TID-7652

Proceedings of the Symposium
on the

Protection Against Radiation Hazards in Space

held in
Gatlinburg, Tennessee
November 5-7, 1962

BOOK 2

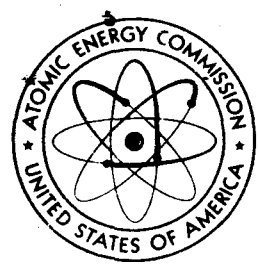

UNITED STATES ATOMIC ENERGY COMMISSION
Division of Technical Information

Code 3

LEGAL NOTICE

This report has been reproduced directly from the best available copy.

Printed in USA. This document consists of 2 books, total price $7.00. Available from the Office of Technical Services, Department of Commerce, Washington 25, D. C.

USAEC Division of Technical Information Extension, Oak Ridge, Tennessee

BOOK 2

Paper D-2

MEASUREMENTS OF SECONDARY SPECTRA FROM HIGH-ENERGY NUCLEAR REACTIONS

Karl Strauch, Harvard University

Abstract

The mechanism of the interaction of a high energy nucleon with a complex nucleus is discussed, and the various types of reaction are described. The available experimental data on secondary particles is summarized, emphasis being placed on those secondaries that might be important for shielding considerations.

Introduction

A beam of high energy neutrons passing through matter is attenuated by inelastic collisions with nuclei present in the material. A beam of high energy charged particles such as protons is attenuated by the same mechanism and in addition the proton kinetic energy decreases as the beam penetrates the material due to collisions with atomic electrons. The higher the energy of a proton, the more important is the role of nuclear collisions before the proton has reached the end of its range: about 15 percent of the protons in a 150 Mev beam will suffer an inelastic nuclear collision before stopping.

Inelastic nuclear collisions result in a variety of secondary particles with complicated energy and angular distributions. This paper uses the existing data to discuss and summarize as far as it is possible the properties of the secondary particles emitted when a high energy neutron or proton interacts with a complex nucleus. The role of secondaries must be considered in the design of shielding for space probes and capsules.

For the purpose of this paper the "high-energy" region is taken to extend from about 80 Mev to 500 Mev. Nucleons with energies higher than this limit do not appear to be present in space in sufficient number to be of importance in shielding considerations[1]. For the sake of completeness these limits will not always be used rigidly.

The probability of inelastic nuclear collisions is measured by the absorption cross section. Measurements of this cross section with both protons and neutrons exist for a variety of elements in the energy region of interest[2-5]. We will be concerned with what happens when an incident nucleon interacts with a nucleus. The general properties of secondary particles expected on the basis of the high energy reaction model will be considered first. Experimental results will then be discussed. The most recent measurements will be stressed; references to older measurements can usually be found in the more recent reports.

Reaction Mechanism

The mechanism of high energy reactions is dominated by two important facts: (1) The de Broglie wave length of the incident nucleon is small compared to the typical distance between nucleons inside the target nucleus. (2) The mean free path in nuclear matter of a high energy nucleon is of the order of the diameter of a light nucleus. The incident nucleon can thus be localized within the target nucleus, and its progress across it described by one or more nucleon-nucleon collisions inside the target nucleus.

A nucleus is a very complex system - various so called "models" exist to describe particular features of the system. The individual particle model which we will find most useful is illustrated in figure 1a. Nucleons exist in definite energy levels inside a potential well of depth V. These nucleons are not at rest, but continuously move around the well - the detailed features of this motion are characteristic of the quantum numbers describing the individual levels. The highest occupied level corresponds to a binding energy B. E. A particle of kinetic energy T_i has, after penetration inside the nucleus, a kinetic energy $T_i + V$.

[1] See papers presented in session A of this conference.

[2] R. Goloskie and K. Strauch, Nucl. Phys. 29, 474 (1962).

[3] A. F. Kirschbaum, University of California, Lawrence Radiation Laboratory report No. 1967 (1954).

[4] R. G. P. Voss and R. Wilson, Proc. Phys. Soc. 236, 41 (1956)

[5] W. P. Ball, Univ. of Calif. Lawrence Radiation Lab, report 1938 (1952).

Let us now consider the first nucleon-nucleon collision as the incident nucleon passes through the nucleus. The incident nucleon has a kinetic energy $T_i + V$ and the target nucleon has a typical momentum probability distribution which corresponds to kinetic energy values smaller than V. If during the collision the momentum transferred to the target nucleon is of the same order or smaller than typical momentum values before the collision, then the final state of the target nucleon is determined by the structure of the residual nucleus. For instance, the nucleon-nucleon collision can raise the target nucleon to an unoccupied excited level. If the incident nucleon leaves without further collision, it emerges, neglecting nuclear recoil, with a kinetic energy $T_i - E_{exc}$. The excited nucleus will return to its ground state usually emitting one or more photons with a combined energy of E_{exc}. This is called a "near-elastic" collision (figure 1b). More complicated excitations of nuclear substructures such as alpha particles or of the nucleus as a whole can also occur.

If the target nucleon receives a momentum which is large compared to typical nucleon moments inside a nucleus, then the effect of the residual nucleus on the final states is small. The collision is similar to a free nucleon-nucleon collision - only the target nucleon has an initial momentum distribution and the binding energy B.E. has to be supplied to the nucleus. If both partners have no further inelastic interactions before leaving the nucleus, they will emergy with energies of roughly $(T_i - B.E.) \cos^2 \theta$ and $(T_i - B.E.) \sin^2 \theta$ respectively where θ is the scattering angle of the incident particle. The residual nucleus can be left in an excited state which will usually decay into the ground state by emission of one or more photons. The name customarily given to this process is "quasi-elastic" collision (figure 1b).

These two simple interactions demanded that only one interaction takes place: this is fairly probably in light nuclei as long as the emerging nucleons have kinetic energies of more than 80 Mev or so. The value of the free nucleon-nucleon cross section increases rapidly below this energy as shown in figure 2[6]. Consequently the nucleon mean free path in nuclear matter decreases rapidly below 80 Mev.

In the more common case two or more collisions take place inside the nucleus and a nuclear cascade is initiated. The energy concentrated in any one nucleon decreases as the cascade progresses until all the energy which has not escaped as intermediate energy secondaries is fairly evenly distributed; the nucleon then "boils-off" this energy by emitting protons and more often neutrons in the Mev energy region. These are the "multiple collision" interactions (figure 1b).

The secondary particle spectrum that results from these processes is sketched in figure 3. Close to the elastic peak at T_{inc} are the near-elastic peaks which correspond to the level structure of the target nucleus. A fairly prominent peak at about (T_{inc} - 20 Mev) corresponds to the excitation of the dipole resonant state first observed in photoproduction. A quasi-elastic peak exists at (T_{inc} - B. E.) $\cos^2\theta$ whose width is determined by the momentum distribution of the target nucleons. The lower energy peaks ride on a rising continuum of cascade particles. Finally a low energy peak due to boil-off particles exists at about 2 Mev for neutrons or at the coulomb barrier energy if they are protons. It must be emphasized that figure 3 is presented mainly as a summary of the possible features of secondary particle spectra in high energy reactions. The relative importance of the near-elastic peaks, the quasi-elastic broad peak, the multiple collision continuum and of the boil-off peak depends strongly on the energy of the incident nucleon and the atomic number of the target nucleus. Some or all of the features sketched on figure 3 are expected for both proton or neutron secondaries with proton or neutron primaries - only the presence of the elastic peak depends on whether or not the secondary spectrum is of the same type as the incident particle.

It must also be remembered that the observation of some or all of the expected peaks in figure 3 depends critically on the experimental energy resolution.

As far as angular distribution of secondary particles is concerned, the reaction model which has been discussed suggests the following:

1. The "near-elastic" events have a strong forward peak similar to elastic scattering. Actually there might well be a dip in the extreme forward direction because of angular momentum considerations for a given excited level.

2. The "quasi-elastic" events have a distribution closely related to free nucleon-nucleon collision angular distributions in the laboratory frame.

3. Cascade particles have a general forward emission, the more pronounced the higher their energy.

4. The low energy boil-off particles are emitted isotropically.

Experimental Data

It is difficult to make detailed predictions using the reaction model discussed in the preceeding section. Phenomenological constants such as nuclear shape, well depth and mean free path must be used[7]. Those features of the secondary particles that depend on specific properties of the target or residual nucleus are especially hard to calculate. Experimental results are therefore necessary to check the validity of the general feature of the reaction model and the detailed theoretical predictions.

Low energy secondary particles will be considered first. Using 160 Mev protons, Fox and Ramsey[8] have obtained proton spectra from 5 - 23 Mev at 60°, 90° and 120° with Zn, Sn, Ta and Pb targets. Figures 4 and 5 show their results with Zn and Pb. Protons with an energy below 10 Mev are emitted isotropically, and the Coulomb barrier inhibits their emission as the target becomes heavier. Gross[9] has used 190 Mev protons to study neutron spectra from 0.5 - 12 Mev at 45°, 90° and 135° emitted by C, Al, Ni, Ag, Au and U targets. Figure 6 shows his results with U: the spectrum has the typical evaporation characteristics and appears to be isotropic - as are the spectra from the other targets. Neutron spectra at 180° have also been obtained earlier with 157 Mev protons incident on C and W targets[10]. The absolute neutron yields obtained in these experiments will be discussed below. Comprehensive studies of photons emitted in high energy nuclear reactions have become available only recently[11-13]. Using 150 Mev protons from the Harwell cyclotron, gamma ray spectra up to 7 Mev have been obtained from a variety of targets from Li to S. Absolute cross sections are also reported and will be discussed below. It is interesting to note that most of the observed gamma-rays can be identified with residual nuclei that can be reached by near-elastic or quasi-elastic collisions.

[7]See for instance paper of H. W. Bertini presented at this session.

[8]R. Fox and N. F. Ramsey, Phys. Rev. 125, 1609 (1962).

[9]E. E. Gross, University of California, Lawrence Radiation Laboratory reports No. 3330 and 3337 (1956).

[10]D. M. Skyrme and W. S. C. Williams, Phil Mag. 42, 1187 (1951).

[11]K. J. Foley, A. B. Clegg and G. L. Salmon, Nucl. Phys. 37, 23 (1962).

[12]K. J. Foley, G. L. Salmon and A. B. Clegg, Nucl. Phys. 31, 43 (1962).

[13]A. B. Clegg, K. J. Foley, G. L. Salmon and R. E. Segel, Proc. Phys. Soc. 78, 681 (1961).

Figure 7 shows the absolute yield measurements as a function of the atomic weight of the target; As checked roughly experimentally, the angular distributions of low energy secondaries are isotropic. This fact was used in calculating the absolute yields. For comparison, a plot of proton inelastic cross sections at 133 Mev[2] is also included. We see that for heavy elements the low energy neutron yield per measured collision rises to 9 - the low energy proton yield is very small. For atomic weights of 30 - 40 mass units, the yield of neutrons, protons and photons per inelastic collision is about 2, 0.8 and 0.5 respectively. These numbers can only be considered as guides - absolute cross sections, especially for neutrons and gamma rays, are hard to obtain accurately. As can be seen by comparing the 190 Mev and 157 Mev neutron yields - it seems unlikely that the differences can be accounted entirely by the difference in incident energy.

For a given target nucleus, the number of low energy particles per inelastic collision should be proportional to the average energy left in the residual nucleus after the direct cascade has terminated. This average energy can be obtained by Monte Carlo type calculations and it should therefore be possible to extrapolate with fair accuracy the above experimental results to other incident energies.

High and medium energy secondaries will be discussed next. Proton spectra will be considered first. Using 96 Mev protons, secondary protons from 40 - 96 Mev have been observed at 40° from a variety of targets from Li to Bi[14]. Figure 8 shows the C spectrum obtained in this work: besides the elastic and near-elastic peaks, there is a strong continuum. The quasi-elastic peak is too broad or too small in size to have been observed at this energy. Fig. 9 shows the Bi spectrum: the experimental resolution is too poor to resolve the near-elastic peaks and the spectrum is dominated by cascade processes. The near-elastic peaks have been studied extensively by the Upsala group[15-18] using 185 Mev protons

[14] K. Strauch and F. Titus, Phys. Rev. 104, 191 (1956).

[15] H. Tyren and Th. A. J. Maris, Nucl. Phys. 4, 637 (1957).

[16] H. Tyren and Th. A. J. Maris, Nucl. Phys. 6, 82 (1958).

[17] H. Tyren and Th. A. J. Maris, Nucl. Phys. 6, 446 (1958).

[18] H. Tyren and Th. A. J. Maris, Nucl. Phys. 7, 24 (1958).

with a variety of targets from Li to Zn.. These near-elastic secondaries are of great interest for the understanding of nuclear structure. However since they occur in only a small fraction of the total available energy range, these secondaries play a relatively small role in the total yield of secondaries. This can be seen in figure 14 on which the yield of near elastic secondaries as obtained in Upsala can be compared with the inelastic cross section. It is for this reason that near-elastic secondaries will not be considered in more detail.

Secondary proton spectra have been obtained at Berkeley with 330 Mev protons[19,20] and at Dubna with 661 Mev protons[21]. The Berkeley experiments were carried out with Li, C, Al, Cu, Cd and Pb targets, and secondary proton spectra in the energy range 50 Mev - 300 Mev were observed at 40° with all targets, and at 26°, 30° and 60° with some targets. The Dubna work was carried out with Be, C, Cu and U targets, secondary protons in the energy range of about 100 Mev - 600 Mev being observed at angles of 7°, 12.2°, 18°, 24° and 30°. Figures 10 and 11 show the Berkeley results at 40° obtained with a C and Pb target respectively. The general features of these spectra are typical of both the 300 Mev and 661 Mev results. The quasi-elastic peak dominates the secondary spectrum from light elements, while cascade particles are very important in the spectra from heavy elements. The Dubna group estimates from their results that quadi-elastic scattering at 30° varies from $\approx$ 60% to $\approx$ 9% of free nucleon-nucleon scattering when going from Be to U. Note that in both experiments the energy resolution is too poor to observe near-elastic peaks in these spectra.

---

[19]W. N. Hess and B. J. Moyer, Phys. Rev. 101, 337 (1956).

[20]J. B. Cladis, W. N. Hess and B. J. Moyer, Phys. Rev. 87, 425 (1952).

[21]L. S. Azligirey, I. K. Vzozov, V. P. Vrelov, M. G. Mescheryakov, B. S. Neganov, R. M. Ryudin and A. F. Shabudin, Nucl. Phys. 13, 258 (1959).

The Dubna work represents the most comprehensive angular study of proton secondaries from several elements. An angular region from 30° to 70° has been studied at Harvard [22] with 95 Mev protons passing through a carbon target. Figure 12 shows the results. The general forward peaking is apparent, with the higher energy secondaries being more forward peaked.

We now turn to spectra of secondary neutrons of high and intermediate energies. Because these could be obtained with internal cyclotron targets, they were some of the earliest spectra measured at Rochester with 244 Mev protons [23], at Harwell with 171 Mev protons[24] and at Harvard with 95 Mev protons[25]. A variety of targets were used. All of these measurements suffered from poor energy resolution. It might be added that neutron spectra from Be of similar poor energy resolution are scattered throughout the literature for a variety of proton energies in articles reporting experiments done with secondary neutron beams.

The development of time-of-flight methods at Harwell has permitted the observation of neutron spectra with much better energy resolution. Results with 143 Mev protons have been reported for many targets in the forward direction[26]: these show a strong charge exchange quasi-elastic peak whose relative importance decreases as the target atomic weight increases. More recent measurements with still better resolution at 95 Mev[27] show the existence of near-elastic peaks similar to those already observed with protons. The usefulness of this work will increase still further when absolute cross sections are reported, and a wider angular region is covered.

---

[22]K. Strauch and F. Titus, Phys. Rev. 103, 200 (1956).

[23]B. K. Nelson, G. Guernsey and G. Mott, Phys. Rev. 88, 1 (1952).

[24]T. C. Randle, J. M. Cassels, T. G. Pickavance and A. E. Taylor, Phil. Mag. 44, 425 (1953).

[25]J. A. Hofmann and K. Strauch, Phys. Rev. 90, 449 (1953).

[26]P. H. Bowen, G. C. Cox, J. B. Huxtable, J. P. Scanlan, J. J. Thresher and A. Langsford, Nucl. Phys. 30, 475 (1962).

[27]private communication

The measurements of intermediate and high energy secondary protons and neutrons as discussed so far have all been carried out with good angular resolution and over a limited angular region. They are very useful in checking the theoretical secondary spectra calculated with the high energy reaction model. In order to get an idea of the importance of intermediate and high energy secondaries, per inelastic collision, the neutron yield, above 45 Mev obtained with 90 Mev protons[25] have been plotted in figure 13. The results have been smoothly extrapolated to 50° and the corresponding proton yields at 40°[14] serve as a rough check of this extrapolation.

Figure 14 shows that at 90Mev there is about a 20 percent probability per inelastic collision of emitting a neutron above 49 Mev at an angle of less than 50°. It is worth noting that the cross section of near-elastic events at 185 Mev is 5 per cent or less of the absorption cross section in three elements.

Bernardini, Booth and Lindenbaum[28] have measured the number of prongs per visible interaction in emulsion. They obtain the following ratios for Ag - Br with 350 - 400 Mev protons and 300 Mev neutrons: secondary proton $E < 30$ Mev: 3.1; 30 Mev $\leq E < 100$ Mev: 0.42; $E > 100$ Mev: 0.35. These emulsion results represent probably the most reliable information available to date on the number of secondary protons/nucleon interaction.

Since photons are primarily emitted by excited nuclei after particle emission has become impossible, few photons are emitted with energies above typical particle binding energies. Special selection rules can however intervene to produce photons with energies higher than about 7 Mev: one such example is the 15.2 Mev photon emitted by carbon[29].

Only photon, proton and neutron secondaries have been discussed in detail. Deuterons, tritons, helium secondaries also exist, but as shown first by Hadley and York[30] with 90 Mev

---

[28]G. Bernardini, E. T. Booth and S. J. Lindenbaum, Phys. Rev. 85, 826 (1952).

[29]D. Cohen, B. J. Moyer, H. Shaw and C. Waddell, Phys. Rev. 96, 714 (1954).

[30]J. Hadley and H. York, Phys. Rev. 80, 345 (1950).

neutrons, their importance is relatively small. In C the number of deuterons with energies above 27 Mev per inelastic collision was found to be 0.12 and this number decreases with increasing weight of both target and secondary. More recent measurements[31,32] confirm the numerically smaller importance of heavy secondaries. Just as the nearly-elastic protons, heavy secondaries, although small in numbers are of considerable interest for nuclear structure investigations.

Conclusion

For the purpose of investigating nuclear structure, the most interesting events among the secondaries in high energy reactions are those resulting from near elastic and pure quasi-elastic processes. It is somewhat unfortunate for the purpose of this conference that the overall importance of these events is small since most of the recent work has been concentrated on picking out these events. However as has been discussed a considerable number of studies of secondary particle spectra exist and these should permit a satisfactory adjustment of the parameters needed for conventional Monte-Carlo type calculations of high energy reactions. Such calculations can of course not give features such as near-elastic peaks which depend on the detailed properties of the target or residual nucleus.

Many of the cross sections reported in the references were obtained by comparison with then accepted values of the proton-proton cross section or of reaction cross sections such as $C^{12}(p, pn)C^{11}$. The absolute values of some of these cross sections have been improved since the original work was done and when high accuracy is required, the quoted cross sections should be corrected accordingly[33].

The author wishes to thank Mr. H. W. Bertini and Dr. F. C. Maienschein for help in compiling the references.

---

[31] L. E. Bailey, University of California, Lawrence Radiation Laboratory Report 3334.

[32] P. F. Cooper and R. Wilson, Nucl. Phys. 15, 373 (1960).

[33] A recent measurement containing references to others: K. Goebel, D. Harting, J. C. Kluyver, A. Kusunegi and H. Schultes, Nucl. Phys. 24, 28 (1961).

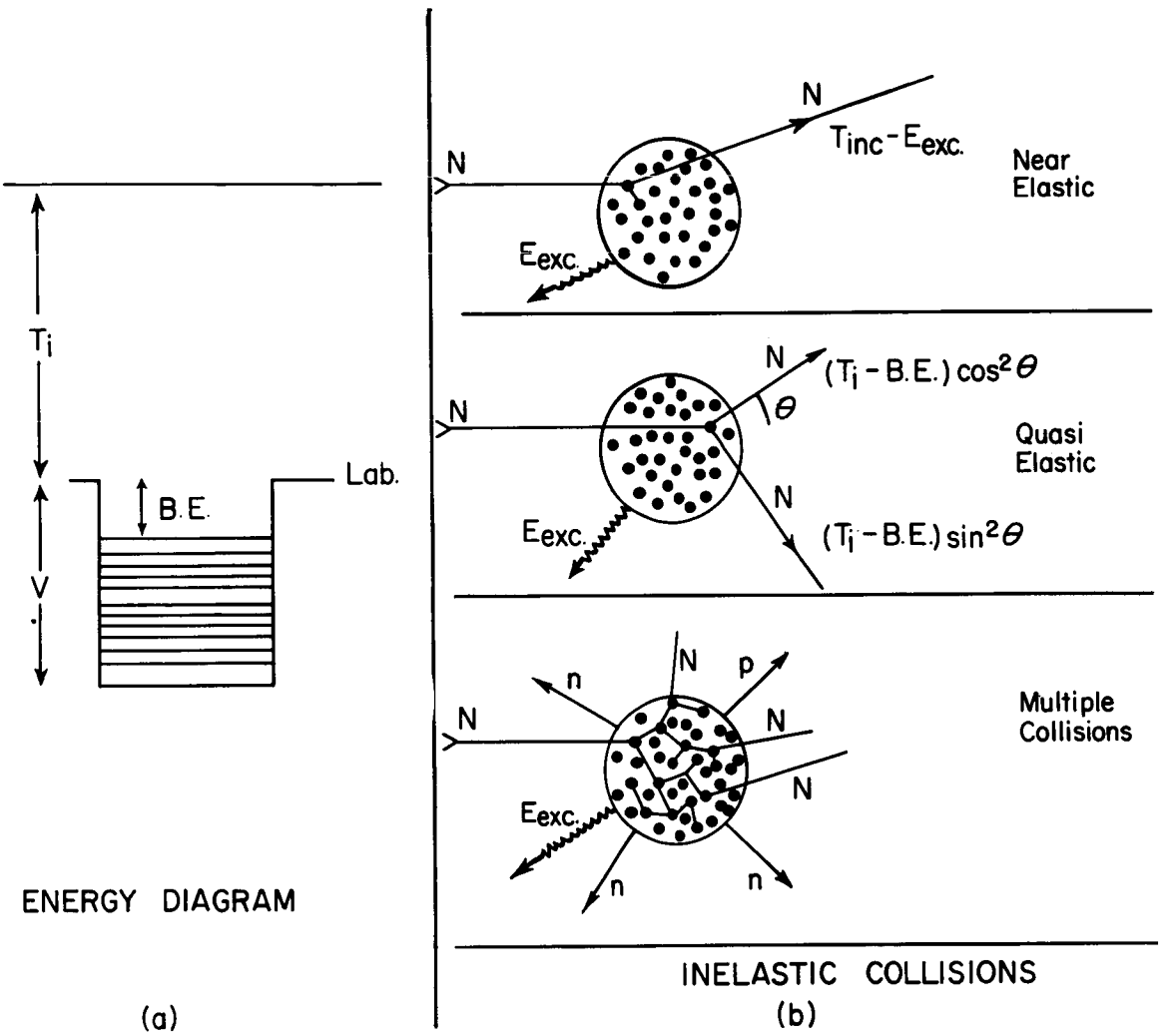

Figure 1a - Schematic representation of a nucleus using single particle model with a square well potential. Only occupied levels are shown.

1b - Schematic diagrams of possible high energy reactions. Secondary particles directly related to the incident particle are indicated by N (nucleon). Boil-off particles are indicated by n (neutron) or p (proton). Photons are represented by accordion lines.

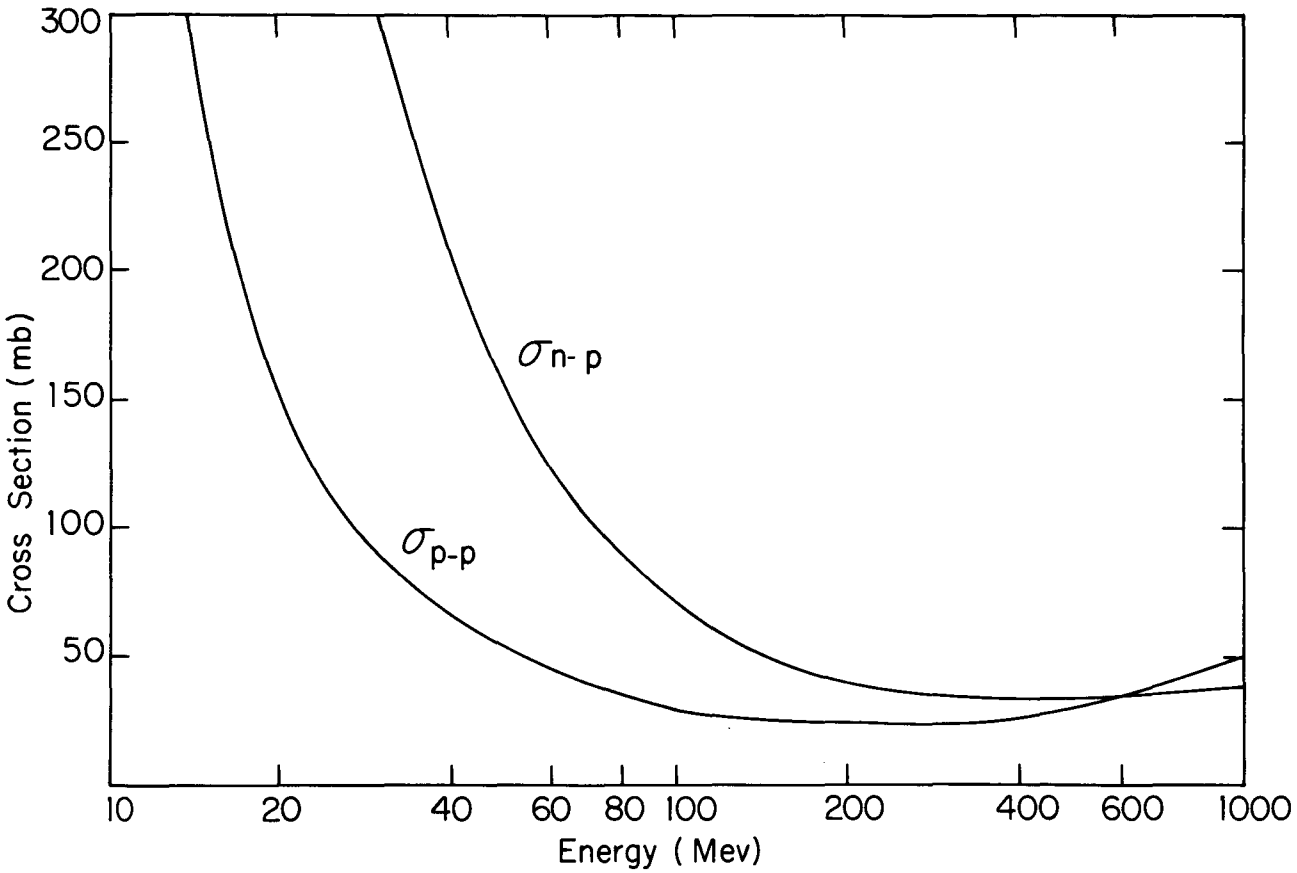

Figure 2 - Free nucleon-nucleon cross sections plotted from the summary of reference 6.

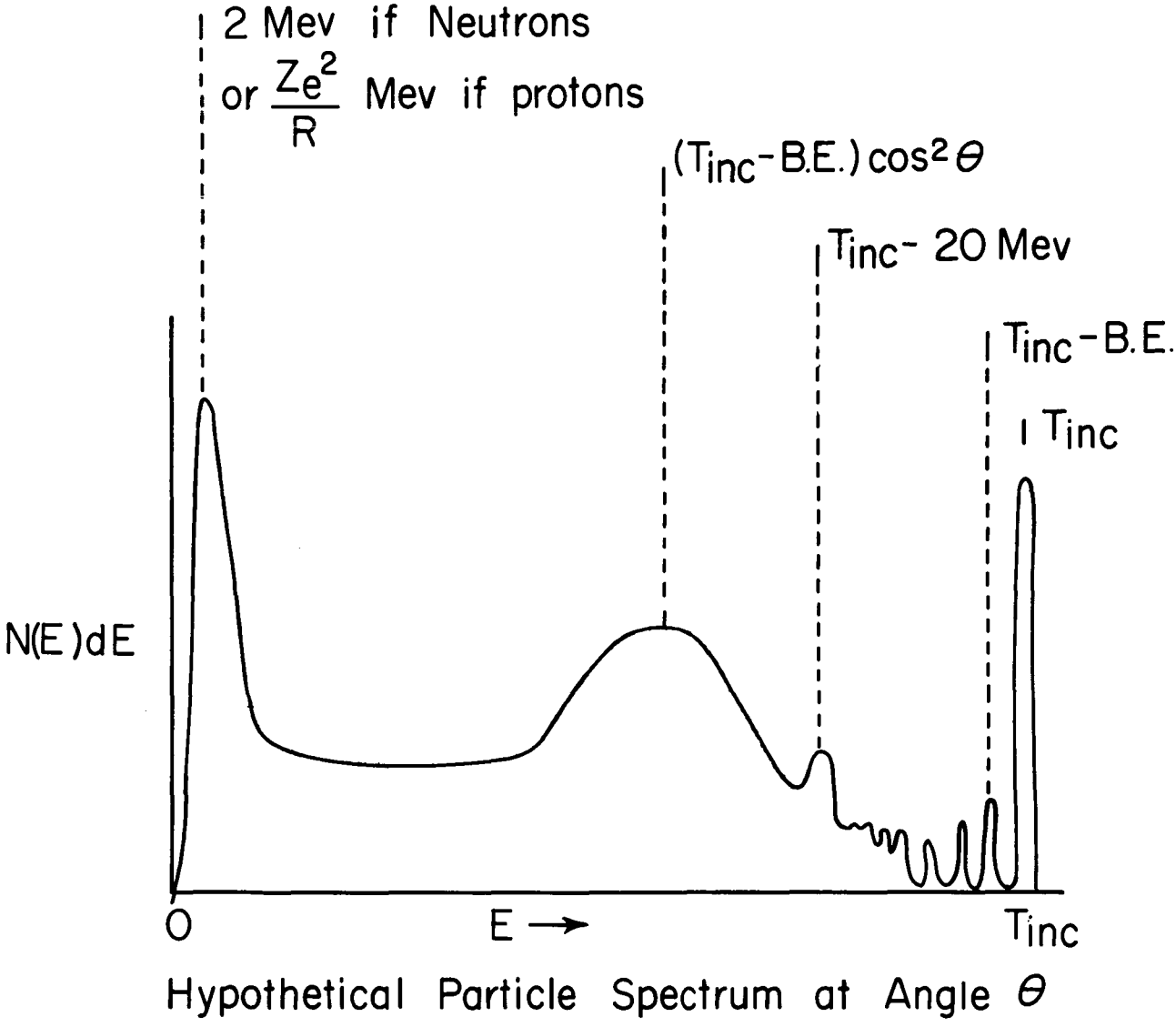

Figure 3 - Hypothetical secondary particle spectrum showing all features that might be expected.

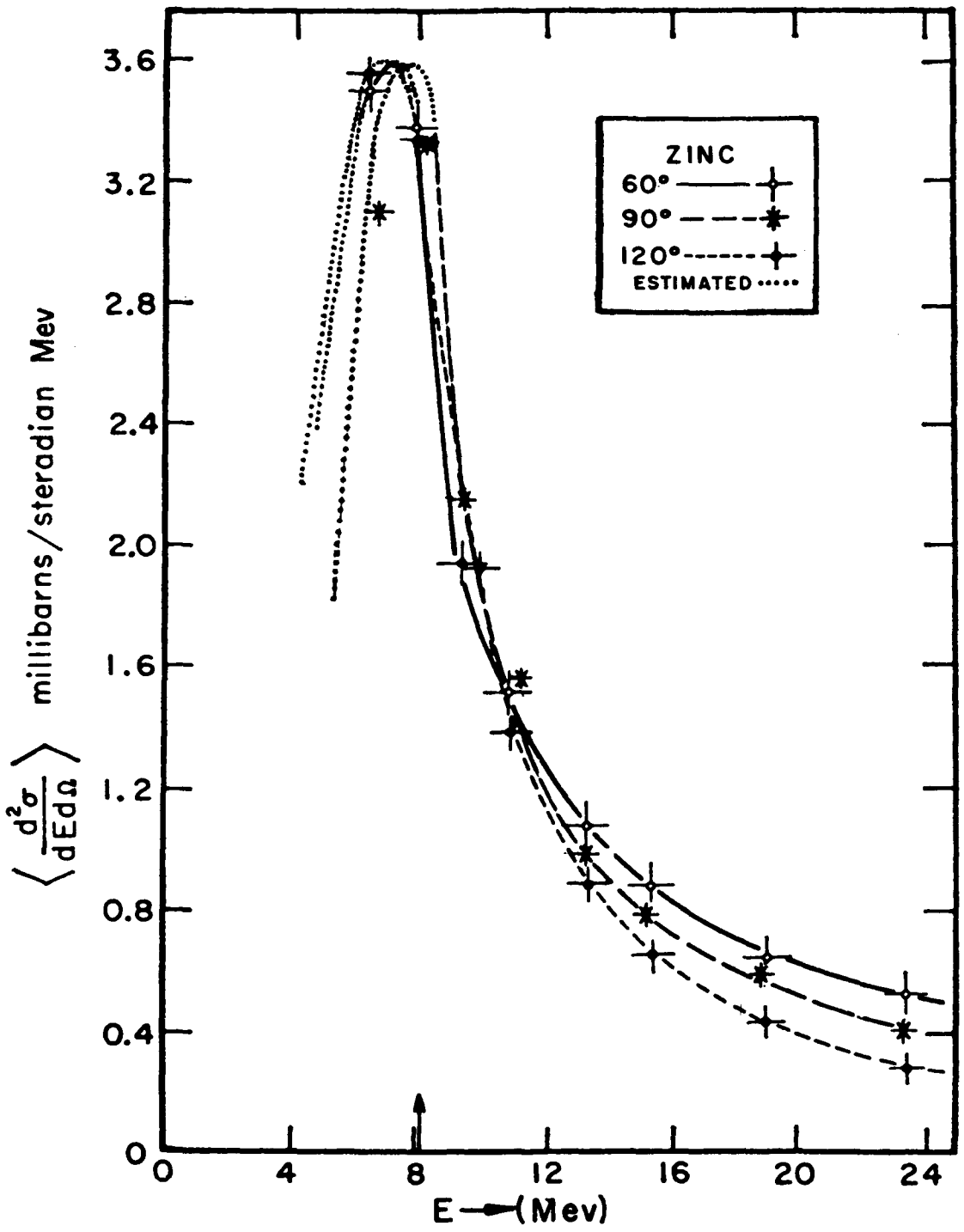

Figure 4 - Spectra of low energy protons emitted by a Zn target bombarded with 160 Mev protons (from reference 8).

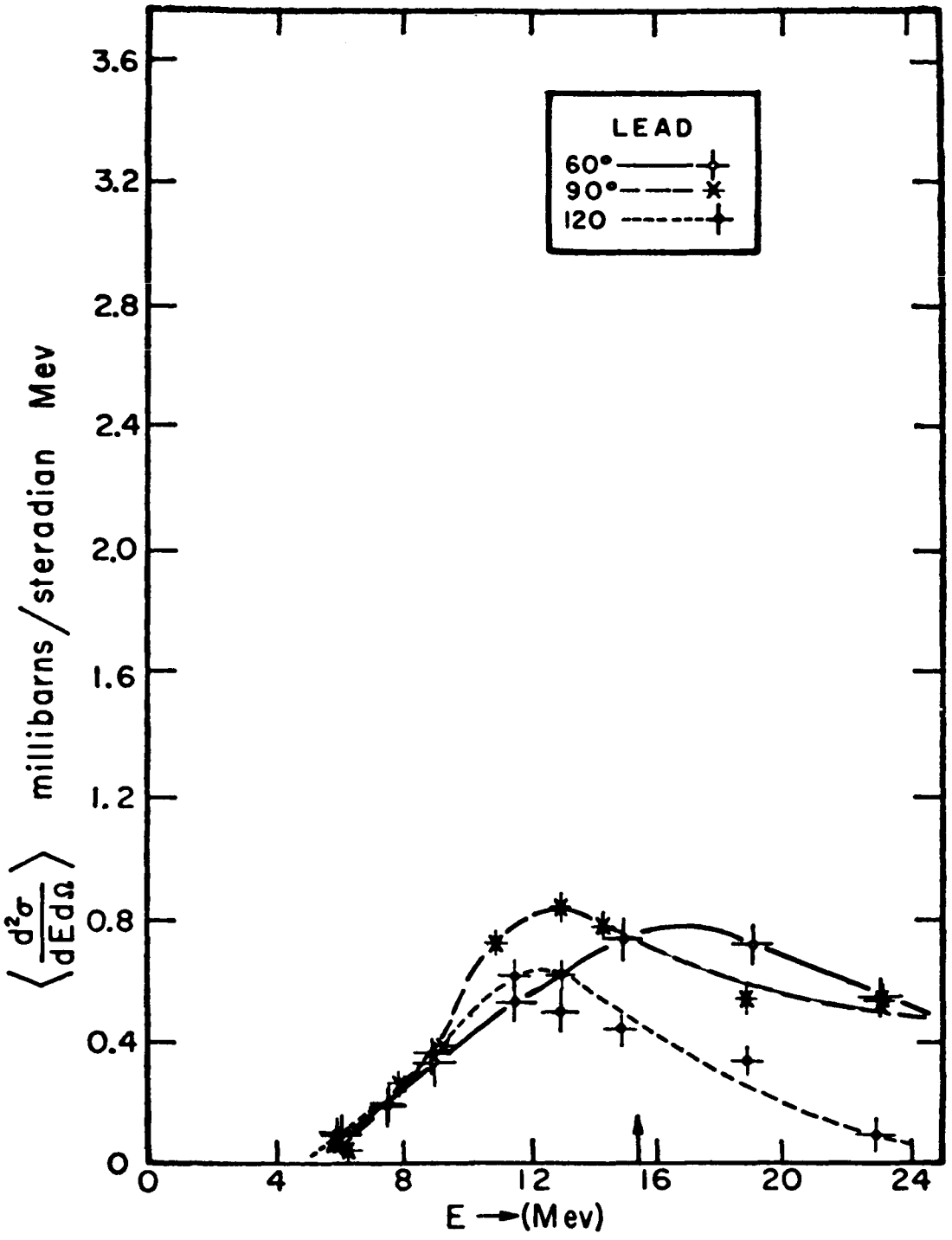

igure 5 - Spectra of low energy protons emitted by a Pb target bombarded with 160 Mev protons (from reference 8).

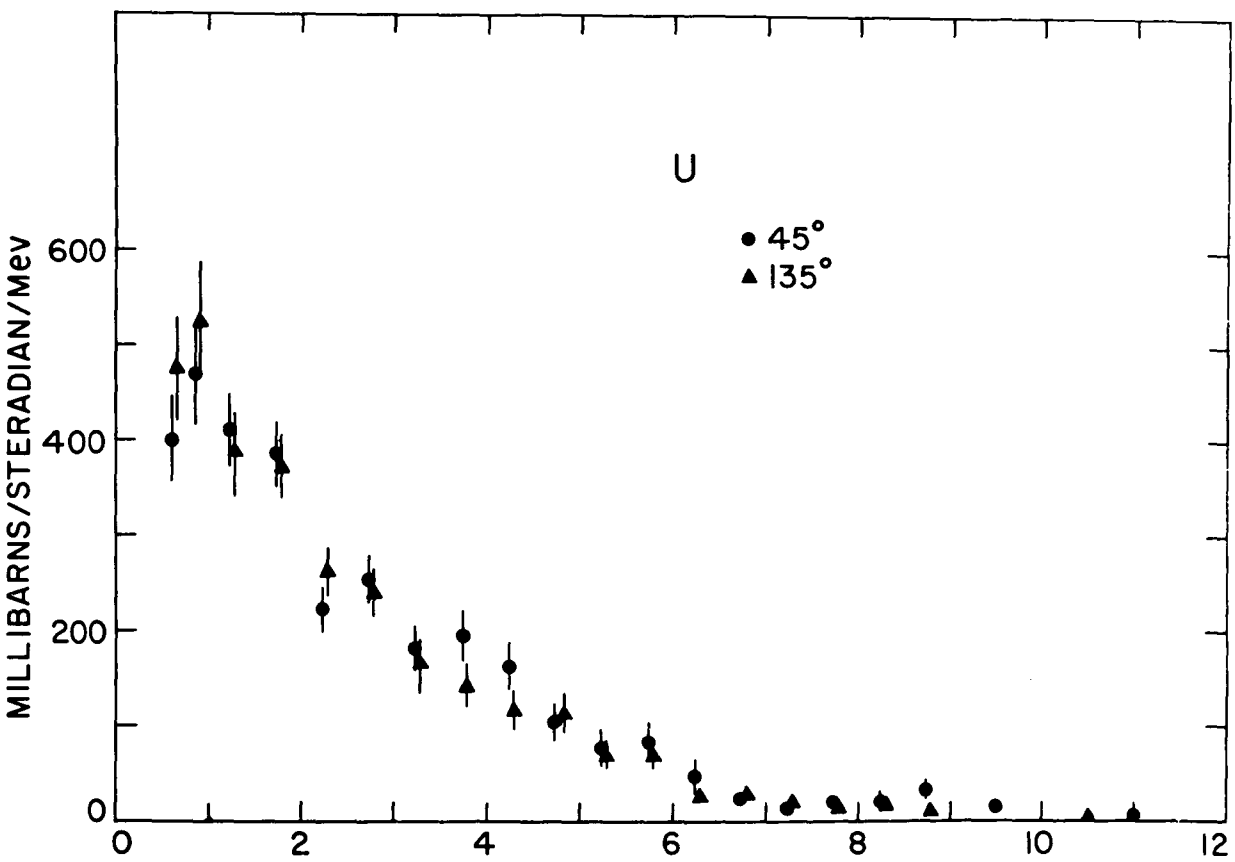

Figure 6 - Spectra of low energy neutrons emitted by an U target bombarded with 180 Mev protons (from reference 9).

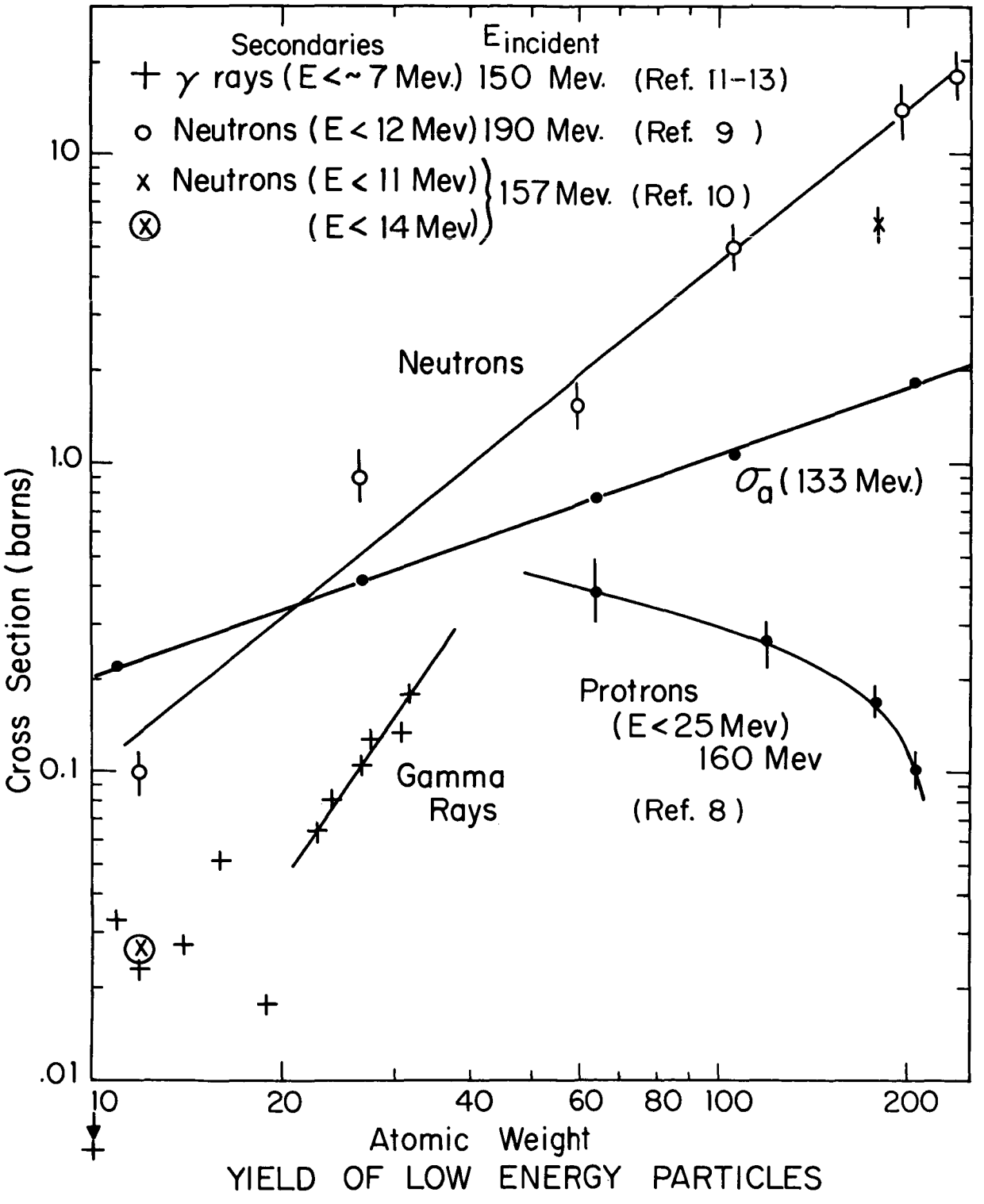

Figure 7 - Yield of low energy secondaries as a function of atomic weight. To guide the eye solid curves have been drawn in region of small scatter.

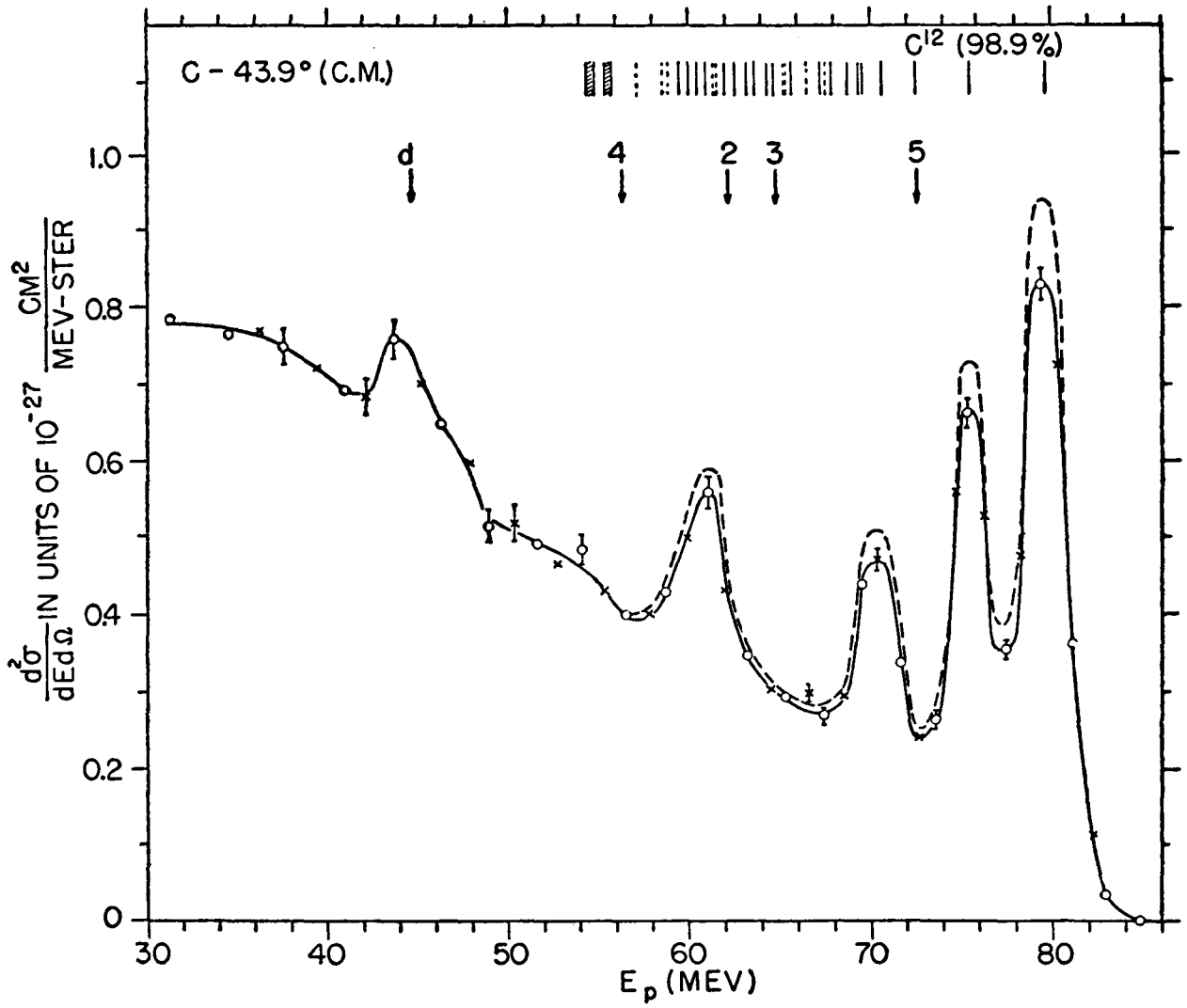

Figure 8 - Proton spectrum observed at 40° from a C target bombarded with 96 Mev protons (from reference 14 where symbols are explained).

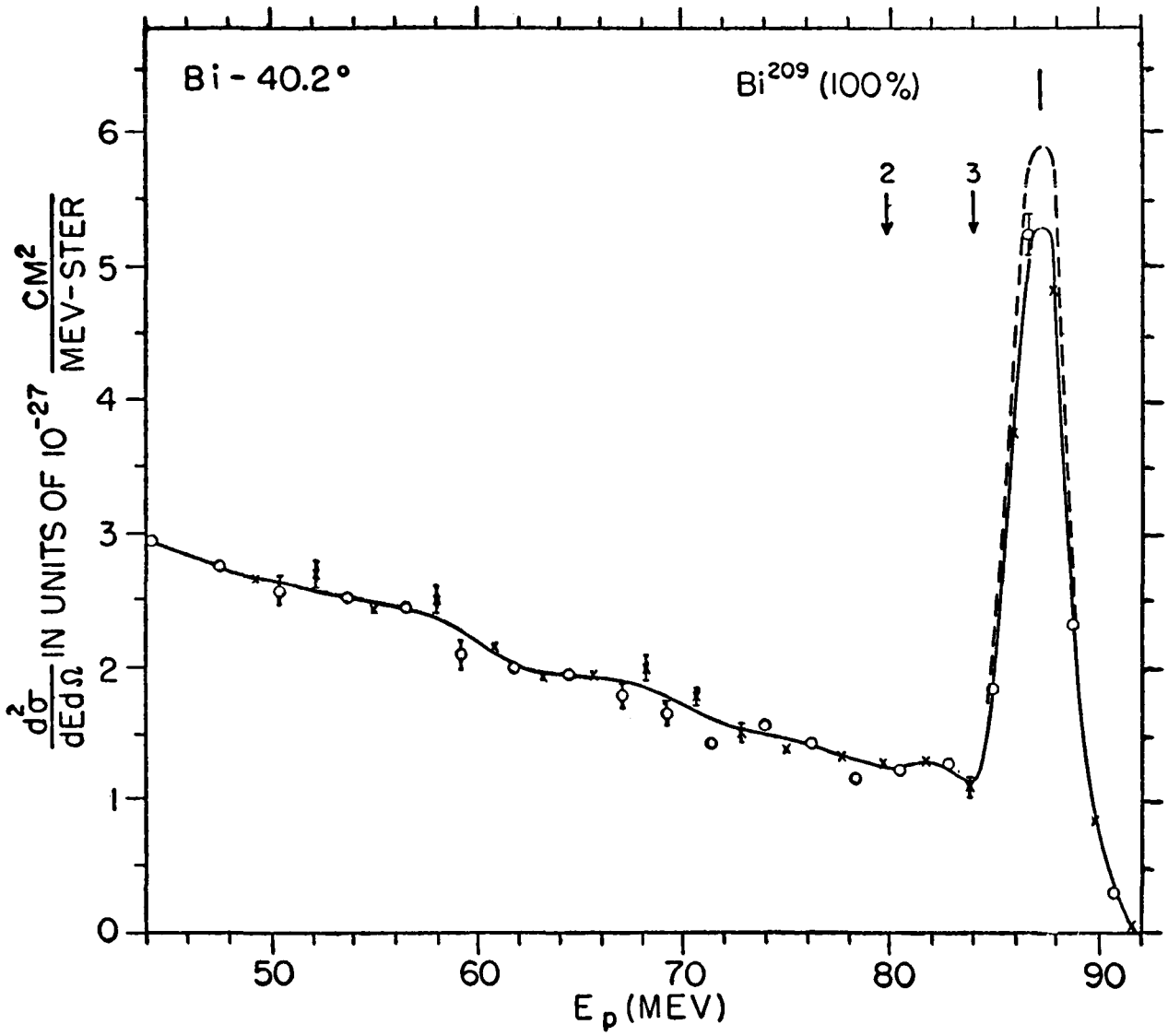

Figure 9 - Proton spectrum observed at 40° from a Bi target bombarded with 96 Mev protons (from reference 14 where symbols are explained).

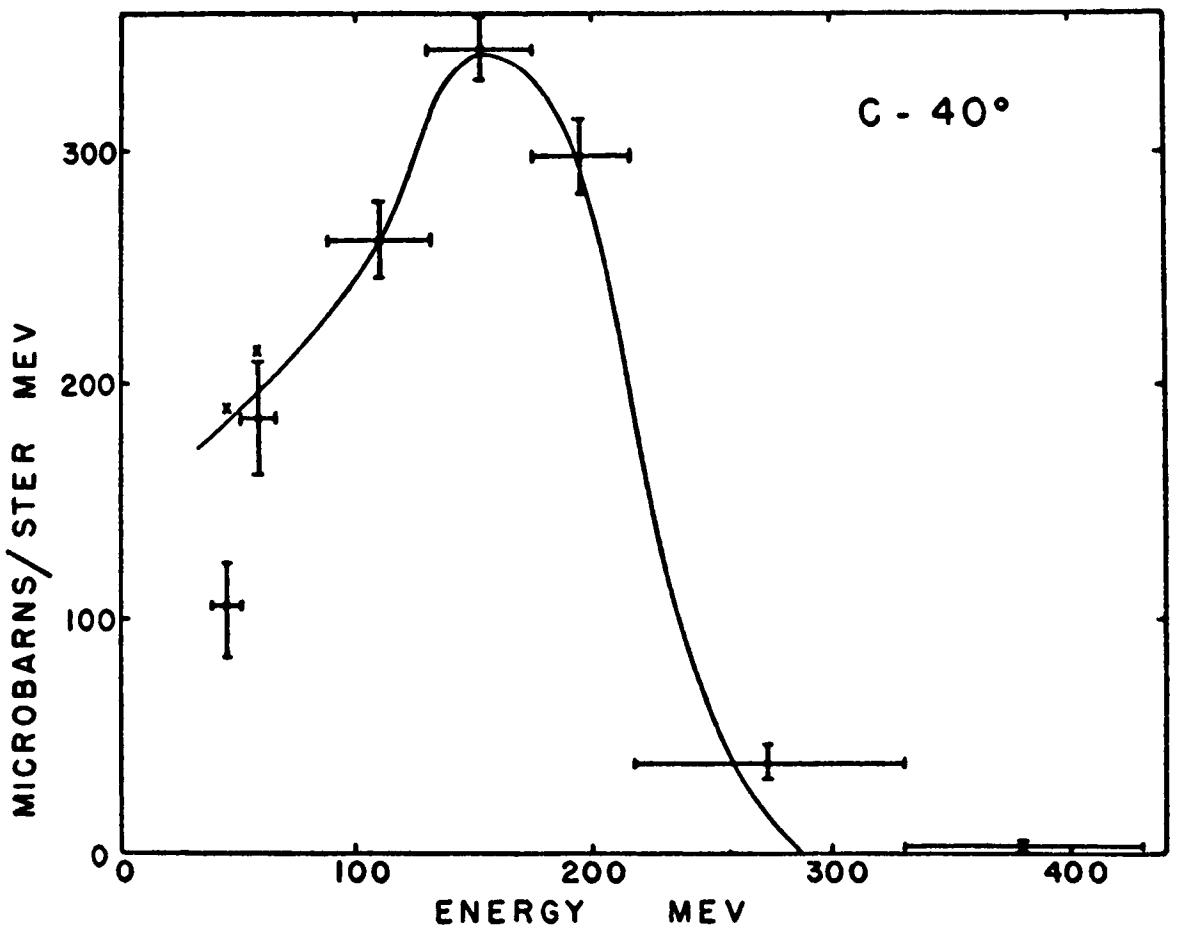

Figure 10 - Proton spectrum observed at 40° from a C target bombarded with 300 Mev protons (from reference 19).

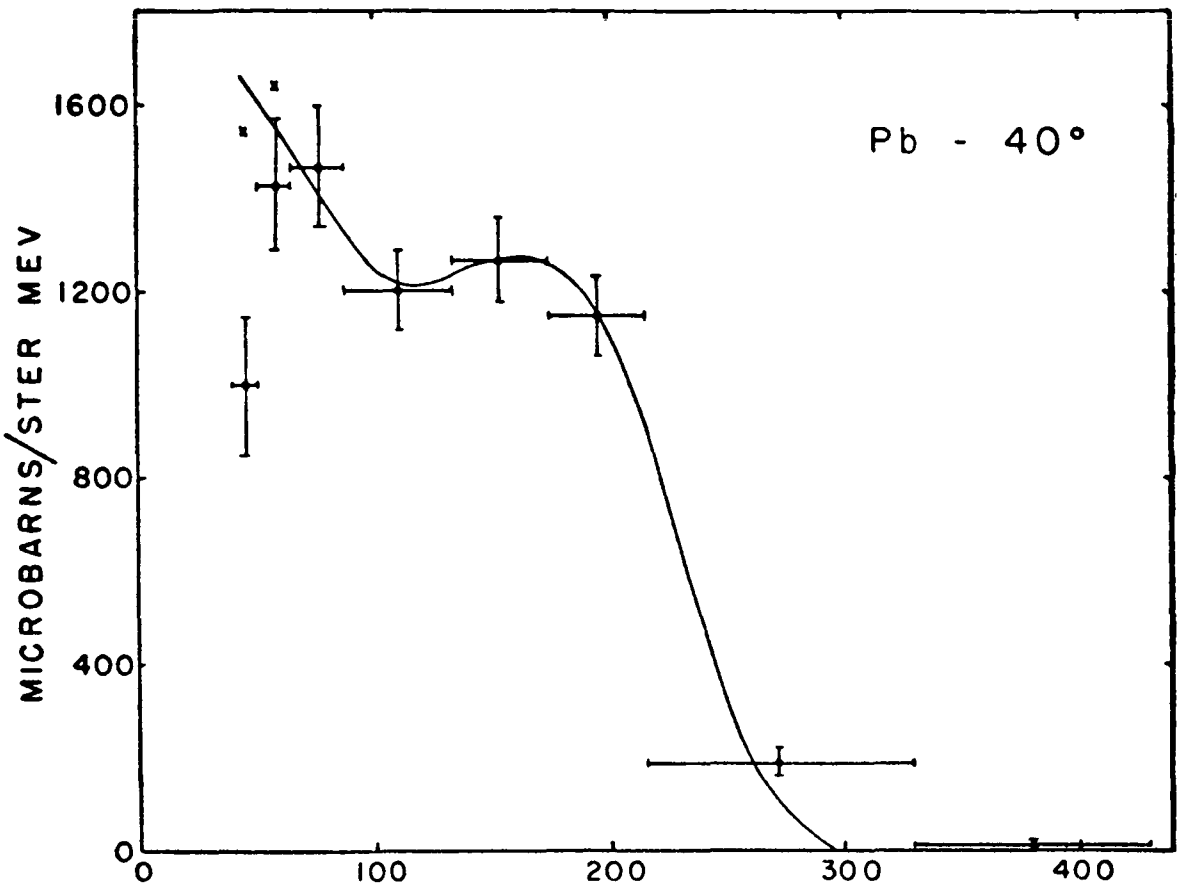

Figure 11 - Proton spectrum observed at 40° from a Pb target bombarded with 300 Mev protons (from reference 19).

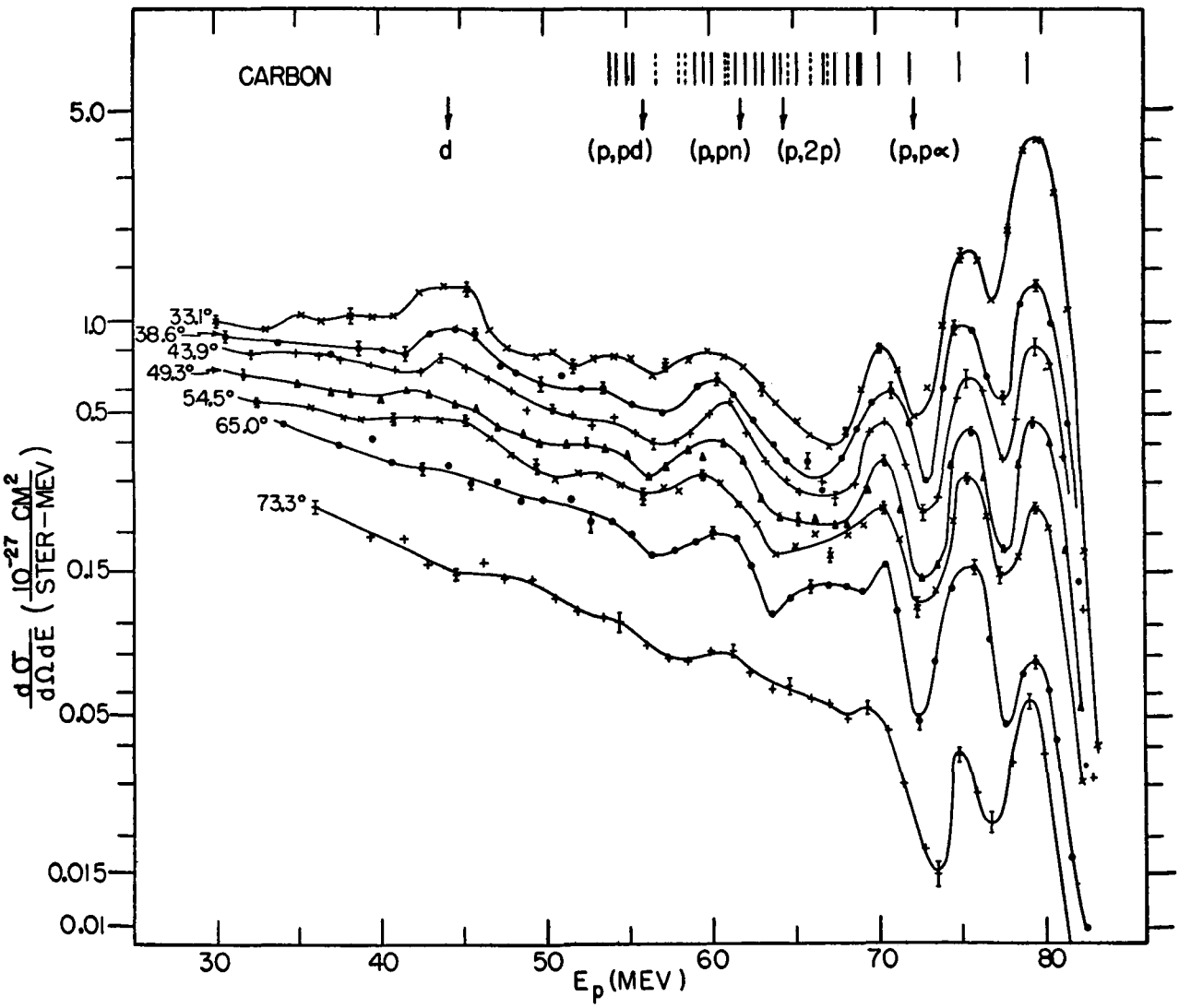

Figure 12 - Energy spectra of protons scattered from a C target bombarded with 95 Mev protons. Energy and angle values are in the p-c center-of-mass system (from reference 22).

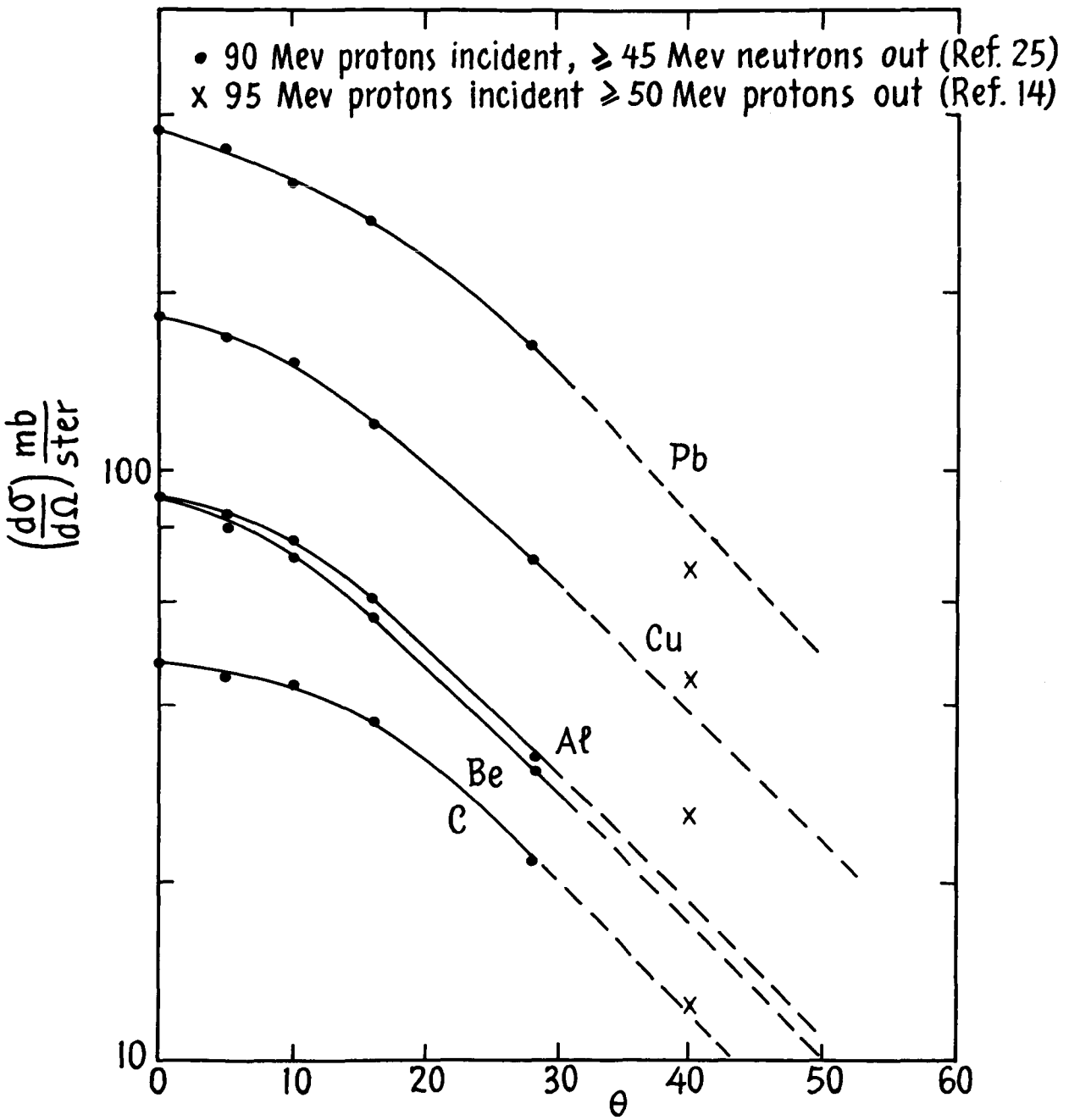

Figure 13 - Angular distribution of high energy secondaries.

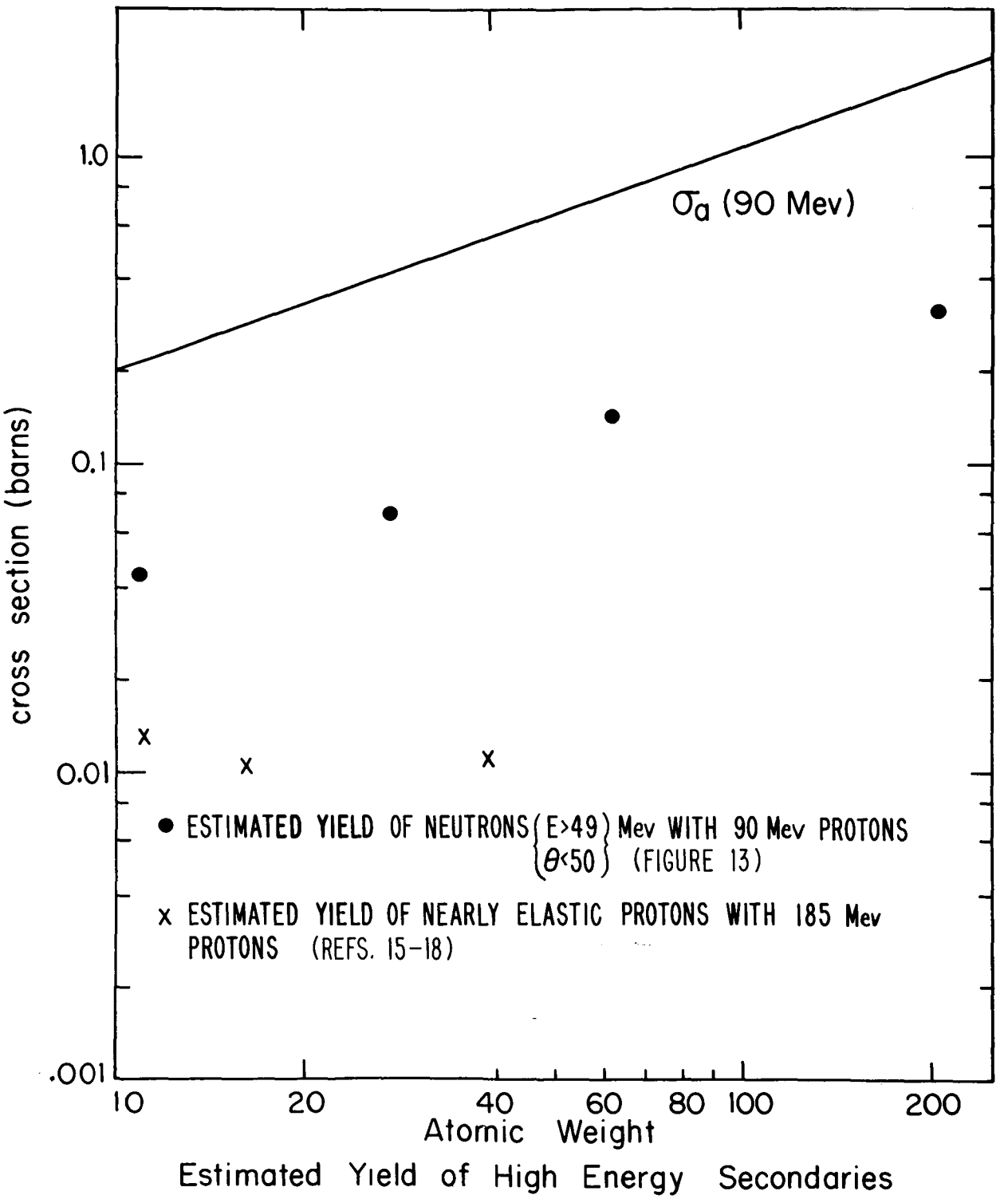

Figure 14 - Estimated yield of high energy secondaries.

Paper D-3

MONTE CARLO CALCULATIONS FOR INTRANUCLEAR CASCADES

H. W. Bertini
Oak Ridge National Laboratory

15140

Abstract

Calculations have been made for nucleons and pions incident on complex nuclei at energies where pion production is not likely (≈ 350 Mev). The interaction with the nucleus as a whole is represented by individual particle-particle collisions within the nucleus where the history of each particle involved in the collision is traced. Extensive comparisons with experiment are made to examine the limits of validity of the model. The effect of a diffuse nuclear edge is examined for certain reactions. It is demonstrated that the model can be used to predict a broad range of experimental results for incident nucleons, whereas the predictions for incident pions are not as reliable as those for nucleons when detailed information is required. It is shown that the bulk of the effects which result when a diffuse nuclear edge is used comes from the increased nuclear dimensions rather than from the edge itself. A compilation of the results for incident nucleons and pions is being prepared, and some preliminary results are presented. The calculation is also being extended to include incident-particle energies up to 2 Gev.

Monte Carlo Calculations on Intranuclear Cascades for Incident-Particle Energies from about 50 to 350 Mev

A code to calculate the reactions of high-energy particles with complex nuclei was described previously.[1,2] The code, which has been written for the IBM-7090 computer and treats incident nucleons and pions on any nucleus greater than helium, is now complete and is being used to obtain a large

1. H. W. Bertini and C. D. Zerby, Neutron Physics Div. Ann. Progr. Rep. Sept. 1, 1960, ORNL-3016, p. 235.

2. H. W. Bertini, Neutron Physics Div. Ann. Progr. Rep. Sept. 1, 1961, ORNL-3193, p. 323.

volume of data which will be illustrated in the next section. This section consists of a brief review of the code and compares some of the calculated results with experimental data.

Nuclear Model and Cross-Section Data

In the nuclear model it is assumed that for incident-particle energies of the order of 50 Mev or higher, the reactions with complex nuclei can be described in terms of particle-particle events that take place inside the nucleus. Each event gives rise to other high-energy particles which in turn make other collisions, and in this way a cascade develops inside the nucleus. These events can be calculated and the history of each particle involved can be traced by using free-particle empirical data and statistical sampling techniques.

The density distribution of nucleons inside the nucleus was made to approximate the continuously varying charge distribution obtained by Hofstadter.[3] This was done by taking three concentric spheres, one nested inside the other with individual uniform densities such that the proton density in each sphere or region corresponded to the average value of the continuous charge distribution over the same region. The region boundaries applied to neutrons as well, and the ratio of the neutron to proton density in each region was taken to be the same as the ratio of the total number of neutrons in the nucleus to the total number of protons. A few calculations were made with a constant nucleon density distribution used throughout the nucleus to determine its effect. These considerations are illustrated in Fig. 1.

In each region the nucleons were assumed to have a zero-temperature Fermi energy distribution. The binding energy of the loosest nucleon was assumed to be constant, 7 Mev, for all regions and all nucleons. The potential for nucleons inside the nucleus was taken to be 7 Mev plus the zero-temperature Fermi energy in each region. This is illustrated in Fig. 2 for a typical case.

The total free-particle cross sections that were used are illustrated in Figs. 3, 4, and 5. The differential cross sections for nucleon-nucleon collisions were taken from the work of Hess,[4] Beretta et al.,[5] and Hughes

---

3. R. Hofstadter, Revs. Modern Phys. 28, 214 (1956).

4. W. N. Hess, Revs. Modern Phys. 30, 368 (1958).

5. L. Beretta, C. Villi, and F. Ferrari, Nuovo Cimento 12, S-499 (1954).

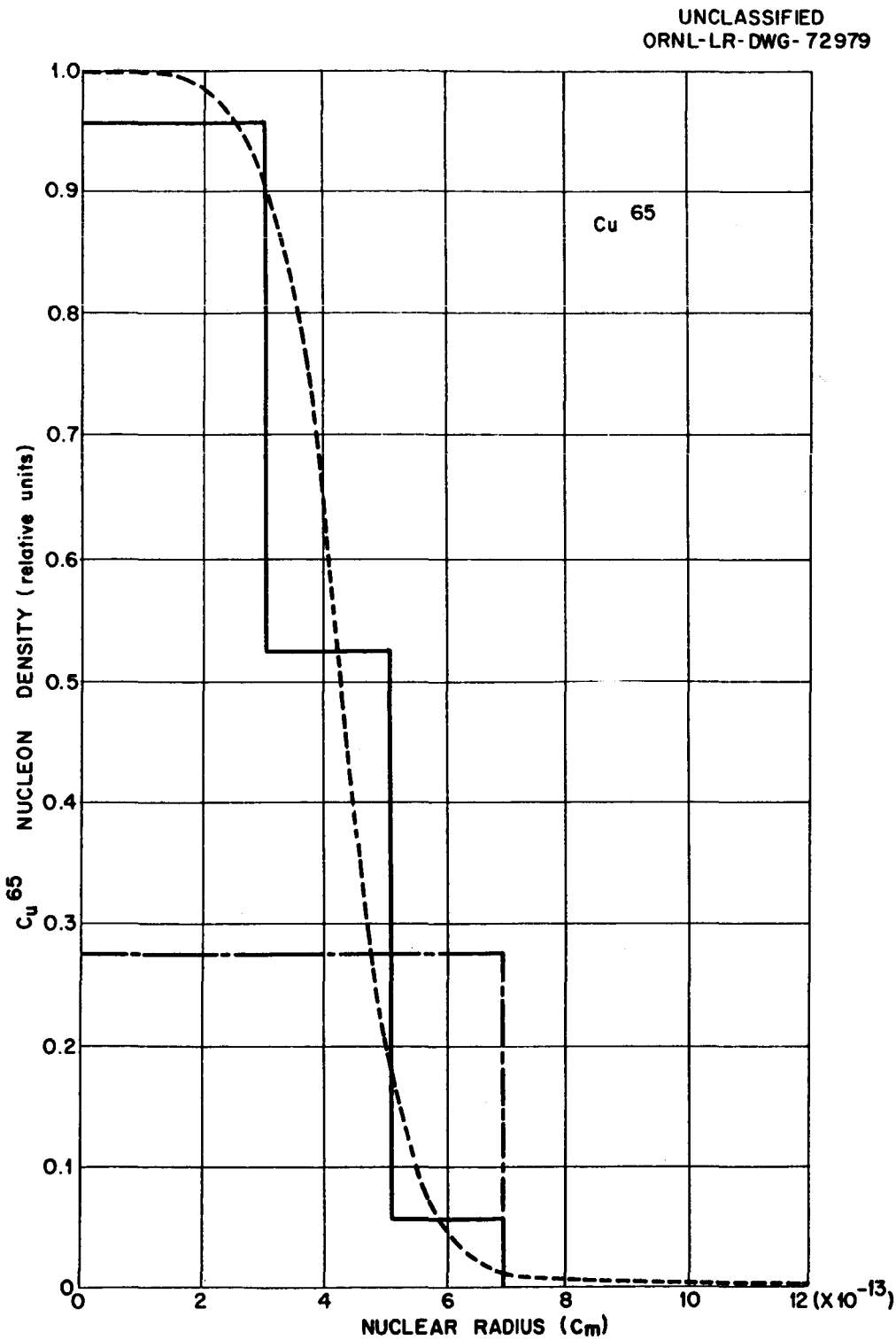

Fig. 1. Nucleon Density Distributions Within the Nucleus. Solid lines: nonuniform distribution; dot-dashed lines: uniform distribution; dotted lines: Hofstadter's curve [Rev. Mod. Phys. 28, 214 (1956)].

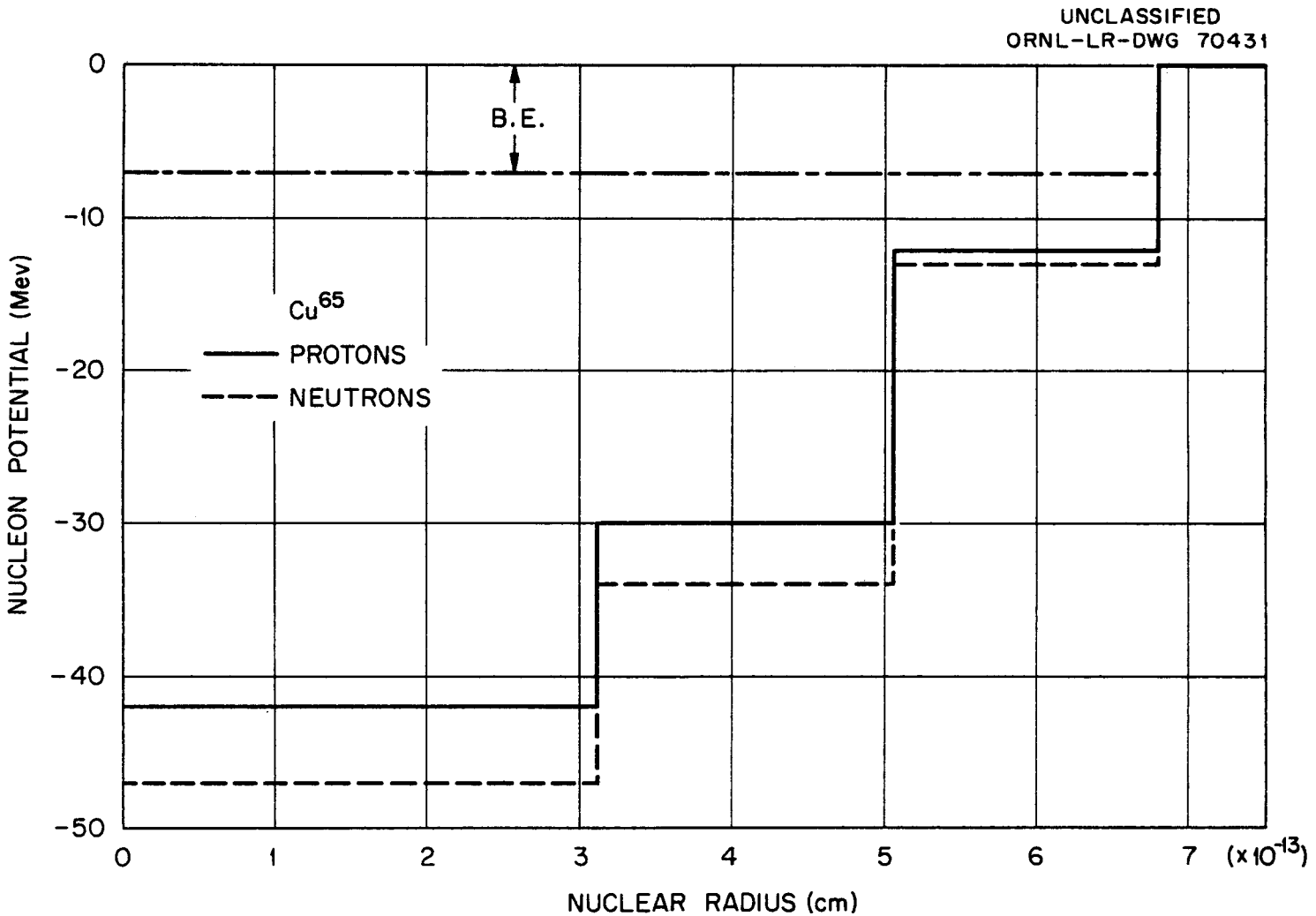

Fig. 2. Nucleon Potential vs Nuclear Radius for a Typical Nucleus. "B. E." is the fixed binding energy of the loosest nucleon.

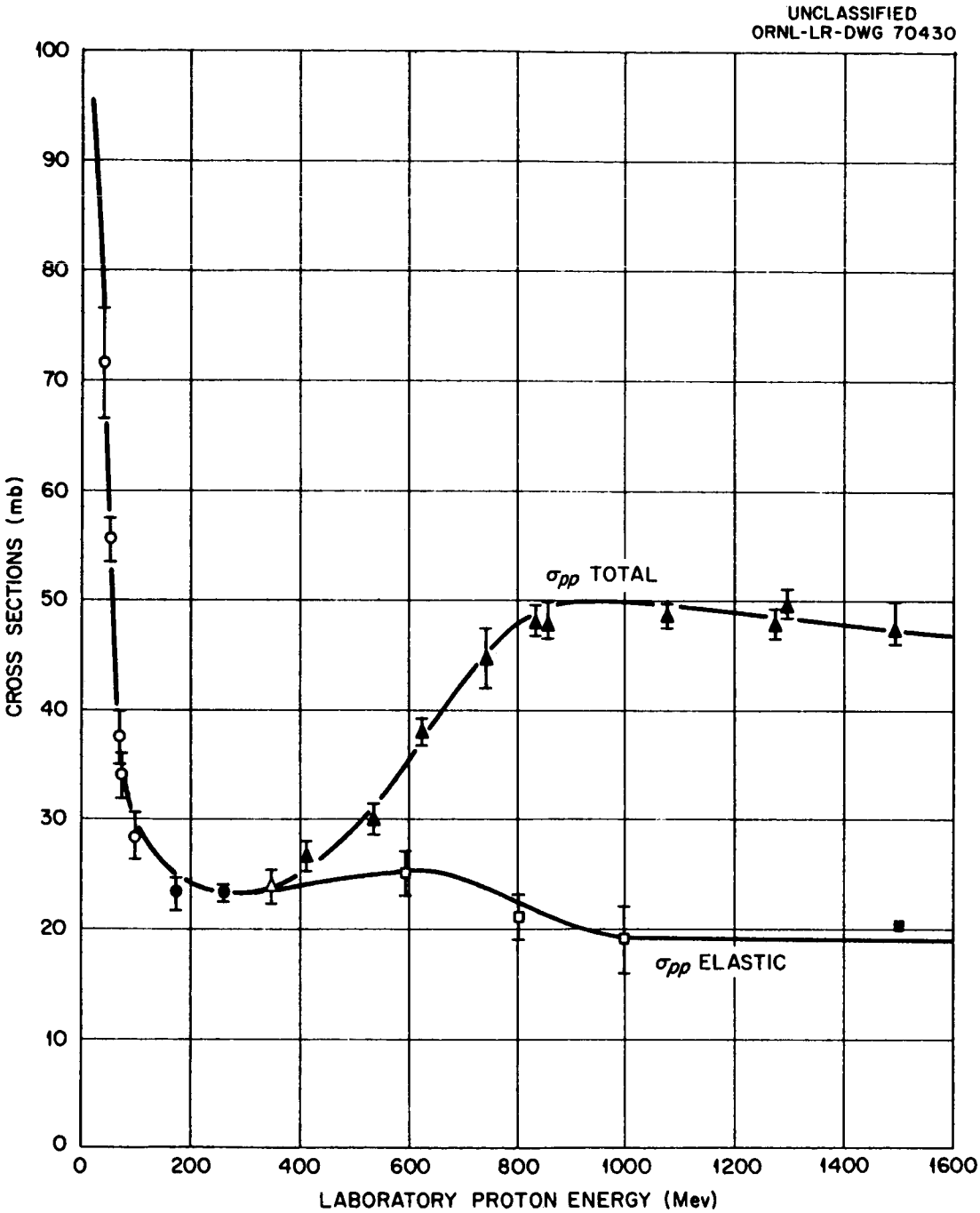

Fig. 3. Proton-Proton Total and Elastic Cross Sections vs Energy. ○ U. E. Kruse, J. M. Teem, and N. F. Ramsey, Phys. Rev. 101, 1079 (1956); ● O. Chamberlain and J. D. Garrison, Phys. Rev. 95, 1349 (L) (1954); △ O. Chamberlain, E. Segrè, and C. Wiegand, Phys. Rev. 83, 923 (1951); ▲ F. F. Chen, C. P. Leavitt, and A. M. Shapiro, Phys. Rev. 103, 211 (1956); □ L. W. Smith, A. W. McReynolds, and G. Snow, Phys. Rev. 97, 1186 (1955); ■ W. B. Fowler et al., Phys. Rev. 103, 1479 (1956).

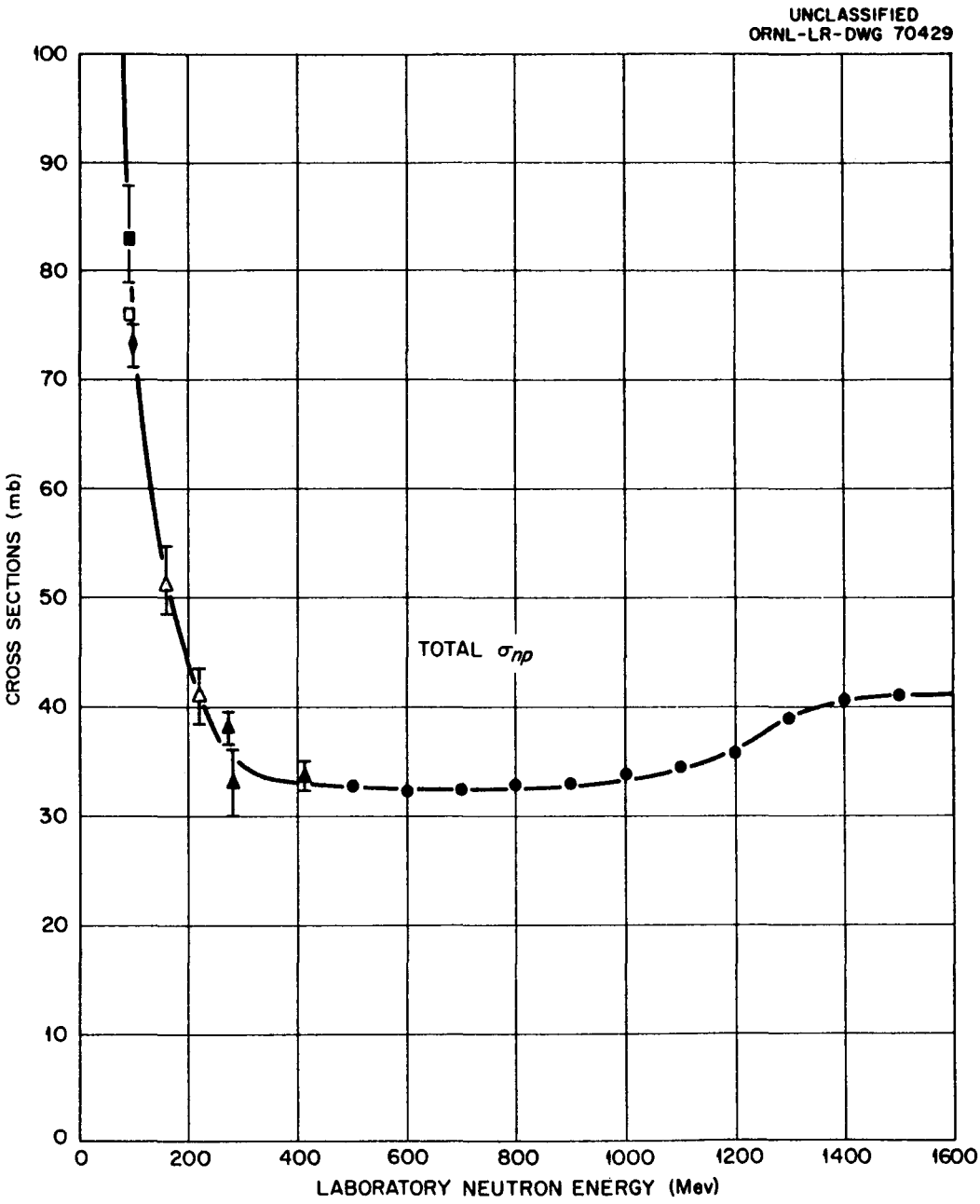

Fig. 4. Neutron-Proton Total Cross Sections vs Energy. ■ L. J. Cook et al., Phys. Rev. 75, 7 (1949); □ J. Hadley et al., Phys. Rev. 75, 351 (1949); ♦ J. DeJuren and N. Knable, Phys. Rev. 77, 606 (1950); △ J. DeJuren and B. J. Moyer, Phys. Rev. 81, 919 (1951); ▲ A. V. Nedzel, Phys. Rev. 94, 174 (1954); ● F. F. Chen, C. P. Leavitt, and A. M. Shapiro, Phys. Rev. 103, 211 (1956).

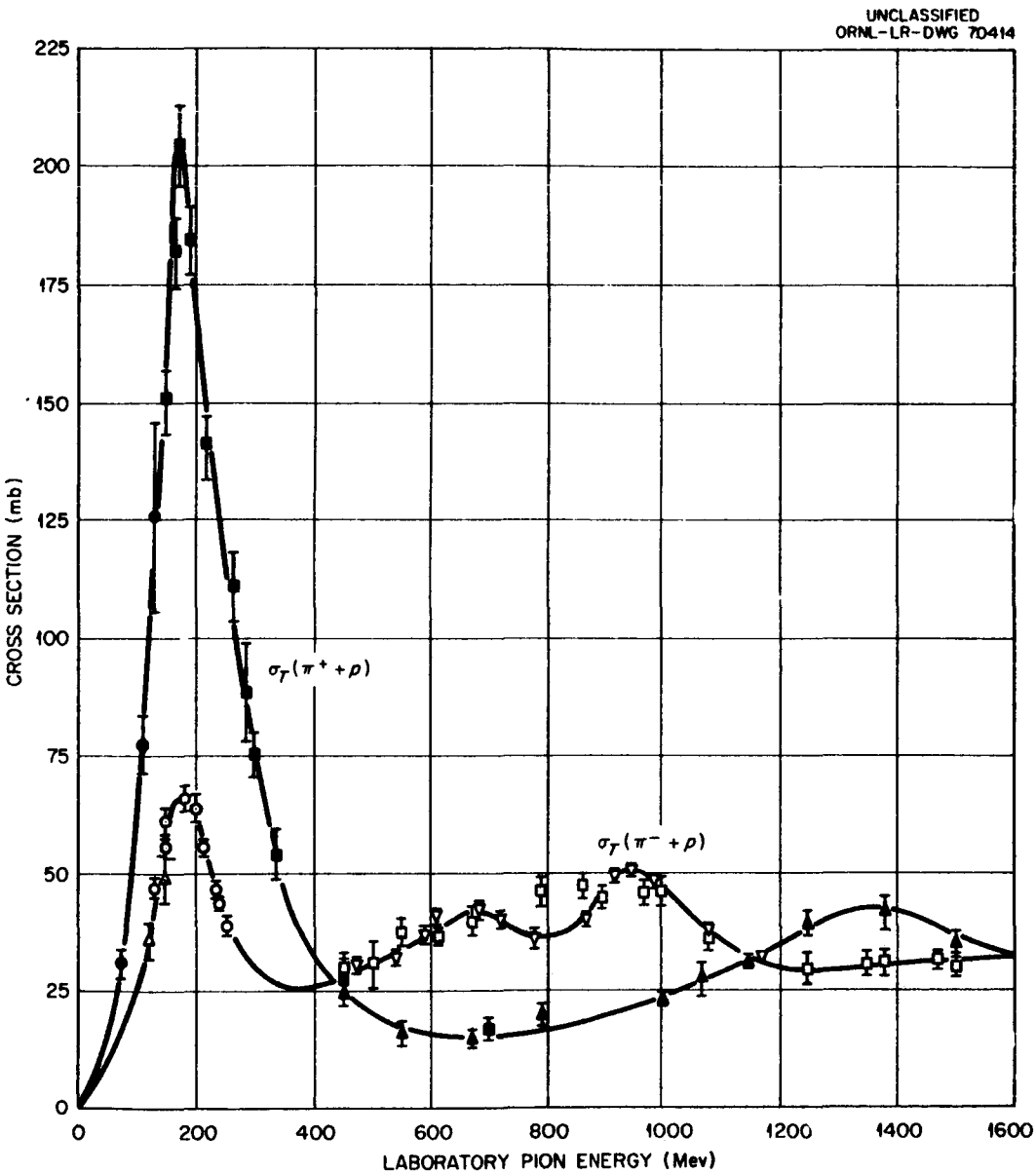

Fig. 5. π^+-Proton and π^--Proton Total Cross Sections vs Energy. ●, △ H. L. Anderson et al., Phys. Rev. 91, 155 (1953); ▣ S. J. Lindenbaum and L. C. L. Yuan, Phys. Rev. 100, 306 (1955); ▲, □ R. Cool, O. Piccioni, and D. Clark, Phys. Rev. 103, 1082 (1956); ○ J. Ashkin et al., Phys. Rev. 96, 1104 (1954); ▽ H. C. Burrowes et al., Phys. Rev. Letters 2, 119 (1959).

Schwartz.[6] The differential cross sections for pion-nucleon collisions were calculated by using the phase shifts of Orear.[7] From the results of these calculations the exchange scattering cross sections and the π^0 cross sections could be deduced with the results given in Fig. 6. The numerical work of Metropolis et al.[8] was used for the pion-absorption cross section. This reaction was assumed to take place with two-particle nucleon clusters inside the nucleus. All the cross-section data were tabulated at every 20-Mev interval.

The basic sampling technique for determining the point of collision, type of collision, and momentum of the struck particle was that described by Zerby et al.[9]

Comparison with Experiment: Incident Nucleons

Table 1 contains comparisons of calculated total nonelastic cross sections with experimental data and Table 2 comparisons of the average excitation energy of the residual nucleus with calculations based on experiment. In both cases the agreement is quite good.

Figures 7 and 8 illustrate the cascade particle spectra in the forward direction for low-energy incident protons. The comparison for carbon, Fig. 7, shows one of the apparent deficiencies of the model. At higher energies this serious discrepancy in the shape of the spectrum in the forward direction is no longer manifest, as is shown in Figs. 9 and 10.

In Figs. 11-13 some comparisons at other angles are illustrated. The high-energy peaks in the experimental spectrum are due to elastic scattering, and the comparisons should be made at the energies below the peaks. Other comparisons, illustrated in Figs. 14-21, indicate low-energy peaks in some of the experimental results. These peaks are caused by nuclear evaporation, and the comparisons should be made at energies greater than about 15 Mev since evaporation is not included in the calculation. Comparisons with some of the data on emulsions are given in Figs. 22-25. Except for incident nucleon energies below 100 Mev on light- to medium-weight nuclei for particles emitted forward, the calculations indicate excellent agreement with experiment for emitted cascade particles. The angular distributions for a few reactions are given in Figs. 26-28.

6. D. J. Hughes and R. B. Schwartz, Neutron Cross Sections, BNL-325 (1958).

7. J. Orear, Phys. Rev. 100, 288 (1955).

8. N. Metropolis et al., Phys. Rev. 110, 204 (1958).

9. C. D. Zerby, R. B. Curtis, and H. W. Bertini, The Relativistic Doppler Problem, ORNL CF-61-7-20 (July 12, 1961).

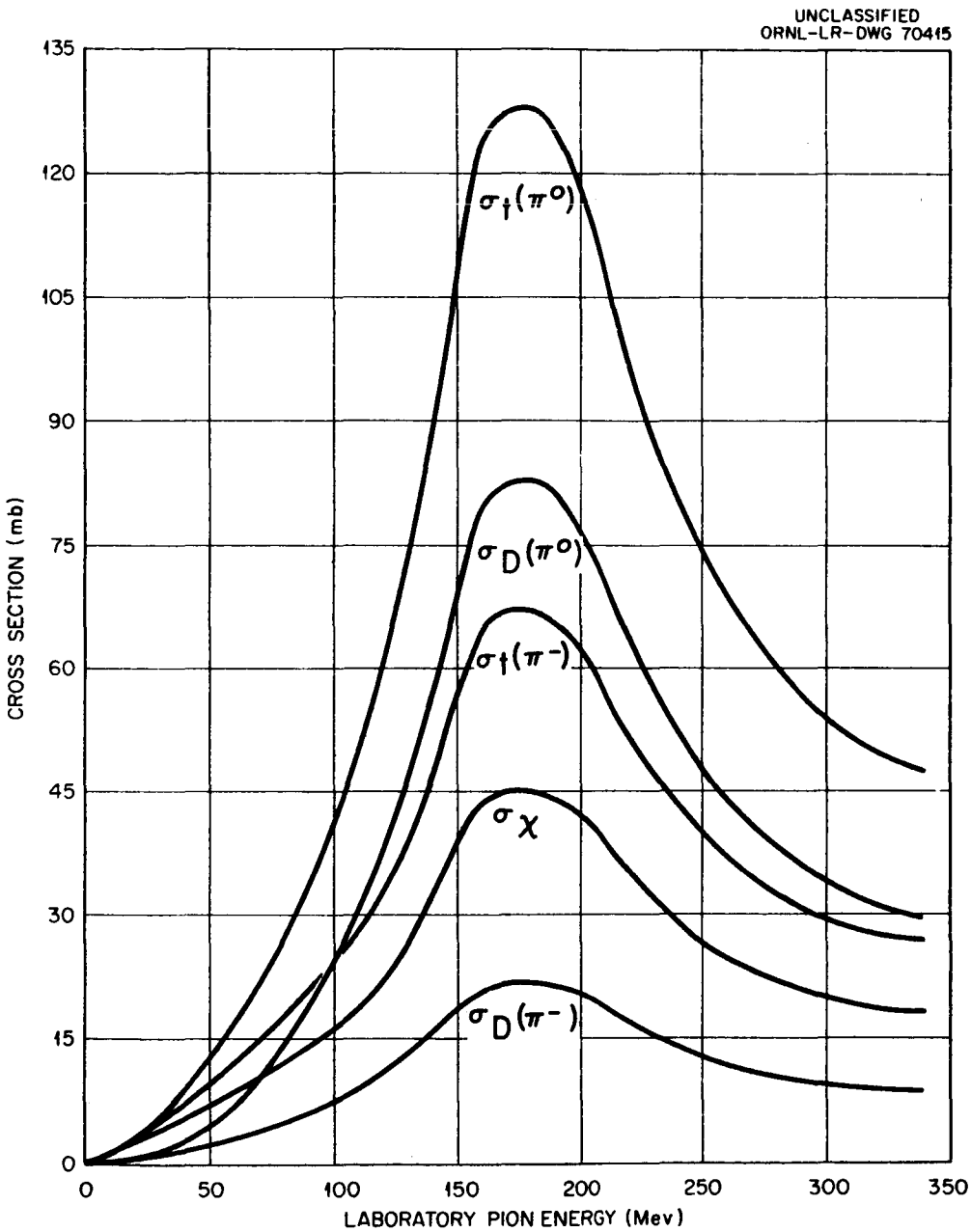

Fig. 6. Calculated Pion-Proton Cross Sections vs Pion Energy. $\sigma_t(\pi^o)$, Total cross section for π^o + p scattering; $\sigma_D(\pi^o)$, Cross section for π^o + p direct scattering; $\sigma_t(\pi^-)$, Experimental π^- + p total cross section included for comparison purposes; σ_X, Cross section for π^- + p, π^+ + n, π^o + p, and π^o + n exchange scattering; $\sigma_D(\pi^-)$, Cross section for π^- + p direct scattering.

Table 1. Calculated and Experimental Nonelastic Cross Sections for Protons and Neutrons Incident on Various Nuclei

Incident Particle	Target	Energy (Mev)	Nonelastic Cross Section (mb)	
			Calculated[a]	Experimental[b]
Proton	Be	185	187 ± 7	172 ± 17
		305	176 ± 7	151 ± 15
	Al	185	417 ± 9	408 ± 41
		305	394 ± 11	334 ± 33
	Cu	170	795 ± 23	
		185		746 ± 75
		240	747 ± 23	667 ± 67
	U	185	1825 ± 38	1900 ± 190
		305	1754 ± 28	1600 ± 160
Neutron	Be	95	217 ± 7	210 ± 8[c]
	Al	84	502 ± 16	500 ± 50[d]
		300	383 ± 11	390 ± 23
	Cu	84	825 ± 23	910 ± 50[d]
		300	725 ± 16	755 ± 33
	Pb	84	1654 ± 26	1850 ± 180[d]
		300	1552 ± 27	1720 ± 80

a. Errors shown are the limits for the standard 68% confidence interval.

b. Unless otherwise noted, all the data come from G. P. Millburn et al., Phys. Rev. 95, 1268 (1954).

c. P. E. Hodgson, Nuclear Phys. 21, 21 (1960).

d. Upper limit.

Table 2. Calculated and Experimental Average Excitation Energies for 190-Mev Incident Protons on Various Nuclei

Target	Excitation Energy (Mev)	
	Calculated	Experimental[a]
C	22	27 ± 5
Al	36	50 ± 8
Ni	59	57 ± 9
Ag	72	69 ± 12
Au	92	83 ± 17
U	95	88 ± 18

a. E. Gross, "The Absolute Yield of Low Energy Neutrons from 190-Mev Protons on Gold, Silver, Nickel, Aluminum, and Carbon," UCRL-3330 (Feb. 29, 1956); "Absolute Neutron Spectra from 190-Mev Protons on Uranium," UCRL-3337 (Mar. 8, 1956).

Table 3. Calculated and Experimental Fast Prong Distributions for Heavy Emulsion Nuclei[a]

Number of Fast Prongs	Percentage of Stars Induced			
	By 300-Mev Neutrons		By 375-Mev Protons	
	Calculated	Experimental[b]	Calculated	Experimental[b]
0	54	30 ± 4	14	29 ± 3
1	42	63 ± 5	76	60 ± 4
2	4	7 ± 2	10	9 ± 2
3	0.4	0	0.5	2 ± 1

a. Fast prongs indicate protons with energies greater than 30 Mev.

b. G. Bernardini, E. T. Booth, and S. J. Lindenbaum, Phys. Rev. 85, 826 (1952).

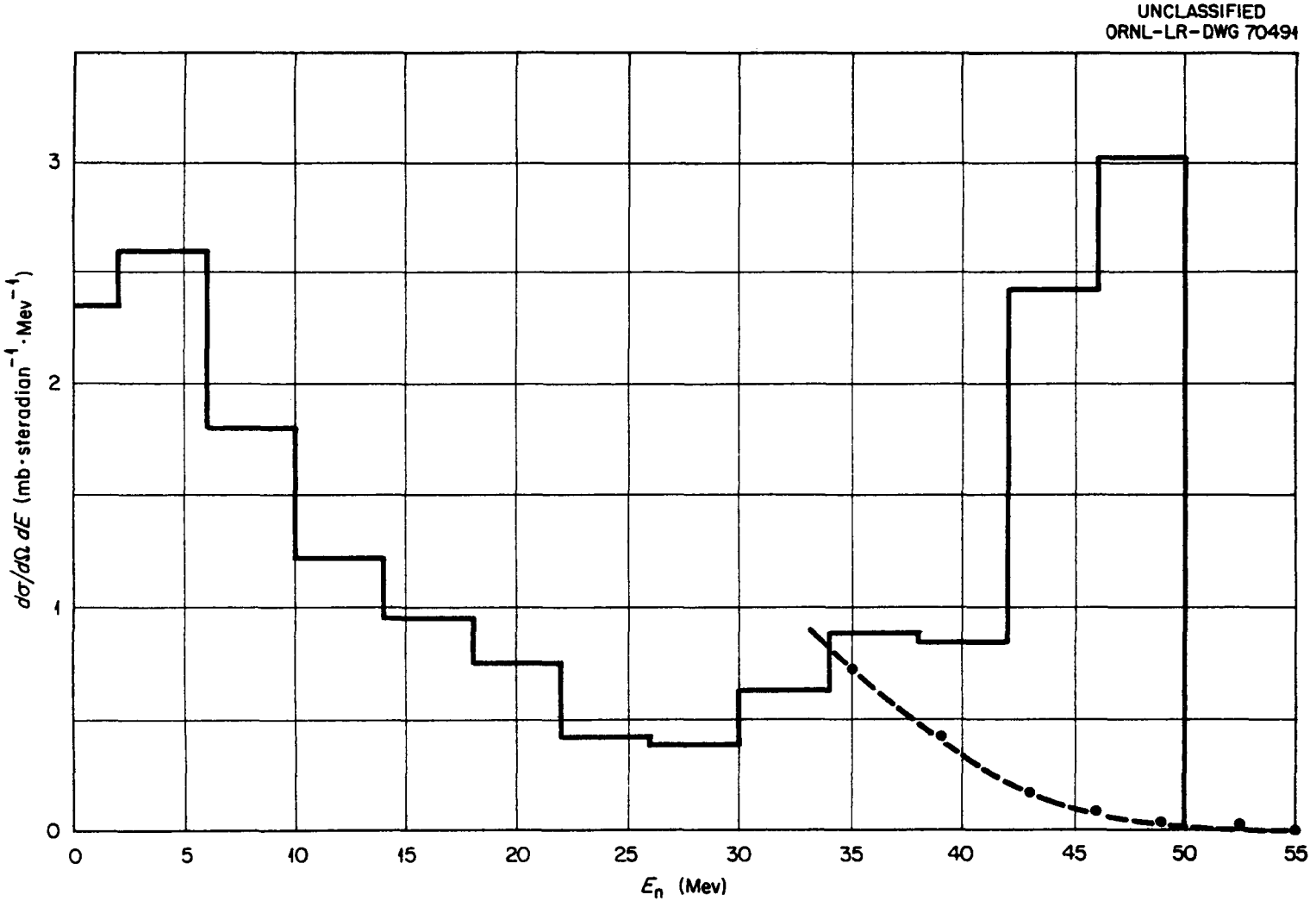

Fig. 7. Neutron Spectra at 0° from 50-Mev Protons on Carbon. Dotted curve: Hofmann's experimental results ("Neutrons Ejected from Nuclei by 50-Mev Protons," Ph.D. Thesis submitted to the Faculty of Arts and Sciences of Harvard University, Cambridge, August 1952); solid lines: calculated spectrum for neutrons emitted in the angular interval 0 to 11°.

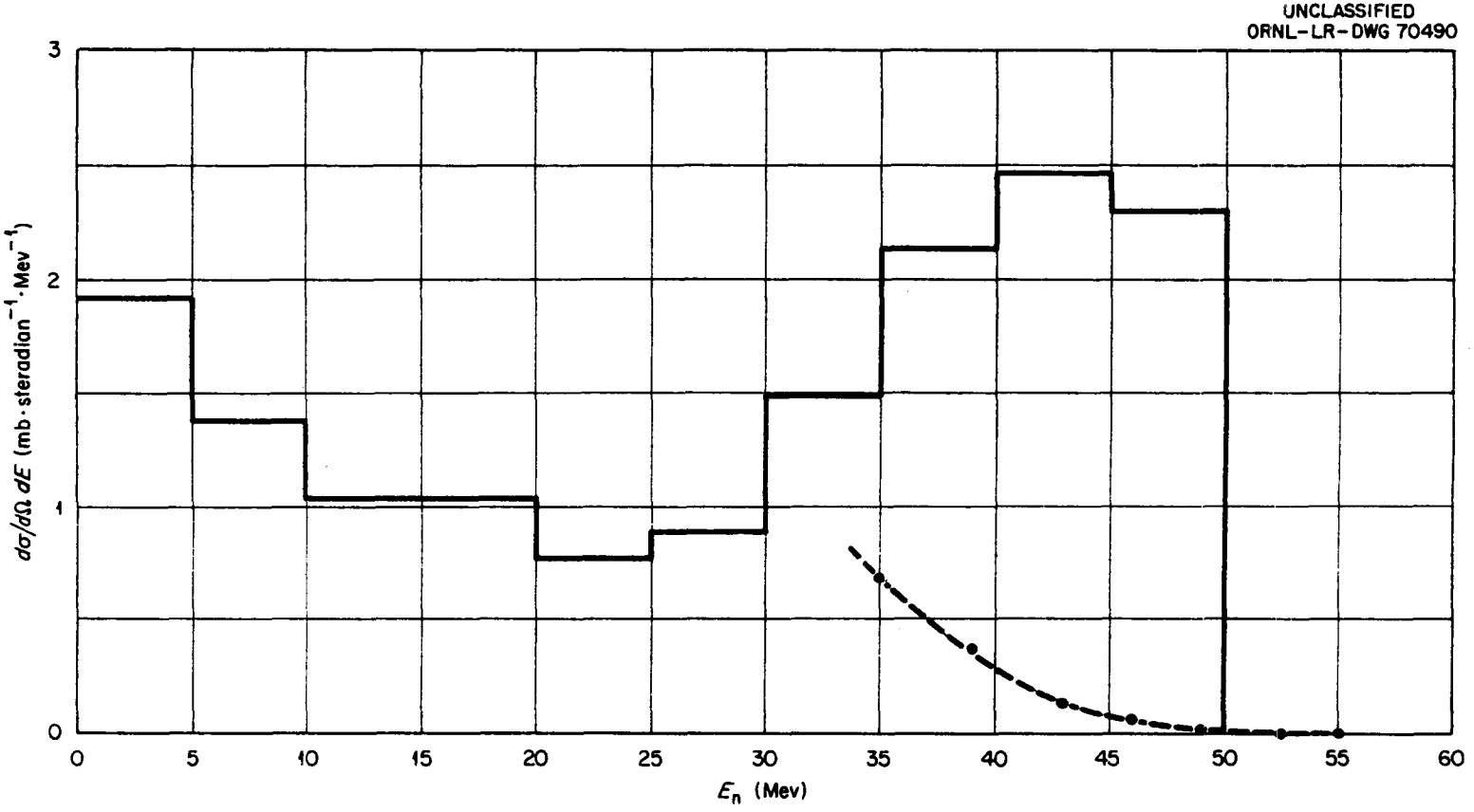

Fig. 8. Neutron Spectra at 16° from 50-Mev Protons on Carbon. Dotted curve: Hofmann's experimental results ("Neutrons Ejected from Nuclei by 50-Mev Protons," Ph.D. Thesis submitted to the Faculty of Arts and Sciences of Harvard University, Cambridge, August 1952); solid lines: calculated spectrum for neutrons emitted in the angular interval 5 to 25°.

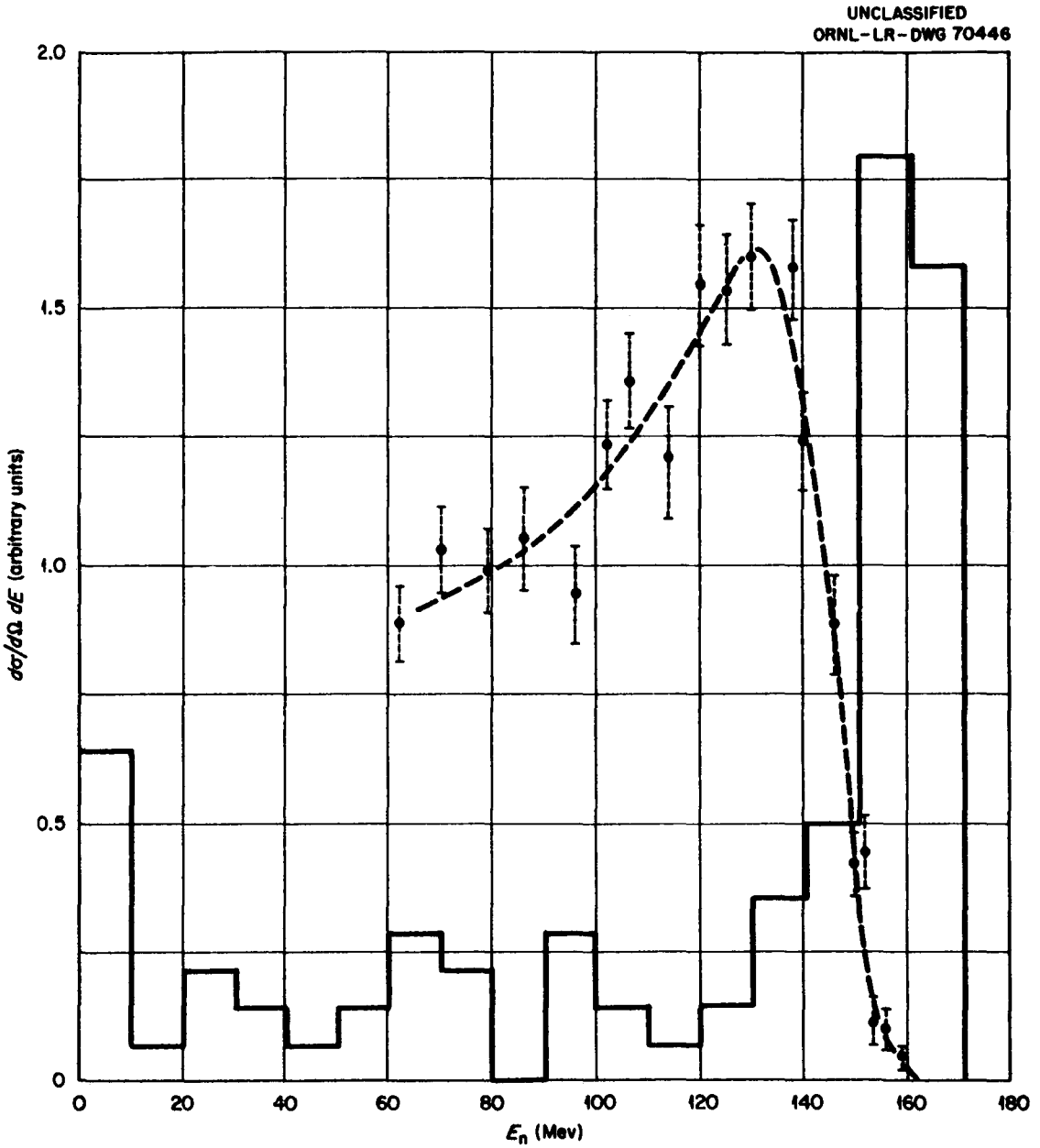

Fig. 9. Neutron Spectra at 2.5° from 171-Mev Protons on Carbon. Dotted curve: experimental results of Cassels et al. [Phil. Mag. 42, 215 (1951)]; solid lines: calculated spectrum of neutrons emitted in the angular interval 0 to 15°; ordinate units are arbitrary.

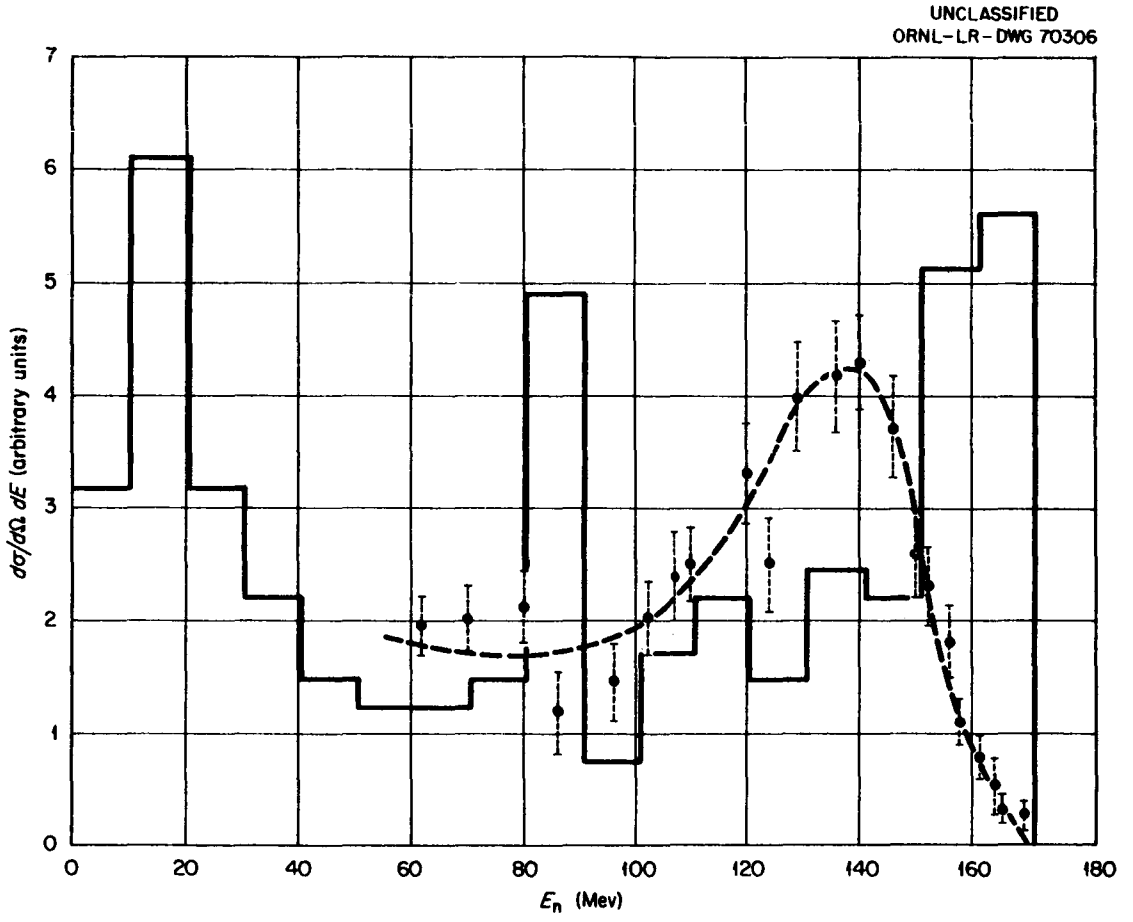

Fig. 10. Neutron Spectra at 2.5° from 171-Mev Protons on Uranium. Dotted curve: experimental results of Cassels et al. [Phil. Mag. 42, 215 (1951)]; solid lines: calculated spectrum of neutrons emitted in the angular interval 0 to 15°; ordinate units are arbitrary.

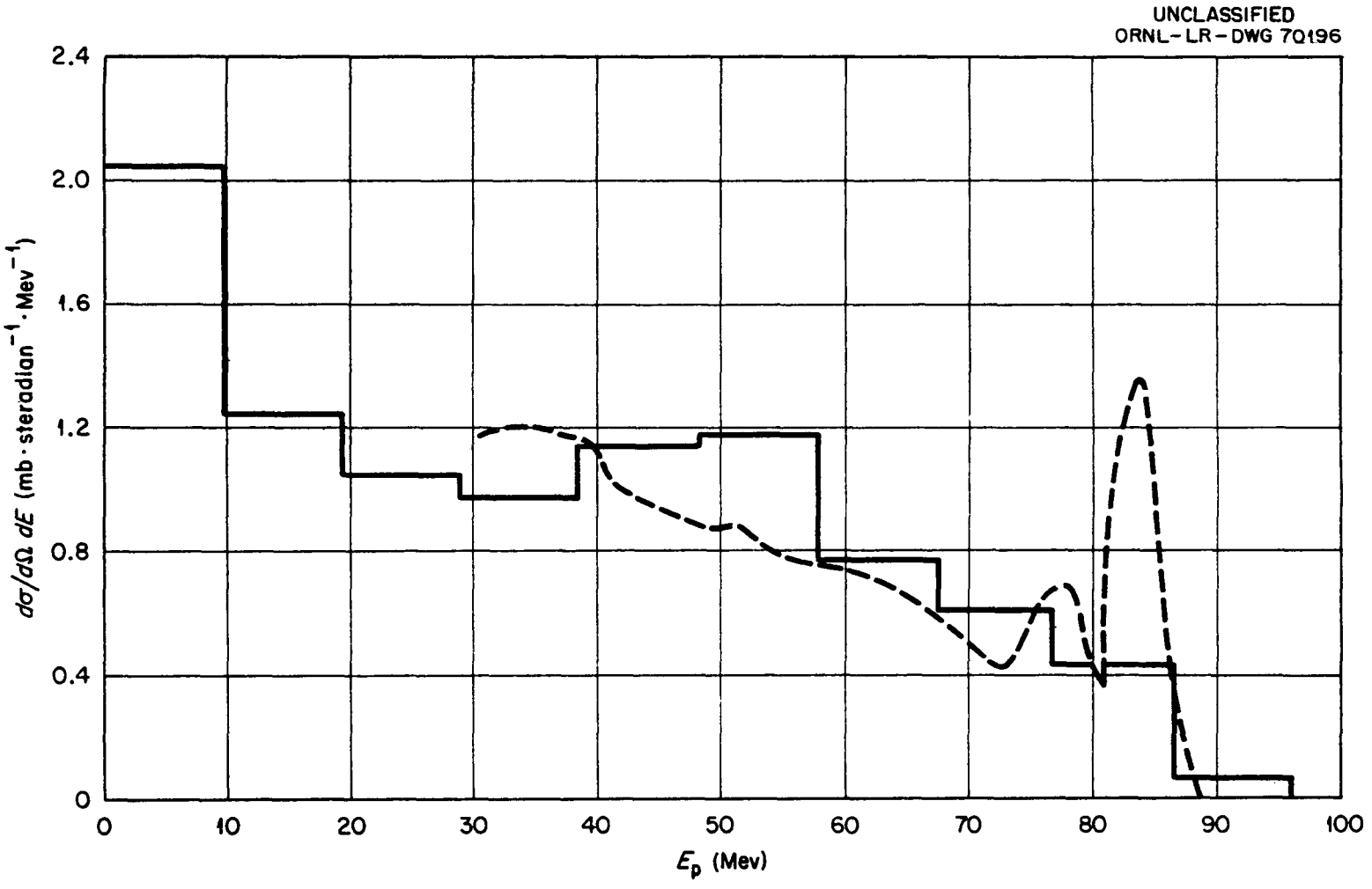

Fig. 11. Proton Spectra at 40° from 96-Mev Protons on Fluorine. Dotted curve: experimental results of Strauch and Titus [Phys. Rev. 104, 191 (1956)]; solid lines: calculated spectrum of protons emitted in the angular interval 30 to 50°.

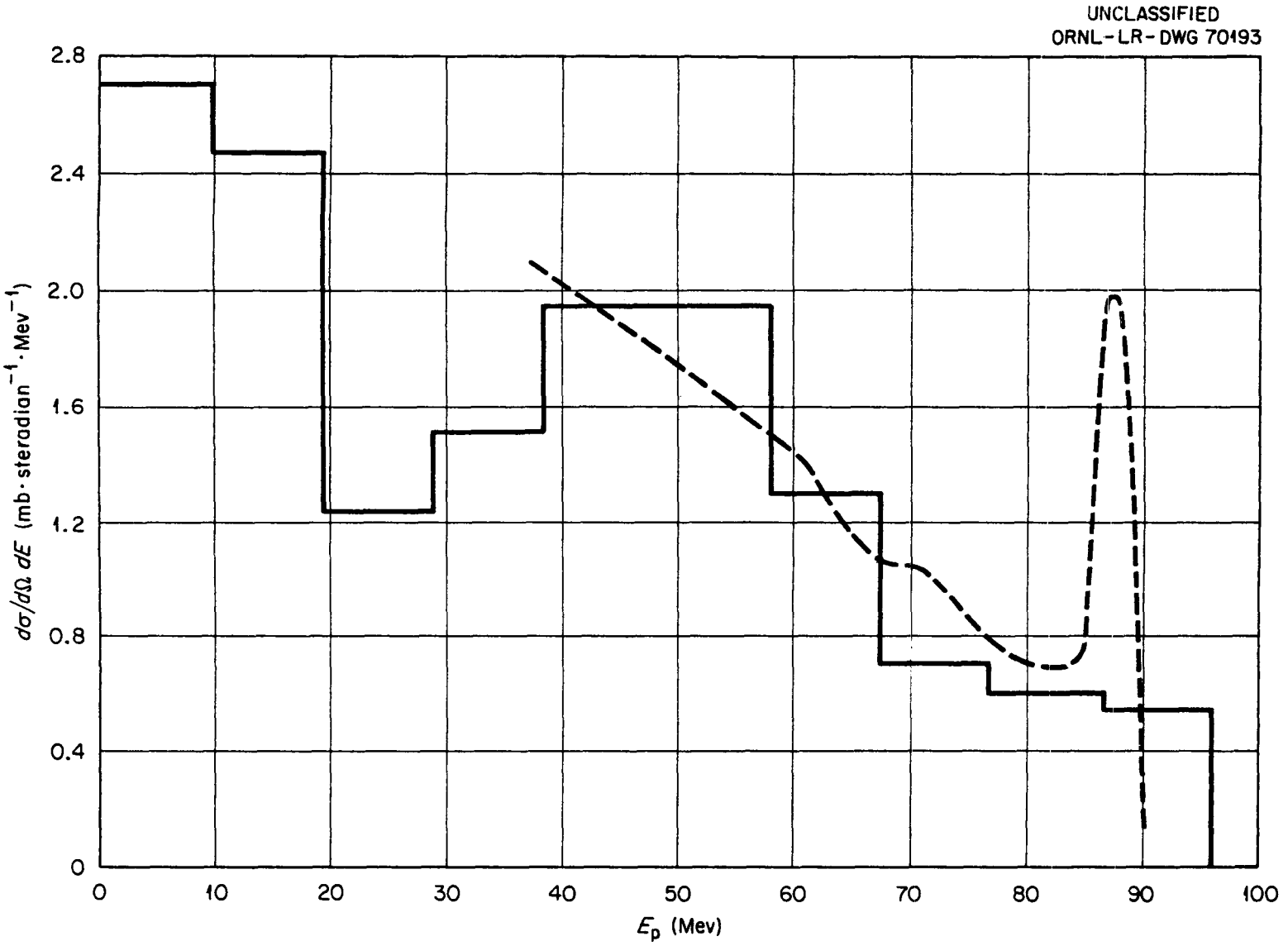

Fig. 12. Proton Spectra at 40° from 96-Mev Protons on Copper. Dotted curve: experimental results of Strauch and Titus [Phys. Rev. 104, 191 (1956)]; solid lines: calculated spectrum of protons emitted in the angular interval 30 to 50°.

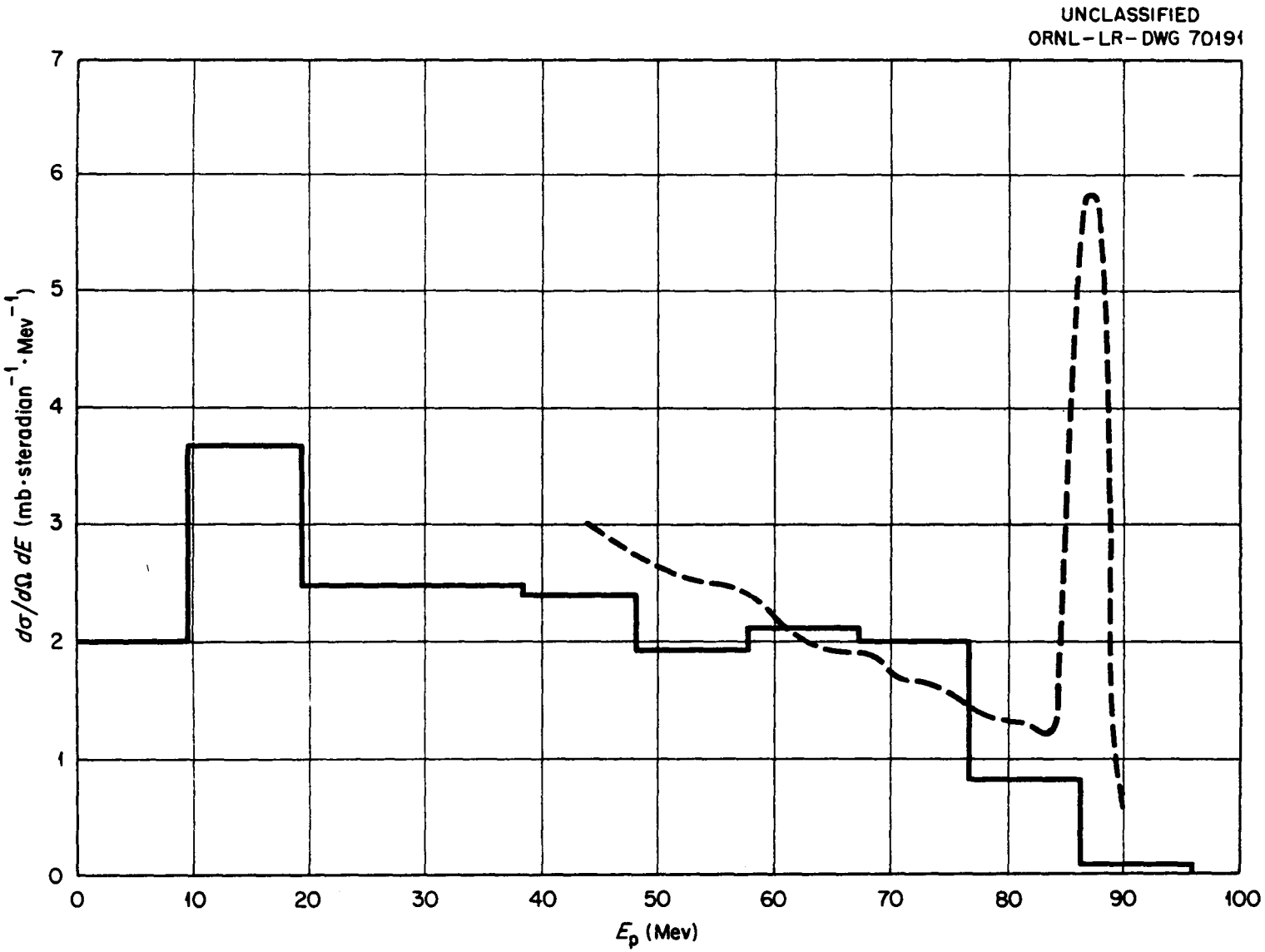

Fig. 13. Proton Spectra at 40° from 96-Mev Protons on Bismuth. Dotted curve: experimental results of Strauch and Titus [Phys. Rev. 104, 191 (1956)]; solid lines: calculated spectrum of protons emitted in the angular interval 30 to 50°.

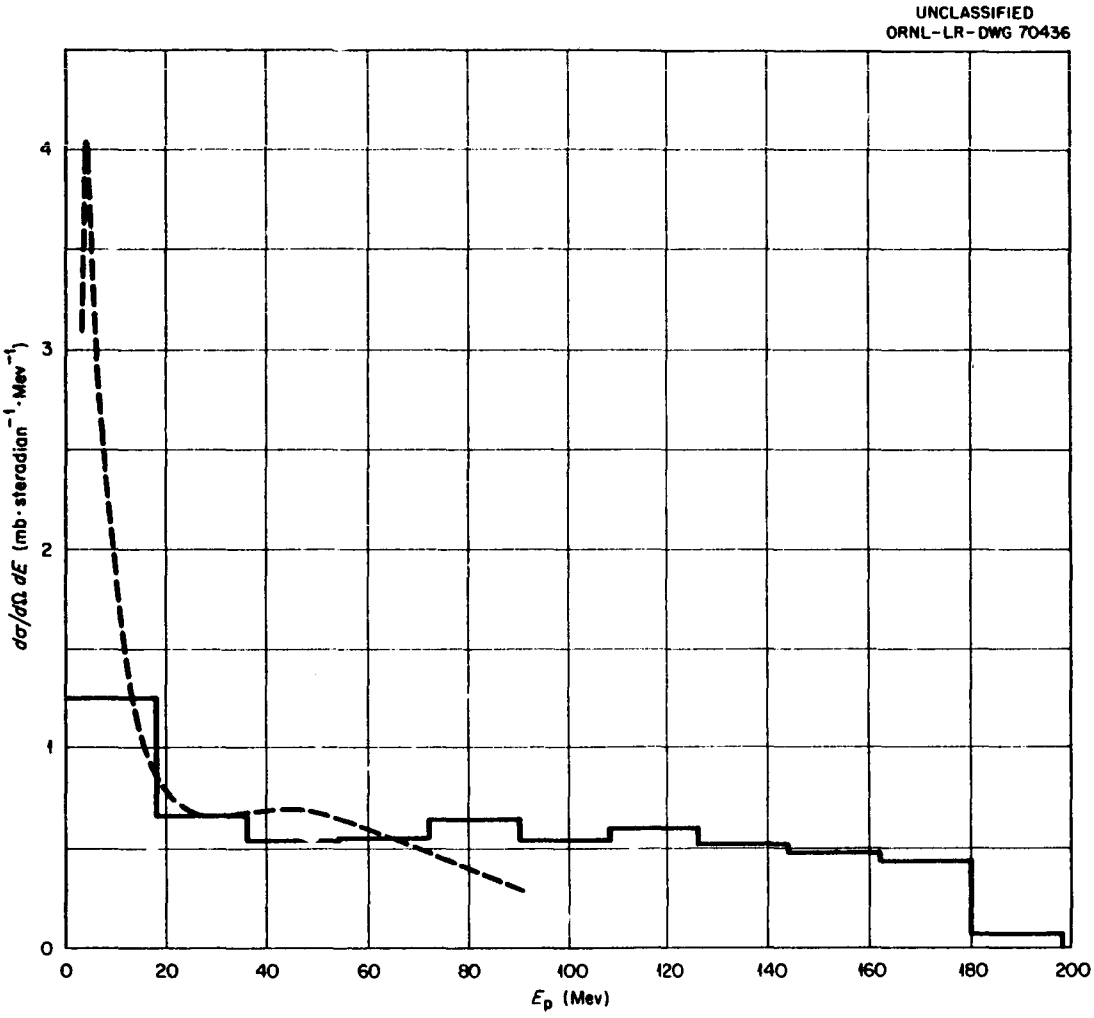

Fig. 14. Proton Spectra from 0 to 65° for 190-Mev Protons on Aluminum. Dashed curve: Bailey's experimental results ["Angle and Energy Distributions of Charged Particles from the High Energy Nuclear Bombardment of Various Elements," UCRL-3334 (Mar. 1, 1956)]; solid lines: calculated spectrum.

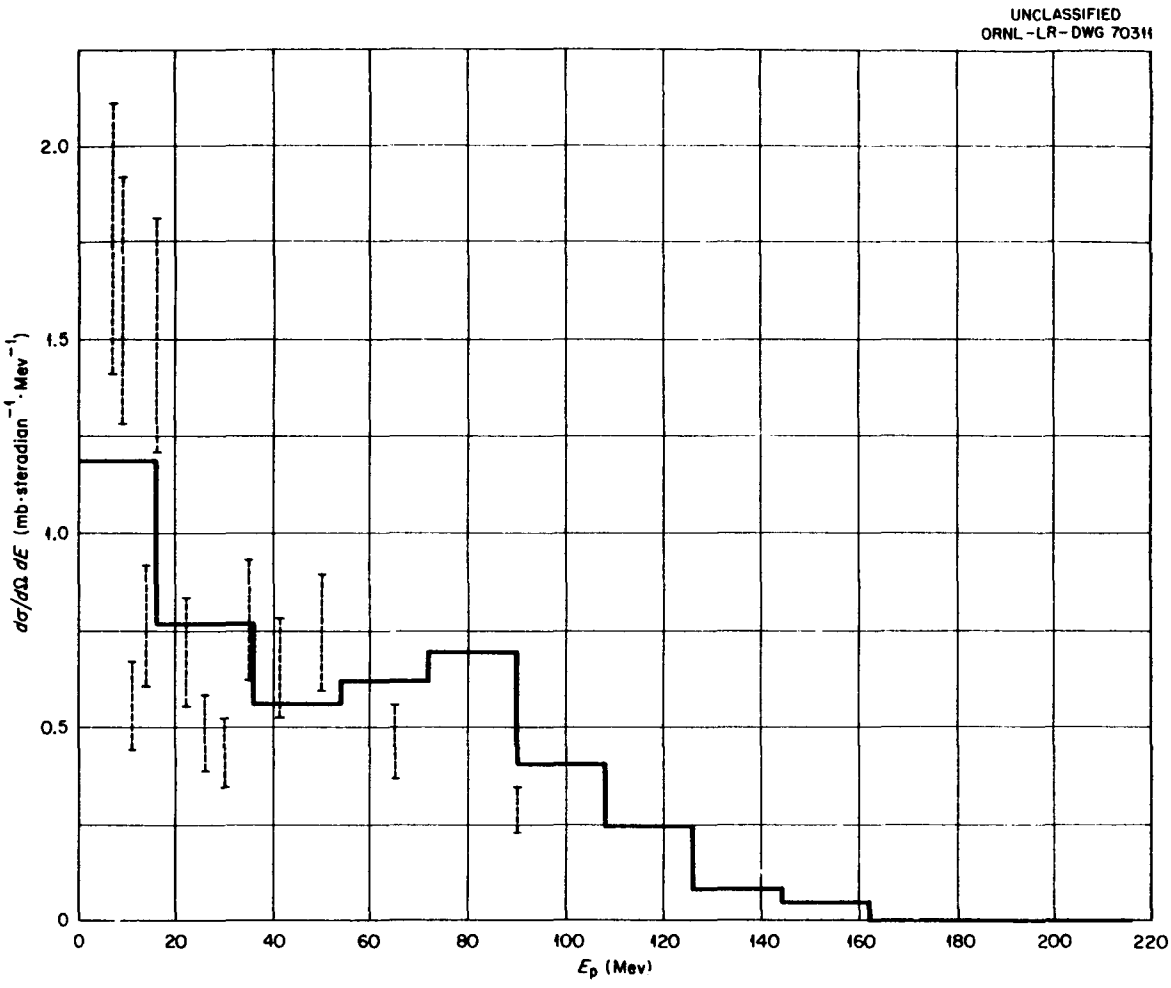

Fig. 15. Proton Spectra from 46 to 65° for 190-Mev Protons on Aluminum. Dotted lines: Bailey's experimental results (UCRL-3334); solid lines: calculated spectrum.

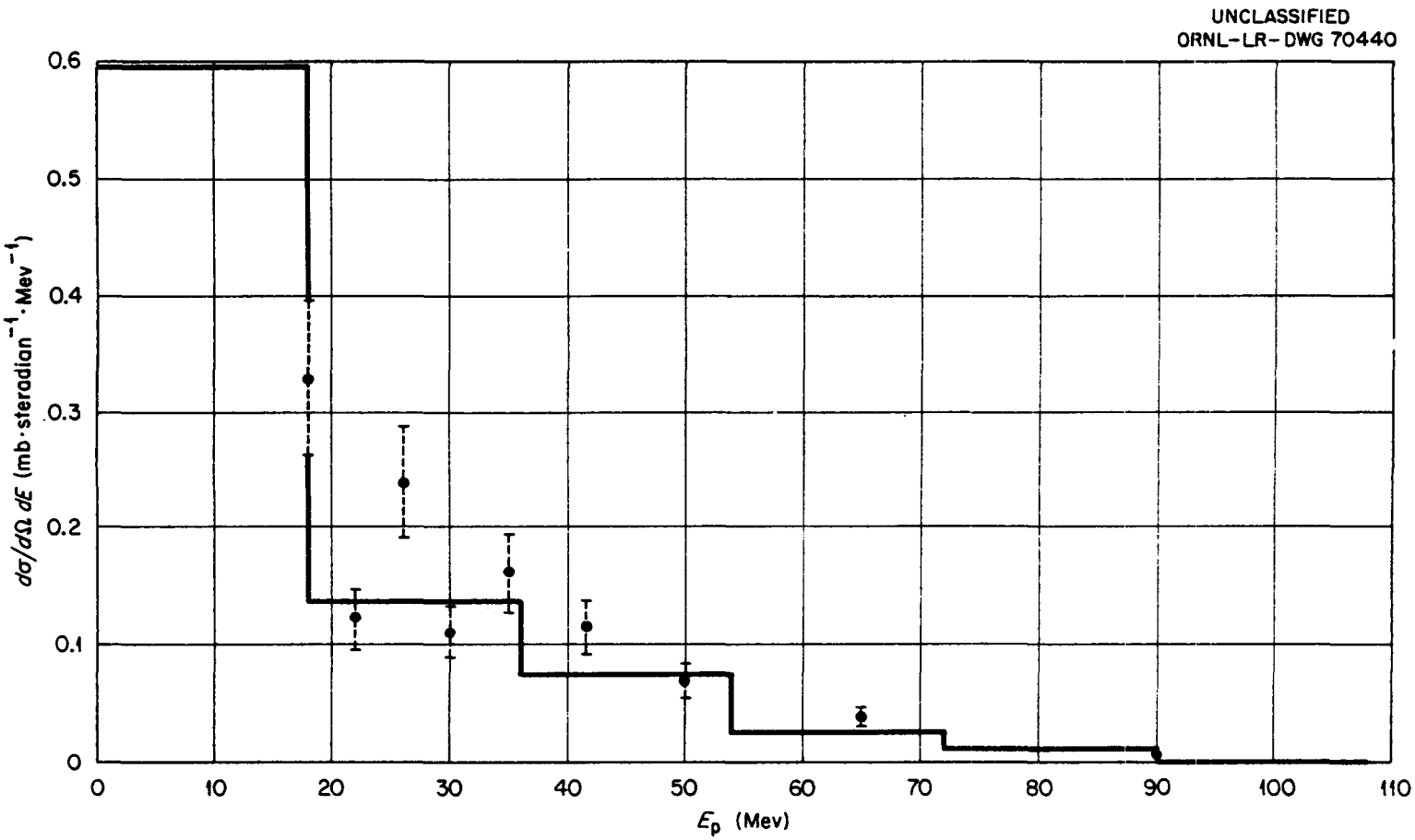

Fig. 16. Proton Spectra from 102 to 117° for 190-Mev Protons on Aluminum. Dotted lines: Bailey's experimental results (UCRL-3334); solid lines: calculated spectrum.

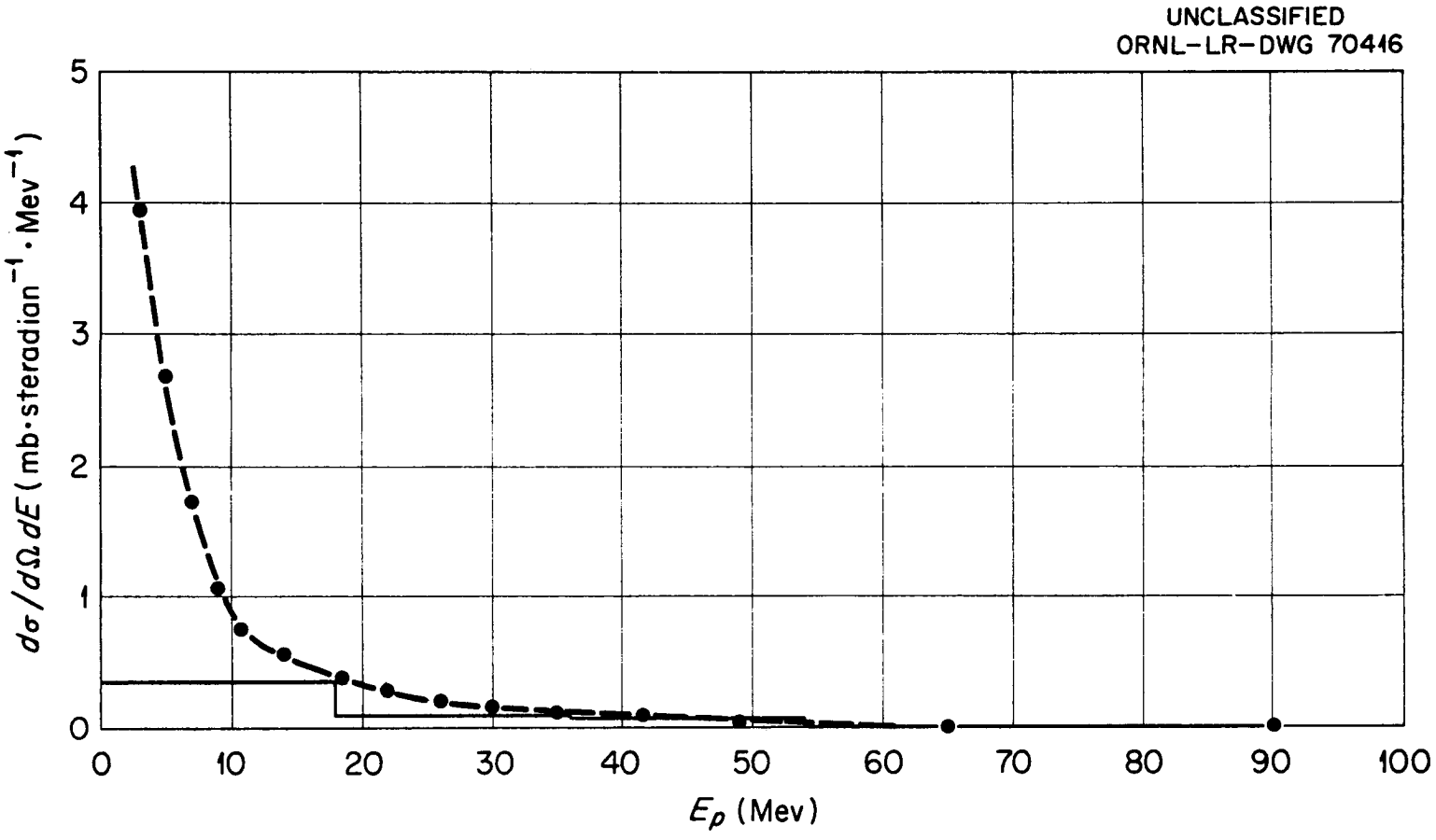

Fig. 17. Proton Spectra from 100 to 180° for 190-Mev Protons on Aluminum. Dotted curve: Bailey's experimental results (UCRL-3334); solid lines: calculated spectrum.

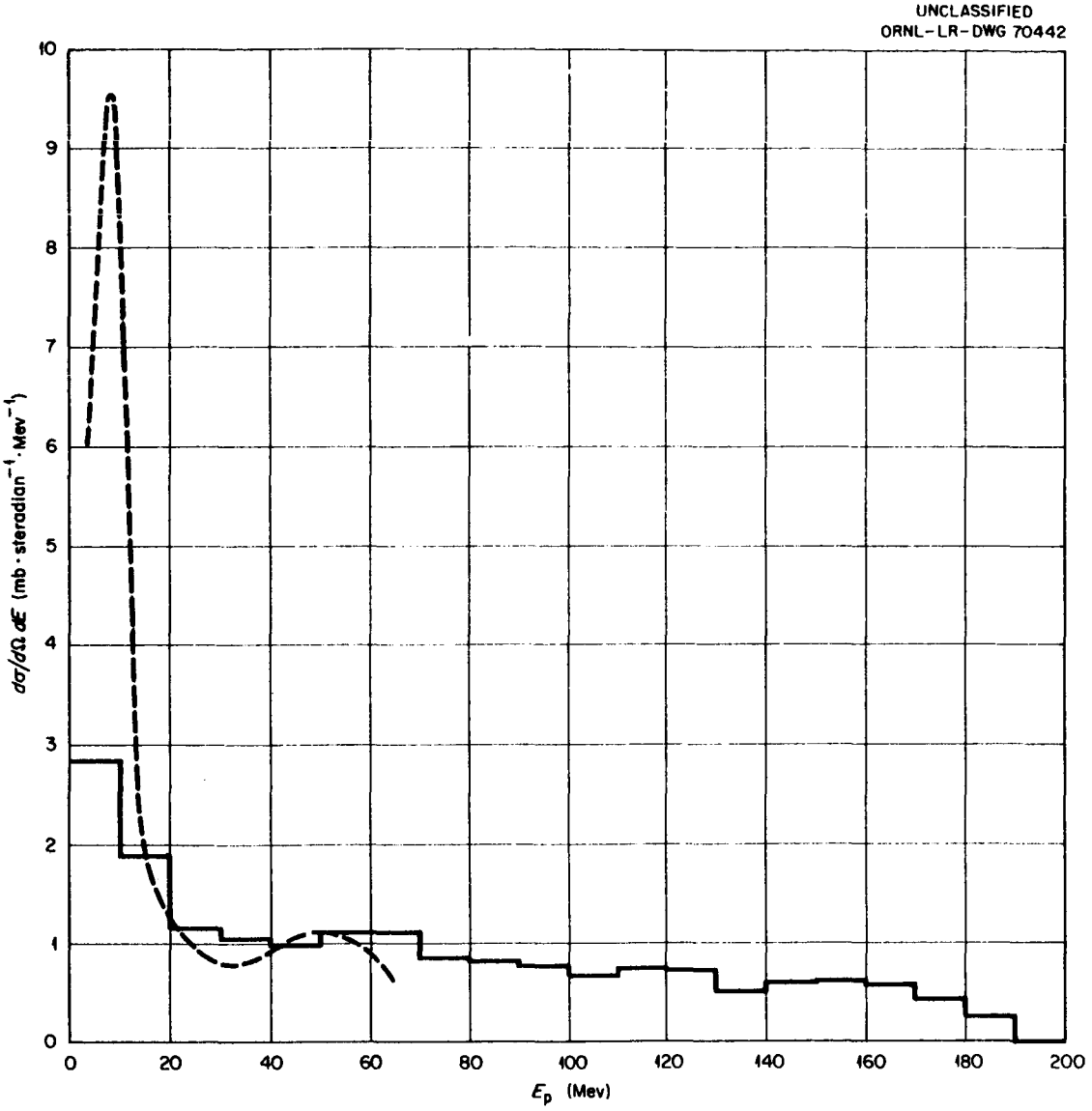

Fig. 18. Proton Spectra from 0 to 65° for 190-Mev Protons on Nickel. Dotted curve: Bailey's experimental results (UCRL-3334); solid lines: calculated spectrum.

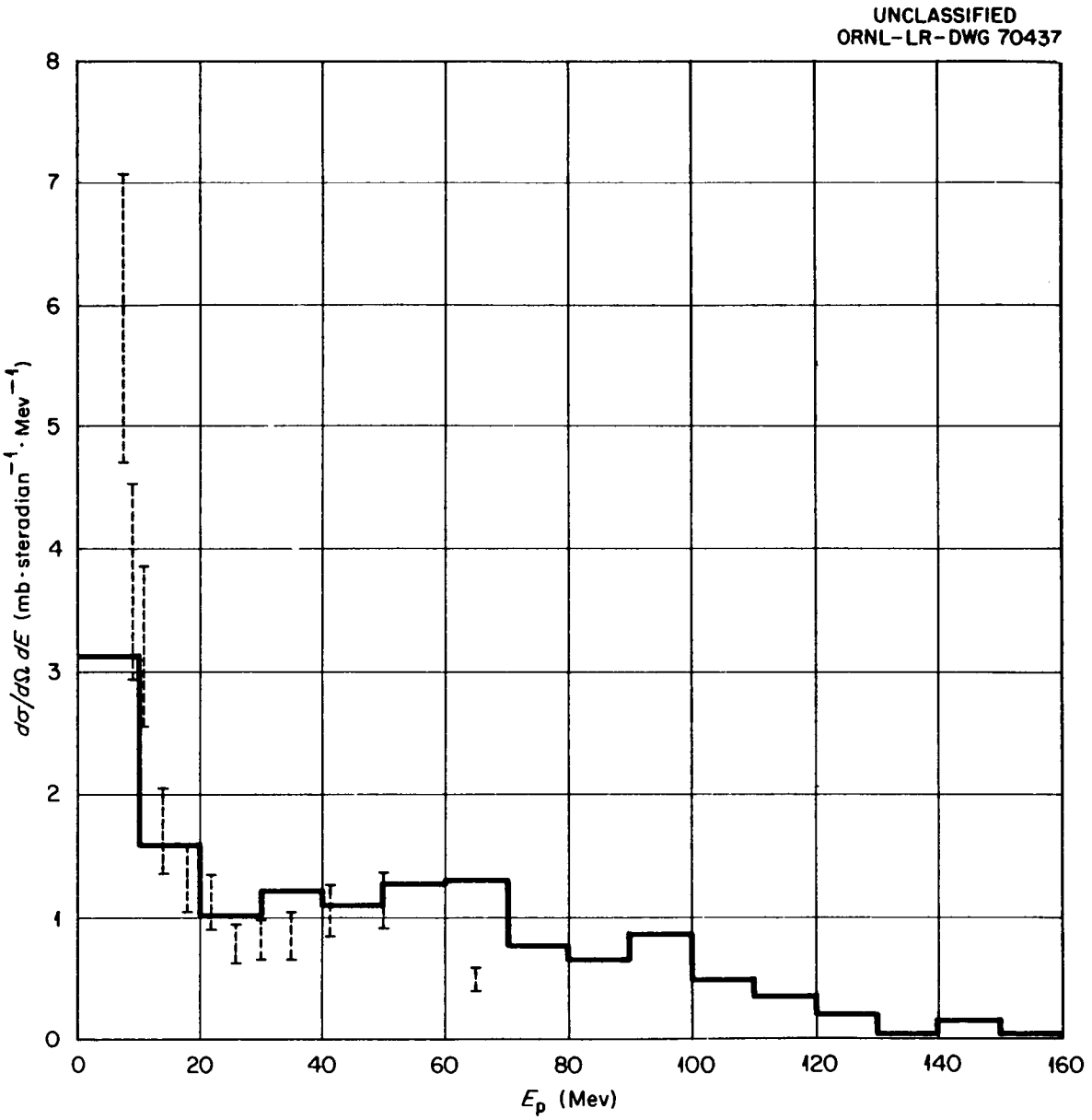

Fig. 19. Proton Spectra from 46 to 65° for 190-Mev Protons on Nickel. Dotted lines: Bailey's experimental results (UCRL-3334); solid lines: calculated spectrum.

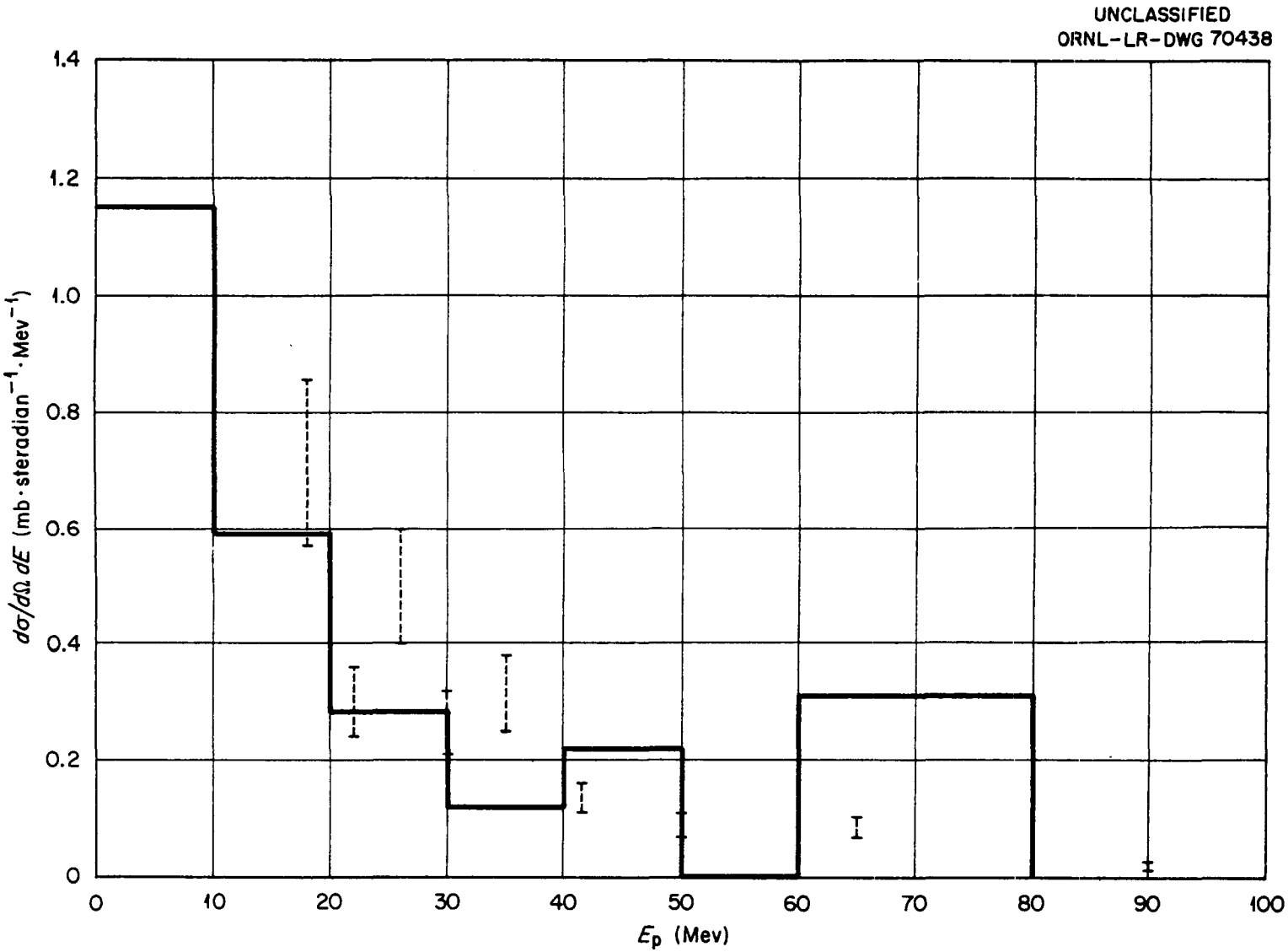

Fig. 20. Proton Spectra from 102 to 117° for 190-Mev Protons on Nickel. Dotted lines: Bailey's experimental results (UCRL-3334); solid lines: calculated spectrum.

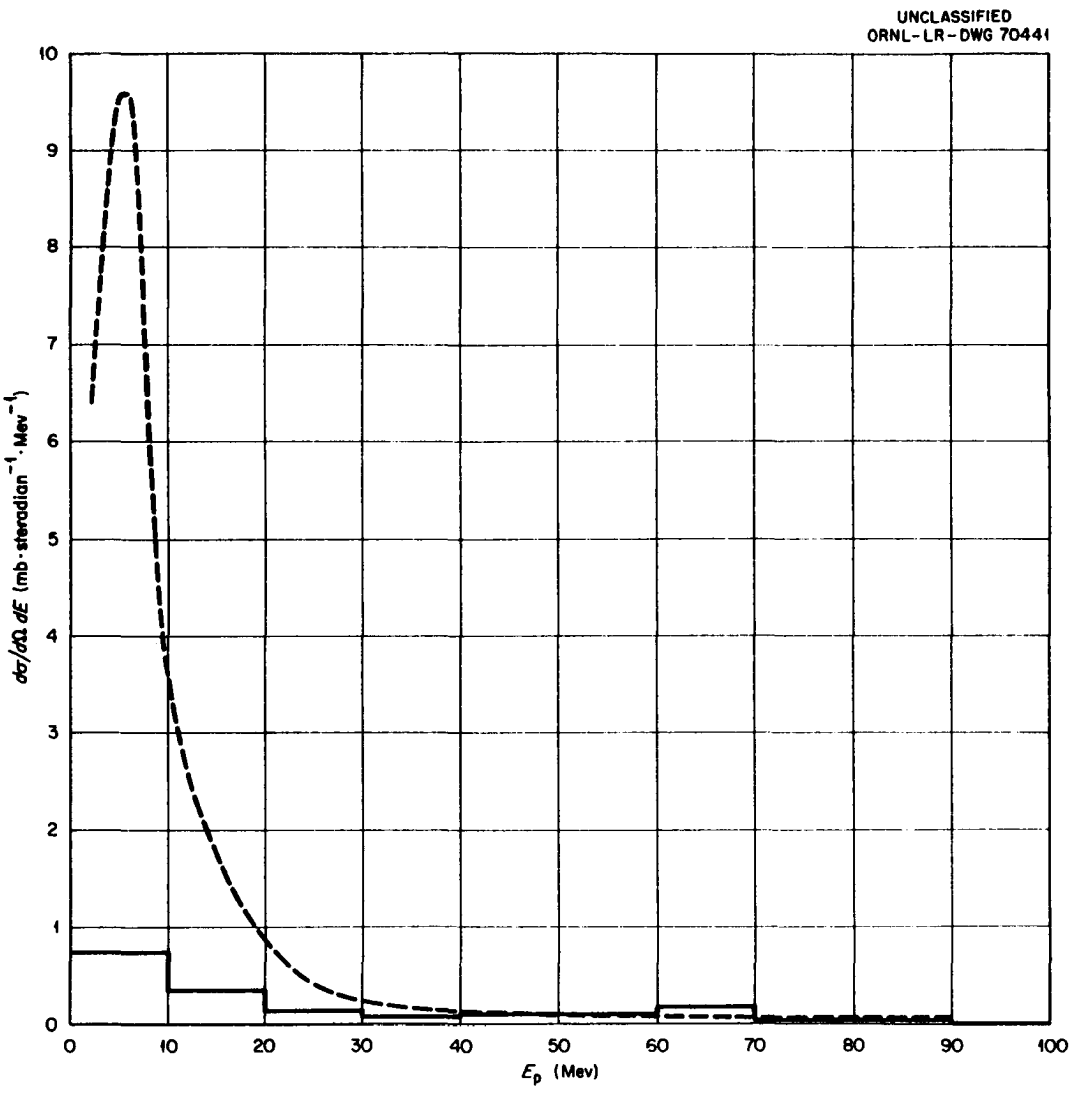

Fig. 21. Proton Spectra from 100 to 180° for 190-Mev Protons on Nickel. Dotted curve: Bailey's experimental results (UCRL-3334); solid lines: calculated spectrum.

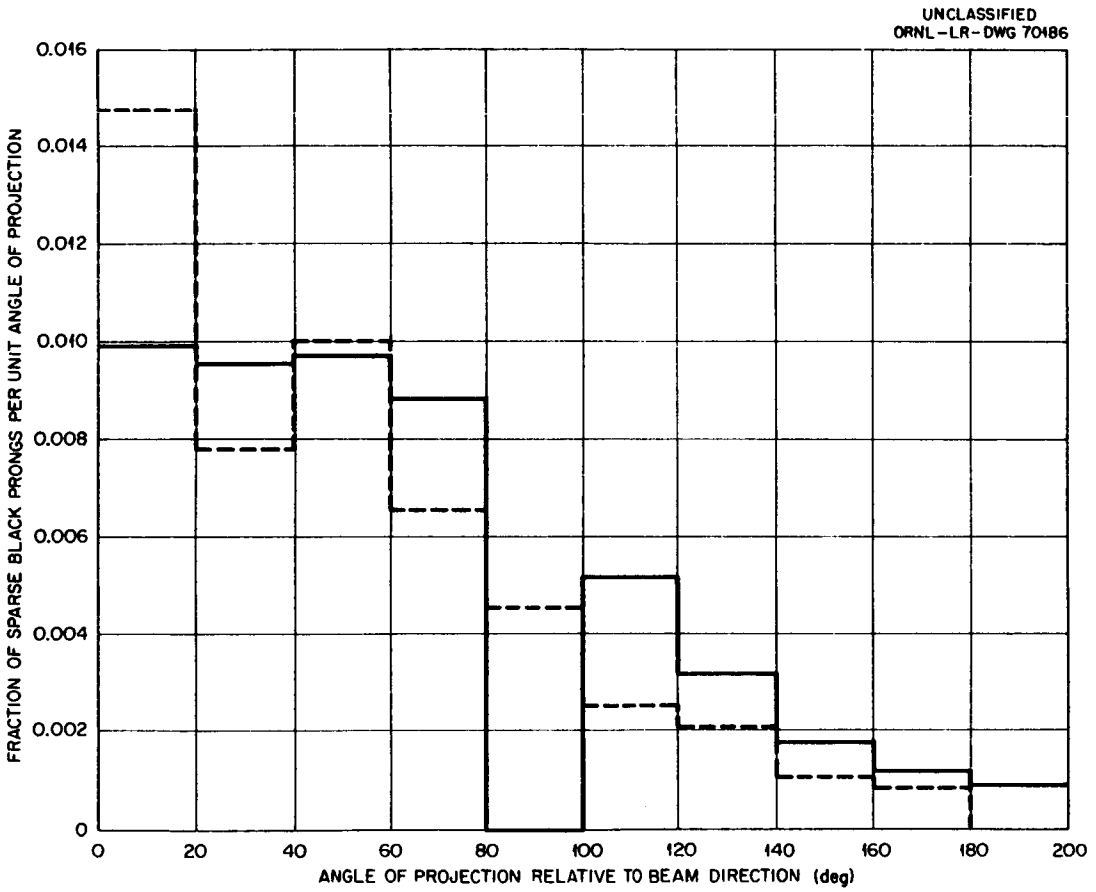

Fig. 22. Angular Distribution of Sparse Black Prongs from 375-Mev Protons on Heavy-Emulsion Nuclei. Dotted lines: experimental results of Bernardini et al. [Phys. Rev. 85, 826 (1952)]; solid lines: calculated distribution for protons emitted with energies from 30 to 100 Mev for 375-Mev protons on Ru^{100}.

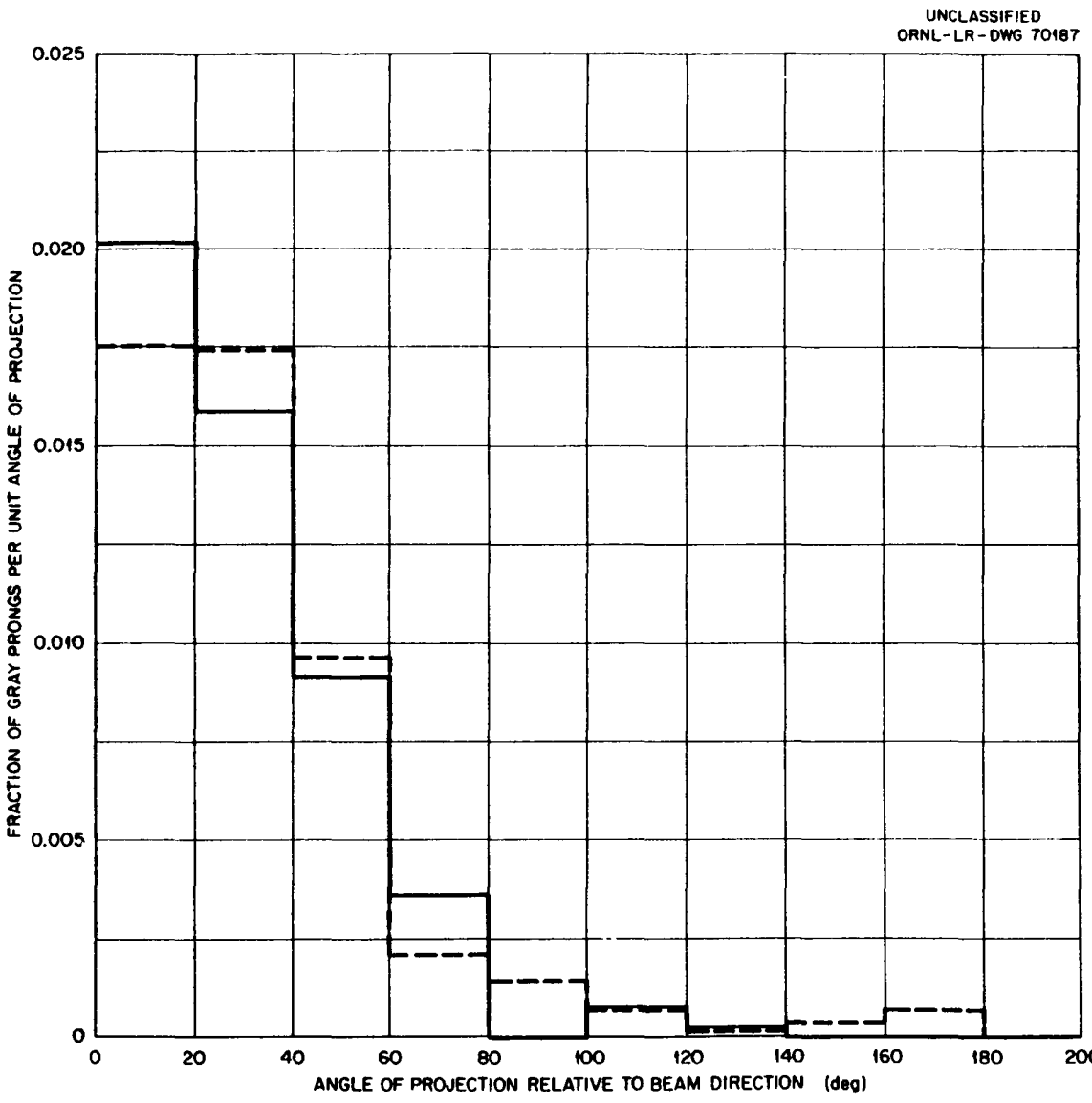

Fig. 23. Angular Distribution of Gray Prongs from 375-Mev Protons on Heavy-Emulsion Nuclei. Dotted lines: experimental results of Bernardini *et al.* [Phys. Rev. 85, 826 (1952)]; solid lines: calculated distribution for protons emitted with energies from 100 to 375 Mev for 375-Mev protons on Ru^{100}.

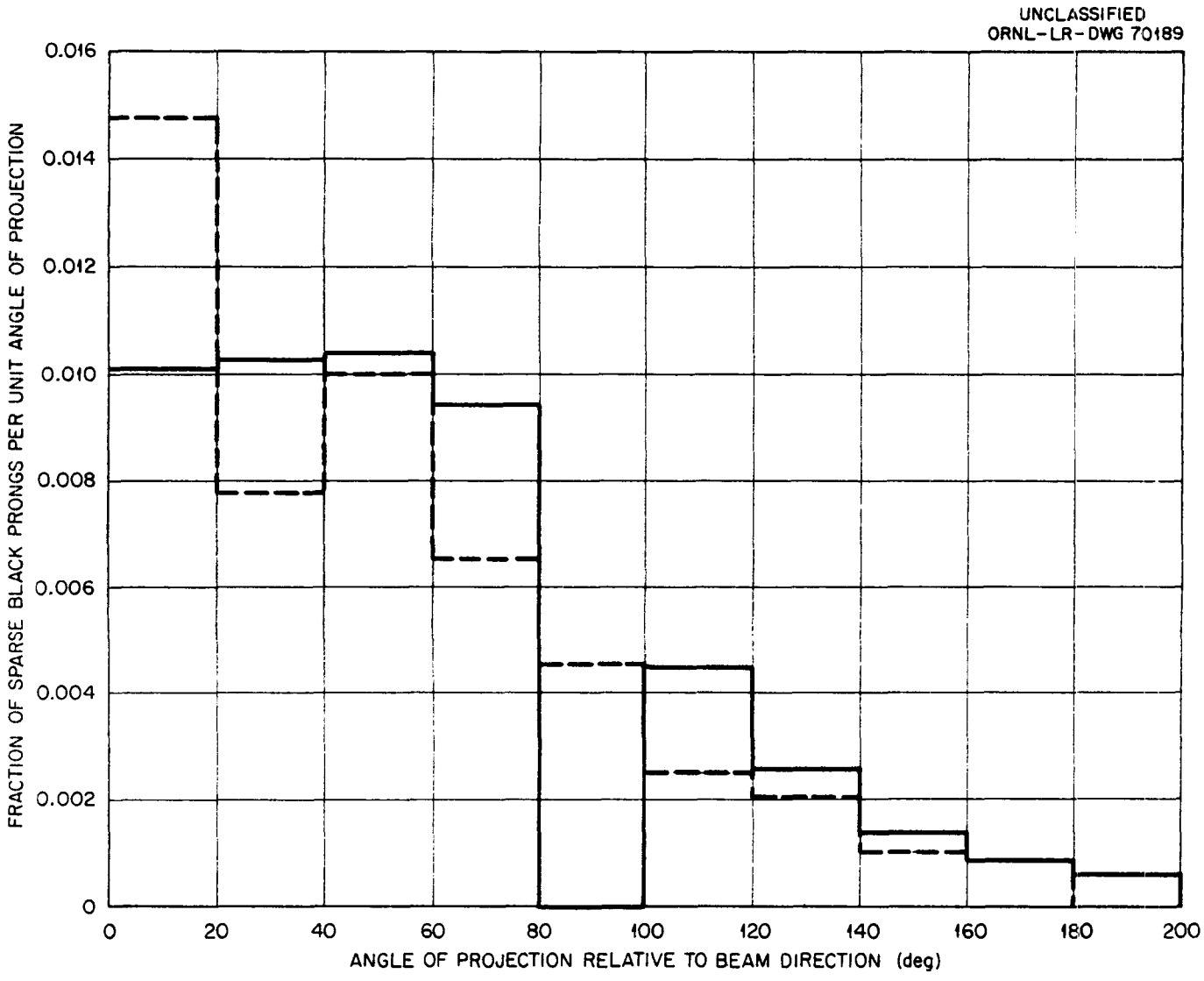

Fig. 24. Angular Distribution of Sparse Black Prongs from 300-Mev Neutrons on Heavy-Emulsion Nuclei. Dotted lines: experimental results of Bernardini et al. [Phys. Rev. 85, 826 (1952)]; solid lines: calculated distribution for protons emitted with energies from 30 to 100 Mev for 300-Mev neutrons on Ru^{100}.

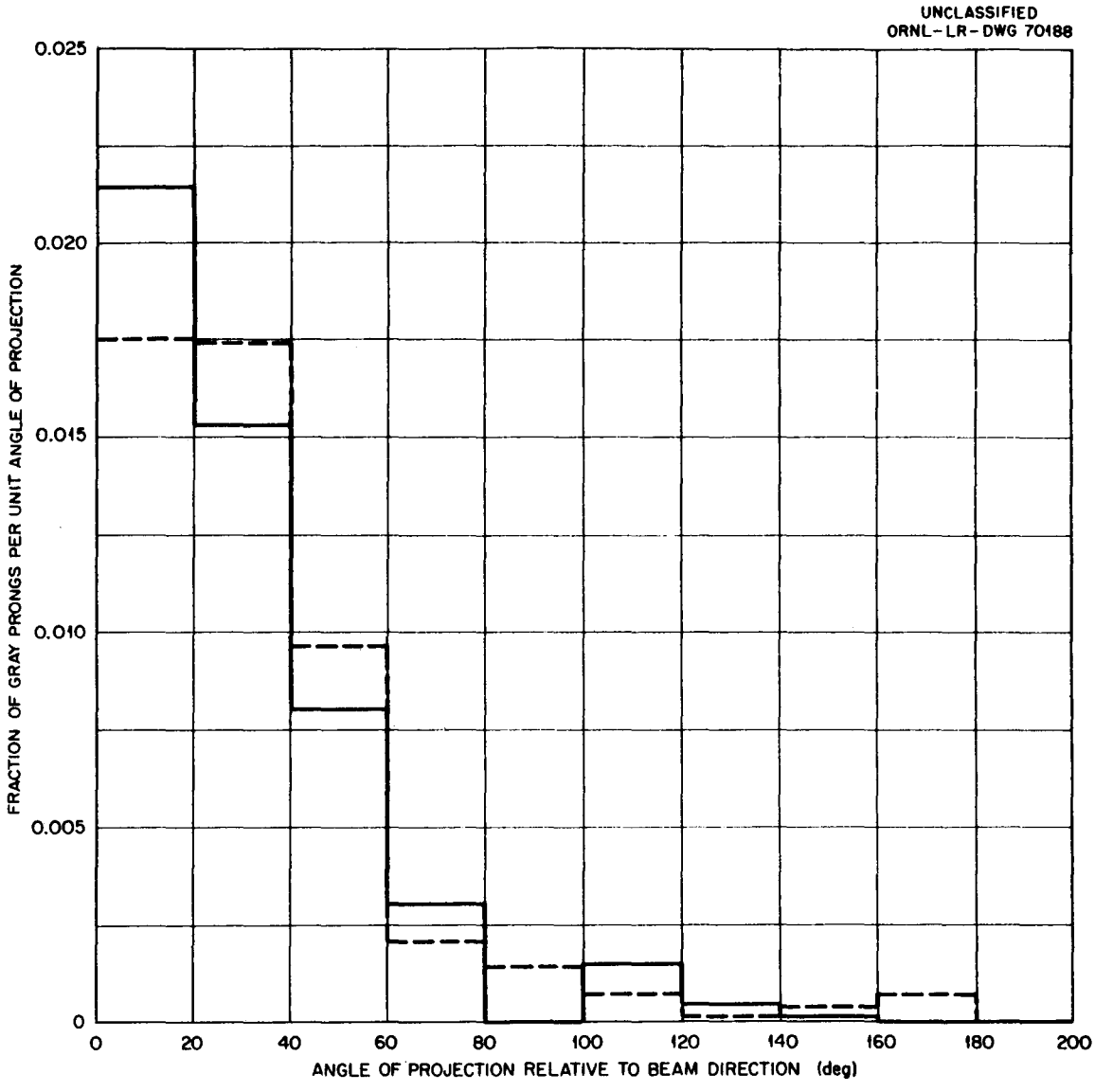

Fig. 25. Angular Distribution of Gray Prongs from 300-Mev Neutrons on Heavy-Emulsion Nuclei. Dotted lines: experimental results of Bernardini *et al.* [Phys. Rev. 85, 826 (1952)]; solid lines: calculated distribution for protons emitted with energies from 100 to 300 Mev for 300-Mev neutrons on Ru^{100}.

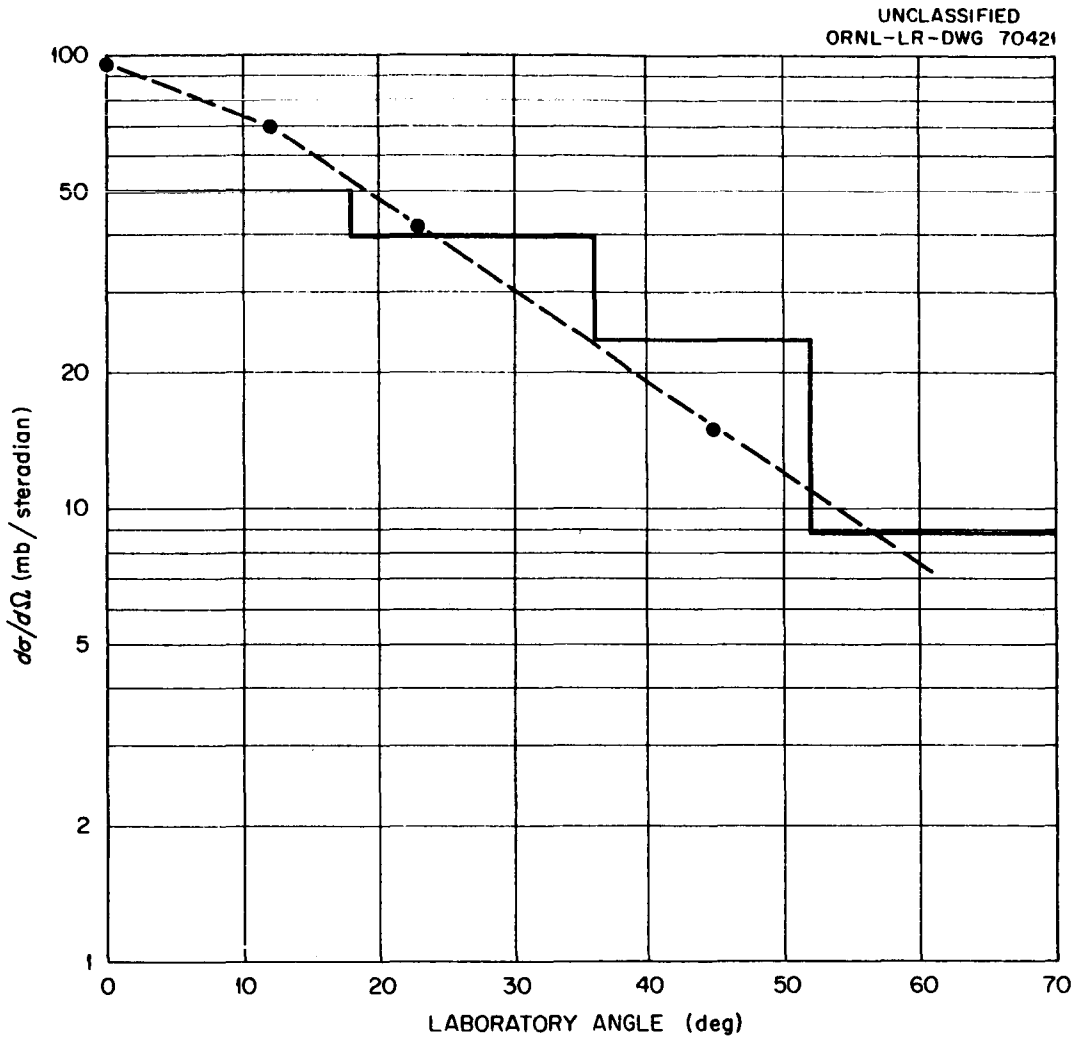

Fig. 26. Angular Distribution of Protons with Energies Greater Than 20 Mev from 90-Mev Neutrons on Carbon. Dotted lines: experimental results of Hadley and York [Phys. Rev. 80, 345 (1950)]; solid lines: calculated distribution.

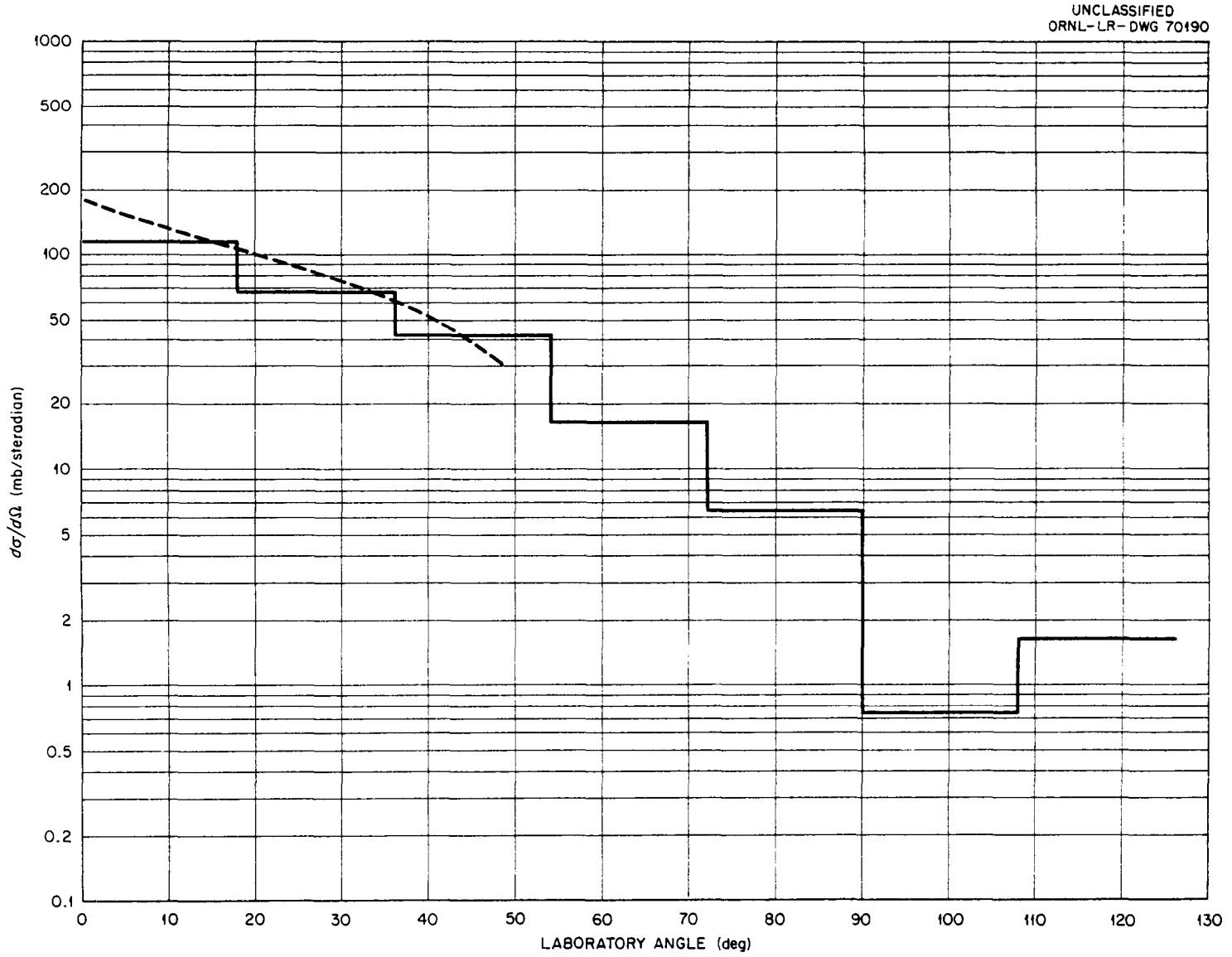

Fig. 27. Angular Distribution of Protons with Energies Greater Than 20 Mev from 90-Mev Neutrons on Copper. Dotted lines: experimental results of Hadley and York [Phys. Rev. 80, 345 (1950)]; solid lines: calculated distribution.

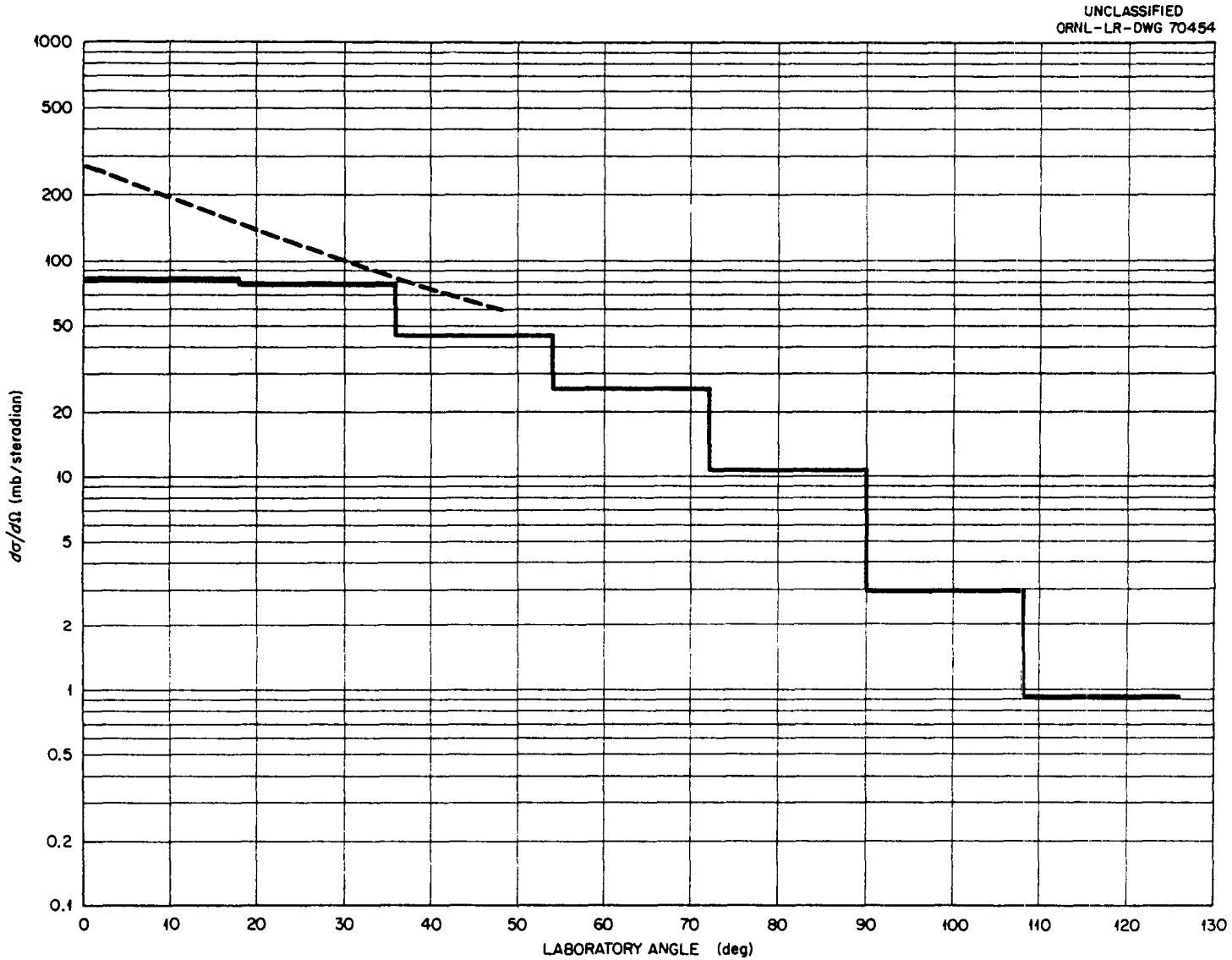

Fig. 28. Angular Distribution of Protons with Energies Greater Than 20 Mev from 90-Mev Neutrons on Lead. Dotted lines: experimental results of Hadley and York [Phys. Rev. 80, 345 (1950)]; solid lines: calculated distribution.

The calculations are compared with some experimental data on cascade particle multiplicities in Table 3. Although the agreement is not bad, the calculation does not predict the symmetry that was observed in the experiments for neutron-induced and proton-induced reactions.

Comparison with Experiment: Incident Pions

The comparison of calculated nonelastic cross sections for incident pions with experimental data is given in Table 4. The agreement is not quite so good as that for incident nucleons.

The energy spectra of nonelastically scattered pions into various angular intervals are shown in Figs. 29-33. The agreement is not bad although all the comparisons for these data are on a relative basis.

A discrepancy between the calculated data and experiments exists for nonelastic scattering at right angles and in the backward direction, as is illustrated in Figs. 34 and 35 for two different nuclear configurations. This discrepancy was observed when previous calculations of this type[9] were compared with the data obtained from use of a smaller radius nuclear model with a constant nucleon density.

The data from emulsion work are compared in Figs. 36 and 37; reasonable agreement is indicated. Other angular distributions are illustrated in Figs. 38-41. Here the calculation indicates the trends properly, but the agreement is not very good on an absolute basis.

The spectra from slow π^- absorption are compared with experimental results in Fig. 42 for a nucleus with a standard configuration and for one with a constant nucleon density distribution and a smaller nuclear radius ($r = 1.3 \times 10^{-13} A^{1/3}$). The agreement is fair and independent of nuclear configuration.

Calculated pion absorption and charge-exchange cross sections are compared with experimental values in Tables 5 and 6, respectively.

The agreement is reasonable for the absorption cross section but not very good for the charge-exchange cross section. This seems to be persistent and difficult to explain since the experiments imply a smaller cross section than the calculated values. However, the free-particle charge-exchange cross section is quite large.

In Table 7 the calculated and experimental charge-exchange plus absorption cross-section data are compared, and except for the last two entries the agreement is quite good.

Conclusions

This calculation seems to reproduce most of the experimental data for incident nucleons very well. The largest discrepancy is in the spectra of cascade particles emitted in the forward direction for small incident nucleon energies on light- to medium-weight nuclei.

Table 4. Calculated and Experimental Total Nonelastic Cross Sections for Pions Incident on Various Nuclei

Pion	Target	Energy (Mev)	Nonelastic Cross Section (mb)	
			Calculated[a]	Experimental
π^+	Li	195	324 ± 10	226 ± 18[b]
	C	185	455 ± 11	325 ± 26[b]
		270	358 ± 10	$296 \begin{smallmatrix}+35\\-28\end{smallmatrix}$[c]
	Pb	50	1563 ± 26	1620[d]
π^-	C	125	458 ± 11	308 ± 43[e]
		150	478 ± 11	430 ± 42[f]
		225	423 ± 11	346 ± 21[g]
	Al	225	653 ± 14	596 ± 30[g]
	Cu	225	1038 ± 19	1058 ± 45[g]
	Sn	225	1471 ± 20	1550 ± 70[g]
	Pb	125	2062 ± 29	2477 ± 385[e]
		150	2145 ± 29	2490 ± 160[f]
		225	1993 ± 29	2290 ± 90[g]

a. Errors indicated apply for a confidence coefficient of 68%.

b. N. I. Petrov, U. G. Ivanov, and U. A. Rusakov, Soviet Phys. -JETP (English Transl.) 10, 682 (1960).

c. W. Kan Chang et al., Soviet Phys. - JETP (English Transl.) 8, 625 (1959).

d. Calculated from the mean free path in nuclear matter given by G. Saphir, Phys. Rev. 104, 535 (1956).

e. J. O. Kessler and L. M. Lederman, Phys. Rev. 94, 689 (1954).

f. R. H. Miller, Nuovo Cimento 6, 882 (1957).

g. V. G. Ivanov et al., Soviet Phys. - JETP (English Transl.) 4, 922 (1957).

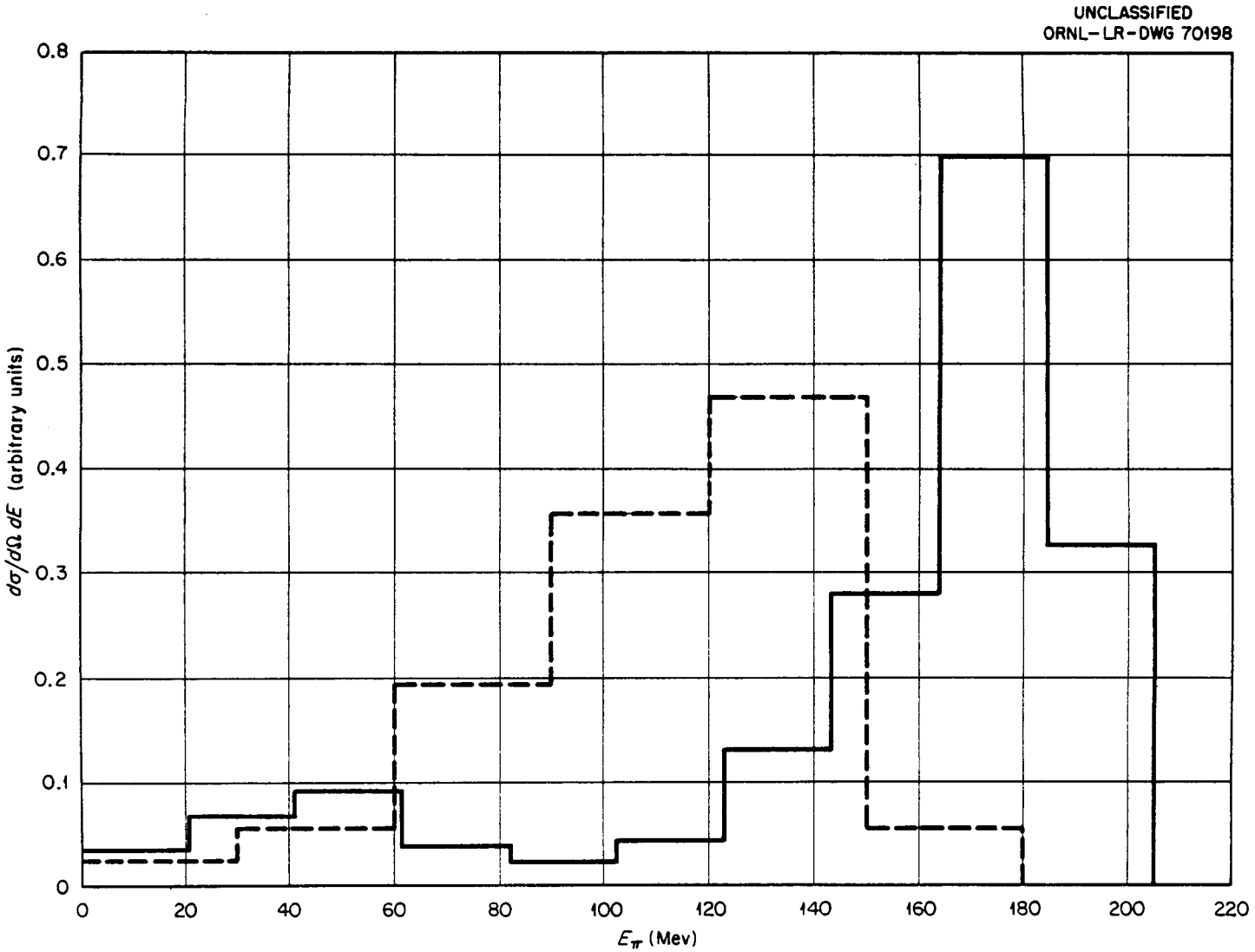

Fig. 29. Energy Spectra of Nonelastic π^+ Emitted in the Angular Interval 0 to 60° from 195-Mev π^+ on Lithium and Carbon. Dotted lines: experimental results of Petrov et al. [Soviet Phys. JETP (English Trans.) 10, 682 (1960)]; solid lines: calculated spectrum; ordinate units are arbitrary.

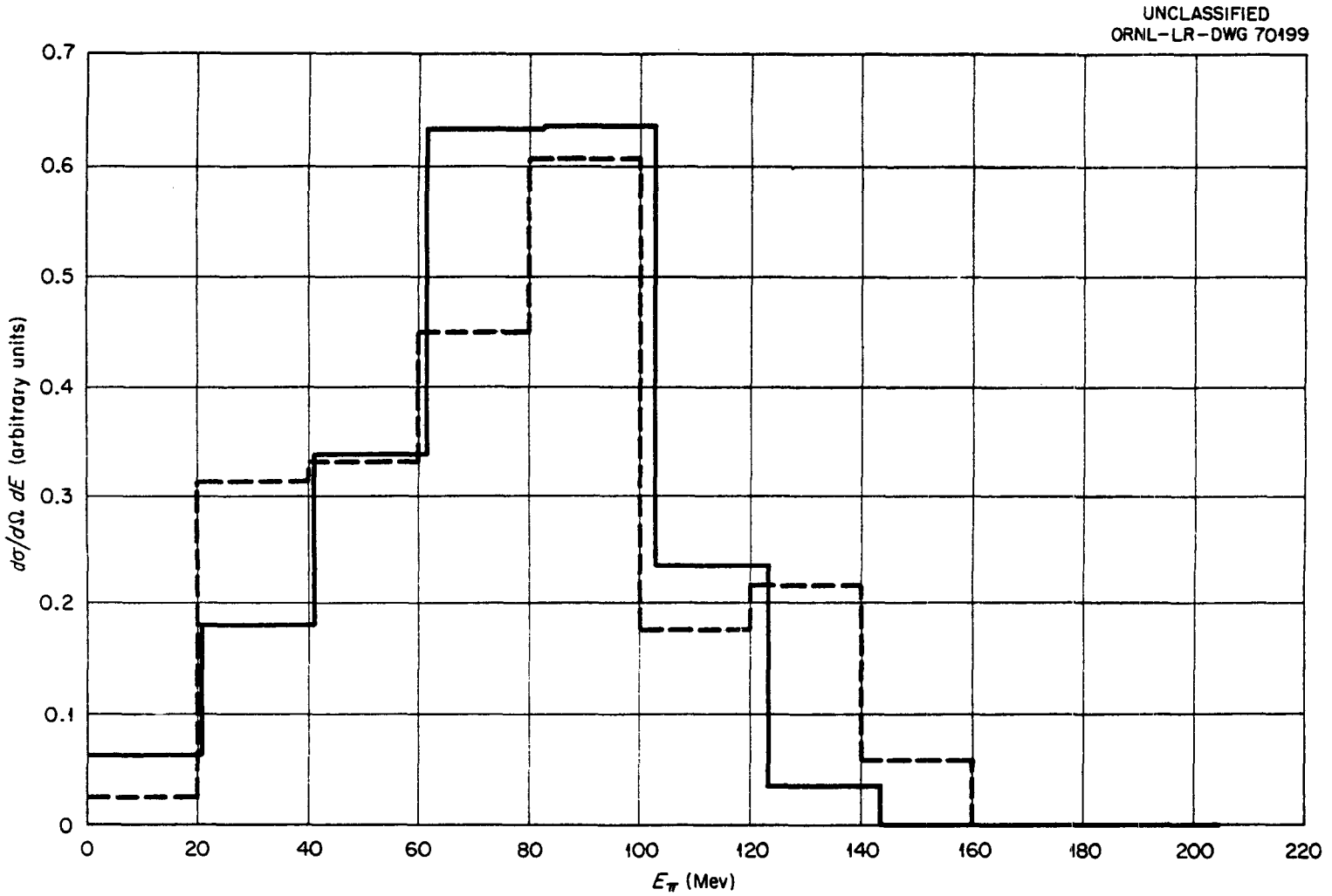

Fig. 30. Energy Spectra of Nonelastic π^+ Emitted in the Angular Interval 120 to 180° from 195-Mev π^+ on Lithium and Carbon. Dotted lines: experimental results of Petrov et al. [Soviet Phys. JETP (English Transl.) 10, 682 (1960)]; solid lines: calculated spectrum. Ordinate units are arbitrary.

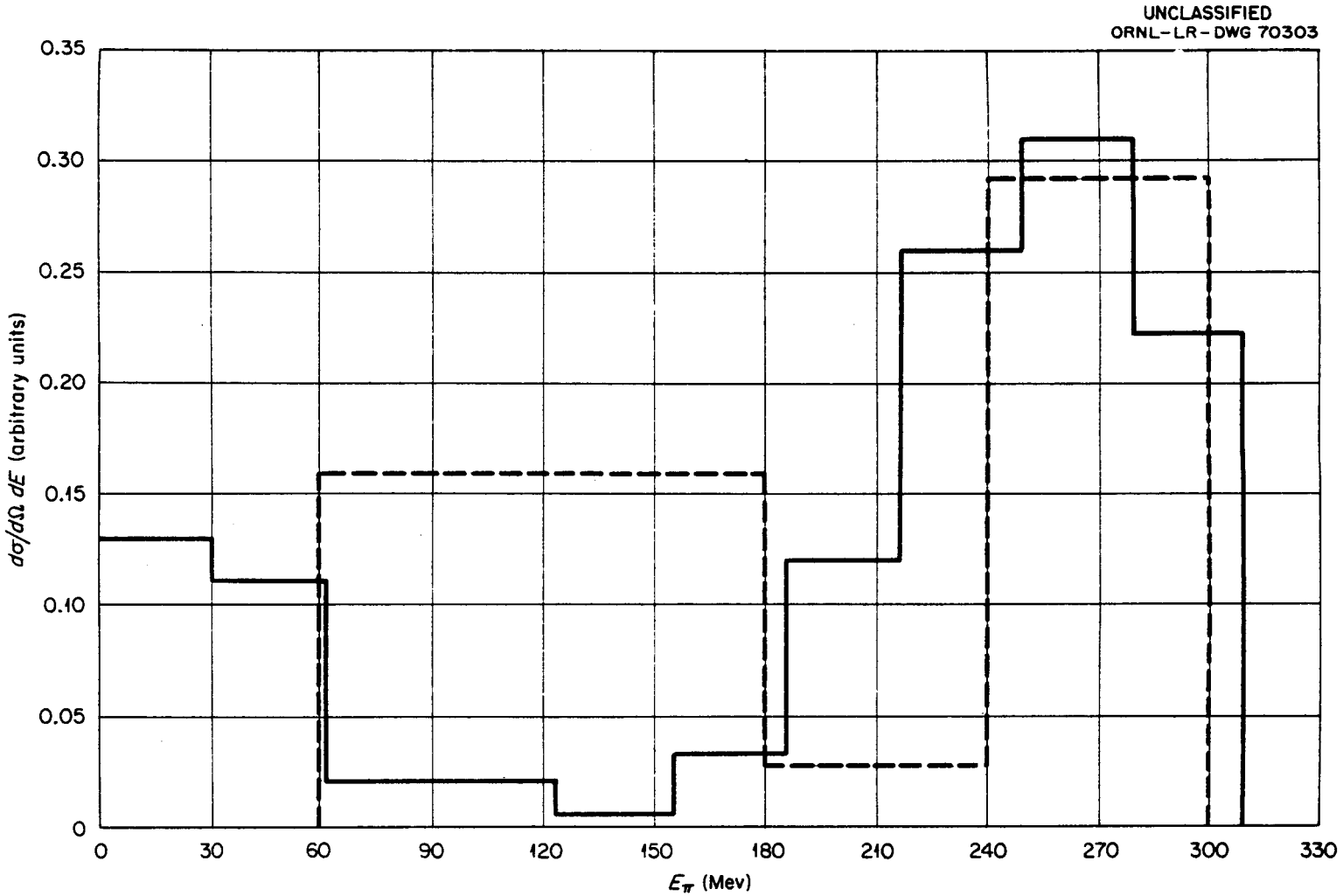

Fig. 31. Energy Spectra of Nonelastic π^- Emitted in the Angular Interval 0 to 60° from 300-Mev π^- on Heavy-Emulsion Nuclei. Dotted lines: experimental values of Willot-Chemel [Ann. Phys. (Paris) 6, 703 (1961)]; solid lines: calculated values for 300-Mev π^- on Ru^{100}.

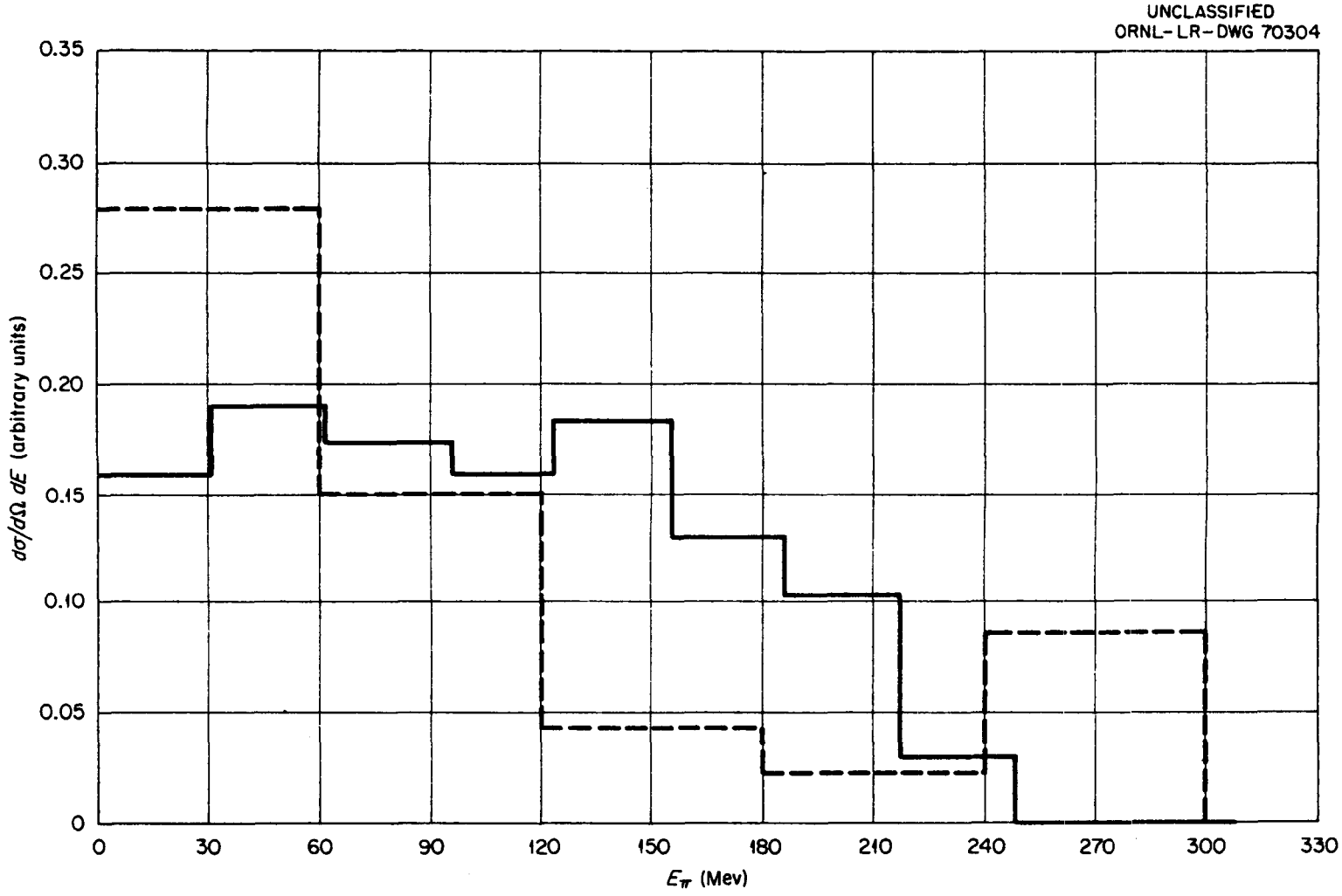

Fig. 32. Energy Spectra of Nonelastic π^- Emitted in the Angular Interval 60 to 120° from 300-Mev π^- on Heavy-Emulsion Nuclei. Dotted lines: experimental values of Willot-Chemel [Ann. Phys. (Paris) 6, 703 (1961)]; solid lines: calculated values for 300-Mev π^- on Ru^{100}.

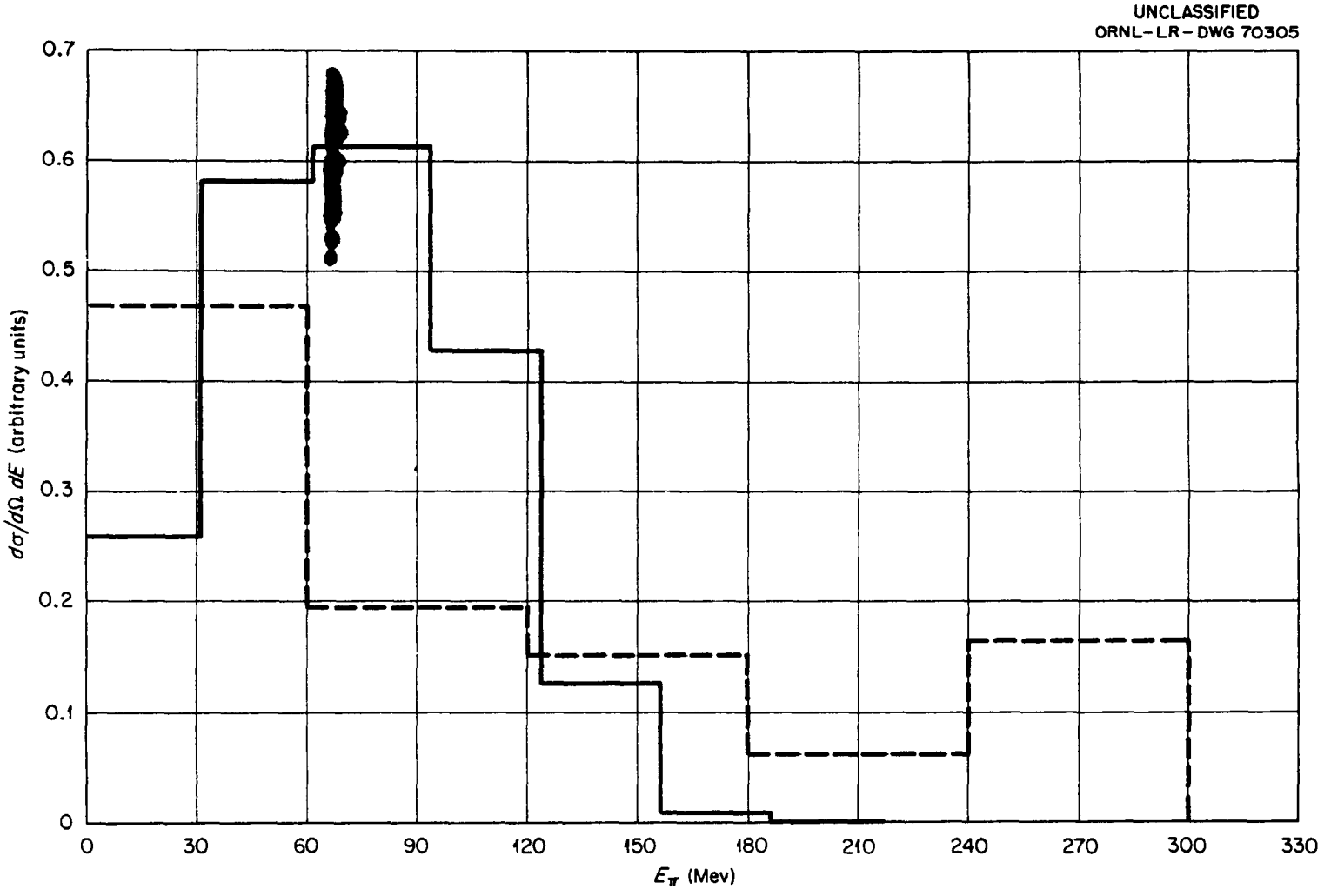

Fig. 33. Energy Spectra of Nonelastic π^- Emitted in the Angular Interval 120 to 180° from 300-Mev π^- on Heavy-Emulsion Nuclei. Dotted lines: experimental values of Willot-Chemel [Ann. Phys. (Paris) 6, 703 (1961)]; solid lines: calculated values for 300-Mev π^- on Ru^{100}.

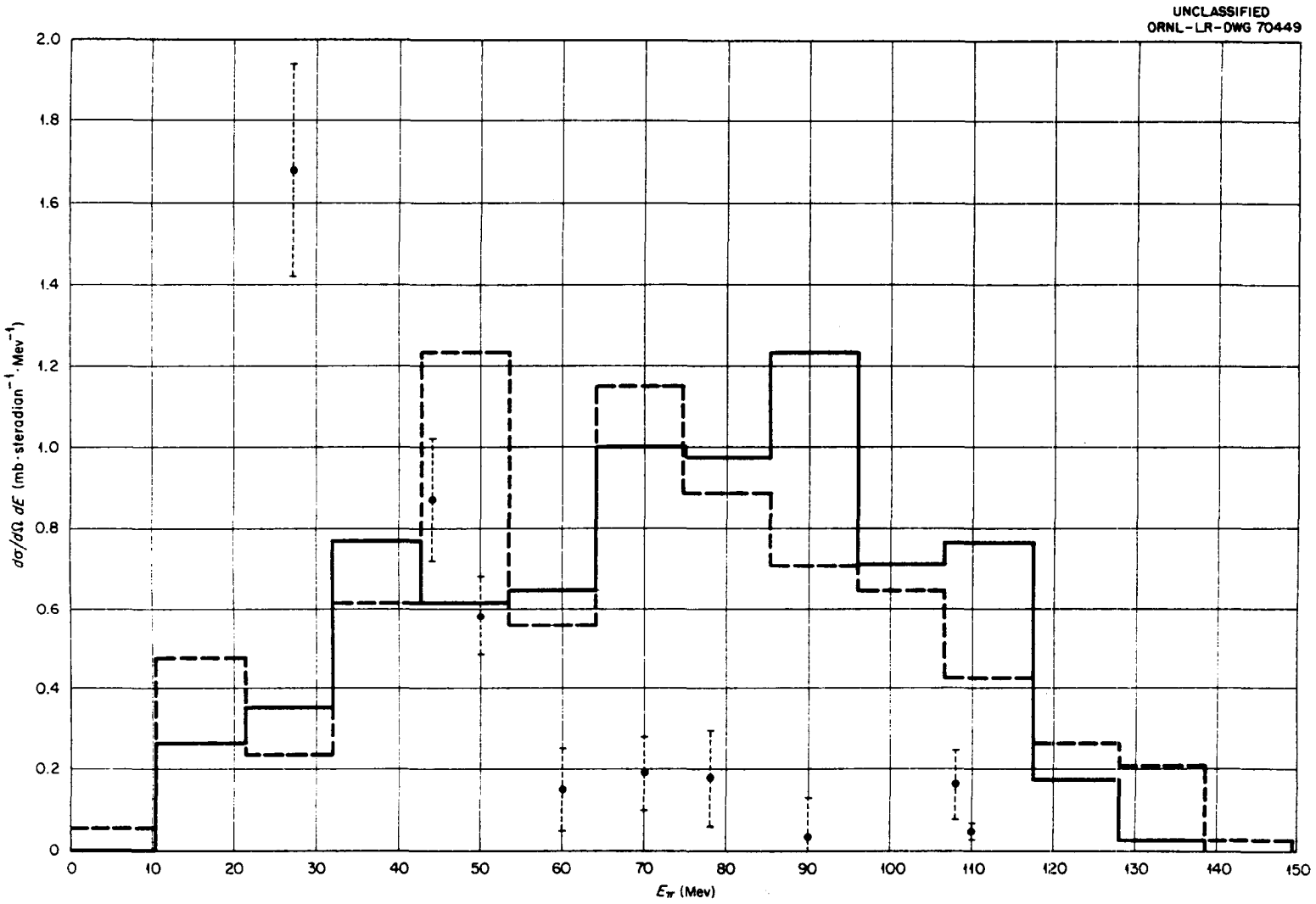

Fig. 34. Nonelastic π^- Spectra at 90° from 150-Mev π^- on Lead. Calculated spectra for π^- in the interval 78 to 102° for nucleus with medium radius. Solid lines: nonuniform nucleon density distribution within the nucleus; dotted lines: uniform density distribution; circles: Miller's experimental values [Nuovo Cimento 6, 882 (1957)].

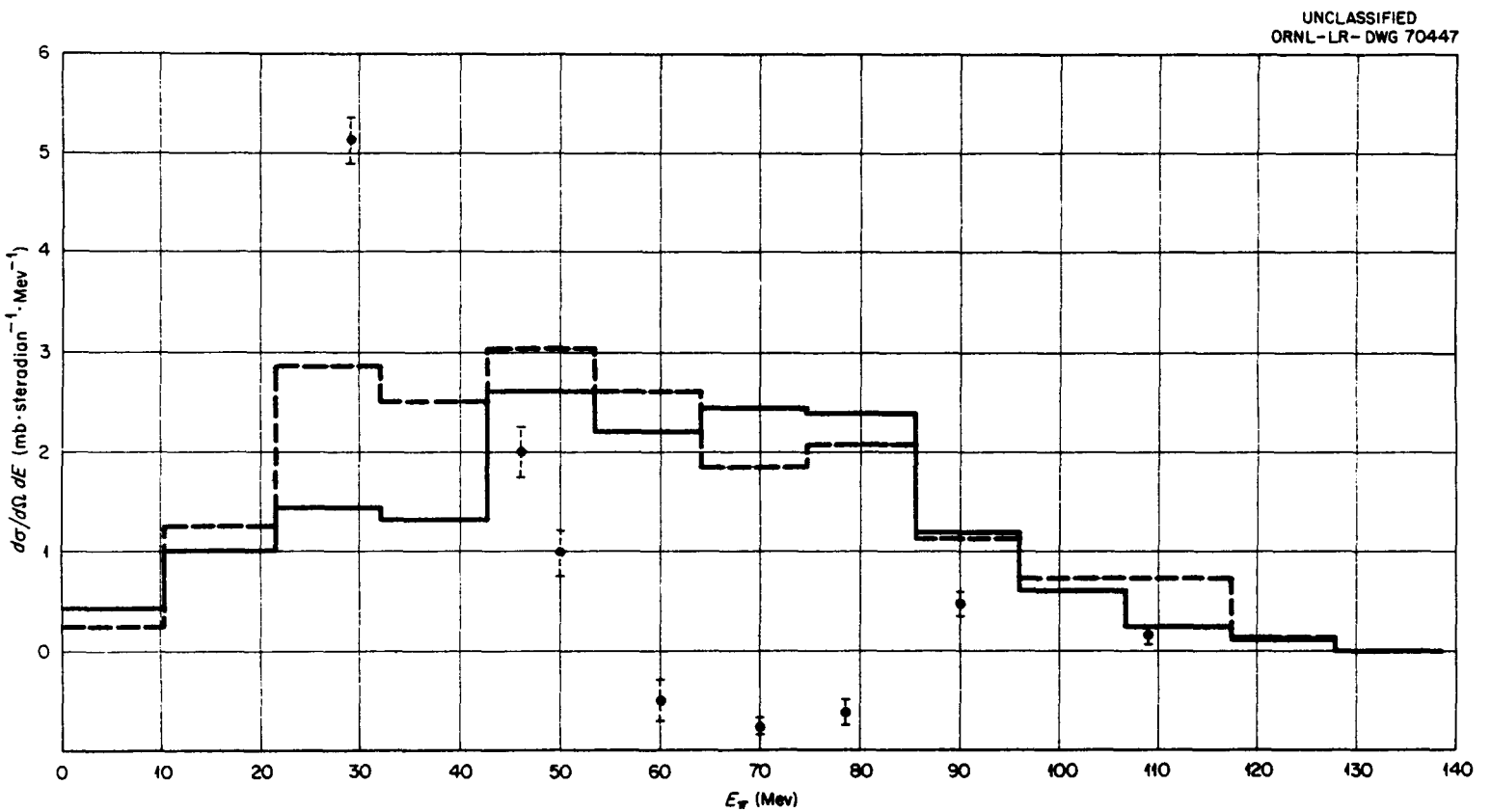

Fig. 35. Nonelastic π^- Spectra at 138° from 150-Mev π^- on Lead. Calculated spectra for π^- in the interval 130 to 148° for nucleus with medium radius. Solid lines: nonuniform nucleon density distribution within the nucleus; dotted lines: uniform density distribution; circles: Miller's experimental values [Nuovo Cimento 6, 882 (1957)].

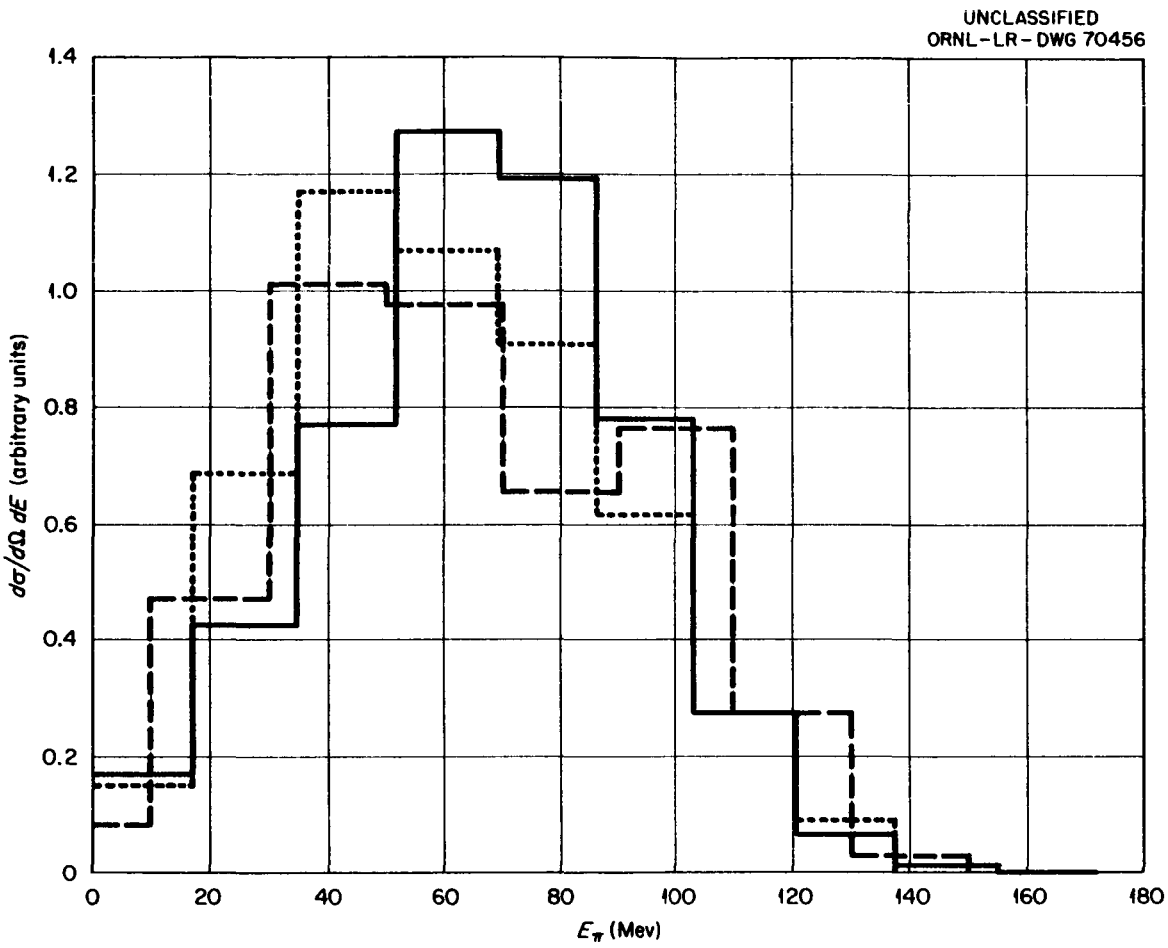

Fig. 36. Nonelastic Spectrum for π^- Emitted Into the Backward Hemisphere from 162-Mev π^- on Heavy-Emulsion Nuclei. Calculated values are for 162-Mev π^- on Ru^{100} with a medium nuclear radius. Solid lines: nonuniform nucleon density distribution within the nucleus; dashed lines: uniform nucleon density distribution; dotted lines: experimental results of Nikolskii et al. [Soviet Phys. JETP (English Transl.) 5, 93 (1957)]; ordinate units are arbitrary.

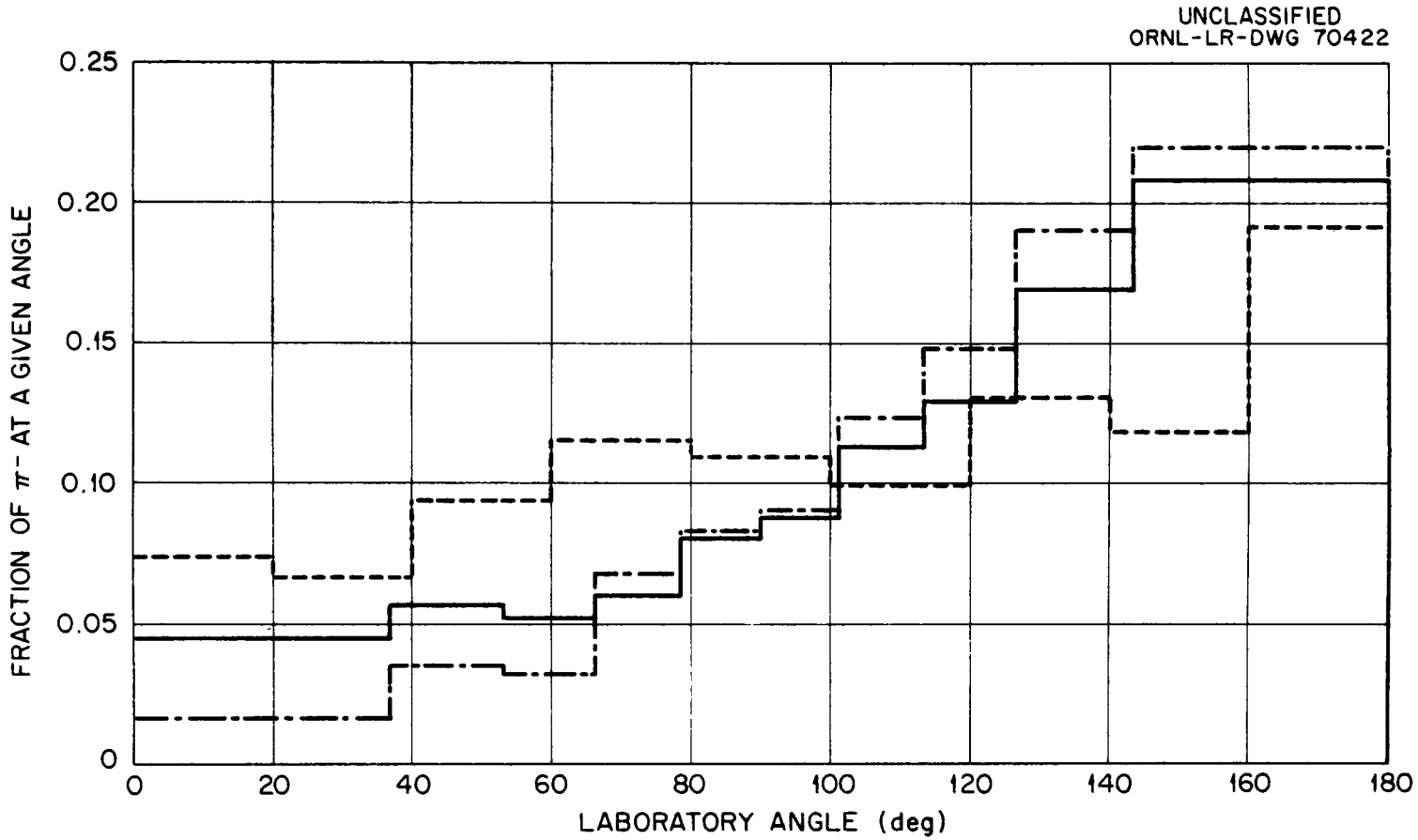

Fig. 37. Angular Distribution of Nonelastic π^- from 162-Mev π^- on Heavy-Emulsion Nuclei. Calculated distribution for nucleus with medium radius. Dotted lines: experimental values of Nikolskii et al. [Soviet Phys. -JETP (English Transl.) 5, 93 (1957)]; solid lines: calculated spectra for a nonuniform nucleon density distribution within the nucleus; dash-dot lines: uniform nucleon density distribution.

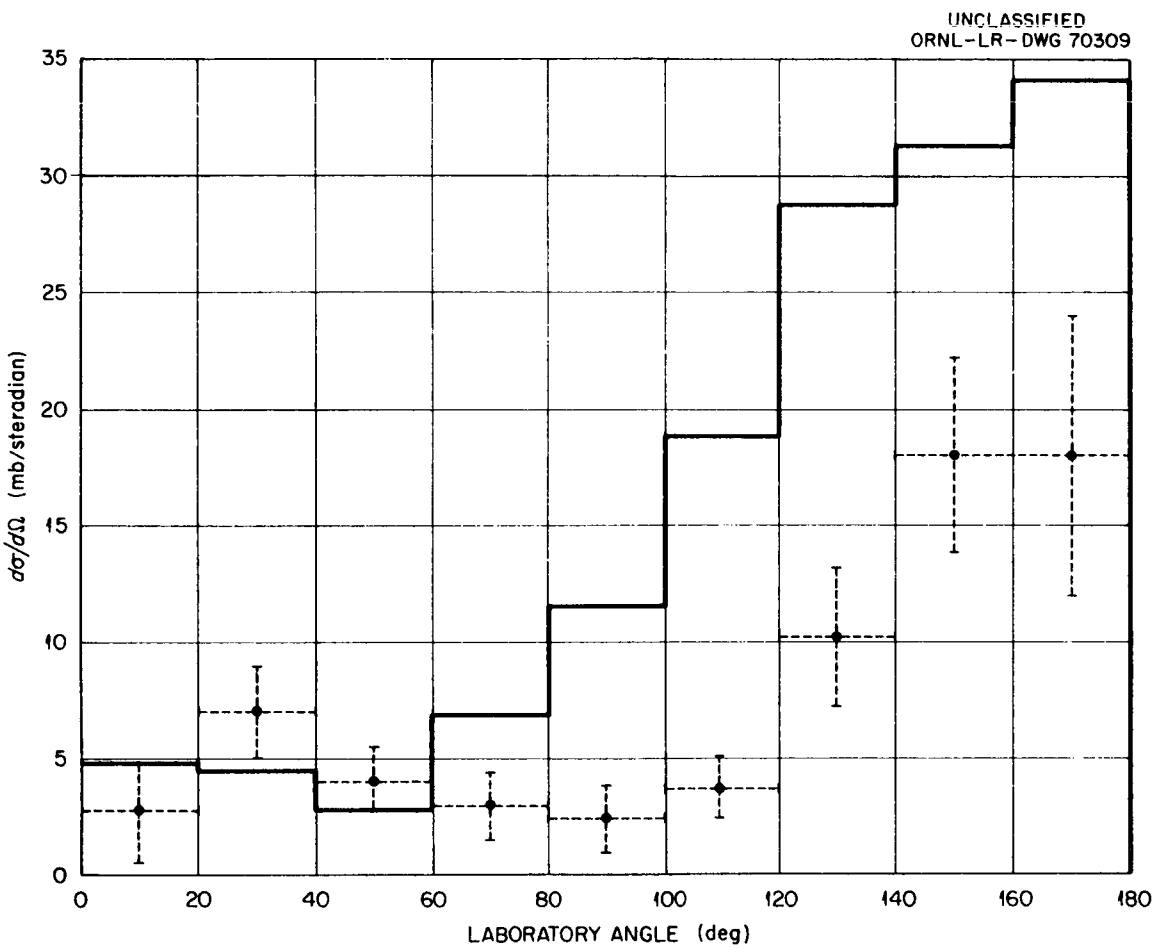

Fig. 38. Angular Distribution of Nonelastic π^- Scattered with Energy Loss Greater than 40 Mev for 125-Mev π^- on Carbon. Circles: experimental values of Kessler and Lederman [Phys. Rev. 94, 689 (1954)]; solid lines: calculated distribution.

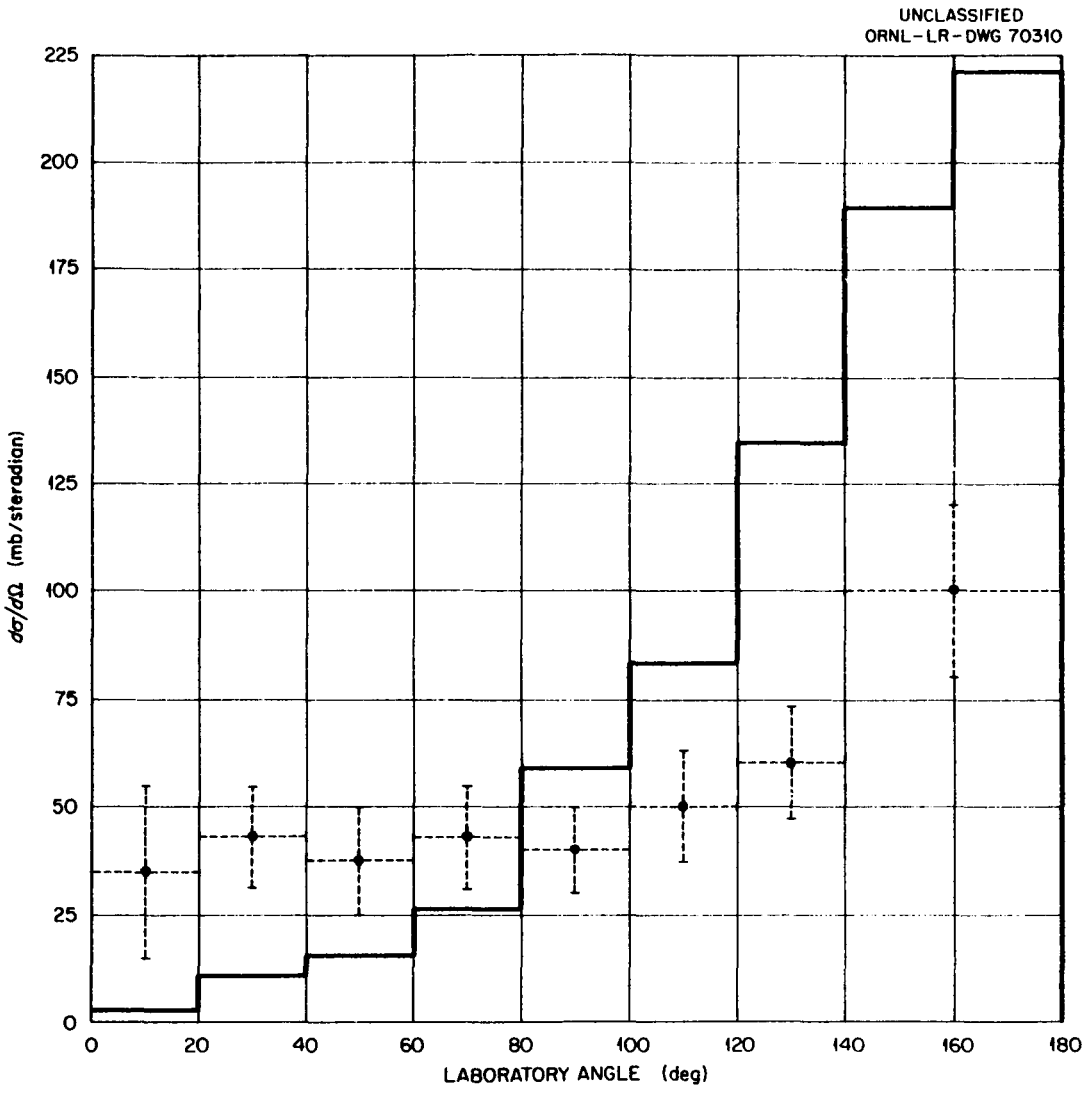

Fig. 39. Angular Distribution of Nonelastic π^- Scattered with Energy Loss Greater Than 40 Mev for 125-Mev π^- on Lead. Circles: experimental values of Kessler and Lederman [Phys. Rev. 94, 689 (1954)]; solid lines: calculated distribution.

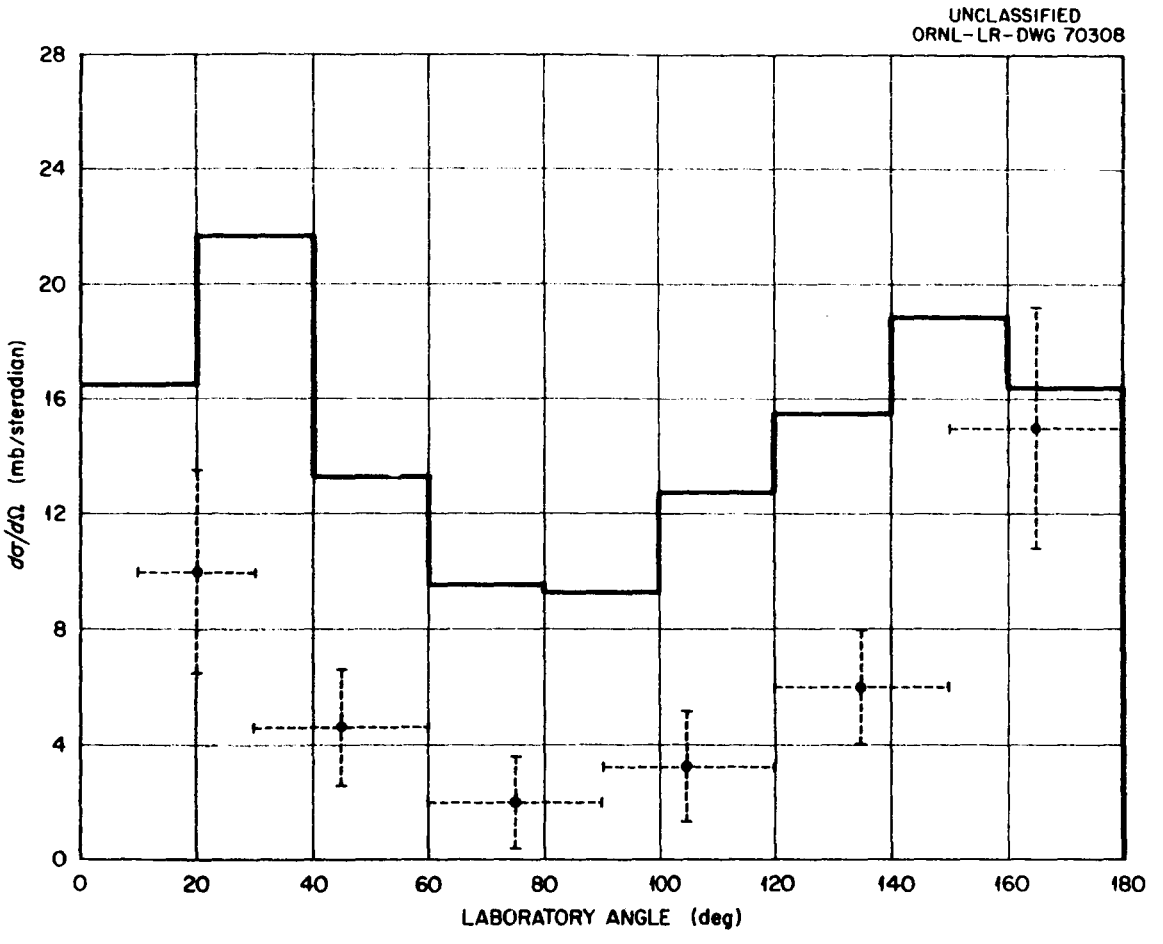

Fig. 40. Angular Distribution of Nonelastic π^+ from 195-Mev π^+ on Lithium. Circles: experimental values of Petrov et al. [Soviet Phys. -JETP (English Transl.) 10, 682 (1960)]; solid lines: calculated π^+ spectrum reduced by the ratio of the experimental to the calculated total nonelastic cross section.

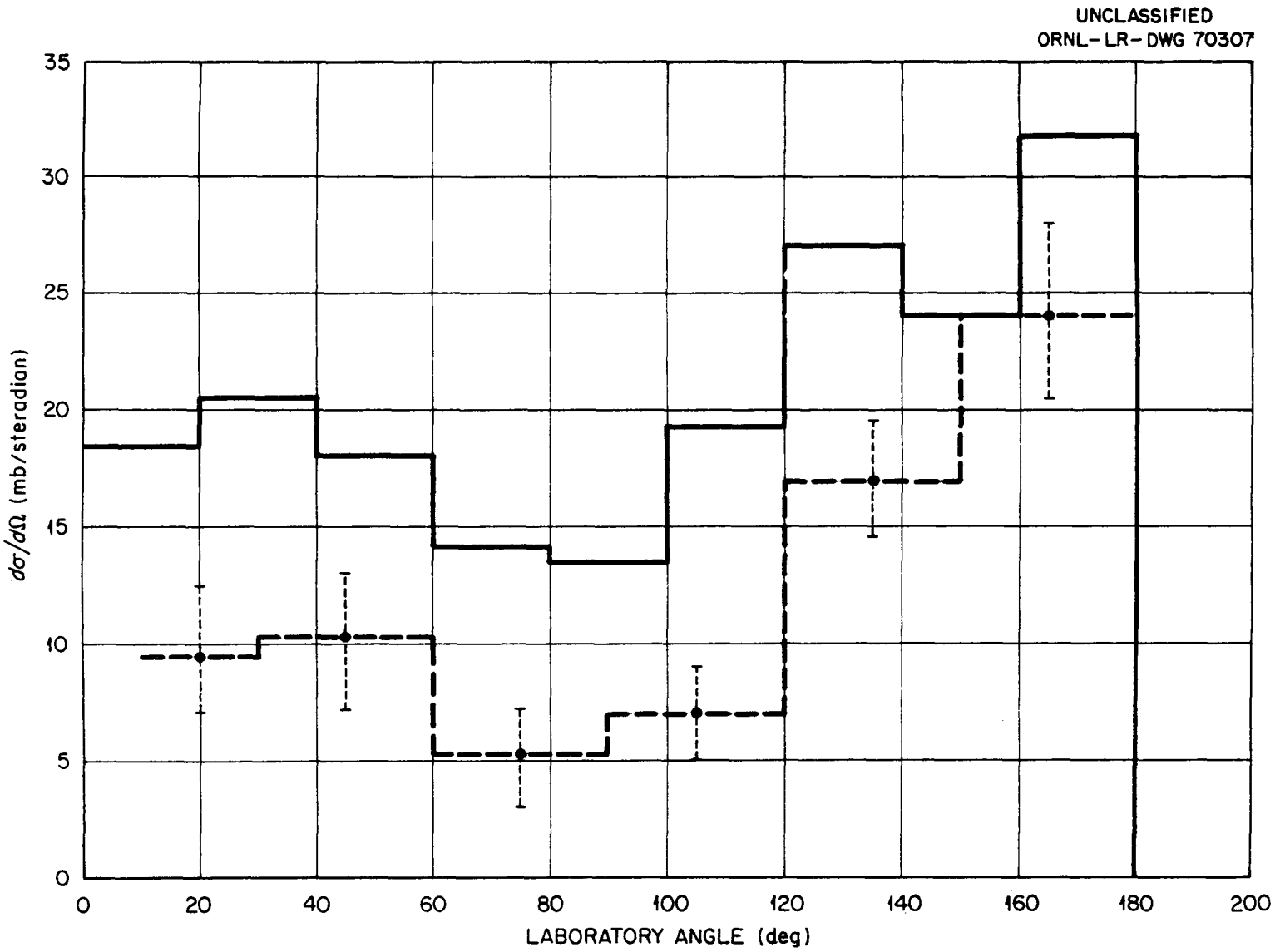

Fig. 41. Angular Distribution of Nonelastic π^+ from 195-Mev π^+ on Carbon. Circles: experimental values of Petrov et al. [Soviet Phys. JETP (English Transl.) 10, 682 (1960)]; solid lines: calculated spectrum.

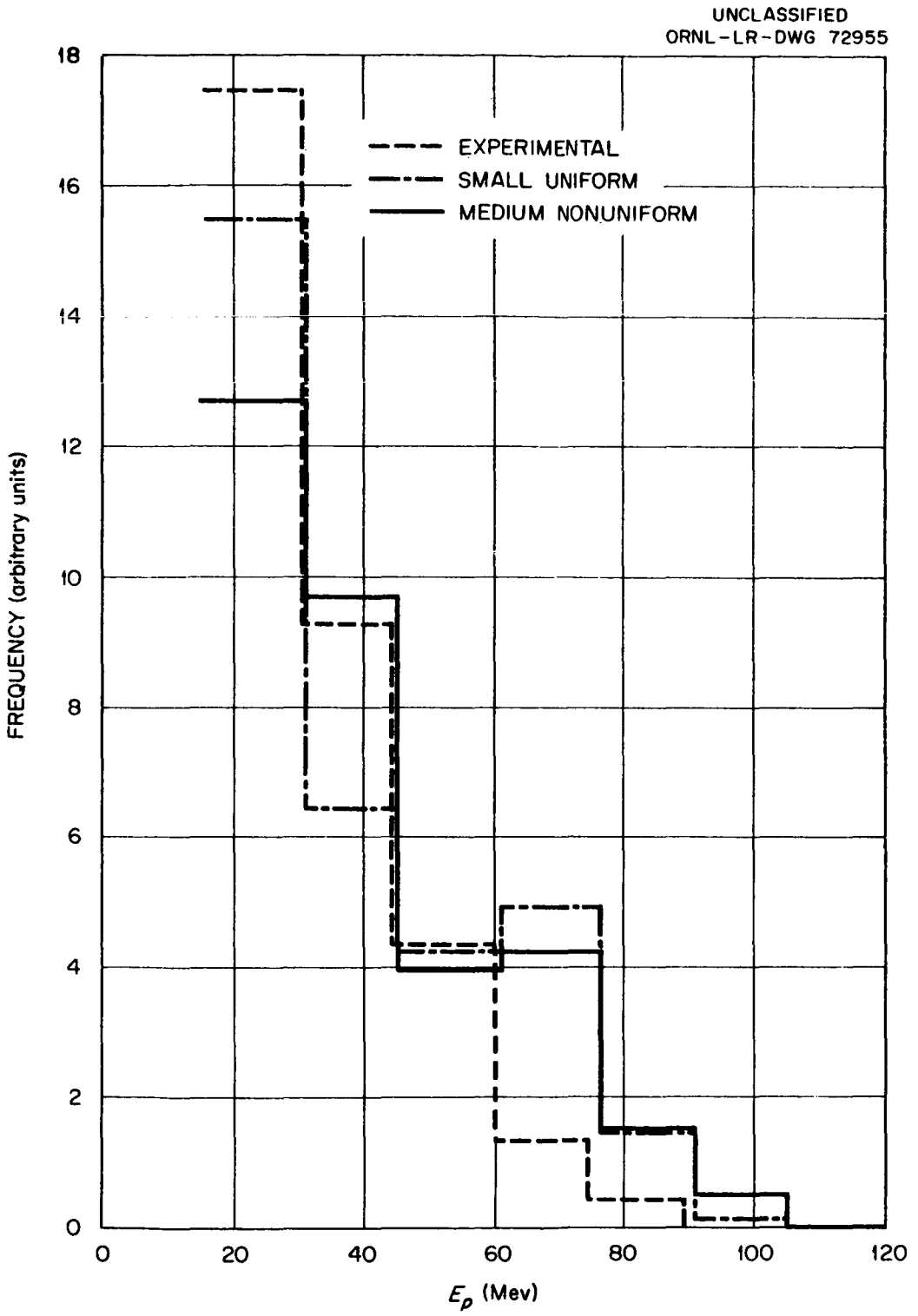

Fig. 42. Energy Spectra of Protons with Energies Greater Than 15 Mev for Slow π^- Absorption on Heavy-Emulsion Nuclei. Calculated values are for 1-Mev π^- on Ru^{100}. Solid lines: calculated spectrum for medium nonuniform nuclear configuration; dash-dot lines: calculated spectrum for small uniform configuration; dotted lines: experimental results of Azimov et al. [Soviet Phys. JETP (English Transl.) 4, 632 (1957)]; ordinate units are arbitrary.

Table 5. Calculated and Experimental Absorption Cross Sections for Pions Incident on Beryllium

Pion	Energy (Mev)	Cross Section (mb)	
		Calculated	Experimental[a]
π^+	20	58	56 ± 9
π^+	30	63	74 ± 13
π^+	40	67	96 ± 20

a. F. H. Tenney and J. Tinlot, Phys. Rev. 92, 974 (1953).

Table 6. Calculated and Experimental Charge-Exchange Cross Sections for Pions Incident on Lead and Carbon

Pion	Target	Energy (Mev)	Cross Section (mb)	
			Calculated	Experimental
π^+	Pb	50	206	27 ± 19[a]
π^-	C	125	61	$20 \begin{smallmatrix} + 20 \\ - 10 \end{smallmatrix}$[b]
π^-	Pb	125	215	$100 \begin{smallmatrix} + 80 \\ - 40 \end{smallmatrix}$[b]

a. G. Saphir, Phys. Rev. 104, 535 (1956).

b. J. O. Kessler and L. M. Lederman, Phys. Rev. 94, 689 (1954).

Table 7. Calculated and Experimental Charge-Exchange Plus Absorption Cross Sections for Pions Incident on Various Nuclei

Pion	Target	Energy (Mev)	Cross Section (mb)	
			Calculated	Experimental
π^+	Li	195	142	164 ± 16[a]
π^+	C	78	174	195 ± 20[b]
		195	205	203 ± 22[a]
		270	146	$165 \begin{smallmatrix} + 34 \\ - 22 \end{smallmatrix}$[c]
π^+	Pb	50	930	880 ± 73[d]
π^-	C	125	206	220 ± 40[e]
		150	209	192 ± 34[f]
	Pb	125	923	1840 ± 350[e]
		150	957	380 ± 310[f]

a. N. I. Petrov, V. G. Ivanov, and V. A. Rusakov, Soviet Phys. JETP (English Transl.) 10, 682 (1960).

b. R. G. Sulukvadze and D. Neagu, Soviet Phys. JETP (English Transl.) 14, 59 (1962).

c. W. Kan Chang et al., Soviet Phys. JETP (English Transl.) 8, 625 (1959).

d. G. Saphir, Phys. Rev. 104, 535 (1956).

e. J. O. Kessler and L. M. Lederman, Phys. Rev. 94, 689 (1954).

f. R. H. Miller, Nuovo Cimento 6, 882 (1957).

The data for incident pions appear to represent the gross features of the experimental data, but they can not be used to predict detailed experimental data as well as the results for incident nucleons.

Compilation of Reactions Calculated for Particles With Energies from About 50 to 350 Mev

The completion of the intranuclear cascade code makes it possible to calculate a vast quantity of data on nuclear reactions. These data are expected to be of value for all problems involving radiation from nucleons or pions in the energy range from about 50 to 350 Mev. A compilation of the data is under way and should be completed within the next three or four months.

The cases to be calculated are as follows: incident neutrons and protons with energies at 25, 50, 100, 150,...400 Mev on C^{12}, O^{16}, Al^{27}, Cr^{52}, Cu^{65}, Ru^{100}, Ce^{140}, W^{184}, Pb^{207}, and U^{238}; and incident π^+ and π^- on the same element with energies at the same intervals but extending only to 300 Mev. The calculation is valid at higher energies for incident nucleons than it is for pions because pion production for incident nucleons, which is ignored in the calculation, takes place at higher energies. The end points in the energy ranges to be used are probably beyond the limits of validity of the calculation but are included for purposes of extrapolation.

The compilation will consist mainly of tables and graphs of data from representative cases. The data for the remaining cases will be available on request. The work will include results from the cascade process alone, from the evaporation process alone,[10] and from the combined processes.

As a reminder, the cascade calculation is based on the assumption that high-energy nuclear reactions can be treated as though the interactions occur on a particle-particle basis within the nucleus. When the particle energy becomes small ($\lambda \rightarrow$ large), this assumption is no longer valid, and the reaction is assumed to be represented by the de-excitation of a highly excited nucleus, which occurs by the evaporation or "boil-off" of nucleons. In the calculations this transition is abrupt and occurs at a somewhat arbitrary energy -- the cutoff energy of the cascade calculation. However, neither the total nucleon multiplicities nor the combined cascade and evaporation spectra are very sensitive to this cutoff energy, as is illustrated in Figs.43-49. The cutoff energies used in the calculations are 1.6 Mev for Al^{27}, 4.2 Mev for Ru^{100}, and 6.7 Mev for Pb^{208}. The lower limit of the proton spectra for lead, Fig.49, is determined by the cascade cutoff energy because there is very little proton evaporation. The correct spectra would drop rapidly for energies smaller than the coulomb barrier; so some care must be exercised in using the data for similar cases. The combined neutron spectrum is illustrated in Fig.46 for Ru^{100} only since it is very similar to those for Al^{27} and Pb^{208}.

---

10. L. Dresner, EVAP - A Fortran Program for Calculating the Evaporation of Various Particles from Excited Compound Nuclei, ORNL CF-61-12-30 (Dec. 19, 1961).

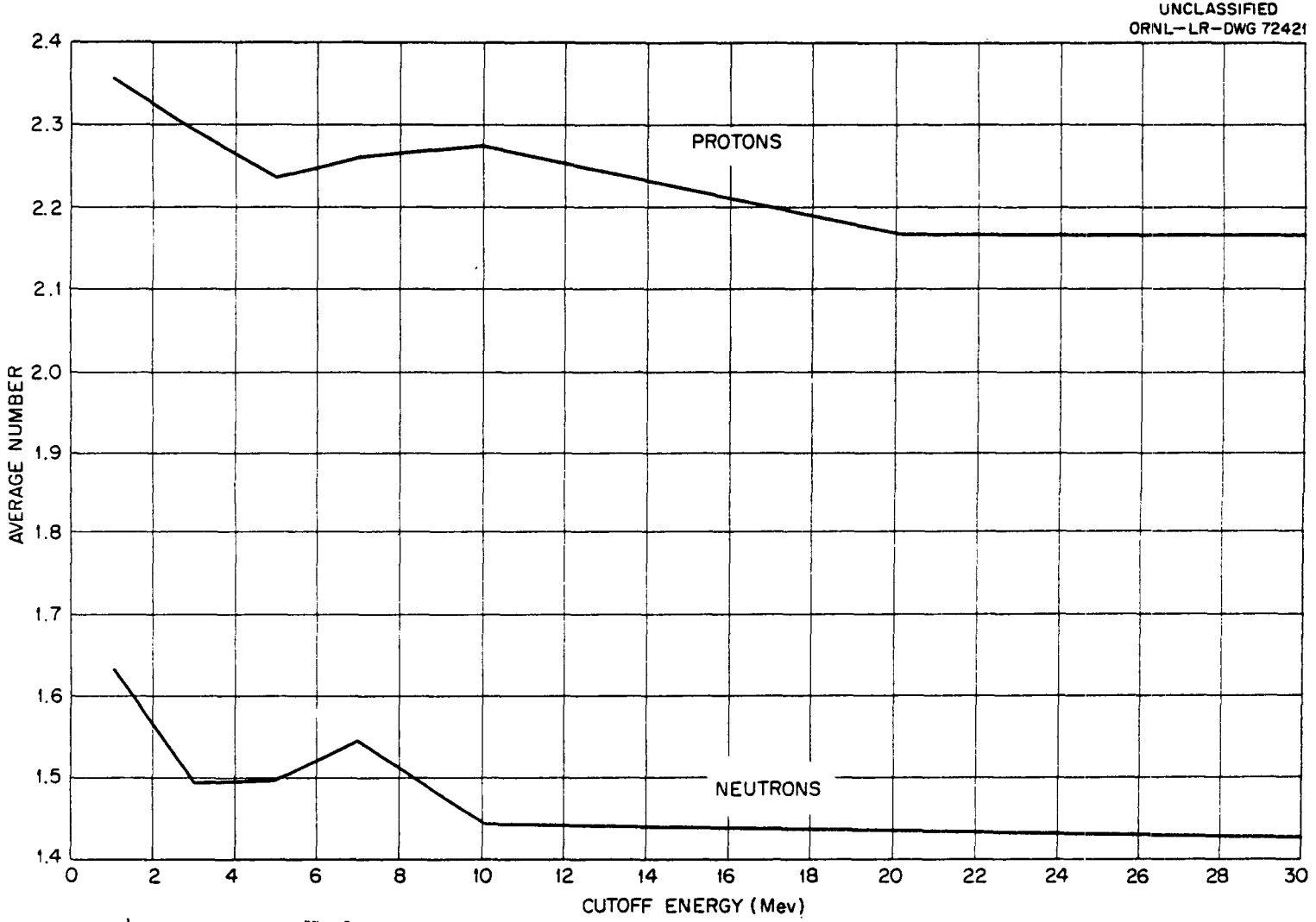

Fig. 43. Average Number of Cascade and Evaporation Protons and Neutrons vs Cutoff Energy for 150-Mev Protons on Al^{27}.

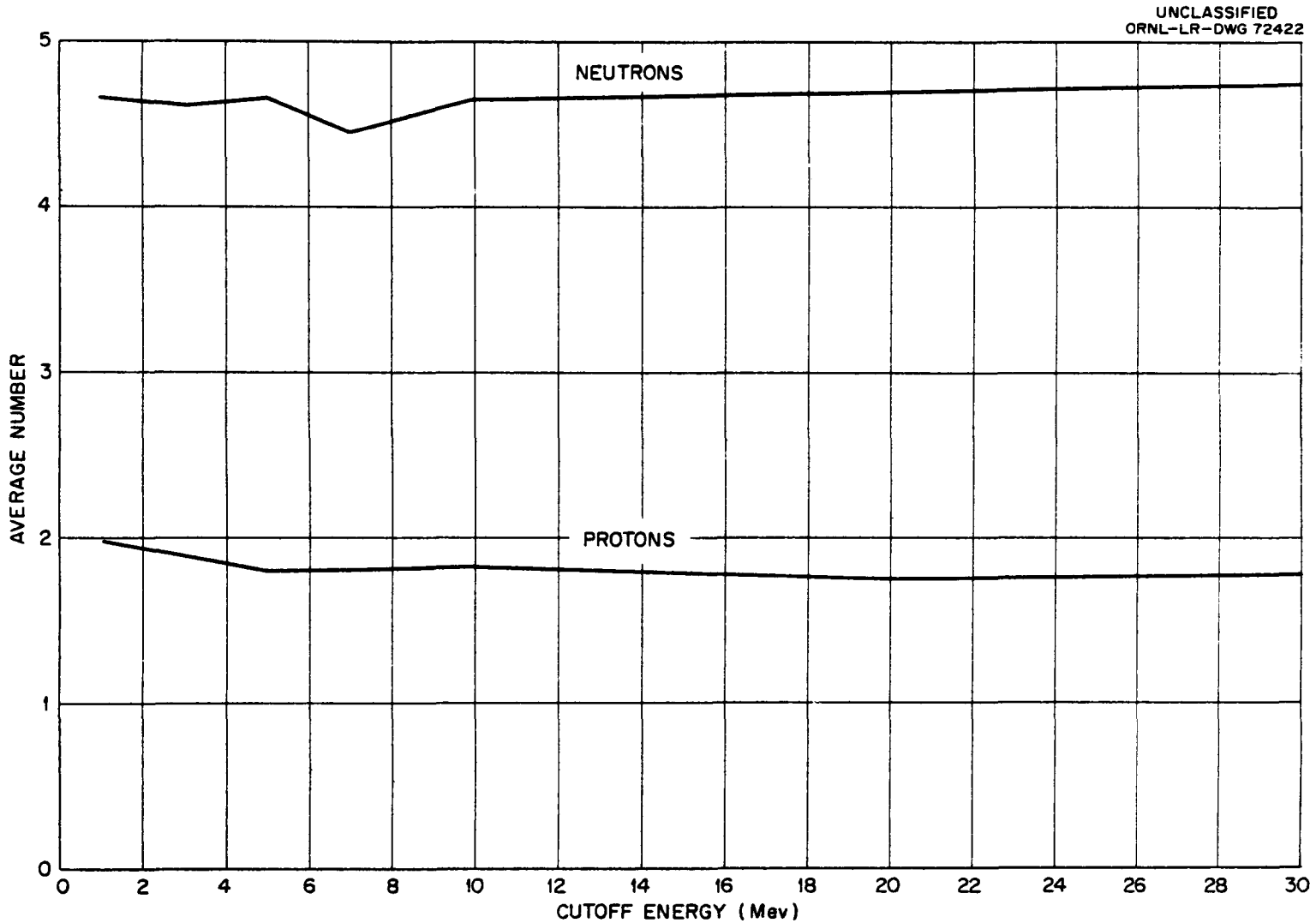

Fig.44. Average Number of Cascade and Evaporation Protons and Neutrons vs Cutoff Energy for 150-Mev Protons on Ru^{100}.

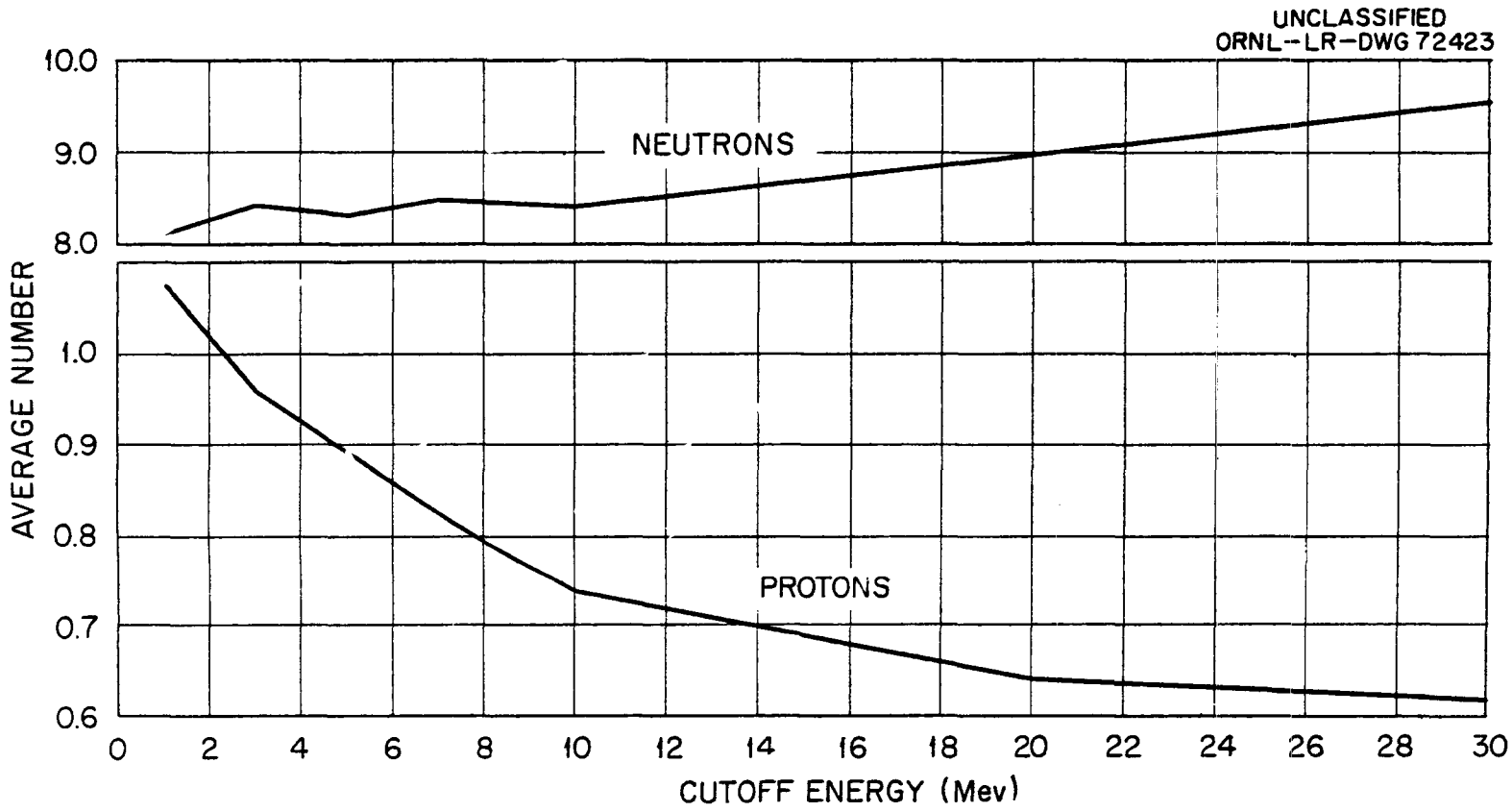

Fig.45. Average Number of Cascade and Evaporation Protons and Neutrons vs Cutoff Energy for 150-Mev Protons on $_{82}Pb^{208}$.

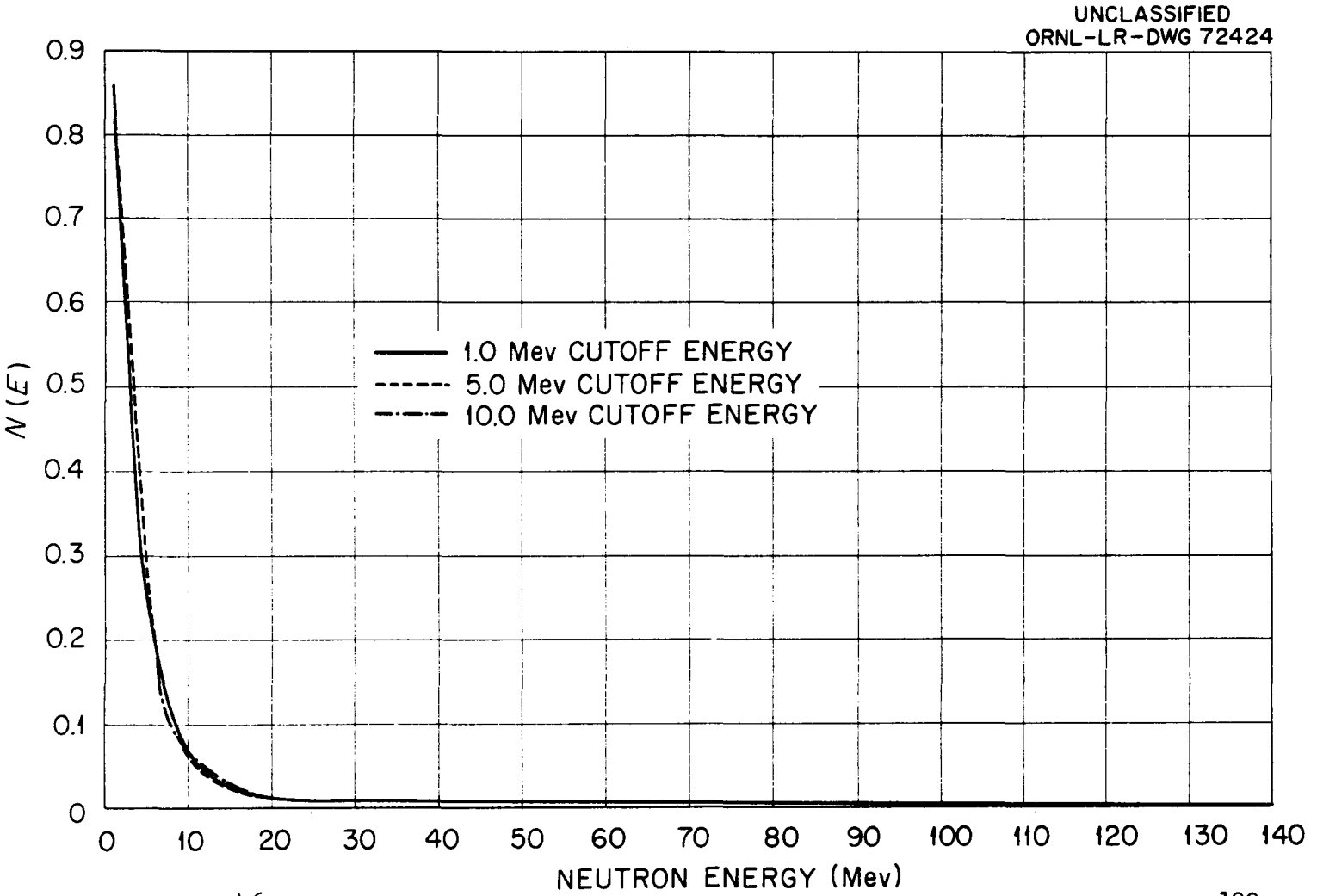

Fig. 46. Cascade and Evaporation Neutron Spectra for 150-Mev Protons on Ru^{100}.

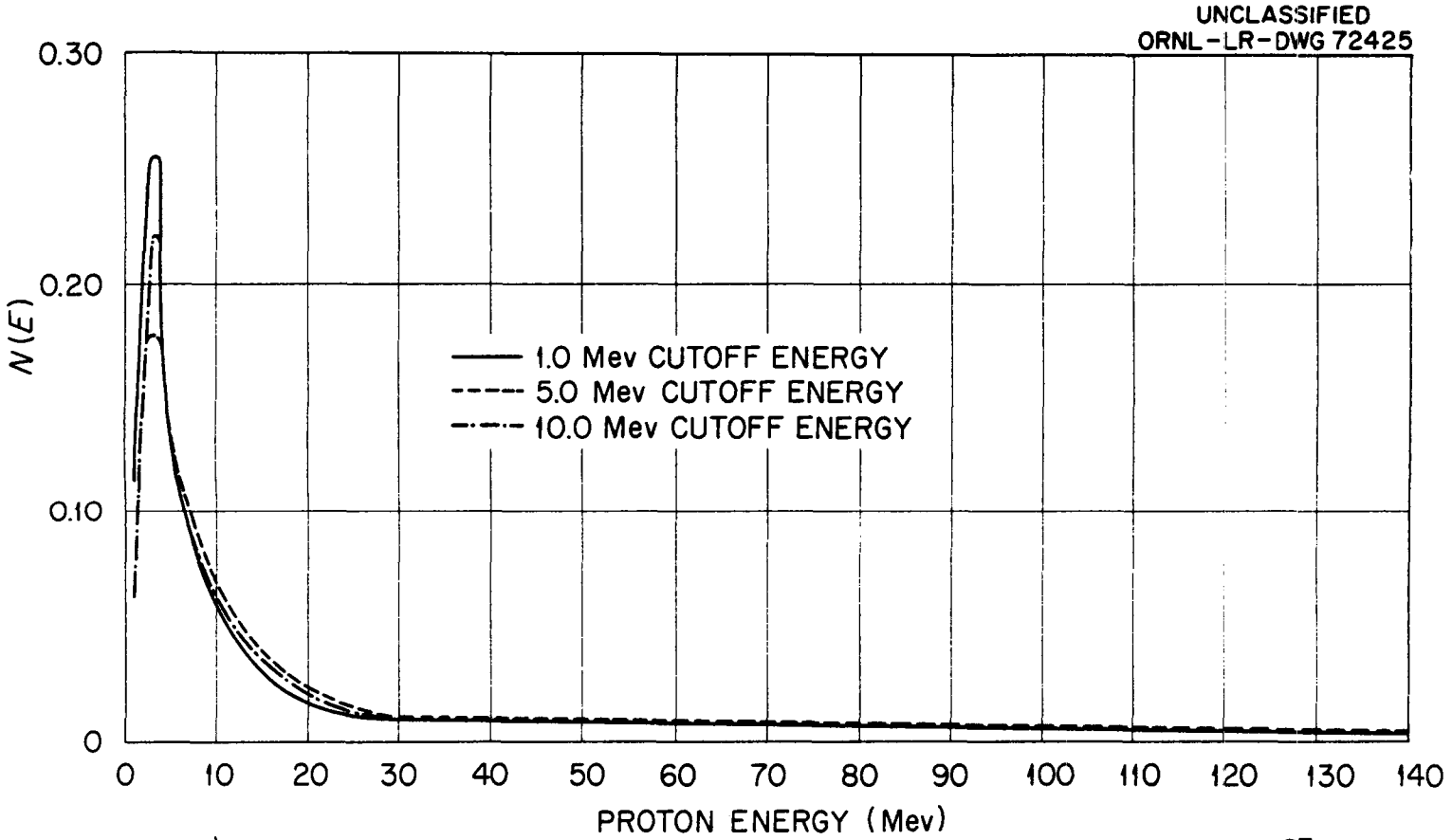

Fig. 47. Cascade and Evaporation Proton Spectra for 150-Mev Protons on Al^{27}.

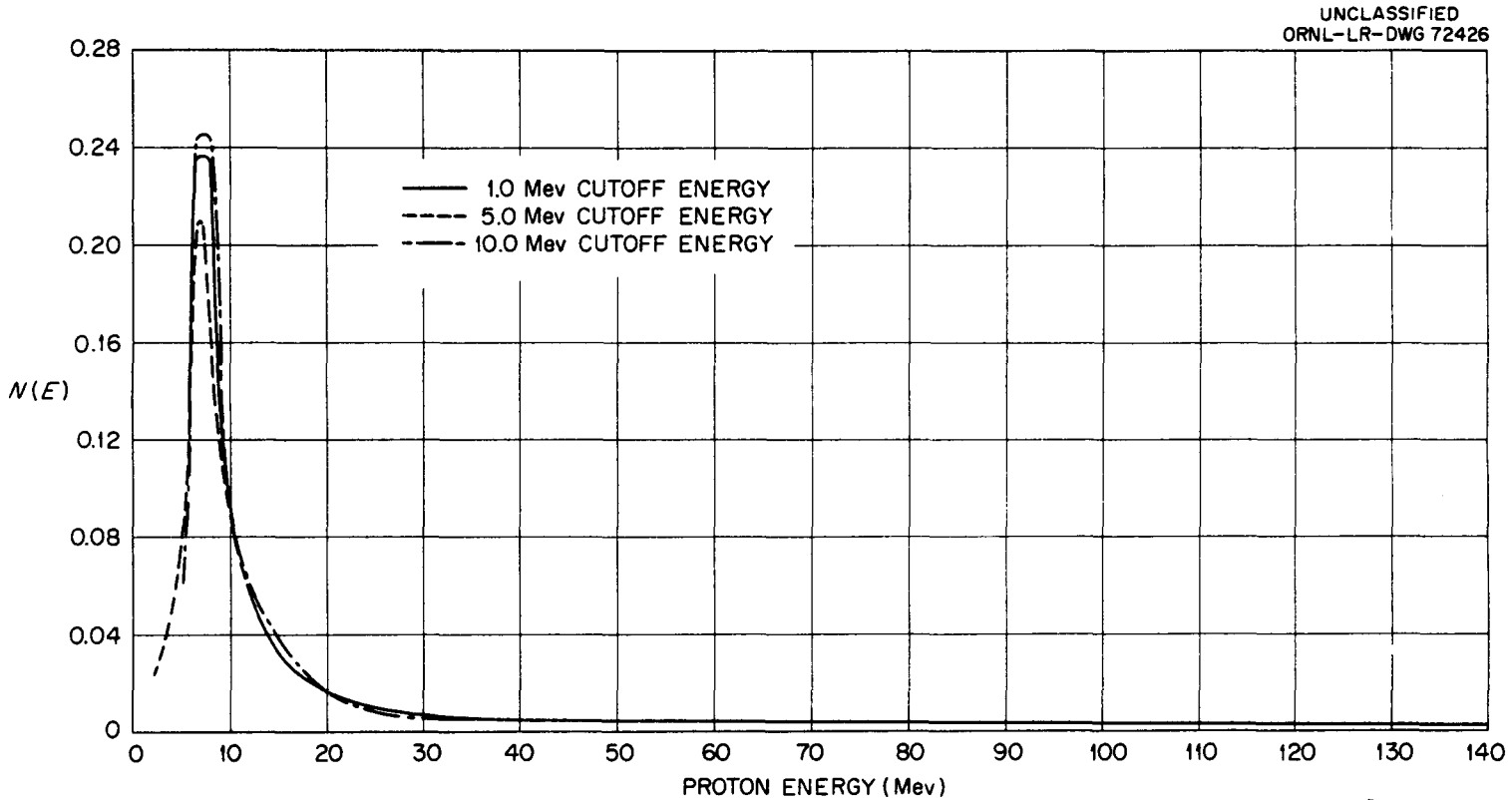

Fig. 48. Cascade and Evaporation Proton Spectra for 150-Mev Protons on $_{44}Ru^{100}$.

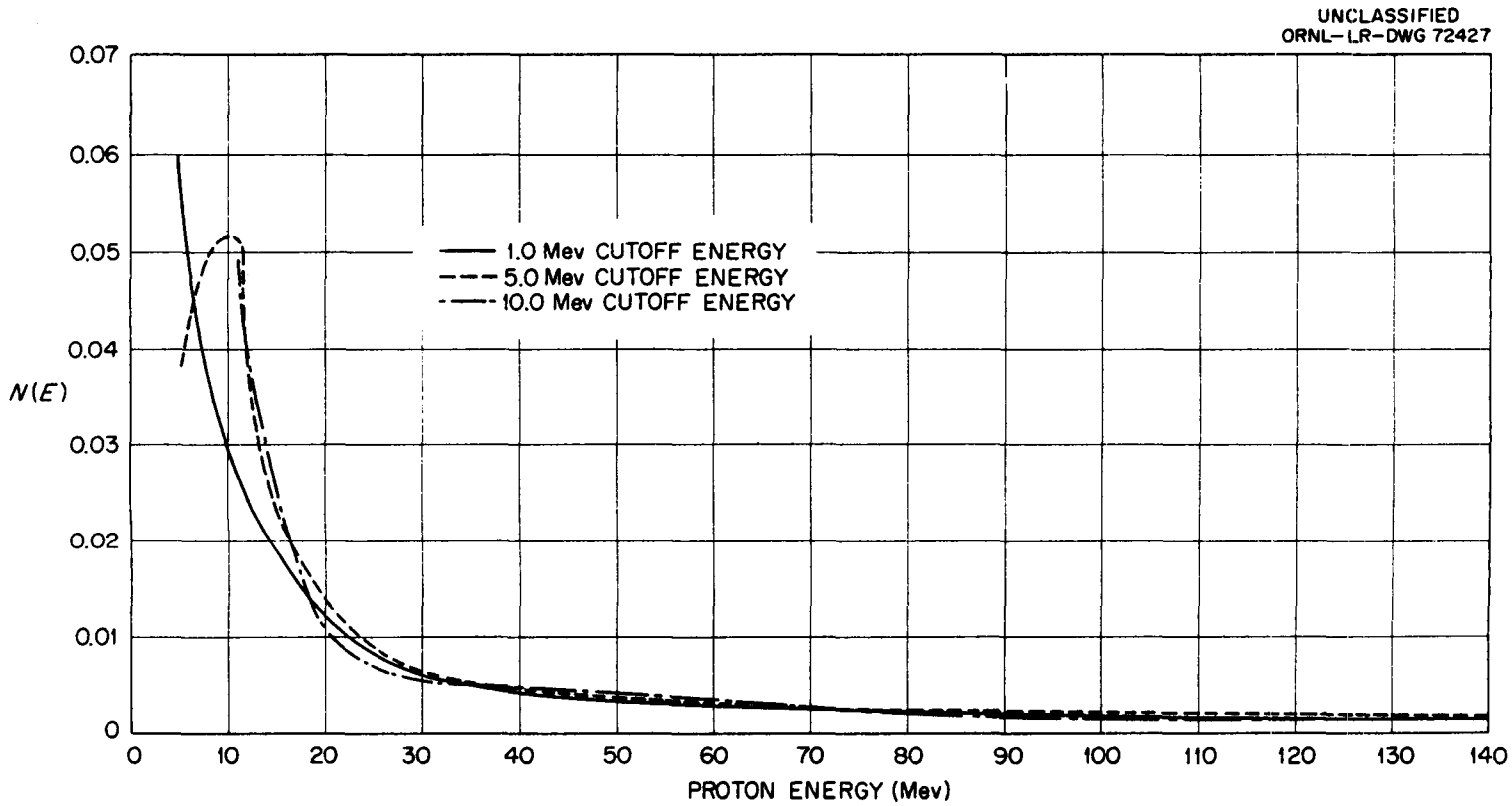

Fig. 49. Cascade and Evaporation Proton Spectra for 150-Mev Protons on $_{82}Pb^{208}$.

A list of the data that will be available on request is as follows:

I. Cascade process

A. For the cascade residual nucleus

1. Parallel and perpendicular momentum distributions and average value of each

2. Momentum distribution and average value

3. Excitation energy distribution and average value

4. Angular distribution

5. Average residual mass

B. For the emission of combinations of cascade particles

1. Cross section for each combination

2. All the distributions above for several specific combinations

C. For each type of emitted cascade particle (proton, neutron, π^+, π^o, π^-)

1. Average number emitted

2. Average energy

3. Energy spectra for all angles

4. $\frac{d\sigma}{d\Omega dE}(E)$ for four angular intervals

5. Differential cross section for scattering into these intervals

6. Average energy of emission into these intervals

7. Angular distribution for all energies

8. $\frac{d\sigma}{d\Omega}(\theta)$ for three energy intervals

9. Cross section for the emission of η particles into three energy intervals (η = 1, 2, ...15)

10. $\frac{d\sigma}{d\Omega}(x)$ for the emission of two protons, where x is the angle between them

D. For incident pions

1. Pion absorption cross section

2. Pion charge-exchange cross section

E. Total nonelastic cross section for the incident particles

II. Evaporation process

A. Cross sections for the various residual nuclei following evaporation

B. For the evaporation particles (protons, neutrons, deuterons, tritons, He^3, alphas)

1. Average number

2. First, second, and third moments of the energy distribution

3. Energy distribution

III. Combined cascade and evaporation process

A. For emitted neutrons and protons

1. Average number emitted

2. Energy spectra

Figures 50-71 exemplify the type of data to be contained in the compilation. The curves drawn through the points of some of the data illustrate the general trends. The deviation of the points from the curves can be quite large in cases where the statistics are poor (Fig. 69).

Some of the data will suffer because of poor statistics, but prohibitive machine time would be involved in providing good statistics for all the data. A reasonable compromise in this respect was attempted.

Monte Carlo Calculations on Intranuclear Cascades for Incident-Particle Energies from About 50 Mev to 2 Gev

The intranuclear cascade calculation for the energy range of incident particles from about 50 to 350 Mev is being extended to higher energies. When completed, the calculation will be able to treat nuclear reactions for incident nucleons up to about 2.5 Gev and incident pions up to about 1.5 Gev.

The nuclear model will remain unchanged, but the particle-particle collisions that occur inside the nucleus will include inelastic collisions, which result in the creation of pions. Only single pion production will be considered for pion-nucleon collisions, and single or double pion production for nucleon-nucleon collisions. The 2.5- and 1.5-Gev energies are higher than the thresholds for the production of pions of greater multiplicity than will be treated in the calculation. Therefore the energy limits of validity of the calculations are nearer to 2 and 1 Gev, respectively, but the production processes which are ignored at the higher energies would constitute only about 15% of all the reactions.

The isobar model will be used for determining the type of reaction products and their angular distribution in the inelastic particle-particle

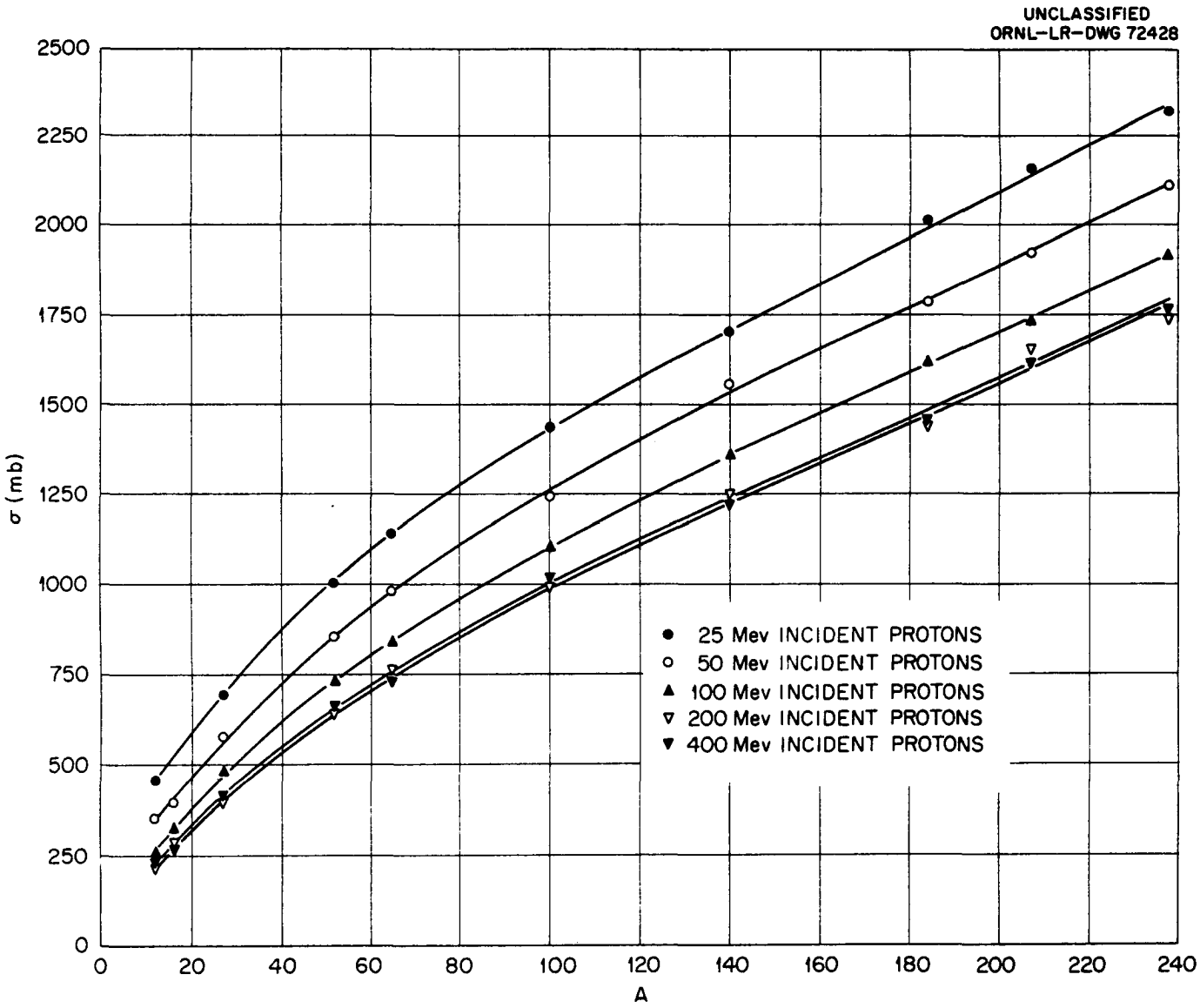

Fig. 50. Total Nonelastic Cross Section vs Atomic Number A for Incident Protons

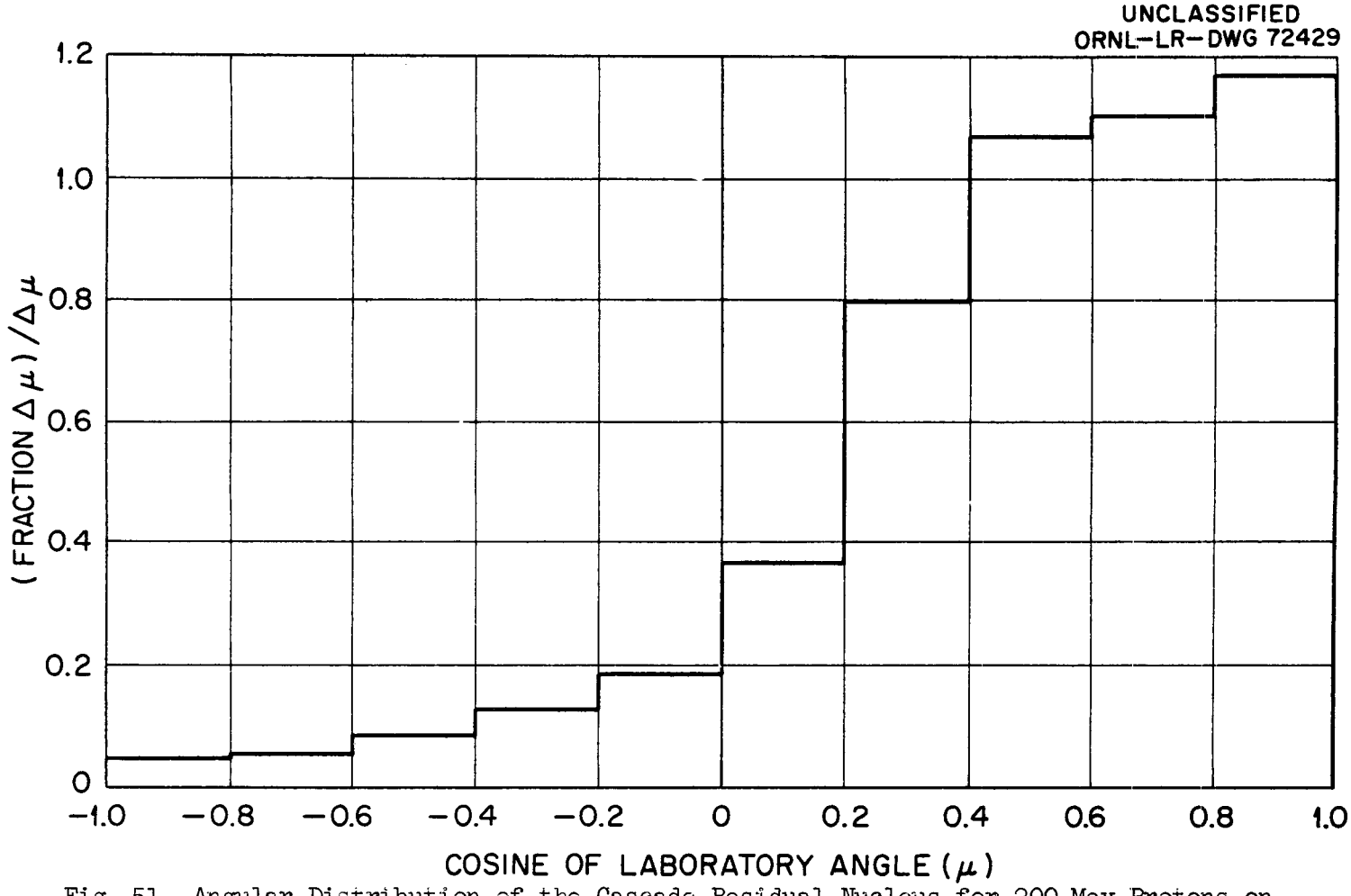

Fig. 51. Angular Distribution of the Cascade Residual Nucleus for 200-Mev Protons on Al^{27}.

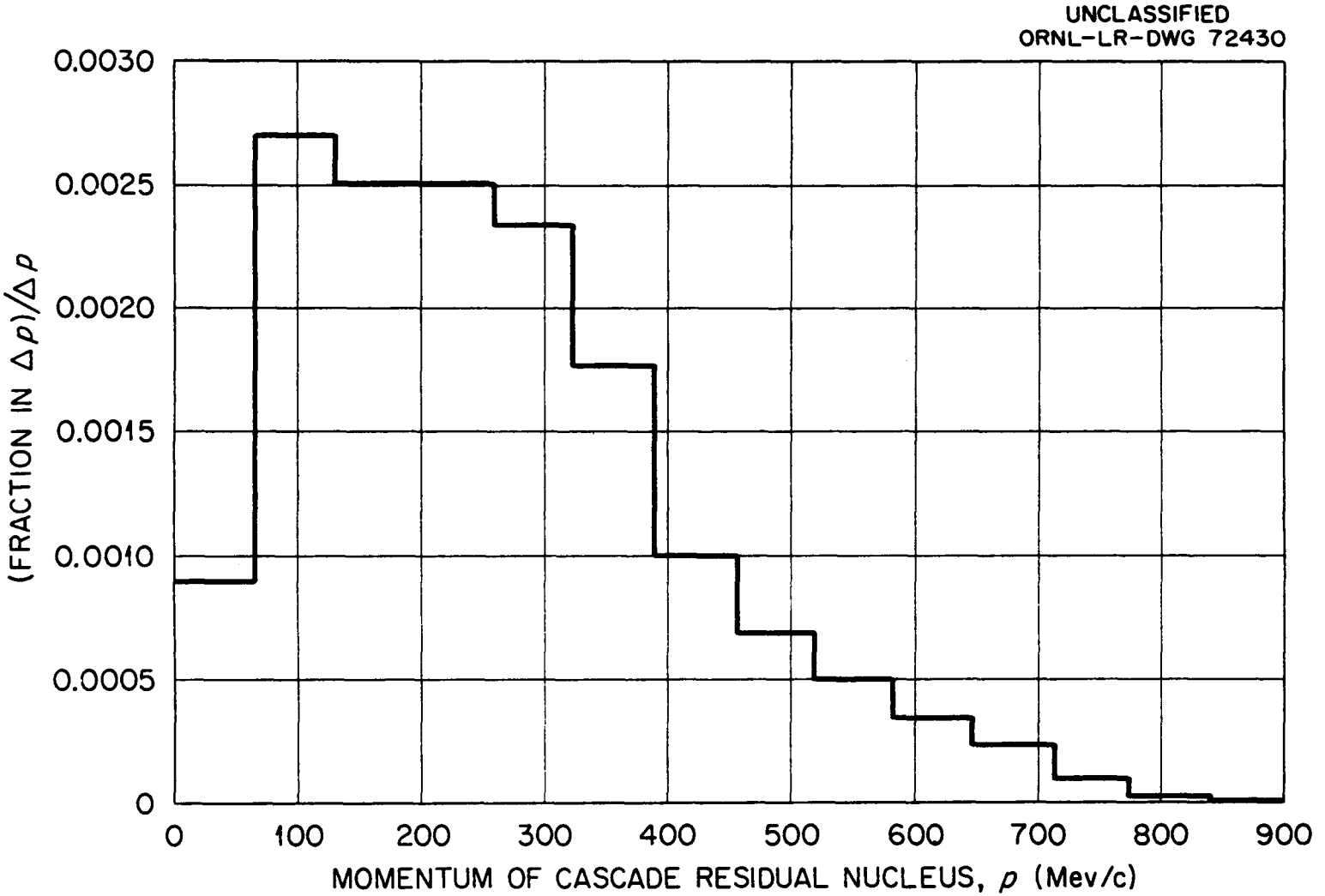

Fig. 52. Momentum Distribution of the Cascade Residual Nucleus for 200-Mev Protons on Al^{27}.
13

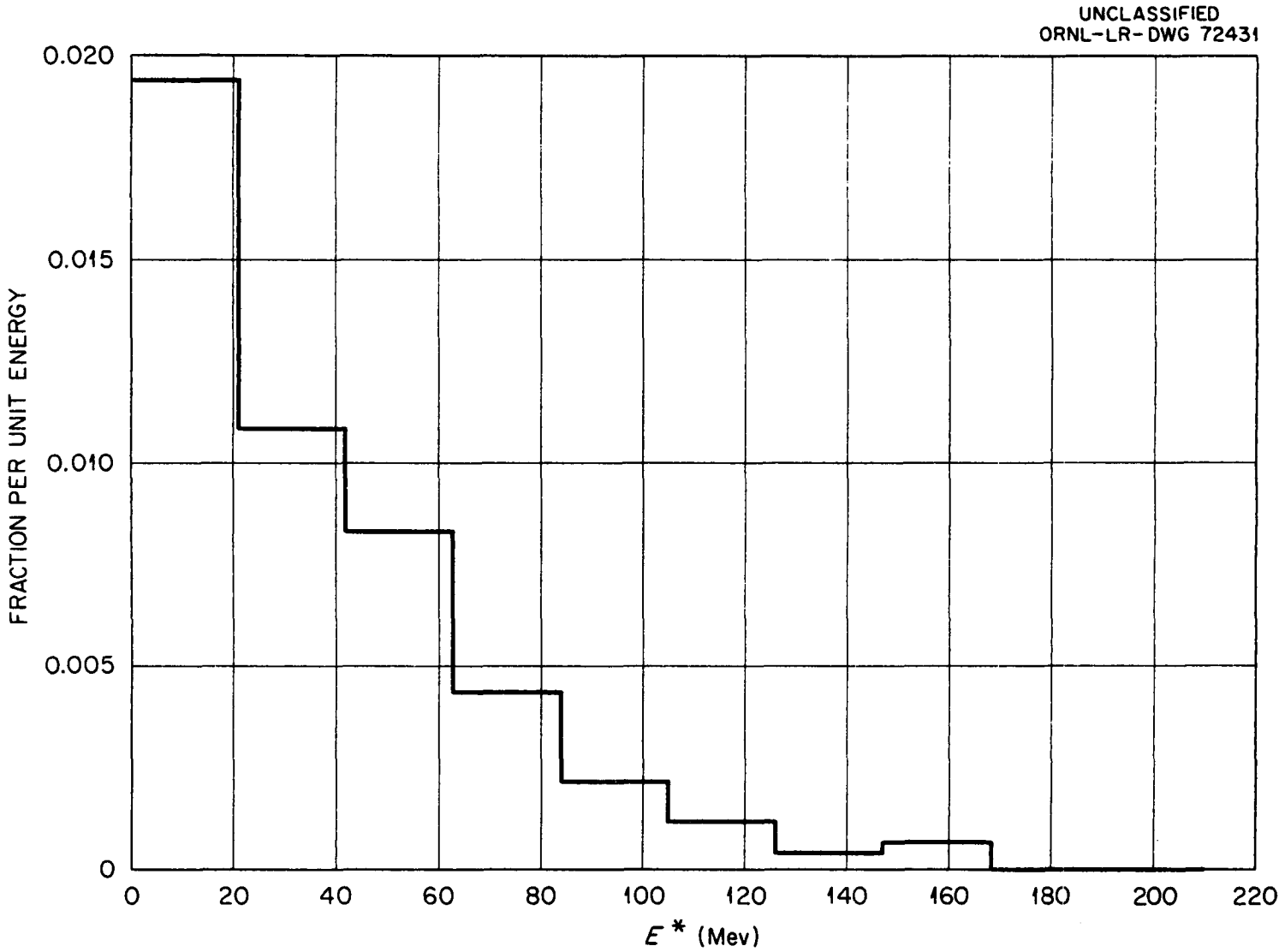

Fig. 53. Excitation Energy Distribution of the Cascade Residual Nucleus for 200-Mev Protons on Al^{27}.[13]

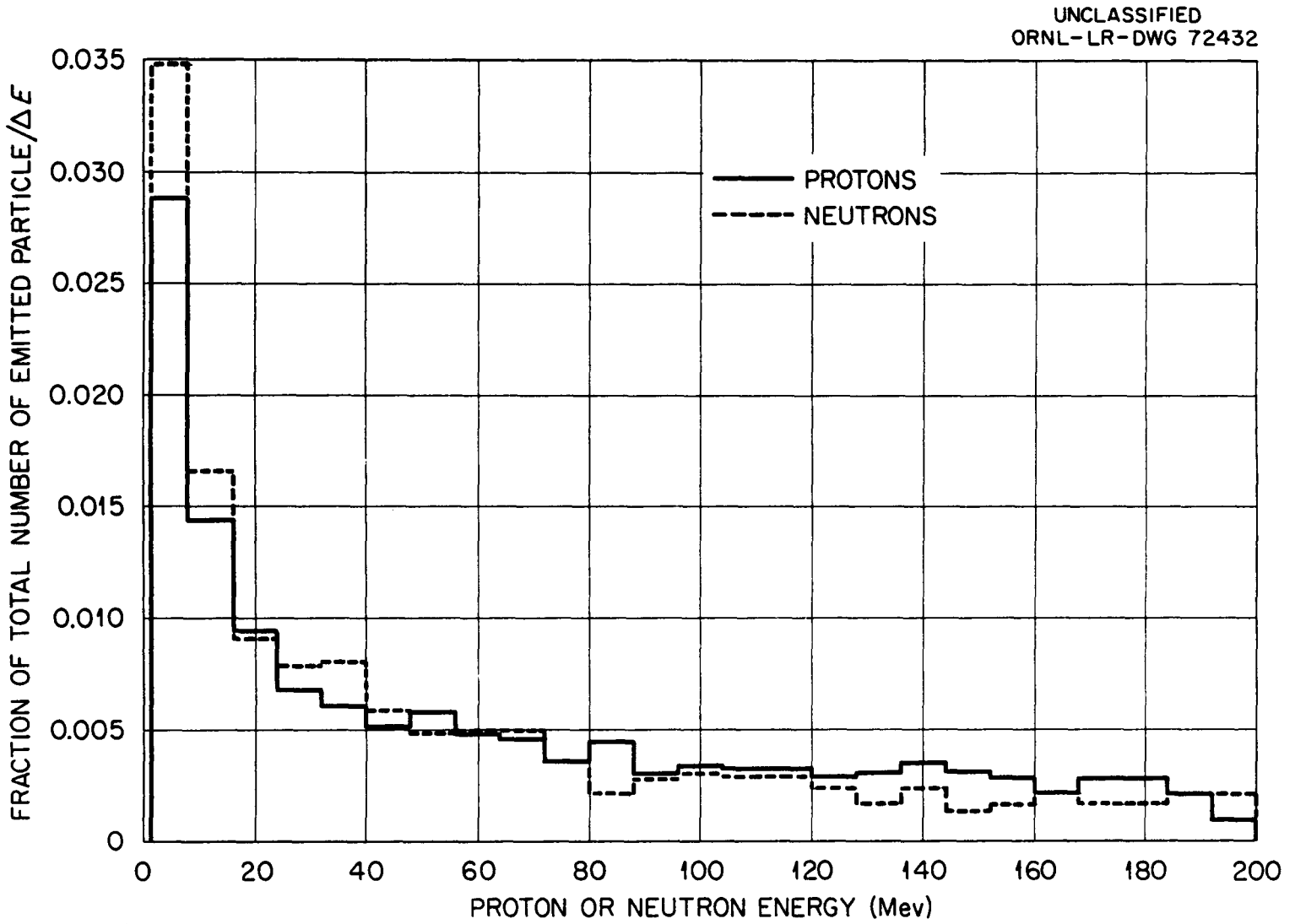

Fig. 54. Energy Spectrum of Emitted Cascade Protons and Neutrons for 200-Mev Protons on Al^{27}.

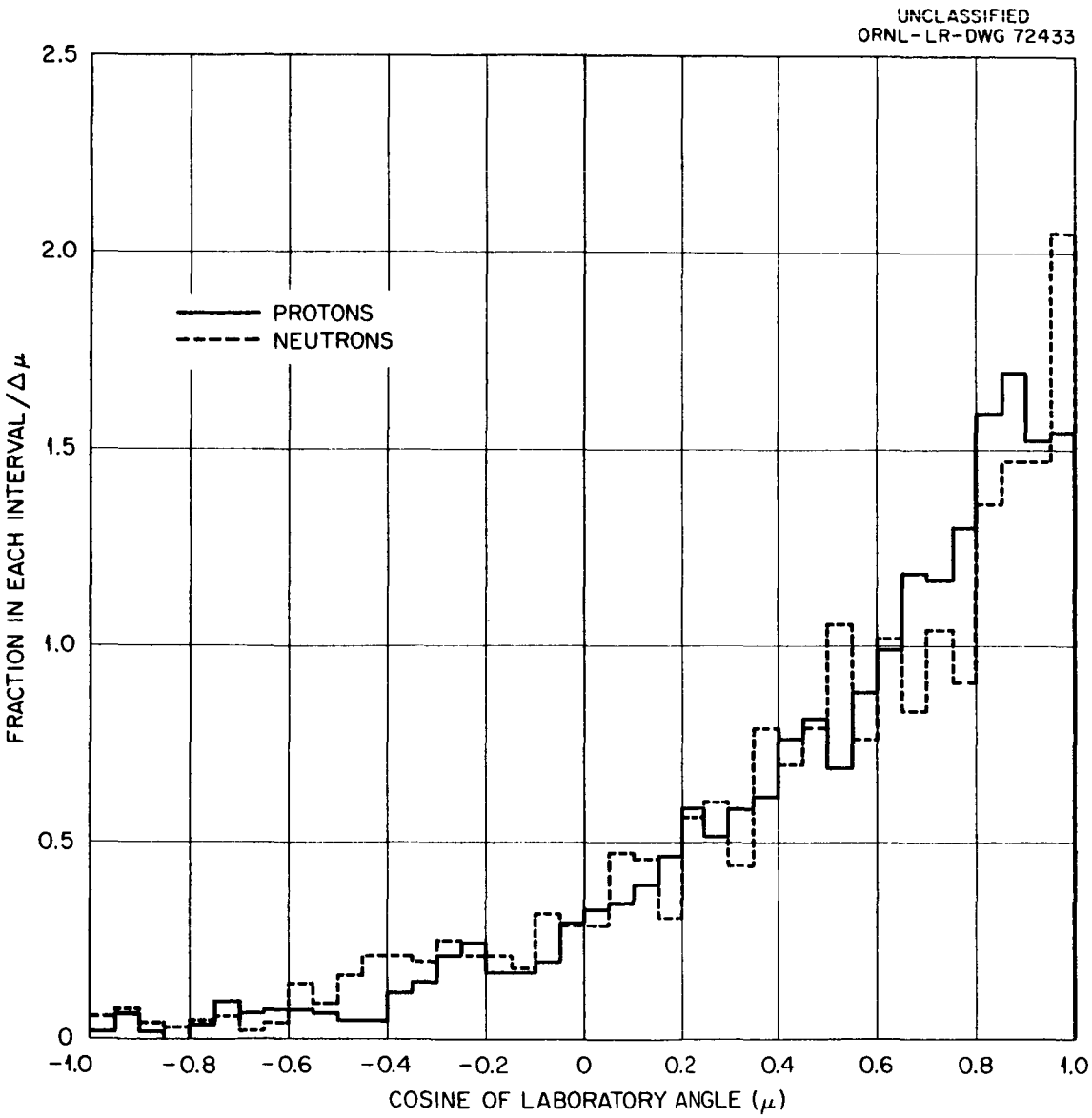

Fig. 55. Angular Distribution of Emitted Cascade Protons and Neutrons for 200-Mev Protons on $_{13}Al^{27}$.

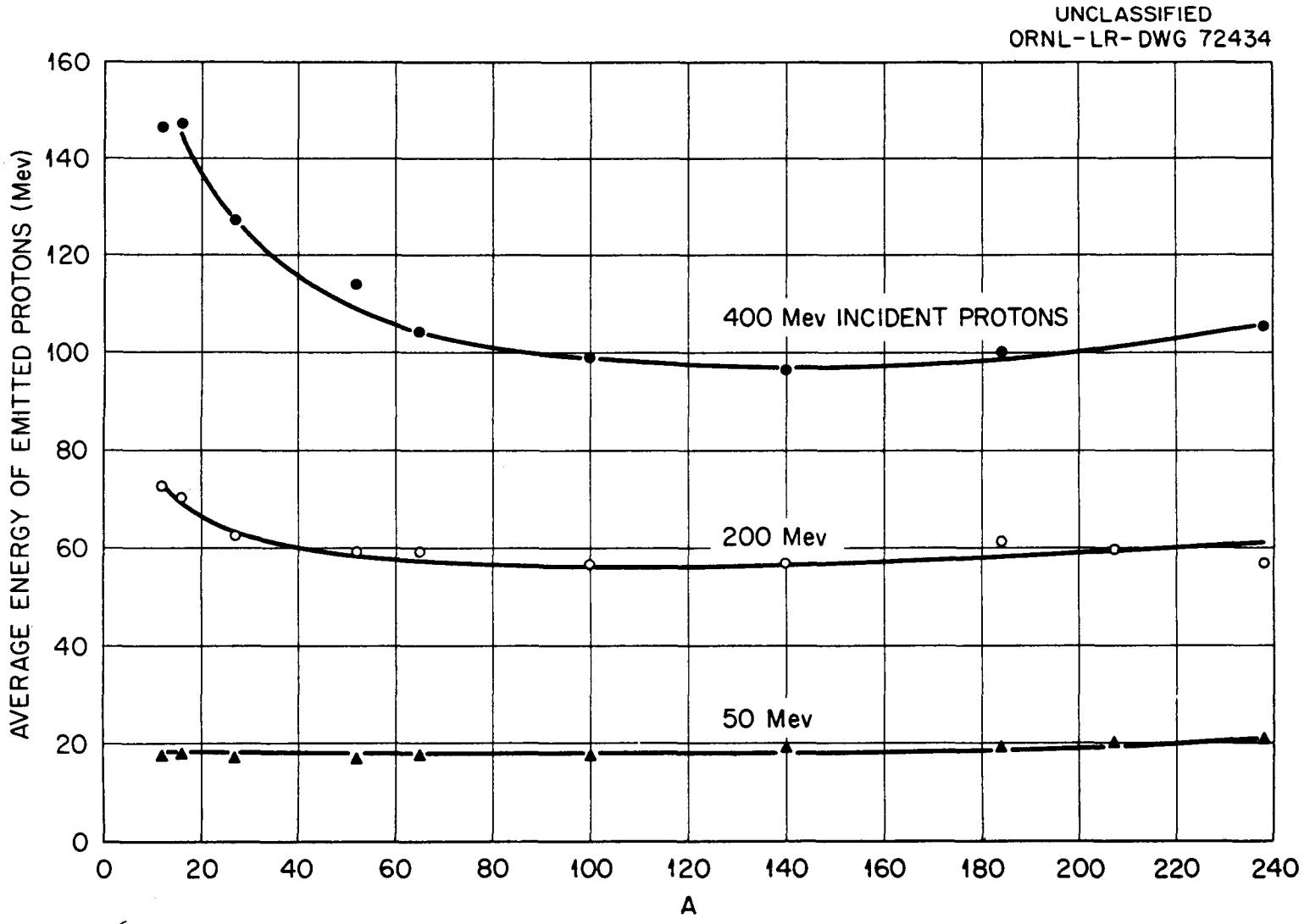

Fig. 56. Average Energy of Emitted Cascade Protons vs Atomic Number A for Incident Protons

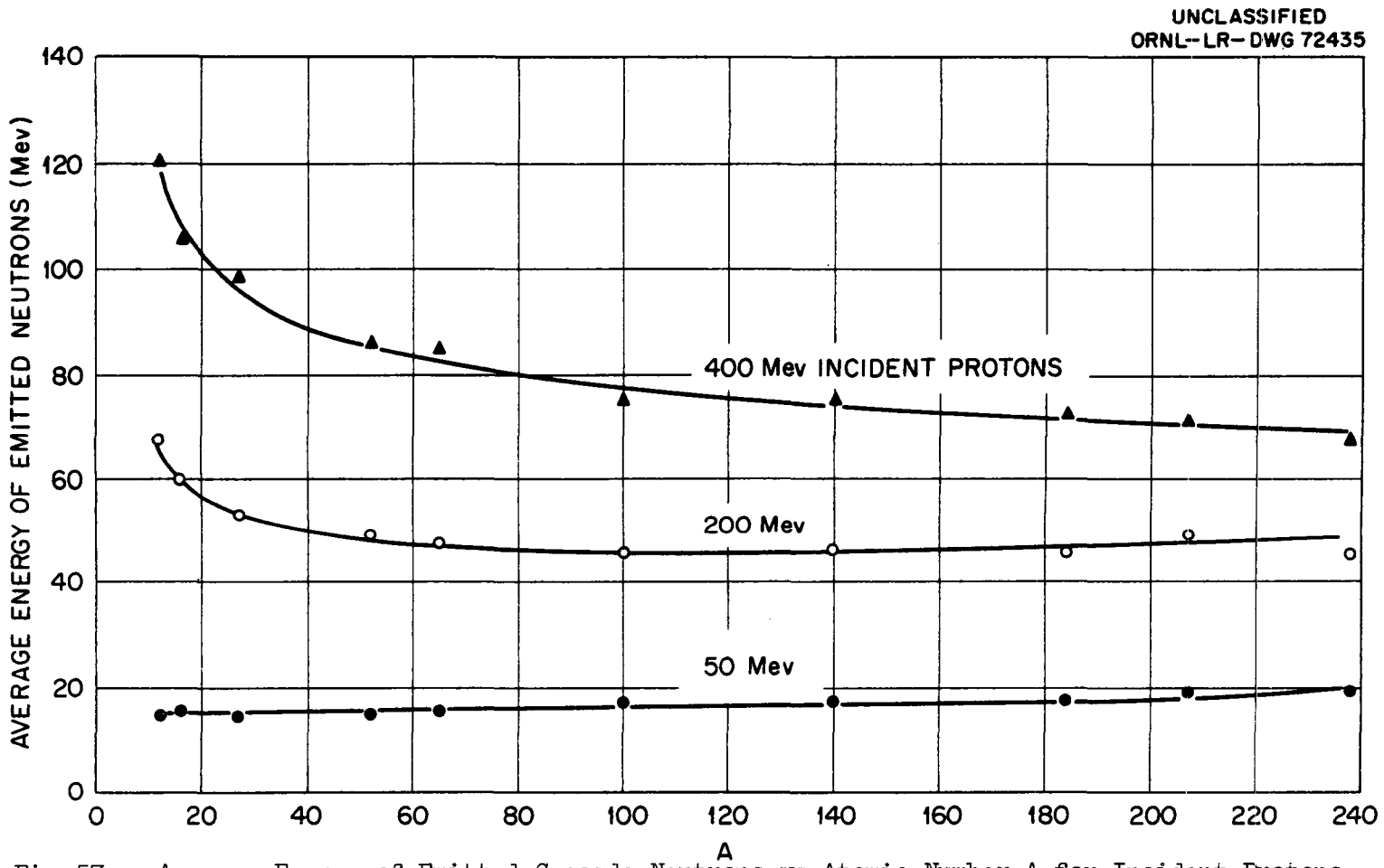

Fig. 57. Average Energy of Emitted Cascade Neutrons vs Atomic Number A for Incident Protons

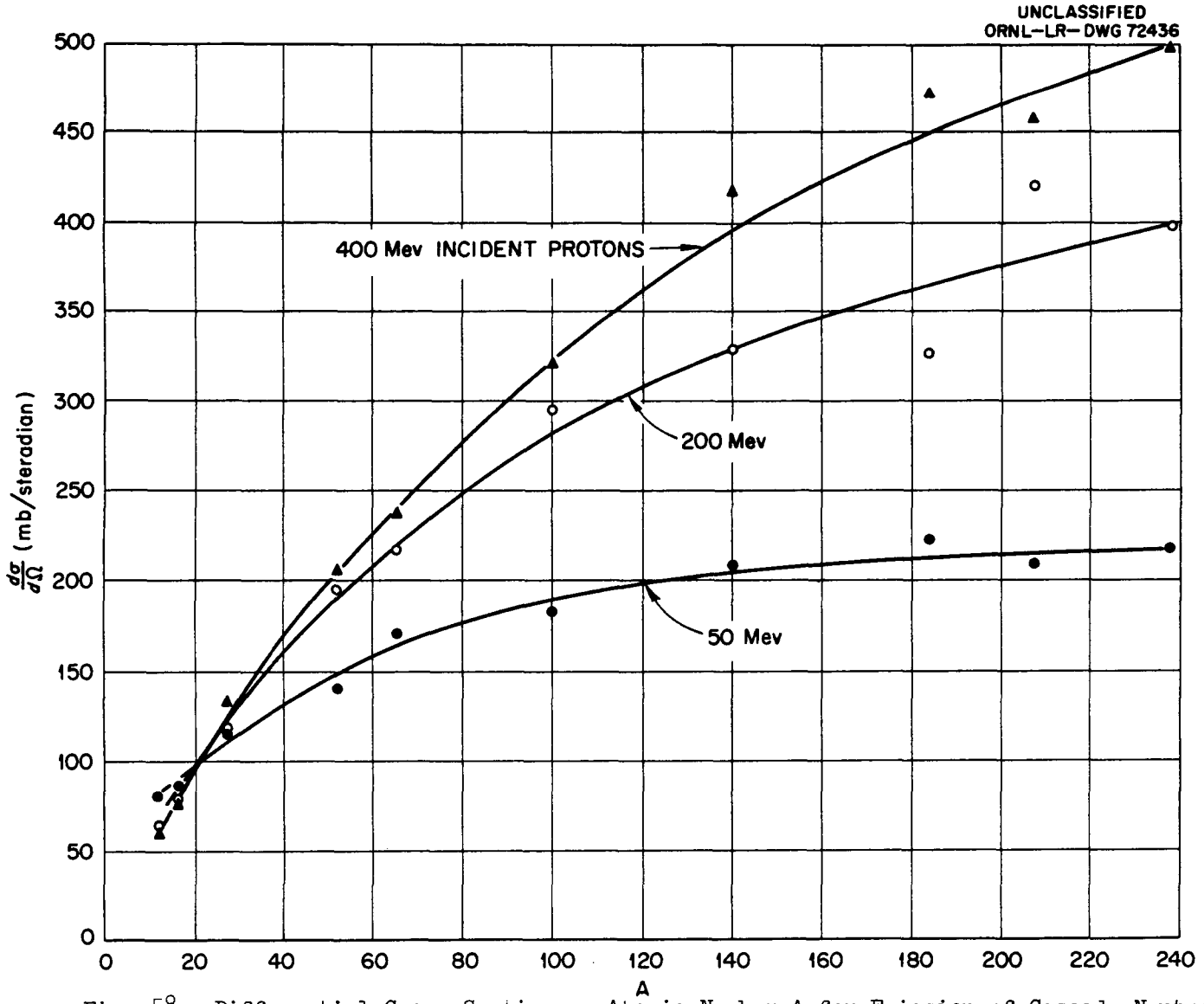

Fig. 58. Differential Cross Section vs Atomic Number A for Emission of Cascade Neutrons into the Laboratory Angular Interval 0 to 30° for Incident Protons.

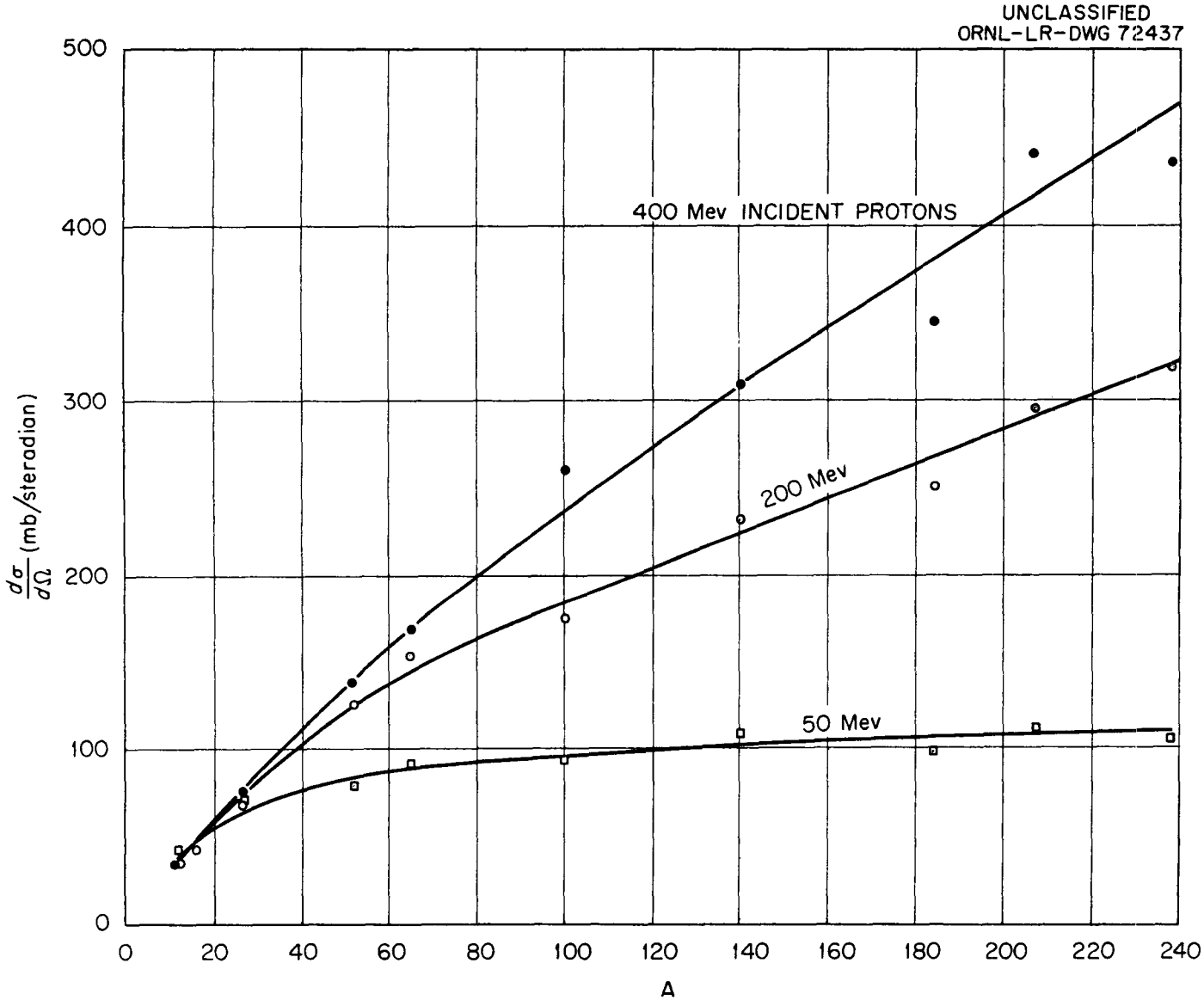

Fig. 59. Differential Cross Section vs Atomic Number A for Emission of Cascade Neutrons into the Laboratory Angular Interval 30 to 60° for Incident Protons.

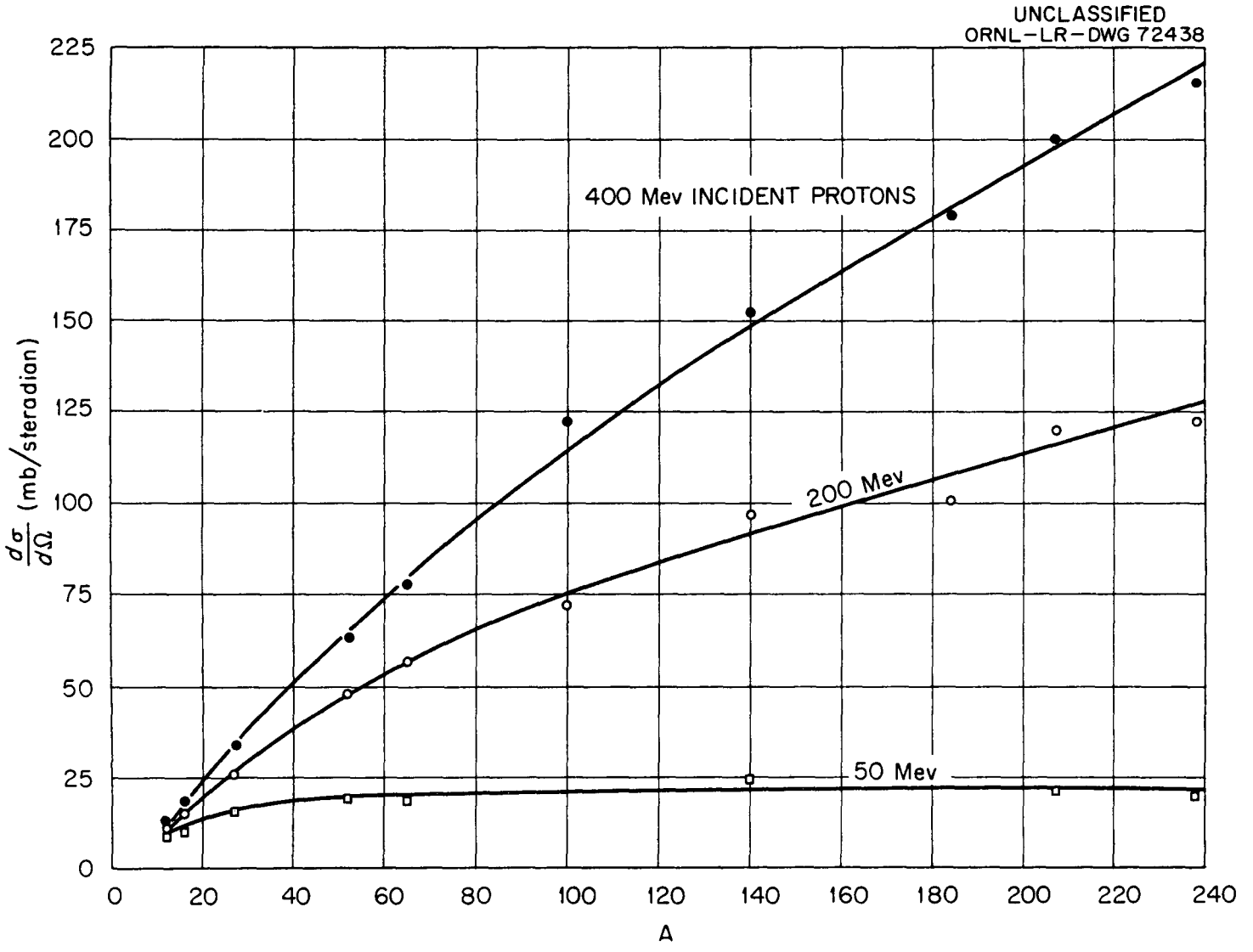

Fig. 60. Differential Cross Section vs Atomic Number A for Emission of Cascade Neutrons into the Laboratory Angular Interval 60 to 120° for Incident Protons.

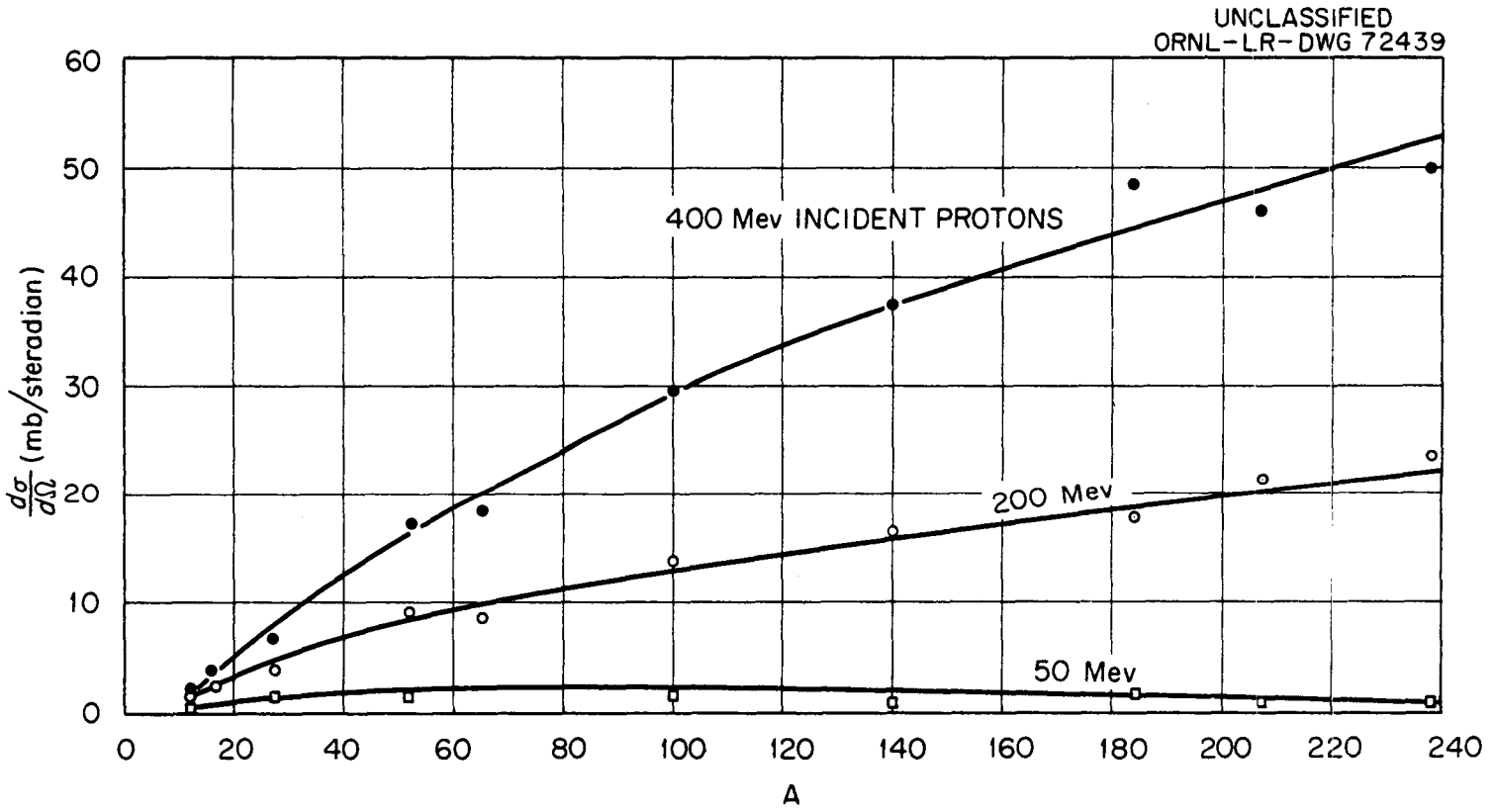

Fig. 61. Differential Cross Section vs Atomic Number A for Emission of Cascade Neutrons into the Laboratory Angular Interval 120 to 180° for Incident Protons.

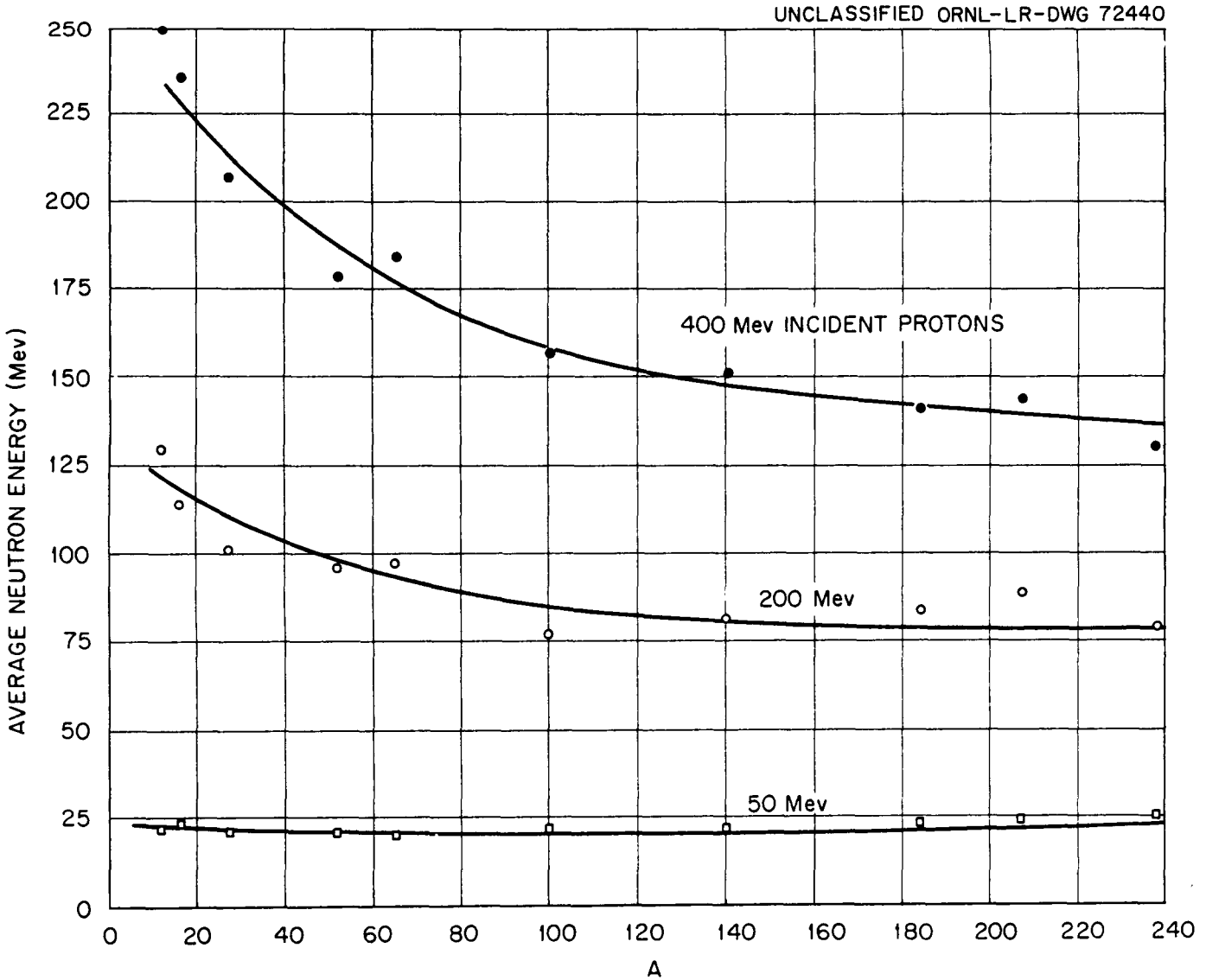

Fig. 62. Average Energy of Cascade Neutrons Emitted into the Laboratory Angular Interval 0 to 30° vs Atomic Number A for Incident Protons.

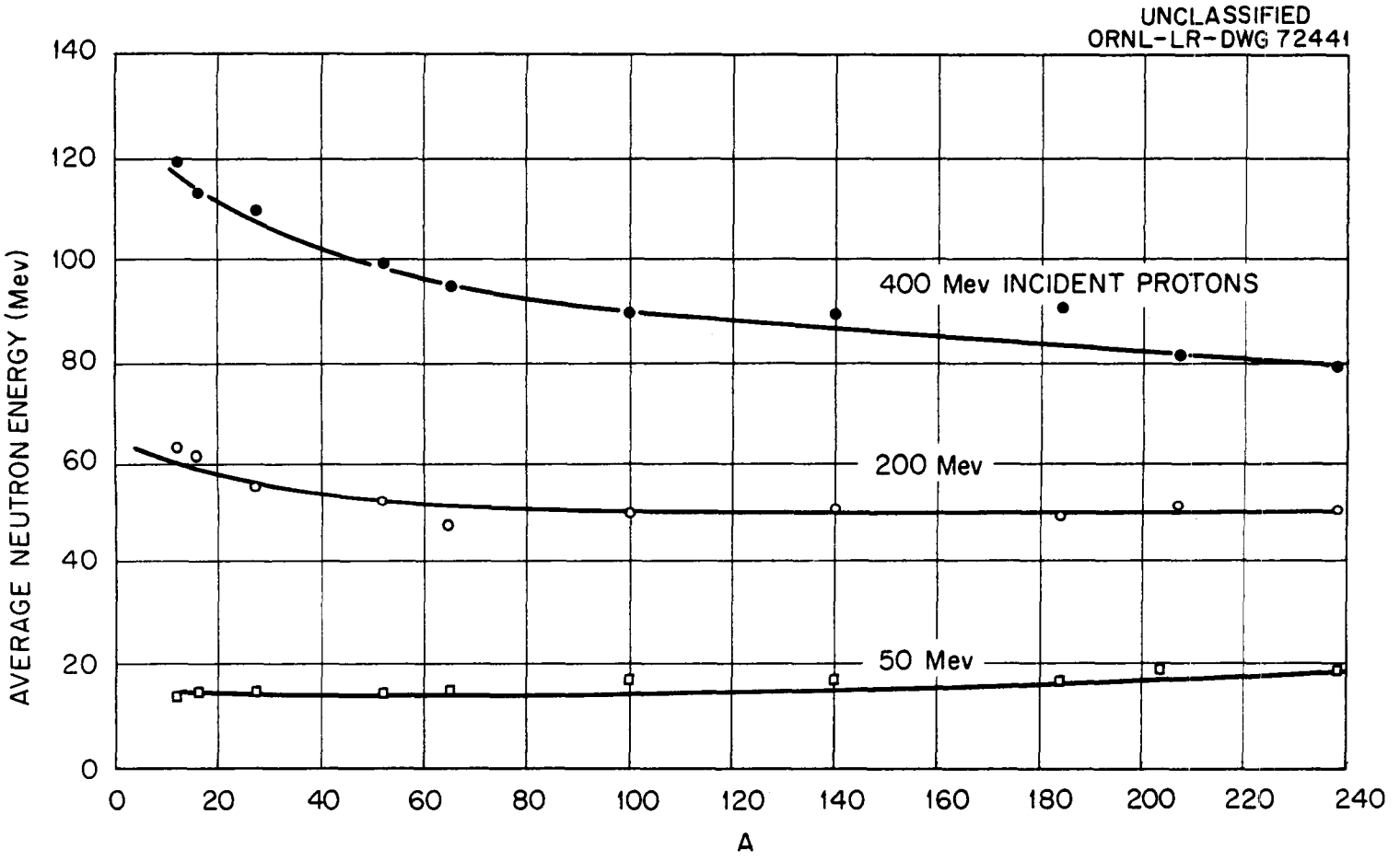

Fig. 63. Average Energy of Cascade Neutrons Emitted into the Laboratory Angular Interval 30 to 60° vs Atomic Number A for Incident Protons.

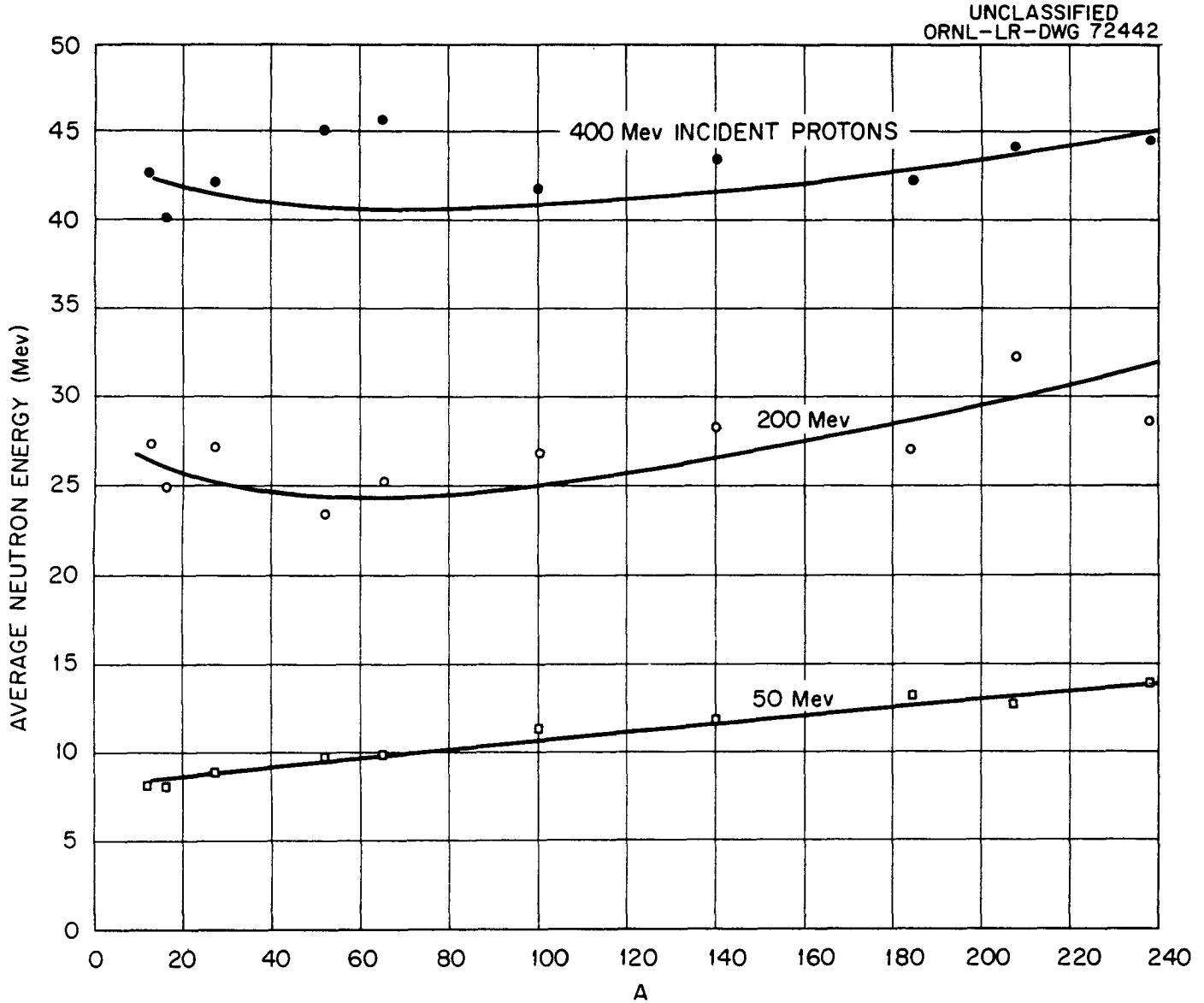

Fig. 64. Average Energy of Cascade Neutrons Emitted into the Laboratory Angular Interval 60 to 120° vs Atomic Number A for Incident Protons.

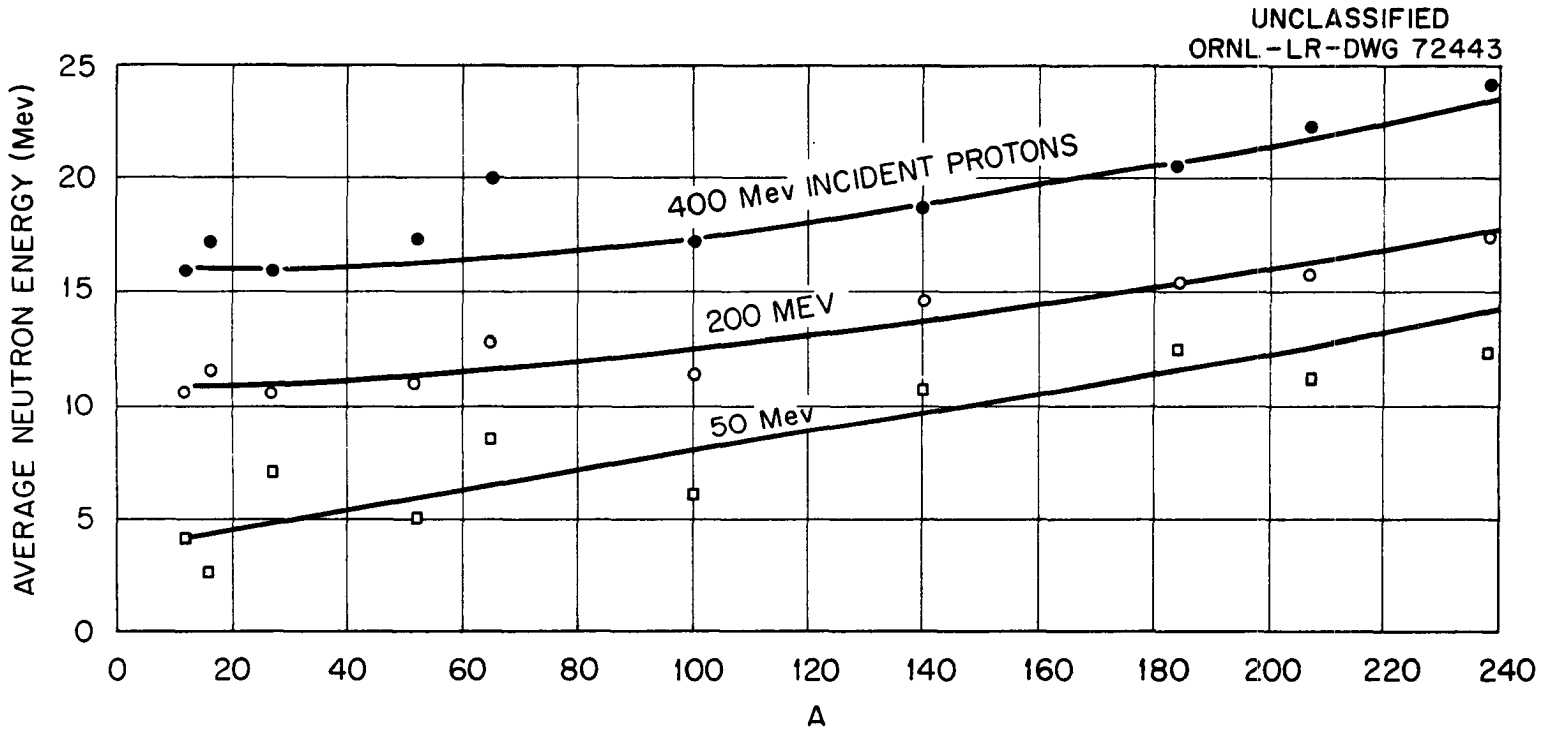

Fig. 65. Average Energy of Cascade Neutrons Emitted into the Laboratory Angular Interval 120 to 180° vs Atomic Number A for Incident Protons.

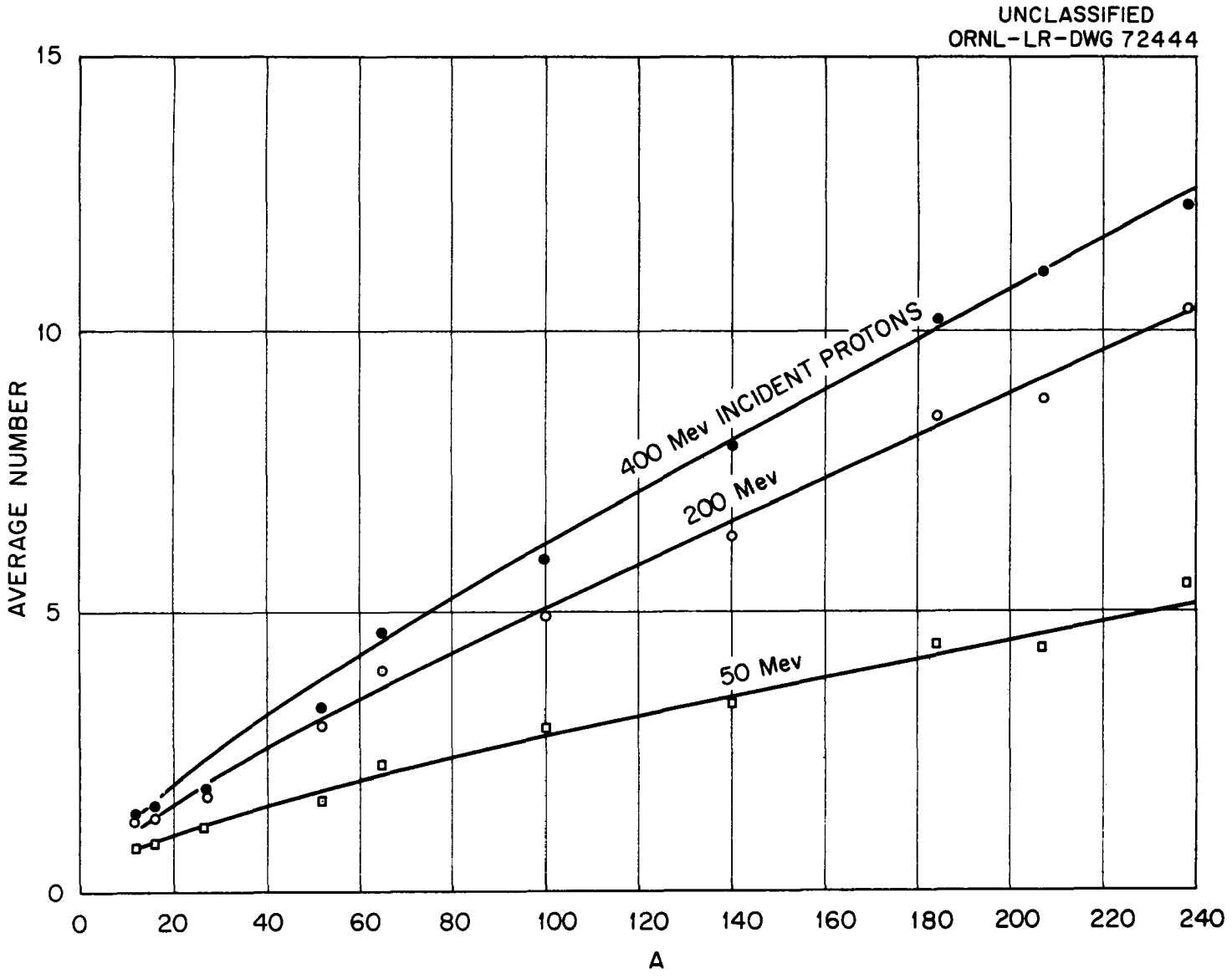

Fig. 66. Average Number of Cascade and Evaporation Neutrons vs Atomic Number A for Incident Protons.

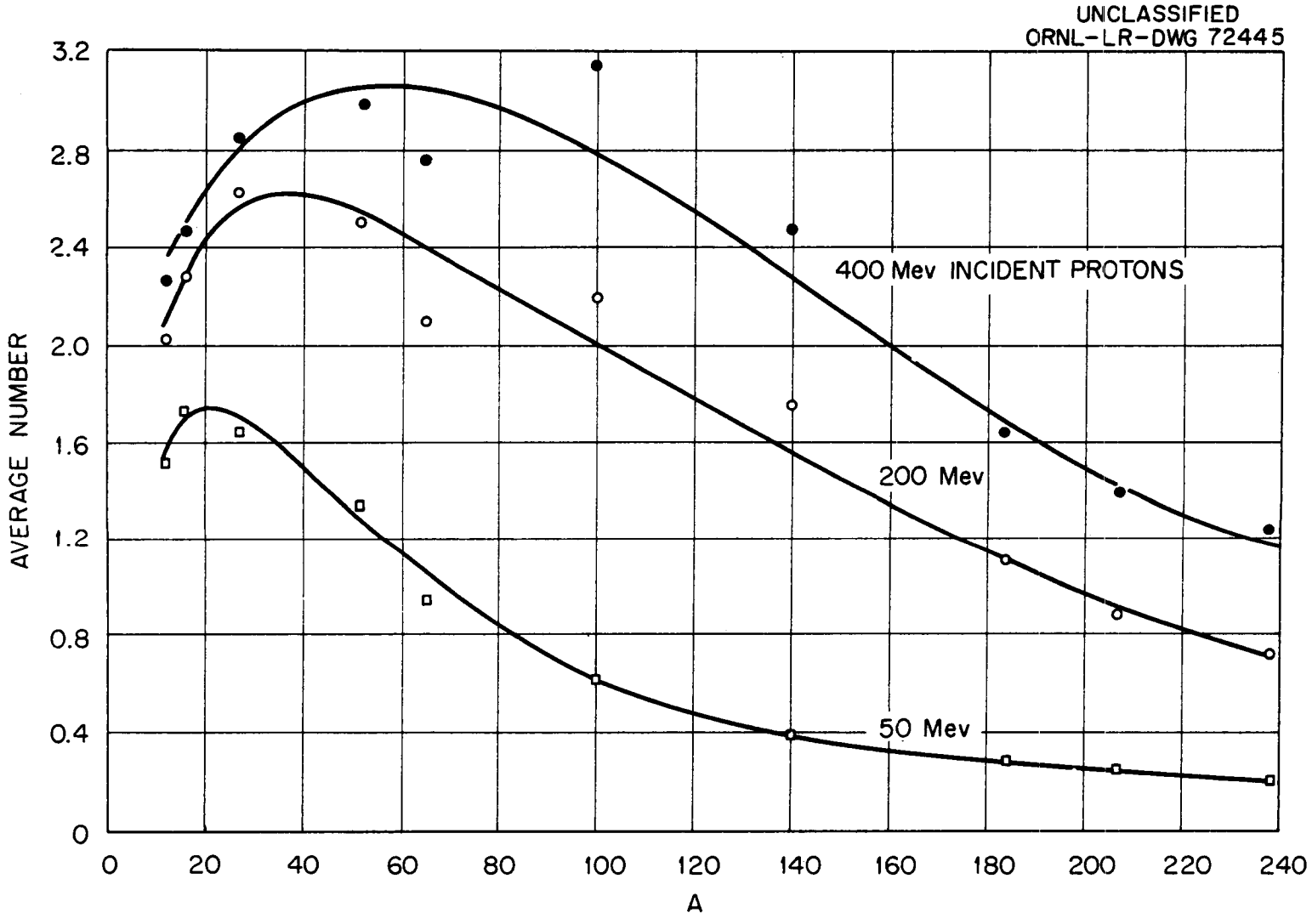

Fig. 67. Average Number of Cascade and Evaporation Protons vs Atomic Number A for Incident Protons.

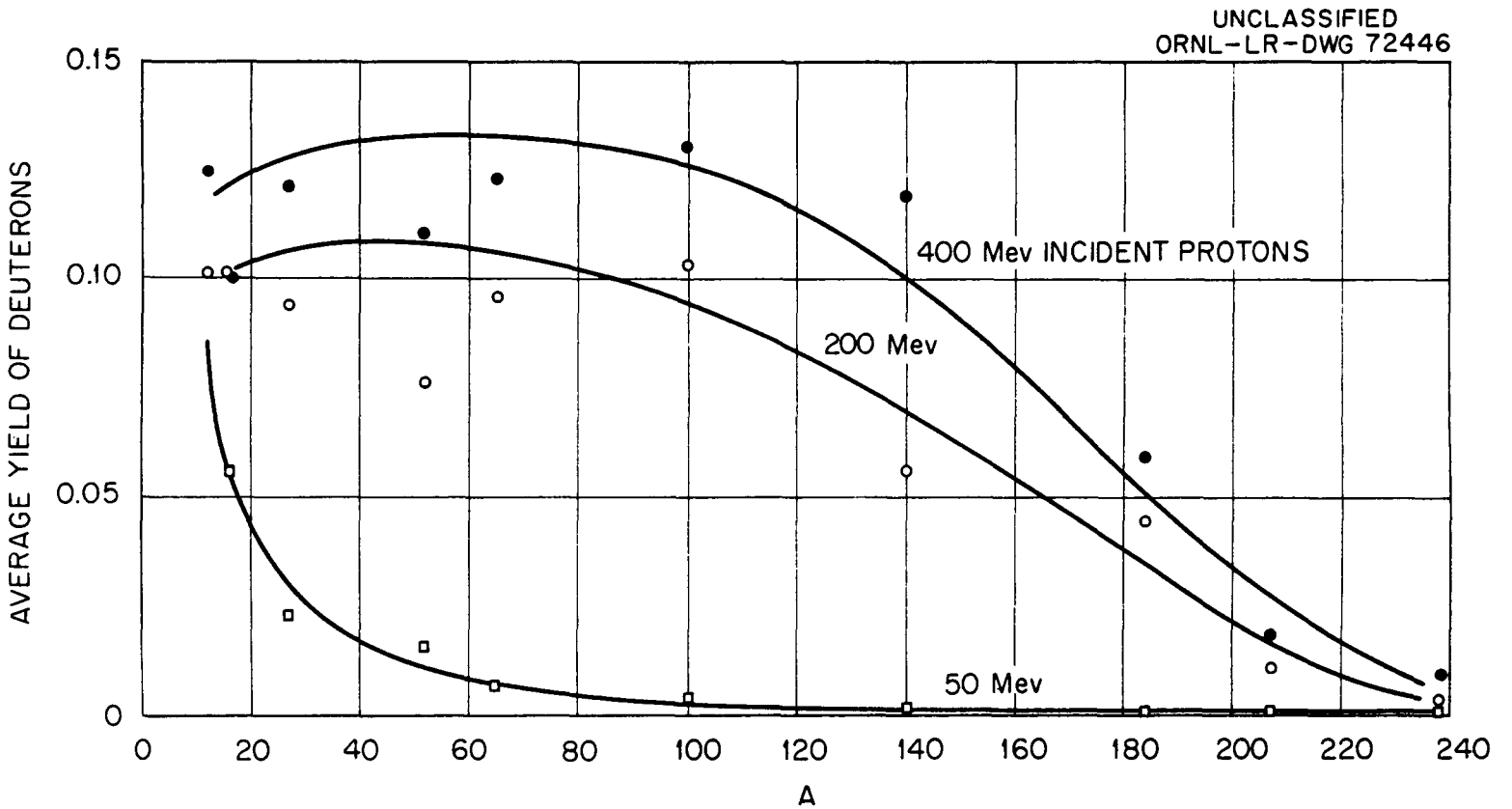

Fig. 68. Average Yield of Evaporation Deuterons per Inelastic Event vs Atomic Number A for Incident Protons.

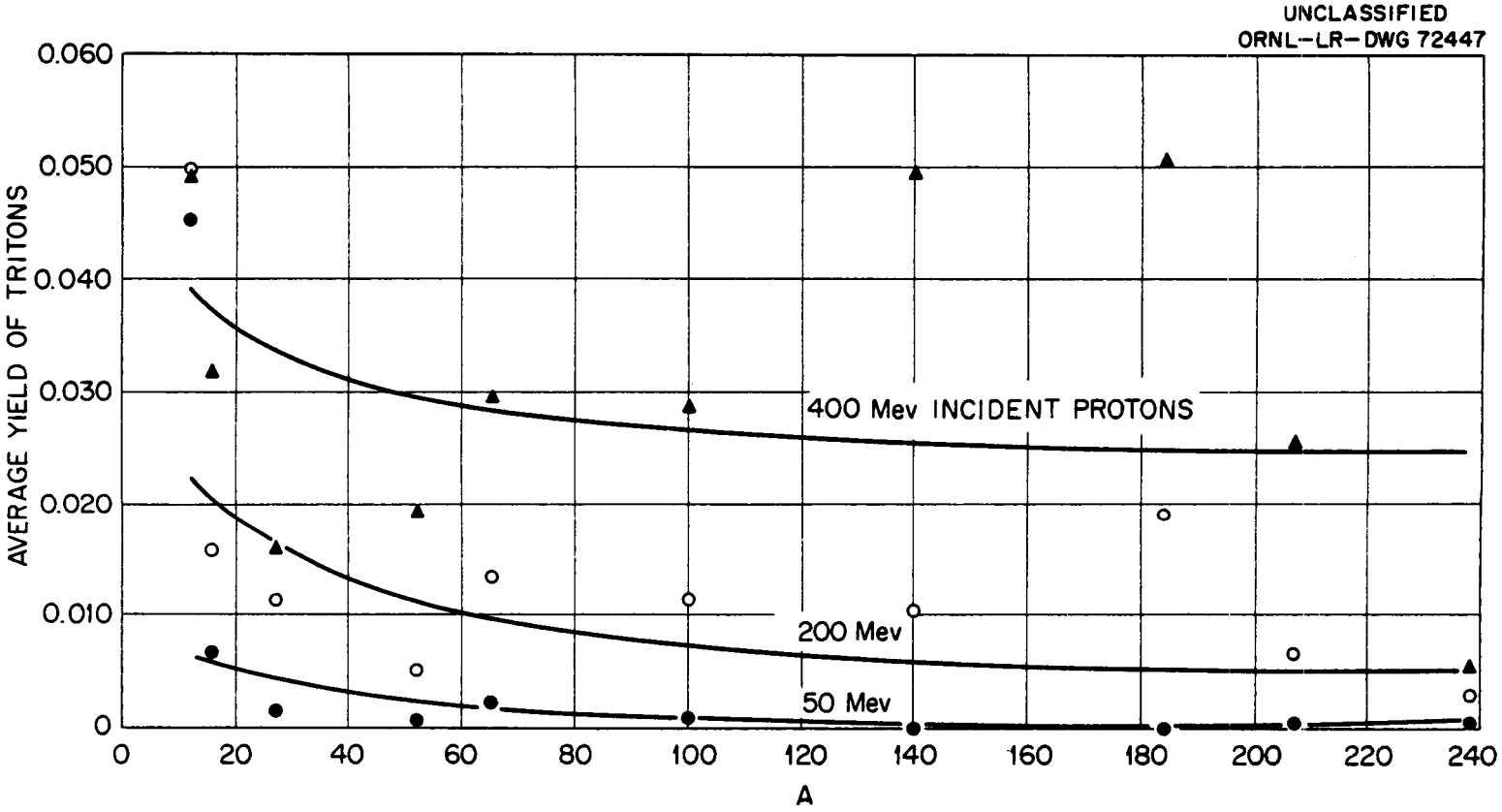

Fig. 69. Average Yield of Evaporation Tritons per Inelastic Event vs Atomic Number A for Incident Protons.

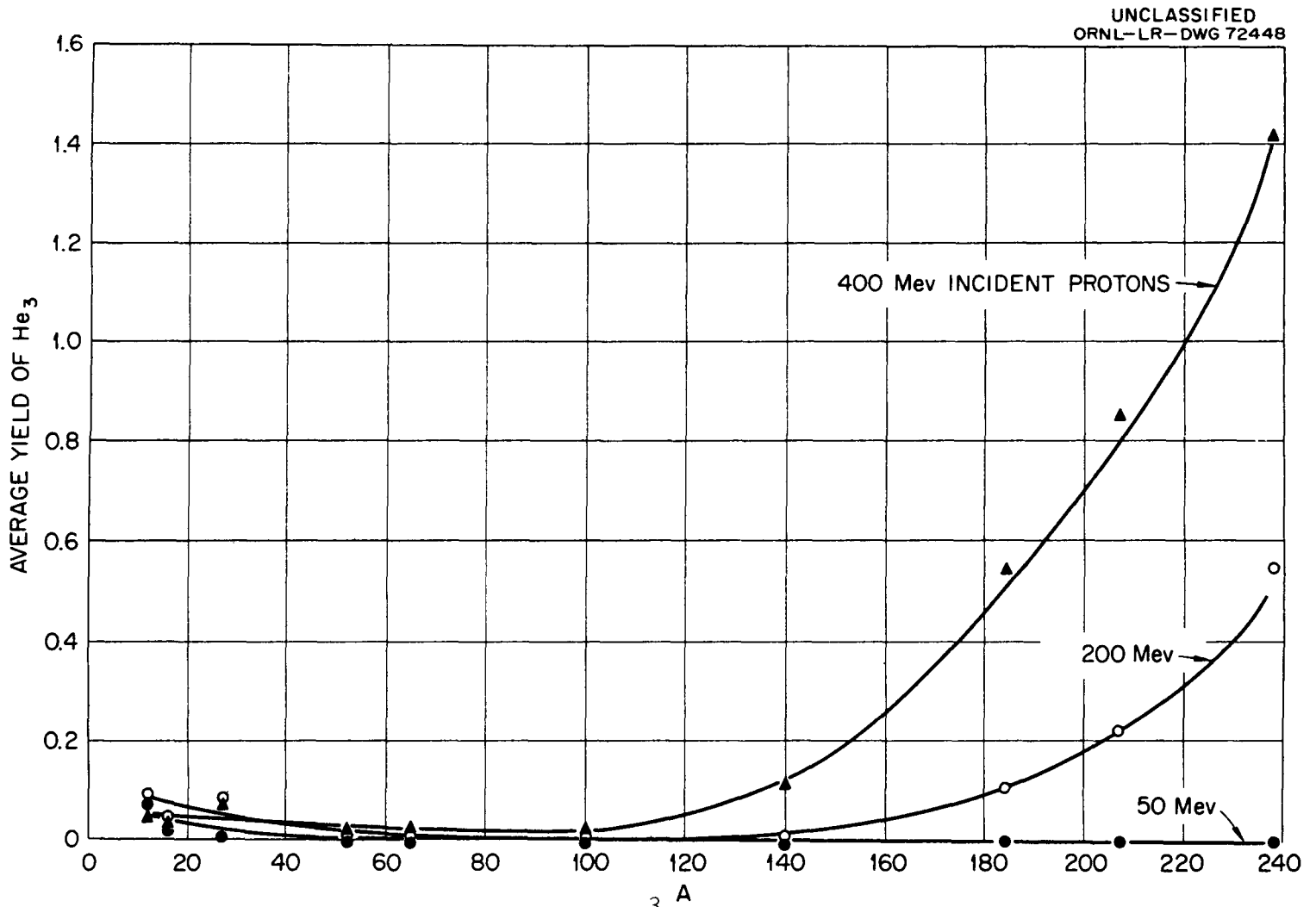

Fig. 70. Average Yield of Evaporation He^3 per Inelastic Event vs Atomic Number A for Incident Protons.

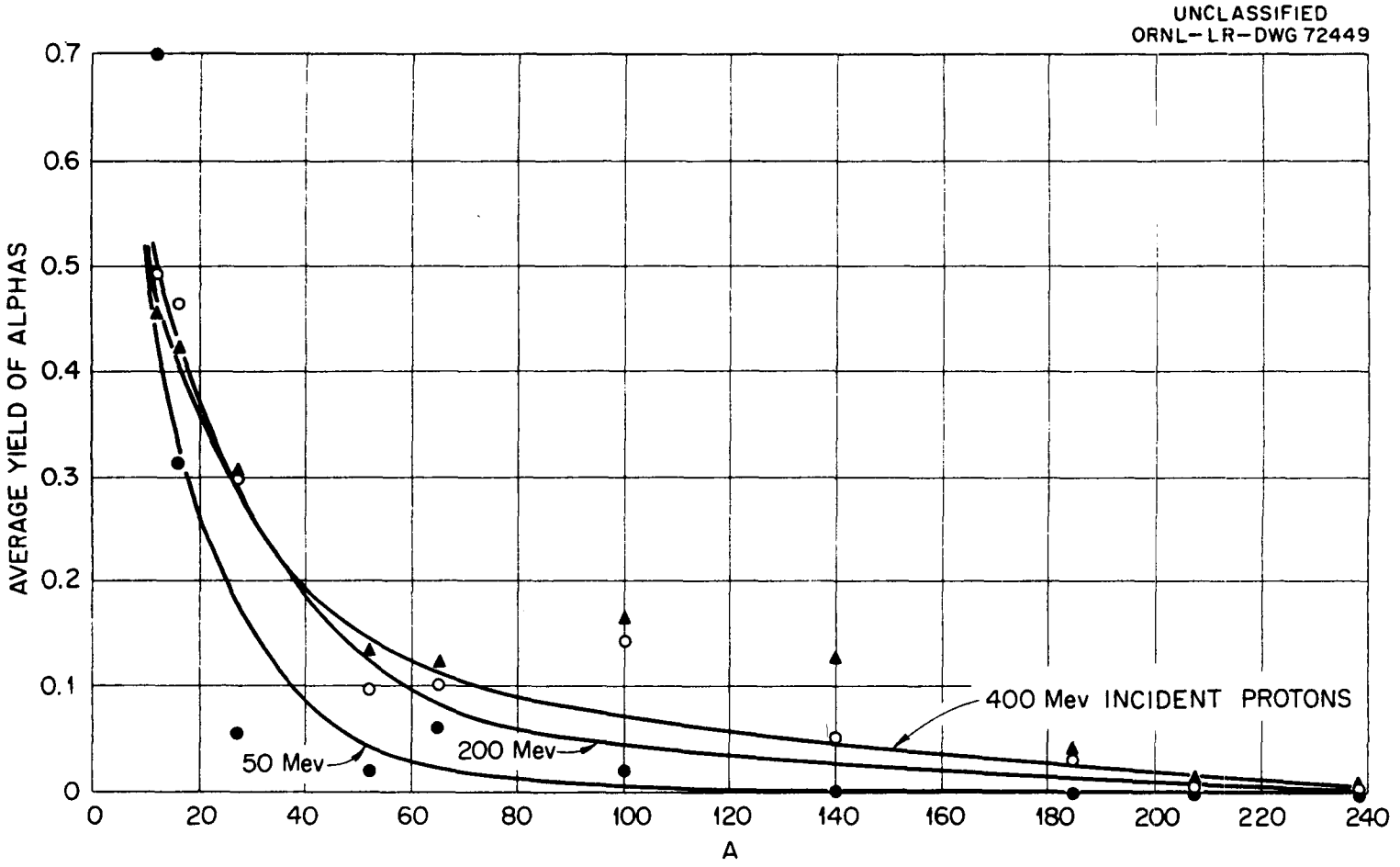

Fig. 71. Average Yield of Evaporation Alphas per Inelastic Event vs Atomic Number A for Incident Protons.

collisions.[11] This model assumes that a T = 3/2, J = 3/2 isobar (excited nucleon state) occurs as a collision product which subsequently decays into a pion and a nucleon; T is the isotopic spin quantum number and J is the total angular-momentum quantum number. In nucleon-nucleon collisions two such isobars can be formed, leading to the decay of two pions and two nucleons. If sufficient energy is available, the model allows for the formation of a T = 1/2 isobar, which can decay into one pion and one nucleon or into two pions and one nucleon. A considerable amount of experimental data (not yet available) would have been required to fix the contribution of the T = 1/2 isobar, and hence this reaction mode was not considered. The data for the description of the production processes decided upon were scarce enough in certain areas, and rather drastic assumptions had to be made in those cases.

Pion Production in Nucleon-Nucleon Reactions

The type of production event, single or double production, in nucleon-nucleon collisions within the nucleus is determined by the free-particle cross section for that event. The data for p-p single production were taken from the paper by Fickinger et al.[12] and are illustrated in Fig. 72. The n-p single-production cross section was assumed to be one-half the p-p cross section for the following reasons: The isotopic spin part of the n-p wave function can be written as a combination of T = 0 and T = 1 isotopic spin states, each comprising one-half the total state. If single pion production occurs through the formation of a T = 3/2 isobar only, the T = 0 state cannot contribute. Therefore only one-half the total n-p state contributes to pion production via the composite T = 1 state, while all of the total p-p state (a pure T = 1 state) contributes.

The p-p double-production cross section[13] is illustrated in Fig. 73. Since double production is assumed to occur via the formation of two T = 3/2 isobars, the T = 0 part of the n-p isotopic spin state does contribute. The cross section for the formation of two isobars through the T = 0 state must be known for the isobaric states being formed to be determined. The cross section for formation of two isobars through the T = 1 state is known (i.e., the p-p double-production cross section). From the expression $\sigma_{T=0} = 2\sigma_{p-n} - \sigma_{p-p}$, the ratio of the total cross sections for n-p scattering in the T = 0 and T = 1 states can be calculated:

$$R = \frac{\sigma_{T=0}}{\sigma_{T=1}} = \frac{2\sigma_{n-p}}{\sigma_{p-p}} - 1.$$

This ratio was assumed to be the same for the formation of two T = 3/2 isobars. The n-p double-production cross section (illustrated in Fig. 73) can then be calculated.

---

11. R. M. Sternheimer and S. J. Lindenbaum, Phys. Rev. 123, 333 (1961); Phys. Rev. 109, 1723 (1958); Phys. Rev. 105, 1874 (1957).

12. W. J. Fickinger et al., Phys. Rev. 125, 2082 (1962).

13. W. O. Lock et al., Phil. Mag. 2, Ser. 8, 215 (1957); W. B. Fowler et al., Phys. Rev. 103, 1479 (1956); F. F. Chen, C. P. Leavitt, and A. M. Shapiro, Phys. Rev. 103, 211 (1956).

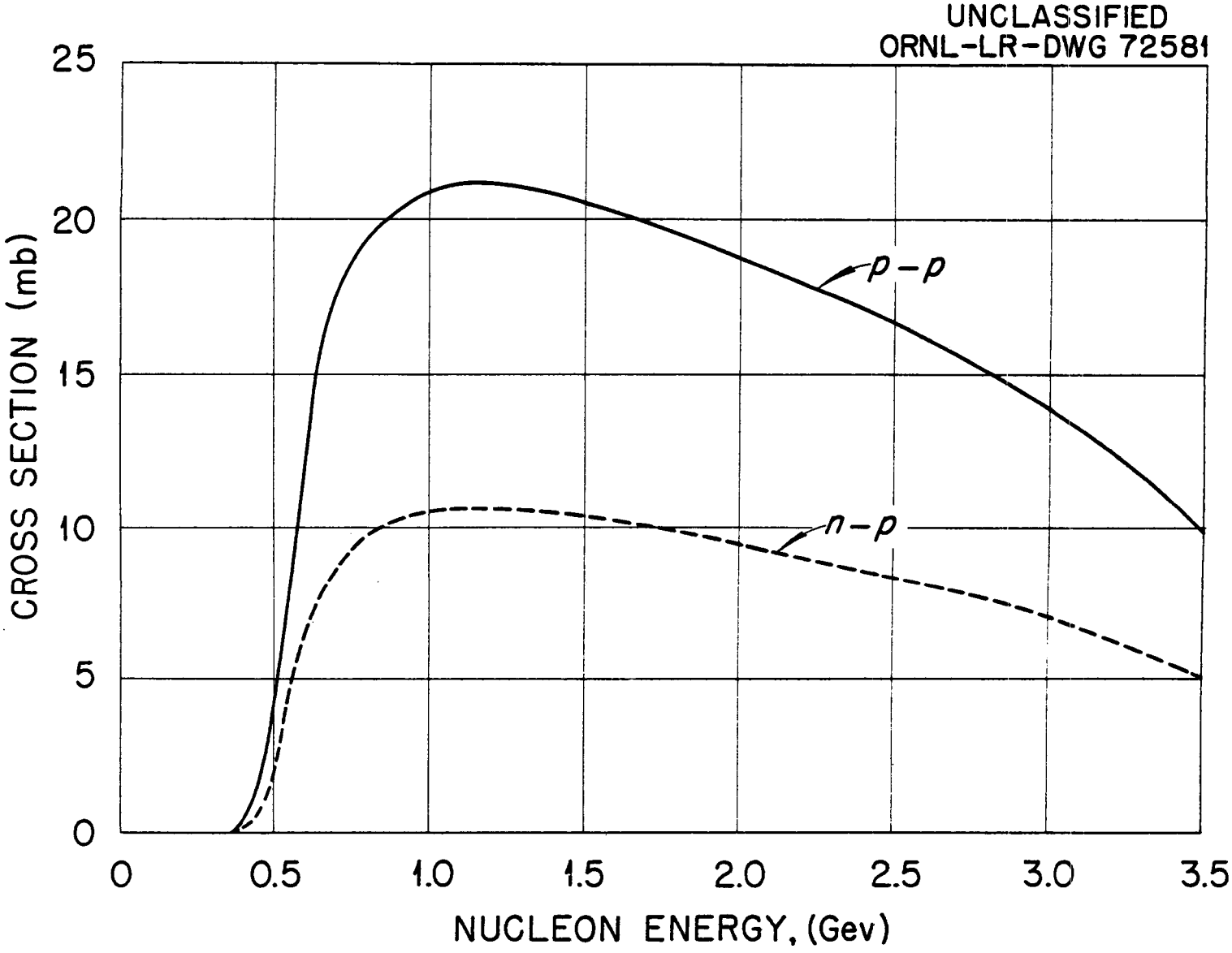

Fig. 72. Single Pion Production Cross Sections for p-p [from W. J. Fickinger et al., Phys. Rev. 125, 2082 (1962)], and n-p Collisions.

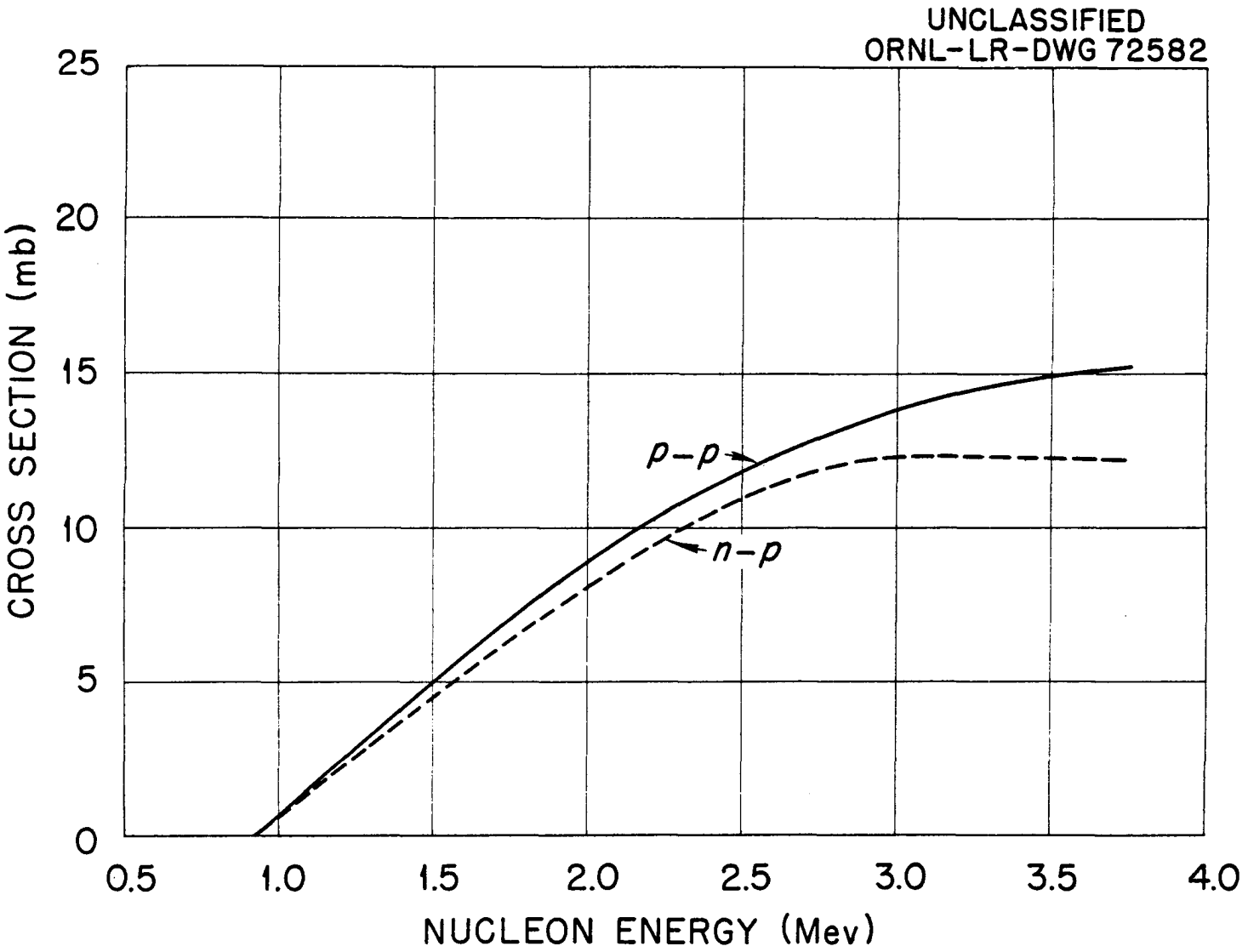

Fig. 73. Proton-Proton [from W. O. Lock et al., Phil. Mag. 2, Ser. 8, 215 (1957); W. B. Fowler et al., Phys. Rev. 103, 1479 (1956); F. F. Chen, C. P. Leavitt, and A. M. Shapiro, Phys. Rev. 103, 211 (1956)] and Neutron-Proton Double-Production Cross Section.

After the type of event is determined, it is necessary to calculate the mass, m, of the isobar. For single pion production this is done using the following expression, which is assumed to give the probability for formation of an isobar of mass m when the relative kinetic energy of the colliding particles is T_r:

$$P(m,T_r) = k\ \sigma_{3/2}\ F(m,T_r) \quad ,$$

where $\sigma_{3/2}$ is the pure T = 3/2 cross section ($\pi^+ + p$ cross section), F is the phase space available to the isobar decay products, and k is a normalizing constant. This expression is a slight modification of the one given by Sternheimer and Lindenbaum.[11] For double pion production the expression

$$P(m_1,m_2,T_r) = k\ \sigma_{3/2}(m_1)\ \sigma_{3/2}(m_2)\ F(m_1,m_2,T_r) \quad ,$$

is used, where m_1 and m_2 are the masses of the two isobars.

When the isobar masses are known, the recoil angles of the isobars must be determined. The code is presently set up with any one of three options in this respect: Isobars are produced in either a forward or backward direction in the center-of-mass (C) system, isotropically in the C system, or in each of them 50% of the time. At present the latter alternative seems best,[14] but the others are included to determine their effects. Relativistic kinematics are used to determine the final momenta of the isobars, and they are allowed to decay isotropically in their own rest mass system to give the produced pions and decay or recoil nucleons.

The Clebsch-Gordon coefficients, in the framework of the isotopic spin formalism, are used to determine the final products.

Pion Production in Pion-Nucleon Reactions

The calculation of the production of pions in pion-nucleon collisions is carried out in exactly the same way as that for nucleon-nucleon collisions. Most of the data needed for these reactions are contained in an excellent article by Falk-Vairant and Vallados.[15] The inelastic cross sections that they give for $\pi^+ + p$ and $\pi^- + p$ reactions were assumed to be all single-production cross sections. These are given in Figs. 74 and 75.

The composite isotopic spin states involved in pion-nucleon collisions are generally the pure T = 3/2 and T = 1/2 state. Each of these can in turn be written in terms of the isotopic spin states of a recoil pion and a T = 3/2 isobar. Here both the composite T = 3/2 and T = 1/2 states contribute to the production process. The phase angle, ϕ, between the matrix

14. A. C. Mellissinos, Rochester University, private communication.

15. P. Falk-Variant and G. Vallados, Rev. Mod. Phys. 33 362 (1961).

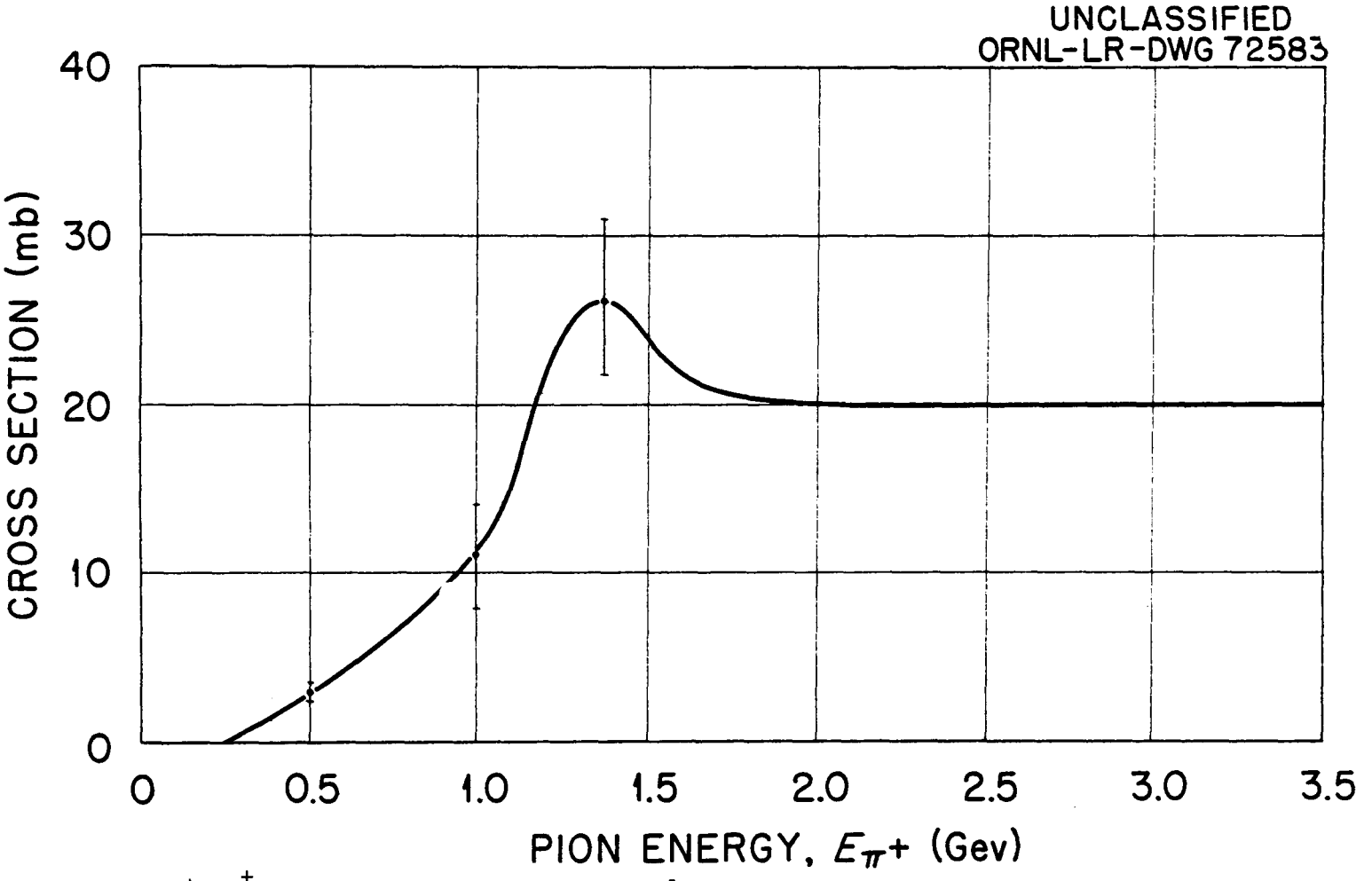

Fig. 74. π^+ + p Inelastic Cross Section [from P. Falk-Vairant and G. Vallados, Rev. Mod. Phys. 33, 362 (1961)].

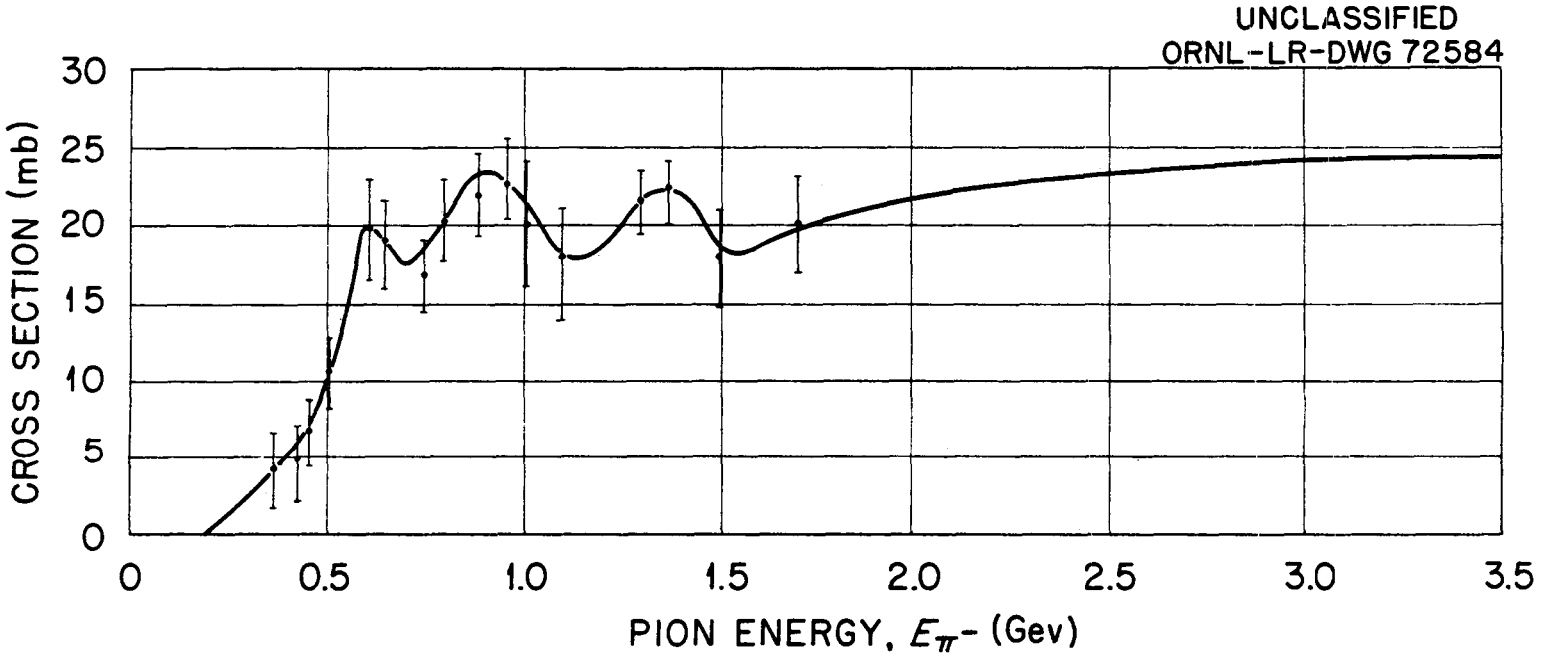

Fig. 75. π^- + p Inelastic Cross Section [from P. Falk-Vairant and G. Vallados, Rev. Mod. Phys. 33, 362 (1961)].

elements of the states and the ratio of the cross sections for production through each of these states must be known, as well as the single-production cross section, in order to determine the mode of formation of the isobar. By using the isotopic spin formalism, the single-production $\pi^- + p$ cross section can be written:

$$\sigma_{s.p.} = \frac{2}{3}\sigma_{11}(1 + \rho_1) \quad ,$$

where $\rho_1 = \sigma_{31}/2\sigma_{11}$, and σ_{31} and σ_{11} are the single-production cross sections for the pure $T = 3/2$ and $T = 1/2$ states, respectively. The $T = 1/2$ nonelastic cross section is given elsewhere.[15] This cross section was assumed to be all single production, and hence ρ_1 could be determined. By again making use of the isotopic spin formalism, the cross section for the reaction $\pi^- + p \rightarrow n + \pi^+ + \pi^-$ can be written

$$\sigma = \frac{2}{3}\sigma_{11}\left(\frac{5}{9} + \frac{26}{45}\rho_1 + \frac{7}{9}a\right) \quad ,$$

where $a = 2\sqrt{\rho_1/5}\cos\phi$, and ϕ is the phase angle mentioned before. The cross section is given by Perkins et al.[16] and by Walker,[17] and therefore a can be calculated. These quantities are sufficient for determining all the formation and decay modes of the $T = 3/2$ isobar for any pion-nucleon reactions.

Status

The coding for the extended intranuclear cascade calculation is nearing completion. Extensive checks must be made and the code debugged; then the code must be run so that extensive comparisons with experiment can be made. The estimated completion time for this portion of the work is about six months.

16. W. A. Perkins et al., Phys. Rev. 118, 1364 (1960).

17. W. I. Walker, Proceedings of the Sixth Annual Rochester Conference for 1956, p IV-16, Interscience, New York.

Paper D-4

EXPERIMENTAL TECHNIQUES FOR THE MEASUREMENT OF NUCLEAR SECONDARIES FROM THE INTERACTIONS OF PROTONS OF A FEW HUNDRED MEV

F. C. Maienschein, T. V. Blosser, H. R. Brashear,
W. R. Burrus, F. M. Glass, W. A. Gibson, N. W. Hill,
C. F. Johnson*, T. A. Love, V. A. McKay,
R. W. Peelle, R. T. Santoro, R. J. Scroggs,
T. F. Sliski, H. J. Stripling, and W. Zobel

Oak Ridge National Laboratory**

1514/over

Abstract

In this paper are described the preparations for a set of experiments which are designed to check space shielding calculations. The experiments are at an early stage and all information must be considered as preliminary. The approximate calculations of Alsmiller[1] have been used to estimate that spectral measurements are most important for secondary neutrons, protons, and gamma rays arising from the interactions of incident protons in the energy range from 20 to 600 Mev. Both "thin" and "thick" targets are needed to check the two pertinent types of calculations, those for the prediction of cross sections and secondary spectra for intranuclear cascades and those for transport through shields. Previous measurements exist only for thin targets and these are all limited in energy resolution or the range of energies and angles covered.

For the present experiments, the choice of spectrometers was conditioned by the need to move the equipment to several accelerators and the very stringent time schedule imposed by the need for shielding information for the Apollo mission to the moon. Thus, for neutron spectroscopy magnetic-deflection of proton recoils was not seriously considered. Three approaches have been followed with extensive development. Proton-recoil telescopes of two types have been studied but current emphasis centers on a dE/dx scintillation spectrometer for the energy range above 50 Mev. Neutron time of flight over a short path is being utilized to cover the energy range from a few Mev to ~50 Mev with reasonable resolution. Finally, a set of Bonner spheres is used for the energy range below 10 Mev.

*On assignment at Oak Ridge National Laboratory from General Dynamics, Fort Worth, Texas.

**Operated by Union Carbide Nuclear Company for the U. S. Atomic Energy Commission.

1. R. G. Alsmiller, Jr., and J. E. Murphy, "Space Vehicle Shielding Studies: Calculations of the Attenuation of a Model Solar Flare and Monoenergetic Proton Beams by Aluminum Slab Shields," ORNL-3317, 1962 (in press).

15140

For proton spectroscopy, the telescopes may be used by removing the hydrogenous radiator. The time-of-flight equipment may also be used for protons although the energy resolution from flight-time measurement becomes inferior to that available from energy absorption in a dE/dx scintillator above about 30 Mev. Flight time can be used to relieve the total absorption vs dE/dx ambiguity. For low-energy protons (less than ~10 Mev) no spectrometer, other than nuclear emulsions, is available nor is this energy region considered to be of particular importance.

Because of the complexity and size, Compton-recoil or pair magnetic deflection spectrometers were not considered for gamma rays. A sodium iodide scintillation spectrometer has an efficiency for neutrons comparable to that for gamma rays in the Mev region, and the resulting neutron-induced background was considered to be overwhelming. Thus a 3-NaI-crystal-pair spectrometer with a high inherent neutron rejection is used above 1.5 Mev. An anticoincidence scintillation spectrometer is used for lower energies.

The various spectrometers, together with dosimeters and threshold detectors have been tested in feasibility studies at the Harvard University Synchrocyclotron (156-Mev protons). Spectral measurements continue at that facility at this time, but the data await analysis. Results from the feasibility studies are discussed.

Introduction

As is discussed in papers by H. W. Bertini, W. E. Kinney et al., and R. G. and F. S. Alsmiller at this symposium, considerable calculational effort has been spent at the Oak Ridge National Laboratory to provide data pertinent to the shielding of space vehicles. The important sources of radiation which must be considered arise from protons trapped in the Van Allen belt(s) and from solar flares. The Van Allen protons will be most troublesome for vehicles with a slow rate of vertical ascent, such as those powered with ion-propulsion engines, while the solar-flare protons will be dangerous for occupants of any extraterrestrial spacecraft. The danger of solar flares is not accurately predictable, however, since their occurrence is statistical, the average rate varying periodically with time. Further, the calculations available, which take into account the production of secondary particles by the interactions of the protons, do not give consistent results for the dose which results from a single

flare.[1-3] Therefore, at present it is not possible to conclude whether the shields required for the approximately seven-day Apollo mission to the moon will be of sufficient thickness to make secondary nuclear interactions of importance. But it is clear that manned interplanetary flights will require shields of such thicknesses that the production of secondary particles must be accurately predicted, and the great cost of extraterrestrial transport emphasizes the need for accurate and not overly conservative calculations.

The calculations necessary for spacecraft shielding are of two basic types: those of cross sections and the spectra of secondary particles for intranuclear cascades and those of the transport of the secondary particles through shields. Energy losses by ionization are included in the transport calculation and are considered to be well understood, but serious uncertainties arise in other parts of the calculations which make experimental checks highly desirable. Thus preparations are under way for a series of experiments to provide such checks. The present status of the preparations is described herein; however, it must be understood that these experiments are at an early stage and that modifications in the equipment and plans may be necessary.

As an aid in determining which measurements would be most pertinent for spacecraft shielding, Alsmiller and Murphy[1] have performed preliminary calculations of the dose resulting from incident monoenergetic protons of various energies. Although these calculations contain many approximations, they represent the best information presently available and several conclusions may be drawn. For example, for shields thinner than the range of the incident protons the dose from the primary protons is dominant; the dose due to secondary protons decreases rapidly with increasing shield thickness, while the dose due to secondary neutrons drops slowly and becomes dominant for thicknesses greater than the incident proton range; and the dose due to secondary mesons is only a few percent of the total dose for any shield thickness appropriate for spacecraft. The dose due to secondary gamma rays was not considered by Alsmiller and Murphy,[1] but Alsmiller et al.[4] and Madey et al.,[5] who estimated the production of inelastic scattering gamma rays, indicate that there will be a significant

---

1. R. G. Alsmiller, Jr., and J. E. Murphy, ORNL-3317, op. cit.

2. R. I. Allen et al., Shielding Problems in Manned Space Vehicles, NR-140 (September, 1961).

3. R. K. Wilson et al., A Study of Space Radiation Shielding Problems for Manned Vehicles, FZK-144 (June 8, 1962).

4. F. S. Alsmiller, R. G. Alsmiller, Jr., and D. K. Trubey, Comparison of Primary Proton Dose with the Dose from Gamma Rays Produced by Inelastic Scattering of Solar Flare Protons, ORNL CF-62-10-29 (1962).

5. R. Madey et al., Trans. Am. Nuclear Soc. 5 (1), 213 (1962).

dose due to secondary gamma rays. In summary, then, it appears that the measurements most needed are for secondary neutrons, protons, and gamma rays. The energy spectra and angular distribution of these particles must be determined in order to provide definitive tests of the theory. (It is assumed that the spectra of the incident primary particles in space will be available from other sources.)

To determine the energies of the incident protons that are the most important, Alsmiller and Murphy[1] calculated two "importance functions." The second of these gives the total secondary dose as a function of incident proton energy and shield thickness for the solar-flare spectrum that occurred on May 10, 1959. The importance function for an aluminum shield of 0.5 collision length (~42 g/cm^2) appears to peak at about 300 Mev and to decrease by a factor of ~10 at 1 Bev. It would be desirable to know the importance function for lower energies, but, unfortunately, the lowest energy point given is at 200 Mev. For thicker shields the importance function is roughly constant from 200 to 600 Mev, with a small decrease at still higher energies. The production of gamma rays is expected to be most important at lower energies, where the proton intensities are highest. Thus the incident-particle energy range of most interest for space shielding lies below about 600 Mev, with a lower limit of perhaps 20 to 50 Mev (lower when secondary gamma rays from nuclear excitation are considered).

Finally, consideration must be given to the choice of target thickness. For checking the intranuclear cascade calculations, experiments are needed with a few "thin" targets with widely varying Z values. For checking the transport calculations, spectra at various angles must be obtained with one or more "thick" targets. Actually, the targets will not be thick with respect to a mean free path for nuclear interactions, but their thickness will be greater than the range of the incident protons.

Previous Research

A number of spectral measurements have been made with synchrocyclotrons, the type of accelerator that covers most of the energy range of interest. Table 1 summarizes the pertinent characteristics of some of these measurements, all of which cover a limited energy range for the outgoing particles, suffer from poor energy resolution, or are otherwise limited. In general, the proton spectra and the neutron spectra with the best resolution show effects of nuclear level structure. Perhaps the most surprising feature of the data is the apparent absence of an exchange peak in the neutron spectra observed at Harvard ($\leq$ 100 Mev) for elements heavier than beryllium. At other laboratories exchange peaks were observed for all Z with energies as low as 143 Mev.

The one set of spectra listed for deuterons and tritons indicates that cascade particles with $Z > 1$ are unlikely to give an effect of more than a few percent. The gamma-ray data, however, when considered together

---

1. R. G. Alsmiller, Jr., and J. E. Murphy, ORNL-3317, op. cit.

Table 1. References to Measurements of Spectra of Secondary Particles from High-Energy Proton Interactions

Observed Particle	Accelerator	Incident Proton Energy (Mev)	Spread of Incident Proton Energy (Mev)	Target Thickness	Materials	Observed Energy Range (Mev)	Observed Angles (deg)	Type of Spectrometer	Energy Resolution	Comments	References
Protons	Harvard	96		~8 Mev	C		3–90	Range telescope	~3 + (a)	Observed level structure in C	Strauch and Titus, *Phys. Rev.* 103, 200 (1956)
Protons	Harvard	96			17 elements from Li to Bi	30–90	40	Range telescope	3–17 Mev including target thickness	Level structure for lower Z	Strauch and Titus, *Phys. Rev.* 104, 191 (1956)
Protons	Harvard	160			Zn, Sn, Ta, Pb	5–23	60, 90, 120	Range telescope and magnetic deflection	Good	Peaks slightly below Coulomb barriers	Fox and Ramsey, *Phys. Rev.* 125, 1609 (1962)
Protons	LRL	190		Thin	C, Al, Ni, Ag, Au	~3–90	0–65, 100–180	Nuclear emulsions and magnetic deflection	Very large angular acceptance	Also measured d and α spectra	Bailey, UCRL-3334 (1956)
Protons	Rochester	240	±8	7 Mev	C	60–190	90	Nuclear emulsions	Poor		Temmer, *Phys. Rev.* 83, 1067L (1951)
Protons	LRL	340	11	4 Mev	H, D, C, O	100–350	30, 40	Magnetic deflection	(a)	Nucleon momentum distributions are deduced	Cladis, Hess, and Moyer, *Phys. Rev.* 87, 425 (1952)
Neutrons	Harvard	50	Large		Li, Be, C, Pb	35–70	0, 5, 10, 16	Telescope	(a)	Li and Be indicate exchange reactions; C and Pb do not	Hoffman, Harvard thesis, 1952
Neutrons	Harvard	100	Large	0.125 in.	Be, C	40–110	0	Telescope	(a)	Li and Be indicate exchange reactions; C and Pb do not	Bodansky and Ramsey, *Phys. Rev.* 82, 831 (1951)
Neutrons	Harvard	95	~20		D, Li, Be, C, Al, Cu, Pb	50–110	0, 5, 10, 16, 28	Telescope	8–10 Mev and (a)	Li and Be indicate exchange reactions; C and Pb do not	Hoffman and Strauch, *Phys. Rev.* 90, 449 (1953)
Neutrons	Harwell	143	3	2.5–7.0 Mev	D, Li, Be, C, Al, Cu, Pb, U	15–140	~0	Time-of-flight	$0.07 \lesssim (\Delta E/E)_n \lesssim 0.14$	Measurements all relative; high-energy peak for all Z	Bowen *et al.*, *Nuclear Phys.* 30, 475 (1962)
Neutrons	Harwell	171		1–2 g/cm^2	Be, C, Al, U	50–200	2.5	Range telescope	(a)	High-energy peak for all Z	Cassels *et al.*, *Phil. Mag.* 44, 425 (1953)
Neutrons	Rochester	244		~0.3–1.0 in.	Be, C, Pb	120–240	0, 15	Telescope	$0.10 \lesssim (\Delta E/E)_n \lesssim 0.15$	High-energy peak for all Z	Nelson *et al.*, *Phys. Rev.* 88, 1 (1952)
Neutrons	LRL	190	±15	4.7–14.6 Mev	C, Al, Ni, Ag, Au, U	0.5–12	45, 90, 135	Nuclear emulsions	(a)	Primarily evaporation neutrons	Gross, UCRL-3330 and UCRL-3337 (1956)
$Z \gtrsim 1$	ORSAY	154			Au^{197}	>30	15, 30, 60	$(dE/dx - E)$ telescope	±20%	$d/p \approx 1/10$, $t/p \approx 1/20$	Genin *et al.*, *J. Phys. Radium* 22, 615 (1961)
Gamma rays	Harvard	35	Large		LiH, Be, B, C, Mg, Al, Si, Cu, Au	~3–~20	90	NaI scintillation		Pulse-height spectra only; serious neutron-induced backgrounds	Culler, Harvard thesis, 1956
Gamma rays	Harvard	24, 56, 90	Large		C, Al	~3–~20	90	NaI scintillation		Pulse-height spectra only; serious neutron-induced backgrounds	Culler, Harvard thesis, 1956
Gamma rays	Harwell	150		20–40 Mev	Li, Be, B, C, N	<15	90	NaI scintillation			Clegg *et al.*, *Proc. Phys. Soc.* 78, 681 (1961)
Gamma rays	Harwell	150		20 Mev	O, F	<15	90	NaI scintillation			Foley *et al.*, *Nuclear Phys.* 31, 53 (1962)
Gamma rays	Harwell	150		20 Mev	Na, Mg, Al, Si, P, S	<15	90	NaI scintillation			Foley *et al.*, *Nuclear Phys.* 37, 23 (1962)
Gamma rays	LRL	30–340			C	8–22	90	180° pair spectrometer		Studied C^{12} level at 15.2 Mev	Cohen *et al.*, *Phys. Rev.* 96, 714 (1954)

[a] Energy resolution limited by energy spread of incident beam.

with one lower energy measurement,[6] are of quite limited value. None of the previous studies were made with a target "thick" from the transport point of view.

Planned Experiments

As described in a previous report,[7] experiments are planned with the primary goal of determining energy spectra at selected angles for secondary neutrons, protons, and gamma rays. Preliminary or feasibility studies were made at the Harvard University Synchrocyclotron (156-Mev protons) in May and August, 1962. The object of these studies was not to produce spectral data but to determine the necessary beam intensities, to measure backgrounds and to check the operation of the spectrometers. Substantial modifications to the equipment were required after each test. The test results have not been analyzed in detail for all spectrometers, and the comments presented in this paper are all tentative. Further measurements were performed at Harvard in October, 1962, and continue at the time of this symposium.

The arrangement of the targets and spectrometers at the Harvard accelerator is described in the next section. Also discussed are the measurements of the proton-beam average intensity and spatial extent, as well as the necessary studies of the complex time behavior of the beam. The use of targets thicker than the range of the primary protons simplifies many experimental problems, especially for measurements near the forward direction. However, both thin and thick targets will be studied (as feasible) in order to check the two types of calculations (cross sections and transport). Targets will be chosen from Be, C, Al, Co, Bi, and H_2O. Copper and lead were used in the preliminary studies. The change to cobalt and bismuth will provide single isotopes, a potential advantage in interpreting nuclear level effects.

The choice of spectrometers was dictated by the need to move the equipment to several accelerators and the stringent time schedule imposed by the need for shielding information for the Apollo mission to the moon. Thus for neutron spectroscopy, magnetic deflection of proton recoils was not seriously considered, but three other approaches have been followed with extensive development. Proton-recoil telescopes of two types have been studied, with current emphasis centering on a dE/dx scintillation spectrometer for the energy range above 50 Mev. Neutron time of flight over a short path is being utilized to cover the energy range from a few Mev to ~50 Mev with reasonable resolution, and, finally, a set of Bonner spheres is used for the energy range below 10 Mev. These three systems are described in Sections II, III, and IV.

---

6. T. Wakatsuki et al., J. Phys. Soc. Japan 15, 1141 (1960).

7. W. A. Gibson, W. R. Burrus, and T. A. Love, Neutron Phys. Div. Ann. Prog. Rep. September 1, 1961, ORNL-3193, p. 325.

In connection with the interpretation of the Bonner sphere data (Section IV) and their extension to higher energy, several threshold detectors were tried. These depended upon fission reactions or $C^{12}(n,2n)C^{11*}$ activation. It was decided not to use these detectors, basically because of their inability to differentiate between neutron- and proton-induced reactions.

In a cooperative effort with the Fort Worth Division of General Dynamics, nuclear emulsions of varying thickness and sensitivity were exposed in the feasibility studies.[8] It has been determined that appropriate exposures were achieved for many of the plates, but they have not yet been subjected to detailed scanning. The separation of proton tracks from neutron-induced proton-recoil tracks is quite difficult at the energies considered here, and the efficacy of the approach remains to be demonstrated. If successfully used, the emulsions should give useful data up to about 25 Mev.

For proton spectroscopy the telescopes may be used by removing the hydrogenous radiator. The time-of-flight equipment may also be used for protons, although the energy resolution from flight-time measurements becomes inferior to that available from energy absorption in a dE/dx scintillator above about 30 Mev. Flight time can be used to relieve the ambiguity between total absorption and dE/dx. For low-energy protons (less than ~10 Mev) no spectrometer, other than the nuclear emulsions, is available; nor is this energy region considered to be of particular importance.

Because of their complexity and size, Compton-recoil or pair magnetic deflection spectrometers were not considered for gamma rays. A NaI(Tl) scintillation spectrometer has an efficiency for neutrons comparable to that for gamma rays in the Mev region, and the resulting neutron-induced background was considered to be overwhelming. Thus a three-crystal (NaI) pair spectrometer with a high inherent neutron rejection was chosen and is described in Section V.

As stated previously, the major goal for the experiments is to provide accurate spectral data for comparison with calculations. A further check may be provided by determining the distribution in depth of the dose resulting in a spherical phantom from the interaction of all secondary particles. Fractionation of the dose with respect to the type of radiation would require dosimeters which are not available. The "integral" dose measurement described in Section VI will, if successful, test whether the interactions of secondary particles in water (or tissue) and the integrations over angle required by the complex geometry can be handled by the calculation.

The electronics for the various spectrometer systems is located in two mobile laboratories so that it may be transported to the accelerators of interest. Connecting cables ~200 feet long permit operation of the experiment from the mobile laboratories. The photograph on page 531 shows

8. Sponsored by the U. S. Air Force, Wright Air Development Division.

part of the 17 relay racks of equipment which is largely transistorized. The design, purchase, fabrication, test, and assembly of the apparatus were possible in the short time available only through the extraordinary efforts of the electronic design, counter, and mechanical design groups of the Instrumentation and Controls Division of ORNL. The tests at Harvard University were greatly facilitated by the cooperation afforded by the synchrocyclotron group, particularly A. M. Koehler and W. M. Preston. Use of the electronic components is described in Sections I - VI. Detailed descriptions of individual components designed for this experiment but of general interest will be prepared for publication elsewhere.

I. Proton Intensity Measurements

The series of experiments currently in progress at the Harvard University Synchrocyclotron[9] has been outlined in the Introduction. For a meaningful interpretation of the experimental data, the detector position as a function of angle and distance from the experimental target must be accurately known. In addition, the spatial and time distributions of protons incident upon the target, as well as the absolute intensity of the proton beam, must be known. Solutions to these problems are individually discussed below.

Experimental Arrangement

The general experimental arrangement is shown in Fig. 1. The Harvard University 95-in. synchrocyclotron is a frequency-modulated machine capable of producing unpolarized protons at an energy of 156 Mev, with an energy spread of 2 Mev, and fluxes up to 5×10^{10} protons/sec. Its frequency range is from 23 to 30 Mc/sec, modulated by a rotating condenser. The nominal beam area is ≤ 7 cm^2. The permanent shield of the machine consists of from 3 to 8 ft of ordinary concrete.

The proton beam emerging from the machine passes through a vertical slit, which was introduced late in the experiments to reduce the effects of backgrounds observed in dosimetry measurements. It is then deflected by the steering magnet and focused by the quadrupole magnet, after which it continues through the beam tube and impinges onto the target. The lead bricks shown were added to further reduce backgrounds.

The target and detector-holding device is shown in the photograph on page 533. The apparatus is first centered on the proton beam by adjustment of the alignment posts at either end. Polaroid film is used as the beam-locating sensor. The target holder and detector arms are then positioned by using an alignment bar extending between the alignment posts. The detectors are rotatable through large angles about the target axis and can be varied in distance from the target up to 100 cm, depending upon which arm is used. All three arms can be used independently, permitting three simultaneous experiments to progress at three different angles and distances.

---

9. F. T. Howard, Cyclotrons and High-Energy Accelerators, ORNL-2644 (January, 1959).

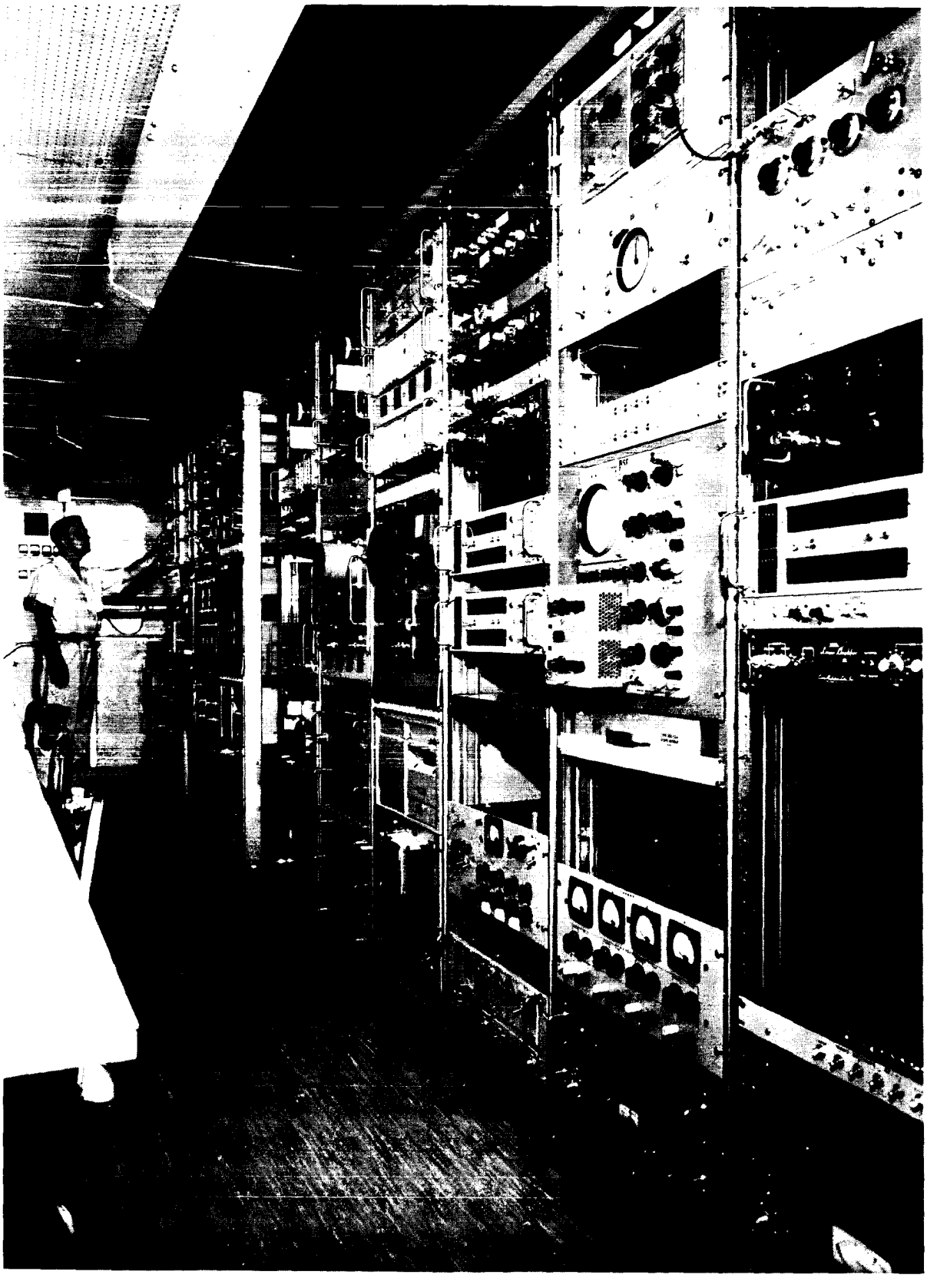

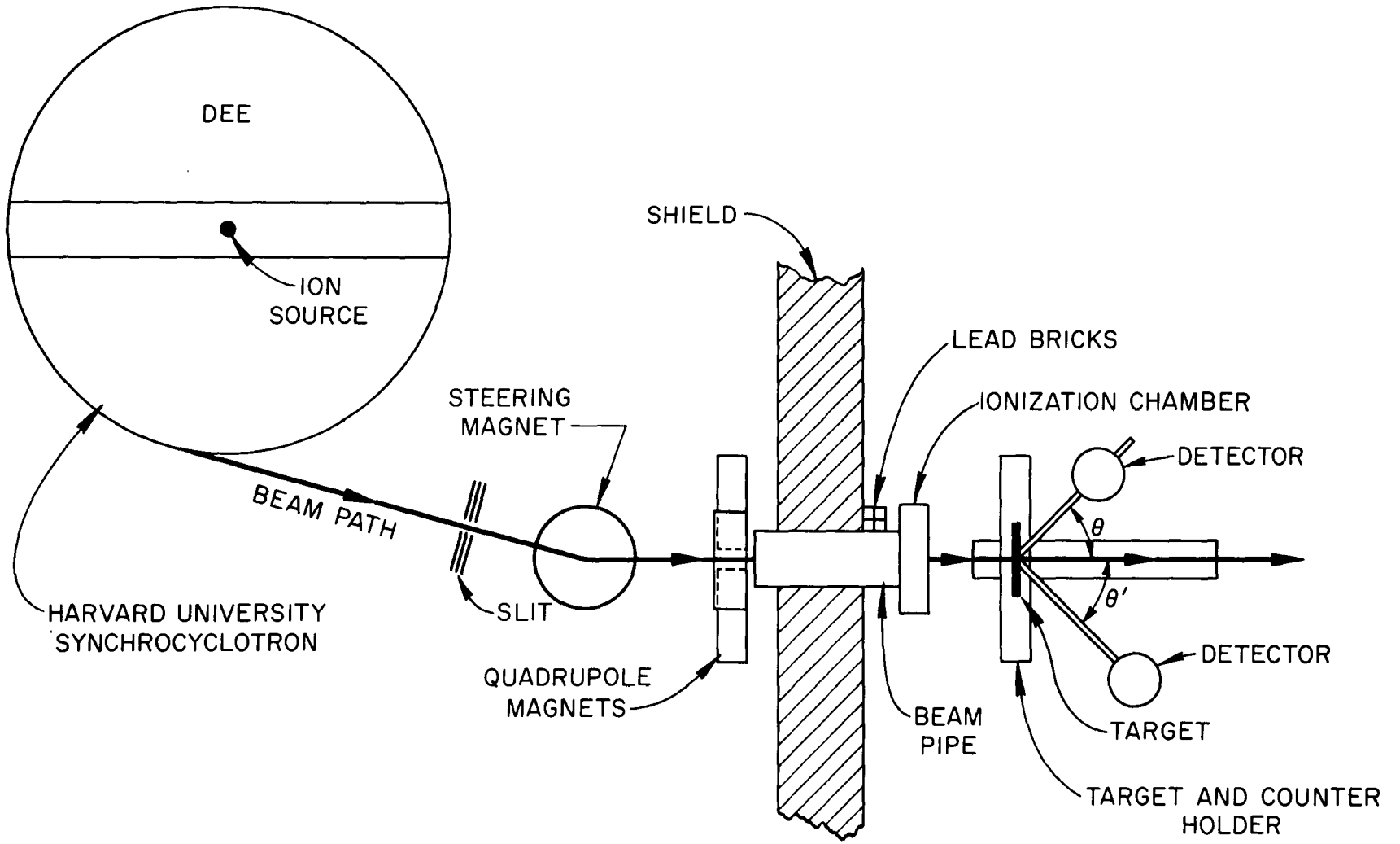

Fig. 1. Experimental Arrangement at Harvard University Synchrocyclotron.

Proton Distribution Over the Beam

Film Studies. The intensity distribution in a plane perpendicular to the beam, called the beam profile, was determined from Polaroid film exposures in the beam at several distances from the beam pipe. The shape of the image was indicative of the condition of focus. Because of the shape of the slit, the ideal cross section should have been a vertically elongated rectangle. In practice, however, the image attained was an oval, with its major axis horizontal. The contradiction is believed to be due to difficulties in adjustment of the quadrupole focusing magnet.

An attempt was made to determine a correlation between the density of Polaroid film negatives exposed in the beam and the number of protons per unit area causing the exposure. A nitrogen-filled ionization chamber at the beam pipe monitored the beam protons while the films were exposed approximately 1 m from the end of the pipe. Densitometer readings of the developed images showed a linear relationship between density and proton flux over the range from 5×10^8 to 1.6×10^{10} protons. Figure 2 shows a graph of relative beam intensity as a function of image width, but sufficient information is not available from the film to accurately determine a density-proton relationship.

Profile Telescope. The need for a more accurate device with which to analyze the distribution of protons in the beam led to the construction of a profile telescope. The profile telescope, diagrammed in Fig. 3, consists of two small cylindrical crystals, with their z axes coincident and parallel to the axis of the proton beam. The signals from the crystals are in coincidence, so that it is possible to count only those protons which pass through both crystals and to minimize the effects of noise, gamma-ray background, and neutron-induced counts present in the individual counters.

The telescope is used to scan the beam horizontally and vertically, counting the number of protons across the beam profile. Figure 4 plots the proton distribution as a function of beam width for both horizontal and vertical profiles. The difference in focus, described above, is clearly shown in these data.

Beam Monitoring

The proton beam was monitored by a Faraday cup and two helium-filled ionization chambers. The Faraday cup was the absolute beam monitor, providing the basis for calibration of the ionization chambers.

The chambers, calibrated in the region of 10^7 to 10^{10} protons per second, gave the values of 74 ± 1.3 and 79 ± 1 ion pairs per proton. The difference in performance is probably due to the variation in plate spanning, gas pressure, or gas composition between the two chambers. Figure 5 shows the performance of ion chamber #2 over a range of nominally 3.5 decades of beam intensity.

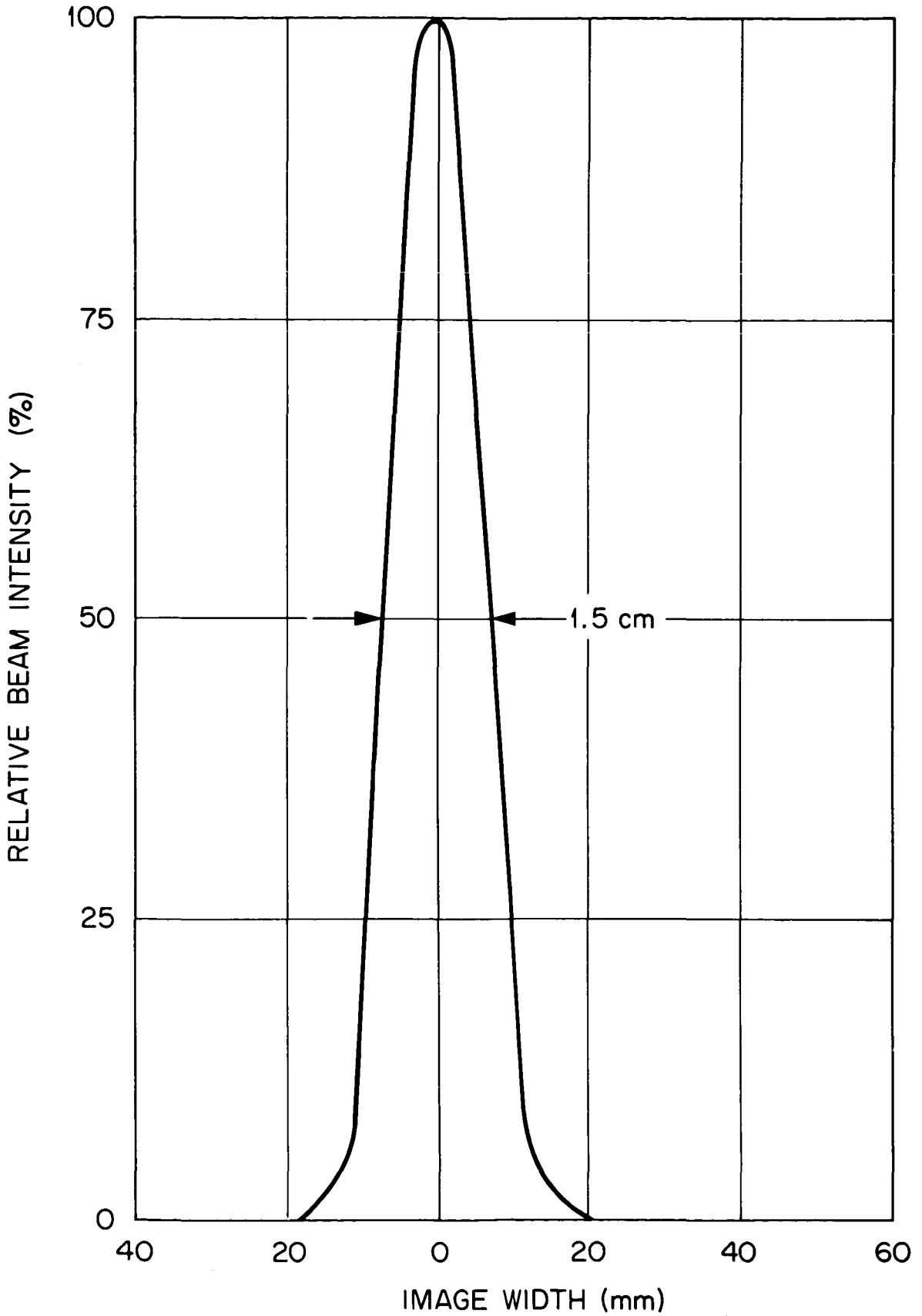

Fig. 2. Relative Beam Intensity as a Function of Image Width.

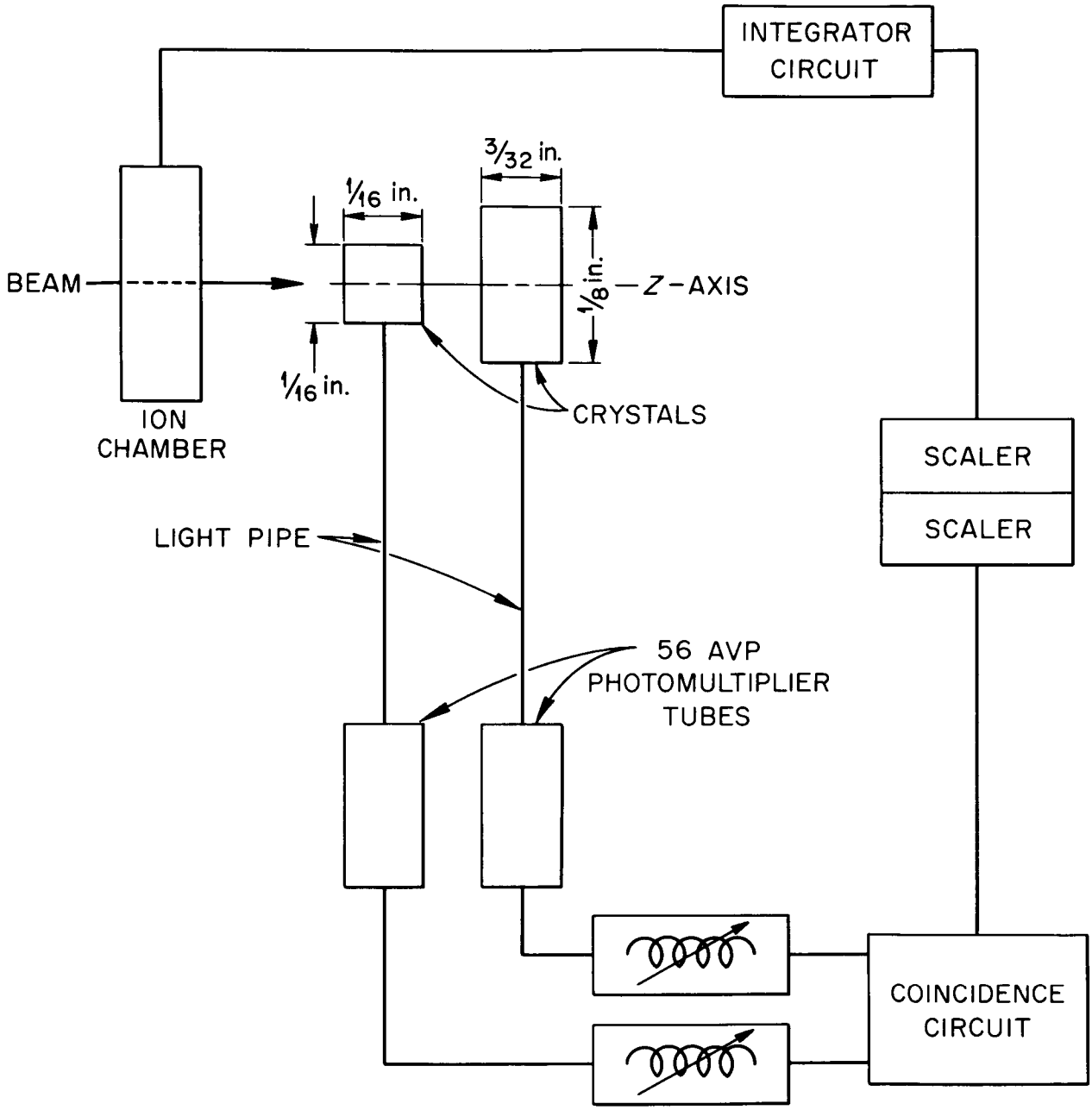

Fig. 3. Schematic of Profile Telescope.

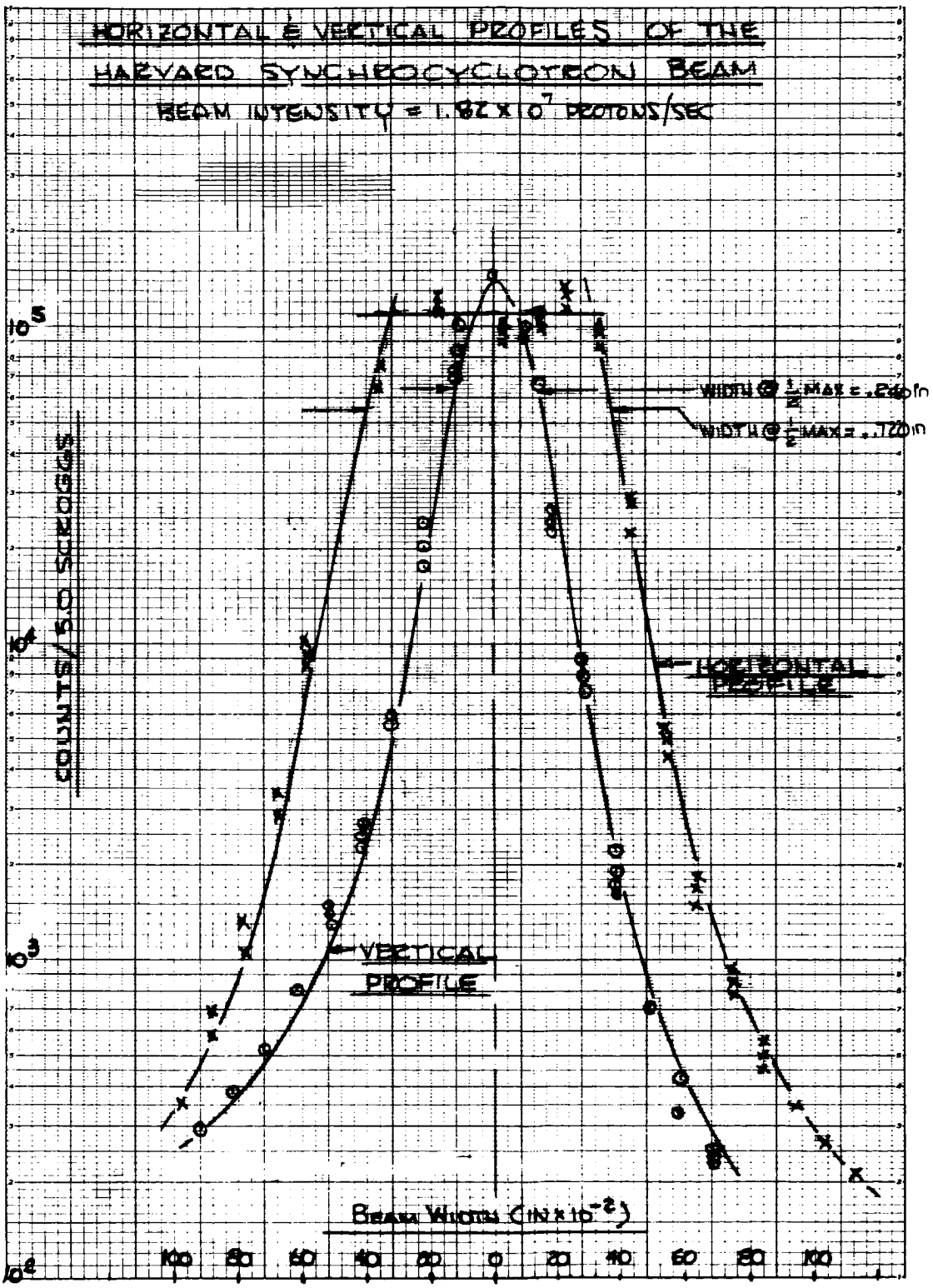

Fig. 4. Horizontal and Vertical Profiles of the Harvard University Synchrocyclotron Beam.

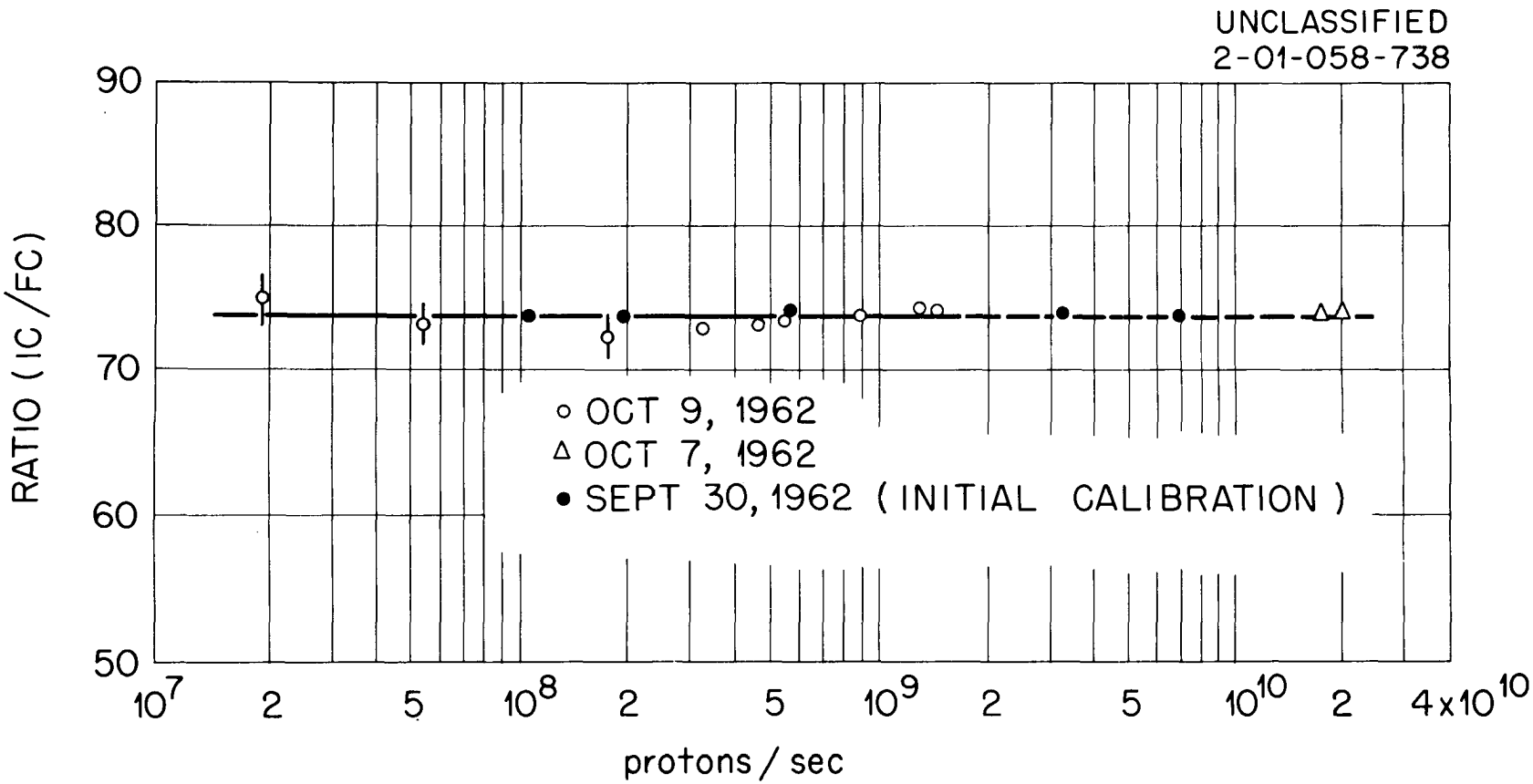

Fig. 5. Performance Curves for Ionization Chamber No. 2.

Time Dependence of the Proton Beam

Protons can be extracted from a synchrocyclotron only when the frequency of the accelerating voltage lies within narrow limits, that is, at the extraction frequency. To minimize the corrections required for random counts in experimental data, it is desirable to extract the beam for as long a period as possible (a continuous beam would be ideal). It is important, therefore, to understand how the duration of the beam is affected by the adjustment of cyclotron parameters and also to have a knowledge of the shape of the individual bursts.

Frequency modulation in the Harvard machine is accomplished with a 16-tooth rotating condenser, which rotates at about 20 rps. There is one proton burst per tooth per revolution, or 320 bursts/sec. The 320-burst/sec modulation is defined as the macrostructure. There is an additional modulation which takes place at the accelerating voltage frequency due to bunching of protons in phase with the accelerating field.

Because of the limited time available in the preliminary studies, the examination of the macroburst was restricted to a feasibility study.

A study of the structure was made for one synchrocyclotron setting. The circuit employed is shown in Fig. 6. The detector, an organic scintillator, was positioned so as to obtain a count rate of somewhat less than one count per macroburst. A marker pulse was obtained on the downswing of the frequency modulation cycle just before proton extraction. The elapsed time between the marker pulse and a proton signal from the scintillator was then analyzed and stored. Since there is a variation from tooth to tooth of the condenser (due to fabrication differences, eccentric alignment, wobble in the mechanical support, etc.), a gate was used which permitted analysis of only the pulse from each sixteenth tooth. The tooth with the widest frequency swing was arbitrarily designated tooth No. 7. As shown in Fig. 6, it was possible to implement all of the necessary gating by using a dual-sweep oscilloscope. The main sweep was set for 500 μsec; the delayed sweep was synchronized to the condenser rotation. Figure 7 shows intensity versus time profiles for teeth 1 and 9. It is evident that the burst shape varies with individual teeth.

A quicker and less detailed determination of the "duty factor," d, for the cyclotron can be obtained from a measurement of the chance coincidence rate, N_{BC}, which is given by:

$$N_{BC} = \left[\frac{(B-B^S)(C-C^S)}{d} + B^S C^S \right] \tau_{BC}$$

where:

$B = B^S + B^P d$ = average count rate in channel B;
B^S = steady count rate when beam is off;
B^P = peak count rate when beam is on; and
τ_{BC} = resolving time of coincidence circuit.

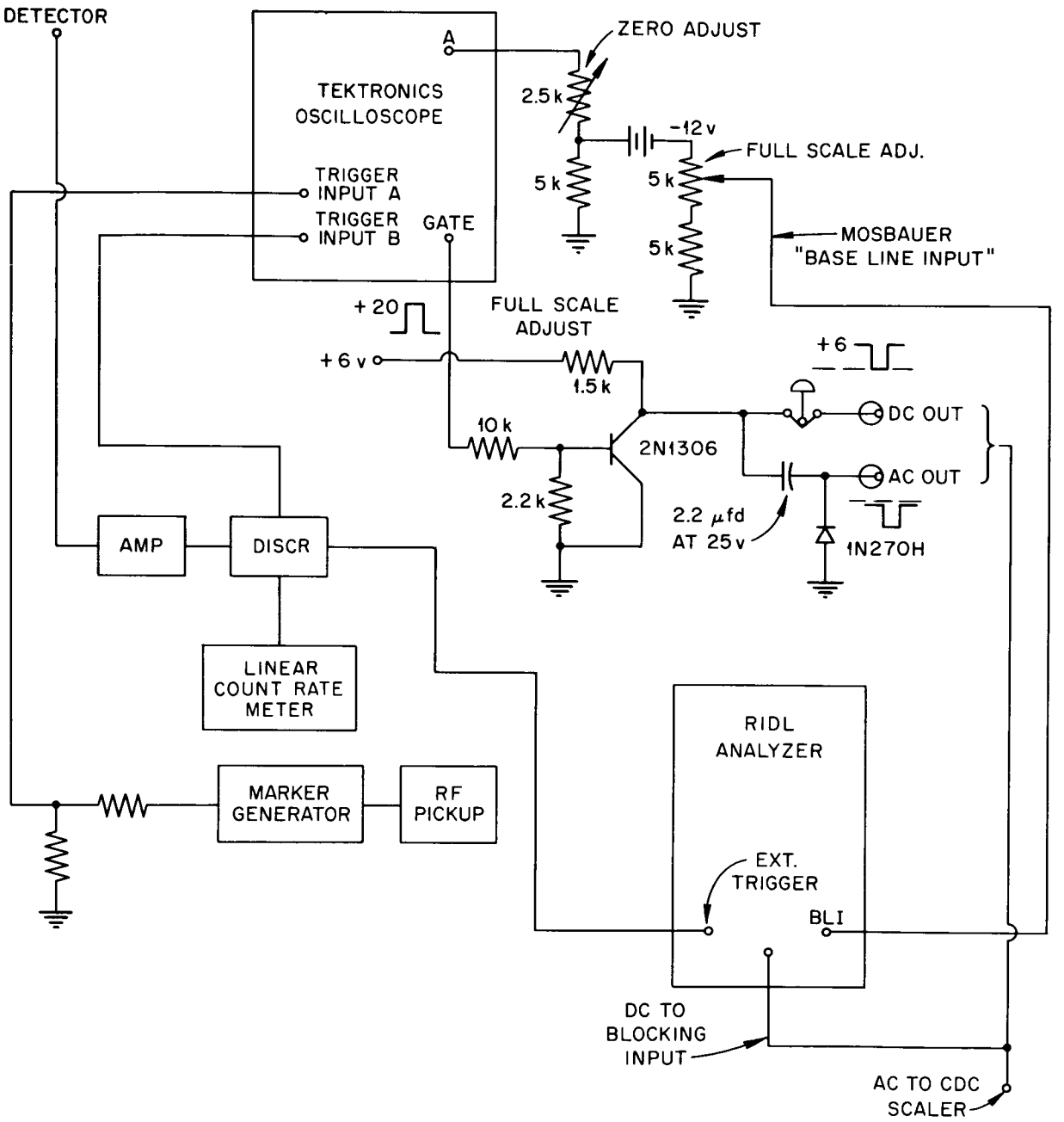

Fig. 6. Circuit Used in Macroburst Studies.

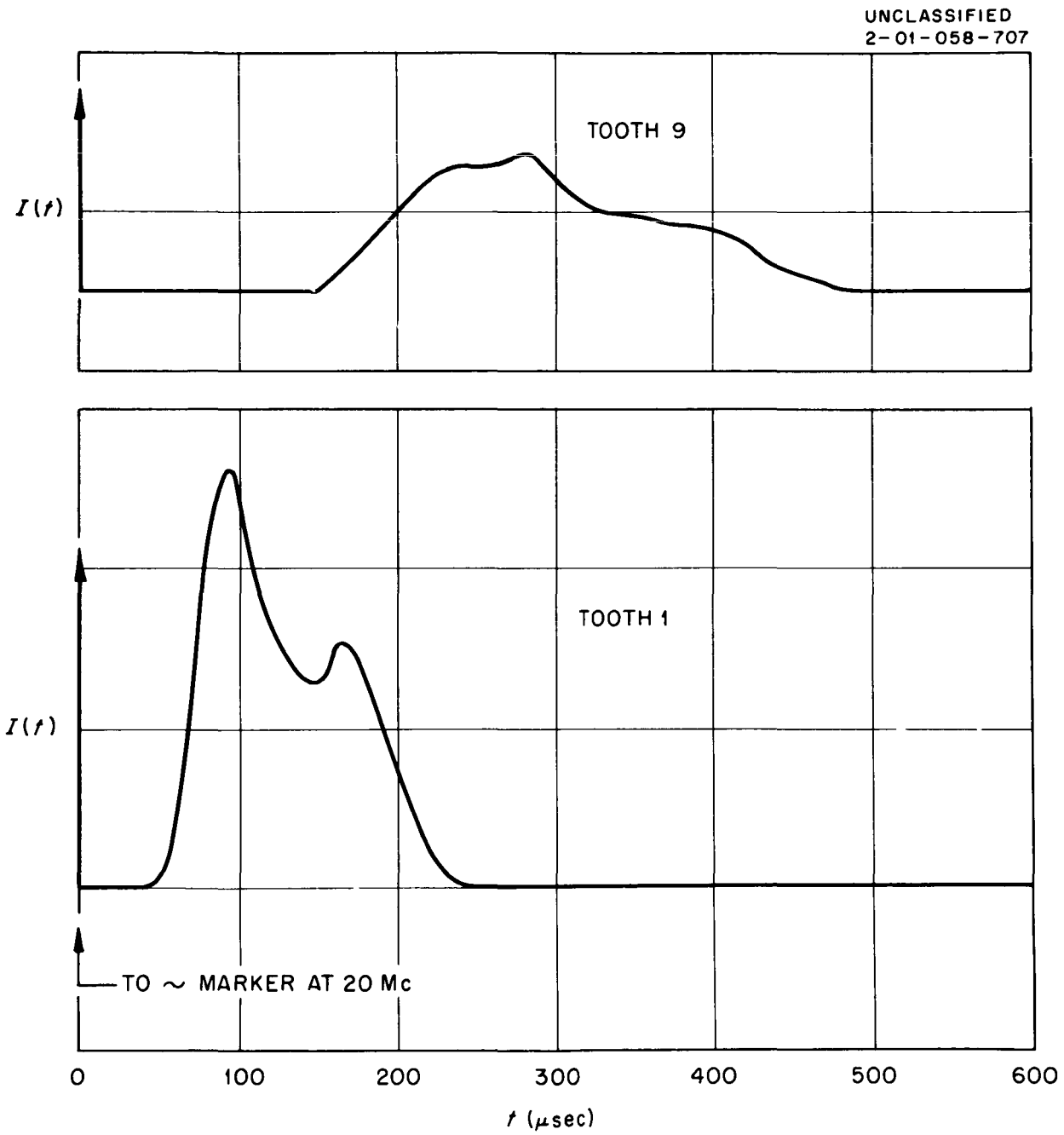

Fig. 7. Intensity as a Function of Time for Teeth 1 and 9.

Measurements using this method are routinely made during the gamma-ray spectral measurements at Harvard using $\tau_{BC} = 3.7 \times 10^{-7}$ sec. However, the NaI(Tl) crystals used give rise to a considerable B^S term due to activation and the neutron flight time. The effect of the B^S term is largely eliminated by using a time gate open only during a cyclotron pulse, but correction for the remaining contribution is difficult. In practice, B^S and C^S are taken as equal to zero and the duty factor determined is an upper limit. Typical values range from 3 to 5%.

A closer analysis of the macroburst shows that it is composed of a series of finer bursts, the microstructure. The fine structure of the beam was analyzed by observing the pulses from an organic scintillator with an oscilloscope. It was also determined by using two detectors placed equal distances from the cyclotron, one in the left corner of the beam and one in the right. Coincidences would be random and at a uniform rate in time were it not for the microstructure. A time calibration against an Ad-Yu delay line gave about 0.755 ns/ch with some nonlinearity. The time interval between the first two peaks in Fig. 8 measures 43.2 ns and between the second pair 43.4 ns, corresponding to about 23.2 mc. The time width of the bursts is shown to average 6.7 ns, and 90% of the protons in the peaks appear to be within a time range of 10 ns. Since both start and stop signals are chosen at random from the microbursts, these time widths would be about 70% as wide in "cyclotron time." Instrument resolving time does not contribute to the width.

The data were very greatly distorted in the valley regions by a now-understood pulse pile-up problem in the time-to-pulse-height converter. Depending on the assumed gross duty factor, 30-40% of the pulses were misplaced in time, enough to explain the valley shown. Anticipated random coincidences would fall about a decade lower. Photographs of a few hundred pulses failed to show any pulses appreciably removed in time from the microbursts. Another effect of the pile-up smearing is to broaden the times listed in the paragraph above.

The first peak shown is higher and perhaps narrower than the others, presumably because it includes a few prompt coincidences from scattered protons, etc. The second and third peaks have the same area, and the apparent difference in width is believed caused by statistical fluctuation.

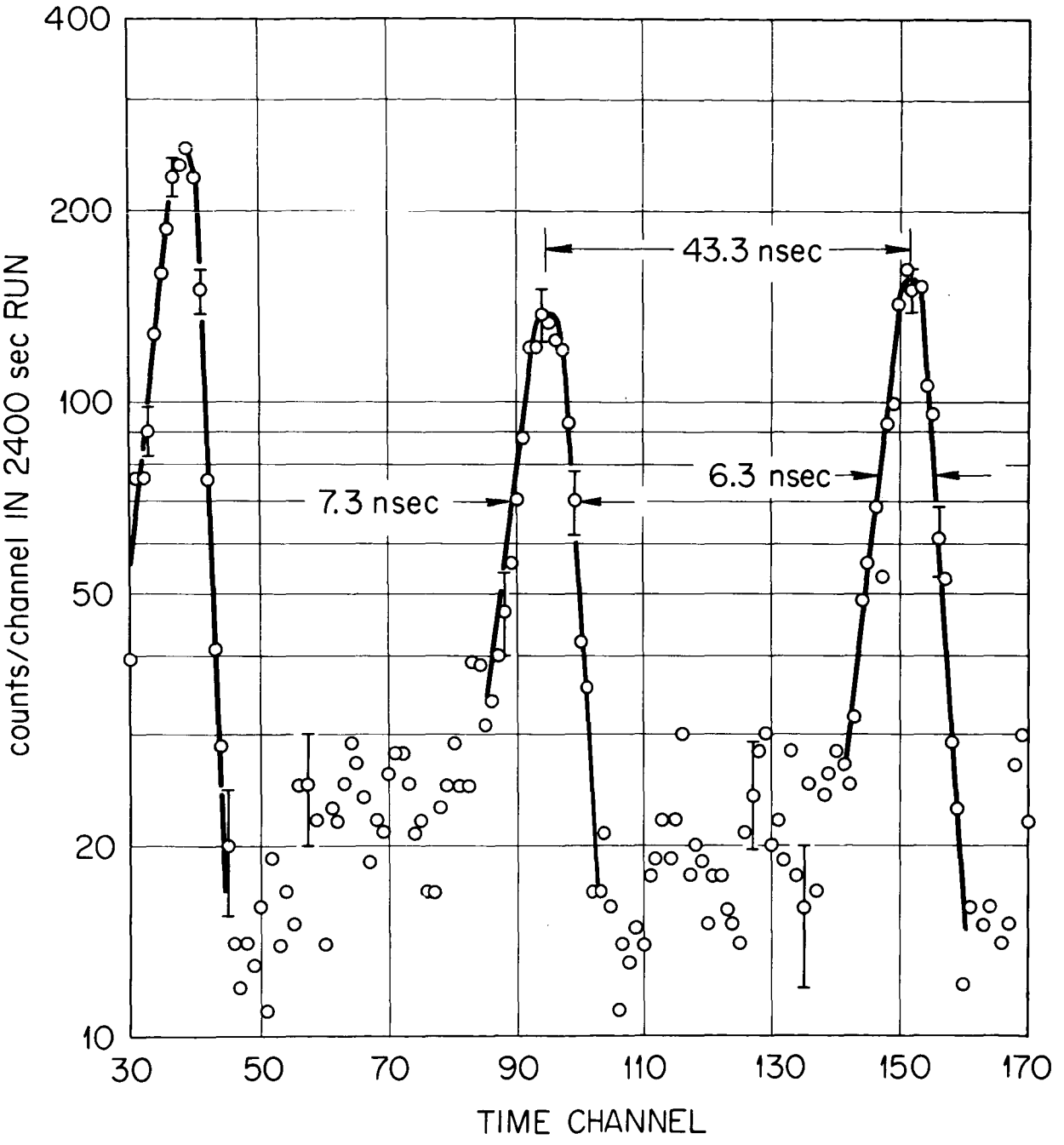

Fig. 8. Beam Microstructure Study Using A and B Counters Intercepting Different Sections of the Beam.

II. Proton-Recoil Telescopes for Spectral Measurements of Neutrons and Protons with Energies > 10 Mev

A brief description of the proton-recoil telescopes proposed for measurements of the energy spectra of neutrons with energies from ~8 Mev to several hundred Mev was given previously,[10] and the efficiency for neutron detection was calculated for neutron energies between 8 and 50 Mev. These instruments have now been constructed and tested in the preliminary experiments at Harvard (see p. 4) on the spectra of neutrons arising from the bombardment of a thick copper slab by 156-Mev protons. The results of these tests and the suggested constructional changes are discussed below.

Spectral Measurements of 8- to 50-Mev Neutrons

The telescope used for the ~8 to 50-Mev neutron range consists of a polyethylene radiator followed by two proportional counters and a NaI crystal. All three counters are placed in coincidence, and a recoil proton originating from the radiator produces pulses in coincidence which gate on a multichannel pulse-height analyzer that records the total energy deposited in the NaI crystal (see Fig. 9). A CsI crystal in front of the radiator is placed in anticoincidence with the other three counters and eliminates counts from protons present in the incident flux. Backgrounds are measured by replacing the polyethylene radiator with a carbon radiator containing the same amount of carbon as the polyethylene.

In the preliminary runs, adequate neutron counting rates were obtained and the single rates in the individual counters were reasonable. However, more than 60% of the triple coincidences representing neutron counts were background. On closer inspection it appeared that these counts were coming from high-energy (n,p) events in the structure of the proportional counters and surrounding material. The bodies of the proportional counters are now being rebuilt to reduce the mass of the counters and hopefully the background.

Spectral Measurements of 50- to 150-Mev Neutrons

The recoil telescope for the 50- to 150-Mev neutron range consists of a polyethylene radiator followed by two organic scintillators and a NaI crystal (see Fig. 10). All three crystals are placed in coincidence and a coincidence pulse from these counters gates on the multichannel analyzer to analyze the pulse from the NaI crystal. An anticoincidence crystal is placed in front of the radiator to eliminate counts from protons in the incident flux.

The NaI crystal is thin (1.5 g/cm^2) compared to the range of a 50-Mev proton and hence the dE/dx of the recoil proton is measured rather than its total energy.[11] The energy deposited in the crystal by the proton is calculated from the pulse height recorded by the multichannel analyzer. For

---

10. W. A. Gibson, W. R. Burrus, and T. A. Love, Neutron Phys. Div. Ann. Prog. Rep. Sept. 1, 1961, ORNL-3193, p. 325.

11. G. L. Guernsey et al., Rev. Sci. Instr. 23, 476 (1952).

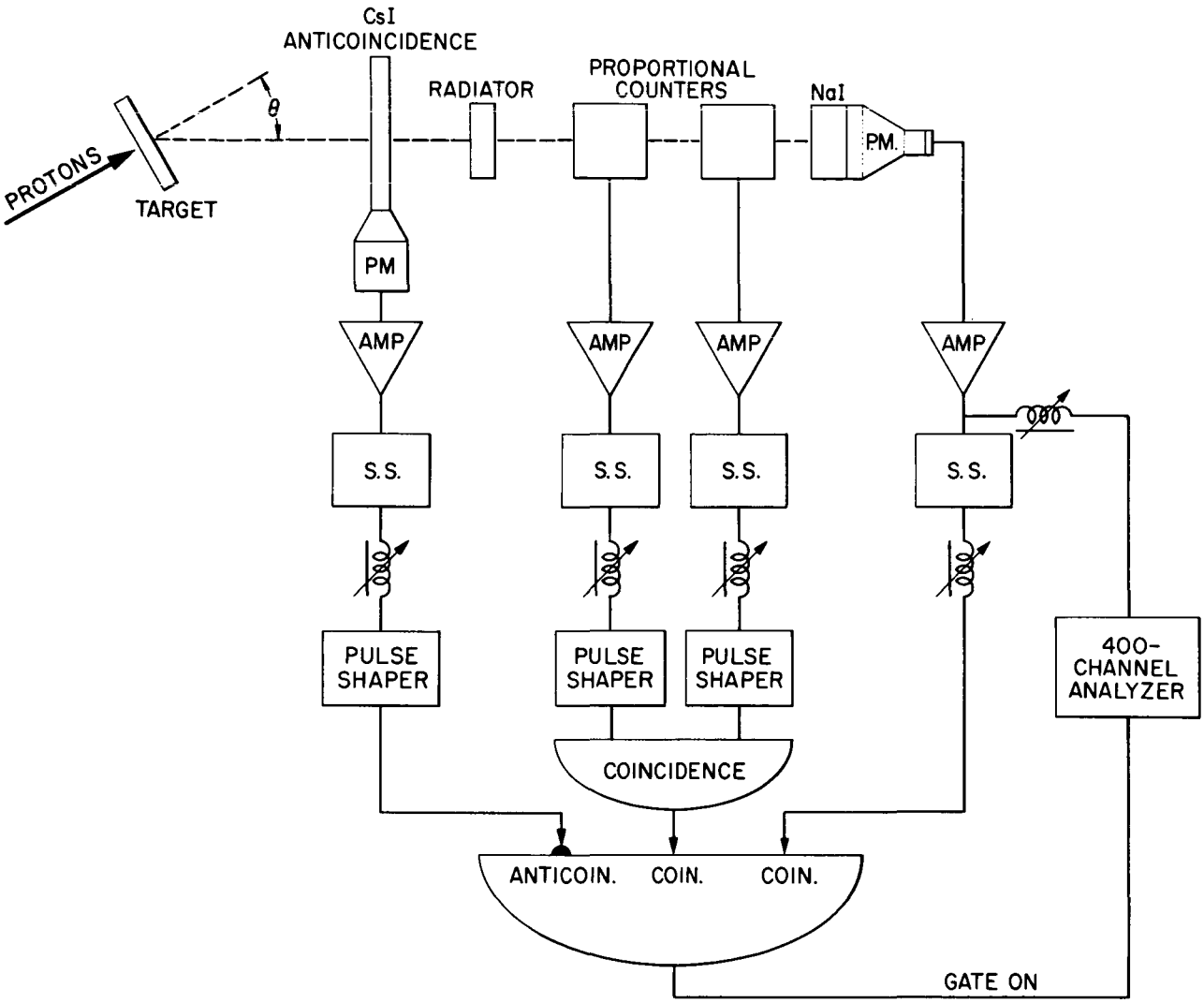

Fig. 9. Block Diagram of Proton-Recoil Telescope Proposed for Measurements of Neutron Spectra Over 8- to 50-Mev Range.

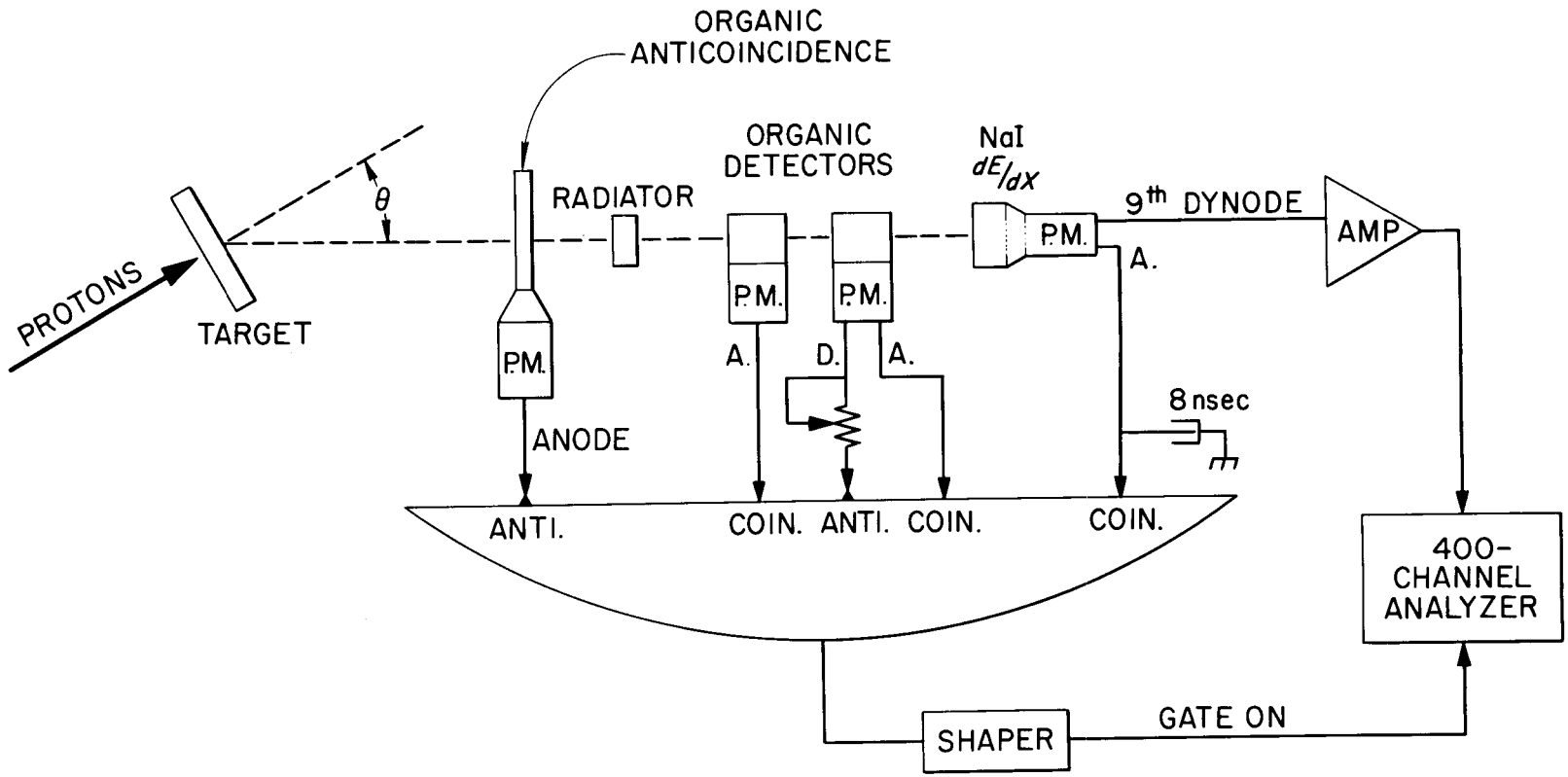

Fig. 10. Block Diagram of Proton-Recoil Telescope Proposed for Measurement of Neutron Spectra Over 50- to 150-Mev Range.

protons which penetrate the NaI crystal, the energy deposited is a direct measure of the dE/dx of the recoil proton and is a unique function of energy for proton energies below the minimum energy for ionization; hence the total energy of the proton is determined from the curves relating dE/dx to energy.

The two major disadvantages of an energy determination by a dE/dx measurement are:

1. For the higher energies the dE/dx changes only slowly with energy and therefore the error in determining the total energy of the proton is much larger than the error in measuring dE/dx.

2. Statistical fluctuations in the energy lost by protons as they pass through the thin NaI crystal (known as the Landau effect[12]) introduce a spread in the pulse-height spectrum obtained for a monoenergetic beam.

The width of the resolution function has been calculated for the crystal used on this telescope and the full widths at half maximum for 50- and 156-Mev protons are 6% and 18%, respectively. The resolution obtained experimentally on the 156-Mev beam supports the calculation.

The advantages of using a thin crystal are that the probability of nuclear interaction is reduced to a negligible value and the geometric effects introduced by a finite thickness crystal are small.

A NaI crystal was chosen rather than an organic scintillator for the dE/dx measurement because of the greater light output of the crystal and because its scintillation efficiency increases with increasing dE/dx below 10 Mev g^{-1} cm^{-2}.[13] Since the dE/dx decreases with increasing proton energy, the two effects add to accentuate the inverse relation between the light output of the crystal and the energy of the proton.

Figure 11 is a plot of the efficiency of the recoil telescope as a function of energy. The solid line is the efficiency for a continuously increasing radiator thickness and a 10% geometric energy resolution, and the dotted lines show the efficiency for radiators of constant thicknesses. The intrinsic resolution of the telescope is approximately 15%. That is, the radiators are chosen so that the lowest energy proton being analyzed loses 10% of its energy in passing through the thickness of the radiator, and the geometries are chosen so that 10% uncertainty in the energy is introduced by variations in the scattering angle of the recoil proton.

Figure 12 is a plot of pulse height as a function of the energy of protons incident upon the NaI crystal. It is seen that a particular energy deposition in the crystal does not correspond to a unique incident proton energy, since a low-energy proton that just stops in the crystal will result in the same size pulse as that produced by a higher energy proton

---

12. Bruno Rossi, High Energy Particles, Prentice Hall, New York (1952), p. 29.

13. R. B. Murray and A. Meyer, Phys. Rev. 122, 815 (1961).

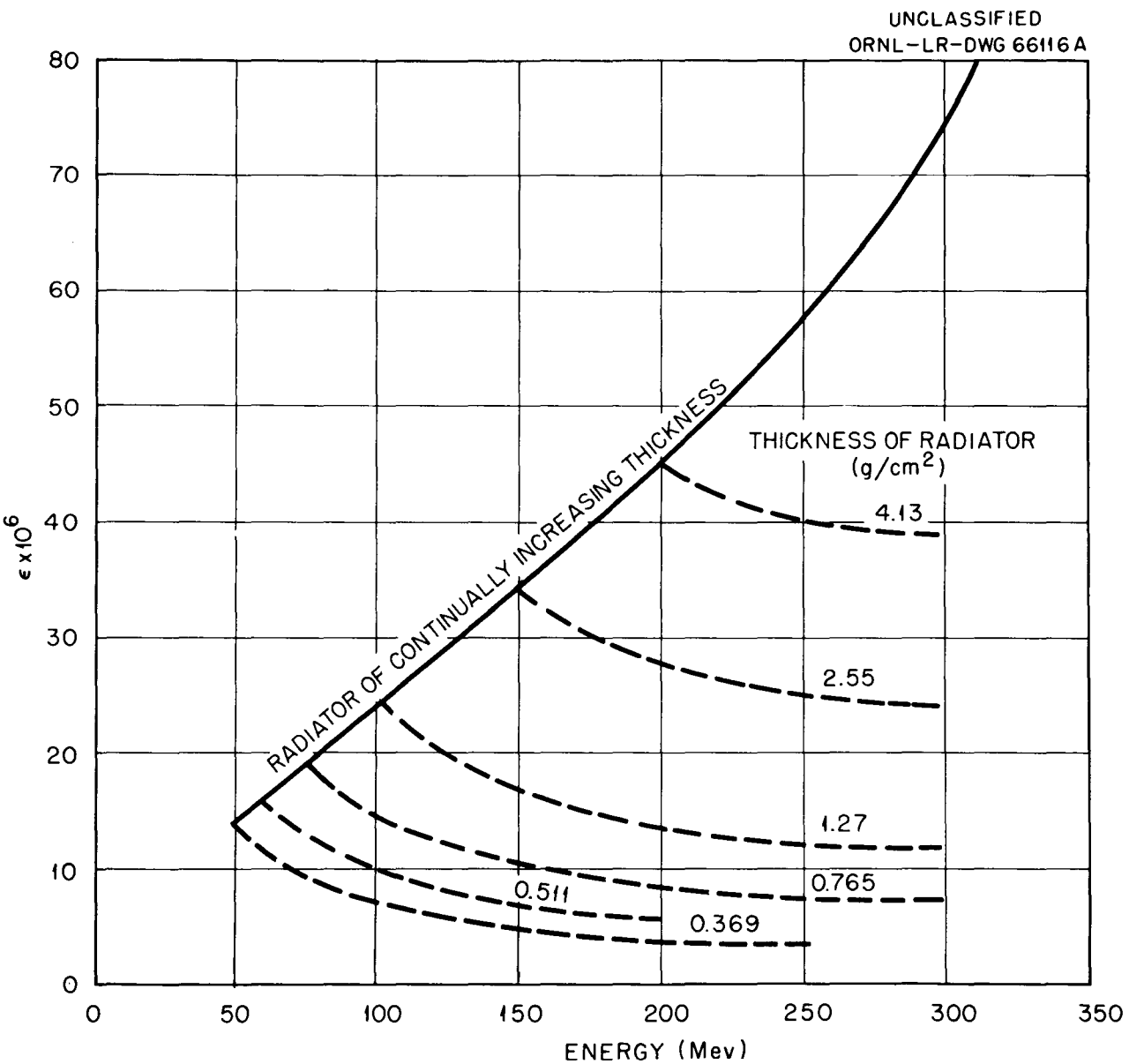

Fig. 11. Calculated Efficiency of High-Energy Proton-Recoil Telescope as a Function of Energy.

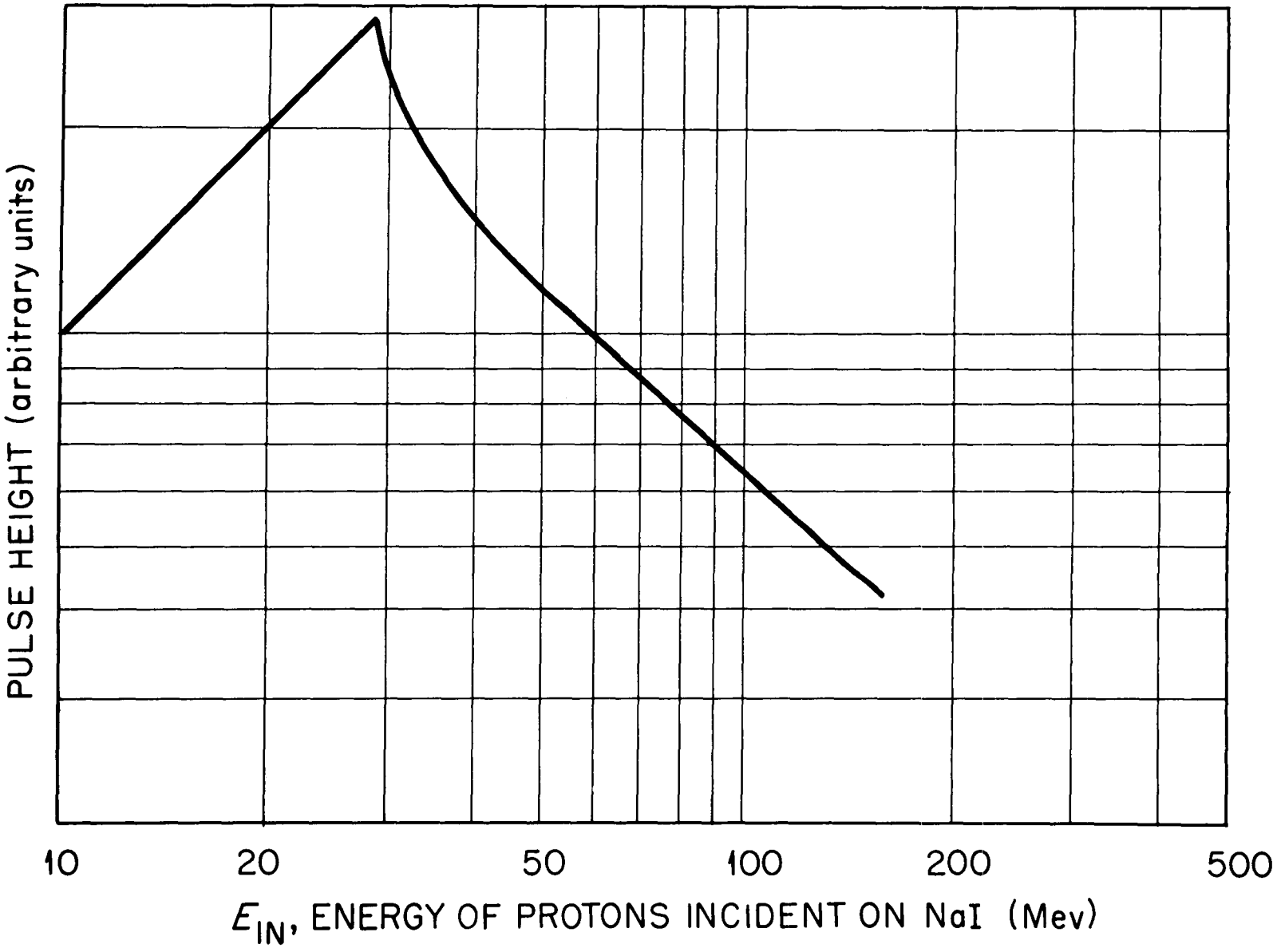

Fig. 12. Pulse Height, as a Function of Incident Proton Energy, for a 0.161-in.-thick NaI Crystal in the Telescope Shown in Fig. 2.

passing through the crystal. The straight-line portion of the graph at low energies results from those protons that stop in the crystal.

To overcome this ambiguity, it is planned to place an upper level discriminator on the organic scintillator preceding the NaI crystal in order to identify the low-energy protons which will stop in the last crystal (the low-energy protons will have a larger dE/dx and therefore deposit more energy in the crystal preceding the NaI crystal than will the higher energy protons).

Figure 13 shows the pulse-height spectrum from the dE/dx crystal with both the background and an estimated contribution from low-energy neutrons subtracted. Figure 14 is a graph of the neutron spectrum obtained by calculating the total energy of the recoil protons from the pulse-height spectrum of Fig. 13. Because of the uncertainty in estimating the low-energy neutron contribution and the large errors in the data, this curve is only indicative of the expected shape of the spectrum.

Since fast decay times are characteristic of organic scintillators, high counting rates were obtained and the operation of the telescope, except for the ambiguity introduced by the low-energy neutrons, was satisfactory. The background was about 10% of the foreground.

Spectral Measurements of Protons

The telescopes described will also be used for measurements of proton spectra, in which case the hydrogenous radiator and the anticoincidence crystal preceding the radiator will be removed and the telescopes will look directly at the target.

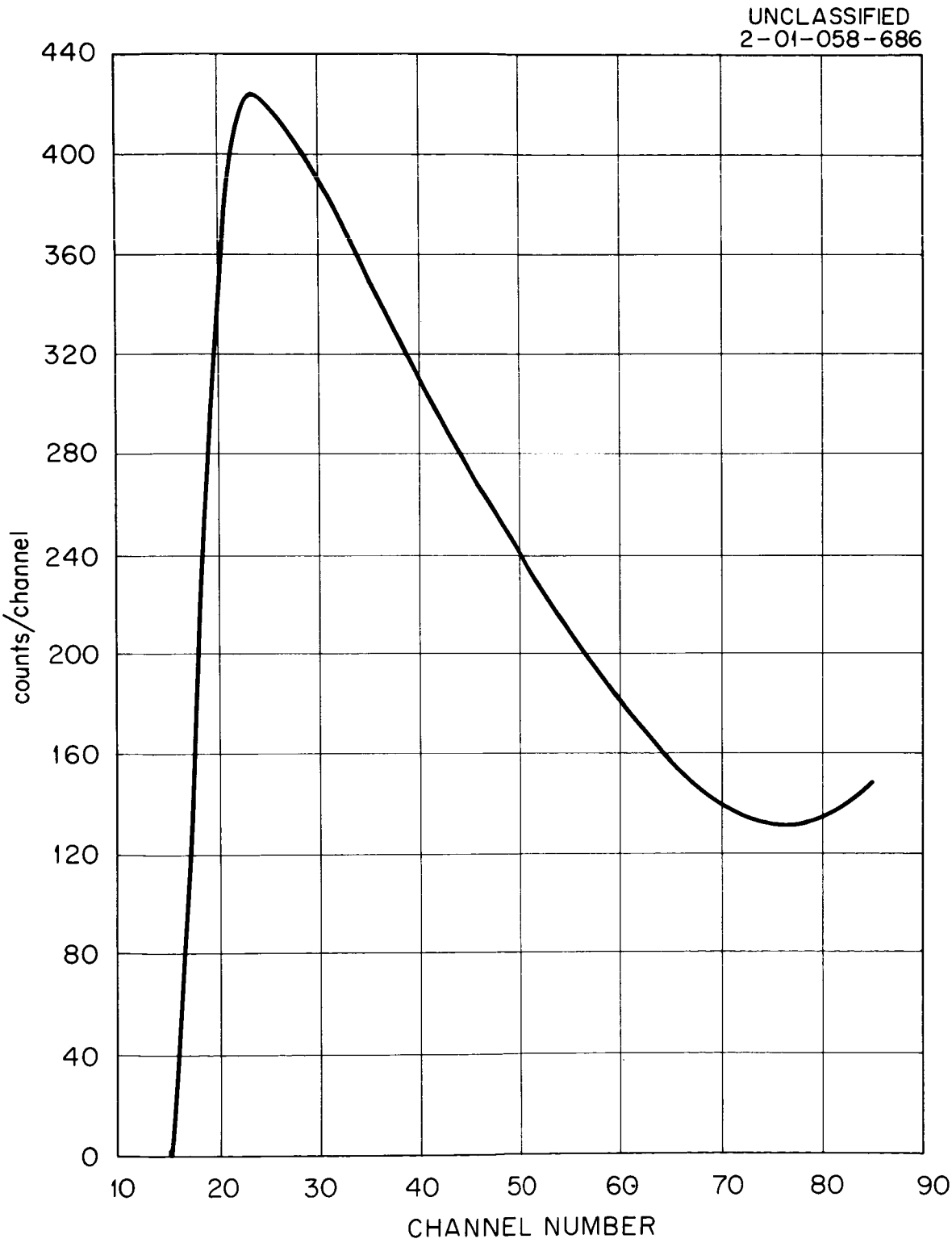

Fig. 13. Pulse-Height Distribution of Neutrons from 31.8-g/cm^2 Copper Target Bombarded by 156-Mev Protons. Curve corrected for background and an estimated correction made for low-energy components.

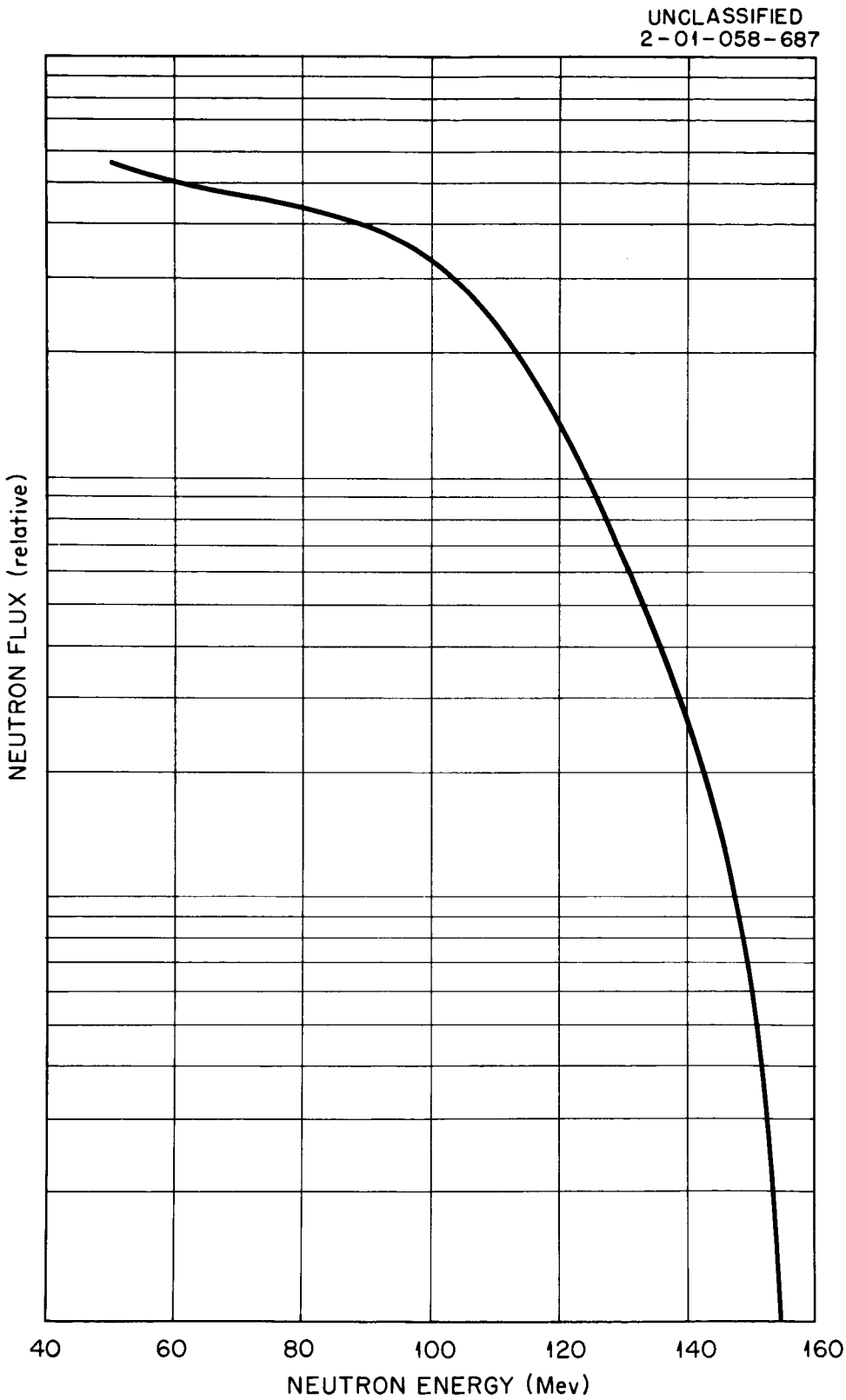

Fig. 14. Spectrum of Neutrons Emitted Forwardly from a 31.8-g/cm^2 Copper Target Bombarded by 156-Mev Protons. Computed from data of Fig. 5.

III. Flight-Time Spectroscopy for Neutron and Proton Yields from Nuclei Bombarded by Protons

The deduction of energies of fast neutrons from measurements of their velocities is a common procedure for the energy region below 20 Mev, even for neutrons resulting from neutron-induced reactions. This "flight-time" method has also been used for very high energies, an example being its recent application at Harwell for neutrons produced in reactions of 143-Mev protons incident on nuclei.[14] Therefore, it was natural to consider flight-time spectroscopy for measuring thick target yields and differential cross sections for interactions of 50- to 700-Mev protons with nuclei.

To measure the velocity of a secondary neutron in the Mev range, the time required for it to travel from the target to a fast-neutron detector, usually a plastic or liquid scintillator, is measured. Thus the pulse from the phototube attached to the scintillator determines one end of the flight-time interval. Either of two systems can be employed for timing the other end of the interval:

1. Particles in the beam can be bunched to an extent consistent with required resolution, and the time that the entire group is incident upon the target can be determined by methods depending on the experiment in question. A neutron chopper is a simple example of this system.

2. The time of each individual incident particle can be determined, as in the associated-particle method in which a timing pulse representing an individual incident fast neutron is derived from a charged particle produced in the reaction with the neutron. For instance, the associated alpha particles may produce timing pulses for fast neutrons from the $D(T,\alpha)n$ reaction.

The first system was used at Harwell[14] by utilizing a natural phase bunch in the cyclotron internal beam once during each cycle of the modulation frequency. At least at the lower end of the range of interesting incident-proton energies, a like system could be used on an external beam provided that a special electrostatic deflection system could be employed to eliminate counts from most of the microstructure bursts. Since the time resolution of the proton burst probably could not be shorter than 4 nsec, a large target room would be required for such a method. Although with this system electronic timing problems would be simpler and there would be less stringent requirements on the detector and target thicknesses, it seems to be out of the question for the experiments required in this program since they must be conducted at other laboratories. Thus the second system has been adopted, and the time that each incident proton reaches the target is deduced from a pulse produced in a detector placed in the beam. This system leads to considerable difficulties with resolution and counting rates, but it is flexible enough that any available external proton beam which can be adjusted to the correct intensity can be used.

---

14. P. H. Bowen et al., Nuclear Phys. 30, 475 (1962).

Experimental Method

Figure 15 shows a plan schematic of the detector apparatus required for neutron-producing reactions, along with a simplified block diagram of the associated electronic apparatus. Detector A consists of a thin (1- or 2-mm) plastic scintillator placed a convenient distance from the target. Since the protons have essentially uniform velocity, the time the proton reaches the target can be inferred from the timing of the light flash in this scintillator. The 5-in.-diam detector B, generally 1-in. thick, is for detection of neutrons originating in the target. At energies below 10 Mev, detection is primarily by means of the recoil protons from n-p scattering, while above 20 Mev various charged-particle reactions with the carbon of the scintillator surely dominate. Detector C, which takes the form of a thin cup surrounding all but one side of detector B, is used in coincidence with the latter to label the detection of charged particles. Coincidences between detectors B and C cause the corresponding time measurement to be stored separately.

The simplified electronic diagram indicates several of the most important features required:

1. The strength of the incident beam is required to put the experiment on an absolute basis and is determined by actually counting the individual protons detected. The time between the pulse from B and the delayed pulse from A is converted to a pulse amplitude and fed into a standard multichannel pulse-height analyzer for storage.

2. The time-to-pulse-height converters deemed appropriate for this experiment are of the general variety which measure the time between "start" and "stop" signals. Since the output of this converter is 1 μsec or so in length, the number of "start" signals must be as small as possible. For this reason the time scale is reversed by delaying the pulse from A.

3. At the beam strength corresponding to a reasonable counting rate, there will be an important (~10%) fraction of cases in which B-A time intervals should not be recorded because two or more protons reach the target so closely spaced in time that one cannot be sure which proton produced the observed pulse in B. Control of such cases is a function of the supervisory circuitry.

4. Additional supervisory circuitry is required to set the lower energy threshold of detector B and to sort the true neutron-produced pulses from those which cause coincidences between detectors B and C. The B counting threshold is very important because it determines the neutron efficiency.

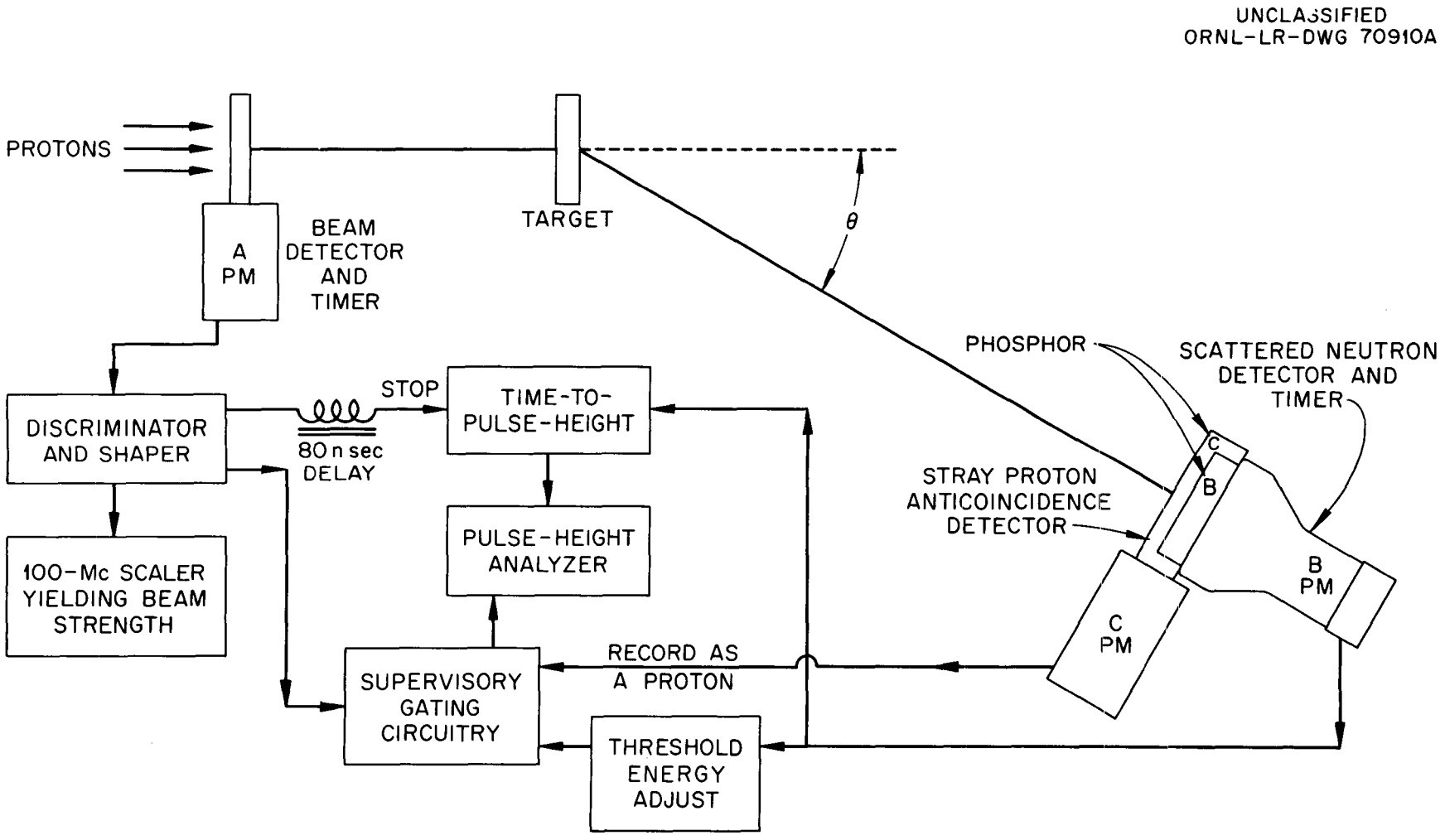

Fig. 15. Detector Plan View and Simplified Block Diagram for Neutron Time-of-Flight Spectrometer.

Two main types of background are likely to be encountered, assuming that detector A responds only to protons from the beam. Gamma rays that do not come from prompt reactions in the target can be detected in B. These lead to a flat background of time-interval measurements. The other important background arises from neutrons generated by the beam. The presence of the beam microstructure synchronizes this background to a certain extent with the protons observed in detector A, and so this background must be expected to be time dependent. The component that results indirectly from reactions in the target is virtually impossible to measure, but that from the floor and perhaps the cyclotron shield can readily be measured by removing the target. Except for gamma rays from radioactivity in the target, the random gamma-ray background is also eliminated by subtracting the target-out counts from those obtained with the target in.

Some understanding of intensity problems can be gained by study of the estimated efficiency curve, Fig. 16, plotted for a scintillator thickness of about 1 in. and a detector bias of just over 1 Mev. If clumsy arrangements involving multiple B detectors are avoided and detector B is placed ~70 cm from the target, the scintillator subtends a fractional solid angle of $\sim 2 \times 10^{-3}$. If one neutron is produced in the target for every ten protons, then in the case of an isotropic yield there would be about one fast neutron detected for some flight time for each 10^5 incident protons. As is developed below, a plausible intensity is $2 \times 10^6 \times f$, where f is the gross duty factor, about 4% at the Harvard synchrocyclotron. Thus, in a typical case it can be anticipated that about 1 count/sec will correspond to some energy of interest. Rates actually observed in tests using a 25-g/cm^2 copper target were two or three times this value.

Table 2 will aid in understanding the time resolution problem. It shows the time required for a 70-cm flight by neutrons of various energies. For the assumed time-measuring system with resolution of about 1 nsec, the best available time resolution for a 50-Mev neutron is 12%, leading to an energy resolution of 25%. The target and detector thicknesses must also be considered. They typically limit energy resolution to 15% by making uncertain the precise length of the flight path. Thus with reasonable target-detector spacings, the equipment can be operated to detect neutrons over 50 Mev only for very low resolution work. Fortunately, the efficiency of Fig. 2 does not seem to vary much in the higher energy region. Table 2 also indicates that at 70 cm the spectrum can be carried down to about 0.5 Mev if an 80-nsec period is allotted to each time measurement. If a 0.5-Mev bias is employed on detector B, efficiency will be reasonably well known for neutrons above 1 Mev. The considerations of this paragraph lead to the energy range limitation for secondary neutrons.

Since if two protons should arrive on the target during an 80-nsec period it is difficult to know which has generated a detected secondary particle, part of the supervisory circuitry is designed to eliminate such proton pairs from consideration. If in the macroburst (see Section I) the intensity averages about 2.2×10^6 protons/sec, and if the microstructure is definite, there is roughly a 0.74 chance ($e^{-0.3}$) that a given pulse will

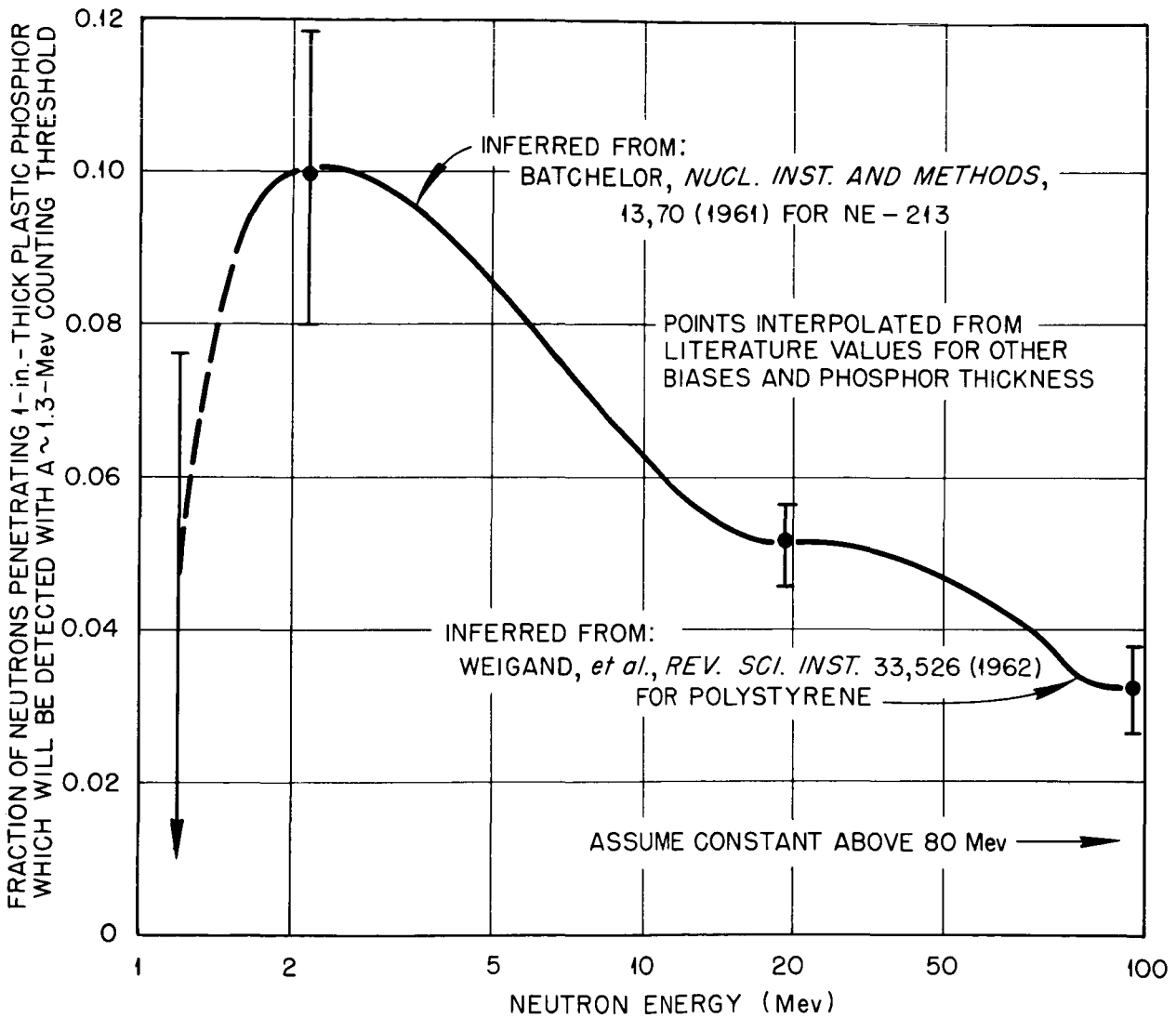

Fig. 16. Estimated Counting Efficiency of the Scattered-Neutron Detector.

Table 2. NEUTRON FLIGHT TIME AND ENERGY RESOLUTION FOR A 70-cm FLIGHT PATH

Kinetic Energy of Secondary Neutron (Mev)	Neutron Velocity (cm/nsec)	Flight Time for 70-cm Path (nsec)	Energy Resolution for 1-nsec Time Resolution[a] (%)
0.5	0.98	71	3
1.0	1.38	51	4
2.0	1.95	36	6
4.0	2.76	25	8
8.0	3.89	18	11
16.0	5.46	13	15
30	7.4	9.5	23
60	10.2	6.8	32
100	12.8	5.5	40
150	15.2	4.6	50

[a]Energy resolutions quoted are for a limitingly thin target and detector and are based on a hypothetical 1.0-nsec time resolution of the system.

be adequately isolated from its neighbors. This probability would lead to a 25% correction by the supervisory electronics to a net counting rate of about 1.5×10^6 protons/sec during the macrobursts. Perhaps a gross microburst intensity as high as 3.3×10^6 protons/sec could be considered, which would give a net rate of 2.1×10^6 protons/sec after correction. It is doubtful if larger corrections by the supervisory circuitry should be allowed, and little counting intensity remains to be gained if the 80-nsec interval is maintained. If there were no microstructure, a clear time interval of $\pm$ 80 nsec around each accepted proton must be provided, which has a probability per proton given by $\exp(-160 \times 10^{-9} \times 2.2 \times 10^6) = e^{-0.35} = 0.70$ for the case of a gross microburst intensity of 2.2×10^6 protons/sec. Therefore, the sharp microstructure helps slightly in utilizing the beam, provided that the amount of free time required is just less than in integral number of cyclotron rf periods.

Preliminary Measurements

An apparatus of the type described above was tested in May, 1962, with protons from the ~156-Mev external beam of the Harvard University Synchrocyclotron. This section discusses very briefly the instrumentation used and shows some of the preliminary results obtained.

Detector A was a single 2-mm-thick polystyrene-based plastic scintillator which gave an ~40% pulse-height resolution from the ~1-Mev energy loss from a single proton. No protons produced pulses of less than half the average pulse height. The bias for pulses to be counted as part of the beam was set just below the half-average pulse-height level by use of a tunnel diode discriminator which fed an amplifier capable of producing a pulse of appropriate shape for the 100-Mc scaler used. Detector B showed 14% resolution (on integrated pulses) for the ~15-Mev energy losses by the primary beam protons.

Light collection in detector C was inadequate, so the resolution for the 1-Mev energy loss from the full-energy beam was about 100%.

Integral lower-bias levels on B and C signal channels were set using conventional slow (1 μsec) electronic circuitry, and the necessary conditions for storage of a pulse were determined in a slow gating circuit. This circuit was operated at much higher than design counting rates because of failure of some of the other supervisory circuitry. In practice, except for a few trial runs, mutually interfering events in the A channel were held to a minimum by operating at a beam strength during the macrobursts of about 0.5×10^6 protons/sec.

Timing signals were formed at the photomultiplier bases in the B and C signal channels by tunnel diode discriminators. The time-to-pulse-height converter formed a voltage pulse by integrating a fixed current during the time between the output signals from these discriminators.

Figure 17 indicates the timing resolution available under the ideal conditions of the full-energy proton beam traversing both the A and B detectors. Artificial delays account for the channel in which the peak appears. For the broad spectrum of pulse heights resulting from a monoenergetic neutron incident on detector B the sharp resolution of the ideal case (~1.2 nsec) is not expected to exist. Figure 18 shows a typical calibration curve for the time-to-pulse-height converter; it was obtained by varying a delay line in the "start" signal channel. A nonlinearity is observable at small pulse heights. Velocity measurements were made by comparing the channel in which the pulse appeared against that in which was centered the full-energy proton peak with the target removed and the detector at 0°. Other distance and delay parameters were, of course, held constant.

Figure 19 shows a typical pulse-height spectrum, obtained at a 10° scattering angle from a copper target 25.2 g/cm^2 thick. The background with the target removed is plotted on the same scale and includes essentially the same random background as the target-in data. Figure 20 shows the same 10° data plotted on a neutron/Mev vs Mev basis. The data were reduced by a computing machine program[15] based on the detector efficiency illustrated in Fig. 16. The spectrum observed at 60° is shown on the same plot. The 120° data (not plotted) appear consistent with that shown for 60°, and the 30° spectrum falls between the two shown. The efficiencies used in reduction of the data should not be catastrophically in error at energies over 3 Mev. The peak in the neighborhood of 6 Mev, which appears at least at 60° and 120°, is unexpected. Because of beam-counting and dead-time difficulties, absolute magnitudes are uncertain by at least 25% plus the undetermined percentage due to efficiency uncertainties.

While the apparatus automatically recorded "proton spectra" for each case studied, it was found that BC coincidences in the apparatus shown were inadequate to assure that the observed charged particles originated in the target. For this reason the proton spectra obtained are interesting but not helpful for estimating the actual proton spectra.

Table 3 gives gross observed counting rates during the entire series of short runs. The values should be helpful in estimating counting rates for future experiments, even though the present runs were too short to produce meaningful spectra. As indicated above, effective proton beam strengths of the order of 1.5×10^6 protons/sec are contemplated during future gross duty-cycle bursts, so at the Harvard cyclotron with a 4% gross duty cycle the apparatus can handle about 2×10^8 protons/hr. Adequate data should be obtainable at low resolution for a limited number of cases.

---

15. The program was designed by R. L. Cowperthwaite, co-op student from the Missouri School of Mines, Rolla, Missouri.

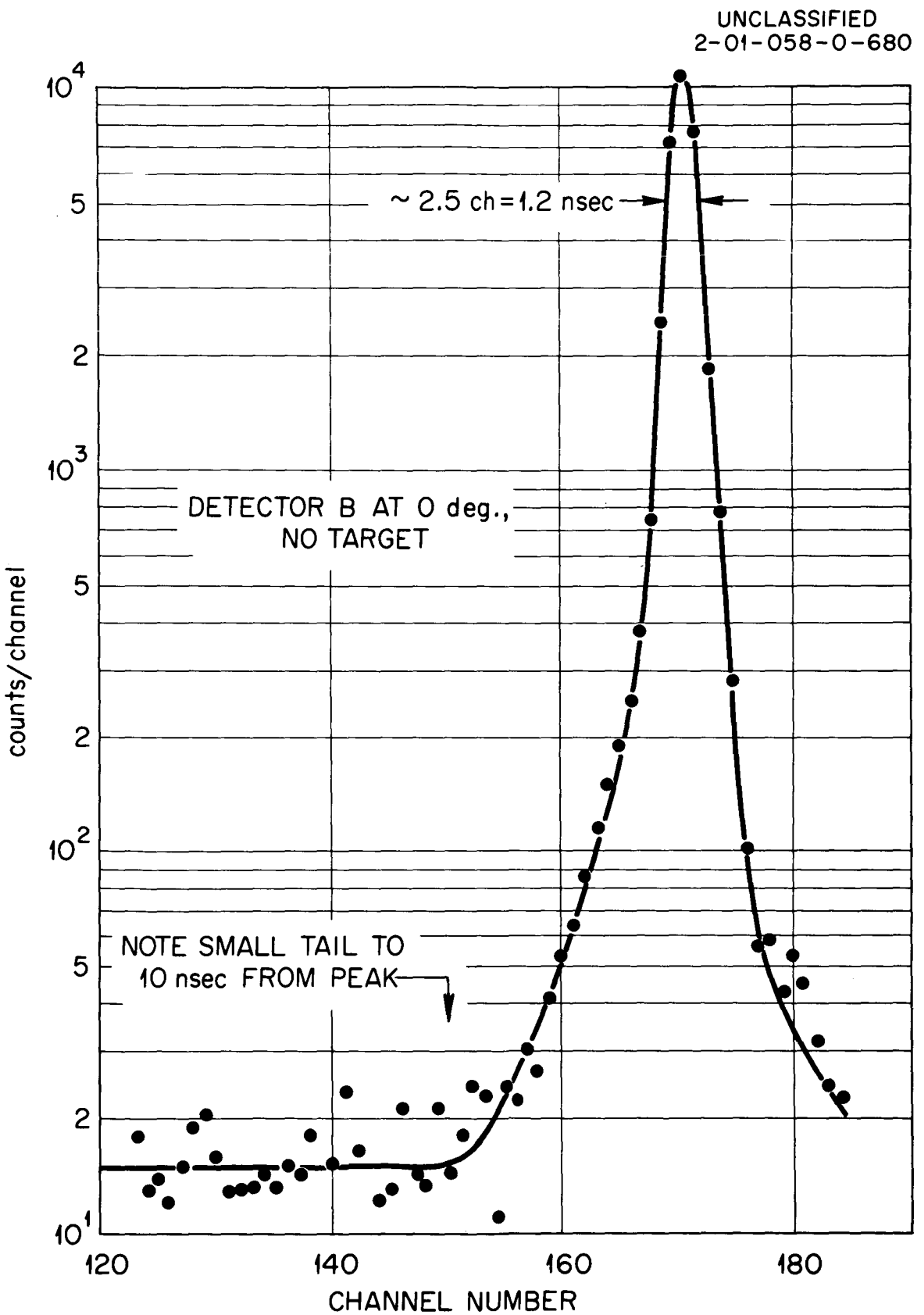

Fig. 17. Time Resolution of Spectrometer System at 0.45 nsec/channel.

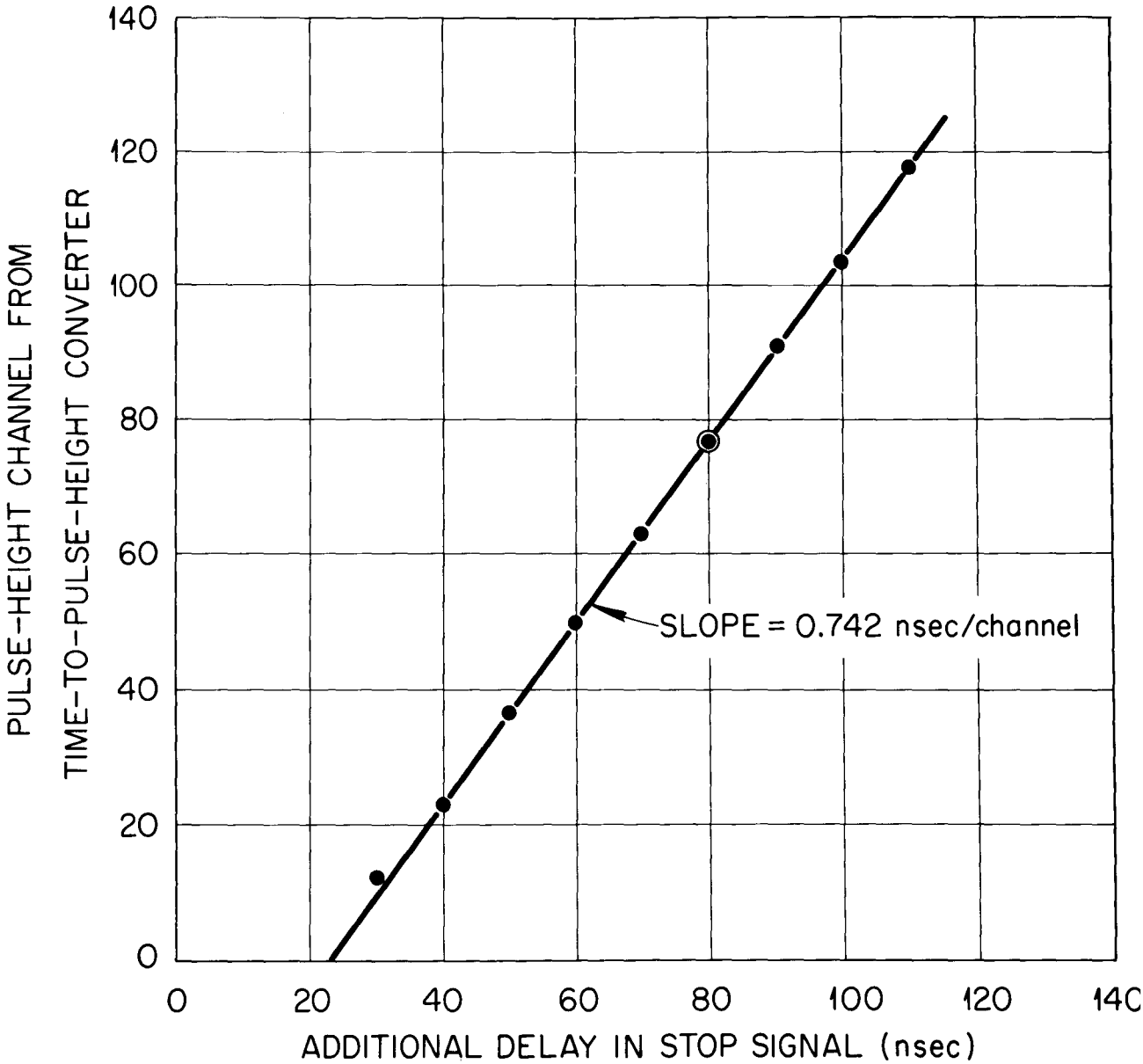

Fig. 18. Typical Calibration Curve of Time-to-Pulse-Height Converter.

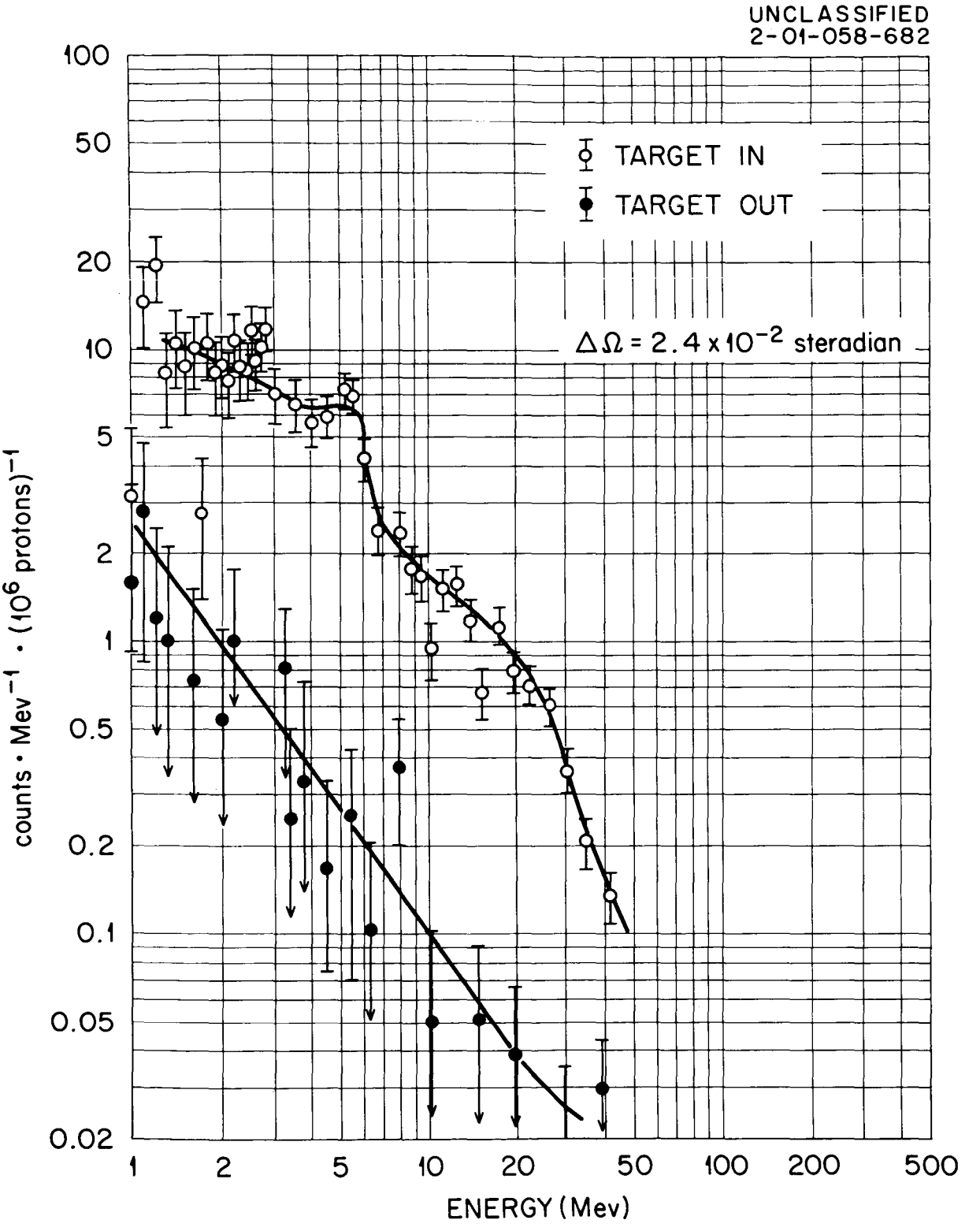

Fig. 19. Neutron Count Spectrum and Target-Out Background for 156-Mev Protons on 25.2 g/cm^2 Thick Copper Target.

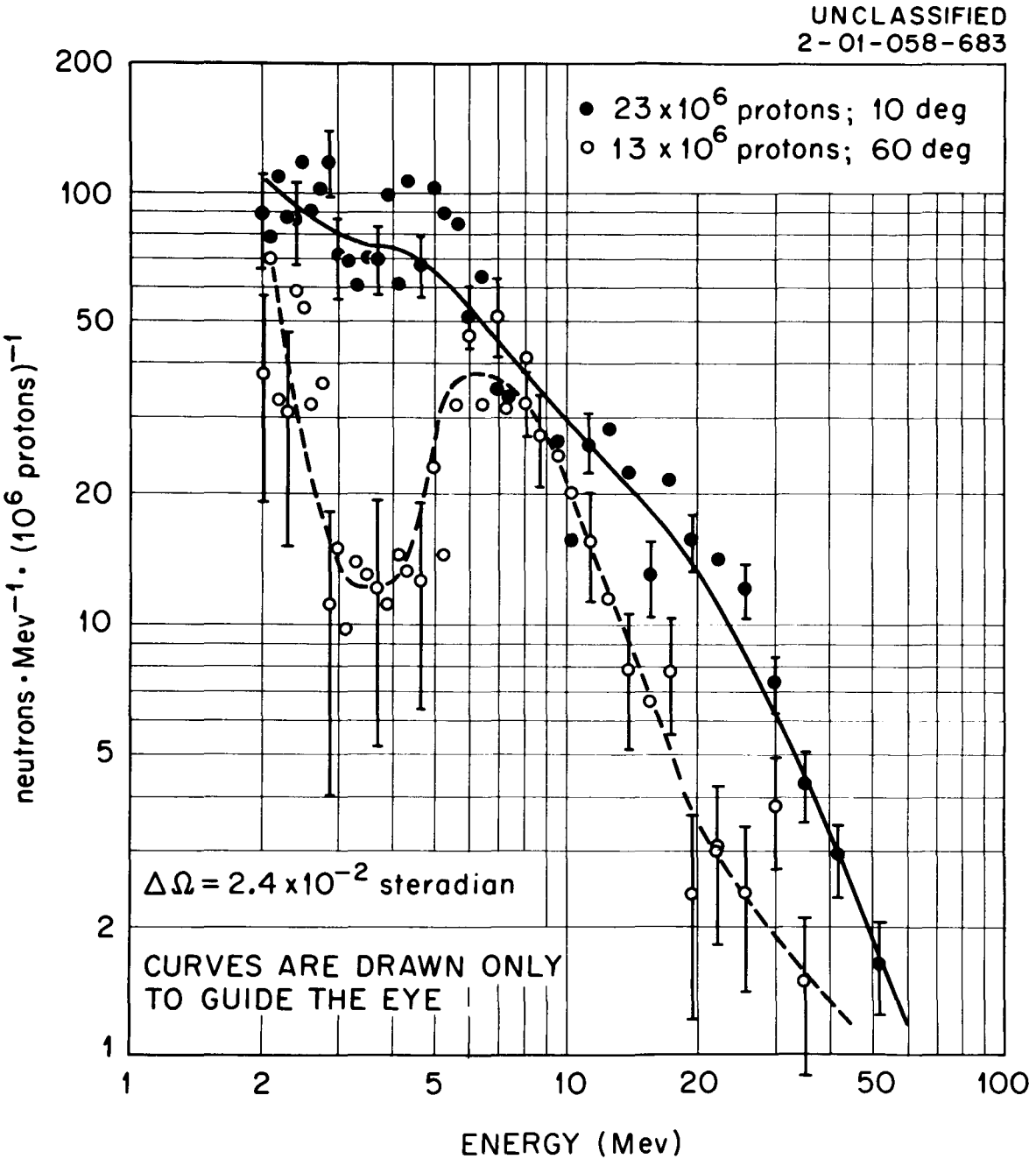

Fig. 20. Neutron Spectrum at Scattering Angles of 10 and 60° from a 25.2 g/cm^2 Copper Target.

Table 3. Summary of Gross Counting Information

Copper Target Thickness (g/cm^2)	θ, Angle from Beam (deg)	Total Protons in Beam	Average Beam Strength (protons/sec)	Total Counts in Time-of-Flight Spectrum	Neutron Counts/10^6 Protons in Energy Bins Shown[a]				
					2–5 Mev	5–10 Mev	10–20 Mev	20–70 Mev	>70 Mev
		$\times 10^6$	$\times 10^3$						
25.2	10	22.7	14	1725	25 ± 1	14 ± 1	11 ± 0.6	9.5 ± 0.6	1.7 ± 0.3
8.6	10	8.1	16	1710[b]	15 ± 1	19 ± 1.5	7.6 ± 1	59[b]	19[b]
0	10	21.9	15	110	0.6 ± 0.1	0.6	0.5	1 ± 0.2	0.4
25.2	30	26.5	53	1690	10.7 ± 0.6	12.8	9.3 ± 0.5	8.8	0.5 ± 0.04
8.6	30	12.9	13	160	1.9 ± 0.4	2.2 ± 0.4	1.7	2.2	1.4
0	30	14.4	14	77	0.8	0.5	0.4 ± 0.2	0.8	0.2
25.2	60	13	13	510	6 ± 0.7	12 ± 1	4	3.5	3.0
8.6	60	8	16	83	3.5 ± 0.7	5.7 ± 0.8	4.0 ± 0.8	3.5	0.7
0	60	15	15	47	0.3	0.2	0.1	0.2	0.3
25.2	120	15	15	406	4.2 ± 0.6	9.8 ± 0.8	3.4	1.6	2.3 ± 0.4
8.6	120	8	16	73	1.2 ± 0.4	3.1	0.9	0.6	0.2 ± 0.1
0	120	16	16	46	0.2	0.3	0.2	0.1	0.1

[a] Representative errors shown are based on counting statistics.

[b] Many protons accidentally registered here as neutrons.

Development of Improved Instrumentation

In the period since the preliminary measurements, efforts have been made to improve the original apparatus in the following ways:

1. The ambiguity in the definition of the incident beam is to be resolved by using two A detectors in fast coincidence with each other.

2. All the electronics in the A-channel, dealing with the incident beam, will be fast.

3. The time isolation of the incident protons used will be more positively assured by using an "isolated signal detector" which yields output pulses for protons isolated from their neighbors by at least 60 nsec. The complementary logic was used during preliminary measurements.

4. Pulse-shape-discrimination methods will be used to insure that random gamma-ray backgrounds are not seriously large. To employ these methods, a Ne-213 liquid scintillator[16] will be employed for the B detector.

5. Fast circuitry will be employed in the scattered particle detectors, B and C, so that measurements can be made at quite small angles with thin targets under conditions such that a substantial portion of the beam passes through these detectors.

6. A separate detection scheme will be employed to allow observation of proton spectra. The scheme includes an arrangement with minimum mass in the scattered beam path and a thin (0.5 mm) plastic detector (C') placed about halfway between the target and the scattered-particle detector (B') to create a telescope arrangement.

7. The anticoincidence detector, C, will be formed from thicker (4 mm) plastic, and an improved light pipe will be used so that effective anticoincidence action will be assured.

Figure 21 shows a block diagram of the equipment to be used in the next trials. It is expected that only minor changes will remain to be made to attain fully satisfactory operation after final testing of the arrangement shown.

Most of the fast circuits shown are in the final design or laboratory testing stage. The circuitry will be based largely on tunnel-diode univibrator designs similar to those described by Whetstone.[17] Adequately

16. Product of Nuclear Enterprises, Ltd., Winnipeg, Canada.

17. A. Whetstone and S. Kounoso, Rev. Sci. Instr. 33, 423 (1962).

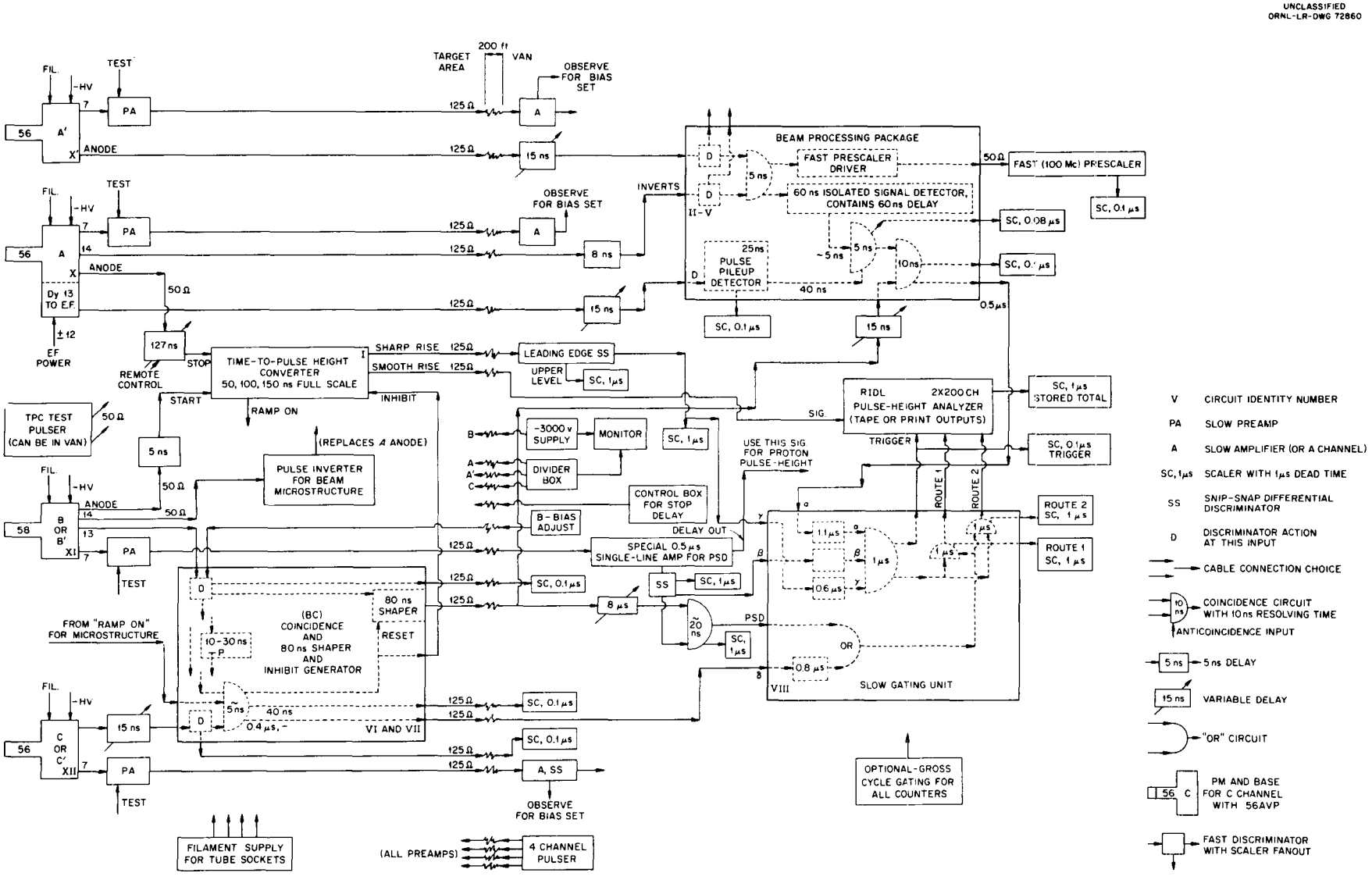

Fig. 21. Block Diagram of Neutron Time-of-Flight Spectrometer.

small propagation delays and rise and fall times can be attained, though some difficulty with dead times is anticipated. Only in the time-to-pulse-height converter will there be a problem caused by "walk" as a function of pulse amplitude from detector B.

If neutron spectra are to be measured over a range from 0.5 to 155 Mev, the light pulses in a 1-in.-thick plastic phosphor will have a dynamic range of 470:1. Since the minimum electronic pulse will be a few milliamperes at its peak, and since under the conditions of the experiment the 58-AVP photomultiplier is capable of producing maximum pulses of only about 0.5 amps, the dynamic range of electronic pulses will be smaller than that of the light pulses. Nevertheless, the electronic pulse range is unusually large, and it is felt that this factor is the source of the major design problems in developing a time-to-pulse-height converter with 1-nsec resolution.

IV. Bonner Spheres and Threshold Detectors for Neutron Spectroscopy

The variety of neutron spectrometers required to encompass the wide range of energies considered in the space vehicle shielding problem is pointed out in the Introduction. For neutron energies < 10 Mev, the use of so-called "Bonner spheres" has been investigated during preliminary experiments at the Harvard University Synchrocyclotron, and the feasibility of augmenting the Bonner sphere data above 10 Mev by threshold detector techniques has been examined. Bonner-sphere data have been obtained for a variety of configurations.

Experimental Procedure - Bonner Spheres

A Bonner sphere[18] basically consists of a thermal-neutron detector surrounded by a spherical mass of polyethylene moderator. For the present work the plans of Bonner have been followed as closely as possible, so that counting efficiency calibrations determined by him could be used. The thermal-neutron detector is a $Li^6I(Eu)$ scintillation crystal, essentially totally absorbing at thermal energies and "transparent" to energies > 100 ev. It is therefore predominantly sensitive to low-energy neutrons. As moderating material is added and the sphere diameter is increased, sensitivity to higher energy neutrons is increased. Table 4 gives the counting efficiencies used, over a neutron energy range from 0.01 ev to 160 Mev, for spheres of five different diameters, as well as for the $Li^6I(Eu)$ detector both with and without a 30-mil-thick cadmium cover. The data from thermal energies to 15 Mev were compiled from large-scale graphs supplied by Bonner and are quoted to be accurate to about 6%. From 15 to 160 Mev, the data represent a crude extrapolation by the author.

A diagram of the simple experimental arrangement for the preliminary experiments is shown in Fig. 22.

---

18. R. L. Bramblett, R. I. Ewing, and T. W. Bonner, Nuclear Instr. and Methods 9, 1 (1960).

Table 4. Counting Efficiencies for Bonner Spheres

Neutron Energy (ev)	Counting Efficiency (counts n^{-1} cm^{-2})						
	Bare Detector	Cd-Covered Detector	2-in.-diam Sphere	3-in.-diam Sphere	5-in.-diam Sphere	8-in.-diam Sphere	12-in.-diam Sphere
1.0 (−2)[a]	0.122	0.000	0.0820	0.0740	0.0420	0.0100	0.0040
1.6 (−2)	0.122	0.000	0.0850	0.0768	0.0448	0.0116	0.0041
2.5 (−2)	0.120	0.000	0.0880	0.0796	0.0476	0.0132	0.0043
4.0 (−2)	0.118	0.000	0.0930	0.0824	0.0504	0.0148	0.0044
6.3 (−2)	0.116	0.000	0.0960	0.0852	0.0532	0.0164	0.0045
1.0 (−1)	0.114	0.000	0.0980	0.0880	0.0560	0.0180	0.0046
1.6 (−1)	0.110	0.000	0.0990	0.0924	0.0600	0.0200	0.0047
2.5 (−1)	0.102	0.000	0.1000	0.0968	0.0640	0.0220	0.0048
4.0 (−1)	0.116	0.116	0.1000	0.1012	0.0680	0.0240	0.0050
6.3 (−1)	0.110	0.110	0.1008	0.1056	0.0720	0.0260	0.0051
1.0 (0)	0.084	0.084	0.1016	0.1106	0.0762	0.0282	0.0052
1.6 (0)	0.076	0.076	0.1020	0.1146	0.0806	0.0300	0.0054
2.5 (0)	0.068	0.068	0.1030	0.1194	0.0850	0.0318	0.0057
4.0 (0)	0.060	0.060	0.1040	0.1224	0.0896	0.0336	0.0059
6.3 (0)	0.052	0.052	0.1000	0.1262	0.0940	0.0354	0.0062
1.0 (1)	0.042	0.042	0.0940	0.1302	0.0986	0.0372	0.0064
1.6 (1)	0.036	0.036	0.0892	0.1338	0.1032	0.0390	0.0067
2.5 (1)	0.028	0.028	0.0862	0.1374	0.1076	0.0408	0.0070
4.0 (1)	0.020	0.020	0.0804	0.1410	0.1120	0.0426	0.0072
6.3 (1)	0.010	0.010	0.0776	0.1446	0.1164	0.0444	0.0075
1.0 (2)	0.002	0.002	0.0746	0.1482	0.1208	0.0462	0.0078
1.6 (2)	0.000	0.000	0.0712	0.1500	0.1258	0.0480	0.0080
2.5 (2)	0.000	0.000	0.0678	0.1520	0.1308	0.0498	0.0083
4.0 (2)	0.000	0.000	0.0646	0.1516	0.1358	0.0516	0.0085
6.3 (2)	0.000	0.000	0.0614	0.1510	0.1408	0.0534	0.0088
1.0 (3)	0.000	0.000	0.0582	0.1500	0.1458	0.0552	0.0090
1.6 (3)	0.000	0.000	0.0548	0.1478	0.1514	0.0574	0.0092
2.5 (3)	0.000	0.000	0.0516	0.1446	0.1570	0.0596	0.0095
4.0 (3)	0.000	0.000	0.0484	0.1412	0.1626	0.0618	0.0097
6.3 (3)	0.000	0.000	0.0452	0.1378	0.1682	0.0640	0.0100
1.0 (4)	0.000	0.000	0.0420	0.1346	0.1740	0.0660	0.0102
1.6 (4)	0.000	0.000	0.0386	0.1290	0.1798	0.0724	0.0116
2.5 (4)	0.000	0.000	0.0354	0.1236	0.1856	0.0790	0.0132
4.0 (4)	0.000	0.000	0.0322	0.1182	0.1914	0.0856	0.0148
6.3 (4)	0.000	0.000	0.0290	0.1126	0.1972	0.0920	0.0164
1.0 (5)	0.000	0.000	0.0258	0.1072	0.2032	0.0986	0.0180
1.6 (5)	0.000	0.000	0.0222	0.0986	0.2082	0.1148	0.0222
2.5 (5)	0.000	0.000	0.0180	0.0900	0.2136	0.1320	0.0274
4.0 (5)	0.000	0.000	0.0132	0.0780	0.2152	0.1578	0.0394
6.3 (5)	0.000	0.000	0.0098	0.0618	0.2118	0.2022	0.0618
1.0 (6)	0.000	0.000	0.0066	0.0596	0.1930	0.2240	0.0900
1.6 (6)	0.000	0.000	0.0044	0.0350	0.1580	0.2250	0.1360
2.5 (6)	0.000	0.000	0.0026	0.0230	0.1240	0.2120	0.1600
4.0 (6)	0.000	0.000	0.0016	0.0148	0.0880	0.1800	0.1650
6.3 (6)	0.000	0.000	0.0010	0.0092	0.0630	0.1640	0.1840
1.0 (7)	0.000	0.000	0.0008	0.0064	0.0420	0.1012	0.1252
1.6 (7)	0.000	0.000	0.0008	0.0056	0.0320	0.0800	0.1040
2.5 (7)	0.000	0.000	0.0008	0.0060	0.0260	0.0680	0.0880
4.0 (7)	0.000	0.000	0.0008	0.0060	0.0260	0.0600	0.0780
6.3 (7)	0.000	0.000	0.0008	0.0060	0.0260	0.0540	0.0720
1.0 (8)	0.000	0.000	0.0008	0.0060	0.0260	0.0520	0.0680
1.6 (8)	0.000	0.000	0.0008	0.0060	0.0260	0.0520	0.0660

[a]Digit in parentheses denotes power-of-ten multiplier.

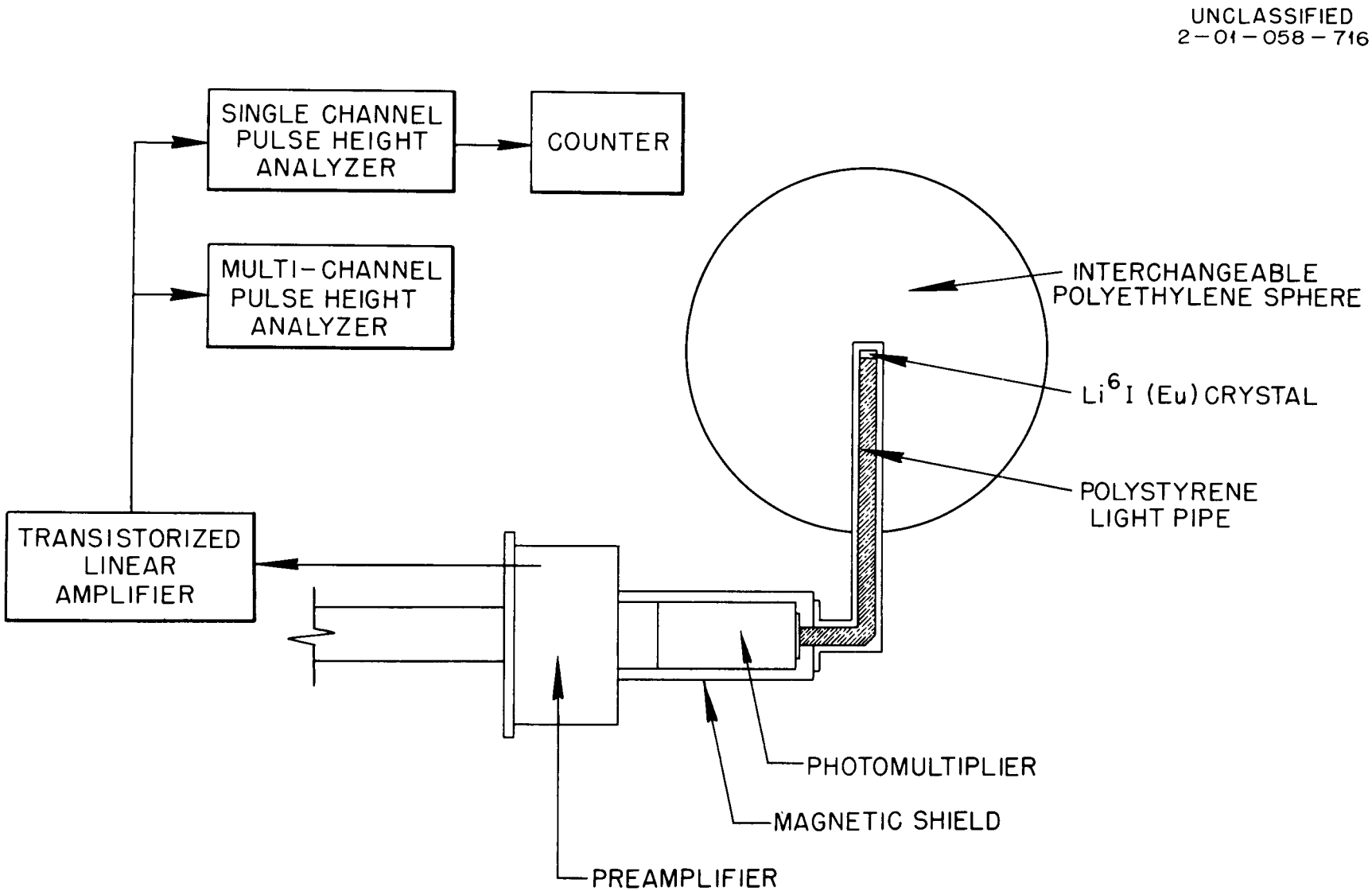

Fig. 22. Experimental Arrangement for Bonner Sphere Tests.

Experimental Results - Bonner Spheres

Pulse-height distributions obtained with 2- and 8-in.-diam polyethylene spheres are shown in Figs. 23 and 24, respectively. In both cases the particles incident on the target were 156-Mev protons, and the Bonner sphere was located 40 cm from the target on a line 30° from the beam-target axis. The target in the case of the 2-in.-diam sphere was a copper disk with a hole punched through its center, while for the 8-in.-diam sphere it was a solid copper disk. Both targets had a thickness of 31.8 g/cm^2. A considerable background is evident in the data from the smaller sphere and punched-out target, mostly due to protons scattered from the primary beam. It should be possible to subtract the background satisfactorily by recording the entire pulse-height distribution and performing a least-squares analysis for the area of the thermal peak. Few pulse-height spectra were recorded in these tests since no significant background had been anticipated.

Net counts recorded for various sphere diameters are shown in Table 5. The values represent the total counts less background for ~10^{10} protons incident on the copper target. Similar data are available but not yet analyzed for a total of 76 configurations. Table 6 lists the targets and angles studied.

Table 5. Total Counts in Thermal Peak for Bonner Spheres of Various Diameters

Detector	Net Counts[a]
Bare $Li^6I(Eu)$	~200[b]
Cd-covered $Li^6I(Eu)$	~ 50[b]
2-in. sphere	300
3-in. sphere	1300
5-in. sphere	3800
8-in. sphere	4900
12-in. sphere	3400

a. ~10^{10} 156-Mev photons incident on 31.8-g/cm^2-thick copper target. Detector 40 cm from target and 30° from beam axis. Beam-off background and counting loss corrections negligible.

b. Background estimated from similar experiments in which aluminum targets were used and pulse-height distributions recorded.

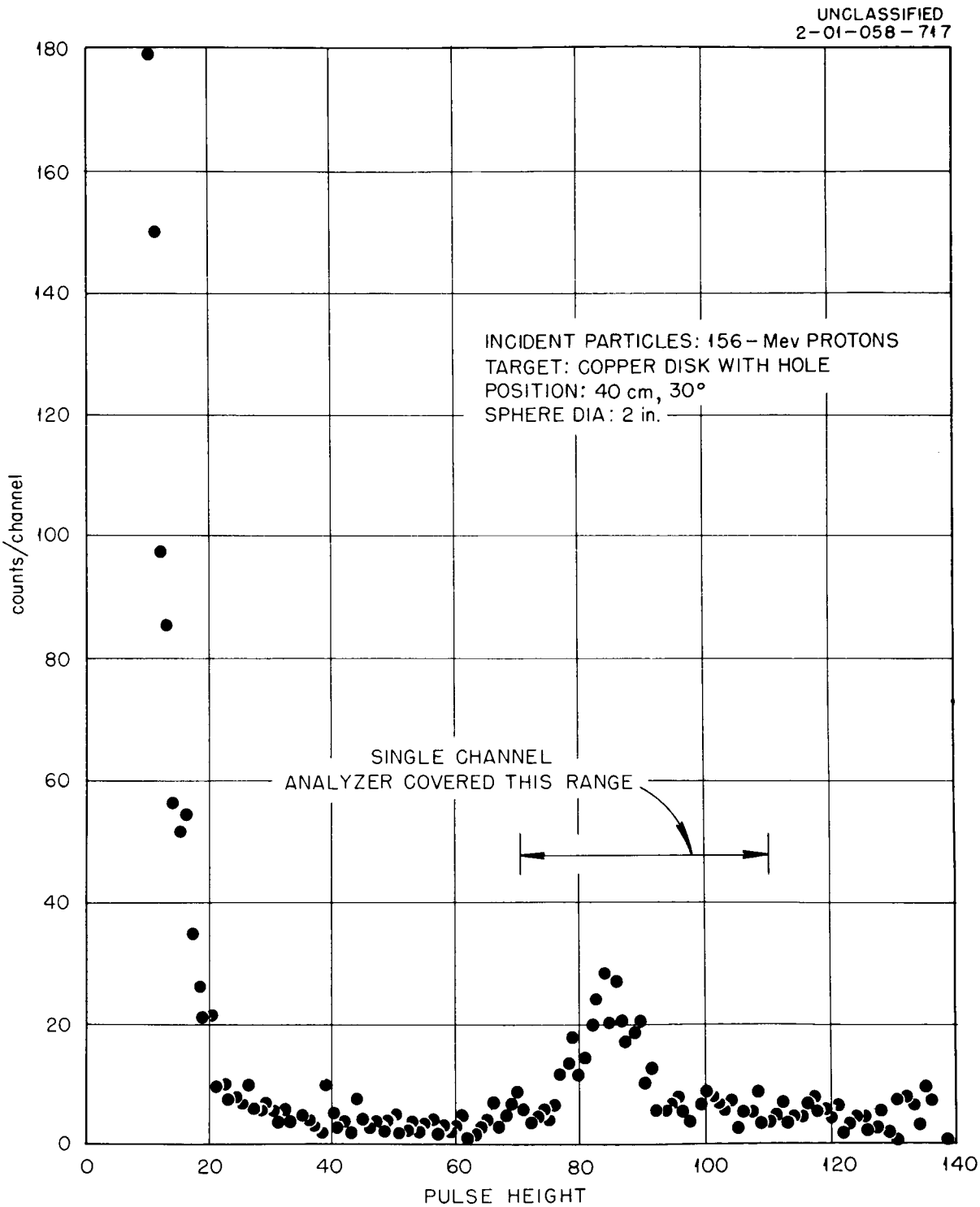

Fig. 23. Pulse-Height Distribution of Neutrons Resulting from 156-Mev Protons Incident Upon Copper, as Detected by a 2-in.-diam Bonner Sphere.

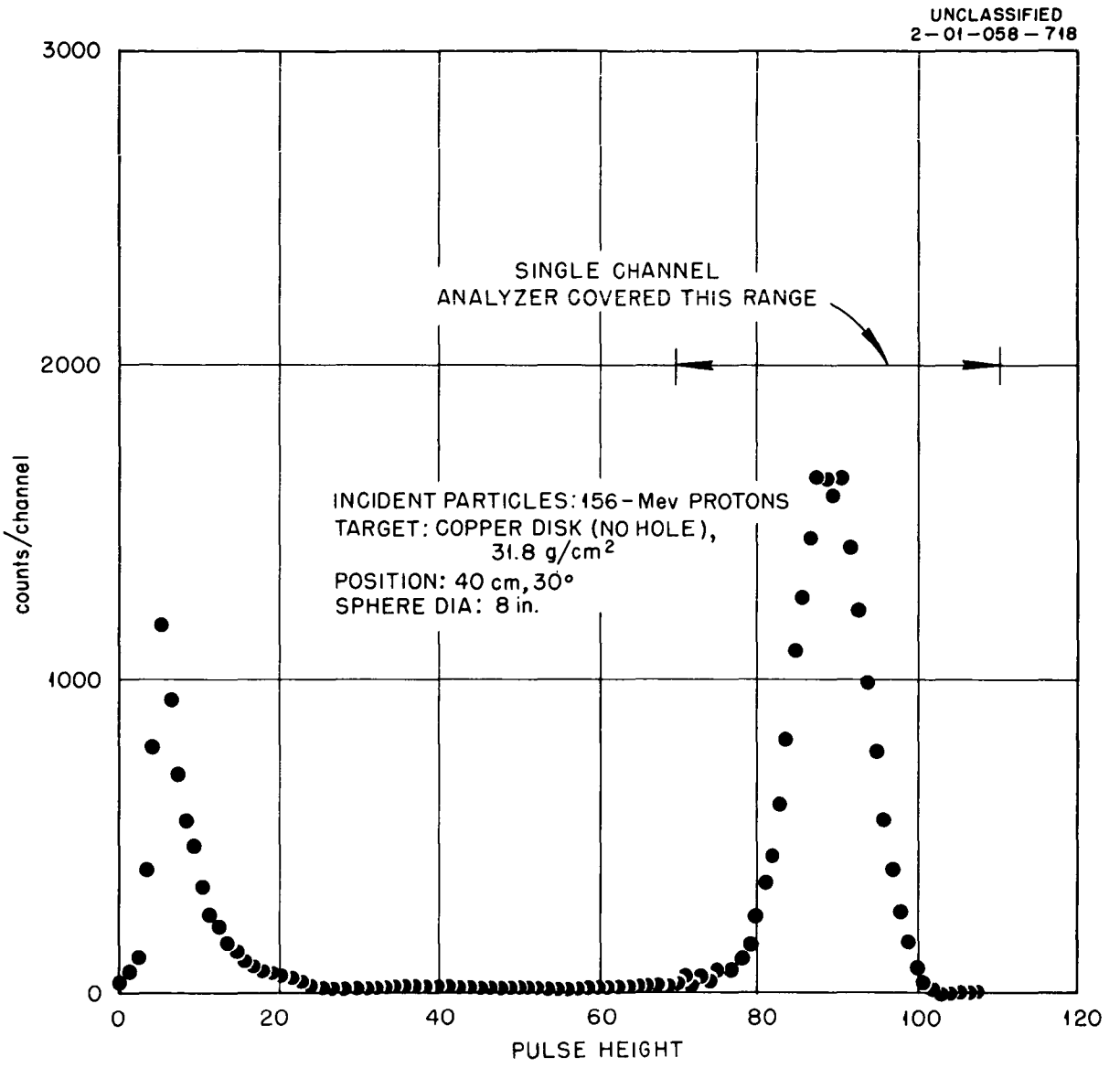

Fig. 24. Pulse-Height Distribution of Neutrons Resulting from 156-Mev Protons Incident Upon Copper, as Detected by an 8-in.-diam Bonner Sphere.

Table 6. Target Configurations for which Bonner Sphere Data were Obtained

Nominal $E_p \approx 156$ Mev

1.2-Range Targets

	Angles
H_2O	0°
C	30°
Al	45°
Co	60°
Cu	135°
Bi	
Pb	
None	

12-Mev Targets

	Angles
Blank Can	30°
H_2O	45°
D_2O	60°
Be	135°
C	
Al	
Co	
Bi	
None	

Experimental Procedure - Threshold Detectors

Three threshold detectors were tested to determine their usefulness for neutron energies > 10 Mev. Two were spiral fission chambers containing ~150 mg of U^{238} and ~150 mg of bismuth. A block diagram of the arrangement is shown in Fig. 25. The organic scintillator shown was used in anticoincidence with the fission chamber to discriminate against proton-induced fission.

The third threshold detector employed the $C^{12}(n,2n)C^{11}$ reaction by measuring the 20.5-m β^+ activity induced in 2 by 2-in. cylinders of Polyfluor plastic scintillator. The cylinders, after exposure to the neutrons, were counted on a conventional pulse-height analyzer using a 6655A photomultiplier. Cross sections used to compute efficiencies for all detectors are given in Table 7.

Experimental Results - Threshold Detectors

The results obtained with the detectors described above are listed in Table 8. Because of the difficulty noted below, the fission chamber counts were taken without the anticoincidence guard. The possibility of proton interaction is reflected in the large errors quoted. The U^{238} fission chamber data, of dubious value, were not used.

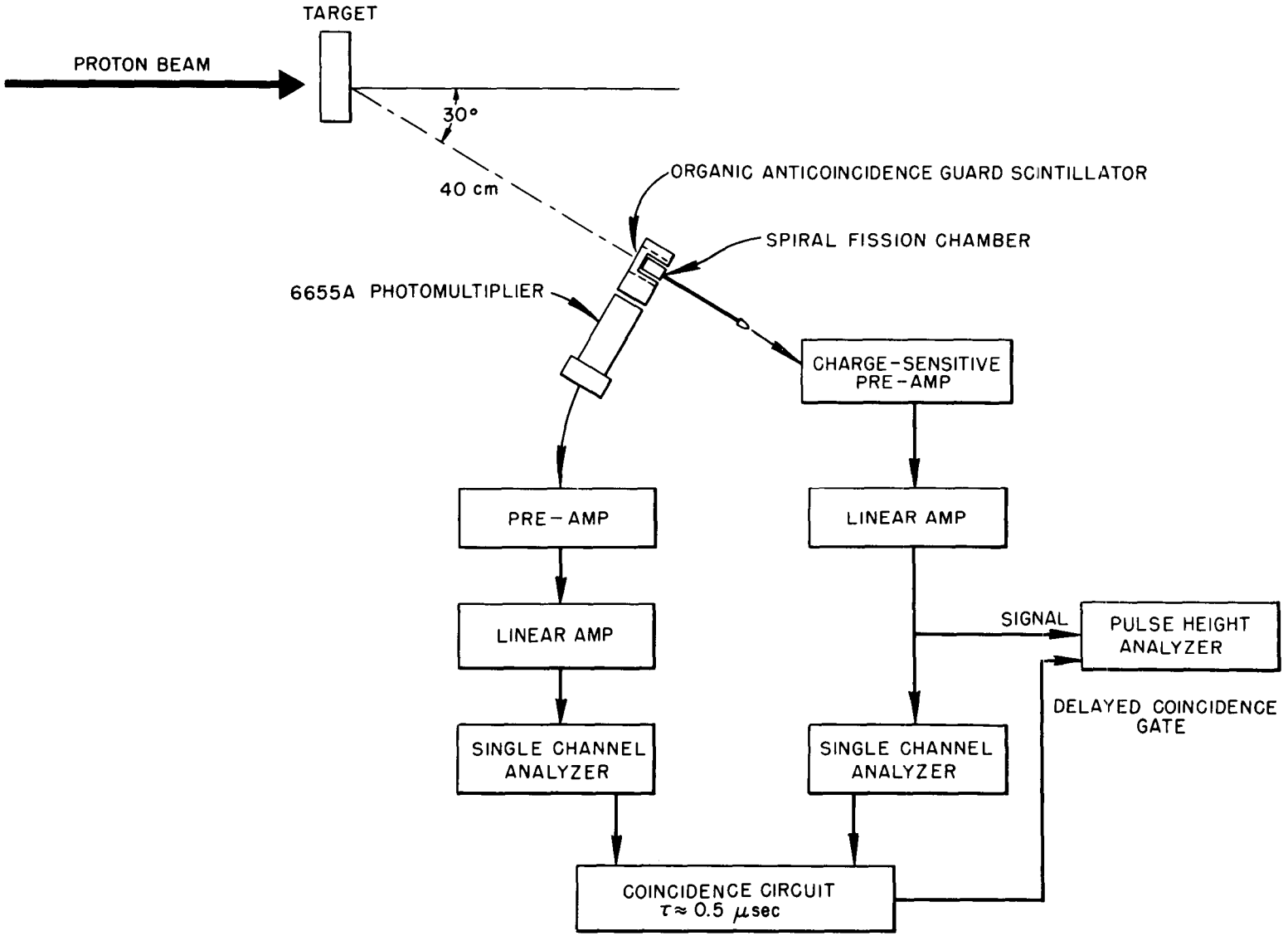

Fig. 25. Arrangement for Threshold Detector Experiments.

Table 7. Cross Sections Used for Threshold Detectors

Energy (Mev)	U^{238} (n,f) (barns) [a]	Bi (n,f) (barns) [b]	C (n,2n) (barns) [c]
0.40	0.000		
0.63	0.001		
1.00	0.18		
1.6	0.30		
2.5	0.58		
4.0	0.56		
6.3	0.70		
10	1.01		
16	1.30		
25	1.60	0.000	0.000
40	1.60	0.007	0.025
63	1.60	0.022	0.030
100	1.60	0.095	0.033
160	1.60	0.150	0.033

a. Accurate within 5% for energies below 16 Mev and probably within 20% for energies up to 160 Mev.

b. Probably accurate within a factor of 2 for energies up to 100 Mev and within a factor of 3 for energies up to 160 Mev.

c. Probably accurate within 30%.

Table 8. Experimental Results for Threshold Detectors

Detector	Number of Atoms in Sensitive Region	Number of Counts[a] per 10^{11} Incident Protons
U^{238} spiral fission chamber (FS-110)	$N_U = 3.8 \times 10^{20}$	1250 ± 80%
Bi spiral fission chamber (FS-109)	$N_{Bi} = 3.66 \times 10^{20}$	25 ± 40%
2 by 2-in. Polyfluor cylinder	$N_C = 5.06 \times 10^{24}$	1.2×10^4 ± 50%[b]

a. Indicated errors include allowance for possible proton interaction. U^{238} data were not used in analysis.

b. Value listed is total activation based on β^+ counting.

It was difficult to obtain satisfactory data with the threshold counters. If the primary proton beam intensity was adjusted so that a count rate of a few counts per second was obtained in the fission counters, then the anti-coincidence guard crystal was jammed. Trouble was also encountered in using the $C^{12}(n,2n)C^{11}$ reaction because of the competing $C^{12}(p,pn)C^{11}$ reaction in the detector. Further development might eliminate these difficulties, but since the energy range above 10 Mev presumably will be adequately covered by other devices, the use of threshold detectors has been abandoned.

Calculation of Neutron Spectra

The raw material from which the neutron spectrum was calculated consisted of the efficiencies of Table 4, the cross sections of Table 7, and the experimental counting rates of Tables 5 and 8. It was known from published measurements and from theoretical calculations of the evaporation neutron spectrum that the neutron spectrum should be fairly slowly varying. This "regularity" of the spectrum was taken into account by assuming that the spectrum $\phi(u)$, where $u = \log_{10}(E/1\ \text{Mev})$, could be expressed as a positive combination of smooth functions,

$$\phi(u) = \sum_{k=1}^{m} q_k R_k(u),$$

where $q_k \geq 0$ and $R_k(u)$ are suitable slowly varying functions. Several typical $R_k(u)$ functions are shown in Fig. 26. Fifty-two such functions were used in the present calculation.

An approximate spectrum was then obtained by solving for the q_k's by the method of optimal combinations.[19] Briefly, the method consists of arbitrarily specifying the response function of a fictitious crude spectrometer and then trying to fit the response function with the counting efficiency functions of the actual detectors. The fictitious spectrometer chosen had a resolution (full width at half maximum) of 0.8 decade in energy.

Results

The results of the present preliminary experiments have been analyzed in the manner described above to give the tentative differential neutron energy spectrum shown in Fig. 27. The choice of the fictitious spectrometer with its resolution of 0.8 decade is reflected in the resolution shown in the figure.

Having obtained the approximate spectrum, one may then calculate the biological dose resulting from such a spectrum. Alternatively, the biological dose may be calculated directly by the method of optimal combinations. It was decided to calculate the entire distribution function, or "importance function," for biological dose, that is, the fraction of the total biological

---

19. Although not specifically identified by this name, this is the method described by W. R. Burrus, Neutron Phys. Div. Ann. Prog. Rep. Sept. 1, 1961, ORNL-3193, p. 44.

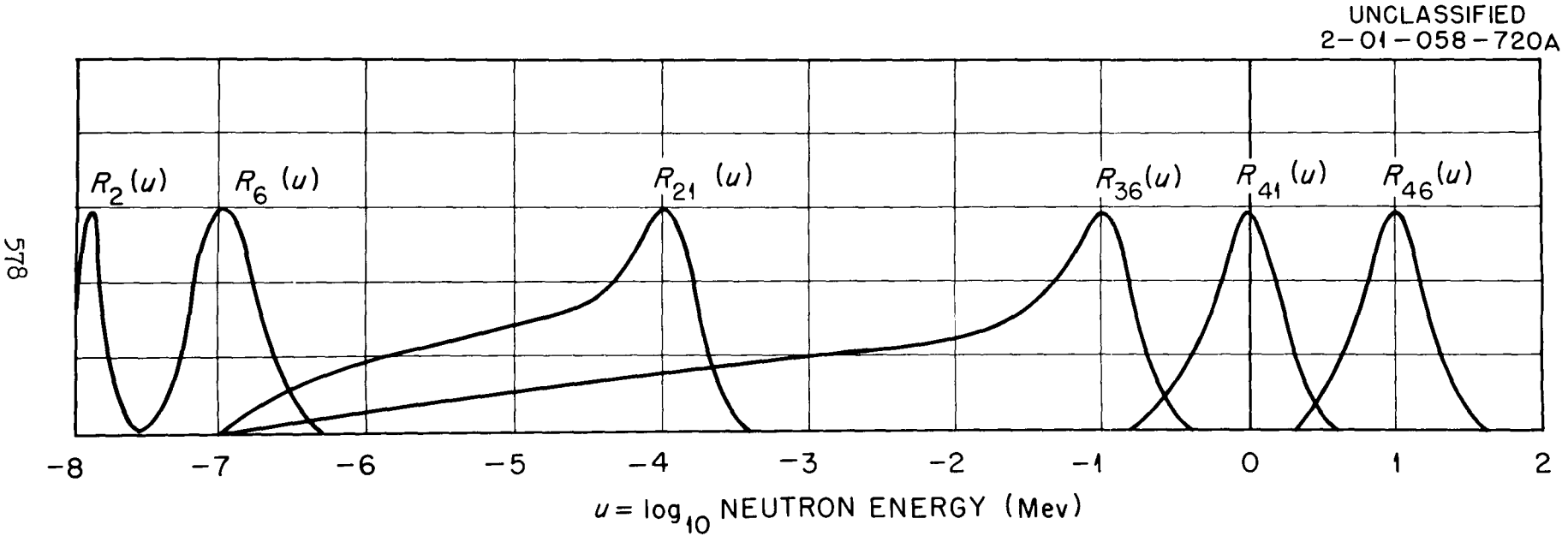

Fig. 26. Six Typical $R_k(u)$ Functions.

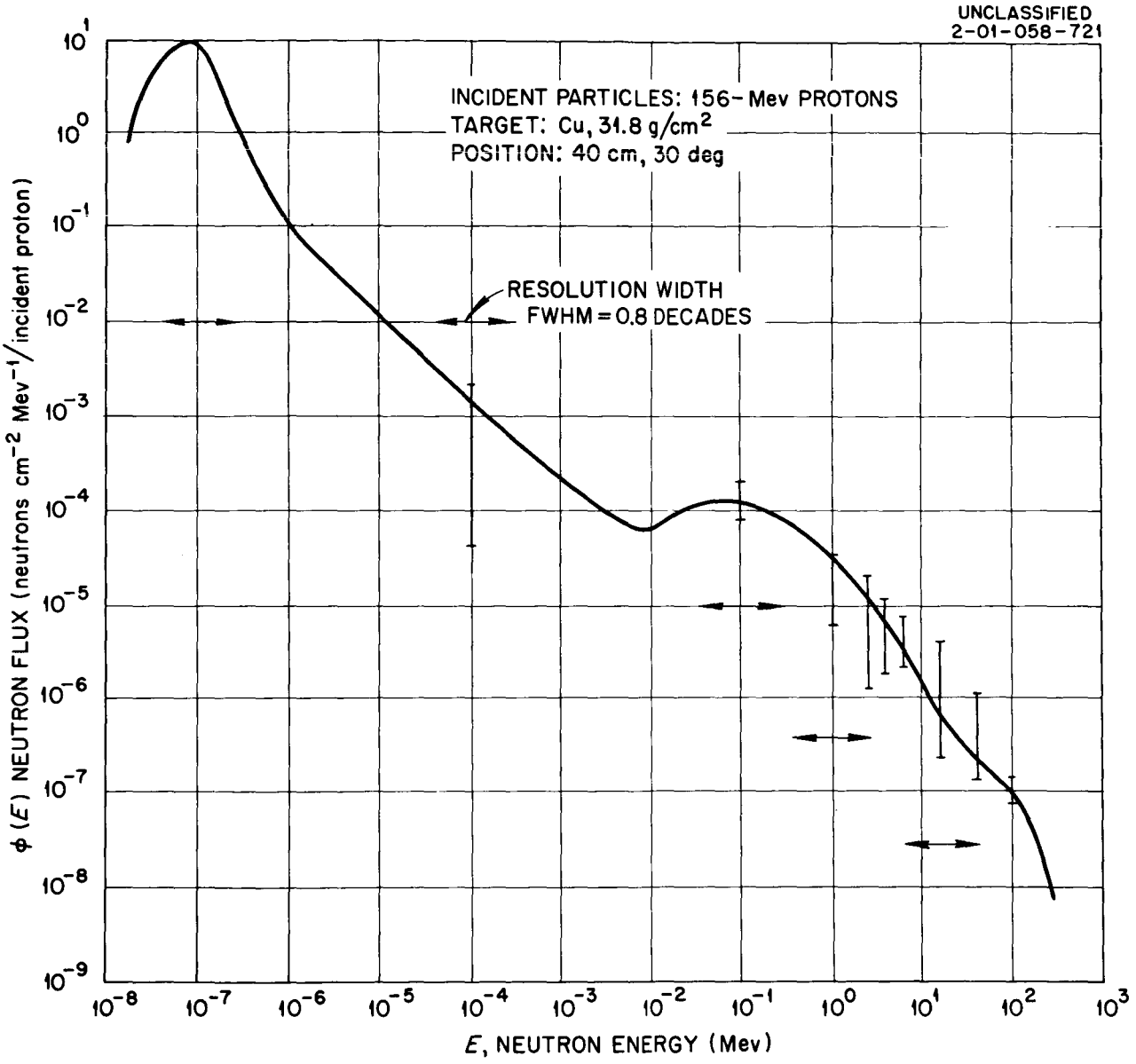

Fig. 27. Differential Neutron Energy Spectrum from 156-Mev Protons on Copper.

dose due to neutrons with energy above E. The result is shown in Fig. 28. From this curve an idea as to which part of the spectrum is most important from a biological damage viewpoint can be obtained. Somewhat unexpectedly, the present work shows that one-half the dose comes from neutrons with energies > 20 Mev and that only ~20% is due to neutrons with energies < 4 Mev.

The relation between biological dose and neutron flux is fairly complicated. In calculating the dose due to the neutron spectrum of the present work, values were taken from NBS Handbook 63[20] for that part of the spectrum below 10 Mev. These values are based on the energy deposited in a 30-cm-thick slab of tissue. They were weighted by a relative biological effectiveness (RBE) taken from NBS Handbook 69[21] and based on the linear energy transfer of the elementary event. Above 10 Mev the assumption was made that the product of the effective RBE and the effective buildup remained constant at the value of 6.5 found for 10 Mev, and the energy removal curve of Gibson[22] was used in lieu of the first collision dose curve. The resulting curves for biological dose and first-collision dose are shown in Fig. 29. The data of Fig. 29, which result in an integrated dose rate of 1.8×10^{-12} (±40%) rem per incident proton, are probably reliable within a factor of ~3 at 160 Mev.

Problems in Use of Bonner Spheres

No measurements of the efficiencies of Bonner spheres in the energy region above 15 Mev are available. Efforts are under way to determine the sensitivity of results to errors in the efficiency in the region from 15 to 160 Mev. In the event that such errors are important, a Monte Carlo calculation of the high-energy response of the spheres appears feasible.

Although direct proton response may be subtracted from the thermal-neutron response peak, secondary neutrons produced within the moderator by p,n interactions are indistinguishable from target neutrons. Additional experiments, with the proton beam directly incident on the sphere, have been performed to estimate the importance of this effect.

Variations in the size of commercially furnished $Li^6I(Eu)$ crystals and small differences in techniques used to analyze the thermal-neutron peak cause slight discrepancies from published calibration values. The spheres to be used in future experiments are being calibrated against a recently obtained standardized Am-Be neutron source.

If dose distributions, such as the curve of Fig. 28, are to be important in future work, better values of flux-to-dose conversion ratios must be sought. It may be more plausible to base conversions on a tissue sphere rather than a tissue slab.

---

20. Protection Against Neutron Radiation up to 30 Million Electron Volts, NBS-63 (1957).

21. Maximum Permissible Body Burdens and Maximum Permissible Concentrations of Radionuclides in Air and Water for Occupational Exposure, NBS-69 (1959).

22. W. A. Gibson, Energy Removed from Primary Proton and Neutron Beams by Tissue, ORNL CF-61-6-48 (June, 1961).

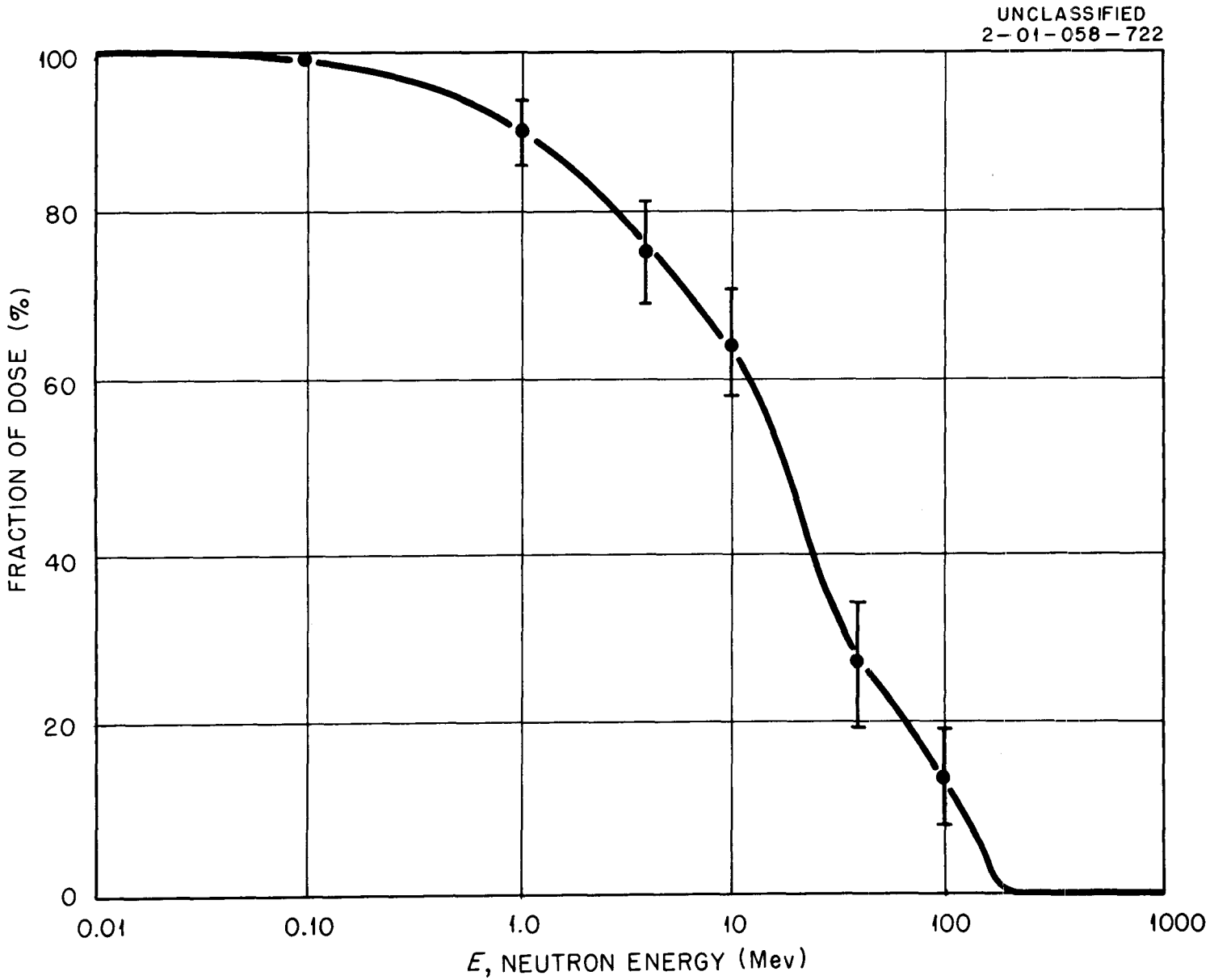

Fig. 28. Biological Dose Distribution.

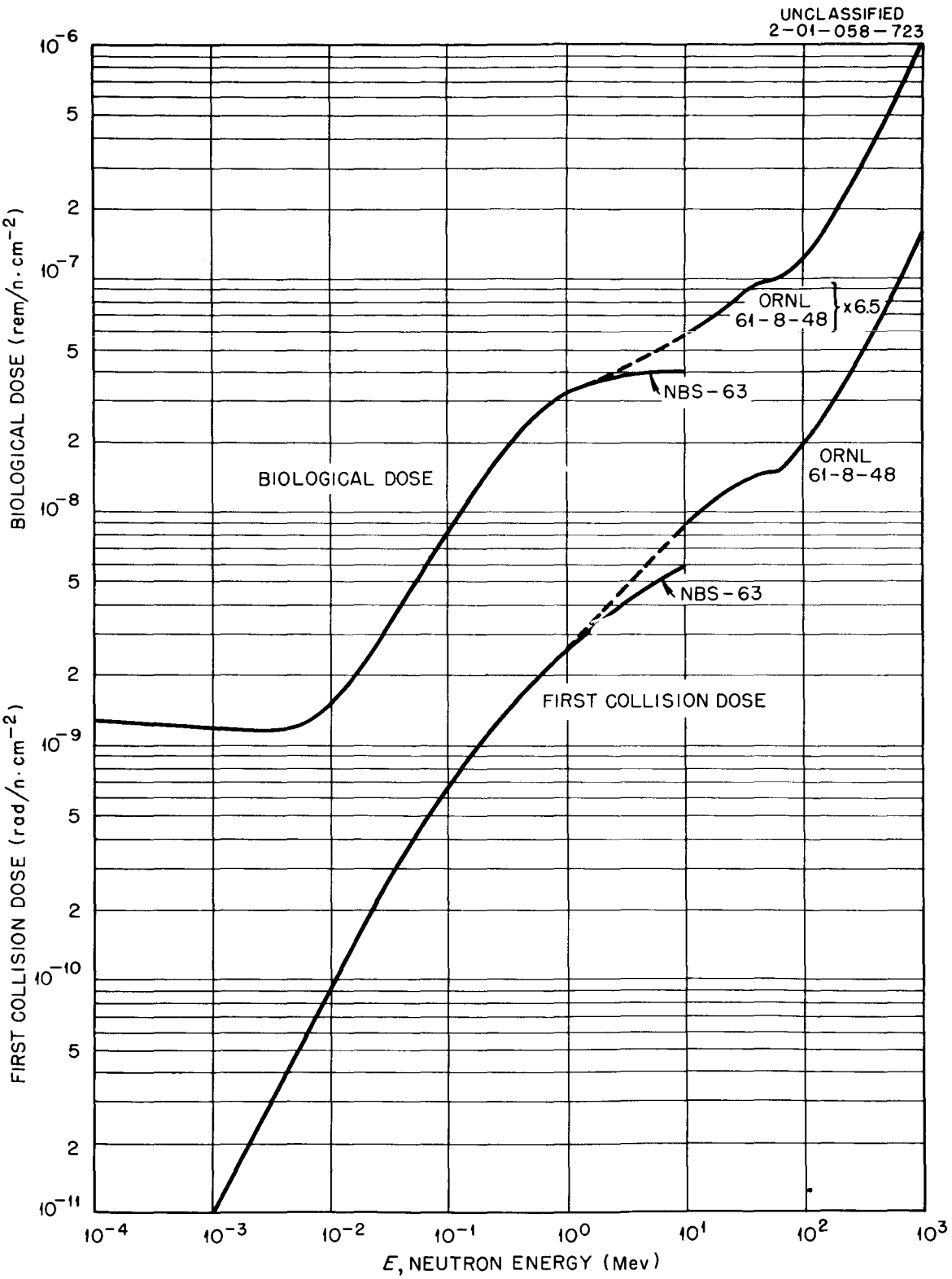

Fig. 29. Biological Dose and Removal Dose as a Function of Neutron Energy.

V. Spectrometry for Gamma Rays From Proton-Bombarded Nuclei

The spectrometer chosen for the preliminary measurements of secondary gamma rays produced by the bombardment of nuclei with ~156-Mev protons was a multicrystal spectrometer. For low-energy (< 2 Mev) photons it will be used as a total-absorption spectrometer, and for photons with energies above 2 Mev, as a pair spectrometer. Multicrystal spectrometers in use at ORNL have been described previously;[23] however, to improve the efficiency, the side crystals were redesigned so that the solid angle subtended by them at the center of the central crystal was greatly increased. The resulting configuration is shown in the photograph on page 586. Each side crystal is a frustum of a cone, with a base diameter of 4.000 in., a top diameter of 3.000 in., and a height of 1.871 in. A semicircular groove is cut into the base along a diameter. Both side crystals are mounted in a thin-walled aluminum can and are optically decoupled. A 3-in. photomultiplier tube, Du Mont Type K-1846, views each side crystal as shown. The central crystal, 1 in. in diameter and $1\frac{1}{2}$ in. in length, fits into the cylindrical hole formed by the semicircular grooves.

A simplified block diagram of electronics, as used for the pair configuration, is shown in Fig. 30. The central crystal is labelled A, the side crystals B and C. The amplifiers are Cosmic Radiation Labs., Inc., Model 901. The introduction of the snip-snap crossover pick-off single-channel analyzers eliminated the requirement for a slow coincidence circuit. The triple coincidence circuit used had a resolving time of ~130 nsec.

For use as a total absorption spectrometer, the snip-snaps in the B and C channels are used as integral discriminators. Their outputs are placed in anticoincidence with the output of the A channel, and the resulting signal is used as the 400-channel analyzer gate.

The detectors are enclosed in a lead housing 6-in. thick on the side nearest the target and at least 4-in. thick on all other sides. During part of the preliminary runs an additional 8-in.-thick layer of lithiated paraffin, intended to reduce the neutron-induced background, surrounded the lead. A collimator through the target side of the housing permits radiation to fall on the central crystal only.

During the initial runs with the pair spectrometer, in which an aluminum target was used, it became apparent that a large background existed that was connected with radiation emanating from the target. The collimator was replaced by a solid lead plug and lithiated paraffin, but the coincidence counting rate was reduced only by about a factor of 2. Removal of the paraffin from the shield did not appear to influence the coincidence counting rate, but removal of the aluminum target reduced it by a factor of more than 10. Similar results were observed later when a copper target was used in the proton beam. The proper functioning of the spectrometer, however, was demonstrated by the data from a carbon target, shown in Fig. 31. It

23. T. A. Love, R. W. Peelle, and F. C. Maienschein, Electronic Instrumentation for a Multiple-Crystal Gamma-Ray Scintillation Spectrometer, ORNL-1929 (Oct. 25, 1955).

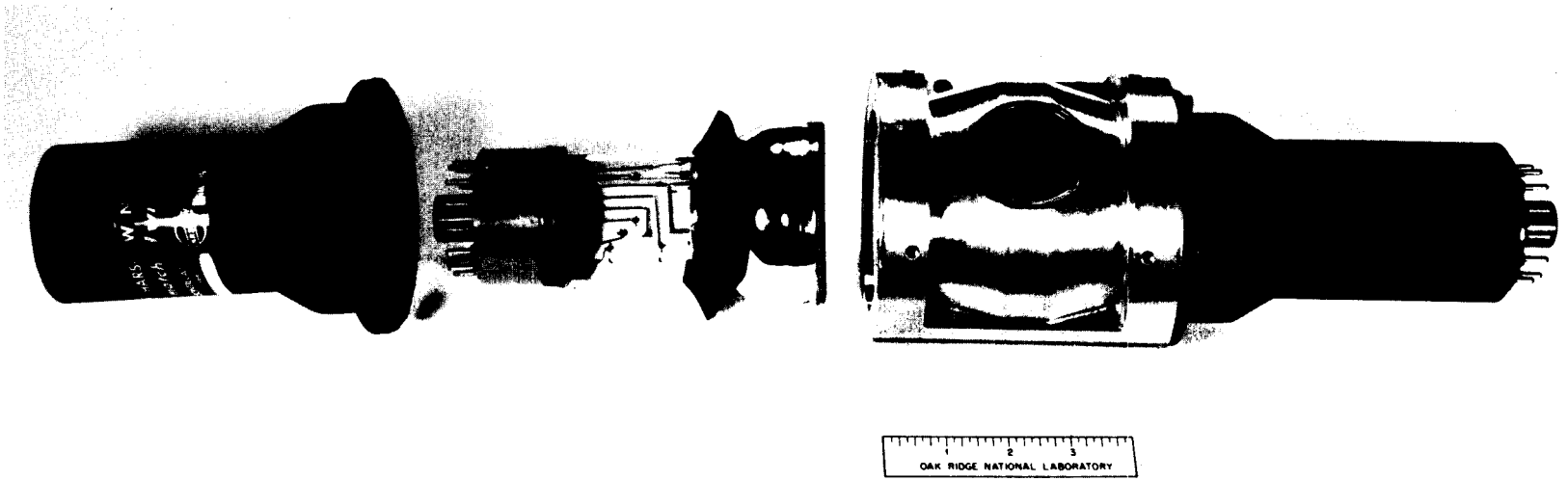

Crystals and Photomultipliers of the Gamma-Ray Spectrometer.

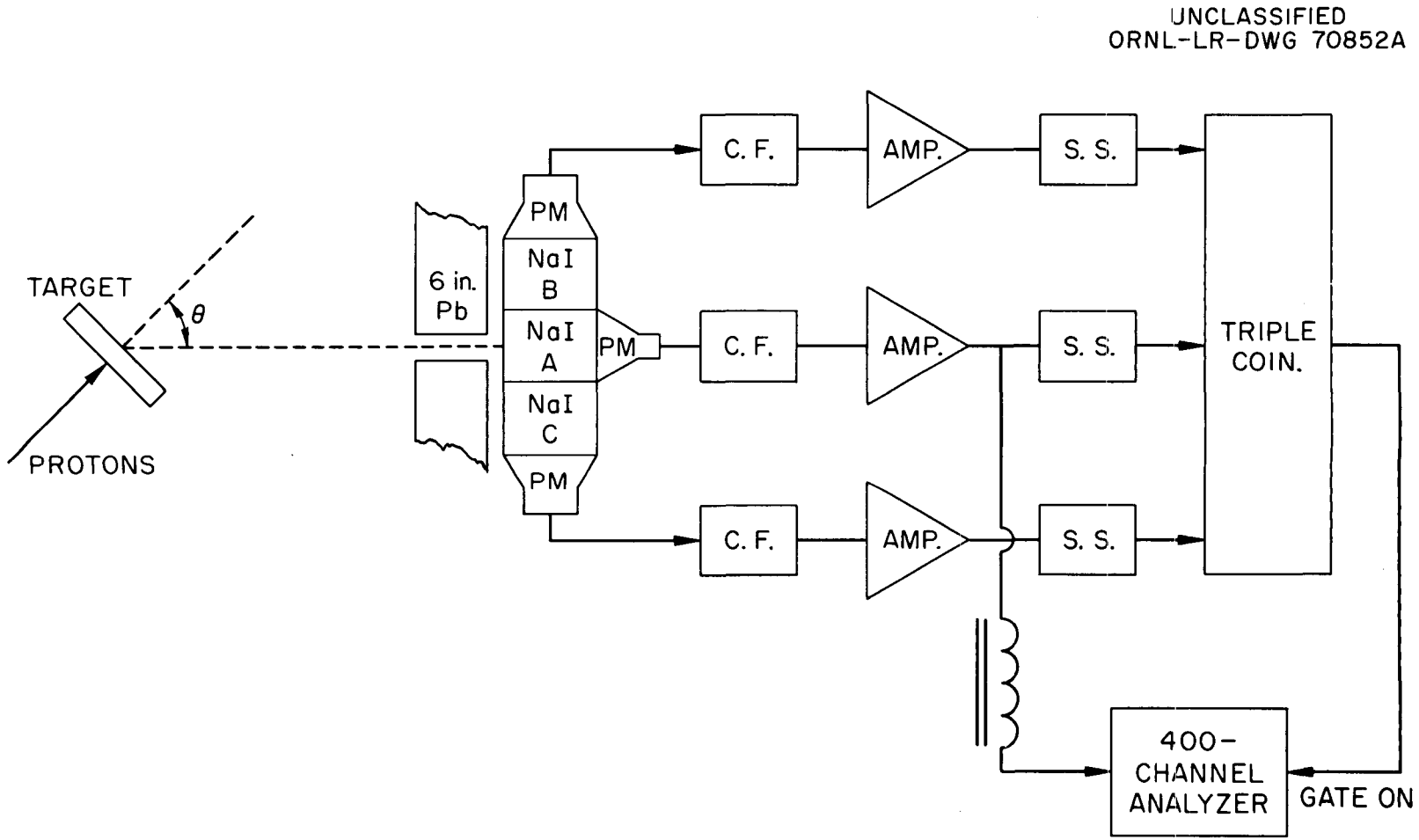

Fig. 30. Original Arrangement of Spectrometer Components in Pair Configuration.

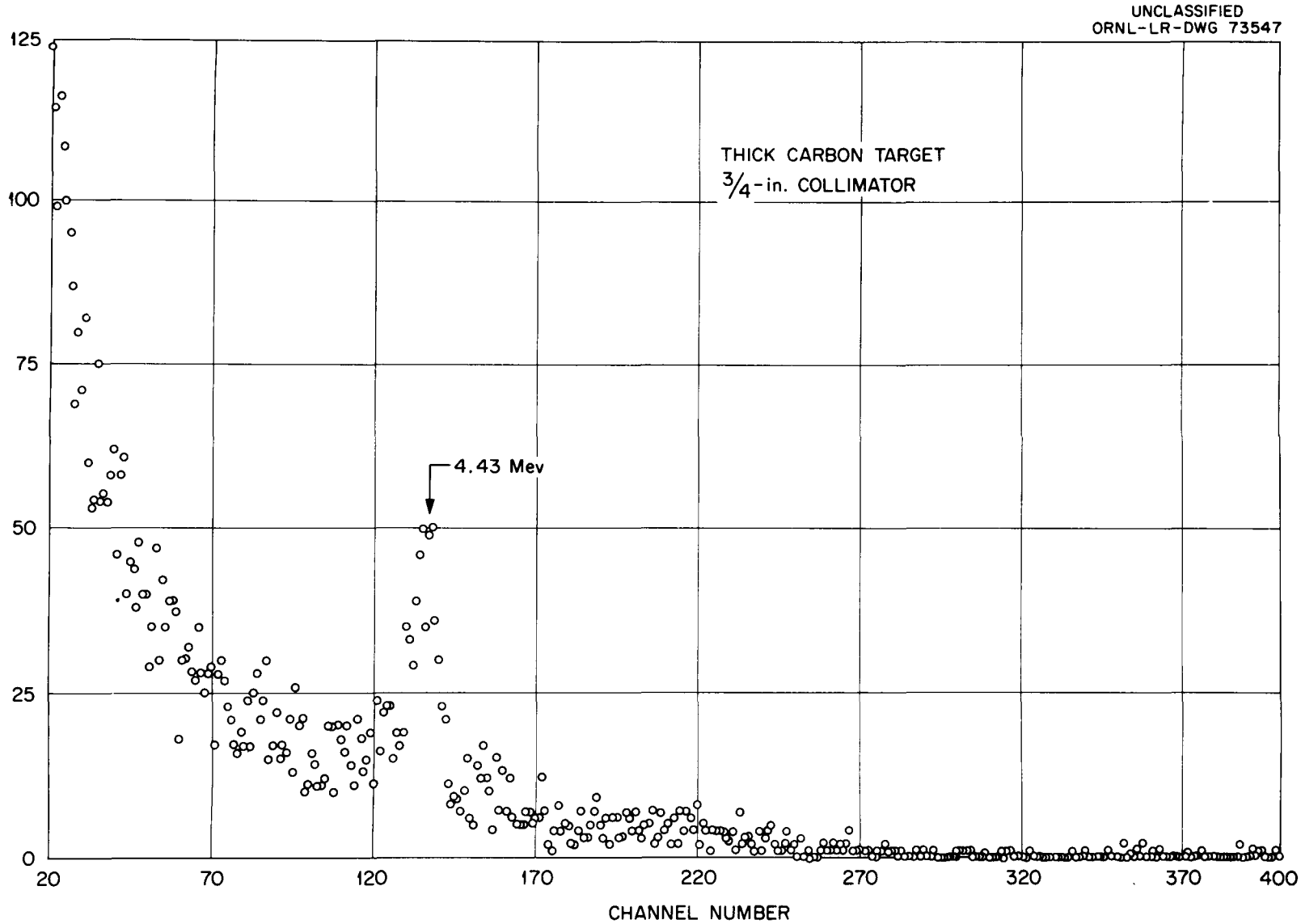

Fig. 31. Uncorrected Pulse-Height Spectrum of Gamma Rays Resulting from Bombardment of a Thick Carbon Target by ~156-Mev Protons.

should be noted that these data are of a very preliminary nature, with no corrections of any type applied. Based upon a rough energy calibration, the very prominent peak appearing at about channel 136 corresponds to a gamma-ray energy of 4.5 Mev. This is in good agreement with the well-known 4.43-Mev gamma ray from carbon.

The results of the trials suggest that the large background is due to neutron-induced radiation. To verify this hypothesis and to minimize the background, several modifications have been made. The shield around the spectrometer has been changed to a greater thickness of lead and a successful attempt was made to reduce the neutron-induced background by using time-of-flight techniques. A block diagram of the revised electronics is shown in Fig. 32. The method depends on the experimental observation that the protons are produced in the machine in bursts, with a frequency depending on the rf of the accelerating voltage. A thin (~1 mm) plastic scintillator detects the beam, and only those gamma rays detected in coincidence with the beam are accepted.

In Fig. 33 is shown the time dependence of the counts recorded in the tunnel diode (TD) fast coincidence circuit of Fig. 32 with the spectrometer viewing a 1.2-proton-range carbon target at 129° and ~145 cm. The peak width of ~12 ns is consistent with the detection of gamma rays in the A crystal. The counting rate at the minimum indicates a small neutron background. At 0°, the neutron background is much larger as would be expected. Figure 34 shows the results at 0° for a distance of ~226 cm.

Preliminary runs were made with the anticoincidence spectrometer and thin (12 Mev) targets of Be, C, and Al. The results for Al, shown in Fig. 35, give peaks at energies corresponding to those previously reported.[24]

24. K. J. Foley et al., Nuclear Phys. 37, 23 (1962).

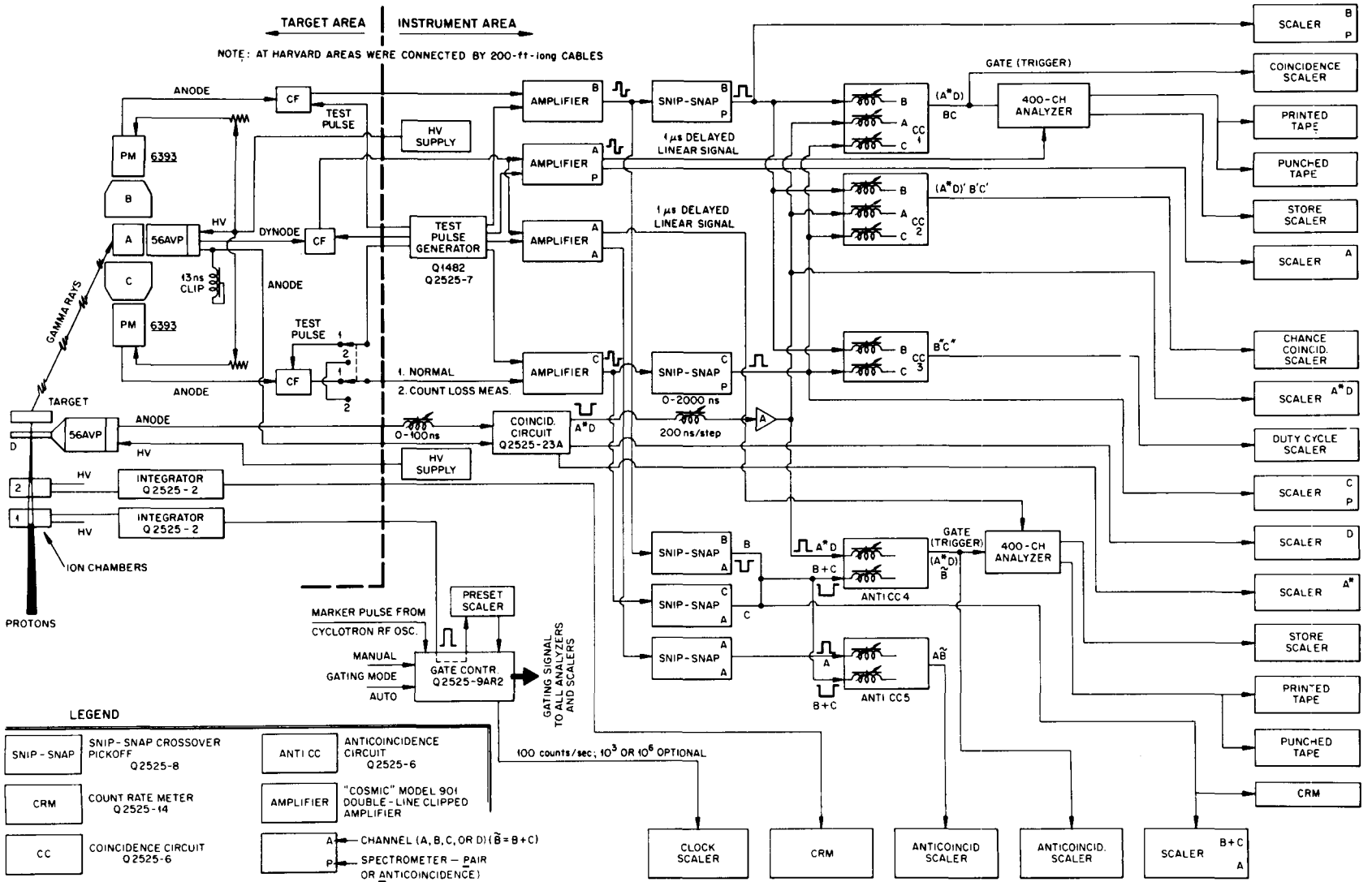

Fig. 32. Block Diagram of Modified Gamma-Ray Spectrometer

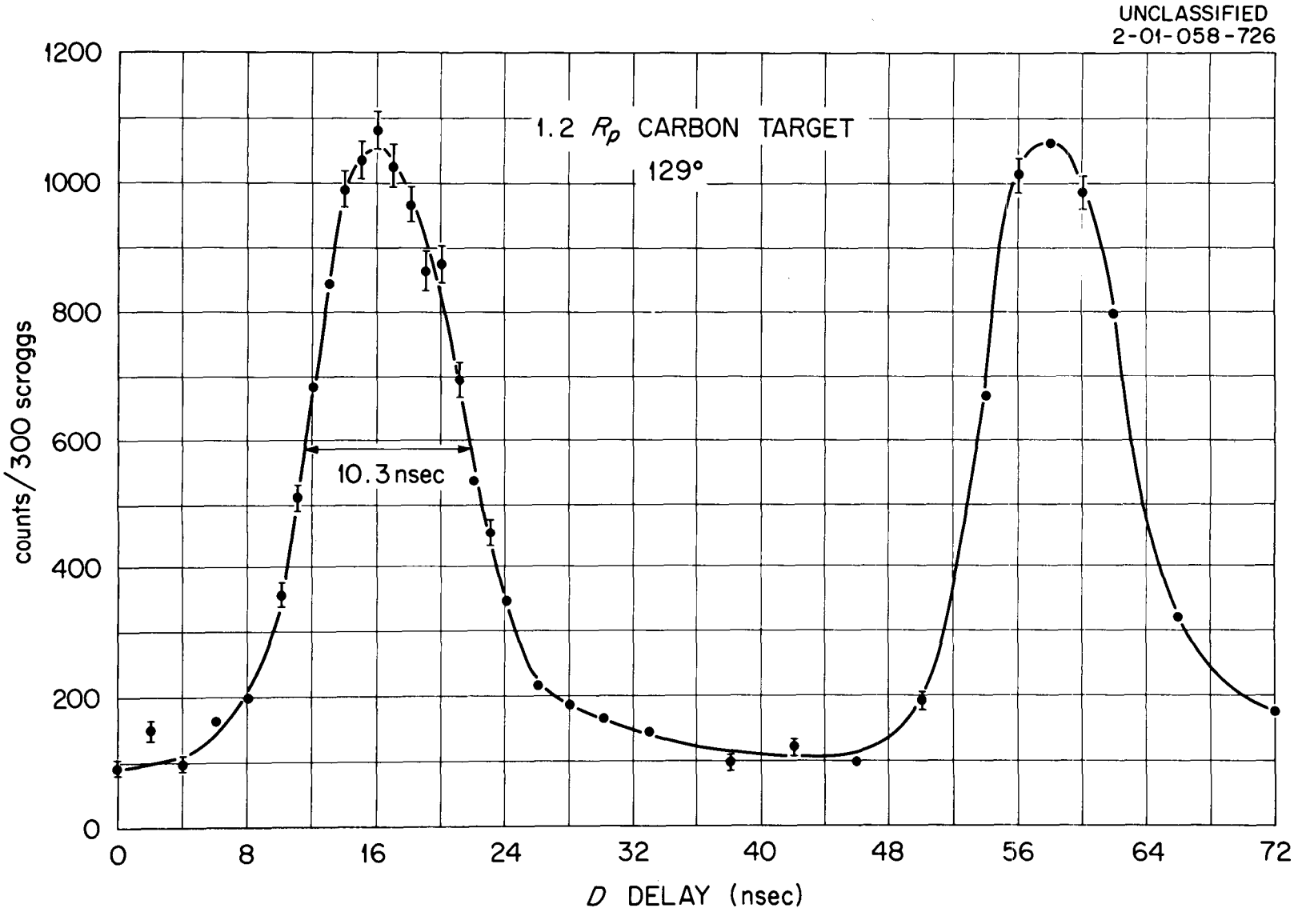

Fig. 33. Delayed Coincidences Between Channel D (Beam Detector) and Channel A (Central Crystal) for a 1.2 R_p Carbon Target at 129° and ~145 cm.

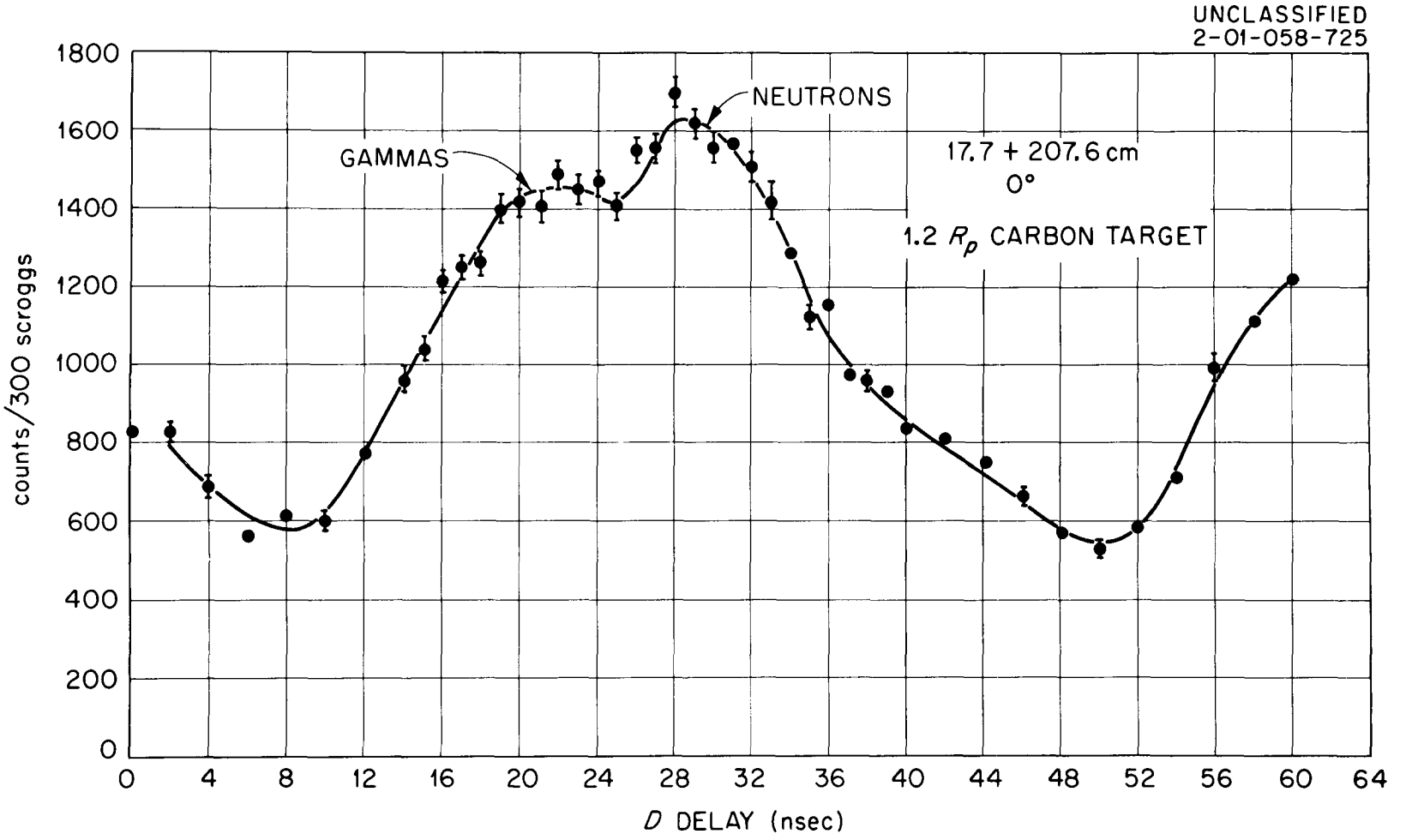

Fig. 34. Delayed Coincidences Between Channel D (Beam Detector) and Channel A (Central Crystal) for a 1.2 R_p Carbon Target at 0° and ~226 cm.

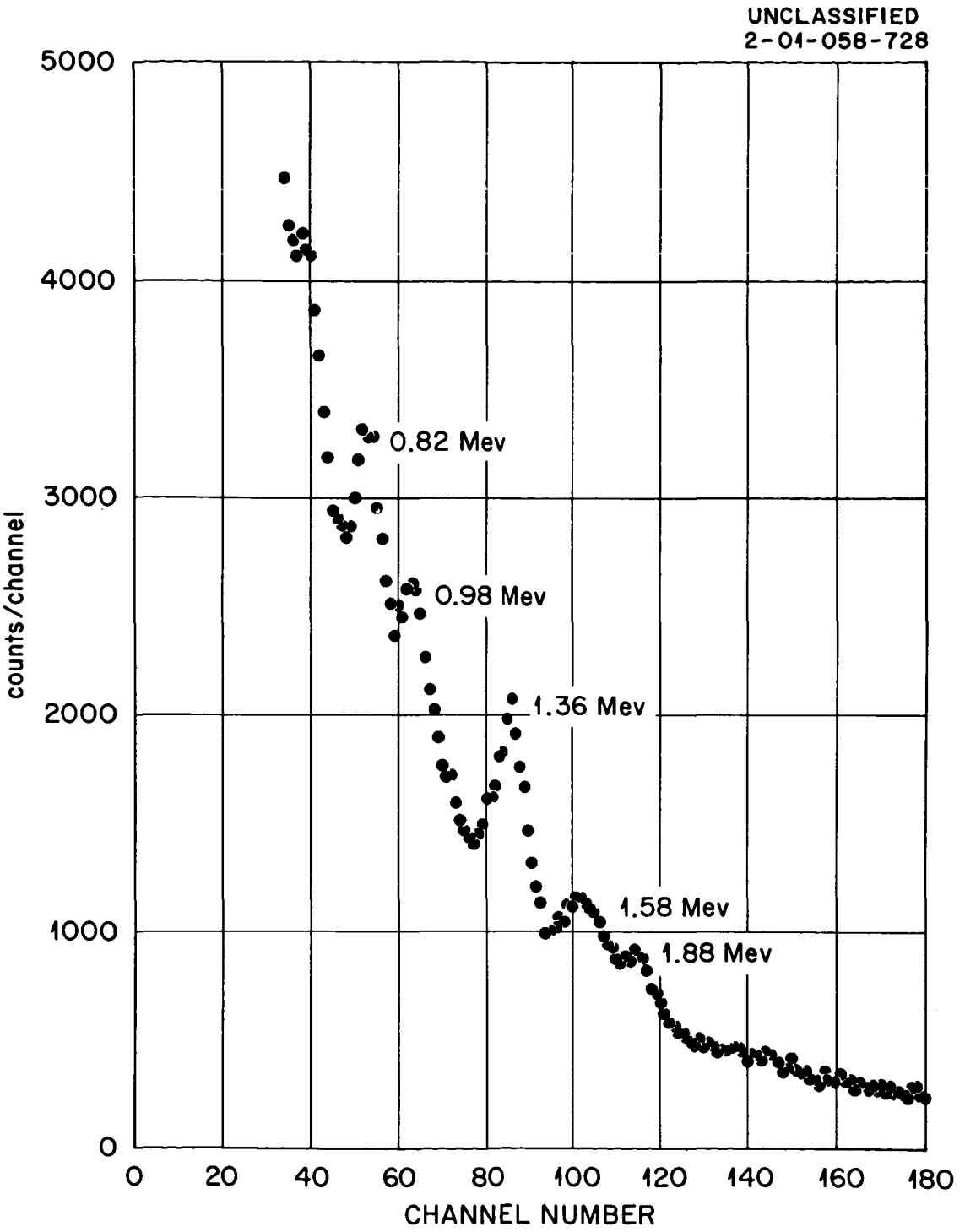

Fig. 35. Gamma Rays from 156-Mev Protons on a 12-Mev-Thick Aluminum Target.

VI. Dosimetry

Measurement of the physical dose resulting from the secondary particles from high-energy reactions would make additional demands upon the calculations. The proper conversion from flux to dose would be required, while for a large object, such as a man or phantom, the penetration through the object and integration over the incident angular distribution would have to be properly taken into account.

The instruments presently used to measure dose from reactor radiations are the results of lengthy development efforts. They measure either the total dose delivered to tissue or the separate contributions from neutrons and gamma rays to the dose.[25] Instruments of either type are not directly useful in the energy range of tens or hundreds of Mev, and another considerable development program will be required to provide dosimeters suitable for such energies. The present effort does not include such a program.

In one of the preliminary experiments at the Harvard accelerator, however, an attempt was made to use dosimeters of the type developed for reactor use in order to obtain very approximate results. A RADSAN, which is a Hurst proton-recoil counter with pulse-height analysis,[26] was used as a neutron dosimeter, and a small, halogen-filled GM counter[27] was used as a gamma-ray dosimeter. The GM counter gives only a single count for any charged particle passing through it, no matter how heavily ionizing, and thus discriminates against proton recoils. Unfortunately, both these instruments respond to high-energy protons with an undetermined efficiency. On a qualitative basis, the walls of the RADSAN were thick enough to stop protons with energies below about 35 Mev. For the relatively thin-walled GM tube, the pertinent parameter in considering the counting efficiency is the reciprocal of the energy loss per unit length, dE/dx. The dE/dx for a 150-Mev proton is roughly equal to that for a 60-kev electron, or three times the dE/dx for an electron in the energy range from ~0.5 to ~10 Mev. Therefore, the efficiency for high-energy protons should be only a few times less than that for recoil electrons produced by gamma rays.

Because of their nondirectional response and low-energy bias, the dosimeters are more responsive to background than are the spectrometers discussed in other sections of this report. Most of their use in the preliminary experiments at Harvard was in attempting to eliminate extraneous room background. As was noted in Section I, backgrounds were reduced by using a slit to restrict the beam and by addition of lead shielding at the point where the beam pipe penetrated the cyclotron shield. The "target-out" background in the horizontal plane of the cyclotron beam was nevertheless

---

25. G. S. Hurst et al., Measurement of Absorbed Dose of Neutrons, and of Mixtures of Neutrons and Gamma Rays, NBS-75, Sec. 3 (1961).

26. E. B. Wagner and G. S. Hurst, Rev. Sci. Instr. 29, 153 (1958).

27. E. B. Wagner and G. S. Hurst, Health Physics 5, 20 (1961).

very large for the gamma-ray dosimeter. This may be noted in Fig. 36. The target-out background increases rapidly as the angle between the beam axis and target counter axis is decreased, that is, as the beam is approached. The effect of shielding by the target at small angles may be seen in the target-in data. Background diminished rapidly as the detector was dropped below the plane of the beam.

In Table 9 are shown the results of measurements with the neutron and gamma-ray dosimeters at 40 cm from 20-cm-diam disk-shaped targets. The scattering angle was 40° for the neutron dosimeter and 50° for the gamma-ray instrument. The values listed, nominally in terms of tissue rad per incident proton, are quantitatively meaningless because of the proton background and are shown only to give an order of magnitude.

Table 9. Response of Dosimeters to Secondary Radiation from 156-Mev Protons Incident on Various Targets

Target	Thickness (g/cm^2)	Dose Rates (see text)	
		Neutrons	Gamma Rays
		($\times 10^{-14}$)	($\times 10^{-14}$)
H_2O	22.2	3.6	0.8
C	23.4	7.2	0.5
Al	26.5	8.9	2.0
Cu	29.4	16.0	2.8
Pb	44	28.0	1.0
none	0	3.8	5.3

Because of their high-energy proton response, the above dosimeters will not be used in future work. However, one dose measurement will be attempted. An ionization chamber will be used in a 42-cm-diam spherical water-filled phantom to determine the response due to all secondaries, regardless of type. The chamber will be moved throughout the phantom to determine the distribution in depth of the response of the ion chamber. The ionization current collected may be related to a physical dose, since the energy required to produce an ion pair depends but little on the type of particle or energy. Correlation with a biological dose, however, is clearly not possible unless the relative biological effectiveness is identical for all of the types of secondaries.

It is estimated that a 20-cc atmospheric-pressure ion chamber with polyethylene walls will yield about 10^{-11} to 10^{-12} amps, depending on position in the phantom, for a beam containing 10^{10} protons (150 Mev) per second. Such a current should be measurable with existing remote-reading electrometers. Determination of backgrounds will require "target-in," "target-out" subtractions. A serious additional background problem will be presented by reflection of secondaries from the laboratory floor.

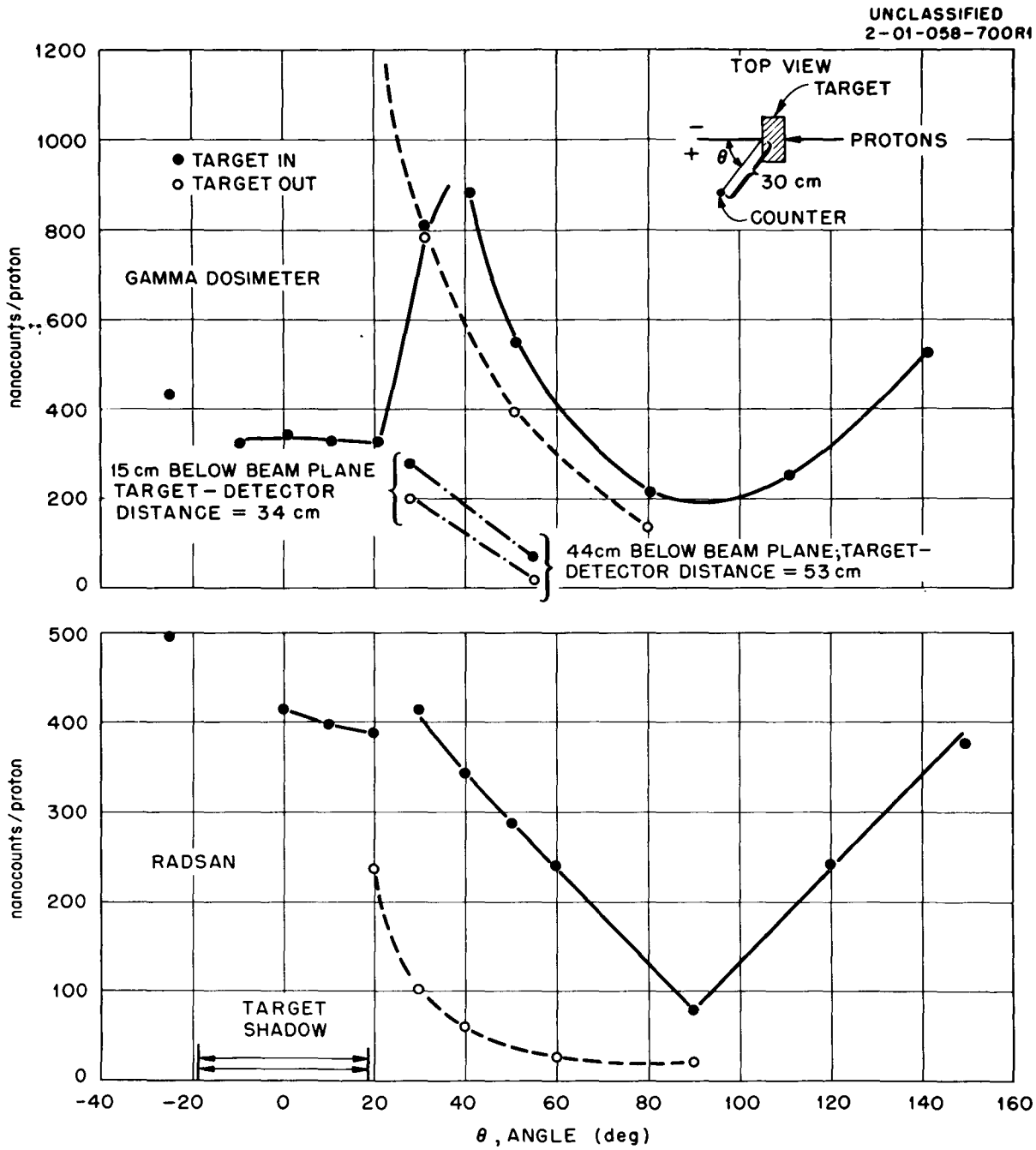

Fig. 36. Angular Distributions with Neutron (RADSAN) and Gamma-Ray Dosimeters Responding to Secondary Particles from a 20-cm-diam by 3.4-cm-thick Cu Target Bombarded by 156-Mev Protons. The target shadow indicates the angular displacement corresponding to the target at the 30-cm radius.

Paper D-5

SECONDARY-PARTICLE DOSE CONTRIBUTIONS INDUCED BY SOLAR PROTON RADIATION*

R. K. Wilson and R. A. Miller
General Dynamics/Fort Worth

15142

Abstract

A study was made to determine the biological hazard due to secondary radiation components produced in bulk shielding by high-energy extra-terrestrial protons. An idealized shield system - spherical-shell shield with a differential-volume water-target at the center - was chosen for the study. A comparison was made of the physical dose due to primary protons penetrating the shield and the secondaries produced in the shield. It was found that (1) shield-target geometry and target model greatly influence the ratio of primary proton-to-secondary component dose, and (2) secondaries may well be important for shield thicknesses greater than about 10 gm/cm^2 in the case of an aluminum shield and a solar-flare proton spectrum.

Introduction

With the prospects of manned flight in cislunar space within this decade, the question arises concerning the potential magnitude of the extraterrestrial radiation hazard to which man will be exposed. Soon after the discovery of the regions of trapped high-energy charged-particles encircling the earth, calculations indicated that no major hazard exists for short transit through these regions. However, the documentation of solar flare effects near the earth indicates that high-energy protons ejected by some solar flares may present a serious radiation hazard to cislunar flight.

Until the questions are answered about the time history and magnitude of the solar cosmic-ray source term, the shielding requirements for a manned space vehicle remain somewhat clouded. However, an area of study which initially requires only a limited amount of source term input - determination of the relative importance of the shielding-produced

*Work supported in part by NASA-MSFC under Contract NAS5-1093.

secondary components - can be considered with some success. Determination of the relative magnitude of the resultant secondary component doses may serve in the future as guidelines for the selection of materials and arrangements for primary component shields.

Dose Components

It should be agreed at the outset that, for such a study of the radiation hazard due to secondary components, a simple geometry be chosen for the shielded system. With this in mind, a spherical-shell shield (Fig. 1) was chosen to represent the system with a point target (differential volume of water) placed at the center. In addition to defining the relative importance of secondaries, a study based on this geometry may serve to define "importance areas" which will require consideration in realistic geometries.

Primary-Proton Component

In order to maintain the simplicity of the system, a point dose for primaries $D_{pp}(T)$ was calculated (Eq. 1) for comparison purposes with the secondary doses. The primary proton dose equation is given by

$$D_{pp}(T) = \int_{E^*(T)}^{E_{max}} dE \left\{ \Phi_p(E) \exp\left[- \int_0^T dx' \sigma_p(E,x') \right] \right\} S_p(E_T), \qquad (1)$$

where $\Phi_p(E)$ is the omnidirectional proton flux in free space as a function of energy E (protons/cm^2-sec-Mev),

$\exp\left[- \int_0^T dx' \sigma_p(E,x') \right]$ is the intensity attenuation due to nuclear collisions, and

$S_p(E,T)$ is the flux-to-dose conversion factor for protons (rads/proton/cm^2) as a function of the energy E_T, with $E_T = g(E,T)$ determined from range-energy curves for the shield material.

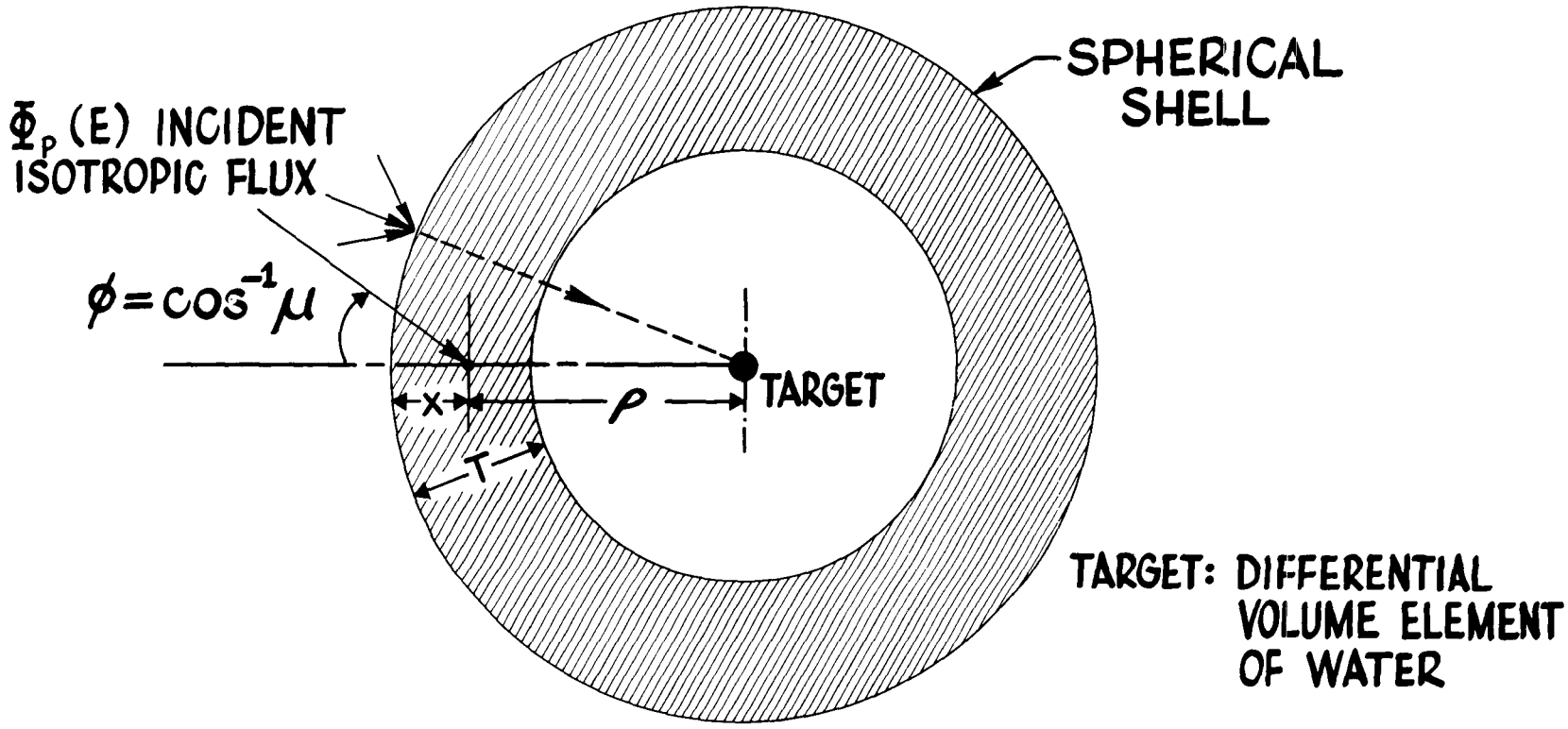

FIGURE I. RADIATION SHIELDING SYSTEM

As indicated by H. J. Schaefer's work[1], the point-target dose may not be the best method for defining shielding requirements; however, all we wish to determine, at this point, is the relative importance of secondaries. In the results section, a comparison of secondary and primary doses will be made on both the point-target and body - phantom basis of defining primary-proton dose received. A body phantom, as the term is used in this paper, is a finite size target representing the astronaut in a "curled-up" position. By using the body phantom method of determining dose, the shielding afforded by other parts of the body is considered in the calculation of the dose at a particular location in the body.

The flux-to-physical dose conversion functions for protons and neutrons shown in Fig. 2 are inferred from results of W. A. Gibson[2]. These curves represent only removal of energy from a particle beam by all processes and not necessarily the deposition of the energy in the body. However, they are presently the best material available for the purpose of representing dose.

Secondary-Particle Component

The type s secondary particle contribution $D_s(T)$ to the total dose can be classically represented by a volume integral of the secondary sources in the shield is given by

$$D_s(T) = \int d\vec{r} \int d\vec{\Omega}' \int dE' \; N_s(\vec{r}, E', \vec{\Omega}') \frac{\Lambda_s(\vec{r}, E', E_t, \vec{\Omega}')}{|\vec{r}|^2} S_s(E_t), \tag{2}$$

where

$N_s(\vec{r}, E', \vec{\Omega}')dE'd\vec{\Omega}'$ is the number of type s secondaries produced as the result of a given primary spectrum per unit volume at $\vec{r}$ in the energy interval dE' about E' and the solid angle interval $d\vec{\Omega}'$ about $\vec{\Omega}'$;

---

1. H. J. Schaefer, Dosimetry of Proton Radiation in Space. U. S. Naval School of Aviation Medicine, Pensacola, Florida, Report No. 19, (June 1961).

2. W. A. Gibson, Energy Removed From Primary Proton and Neutron Beams by Tissue. ORNL-3260 (September 1962).

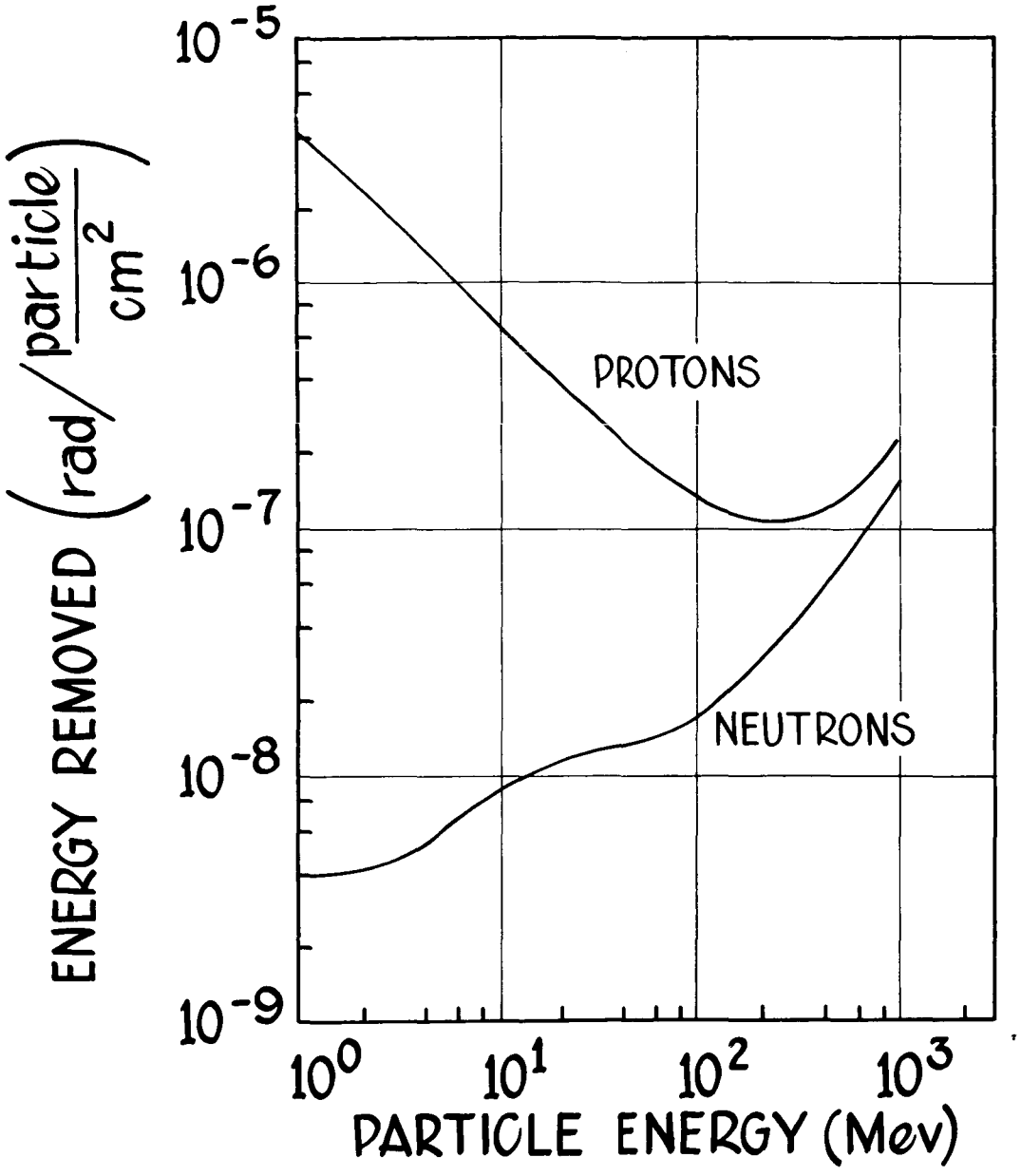

FIGURE 2. ENERGY REMOVED FROM PRIMARY-PROTON AND -NEUTRON BEAMS BY TISSUE

$\Lambda_s(\vec{r}, E', E_t; \vec{\Omega}')$ is a transfer function which considers the type s particle transport from secondary source location, $\vec{r}$, to the target (the term ideally would consider the energy degradation, tertiary production, and angular dependence of the secondary source);

$S_s(E_t)$ is the flux-to-dose conversion factor for type s secondaries which reach the target with degraded energy E_t;

$d\vec{r}$ is the volume (for the spherical shell, $d\vec{r} = \rho^2 d\rho\, d\mu\, d\phi$); and

$|\vec{r}|$ is the distance from the secondary-source location to the target (for the spherical shell, $|\vec{r}| = \rho$).

The secondary-particle source term is given by the equation

$$N_s(\vec{r}, E'', \vec{\Omega}') = \int d\vec{\Omega} \int_{E_s^*(x)}^{E^+} dE'' \left\{ \Phi(x, E'', \vec{\Omega}) \exp\left[- \int_0^{x/\mu} dx' \sigma_R(E'', x') \right] \right.$$
$$\left. \sigma_s^R(E'')\, \bar{n}_s(E'') f_s(E'', E; \vec{\Omega}, \vec{\Omega}') \right\}, \qquad (3)$$

where

$\Phi(x, E'', \vec{\Omega})$ is the primary-proton flux (energy degraded, but not attenuated in intensity) at the secondary-source location x, energy E";

$\exp\left[- \int_0^{x/\mu} dx' \sigma_R(E'', x') \right]$ is the intensity attenuation factor for a proton which arrives at the point x, making an angle $\cos^{-1}\mu$ with the radius, and with energy E";

$E_s^*(x, \mu)$ is the minimum-energy proton at x that can cause a reaction resulting in a type s secondary;

E^+ is some arbitrary upper limit to the energy spectrum;

$\sigma_s^R(E'')$ is the reaction cross section for type s secondary production at the location x by a proton of energy E"; and

$\bar{n}_s(E")$ is the average number of type s secondaries produced per reaction by a proton of energy E";

$f_s(E", E; \vec{\Omega}, \vec{\Omega}')$ is the type s secondary energy and angular distribution function so normalized that

$$\int_{4\pi} d\vec{\Omega}' \int dE \, f_s(E", E; \vec{\Omega}, \vec{\Omega}') = 1 \qquad (4)$$

Simplifications. An obvious question at this point concerns the assumptions which can be made in order to simplify these equations. One approach which has been used by several investigators[3,4] has been to assume that only primary protons moving initially in the direction of the target produced secondaries which would contribute to the dose. This assumption is based on the fact that high-energy secondaries* are given off essentially in the direction of the incident, reaction-producing proton. However, low-energy secondaries are produced with an angular distribution which is more nearly isotropic, and the "straight-ahead" approximation cannot be used without some modification in the "spirit" of its use (see Fig. 3).

If this "straight-ahead" assumption is to be used for all secondary components, it is necessary to determine some approximate secondary-source intensity in the direction of the target for each secondary component. One approach is suggested by considering the reaction rate R (reactions/gm-Mev) of protons with energy E" at the location x as given below:

---

3. J. H. Tolan, Ed., Shielding Problems in Manned Space Vehicles. Lockheed Nuclear Products (Marietta, Ga.), Report NR-140 (September 1961).

4. R. G. Alsmiller, Jr., et al., Nuclear-Meson Cascade Calculations: Traverse Shielding for a 45-Gev Electron Accelerator (Part 1). Oak Ridge National Laboratory Report ORNL-3289 (1962).

* High-energy secondaries are defined here as those secondaries which are produced essentially in the direction of the primary (fairly well approximated by an energy limit of $E_s > 20$ Mev).

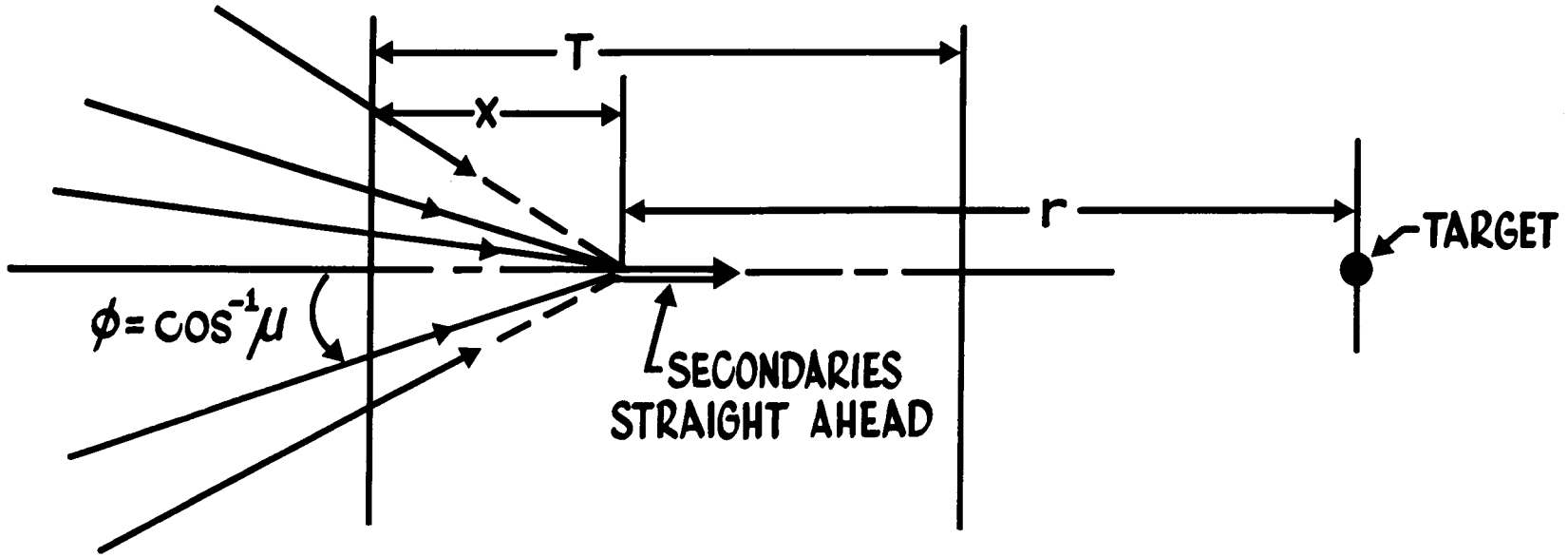

FIGURE 3. SECONDARY-PARTICLE STRAIGHT-AHEAD GEOMETRY

$$\sigma_s^R(E'')\int d\vec{\Omega}\ \Phi(x,E'',\vec{\Omega}) = R. \tag{5}$$

The question is: How can the type s secondary flux in the direction of the target be related to the reaction rate, R_o, due to primary protons moving initially in the inward radial direction? The answer is found in the ratio $A(x,E'')$ of the normalized secondary flux to the reaction rate R_o (Eq. 6):

$$A(x,E'') = \frac{\sigma_s^R(E'')}{R_o}\left\{\int_{2\pi} d\vec{\Omega}\ \Phi(x,E'',\vec{\Omega})\int_0^{E''} dE\ f_s(E'',E;\vec{\Omega},\vec{\Omega}_o)\right\} \tag{6}$$

Ultimately, $A(x,E'')$ serves as a "weight" function which allows the explicit integration over $\vec{\Omega}$ to be dropped in the secondary source term (Eq. 3).

For the region of the shield from which most of the secondaries are produced near the incident face (in the case of a "typical" flare spectrum), $A(x,E'')$ is reasonably constant as a function of x. The energy dependence of $A(x,E'')$ is considered through the type of secondary component which the primary produces, i.e., evaporation or cascade particles. On the basis of the above remarks, it can be seen that not much generality is lost in assuming that $\bar{A}$ (an average A) can be determined for each of the secondary components. For cascade neutron and proton particles, which are the result of direct high-energy interaction in the nucleus, $\bar{A}$ is found to be approximately equal to 1. It was found that an $\bar{A}$ equal to 1/4 could be used to weigh the source intensities for evaporation and low-energy cascade particles.

As a result of these several approximations, the secondary-component dose equation can be written in the form

$$D_s(T) = \bar{A}\int_0^T dx \int dE' \left\{ \int_{E_s^*(x)}^{E} dE\,\Phi_p(E)\ \exp\left[-\int_0^x dx'\sigma_R(E,x')\right] \right.$$
$$\left. \sigma_s^R(E'')\ \bar{n}_s(E'')g_s(E'',E)\right\} \Lambda_s(x,E',E_t)S_s(E_t) \tag{7}$$

where the terms not defined previously are

$\Phi_p(E)$ is the omnidirectional-proton flux incident on the system in terms of the free-space proton energy E (protons/cm^2-sec-Mev),

$\exp\left[-\int_0^T dx'\sigma_R(E,x')\right]$ is the intensity attenuation due to nuclear-collision removal, and

$g_s(E'',E)$ is the type s secondary-particle energy distribution function.

Results of Dose Calculations

The secondary-component-dose equations were solved as a function of shell thickness for several incident-proton spectra and material compositions[5]. Figure 4 shows the variation of the physical dose rate with thickness of an aluminum shield for the 10 May 1959 flare spectrum[6] (measured 33 hours after onset). In order to appreciate the relative significance of the secondary components, the primary-proton dose contribution is given in terms of both the point-target and body-phantom (52-cm-diam sphere of water, representing a man in the fetal position) volume dose, evaluated 5 cm below the surface of the phantom. If the secondary-component doses are compared to that due to the primaries evaluated in terms of the body-phantom model, one observes that the secondaries are indeed significant*. The relative flatness of the neutron-dose curve as a function of shield thickness can best be explained by the realization that the low-energy portion of the flare spectrum generates the majority of the secondaries. From the spectrum shown in Fig. 4, one can see that more than 95% of the particles incident on the shield are removed by ionization losses before they penetrate 10 gm/cm^2 of aluminum. Some of these particles, however, undergo neutron-producing reactions before they are stopped through energy degradation by ionizing losses.

5. R. K. Wilson, R. A. Miller, and R. L. Kloster, A Study of Space Radiation Shielding Problems for Manned Vehicles. GD/FW Report FZK-144 (June 1962).

6. J. R. Winckler and P. D. Bhavsar, J. Geophys. Res. 65, (1960) 2637.

* If the respective RBE (relative biological effectiveness) values were used to determine biological dose, the secondary component doses would doubtlessly appear even more important; however, the RBE values for the high-energy secondaries presently are only estimated.

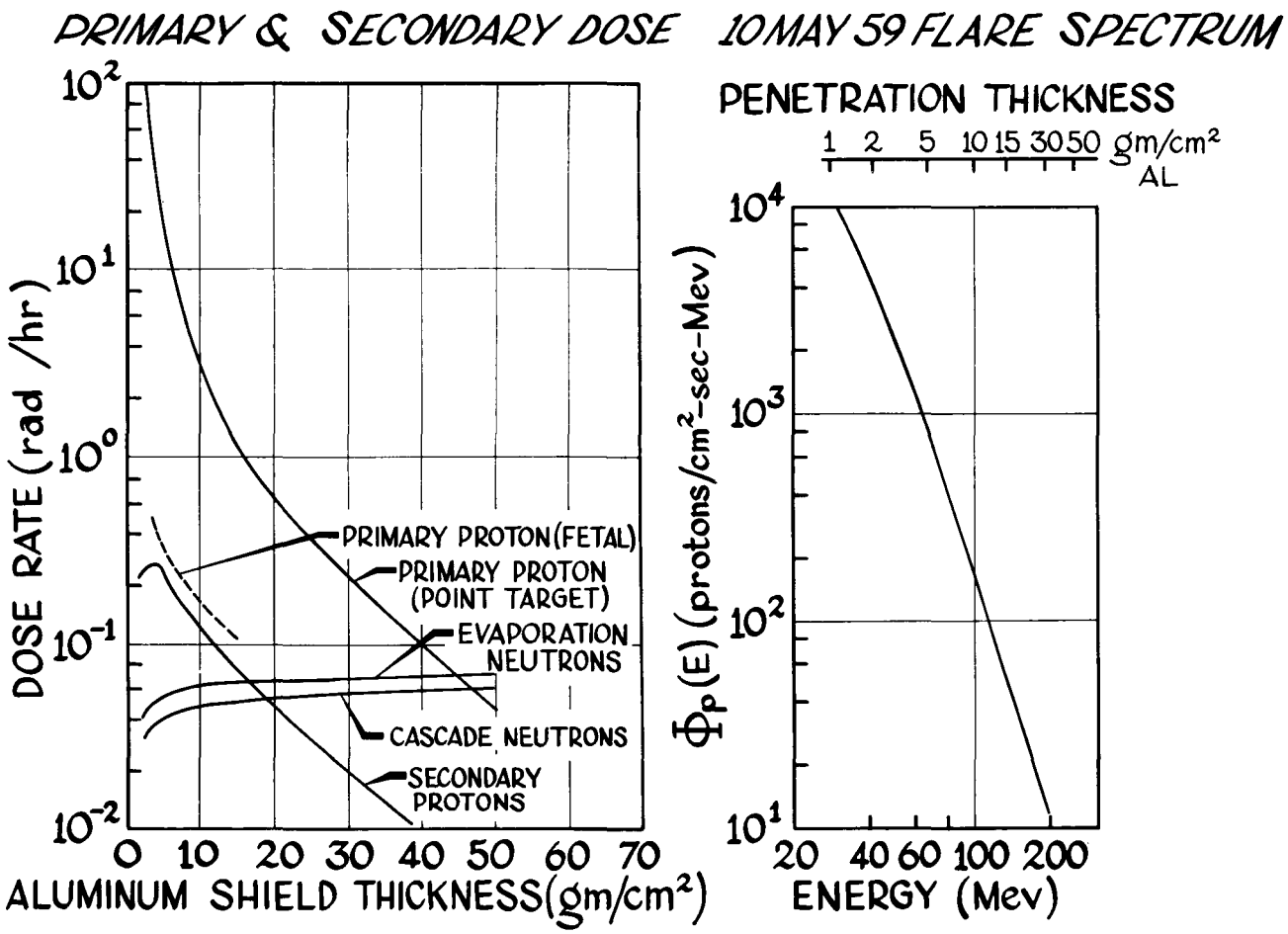

FIGURE 4. CALCULATED DOSE COMPONENTS FOR THE 10 MAY 1959 SOLAR-FLARE PROTON SPECTRUM AS MEASURED 32 HOURS AFTER ONSET (SHIELD GEOMETRY SHOWN IN FIGURE 1)

Thus, it is seen that the greater portion of the secondaries are formed near the outer surface of the shield. This would suggest the need for selection of a low-secondary-producing outer surface of a vehicle.

The order of magnitude difference in the two methods of defining dose for a particular thickness of shielding gives some idea of the problems encountered in defining the radiation dose an astronaut would receive. This difference in primary-proton dose is principally a problem of geometry and the consideration of a finite size target. The geometry of a space capsule can thus be seen to affect greatly the dose received.

The dose-rate curves shown in Fig. 5 for the same shield and the Van Allen inner-belt proton spectrum[7] indicate the secondary contribution is much less significant for this spectrum. This result is primarily due to the much harder inner belt spectrum (Fig. 5). With the hard spectrum, the secondaries are formed rather uniformly across the shield and not just at the surface.

Conclusion

It can be concluded from the results presented that, under the assumption a solar-flare primary-proton hazard exists for manned-space flight, the secondary-particle production in the vehicle skin must be considered. Certainly it should not be inferred that the secondaries will be an all-consuming problem, but rather that they warrant further study and consideration in the selection and arrangement of shielding materials.

---

7. S. C. Freden and R. S. White, Phys. Rev. Letters 3, 9 (1959).

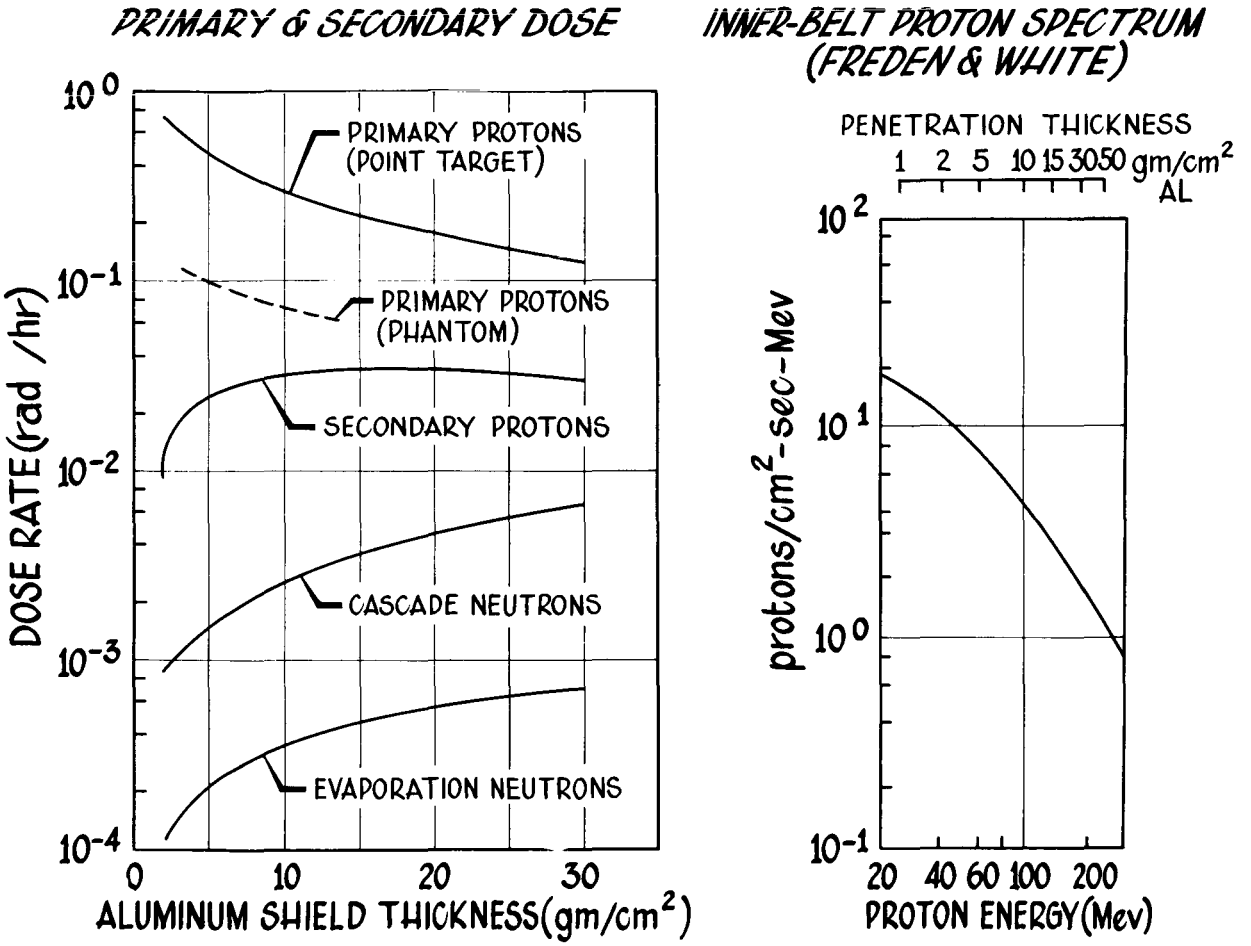

FIGURE 5. CALCULATED DOSE COMPONENTS FOR THE INNER VAN ALLEN BELT PROTON SPECTRUM (SHIELD GEOMETRY SHOWN IN FIGURE 1)

Paper D-6

A SERIES OF MONTE CARLO CODES TO TRANSPORT NUCLEONS THROUGH MATTER

W. E. Kinney, R. R. Coveyou, and C. D. Zerby
Oak Ridge National Laboratory

Abstract 15743

A series of Monte Carlo codes for the IBM-7090 computer has been written to transport nucleons of energy less than 400 Mev through complex configurations composed of four or fewer materials. The nucleons above 50 Mev are treated by a high-energy transport code which uses an intra-nuclear cascade subroutine to compute the production of secondary nucleons. Below 50 Mev, protons are allowed to proceed straight ahead with no nuclear interactions and neutrons are transported by the already existing 05R code. Doses in tissue behind aluminum slabs of varying thickness estimated from 1940 400-Mev source protons and their descendants showed the primary beam dose to be more than a factor of two larger than the dose due to all secondaries.

The interaction of a high-energy nucleon with the material of a radiation shield initiates a complex avalanche of lower energy secondary particles which proceeds through the shield, increasing in population and decreasing in total energy. It is essential to the design of a space vehicle shield to know the behavior of such an avalanche as a function of energy and shield thickness.

In general, a high-energy nuclear interaction produces first of all several secondary nucleons which are due to direct interactions of the incident particle with the nuclear constituents and which have energies ranging from a few Mev to a large fraction of the incident particle energy. There is left a highly excited recoiling nucleus which rids itself of most of its excess energy by evaporating nucleons and heavy particles of relatively low energy of the order of a few Mev.

A calculational method which may include as much detail as desired and which is relatively easy to program for a computer is the Monte Carlo method. It performs an idealized experiment on a system whose properties are completely known with counters of known resolution and 100% efficiency. As with any counting experiment, however, it is subject to counting uncertainties and so a balance must be struck between counting statistics and the cost of a calculation.

The Monte Carlo method has been used in 05R,[1] a code for the IBM computers to treat neutron transport at fission energies and below. At energies greater than fission, two circumstances prevent a high-energy nucleon transport code from being a simple extension of 05R. First, nuclear interactions absorb the parent nucleon and produce a number of secondary nucleons. In 05R a neutron never disappears by absorption at a collision but rather continues with its statistical weight multiplied by the nonabsorption probability at the energy of the collision. Secondly, protons lose energy in flight due to ionization collisions, and account must be taken of this effect. For these reasons, then, the nucleons are transported by a separate code down to some appropriate boundary energy, while below the boundary protons are transported straight ahead and neutrons are treated by 05R. A suitable boundary energy is 50 Mev since that is an energy below which most evaporation particles are emitted, the direct interaction calculational model does not apply, and the proton range is small.

The series of codes will first be described in a general way. The high-energy transport and 05R source preparation codes will next be discussed in some detail. Finally some typical results will be presented and future plans indicated.

A General Description

The series of codes, all written for the IBM-7090, will transport nucleons of energies up to 400 Mev through arbitrary complex configurations containing four or fewer media each of which may be composed of as many as ten isotopes. A very schematic flow chart of the code series is given in Fig. 1. The nucleons are introduced into the system and transported through the 400- to 50-Mev region by the high-energy transport code. When a nucleon escapes from a medium, has a collision, or slows down past 50 Mev, details of the event such as the position and velocity of the nucleon at the time of the event are recorded on a history tape. The only task assigned to the code is the tracing of particle paths in phase space and recording information at significant points along the paths. This method was originally used in 05R to allow freedom in the manner of analyzing the particle trajectories and also to allow saving the data for possible future reanalysis for additional information.

The 05R source preparation routine uses the history tape from the high-energy transport code to do four things: (1) estimate the desired high-energy nucleon distributions, (2) complete the intra-nuclear cascades by evaporating additional nucleons from the highly excited residual nuclei, (3) estimate the distribution of protons below the boundary energy, and (4) prepare a neutron source tape for 05R of neutrons below the boundary energy.

---

1. R. R. Coveyou, J. G. Sullivan, and H. P. Carter, "The 05R Code: A General Purpose Monte Carlo Reactor Code for the IBM-704 Computer," Codes for Reactor Computations, p. 267, International Atomic Energy Agency, Vienna, 1961.

05R transports neutrons below 50 Mev starting them according to the source tape from the source preparation routine. The position of collisions and escapes and the velocities of the neutrons before and after collisions are recorded on the 05R history tape. Finally, the 05R analysis code uses the 05R history tape to estimate the desired distributions of neutrons below 50 Mev.

The High-Energy Transport Code

A general flow chart of the high-energy transport code is given in Fig. 2. The calculation starts by specifying the upper and lower energy limits of the calculation, the atomic number, atomic weight, nuclear density, and effective ionization potential for each isotope of each medium, the desired number of source particles to be treated, a description of the geometry of the problem, and any source information required by the source subroutine.

A range table is then prepared containing values of the range at 101 equally spaced values of the energy between the upper and lower energy limits. An inverse range or energy table containing values of the energy corresponding to 101 equally spaced values of the range from the maximum range to zero range is also computed. Quantities in both tables are assumed to vary linearly between entries.

Flexibility in the geometry is achieved by using Irving's general purpose geometry subroutine.[2] Briefly, it subdivides space into a number of parallelepipeds each of which may be further subdivided by several quadratic surfaces. Given the end points of a line, the subroutine gives the coordinates of the point of intersection of the line with the nearest intervening surface, if any.

The repetitive portion of the code starts by calling the source subroutine to select a source particle. This subroutine is arbitrary and is written to satisfy the requirements of the problem at hand.

A flight distance, d, is next selected from the distribution $\Sigma e^{-\Sigma d}$, where Σ is the total macroscopic geometric cross section.* If the particle being treated is a proton, its energy at the end of the flight is computed by interpolation in the inverse range table. If a proton has crossed the lower energy limit within the distance d or if the particle, proton or neutron, has escaped from the system, the position of the energy or spatial boundary crossing is recorded on the history tape and interest in the particle ceases for this code. If the particle has

---

2. D. Irving, Neutron Physics Division Annual Progress Report for Period Ending September 1, 1962, Oak Ridge National Laboratory Report ORNL-3360, p. 230 (1962).

*The largest proton cross section in the energy range, the n-p cross section at the lower energy limit, plays the role of a geometric cross section for hydrogen.

neither slowed past the energy boundary nor escaped, it suffers a nuclear interaction. The jth nucleus is selected as the target nucleus by the requirement that

$$\sum_{i=1}^{j-1} (\Sigma_i/\Sigma) < R < \sum_{i=1}^{j} (\Sigma_i/\Sigma),$$

where R is a random number uniform on the unit interval, Σ_i is the ith isotope geometric macroscopic cross section and

$$\Sigma = \sum_i \Sigma_i.$$

If the target is not hydrogen, Bertini's cascade subroutine[3] is given the energy and type of incident particle and the atomic weight and number of the target and it returns the number, type, energy, and direction cosines of the cascade products. The subroutine has built into it an energy variation of the interaction cross sections and allows the passage of the incident particle through the nucleus with no interaction whatever. Collisions with hydrogen are treated by storing the n-p and p-p cross sections as functions of energy. A random number R is tested against $[\sigma_{np}(E)/\sigma_{max}]$ or $[\sigma_{pp}(E)/\sigma_{max}]$ for incident neutrons or protons, respectively, where $\sigma(E)$ is a microscopic cross section at energy E and σ_{max} is the pseudo-microscopic geometric cross section for hydrogen. If R is less than the ratio, a scattering takes place as an apparent cascade with two particles emitted. If R is greater than the ratio, the particle continues with no collision.

When there is a nuclear collision, the following details are recorded on the history tape:

1. The type of colliding particle, neutron or proton,
2. the position, energy, and velocity of the colliding particle at its birth,
3. the position of the collision and the energy of the colliding particle at collision,
4. the number, type, energy, and velocity of the product nucleons having energies above the lower energy limit,

---

3. H. W. Bertini, Neutron Physics Division Annual Progress Report for Period Ending September 1, 1961, Oak Ridge National Laboratory Report ORNL-3360, p. 137 (1962).

5. the number, type, energy, and velocity of the product nucleons having energies below the lower energy limit,

6. the atomic number and weight, and the excitation and recoil energies of the residual nucleus.

The data for the product nucleons with energies above the lower energy limit are saved in the fast memory as well as being put on the history tape so that they may be transported in turn. The colliding particle, of course, disappears and the question is asked whether or not all the descendants of the starting source particle with energies above the lower energy limit have been treated. If they have not, the next descendant is chosen as the transported particle, a flight distance is selected, and the entire process is repeated. When all the descendants have been treated, a test is made to see whether or not the desired number of source particles have been considered. If they have not, another source particle is selected by calling the source subroutine and the steps are repeated from point 1 in the flow chart.

The 05R Source Preparation Routine

The functions of the 05R source preparation routine are summarized in Fig. 1 and the flow chart shown in Fig. 3 indicates how they are performed. A record is first read into the memory from the high-energy transport history tape and an arbitrary Analysis I subroutine is called to analyze the particle history and determine its contribution to whatever distributions are being estimated.

If the record was that of a particle which escaped from the system, the code has no further interest in the particle. If the record shows the particle (necessarily a proton) slowed down past the lower energy limit of the high-energy code, the arbitrary "Analysis II" subroutine is called to treat protons below that energy limit. If the record is one of a particle interaction then the code determines whether there are any product nucleons below the lower energy limit and, if there are, treats protons with the "Analysis II" subroutine and writes the neutron data on the 05R source tape. Finally, particles are evaporated from the excited residual nucleus by calling a subroutine version of Dresner's evaporation code[4] with the resulting protons being referred to "Analysis II" and the neutron data being put on the 05R source tape. Provision is also made in the code to record the spatial distribution of evaporated heavy particle energy and final residual nucleus energy.

The 05R Code and Its Analysis Routine

The 05R code has been described elsewhere.[1] For its application here, provision was made to treat nonelastic events by means of an

---

4. L. Dresner, EVAP - A Fortran Program for Calculating the Evaporation of Various Particles from Excited Compound Nuclei, Oak Ridge National Laboratory Report ORNL-CF-61-12-30 (Dec. 19, 1961).

abbreviated version of Dresner's evaporation subroutine which allows only nucleon and alpha particle emission. (It should be pointed out that a present limitation in 05R is the restriction of elastic scattering to a P_1 center-of-mass angular distribution.) 05R writes a history tape similar to that of the high-energy transport code, recording the details of the neutron paths in phase space. The 05R analysis routine has been left entirely open to be written as the needs of a particular problem dictate.

Typical Results

Some results from the series of codes treating 400-Mev protons incident normally on infinite slabs of aluminum are shown in Fig. 4. The partial dose rates in rads per hour per unit incident current in a thin tissue slab behind aluminum shields of varying thickness are plotted as a function of thickness. The flux-to-dose conversion factors were those used by Alsmiller[5] and are shown in Fig. 5. It is of interest to notice that the contribution of all the secondary doses never comes up even to one-half the primary dose contribution. The statistical fluctuations are not indicated but become quite large for the secondary protons at thicknesses larger than 50 cm. The results were obtained from 1940 incident protons and the machine time required was 32 minutes in the high-energy transport code, 18 minutes in the 05R source preparation routine, 18 minutes in 05R, and 20 minutes in the 05R analysis.*

Future Plans

It is planned to raise the upper energy limit of the code above the present 400 Mev as Bertini's intra-nuclear cascade calculation is improved to apply to the higher energies. It will then become necessary to include pions as well as nucleons. 05R is in the process of being changed to accommodate a more general elastic scattering angular distribution than is presently allowed.

---

5. R. G. Alsmiller, Jr., F. S. Alsmiller, and J. E. Murphy, Nucleon-Meson Cascade Calculations: Transverse Shielding for a 45-Gev Electron Accelerator, Part I, Oak Ridge National Laboratory Report ORNL-3289 (1962).

*The machine times go down as (1) the medium thickness decreases, (2) the atomic weights of the elements in the medium decrease thus yielding fewer secondaries in a nuclear interaction, (3) the incident nucleon energy decreases, and (4) the analysis routines simplify. To compute partial doses as a function of depth in 30 cm of tissue using 2000 400-Mev protons required 11 minutes in the high-energy code, 9 minutes in the 05R source preparation routine, 14 minutes in 05R, and 2 minutes in the 05R analysis.

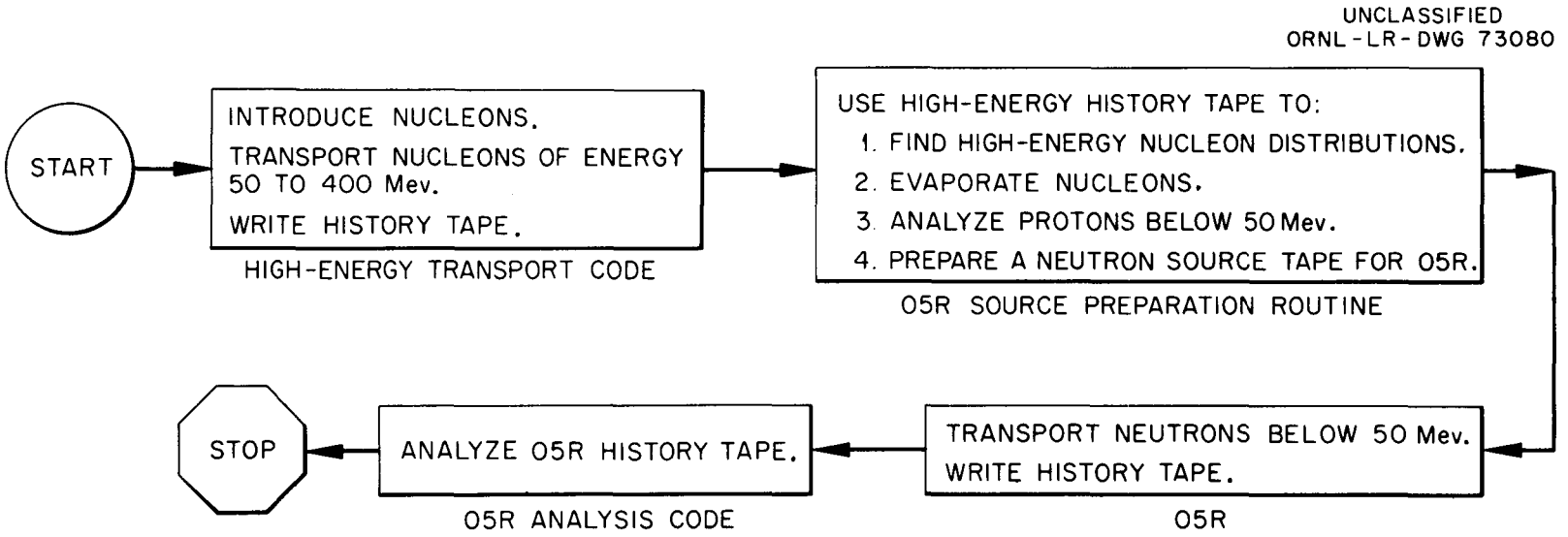

Fig. 1. A Flow Chart for the Series of Nucleon Transport Code.

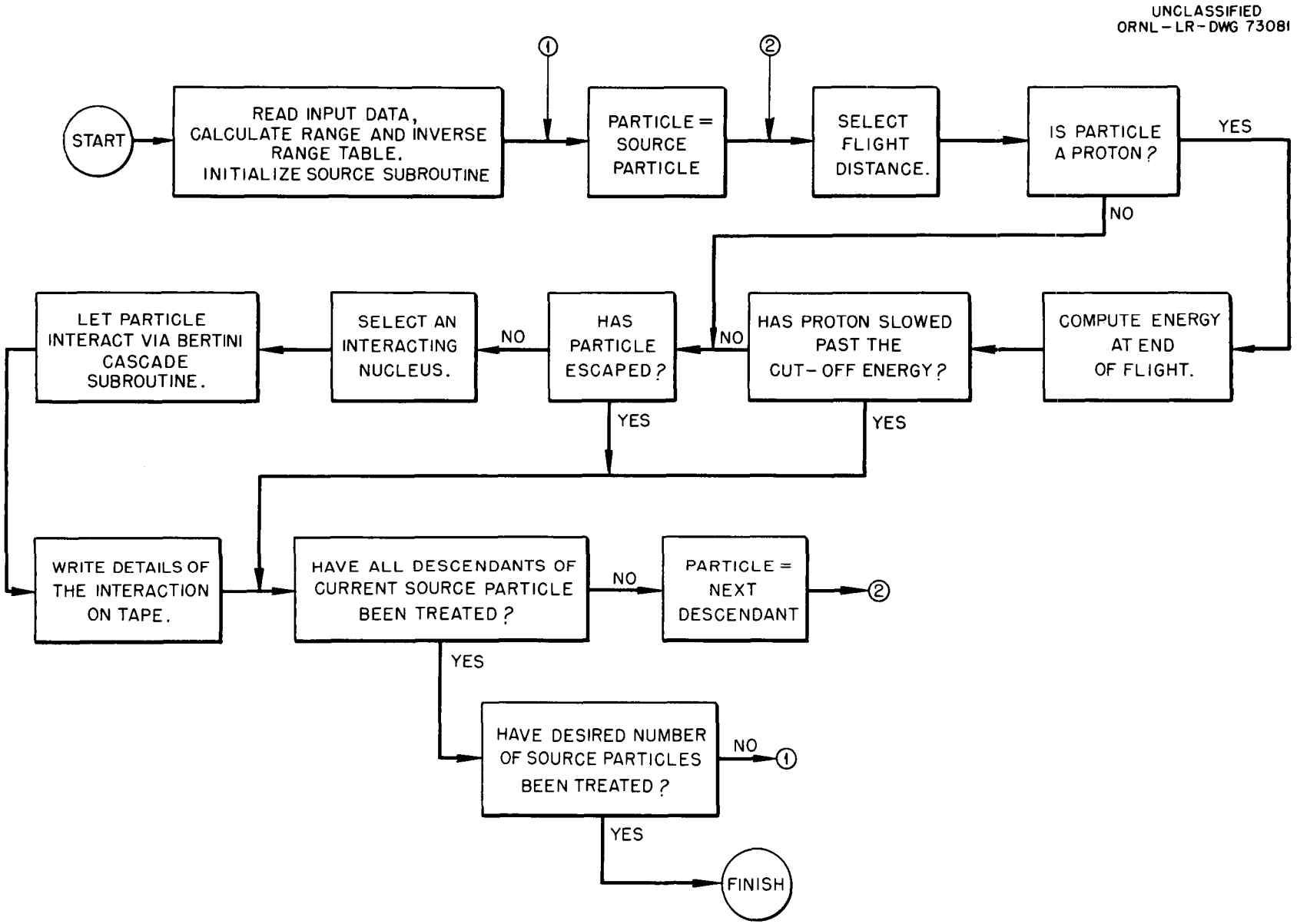

Fig. 2. A Flow Chart for the High-Energy Transport Code.

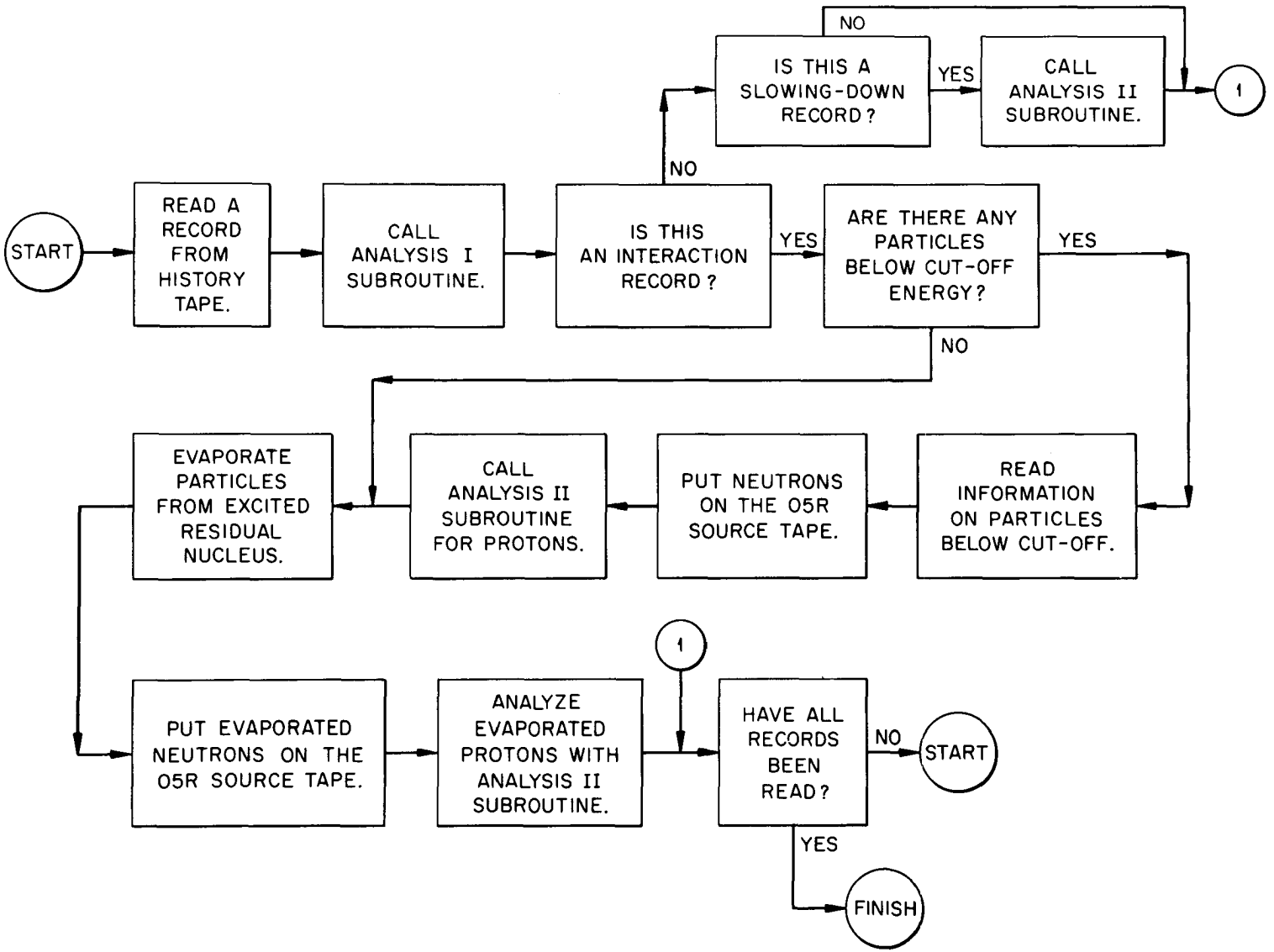

Fig. 3. A Flow Chart of the 05R Source Preparation Routine.

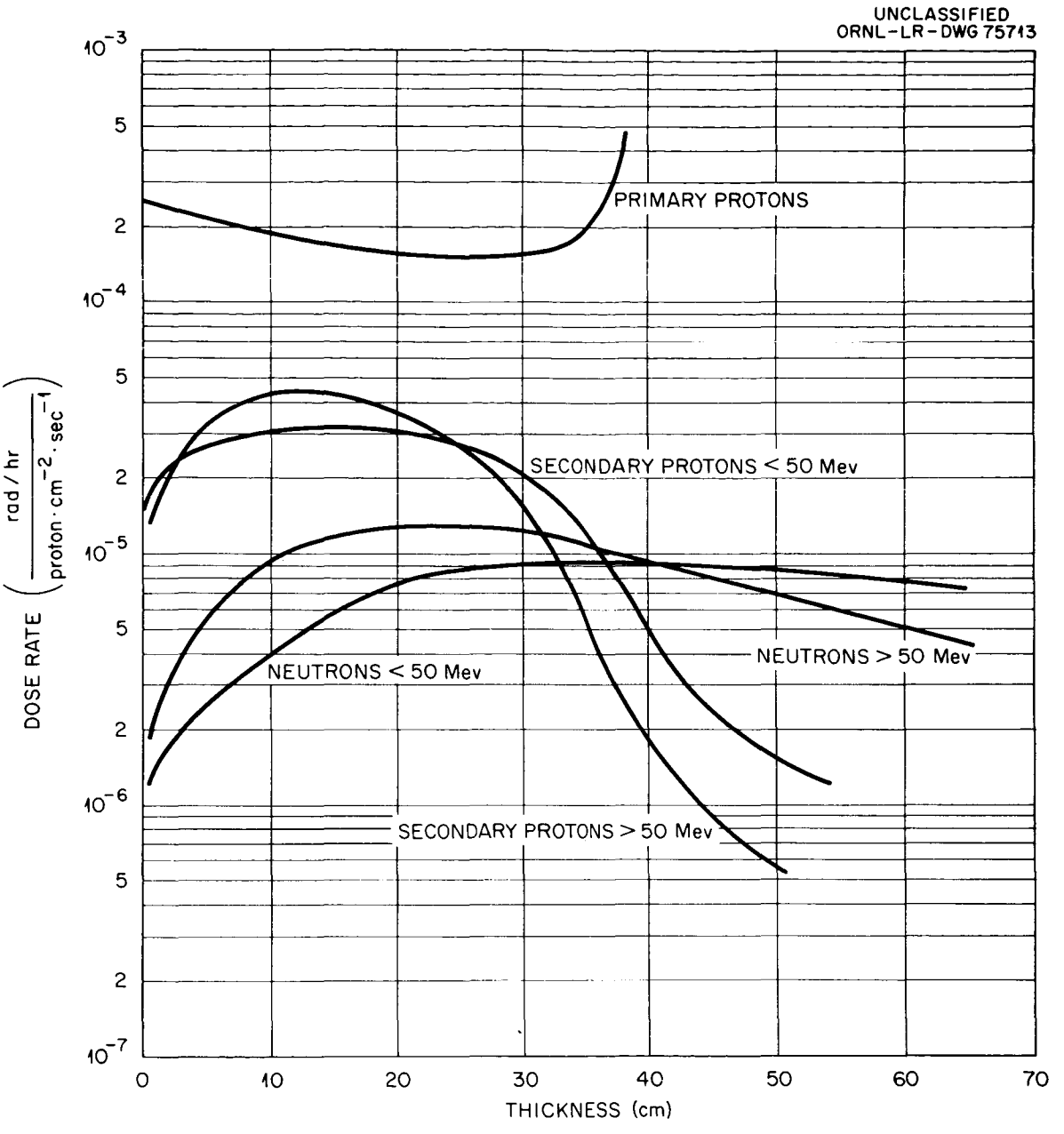

Fig. 4. Partial Tissue Dose Rates Behind Aluminum Slabs vs. Slab Thickness for 400-Mev Incident Protons.

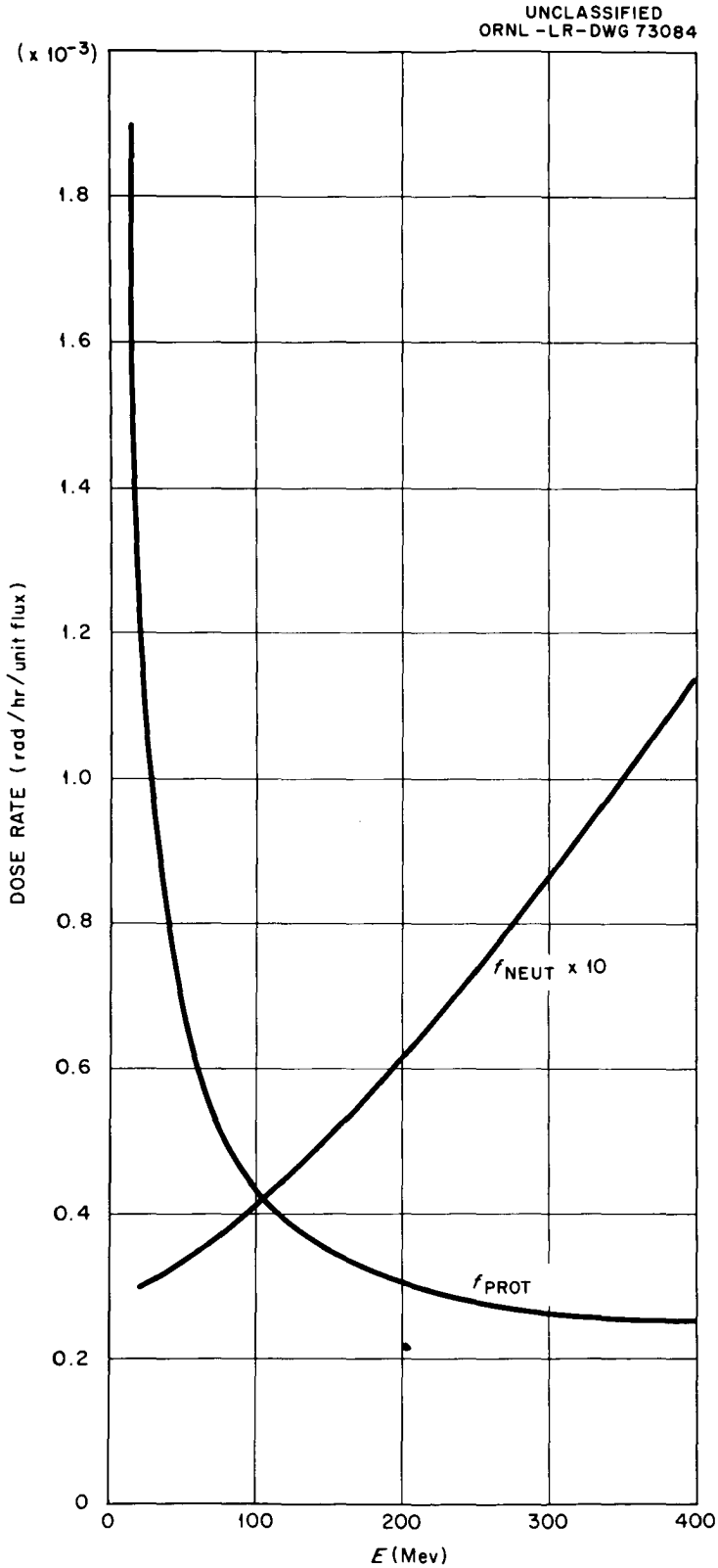

Fig. 5. Neutron and Proton, Flux-to-Dose Conversion Factors vs. Energy.

Paper D-7

THE CALCULATION OF RADIATION DOSE IN TISSUE FROM HIGH-ENERGY PROTONS*

J. E. Turner, J. L. Feuerbacher, C. D. Zerby, W. E. Kinney,
J. Neufeld, W. S. Snyder, and R. L. Woodyard
Health Physics Division and Neutron Physics Division
Oak Ridge National Laboratory**
Oak Ridge, Tennessee

15144

Abstract

The Oak Ridge National Laboratory is developing Monte-Carlo calculations for the paths and interactions of particles of various kinds and energies and for secondary particles they produce when incident on phantoms of a given composition, i.e., for materials and combinations of materials of given atomic number Z and mass number A. These calculations provide histories of the particles involved, as described in the preceding paper. For the estimation of dose from high-energy radiation, particle histories have been analyzed in a tissue slab of thickness 30 cm from normally incident protons with energies of 100, 150, 200, 250, 300, 350, and 400 Mev. Calculations at still higher energies are in progress. The results of the calculation of rad and rem dose as a function of depth in the tissue slab are presented. Also shown at each incident energy is the relative contribution of recoil nuclei (and other particles with mass number $A > 1$) to the total absorbed energy per unit mass. For the purpose of estimating rem dose, the recommendations of the National Committee on Radiation Protection and Measurements (NCRP) published in NBS Handbook 59 were used. For values of linear energy transfer (LET) greater than those considered in Handbook 59 (viz., for LET > 1750 Mev/cm) an RBE (relative biological effectiveness) value of 20 was used. A method for analyzing particle histories is utilized which will later permit computations of rem dose curves under very general assumptions about the dependence of RBE on LET. The rem dose as presented here uses the estimation of LET as formulated by Neufeld and Snyder and is calculated using their methods.

---

* Supported by National Aeronautics and Space Administration.

** Operated by Union Carbide Corporation for the U. S. Atomic Energy Commission.

This paper presents results which are available at this time on the calculation of radiation dose due to high-energy protons incident on tissue. The highest incident proton energy considered here is 400 Mev, which is the maximum energy at which the presence of pions is not being considered. Calculations up to several Bev incident nucleon energy are in progress. Assuming the charge independence of nuclear forces, one can apply much of the data from nuclear interactions discussed below for incident protons directly to incident neutrons of the same energies. The essential difference between the penetration of high-energy protons and high-energy neutrons through matter arises through the circumstance that protons lose energy by ionization as well as in nuclear interactions.

The calculations of the penetration of high-energy incident protons and the secondary particles to which they give rise are described elsewhere.[1,2] The information from these studies from which energy deposition per unit mass in a medium can be calculated is summarized by the example shown in Fig. 1. The figure represents the history of one incident proton and secondaries, derived on the basis of the above mentioned Monte-Carlo calculations. The line (1) represents the path of a proton incident normally at a point P on a tissue slab 30 cm thick having infinite extension in space in directions perpendicular to the velocity vector of the incident proton. (The distribution of dose in such a slab will approximate the expected dose distribution in man; calculations will be modified later to treat other geometries.) The incident proton (1) penetrates the slab to some point A at which a nuclear interaction takes place. (Depending upon the incident proton energy, a certain fraction of incident protons will not experience a nuclear interaction.) In the example in Fig. 1 the interaction between the incident proton (1) and a nucleus in the tissue slab gives rise to a proton (2) and two neutrons (3) and (4); the track (5) represents the recoiling residual nucleus following the nuclear interaction. Proton (2) is stopped in the slab, neutron (3) escapes, and neutron (4) interacts at B with another nucleus, giving rise to a proton (6), a neutron (7), and another recoiling nucleus (8). Proton (6) comes to rest; neutron (7) is elastically scattered at C and subsequently escapes from the slab. For each nuclear track shown in the figure, the following information is given:

type of particle,
position coordinates of particle at birth,
energy at birth,
direction cosines of velocity vector at birth,
position coordinates of particle at next interaction.

---

1. H. W. Bertini, "Monte-Carlo Calculations on Intranuclear Cascades," this Symposium.

2. W. E. Kinney, R. R. Coveyou, and C. D. Zerby, "A Series of Monte-Carlo Computer Codes to Compute the Transport of Nucleons Through Matter," this Symposium.

The nuclei remaining after the cascade and evaporation processes are identified, and the initial kinetic energy of recoil and the residual excitation energy of each nucleus are given. It should be pointed out that Fig. 1 schematically represents particle trajectories which, of course, are calculated in three dimensions.

For the calculation of radiation dose in the tissue slab, the particle histories for a number of incident protons are analyzed. For analysis, the slab is divided into a number of sub-slabs parallel to the slab faces, and the total energy deposited in each sub-slab from all events involving the incident protons and their products is first calculated. By symmetry, the total energy deposited in any sub-slab from one incident particle at P is equal to the energy deposited per unit volume in that sub-slab from a uniform, normally incident broad proton beam having unit flux. Consequently, the calculation of the total energy deposited in a given sub-slab from a number of normally incident protons at the single point P on the slab boundary provides directly the energy absorbed per unit mass, or rad dose, in that sub-slab from a broad beam of normally incident protons.

Results of the calculation of rad dose as a function of depth in tissue slabs for incident protons of energies 100, 150, 200, 250, 300, 350, and 400 Mev are presented in Figs. 2-8. The figures show both the total rad dose and the rad dose due to heavy particles (i.e., particles with mass number $A \geq 2$, which arise as recoil nuclei and as nuclear evaporation products.) At each energy 1000 incident protons were used, and the energy deposition was calculated in each of 150 successive sub-slabs of thickness 2 mm. The total rad dose is generally quite uniform throughout the slabs in which the primary protons do not come to rest (Figs. 5-8). For the energies 200 Mev and below, protons coming to rest show the familiar Bragg peak.* At depths beyond the peak there is a small dose arising from interactions of secondary neutrons with nuclei of the slab. This dose was calculated and found to be about two orders of magnitude less than the dose at depths on the other side of the Bragg peak. Accordingly, in Figs. 2-4 it should be realized that there is a small dose beyond the straight-ahead depth of penetration of primary protons which come to rest in the slab.

While the rad dose is of interest, presumably the important quantity for radiation protection purposes is the rem dose, which considers explicitly the relative biological effectiveness (RBE) of the various components contributing to the absorbed energy per unit mass, or rad dose. The rem dose estimations for each incident proton energy are also shown in Figs. 2-8. Presently available values of RBE are based upon the rate of linear energy transfer (LET) of radiation in tissue and apply to low-level chronic exposure to radiation. The current recommendations of the National Committee on Radiation Protection and Measurements (NCRP) for exposures under these conditions are incorporated

*A smoothing routine was used in the calculation, which produces the smooth variation of dose shown over the otherwise discontinuous analytic expression for dose at the end of the proton range.

in Fig. 9.[3] The highest value of LET for which recommendations are given is 1750 Mev/cm path length. For the rem dose estimations the value RBE = 20 was used for particles having a LET greater than this, corresponding to the dashed portion of the curve shown in Fig. 9. All of the recoil nuclei in the present calculation have LET values greater than 1750 Mev/cm.[4]

Inasmuch as the LET for all recoiling nuclei (except hydrogen) arising in tissue exceeds the maximum value considered by the NCRP, an estimation of rem dose even within the framework of the existing recommendations for RBE for chronic, low level exposure cannot be completely made. From the results presented in Figs. 2-8 one can make quick estimates of rem dose from rad dose by considering the rem dose as due, approximately, to two distinct groups: (1) protons and (2) heavy particles (i.e., all particles with $A \geq 2$). For the first group, the RBE is essentially unity. For example, with reference to Fig. 9, the LET for protons of energies greater than about 20 Mev is less than 40 Mev/cm, and so, to a first approximation, most of the total proton dose can be considered to have RBE = 1. (In Figs. 2-8 the total proton dose is represented by the difference of the total rad dose and heavy particle dose curves.) For this group, then, the rad and rem doses are approximately numerically the same. In the second group, a large fraction of the energy deposited comes from recoiling nuclei, for which RBE = 20 has been used at all energies. For this group, then, the rem dose is numerically approximately 20 times the rad dose. Thus, for an order of magnitude estimate, one has

$$\text{Rem Dose} \cong (\text{Proton Rad Dose}) \times 1 + (\text{Heavy Particle Rad Dose}) \times 20.$$

One sees in Figs. 2-8 that this approximate relationship is borne out.

The question of appropriate RBE values to use for exposure conditions anticipated in space missions remains an outstanding problem in space dosimetry at the present time.[5] The problem arises both through (1) the different conditions of exposure encountered in space missions

---

3. Taken from Table 3, p. 48, Permissible Dose from External Sources of Ionizing Radiation, Recommendations of the National Committee on Radiation Protection and Measurements, National Bureau of Standards Handbook 59, Washington, D. C., 1954.

4. J. Neufeld and W. S. Snyder, "Estimates of Energy Dissipation by Heavy Charged Particles in Tissue," Selected Topics in Radiation Dosimetry, pp 35-44, Bruder Rosenbaum, Vienna, 1961.

5. W. S. Snyder, "Some Data on the Relationship of RBE and LET," this Symposium.

as opposed to the exposure conditions previously dealt with and through (2) the relatively large fraction of the dose deposited at LET values which are orders of magnitude larger than those encountered previously in most work in radiation dosimetry. An investigation of these problems will be made from an analysis of the LET spectrum based upon accumulating biological evidence. The incorporation of RBE in the dose codes has been made in a way which will permit a wide range of RBE values to be considered without repeating the entire calculation. The method employs a polynomial expansion of expressions for rem dose in powers of energy, the coefficients of the polynomial corresponding to a particular choice of RBE values.

Acknowledgments

The contributions of H. A. Wright and K. Katoh in various phases of the dose calculations are gratefully acknowledged. The present calculations have made use of several previous calculations which were constructed through the efforts of many people. In particular, we would like to recognize the contributions of R. R. Coveyou, H. W. Bertini, and L. Dresner..

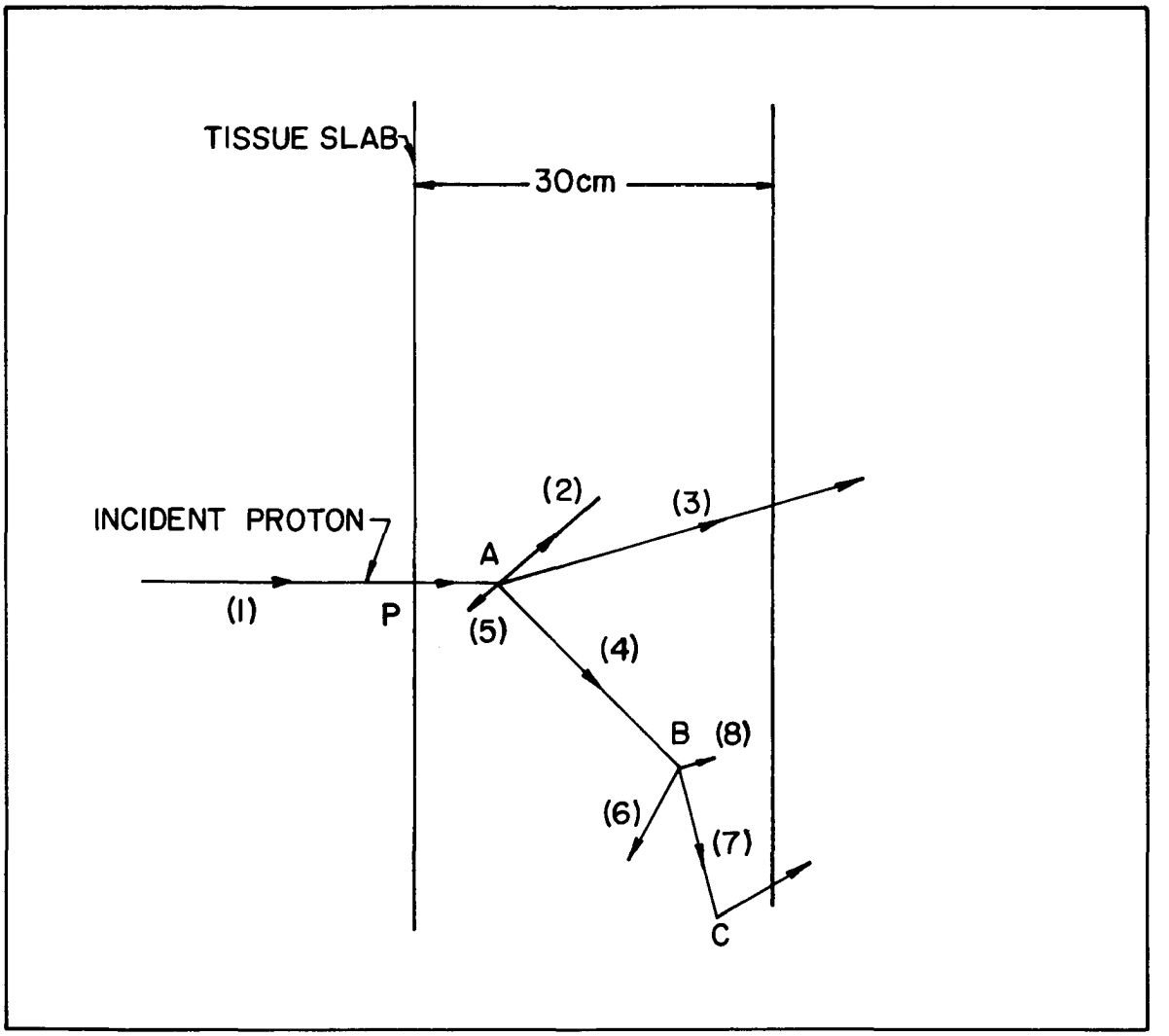

FIG. 1 SCHEMATIC REPRESENTATION OF TYPICAL PRIMARY AND SECONDARY PARTICLE TRAJECTORIES

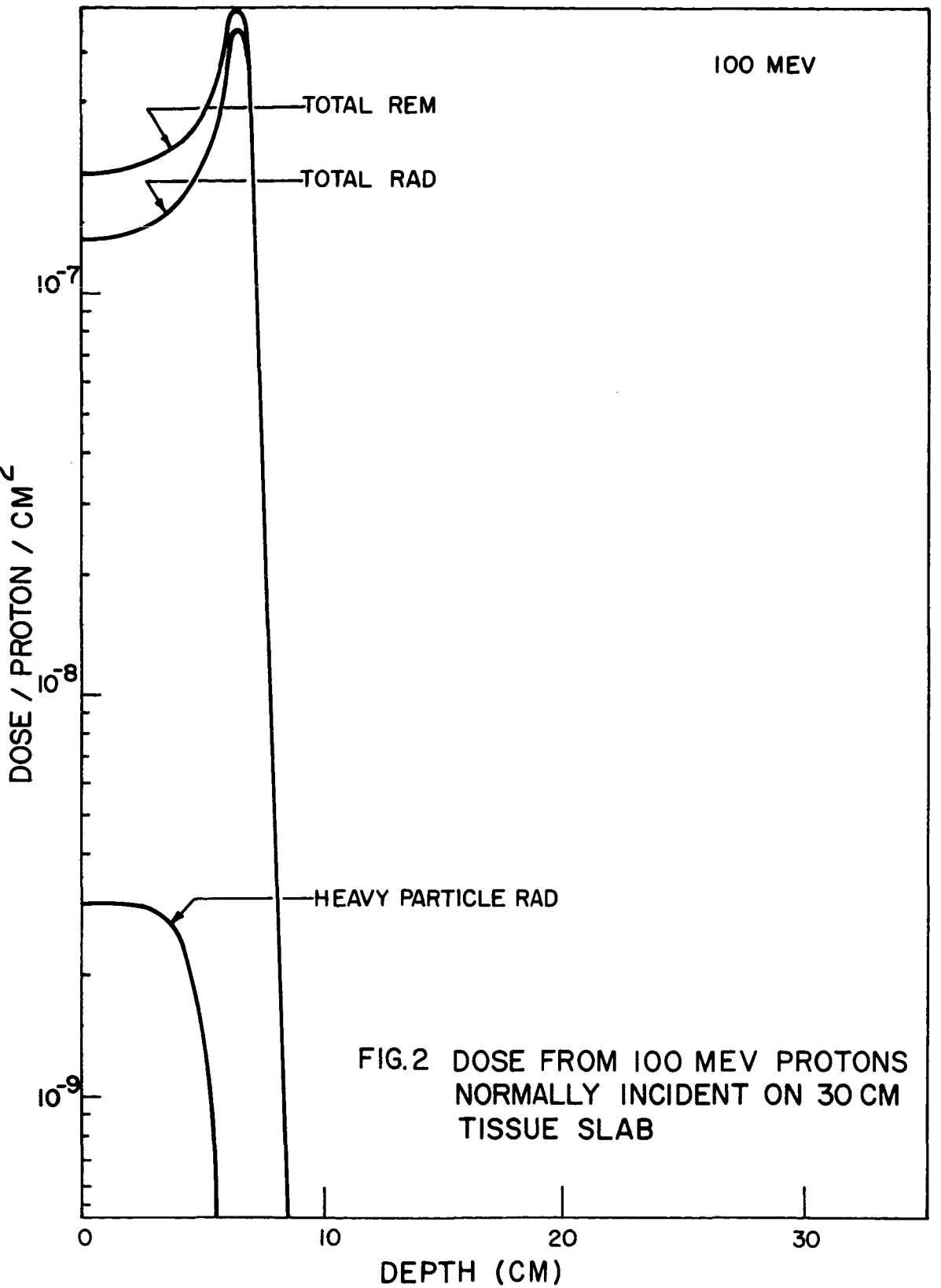

FIG. 2 DOSE FROM 100 MEV PROTONS NORMALLY INCIDENT ON 30 CM TISSUE SLAB

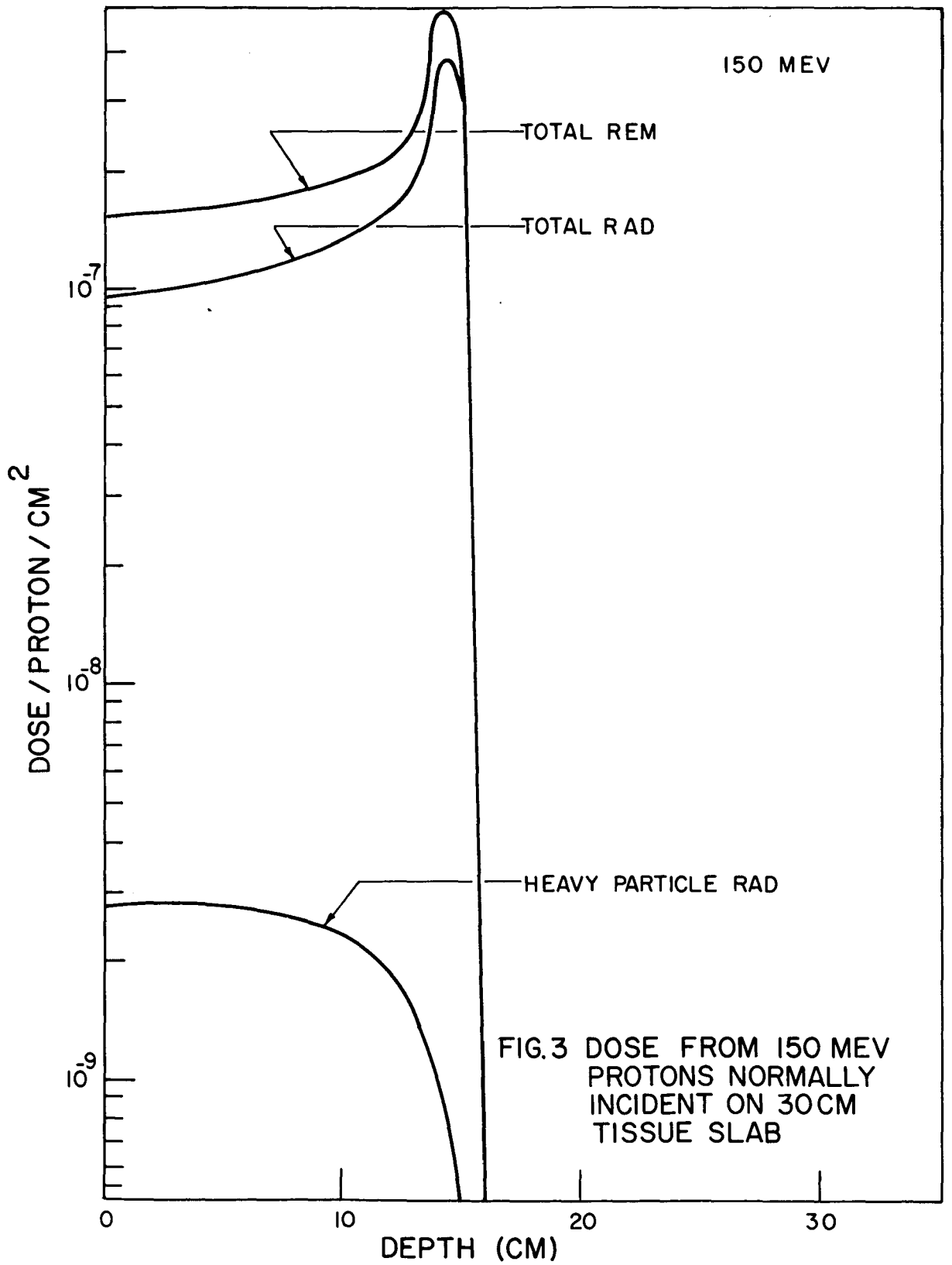

FIG. 3 DOSE FROM 150 MEV PROTONS NORMALLY INCIDENT ON 30 CM TISSUE SLAB

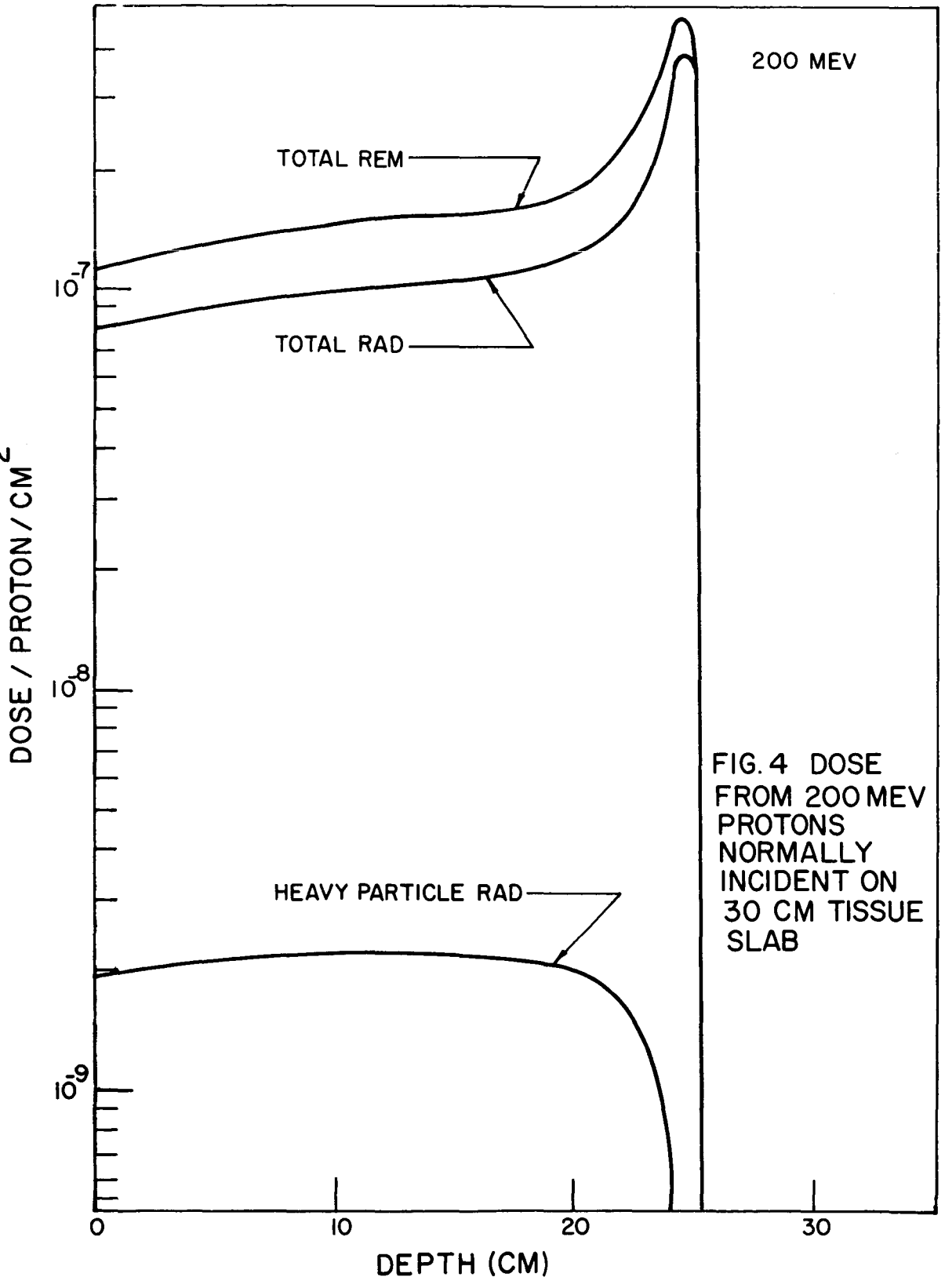

FIG. 4 DOSE FROM 200 MEV PROTONS NORMALLY INCIDENT ON 30 CM TISSUE SLAB

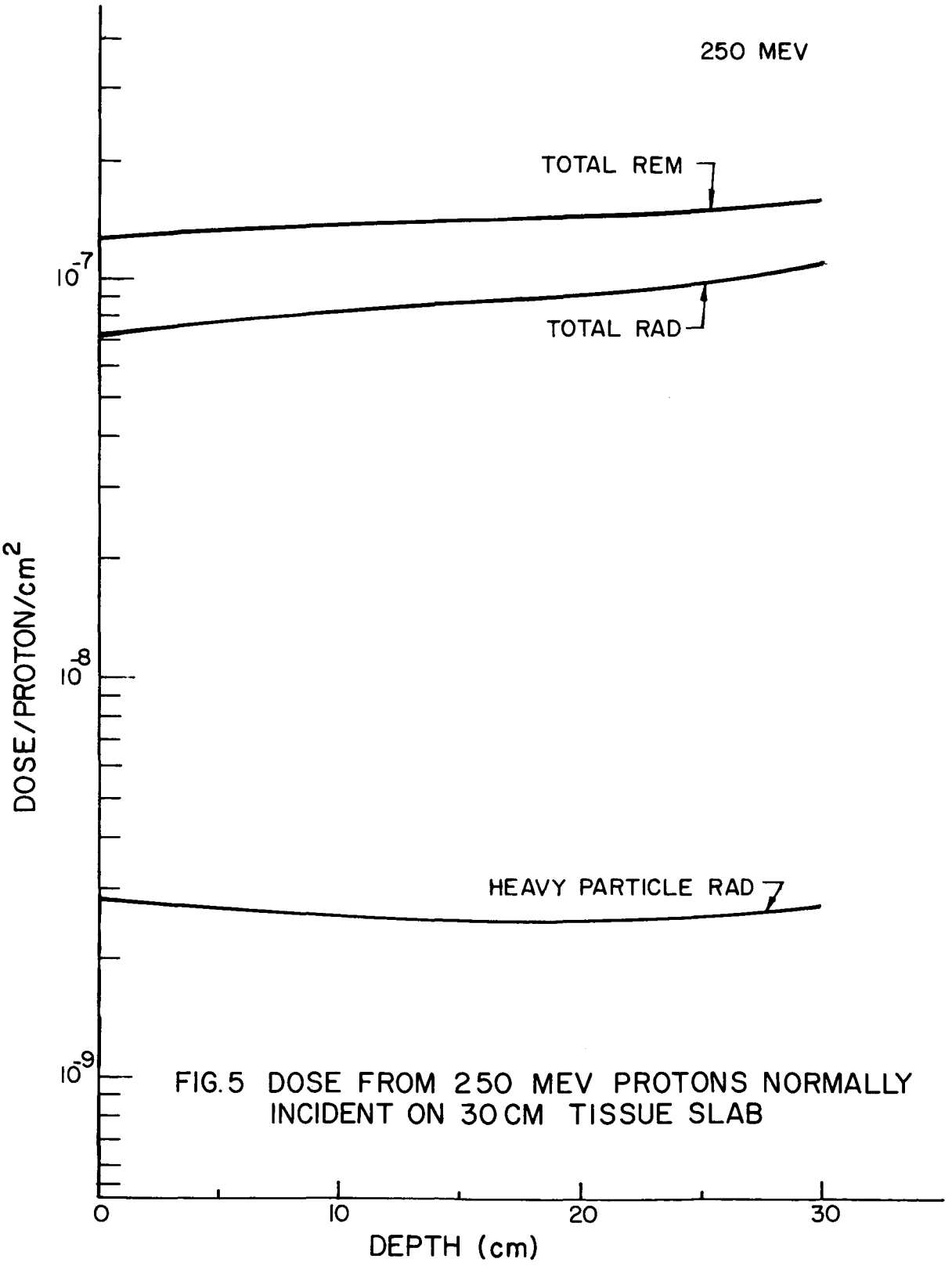

FIG. 5 DOSE FROM 250 MEV PROTONS NORMALLY INCIDENT ON 30 CM TISSUE SLAB

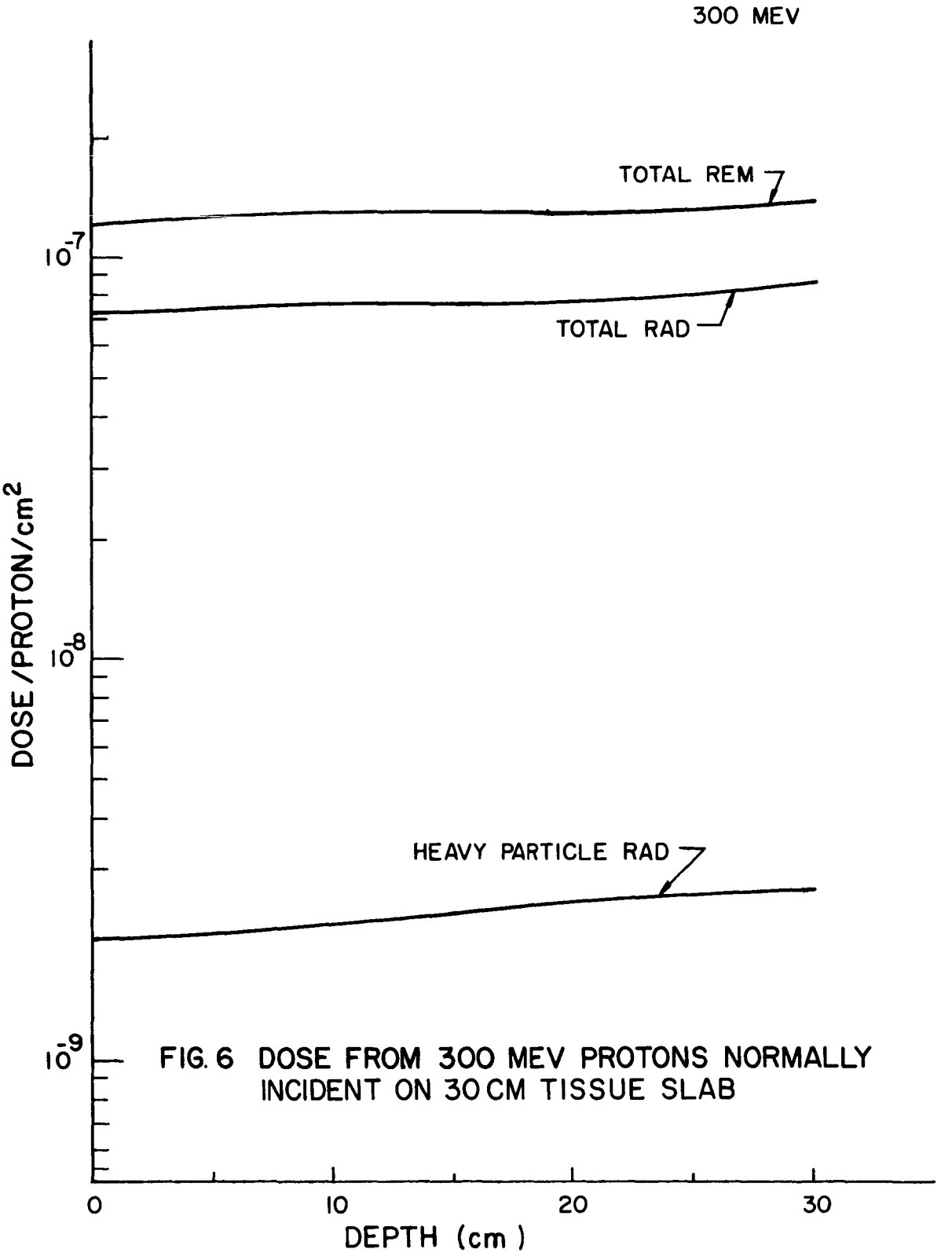

FIG. 6 DOSE FROM 300 MEV PROTONS NORMALLY INCIDENT ON 30 CM TISSUE SLAB

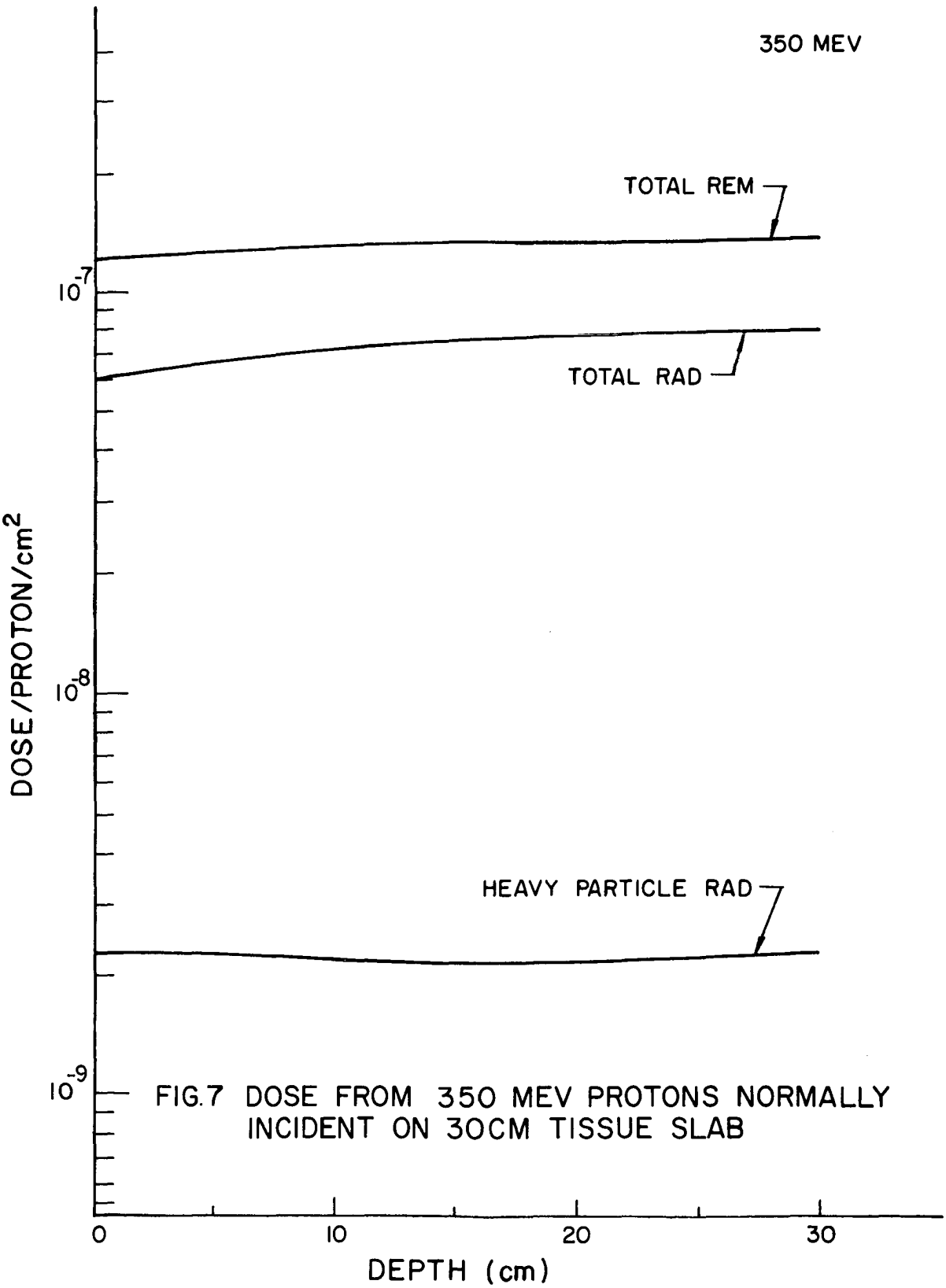

FIG. 7 DOSE FROM 350 MEV PROTONS NORMALLY INCIDENT ON 30CM TISSUE SLAB

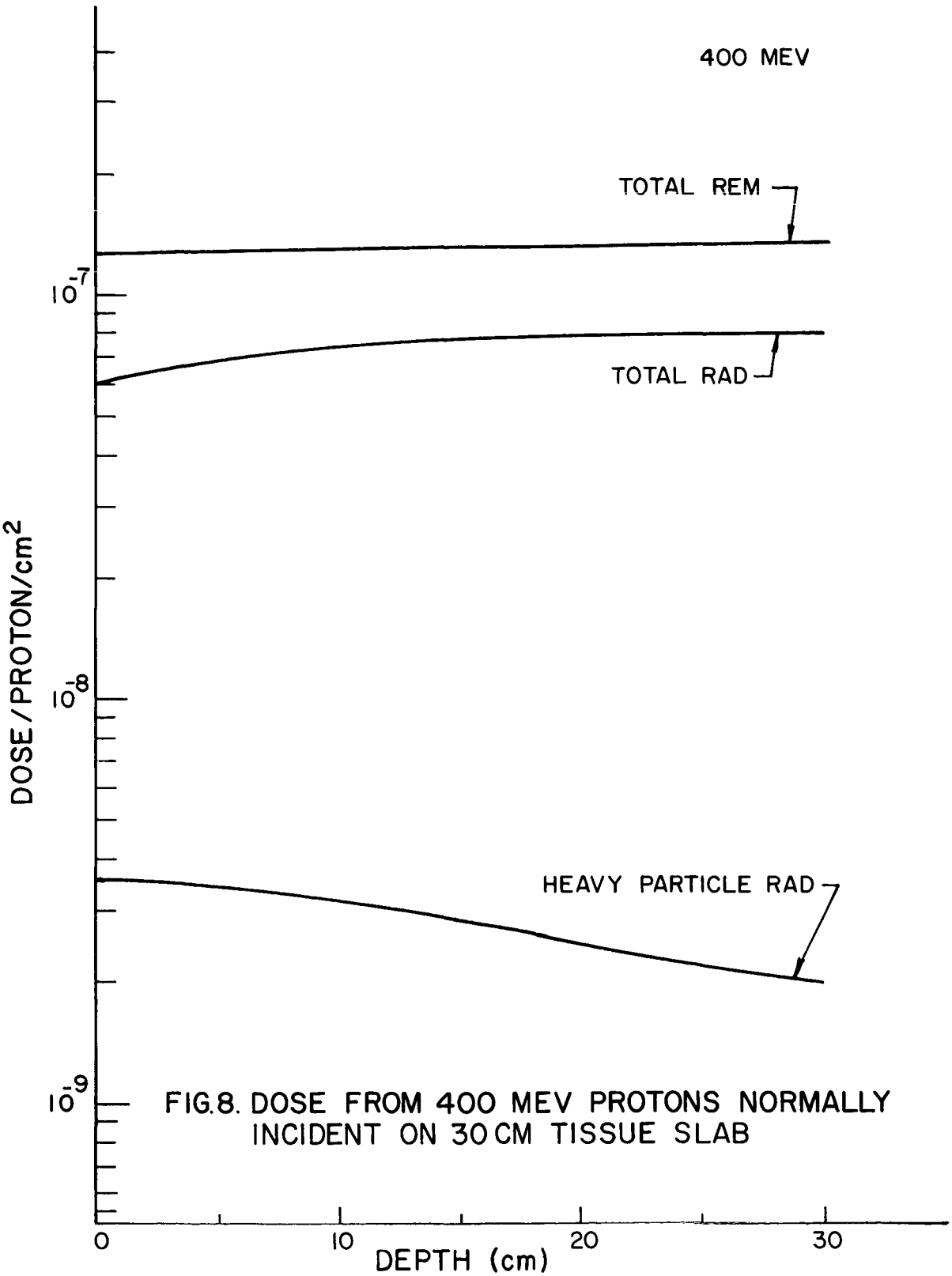

FIG. 8. DOSE FROM 400 MEV PROTONS NORMALLY INCIDENT ON 30 CM TISSUE SLAB

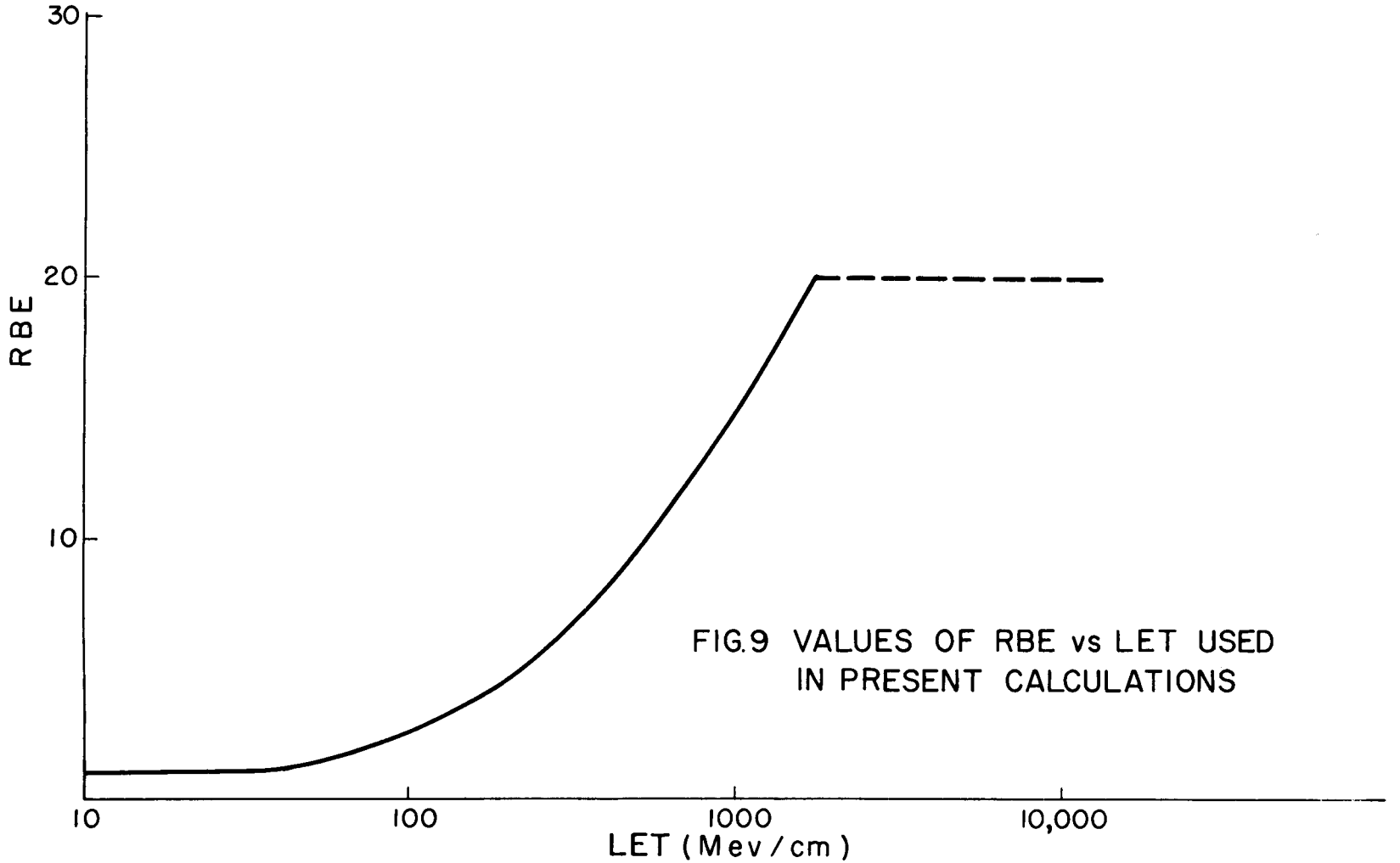

FIG.9 VALUES OF RBE vs LET USED IN PRESENT CALCULATIONS

15145

Paper D-8

SPACE PROTON DOSES AT POINTS WITHIN THE HUMAN BODY

David L. Dye
The Boeing Company

15145 cm

Abstract

Distribution patterns of absorbed dose influence the radiation response of a mammalian system, because of differing radiosensitivities of different organ systems. In a man exposed to space radiations; e.g., an astronaut, body self-shielding produces nonuniform dose distributions which depend upon external shielding configurations and the incident radiation parameters. In this paper are presented the doses at twelve specific points in the body of a seated man exposed to isotropic incident space protons, where the man is inside various thicknesses of external vehicle shell shielding. The body points, selected for their radiobiological interest, are in (or on) sternum, chest skin, femur, spinal column, eye, central gut, and a series at various lateral depths on the waist. The protons reaching these specific points from all directions traverse tissue thicknesses that were determined from scale drawings of a statistically standard man (75-percentile). The proton penetration, secondary radiation generation, and total dose delivered to each specific body point was calculated using an IBM (Fortran) computer code.

For feasibly thin aluminum shields and typical spectra, the secondary dose is a small fraction of the total proton dose for most of the body points. The doses at a given point vary with both spectral shape and external shielding, as well as point to point. Power law spectra, $E^{-n}dE$, normalized to one proton/cm^2-sec of $E > 100$ Mev, with $2 \leq n \leq 5$, and the Freden and White trapped proton spectrum, were considered. Resulting dose values for n = 3 to 4 (a

typical solar flare-associated proton spectrum) vary from about 10^{-4} to 10^{-8} rad/proton/cm^2 > 100 Mev for the various body points for a 1 gm/cm^2 external shield, and from 10^{-7} to 10^{-8} rad/proton/cm^2 > 100 Mev for a 10 gm/cm^2 external shield.

Introduction

Dose distribution patterns in a biological system have an important influence on the radiation effects in that system. In the human body exposed to a typical space proton environment, there is some self-shielding that reduces the body interior doses with respect to the skin doses and thus affords some measure of radiation protection. Previous studies have been made of the depth-dose patterns resulting from several simple proton spectra impinging on slab shields and penetrating into tissue slabs.[1,2] These early results show the dependence of depth-dose on spectral shape and exterior shielding, but the simplified geometry used leaves one still wondering just what the absorbed doses are inside a biologically interesting shape such as the human body.

The earlier results were calculated by means of an IBM 7090 computer code.[2] A slightly modified version of this same program was used in part of the present calculation. A principal feature of the present program is that it calculates a series of dose values due to penetrating protons in a set of slab geometries, then sums these dose values, weighted as necessary by the fractional solid angles subtended by each slab problem, to obtain the proper total dose at an interior point. For the work here reported, the seated human (75-percentile male) body was used, with various spherical shells around it. Doses were computed at a number of body-interior points: femur, sternum,

---

1. D. L. Dye and J. C. Noyes, Biological Shielding for Radiation Belt Particles, J. Astron. Sci. VII, 64 (1959).

2. D. L. Dye and G. Butler, Computer Calculations of Doses from Protons in Space, J. Astron. Sci. IX, 63-71 (1962).

backbone, eye lens, central gut, and at waist level.[3] The results of these computations are tabulated here and show a dependence on spectral and shielding parameters similar to the earlier results. However, these values now represent useful doses (per isotropic incident proton/cm^2 of E > 100 Mev) at the specific body points. If the incident isotropic flux and spectrum is known exactly--an unlikely eventuality--then the proton ionization dose at any of these points may be known accurately.

The dose due to secondaries generated in nuclear interactions has been estimated variously [4,5] but it is small for thin shields. A computer program has been developed to determine the tissue doses due to the secondaries generated by the incident primary protons in the shielding material. The secondary component includes inelastic scattering-produced gamma rays, low-energy evaporation nucleons, and high-energy knock-on nucleons. Part of the tertiary neutron and gamma effects were included, by adding the secondary proton spectrum to the primary at every point, so the total was used in interior sublayers. The results justify the usual procedure of neglecting the secondaries from incident space protons of typical energy spectra.

The Computer Programs

Primary Dose Code

Spectral Modification. In the present version of the primary proton dose calculation, an incident proton spectrum is degraded through shielding layers according to formulas 1 to 3 of Ref. 2. However, instead of interpolating between tabulated range-energy points, as was

---

3. D. L. Dye, A Geometrical Analysis of the Seated Human Body for Use in Radiation Dosage Calculations, The Boeing Company, D2-90107, (1962).

4. R. I. Allen, et al., Shielding Problems in Manned Space Vehicles, Lockheed Aircraft Corp., NT-140, (1961).

5. R. K. Wilson, et al., A Study of Space Radiation Shielding Problems for Manned Vehicles, General Dynamics Corp., FZK-144 (1962).

done in Ref. 2, we have made a least squares fit to those tables[6] to obtain analytic expressions for proton range as a function of energy and energy as a function of range. Thus, the proton range function is defined empirically to be:

$$\text{RNGEF(E)} = \exp(\text{A1} + \text{A2} \log \text{E} + \text{A3} \log^2 \text{E}), \tag{1}$$

and the proton energy function is (by quadratic inversion):

$$\text{ENGYF(R)} = \exp\left[\frac{-\text{A2} + \sqrt{\text{A2}^2 - 4\text{A3}(\text{A1} - \log \text{E})}}{2\text{A3}}\right], \tag{2}$$

where E is proton energy, R is proton range, and the A's are coefficients of the fit which depend on the shielding material. Equation 1 was chosen as the form to which to fit by least squares the range-energy tables because range is approximately a power law function of energy; that is,

$$R = kE^n, \tag{3}$$

with k and n slowly varying functions of E over the range of interest, $1 \lesssim E \lesssim 1{,}000$ Mev.

Use of an analytic range function provides simply for the solution to the spectral modification with penetration into shielding material. It also allows one readily to compute the output spectrum on a specified energy grid, so that spectra are easily added at an interior point.

If a monodirectional proton spectrum P(E)dE is incident on a shield layer of thickness X, then the penetrating spectrum P'(E')dE' may be computed by means of the recipe:

$$\text{E}' = \text{ENGYF(RNGEF(E)} - \text{X}), \tag{4}$$

$$\text{P}'(\text{E}')\text{dE}' = \text{P(E)dE}(\text{dE}'/\text{dE}), \tag{5}$$

and

$$(\text{dE}'/\text{dE}) = \frac{(\text{dR/dE})_{\text{E}}}{(\text{dR/dE})_{\text{E}'}} \tag{6}$$

---

6. M. Rich and R. Madey, Range Energy Tables, UCRL-2301 (1954)

where the subscripts mean that the derivative is evaluated at E and E', respectively.

In the present IBM code, an output energy grid E'(K) is specified, so the E(K) values needed to obtain it are computed by Eq. 4. Then the incident specified spectrum P(K) is rearrayed, by interpolation, onto this input energy grid. Then the "energy spread factor", determined by Eq. 6, is multiplied into the spectrum P to obtain the output spectrum P' arrayed on the specified output energy grid E'(K), according to Eq. 5.

This spectrum degrading process is repeated for each layer of shielding material until the point of interest for dose calculation is reached. The actual dose computation is done as it was earlier in versions of this code; namely, by:

$$\text{DOSE} = \int_{1}^{1{,}000\ \text{Mev}} P'(E')\ \text{DOSF}(E')\ dE' \qquad (7)$$

where DOSF(E) is proportional to dE/dX for tissue.

Vehicle Analysis. It is desired to compute a dose absorbed by some material such as tissue, within a complicated arbitrary shielding configuration such as a space vehicle or a human body, due to an arbitrary angular distribution of incident protons. The way this is done may be seen by referring to Fig. 1. Briefly, the three-dimensional material configuration is analyzed in a large number of one-dimensional problems, so that the code just described can solve the three-dimensional problems.

Looking outward from an interior point P in all directions, one sees various solid angular regions $\Delta\Omega$, over each of which the shielding layers are approximately the same. If the radiation reaching P is direct, or primary and unscattered, then we may approximate the dose at P by the sum:

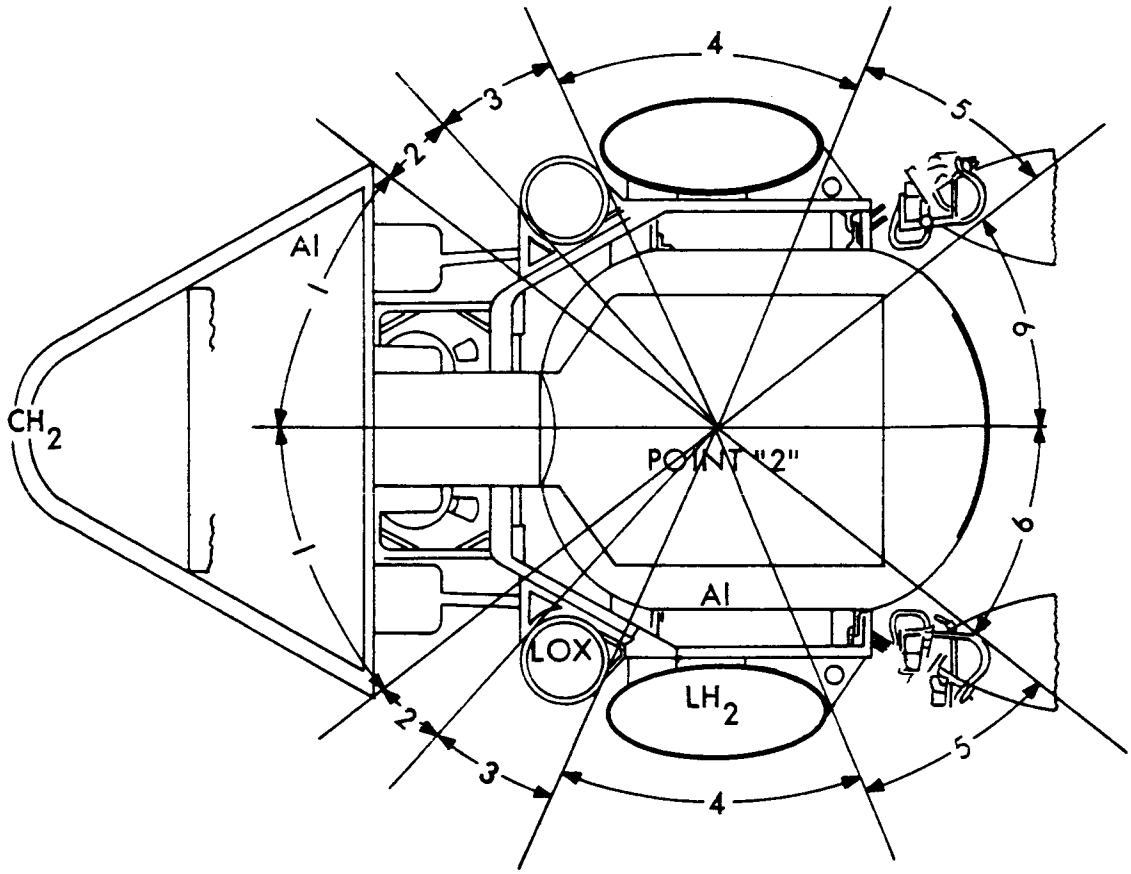

REGION	FRACTIONAL SOLID ANGLE	SHIELDING IN REGION
1	.10	3" CH_2 +4.7" Al
2	.07	1.25" Al
3 (with fuel)	.14	.02" Al +15" O_2 +1.5" Al
3 (without fuel)	.14	1.52" Al
4 (with fuel)	.4	.02" Al +18" H_2 +1.6 Al
4 (without fuel)	.4	1.62" Al
5	.13	2.2" Al
6	.18	3.1" Al

TYPICAL SPACE VEHICLE SHIELDING THICKNESS ANALYSIS

FIGURE 1

$$\text{DOSE}(P) = F \sum_{IP=1}^{NP} \left[\text{DOSE}(S_{IP})\right] \left[\text{ANG}(IP)\right] \left[\Delta\Omega_{IP}\right], \qquad (8)$$

where: $\text{DOSE}(S_{IP})$ is the absorbed dose computed behind a layer shield S_{IP},

S_{IP} represents the one-dimensional shielding configuration of whatever layers, materials, and thicknesses specified for the solid angular region indexed by IP,

ANG(IP) is the fraction of the flux coming from the IP direction, calculable from the angular distribution of the incident radiation, and normalized to be a constant unity value for isotropic flux,

F is the incident flux assumed suitably normalized,

$\Delta\Omega_{IP}$ is the fractional solid angle subtended about the point of interest P by the constant shielding region IP, and

NP is the total number of such regions needed to complete the full solid angle, so that the vehicle shielding is analyzed into sufficiently small angular regions to obtain the desired accuracy.

In Fig. 1, six regions were chosen to illustrate the concepts, but an actual analysis might use more. In the body point results reported here, 15 to 25 regions were used in most cases. It was found that little change in the final dose answer is obtained with larger numbers of subregions than this; that is, the dose calculation converges with relatively large $\Delta\Omega$ values for practical cases.* Equation 8 describes the method of calculating a dose to an interior point due to incident primary, straight-through, radiation of arbitrary incident angular

*See the paper by J. W. Keller, this symposium, for some further comments on the need for an adequately fine analysis.

distribution. Because in practice a space vehicle is likely to be drifting or slowly tumbling, the results computed and here reported are for isotropic distributions. Also, DOSE(S) was normalized to one proton/cm^2 of energy E > 100 Mev (for power law spectra), so the normalization of F, incident flux, must be compatibly defined.

Thus, in a vehicle shielding design problem, a geometrical analysis is made of the proposed design to determine a number of "constant-shielding" regions about an interior point. The dose at that point is calculated, one-dimensionally, for each of the constant-shielding regions and the weighted sum, Eq. 8, is performed using the dose values and the fractional solid angles for each region. The vehicle analysis part is a drafting board problem, and can be done quickly and with adequate accuracy for most practical vehicle configurations. But the power of this method is in the fact that any complex arrangement can be analyzed in these terms. The dose results presented here apply to specific points inside a very complex shielding arrangement--the tissue of the human body.[3]

Secondary Dose Code

Secondary Radiation Components. In addition to the dose due to primary penetrating protons, there is some energy deposition by the secondary radiations generated by the incident protons. These secondaries include gamma rays, and evaporation and knock-on nucleons. The neutrons and protons are generated in nuclear reactions where an incident proton excites a shield material nucleus. Some neutrons and protons of high energy (up to about the incident proton energy) can theoretically be produced. The bulk of the secondary neutrons and protons, perhaps with ten times the intensity of the high energy tail, are produced by evaporation from the excited nucleus. These evaporation nucleons are generated isotropically and have energies of 5 to 25 Mev, and proton numbers are roughly one half the neutron numbers. The statistical theory of the nucleus, which formally describes the excitation and evaporation processes, is invalid for the low atomic number

nuclei, such as carbon or aluminum, so the proton interaction probabilities were not computed using that theory. Rather, experimental data[7] were used to estimate the total neutron production probabilities as a function of incident proton energy.

Gamma rays emerge from excited nuclei, having energies depending on the specific nuclei and excitation levels. The excitation may be residual from a higher energy nucleon-producing interaction, or it may be from an inelastic scattering process in which the incident proton loses a relatively small amount of energy to the nucleus. From either cause, a discrete gamma ray spectrum results from the passage of high energy protons through matter.[8]

The secondary dose code was developed to compute, for all three components, the secondary fluxes and spectra generated in successive layers of the shielding, the secondary flux and spectra penetrating through the material between the generation layer and the interior point of interest, and the total absorbed dose at the interior point.

Description of the Code. The secondary code will not be described here in detail, as it is to be reported elsewhere.[9] Only enough discussion will be given to indicate how the preliminary results depend on the assumed secondary radiation production data, since these data are likely to be better known as more nuclear physics research is done. Then, presumably, better results will be obtained.

---

7. W. E. Crandall and G. P. Millburn, Neutron Production at High Energies, J. Appl. Phys. 29,698 (1958).

   See also R. Wallace and C. Sondhaus, (especially Figs. 12-16) this symposium, and UCRL-10439.

8. R. Madey, A. G. Duneer, Jr., and T. J. Krieger, Gamma Dose from Solar Flare Protons Incident on an Aluminum Shield, Trans. Am. Nuc. Soc. June 1962 meeting.

9. D. L. Dye, Space Proton Doses at Points Within the Human Body, The Boeing Company, D2-90106 (1962).

GENERATION AND TRANSMISSION OF SECONDARY RADIATIONS

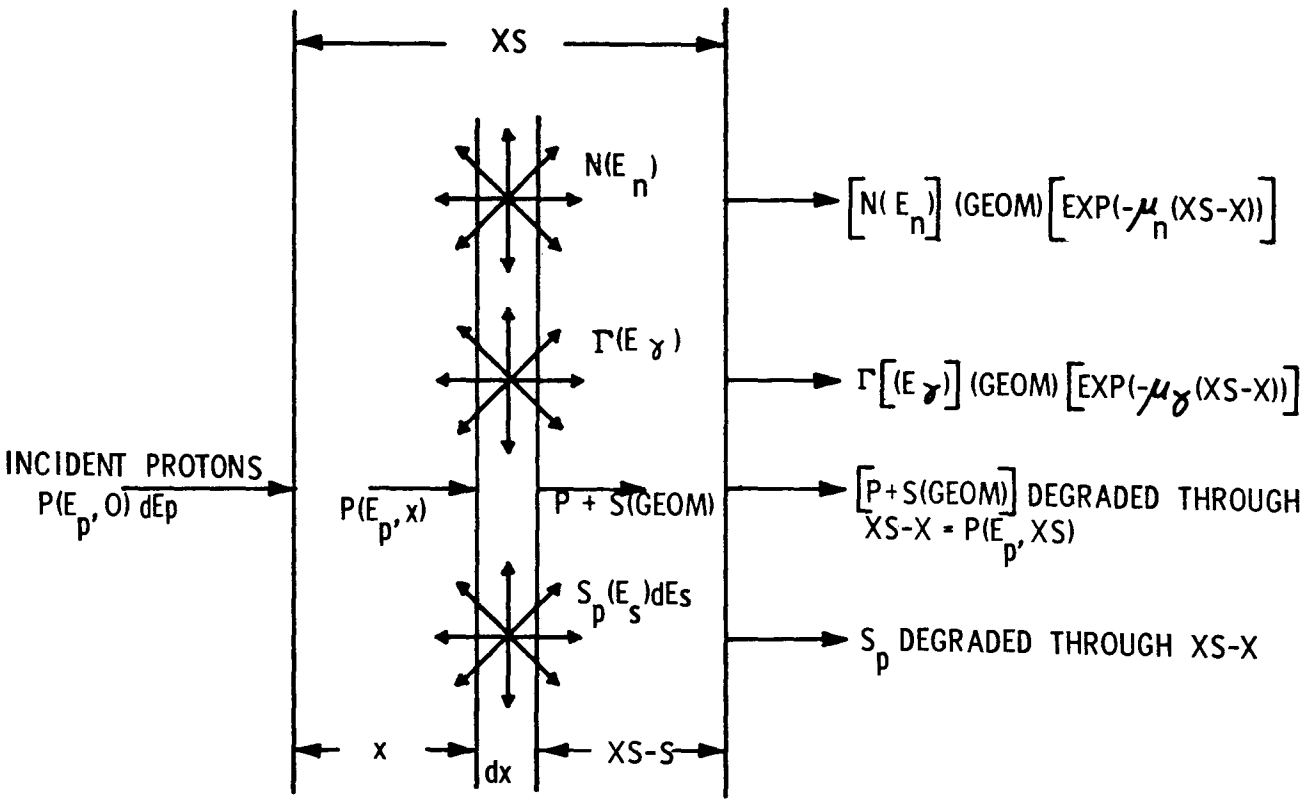

FIGURE 2

Consider a layer of shielding material, Fig. 2, of total thickness XS. At a depth X, in a layer dX thick, the secondary radiation is being generated according to:

$$N(E_n) = \frac{6 \times 10^{23} dX}{A} \int P(E_p,X)\ XNMULT(E_p,E_n)\ \sigma_n(E_p)\ dE_p, \qquad (9)$$

$$\Gamma(E_\gamma) = \frac{6 \times 10^{23} dX}{A} \int P(E_p,X)\ XGMULT(E_\gamma)\ \sigma_\gamma(E_p)\ dE_p, \qquad (10)$$

and

$$S_p(E_s)E_s = \frac{6 \times 10^{23} dX}{A} \int P(E_p,X)\ XPMULT(E_p,E_s)dE_s\ \sigma_s(E_p)\ dE_p. \qquad (11)$$

Where: A is atomic number of the shield material,

$N(E_n)$ is the flux of neutrons generated in an energy group having energy E_n,

$\Gamma(E_\gamma)$ is the flux of photons generated having energy E_γ,

$S_p(E_s)dE_s$ is the differential energy distribution of secondary protons generated having energy E_s to $E_s + dE_s$,

$P(E_p,X)dE_p$ is the proton energy spectrum at depth X, the flux having energy between E_p and $E_p + dE_p$,

$XNMULT(E_p,E_n)\ \sigma_n(E_p)$ is the yield of neutrons having energy E_n, per incident unit flux of protons having energy E_p,

$XGMULT(E_\gamma)\ \sigma_\gamma(E_p)$ is the yield of gamma rays having energy E_γ (due to inelastic scatter or other processes) produced per incident unit proton flux of Energy E_p. XGMULT depends primarily on the nuclear levels of the struck nucleus, while σ_γ is the cross section for an interaction,

$XPMULT(E_p,E_s)dE_s\ \sigma_s(E_p)$ is the differential yield of secondary protons having energy E_s to $E_s + dE_s$ from processes induced by incident protons of energy E_p.

The multiplicity factors (XNMULT, XGMULT, XPMULT) are normalized to one "particle" produced so that experimentally determined total yield cross sections may be used.[7,10]

---

10. T. Watasuki et al., Gamma Rays from Several Elements Bombarded by 10 and 14 Mev Protons, J. Phys. Soc. Japan 15, 1141 (1960).

A geometrical weighting factor (GEOM) is assigned to the radiation generated in any given material layer. This factor depends upon the angular distributions of the secondaries and upon the relative sizes of the vehicle shield and the dose point of interest. The fraction of the secondaries produced in a given sublayer within the shielding that is directed toward the interior dose point is given by multiplying N_s, Γ_s, or S_p by GEOM for that layer.

The neutrons and gamma rays are assumed to be absorbed by intervening shielding according to exponential laws. The protons generated in dX are added to $P(E_p, X + dX)dE_p$. (This is the reason we needed the differential energy distribution for $S_p(E_p)$). Thus, the spectrum for the next dX is enhanced by the secondary protons generated in previous sublayers.

In the actual code computation, the layer XS thick is broken up into NSL finite-thickness sublayers, where NSL is determined by a specified maximum sublayer thickness, except that NSL never exceeds another specified parameter, NSUBL. This last restriction saves computer time for thick shields.

The absorption of the neutrons and gammas is carried through all intervening shielding layers to the dose point inside, and the dose there calculated using well-known dose conversion factors. The code is dimensioned for 10 different materials and/or layers. The secondary protons are also carried through the intervening shielding separately from the total (primary plus secondary) proton flux, so as to show secondary proton dose separately. For this, the proton spectrum modification and dose code described in the previous section is used. After the absorbed doses, in rads, are computed at the interior point for each secondary component, these doses are individually converted to biological dose, in rem, by multiplying by the appropriate, specified, RBE. The individual component, as well as the total, secondary biodose is then read out. Finally, the weighted sum, Eq. 8, is done to obtain total dose from all directions at the point.

Data Used in the Secondary Dose Computation. In addition to the proton range-energy tables used in the primary dose computation, a number of nuclear and other parameters are needed in the secondary code. These include: the yield cross sections σ_n, σ_γ; the multiplicities XNMULT, XPMULT, and XGMULT; the discrete gamma ray energies generated in the specific shielding materials, designated EGAM; the gamma and neutron absorption coefficients and dose conversion factors for these energies; the angular distribution factors, GEOM, for each layer; and the maximum sublayer thickness, XLMAX, for each material. Neutron yield cross sections were found from the empirical relation

$$\sigma_n = C_1 E^{0.4}$$

which fits the experimental data[7] for aluminum and carbon (assumed the same as tissue) with $C_1 = 0.07$ and $C_1 = 0.035$, respectively. (For iron, $C_1 \simeq 0.3$.) Gamma ray yield cross sections and energies were also inferred from reported experiments [10,11] and the σ_γ values used are plotted, along with σ_n, in Fig. 3. Two different σ_γ curves were used, one in which σ_γ approaches σ_{total} at high energies, and one in which it is held constant at its low energy maximum (~ 2 barns) at high energies. This latter case is labelled "upper limit". The inelastic scatter gamma ray energies, EGAM, and multiplicities, XGMULT, for aluminum and tissue, and the NBS Handbook dose conversion coefficients, are given in Table 1.

The secondary nucleon energy distributions are somewhat less well known, and as better data become available, better dose values can be obtained by using them in this code. For the present calculation, an evaporation hump ranging from 5 to 25 Mev for secondaries was assumed for all incident proton energies above 25 Mev, and a high-energy tail was assumed to extend out to 0.5 the incident proton energy,

---

11. G. Schrank et al., Inelastic Scattering of 17-Mev Protons, Phys. Rev. 127, 2159 (1962). This paper gives many references to experimental determinations.

Table 1. Gamma Ray Energies, Multiplicities, and Dose Coefficients Assumed for the Secondary Dose Computation

Material	EGAM (Mev)	XGMULT	DOSGAM (Tissue) (rad/proton/cm^2)
Aluminum	1.4	0.45	4.8×10^{-9}
	2.2	0.19	4.0×10^{-9}
	3.0	0.25	3.5×10^{-9}
	5.0	0.08	3.3×10^{-9}
	8.0	0.03	3.2×10^{-9}
Tissue	4.4	0.88	3.0×10^{-9}
	6.1	0.06	2.9×10^{-9}
	7.0	0.06	2.9×10^{-9}

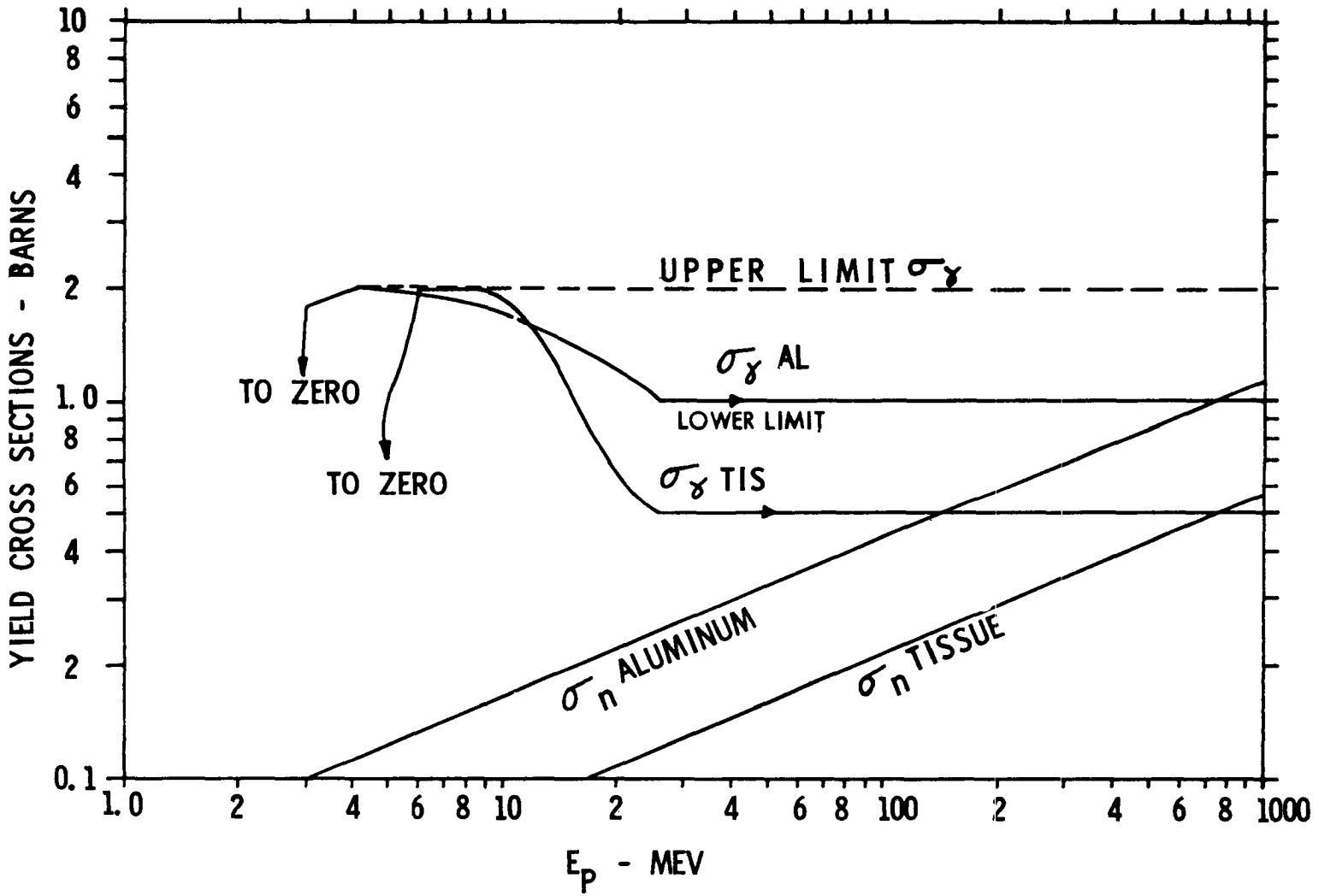
YIELD CROSS SECTIONS - BARNS
10
8
6
4
2
1.0
8
6
4
2
0.1
UPPER LIMIT σ_γ
σ_γ AL
LOWER LIMIT
TO ZERO
TO ZERO
σ_γ TIS
σ_n ALUMINUM
σ_n TISSUE
1.0
2
4
6
8
10
2
4
6
8
100
2
4
6
8
1000
E_P - MEV

FIGURE 3

containing about 10 percent of the total secondary nucleons.* The secondary spectrum was normalized, for each incident proton energy in the integration of Eq. 11, to one nucleon over the whole energy range $1 < E_s < E_p/2$. More detail is given elsewhere.[9]

The GEOM factors were assumed to be constant for each shielding layer, and were taken as 0.5 for both outer aluminum and inner tissue layers in the results to be given here.

Human Geometry

The absorbed dose at each of several points in a seated astronaut is desired. The points of specific interest are those that are parts of radiosensitive physiological systems, such as hematopoetic and spinal marrow, gut, and eye lens. Twelve such body points were chosen, located as indicated in Table 2, on a 75-percentile seated man. This body geometry is based on data given[12] in an anthropometric study of Air Force personnel. (Seventy-five percent of the men had smaller body measurements than those used.) Scale drawings of this composite astronaut's body were made and used to determine the tissue thicknesses around each of the selected body points in all directions.[3] For each specific body point listed in Table 2, this descriptive geometry problem was solved; the point is taken as the center of a large sphere on which isothickness contours are projected. These contours mark out a set of solid angular regions; a region's projected area on the sphere divided by the total sphere area is the fractional solid angle of that region. Depending on the accuracy required, one may choose any set of regions to define the fractional solid angles for the human geometry problem.

The isothickness contours are obtained by drawing a series of cross sectional views of the body at different angles ϕ from the

---

12. Hertzberg, Daniels, and Churchill, Anthropometry of Flying Personnel--1950, WADC Technical Report 52-321 (1954).

*The form of this secondary nucleon distribution is not unlike that given in this symposium by Dr. K. Strauch as a "hypothetical particle spectrum", built-up on the high energy end to account for secondary angular distributions.

TABLE 2. DESCRIPTION OF BODY POINTS ANALYZED

BODY POINT	LOCATION	SYMBOL
CENTRAL GUT	10 CM UP FROM SEAT, AND 10 CM FORWARD FROM BACK OF SEAT.	GUT
CHEST CENTER	ON THE SKIN SURFACE, 55 CM UP FROM SEAT.	CHEST 0
CHEST CENTER	2 CM IN FROM THE SKIN, IN STERNUM, 55 CM UP FROM SEAT, NEGLECTING LUNGS.	CHEST 2
CHEST CENTER	2 CM DEEP, IN STERNUM, AS BEFORE, TAKING ACCOUNT OF AIR IN LUNGS.	CHEST 2 L
SPINAL CORD REGION	55 CM UP FROM SEAT, 2 CM DEEP IN BODY.	BACK 2
FEMUR	LEG CENTER, 38 CM FORWARD FROM BACK OF SEAT, 9 CM UP FROM SEAT LEVEL (NEGLECTING BONE).	FEMUR
FEMUR	SAME POINT AS BEFORE, TAKING ACCOUNT OF BONE STRUCTURE	FEMUR B
EYE LENS	RIGHT EYE SURFACE, NEGLECTING FACIAL AND CRANIAL BONY STRUCTURE.	EYE
WAIST, RIGHT SIDE	ON THE SKIN, 25 CM UP FROM SEAT LEVEL.	WAIST 0
WAIST, RIGHT SIDE	25 CM UP FROM SEAT LEVEL, 1 CM IN FROM SKIN, ON THE MID-SAGGITAL LINE.	WAIST 1
WAIST, RIGHT SIDE	25 CM UP FROM SEAT LEVEL, 4 CM IN FROM SKIN, ON THE MID-SAGGITAL LINE.	WAIST 4
WAIST, RIGHT SIDE	25 CM UP FROM SEAT LEVEL, 6 CM IN FROM SKIN, ON THE MID-SAGGITAL LINE.	WAIST 6
WAIST, RIGHT SIDE	25 CM UP FROM SEAT LEVEL, 8 CM IN FROM SKIN, ON THE MID-SAGGITAL LINE.	WAIST 8

anterior-posterior plane; and by drawing a series of horizontal cross sectional views at various planes above and below the point of interest. A tissue thickness is then obtained by determining the true distance from the point to the body surface along every (latitude) direction θ in the ϕ plane. Figure 4 illustrates the method for a specific point. The result of this descriptive geometry problem is a map on the projection sphere showing lines of constant tissue thickness between the point of interest and the body exterior along the θ, ϕ direction. Figure 5 shows a typical isothickness contour for a body point, in the spinal column. In this procedure, the human body is assumed to be a homogeneous tissue mass except for certain cases below.

Conceptually simple, but computationally tedious, extensions of the interior body point dose calculations for the STERNUM, FEMUR, WAIST 4, and EYE LENS positions were also analyzed with slight geometric variations. These variations were intended: (1) to solve more realistic problems that include bones and lung absorption effects, (2) to give an idea as to the dose error made in neglecting bones and lungs; i.e., in assuming the body to be homogeneous, (3) to assess the shielding effectiveness of partial body shielding built in as a chair, and (4) to assess the effect of goggles in eye protection.

Incident Proton Spectra

Five different incident proton spectra were considered; four having power law forms, the other approximating the Van Allen belt spectrum. The power law forms, normalized to one proton/cm^2 of $E > 100$ Mev, are given by:

$$N(E)dE = (n - 1)(100)^{n-1} E^{-n} dE \text{ for } 20 \text{ Mev} \leq E \leq 1{,}000 \text{ Mev}$$

for the parameter n with values 2, 3, 4, and 5. They are flat at the 20 Mev value for the interval $1 \leq E \leq 20$ Mev. The Van Allen spectrum is normalized to one proton/cm^2 of $E > 40$ Mev, and has an E^{-2} form above 100 Mev, with the lower energy part of Hess's theoretical form matched to it at 100 Mev.

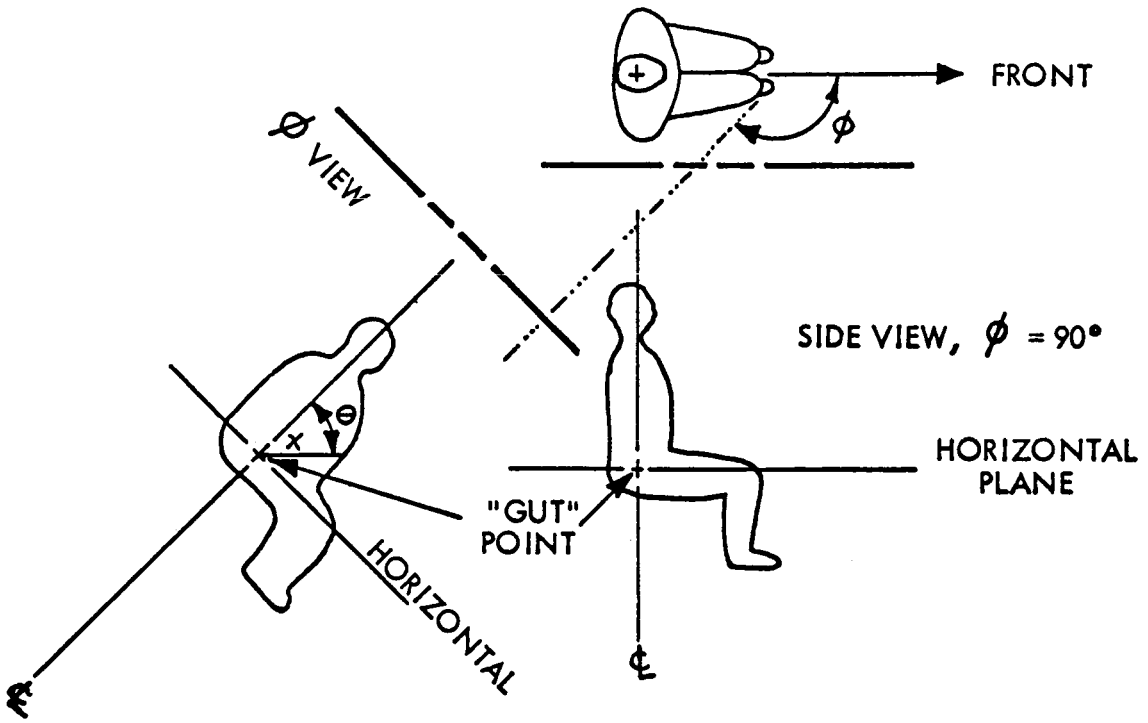

FIGURE 4

℄ IS VERTICAL AXIS, PASSING THROUGH THE POINT OF INTEREST

ϕ IS LONGITUDE ANGLE

θ IS LATITUDE ANGLE

x IS THICKNESS, A FUNCTION OF θ AND ϕ FOR THIS POINT

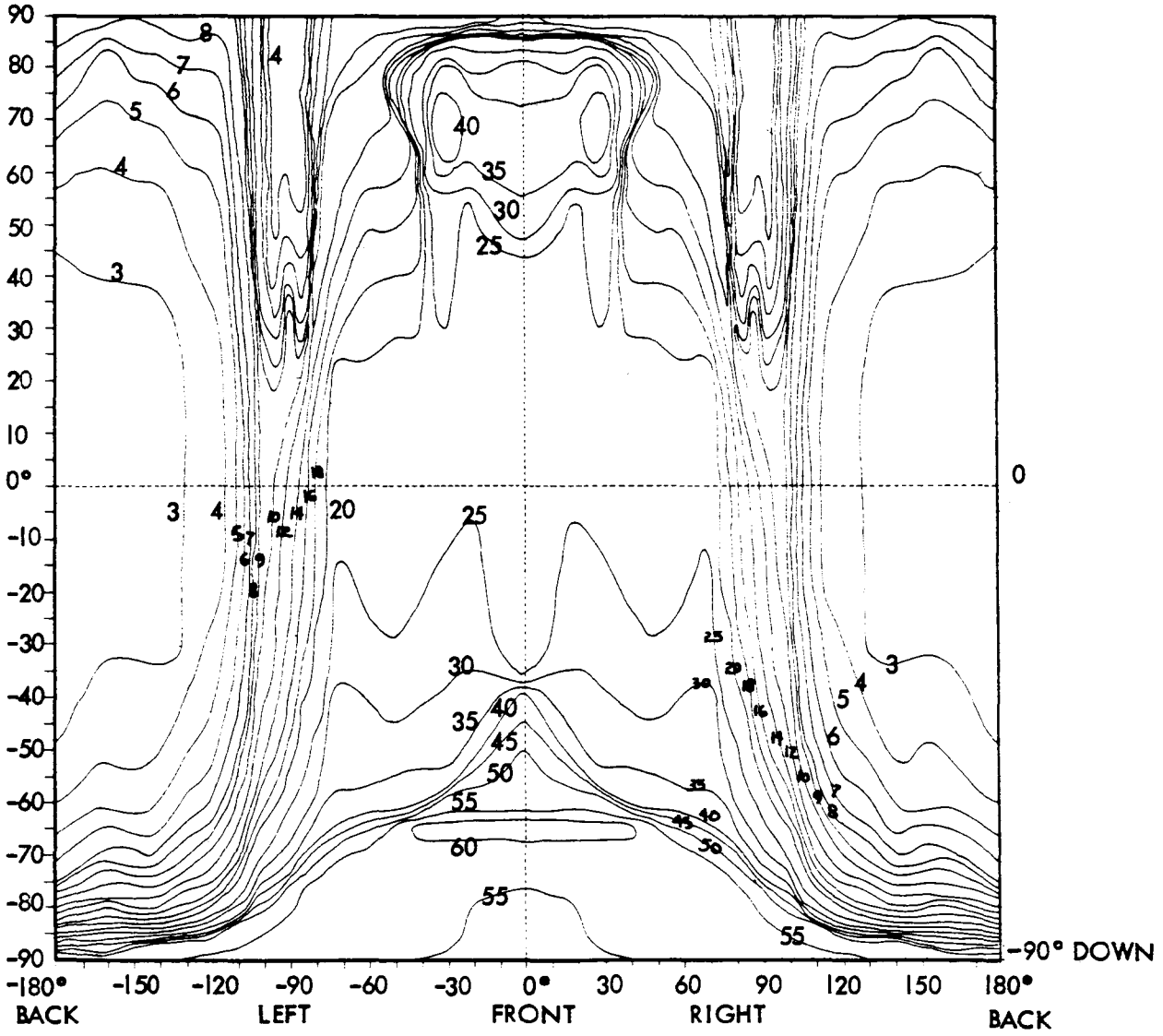

SPINAL COLUMN

FIGURE 5

Dose Results

Figure 6 shows the penetrating primary proton dose and the secondary dose plotted separately for the E^{-3} spectrum and for one-dimensional cases. It is seen that the nuclear data assumptions made here lead to a relatively small secondary radiation dose, even with "upper limit" inelastic scatter cross sections. It should be noted that for steeper primary spectra the primary absorption is greater, so that the secondary dose is a larger fraction of the primary than for spectra having smaller n values.[9] However, the secondary dose is clearly a small fraction of the primary proton dose for tissue thicknesses up to 20 gm/cm^2 and aluminum shields of up to 10 gm/cm^2, for typical space proton spectra. Further, the solid angle subtended by tissue thickness greater than 20 gm/cm^2 around the deepest body points considered (GUT, WAIST 8) totals only about 20 percent[3], and it is even less for most radiosensitive organs. Thus the total dose to these organs is essentially equal to the primary proton dose, computed by Eq. 8, for feasibly thin external aluminum shields.

Tables 3 through 7 show the total doses at each of the body points considered for a variety of aluminum shells for the E^{-2}, E^{-3}, E^{-4}, E^{-5}, and Van Allen spectra, respectively. The units are tissue rad per incident isotropic proton/cm^2 having $E > 100$ Mev. These values utilize the three-dimensional human geometry analyses, Eq. 8, and the solid-line cross section data of Fig. 3. The nuclear data used are thus reasonable composites of published experimental information.

In addition to the twelve body points with only external shell shielding, four special cases are listed. In the case WAIST 4S, a shielding chair of either 2 gm/cm^2 or 4 gm/cm^2 polyethylene is considered with three outer aluminum shell values. The line labelled FEMUR B is a 72-region case in which the structure of the bone was considered. The line labelled EYE G is a case in which 0.25 cm of lead glass was added to the zero tissue thickness region of the EYE analysis; that is, to the front of the eye lens. The case CHEST 2

PRIMARY & SECONDARY DOSES DUE TO E^{-3} SPECTRUM PROTONS MONODIRECTIONAL FLUX, NORMALIZED TO 1 PROTON / CM^2 OF E > 100 MEV

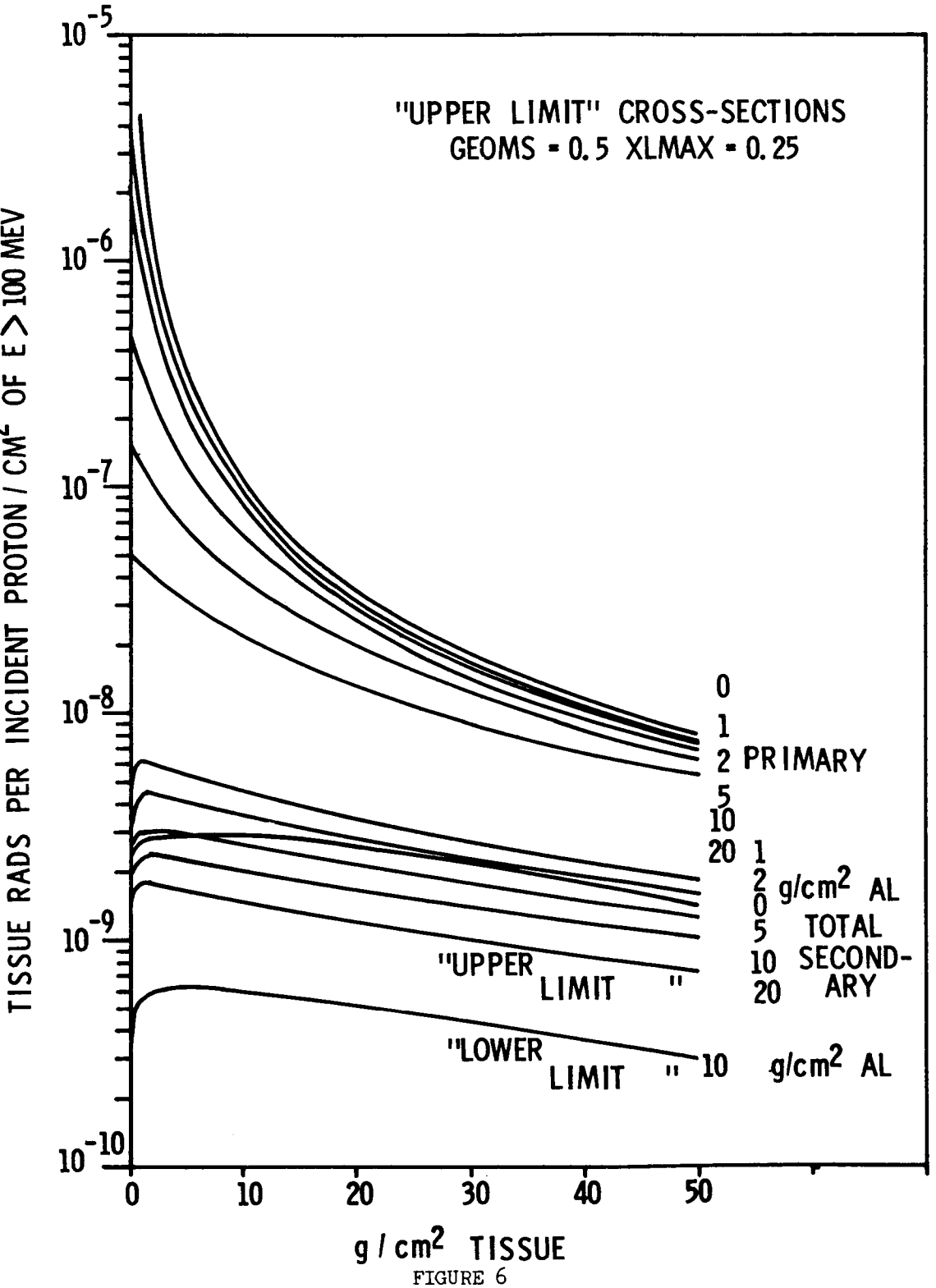

FIGURE 6

Table 3. Doses at Specific Body Points Due to Incident Isotropic Proton Flux with n = 2 Spectrum, for Various Aluminum Shell Shield Thicknesses (rads per proton/cm^2 of E > 100 Mev)

Body Points	Aluminum Shell Thickness (gm/cm^2)						
	0	1	2	4	6	8	10
GUT	5.4×10^{-8}	5.1×10^{-8}	4.8^{-8}	4.3×10^{-8}	3.9×10^{-8}	3.6×10^{-8}	3.3×10^{-8}
CHEST 0	3.0×10^{-6}	6.5×10^{-7}	3.3×10^{-7}	1.7×10^{-7}	1.2×10^{-7}	8.9×10^{-8}	7.3×10^{-8}
CHEST 2	1.3×10^{-7}	1.1×10^{-7}	9.2×10^{-8}	7.2×10^{-8}	6.1×10^{-8}	5.2×10^{-8}	4.6×10^{-8}
CHEST 2L (Sternum)	1.4×10^{-7}	1.2×10^{-7}	1.0×10^{-7}	8.0×10^{-8}	6.7×10^{-8}	5.8×10^{-8}	5.1×10^{-8}
BK 2 (Spinal Column)	1.4×10^{-7}	1.1×10^{-7}	9.5×10^{-8}	7.5×10^{-8}	6.2×10^{-8}	5.4×10^{-8}	4.7×10^{-8}
WAIST 0	2.4×10^{-6}	5.2×10^{-7}	2.7×10^{-7}	1.4×10^{-7}	1.0×10^{-7}	7.9×10^{-8}	6.5×10^{-8}
WAIST 1	1.3×10^{-7}	1.1×10^{-7}	9.5×10^{-8}	7.5×10^{-8}	6.2×10^{-8}	5.4×10^{-8}	4.7×10^{-8}
WAIST 4	7.6×10^{-8}	6.9×10^{-8}	6.3×10^{-8}	5.4×10^{-8}	4.8×10^{-8}	4.3×10^{-8}	3.9×10^{-8}
WAIST 6	6.1×10^{-8}	5.7×10^{-8}	5.3×10^{-8}	4.7×10^{-8}	4.2×10^{-8}	3.8×10^{-8}	3.5×10^{-8}
WAIST 8	5.5×10^{-8}	5.2×10^{-8}	4.9×10^{-8}	4.3×10^{-8}	3.9×10^{-8}	3.6×10^{-8}	3.3×10^{-8}
WAIST 4S (2 gm/cm^2 CH_2 chair)	6.6×10^{-8}		5.6×10^{-8}		4.4×10^{-8}		
(4 gm/cm^2 CH_2 chair)	5.9×10^{-8}		5.1×10^{-8}		4.4×10^{-8}		
FEMUR	8.0×10^{-8}	7.2×10^{-8}	6.6×10^{-8}	5.7×10^{-8}	5.0×10^{-8}	4.5×10^{-8}	4.1×10^{-8}
FEMUR B	8.0×10^{-8}	7.3×10^{-8}	6.7×10^{-8}	5.8×10^{-8}	5.2×10^{-8}	4.7×10^{-8}	4.5×10^{-8}
EYE	2.5×10^{-6}	5.6×10^{-7}	3.1×10^{-7}	1.7×10^{-7}	1.2×10^{-7}	9.1×10^{-8}	7.5×10^{-8}
EYE G (2.5 mm glasses)	1.1×10^{-6}	4.4×10^{-7}	2.6×10^{-7}				

Table 4. Doses at Specific Body Points Due to Incident Isotropic Proton Flux with n = 3 Spectrum, for Various Aluminum Shell Shield Thicknesses (rads per proton/cm^2 of E > 100 Mev)

Body Points	Aluminum Shell Thickness (gm/cm^2)						
	0	1	2	4	6	8	10
GUT	5.6×10^{-8}	5.0×10^{-8}	4.6×10^{-8}	3.9×10^{-8}	3.4×10^{-8}	2.9×10^{-8}	2.6×10^{-8}
CHEST 0	2.8×10^{-8}	3.5×10^{-6}	1.2×10^{-6}	3.9×10^{-7}	2.1×10^{-7}	1.3×10^{-7}	9.5×10^{-8}
CHEST 2	2.8×10^{-7}	2.0×10^{-7}	1.5×10^{-7}	9.9×10^{-8}	7.3×10^{-8}	5.6×10^{-8}	4.6×10^{-8}
CHEST 2L (Sternum)	2.9×10^{-7}	2.1×10^{-7}	1.6×10^{-7}	1.1×10^{-7}	8.2×10^{-8}	6.4×10^{-5}	5.2×10^{-8}
BK 2 (Spinal Column)	3.0×10^{-7}	2.1×10^{-7}	1.6×10^{-7}	1.0×19^{-7}	7.6×10^{-8}	5.8×10^{-8}	4.7×10^{-8}
WAIST 0	2.2×10^{-5}	2.7×10^{-6}	9.2×10^{-7}	3.2×10^{-7}	1.7×10^{-7}	1.1×10^{-7}	8.1×10^{-8}
WAIST 1	2.9×10^{-7}	2.0×10^{-7}	1.6×10^{-7}	1.0×10^{-8}	7.5×10^{-8}	5.8×10^{-8}	4.7×10^{-8}
WAIST 4	1.1×10^{-7}	9.0×10^{-8}	7.7×10^{-8}	5.9×10^{-8}	4.8×10^{-8}	4.0×10^{-8}	3.4×10^{-8}
WAIST 6	7.2×10^{-8}	6.4×10^{-8}	5.7×10^{-8}	4.6×10^{-8}	3.9×10^{-8}	3.3×10^{-8}	2.9×10^{-8}
WAIST 8	6.0×10^{-8}	5.3×10^{-8}	4.8×10^{-8}	4.0×10^{-8}	3.4×10^{-8}	3.0×10^{-8}	2.6×10^{-8}
WAIST 4S (2 gm/cm^2 CH_2 chair)	8.3×10^{-8}		6.3×10^{-8}		4.1×10^{-8}		
(4 gm/cm^2 CH_2 chair)	7.0×10^{-8}		5.4×10^{-8}		3.7×10^{-8}		
FEMUR	1.1×10^{-7}	9.3×10^{-8}	8.0×10^{-8}	6.3×10^{-8}	5.1×10^{-8}	4.2×10^{-8}	3.6×10^{-8}
FEMUR B	1.1×10^{-7}	9.4×10^{-8}	8.2×10^{-8}	6.4×10^{-8}	5.3×10^{-8}	4.4×10^{-8}	3.8×10^{-8}
EYE	2.2×10^{-5}	2.9×10^{-6}	1.0×10^{-6}	3.6×10^{-7}	2.0×10^{-7}	1.3×10^{-7}	9.6×10^{-8}
EYE G (2.5 mm glasses)	7.1×10^{-6}	1.9×10^{-6}	8.3×10^{-7}				

Table 5. Doses at Specific Body Points Due to Incident Isotropic Proton Flux with n = 4 Spectrum, for Various Aluminum Shell Shield Thicknesses (rads per proton/cm^2 or E > 100 Mev)

Body Points	Aluminum Shell Thickness (gm/cm^2)						
	0	1	2	4	6	8	10
GUT	6.3×10^{-8}	5.6×10^{-8}	4.7×10^{-8}	3.8×10^{-8}	3.1×10^{-8}	2.6×10^{-8}	2.0×10^{-8}
CHEST 0	2.2×10^{-4}	1.7×10^{-5}	3.9×10^{-6}	8.4×10^{-7}	3.3×10^{-7}	1.7×10^{-7}	1.1×10^{-7}
CHEST 2	5.7×10^{-7}	3.4×10^{-7}	2.3×10^{-7}	1.3×10^{-7}	8.1×10^{-8}	5.6×10^{-8}	4.4×10^{-8}
CHEST 2L (Sternum)	5.9×10^{-7}	3.6×10^{-7}	2.4×10^{-7}	1.4×10^{-7}	8.8×10^{-8}	6.2×10^{-8}	4.7×10^{-8}
BK 2 (Spinal Column)	6.0×10^{-7}	3.6×10^{-7}	2.5×10^{-7}	1.4×10^{-7}	8.5×10^{-8}	6.1×10^{-8}	4.7×10^{-8}
WAIST 0	1.6×10^{-4}	1.3×10^{-5}	2.8×10^{-6}	6.3×10^{-7}	2.6×10^{-7}	1.4×10^{-7}	9.4×10^{-8}
WAIST 1	5.7×10^{-7}	3.5×10^{-7}	2.4×10^{-7}	1.4×10^{-7}	8.6×10^{-8}	6.0×10^{-8}	4.5×10^{-8}
WAIST 4	1.5×10^{-7}	1.1×10^{-7}	8.9×10^{-8}	6.2×10^{-8}	4.6×10^{-8}	3.5×10^{-8}	2.9×10^{-8}
WAIST 6	8.3×10^{-8}	7.0×10^{-8}	5.8×10^{-8}	4.3×10^{-8}	3.4×10^{-8}	2.7×10^{-8}	2.3×10^{-8}
WAIST 8	6.4×10^{-8}	5.5×10^{-8}	4.7×10^{-8}	3.6×10^{-8}	3.0×10^{-8}	2.4×10^{-8}	2.0×10^{-8}
WAIST 4S (2 gm/cm^2 CH_2 chair)	1.0×10^{-7}		6.6×10^{-8}		3.8×10^{-8}		
(4 gm/cm^2 CH_2 chair)	8.3×10^{-8}		5.7×10^{-8}		3.3×10^{-8}		
FEMUR	1.4×10^{-7}	1.2×10^{-7}	8.9×10^{-8}	6.3×10^{-8}	4.8×10^{-8}	3.8×10^{-8}	3.1×10^{-8}
FEMUR B	1.3×10^{-7}	1.1×10^{-7}	8.9×10^{-8}	6.5×10^{-8}	5.0×10^{-8}	3.9×10^{-8}	3.1×10^{-8}
EYE	1.7×10^{-4}	1.4×10^{-5}	3.0×10^{-6}	6.1×10^{-7}	3.1×10^{-7}	1.8×10^{-7}	1.2×10^{-7}
EYE G (2.5 mm glasses)	3.9×10^{-5}	8.4×10^{-6}	2.3×10^{-6}				

Table 6. Doses at Specific Body Points Due to Incident Isotropic Proton Flux with n = 5 Spectrum, for Various Aluminum Shell Thicknesses (rads per proton/cm^2 of E > 100 Mev)

Body Points	Aluminum Shell Thickness (gm/cm^2)						
	0	1	2	4	6	8	10
GUT	5.8×10^{-8}	5.4×10^{-8}	4.2×10^{-8}	3.3×10^{-8}	2.5×10^{-8}	2.2×10^{-8}	1.9×10^{-8}
CHEST 0	1.6×10^{-3}	7.8×10^{-5}	1.0×10^{-5}	1.4×10^{-6}	4.8×10^{-7}	2.3×10^{-7}	1.2×10^{-7}
CHEST 2	1.1×10^{-6}	6.2×10^{-7}	3.4×10^{-7}	1.6×10^{-7}	8.7×10^{-8}	5.9×10^{-8}	4.2×10^{-8}
CHEST 2L (Sternum)	1.1×10^{-6}	6.0×10^{-7}	3.6×10^{-7}	1.7×10^{-7}	9.7×10^{-8}	6.5×10^{-8}	4.7×10^{-8}
BK 2 (Spinal Column)	1.1×10^{-6}	6.0×10^{-7}	3.7×10^{-7}	1.7×10^{-7}	1.0×10^{-7}	6.4×10^{-8}	4.9×10^{-8}
WAIST 0	1.2×10^{-3}	6.0×10^{-5}	7.9×10^{-6}	1.1×10^{-6}	3.8×10^{-7}	1.8×10^{-7}	1.0×10^{-7}
WAIST 1	1.0×10^{-6}	5.4×10^{-7}	3.3×10^{-7}	1.5×10^{-7}	8.9×10^{-8}	5.8×10^{-8}	4.1×10^{-8}
WAIST 4	1.8×10^{-7}	1.3×10^{-7}	9.8×10^{-8}	6.3×10^{-8}	4.4×10^{-8}	3.3×10^{-8}	2.6×10^{-8}
WAIST 6	8.3×10^{-8}	5.7×10^{-8}	5.9×10^{-8}	4.1×10^{-8}	3.1×10^{-8}	2.5×10^{-8}	2.2×10^{-8}
WAIST 8	6.8×10^{-8}	5.9×10^{-8}	4.7×10^{-8}	3.3×10^{-8}	2.7×10^{-8}	2.2×10^{-8}	19.0×10^{-9}
WAIST 4S (2 gm/cm^2 CH_2 chair)	1.1×10^{-7}		6.7×10^{-8}		3.4×10^{-8}		
(4 gm/cm^2 CH_2 chair)	8.9×10^{-8}		5.4×10^{-8}		3.0×10^{-8}		
FEMUR	1.7×10^{-7}	1.4×10^{-7}	9.9×10^{-8}	6.3×10^{-8}	4.5×10^{-8}	3.4×10^{-8}	2.7×10^{-8}
FEMUR B	1.5×10^{-7}	1.3×10^{-7}	9.6×10^{-8}	6.4×10^{-8}	4.7×10^{-8}	3.7×10^{-8}	2.75×10^{-8}
EYE	1.2×10^{-3}	6.2×10^{-5}	8.3×10^{-6}	1.2×10^{-6}	4.2×10^{-7}	2.0×10^{-7}	1.1×10^{-7}
EYE G (2.5 mm glasses)	1.9×10^{-4}	3.7×10^{-5}	5.5×10^{-6}				

Table 7. Doses at Specific Body Points Due to Incident Isotropic Proton Flux with Van Allen Spectrum, for Various Aluminum Shell Shield Thicknesses (rads per proton/cm^2 of E > 40 Mev)

Body Points	Aluminum Shell Thickness (gm/cm^2)						
	0	1	2	4	6	8	10
GUT	$3.1x10^{-8}$	$2.9x10^{-8}$	$2.8x10^{-8}$	$2.5x10^{-9}$	$2.3x10^{-8}$	$2.1x10^{-8}$	$1.9x10^{-8}$
CHEST 0	$3.8x10^{-7}$	$1.3x10^{-7}$	$1.0x10^{-7}$	$7.5x10^{-8}$	$6.0x10^{-8}$	$5.0x10^{-8}$	$4.2x10^{-8}$
CHEST 2	$6.0x10^{-8}$	$5.4x10^{-8}$	$4.9x10^{-8}$	$4.1x10^{-8}$	$3.5x10^{-8}$	$3.0x10^{-8}$	$2.7x10^{-8}$
CHEST 2L (Sternum)	$6.7x10^{-8}$	$6.0x10^{-8}$	$5.4x10^{-8}$	$4.6x10^{-8}$	$3.9x10^{-8}$	$3.4x10^{-8}$	$3.0x10^{-8}$
BK 2 (Spinal Column)	$6.2x10^{-8}$	$5.6x10^{-8}$	$5.0x10^{-8}$	$4.2x10^{-8}$	$3.6x10^{-8}$	$3.1x10^{-8}$	$2.7x10^{-8}$
WAIST 0	$3.1x10^{-7}$	$1.2x10^{-7}$	$9.4x10^{-8}$	$6.9x10^{-8}$	$5.5x10^{-8}$	$4.5x10^{-8}$	$3.8x10^{-8}$
WAIST 1	$6.4x10^{-8}$	$5.7x10^{-8}$	$5.2x10^{-8}$	$4.3x10^{-8}$	$3.7x10^{-8}$	$3.1x10^{-8}$	$2.8x10^{-8}$
WAIST 4	$4.4x10^{-8}$	$4.0x10^{-8}$	$3.7x10^{-8}$	$3.2x10^{-8}$	$2.8x10^{-8}$	$2.5x10^{-8}$	$2.3x10^{-8}$
WAIST 6	$3.6x10^{-8}$	$3.3x10^{-8}$	$3.1x10^{-8}$	$2.7x10^{-8}$	$2.4x10^{-8}$	$2.2x10^{-8}$	$2.0x10^{-8}$
WAIST 8	$3.2x10^{-8}$	$3.0x10^{-8}$	$2.8x10^{-8}$	$2.5x10^{-8}$	$2.3x10^{-8}$	$2.1x10^{-8}$	$1.9x10^{-8}$
WAIST 4S ($2\ gm/cm^2$ CH_2 chair)	$3.8x10^{-8}$		$3.3x10^{-8}$		$2.5x10^{-8}$		
($4\ gm/cm^2$ CH_2 chair)	$3.4x10^{-8}$		$3.0x10^{-8}$		$2.4x10^{-8}$		
FEMUR	$4.5x10^{-8}$	$4.2x10^{-8}$	$3.8x10^{-8}$	$3.3x10^{-8}$	$2.9x10^{-8}$	$2.6x10^{-8}$	$2.4x10^{-8}$
FEMUR B	$4.7x10^{-8}$		$4.0x10^{-8}$		$3.0x10^{-8}$		
EYE	$3.3x10^{-7}$	$1.3x10^{-7}$	$1.0x10^{-7}$	$7.7x10^{-8}$	$6.2x10^{-8}$	$5.1x10^{-8}$	$4.3x10^{-8}$
EYE G (2.5 mm glasses)	$1.5x10^{-7}$	$1.0x10^{-7}$	$8.6x10^{-8}$				

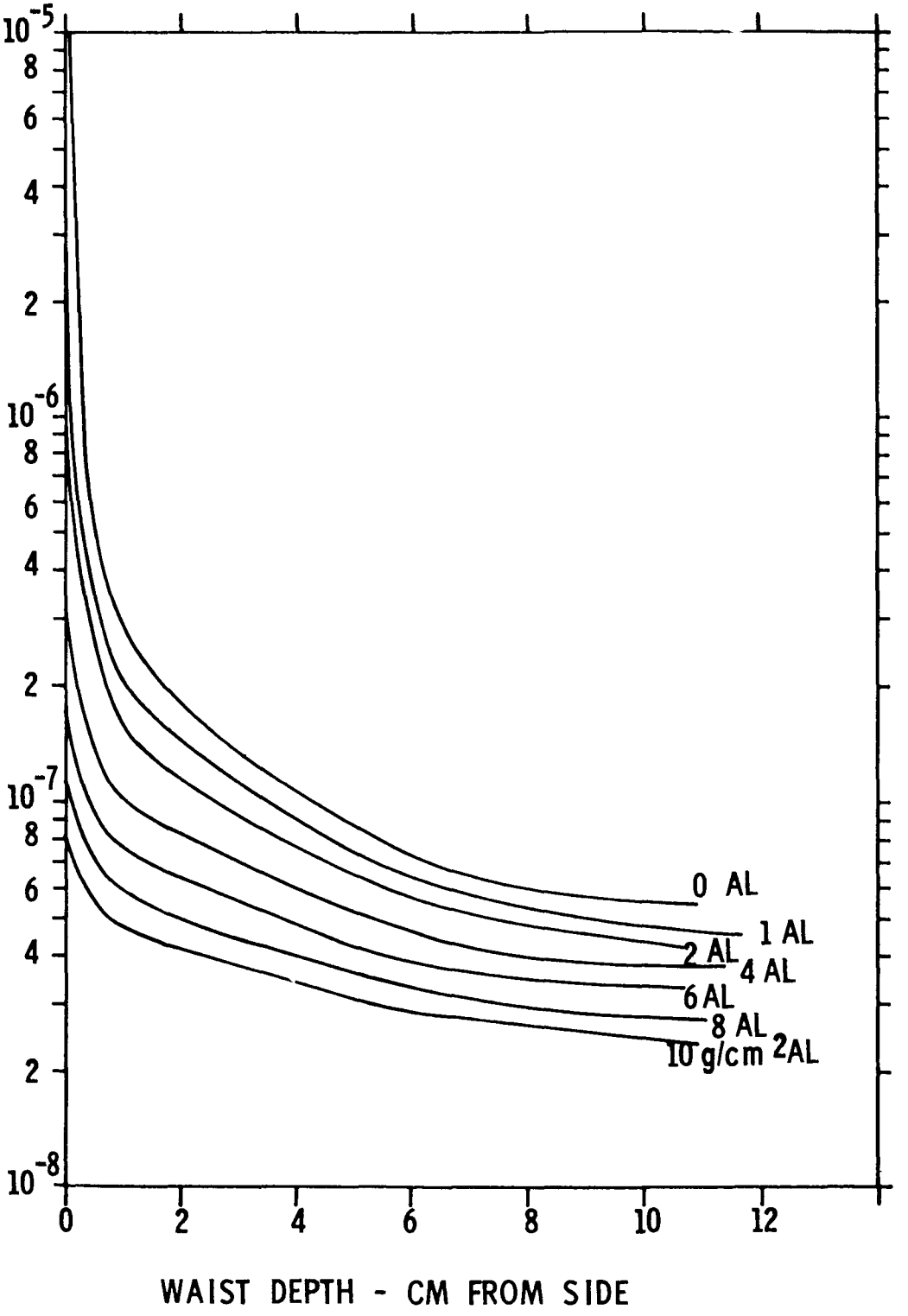
PRIMARY PROTON DOSE vs LATERAL WAIST DEPTH FOR VARIOUS ALUMINUM SHELL SHIELD THICKNESS. E^-3 SPECTRUM
10^-5
8
6
4
2
10^-6
8
6
4
2
10^-7
8
6
4
2
10^-8
0 AL
1 AL
2 AL
4 AL
6 AL
8 AL
10 g/cm 2AL
0
2
4
6
8
10
12
WAIST DEPTH - CM FROM SIDE

FIGURE 7

ignores air in the lungs and bilateral asymmetry due to the heart; CHEST 2L takes these into account. It is seen from Tables 3 through 7 that to take account of lung air or bone structure is hardly worth the extra analysis effort and computing time for the proton dose.

The depth-dose pattern in the human body is felt to be of special significance[13] and so the doses at points laterally along the waist are plotted in Fig. 7 to show the representative pattern. It is seen from Fig. 7 and the tabulated values that a midline dose of 15 to 30 percent the skin dose is typical, dpending on shielding and spectrum in obvious ways.

Because of the normalization used in the values reported here, they may readily be applied to environment data. If a trajectory is known, the trapped proton flux of $E > 40$ Mev may be computed and integrated over the orbit.[14] If a specific solar flare proton event is estimated to have a spectrum denoted by n and size in protons/cm^2, both parameters integrated over the whole event, (or instantaneous flux in protons/cm^2-sec), then total dose (or dose rate) may be determined to any of the body points. An estimated flare size-probability curve can be converted to significant dose-probability[15] using these data and vehicle shielding assumptions. By simple descriptive geometry techniques and the codes here reported, the shielding required in specific vehicle designs may be computed so as to maintain a desired lower probability limit for specified organ tolerance dose.

---

13. K. L. Jackson, The Lethal Effectiveness of a Solar Flare-type Dose Distribution Delivered to the Rat, this symposium.

14. F. C. Perry, Proton Fluxes Along Trajectories Through the Inner Van Allen Belt, this symposium.

15. E. L. Chupp, D. L. Dye, B. W. Mar, L. O. Oncley, and R. W. Williams, Analysis of Solar-Flare Hazards to Manned Space Systems, The Boeing Company, D2-11608 (1961)

Paper E-1

LONG RANGE NASA SHIELDING REQUIREMENTS

J. Warren Keller
Headquarters, National Aeronautics and Space Administration
Washington, D.C.

Abstract

The NASA being confronted with the relatively short range problem of shielding for Project Apollo is faced with the task of developing a shielding technology which can be applied not only to Apollo but to future manned or unmanned missions as well. This task is the responsibility of the Office of Advanced Research and Technology working through the NASA centers and their contractors.

Future missions will present in many cases much more severe shielding problems than those encountered in Apollo, primarily because of their longer duration in affected regions in space. In this paper several types of future missions are discussed in a quite general manner to establish the magnitude of the shielding problems that may exist. Also, some of the uncertainties in environmental data and shielding calculations are discussed in an effort to clear up some misconceptions which exist as to the need for a significant shielding effort with respect to future missions.

It is obvious that the available on-board mass in the form of equipment, fuel, etc., must be utilized as shielding where possible. However, high effectiveness in the utilization of such mass may be difficult. The importance of accurate determination of such effectiveness is pointed out.

An effort is made to outline a general approach to the space vehicle shielding problem.

Introduction

All space vehicles will, to some degree, be exposed to particulate radiation fields in space. Consequently, the NASA, besides being confronted with the relatively short range problem of radiation shielding for Project Apollo, is faced with the task of developing a shielding technology which can be applied not only to Apollo but to future manned or unmanned missions as well. This task is the responsibility of the

Office of Advanced Research and Technology, within NASA Headquarters, working through the various NASA centers and their contractors.

The importance of the radiation portion of the total vehicle environment will depend to a very large extent upon the given mission. While the Apollo vehicle may be exposed to each of the major components of the indigenous radiation in space, future missions will present, in many cases, much more severe shielding problems for man and equipment, primarily because of their longer duration in the affected regions.

The purposes of this paper are:

(1) to outline, in a general sense, the nature and possible magnitude of the radiation shielding problem for several categories of future missions,

(2) to discuss some of the uncertainties in environmental data and shielding calculations and some of the reasons for wide variations in the results of dose calculations,

(3) to attempt to clear up some misconceptions as to the need for a significant shielding effort with respect to future space vehicle missions, and

(4) to outline a general approach to the space vehicle shielding problem.

A significant problem exists with respect to the protection of certain components of unmanned vehicles from damaging radiations in space. This problem, however, will not be considered in this paper, which is devoted primarily to the problem for manned missions. Also the problem of shielding against radiation leakage from on-board reactor power sources is not considered.

Mission Categories

Most future manned missions may be categorized, in a broad sense, into groups based on the nature of the radiation environment which will be encountered. In this section several such categories are discussed, in a quite general manner, to establish the nature and magnitude of the shielding problems that will exist.

The curves of dose as a function of shield thickness for each of the categories considered are for infinitesimally small samples of tissue located at the center of a spherical shield (model discussed later in this paper) and were derived primarily from data given in the sources below. [1-5]

---

1. Keller, J. W., A Study of Shielding Requirements for Manned Space Missions, Convair-Ft. Worth Report FZK-124 (1960).

2. Bailey, D. K., "Time Variations of the Energy Spectrum of Solar Cosmic Rays in Relation to the Radiation Hazard in Space" Journal of Geophysical Research, 67, pp 391-296 (1962).

References 3-5 continued on next page.

The curves should be considered only as approximations to the actual doses and should not be taken as definitive. However, they should be of sufficient accuracy to illustrate rather well the relative importance of the various components and the magnitude of the shielding problems. The curves for the solar protons are based on observations over a portion of the last solar cycle. There is, of course, no assurance that this represents the worst possible case.

Two-Week Lunar Mission- Figure 1, illustrates the radiation environment for a two week lunar mission such as Apollo and is included primarily as a point of comparison with the immediate short range shielding problem. The solar proton component is based on the occurrence of a single "typical" large event[2] which in itself is a rather unlikely happening. Even with the occurrence of such an event one is well below the dose limits[6] presently considered for Apollo if only quite thin shields are used. The galactic cosmic radiation and the Van Allen belts are seen to be of very little significance for this type of mission.

Interplanetary Missions- The radiation problem for interplanetary missions will depend to a large extent upon the manner in which the missions are carried out. Consequently these types of missions are divided into two categories for consideration of the radiation problem. The first category [Fig. 2(a)] represents those missions which are characterized by high thrust, rapid traversal of the Van Allen radiation belt of which the two-week lunar mission discussed previously may be considered a special case. The second category [Fig. 2(b)] on the other hand, is representative of missions accomplished with low thrust vehicles, such as those utilizing electric propulsion, which spiral slowly through the region of the trapped radiation. The curves for both cases are based arbitrarily upon a two to three year mission duration.

---

3. Malitson, H. H., and Webber, W. R., A Summary of Solar Cosmic Ray Events, Solar Proton Manual, Goddard Space Flight Center Report X-611-62-122, pp 1-17, (1962).

4. Schaefer, H. J., "Radiation and Man in Space", Advances in Space Science, Vol. 1, (edited by F. I. Ordway, III), Academic Press, New York (1959).

5. Tobias, C. A., Radiation Hazards in High Altitude Aviation, WADC Technical Report 52-119, May 1952.

6. Gill, W. L., "Shielding Requirements for Apollo", paper presented at symposium on "Protection Against Radiation Hazards in Space", Gatlinburg, Tennessee, Nov 5-7, 1962.

It is seen that the radiation problems encountered in these two categories differ. In the high thrust case the problem is primarily that resulting from solar protons while in the case of the low thrust trajectory the trapped radiation presents the major problem. This difference of course, arises not through any difference in the solar proton or galactic cosmic ray environments but from the difference in exposure time in the Van Allen belt. It is noted that whereas about 10 gm/cm^2 will reduce the dose to a few hundred rem in the high thrust case, 80-100 gm/cm^2 are required to accomplish a similar reduction in the low thrust case. Also for large shield thicknesses, as in the case of the low thrust mission, secondary production in the shield (not considered in the curve in Fig. 2(b)) will become important making the dose still greater than that indicated in the figure.

It is seen from the graphs that as long as the tolerant mission dose is kept above several 10's of rem the controlling components as far as the shielding problem is concerned are the solar protons and the Van Allen belt protons for the high thrust and low thrust cases respectively. On the other hand, if the tolerant dose were lowered below this level one would be faced with the problem of shielding against primary cosmic rays - a very difficult task. Unless one is forced to live with such low tolerant doses much more shielding will be required for the low thrust than for the high thrust missions. On the other hand, the low thrust vehicles are likely to be able to afford considerably more shielding (weight-wise) than those using high thrust propulsion techniques.

Another source of radiation which may be a factor in interplanetary missions but has not been included in the above considerations is the existence of radiation belts surrounding other planets having magnetic fields. Some attention has been given to this problem by others.[7]

The picture as presented in Fig. 2(a) would also be indicative of the shielding problem for personnel manning a lunar base.

Orbital Missions- The nature of the radiation problem for orbital missions in the region occupied by the trapped radiation belt is indicated in Fig. 3. Here the missions may be divided into two general categories- (1) those utilizing equatorial orbits [Fig. 3(a)] and (2) those calling for polar orbits [Fig. 3(b)]. The primary type of mission for which these categories would apply would be the manned space station. Since it would be highly desirable to be able to leave a crewman in such a station for a period of from six months to a year the curves in Fig. 3 are based on a one year period. Contracting

7. Singer, S. F., "Some Considerations of Expected Radiation Belts of Planets Mars and Venus", Advances in Astronautical Sciences, Vol. 6, The MacMillan Co., New York (1961).

or expanding this period, however, would not significantly effect the relative importance of the various components as indicated but would only change their absolute magnitude. The shaded areas indicated for the Van Allen belt radiation in Fig. 3 are representative of the variation in radiation intensity over altitudes from about ~900 to ~7500 km.

The chief difference in the radiation environment for the polar orbit as opposed to the equatorial orbit is the disappearance of the solar proton radiation in the latter case. This, of course, is due to the shielding afforded by the earth's magnetic field, as is the variation noted for the galactic cosmic radiation. Also a difference is noted in the magnitude for the trapped radiation component for the two cases since, in the case of the polar orbit, less time is spent in the region of high proton flux. For any orbital inclination between the two extremes represented in Figs. 3(a) and 3(b) the magnitudes of the components will lie intermediate to those shown for the two cases. The effects of the trapped electrons in the Van Allen belt are not indicated on the curves in Figs. 1, 2, or 3 since their effects to man are not comparable with those posed by the protons for shielding thicknesses of interest.

It is seen that for any manned orbital vehicle operating at altitudes between ~900 and ~7500 kilometers the Van Allen belt protons present the controlling component of the radiation as far as biological shielding is concerned and are of a magnitude so as to require rather thick shields if the desired staying times for space station crews are to be obtained. The sensitivity of the required shielding on altitude is illustrated quite well in Fig. 3 since the spread in shield thickness to attain the same dose varies by as much as ~100 gm/cm^2 over the range of altitudes considered.

Of course all orbital operations need not be in the regions between ~900 and ~7500 kilometers. For orbits at higher altitudes the shielding problem slowly approaches the case illustrated in Fig. 2(a) while those at lower altitudes approach those shown in Figs. 3(a) and 3(b) with the Van Allen component removed.

It is apparent from the foregoing discussion that for the early manned missions (missions in the category represented by Fig. 2(a), or space stations orbiting beneath the trapped radiation belts) the shielding problem will be governed primarily by the providing of protection from the solar proton environment.

It is also clear that missions will surely be undertaken in a later time period for which the governing radiation component as far as shielding is concerned will be the trapped protons. Based on observations to date the shielding problem for these missions will be much more severe (weight-wise) than those imposed by the solar protons due partially to the harder spectrum which characterizes the trapped

radiation. As was pointed out earlier such large shielding thicknesses give rise to the additional problem of secondary production. Indeed, in some cases, these missions will be relegated to the later time period principally because of the magnitude of the shielding problem.

Preliminary studies[8-9] have indicated that electromagnetic shielding (using superconducting magnets) may be superior to passive shielding in cases where a high energy cut-off is required and/or large volumes are to be shielded. Consequently, it appears that such systems may be particularly useful for these missions. Superconducting magnets of the nature needed for such an application are a number of years off since they represent a rather large advancement in the present state of the art, however, studies are continuing in this area. A detailed discussion of such systems is beyond the scope of this paper.

Discussion of Uncertainties

Before a logical approach to the problem of developing a technology for use in designing space vehicle shields can be formulated an assessment must be made of the uncertainties which exist in both the environmental data and existing techniques for shielding calculations. A detailed discussion of such uncertainties was given in an earlier paper.[10]

In this section several selected topics are discussed which may have an important influence on the proper approach to the shielding problem. It is hoped that some apparent misconceptions which have arisen recently concerning the magnitude of the shielding problem may be illuminated by these discussions.

Typical Solar Flare- During the last few months much attention has been directed toward the "typical" solar flare presented by Dr. D. K. Bailey.[2] This hypothetical solar proton event represented an attempt at correlating continuous radio observations with direct balloon, satellite, and rocket observations to arrive at a time history for a typical large event.

---

8. Levy, R. H., "Radiation Shielding of Space Vehicles by Means of Superconducting Coils" ARS Journal, 31, pp 1568-1570 (1961).

9. Dow, N. F., Shen, S. P., and Heyda, J. F., "Evaluation of Space Vehicle Shielding," General Electric Space Sciences Laboratory Report R62SD31, April 1962.

10. Keller, J. W., "Uncertainties in Space Radiation Shielding Calculations," paper presented at ARS Space Flight Report to the Nation, New York, N.Y., October 9-15, 1961.

A cross plot of Bailey's flux versus energy curves (time as a parameter) are shown in Fig. 4(a) in the form of integral flux as a function of time with energy as the parameter. The dashed portion of the curves represent extrapolations in time beyond that given by Bailey. The dotted curve in Fig. 4 represents a curve derived by Fichtel, Guss, and Ogilvie[11] to envelope the highest integral fluxes >100 Mev which have been experimentally observed for solar proton events to date and is included for comparison with the Bailey "typical" event.

The time integrated integral and differential spectra derived from the curves in Fig. 4(a) are shown in Fig. 4(b) while the time integrated dose (for the entire event) is given as a function of shield thickness in Fig. 5(a). The curve in Fig. 5(a) again represents the dose in an infinitesimally small tissue sample at the center of a spherical shield.

Shortly after Bailey's paper was published the tolerance dose values[6] which are proposed for project Apollo became known. These dose values are more liberal (and perhaps more realistic) values than many persons had allowed themselves to consider in the past. Using Bailey's flare, Schaefer[12] made depth-dose calculations in a spherical phantom wrapped by shielding[12] (model to be discussed later) which yielded values which were of little concern (i.e. skin dose of 19r behind 8 gm/cm^2 of shielding) when compared to the allowable dose values. It has since that time, been generally accepted in many quarters that the Bailey model flare has resulted in greatly reduced doses compared to earlier calculations based on direct observations.

If the earlier dose calculations are compared with dose calculations for the Bailey flare which are made in the same manner (i.e. dose in infinitesimally small sample of tissue at the center of a spherical shield) the agreement is quite striking. Fig. 5(b) is a comparison in this manner with the earlier calculations of Foelsche[13] based on direct experimental measurements for three large events. Foelsche's curves are very nicely bracketed by those based on Bailey's typical flare (solid dots) and his estimates of possible upper limits for observed flares (triangles and circles).

It is evident, that the magnitude of the shielding problem has been somewhat reduced by the appearance of liberal tolerant doses and not by the acceptance of the Bailey "typical" flare. It would not

---

11. Fichtel, C.E., Guss, D. E., and Ogilvie, K. W., Details of Individual Solar Particle Events, Solar Proton Manual, Goddard Space Flight Center Report X-611-62-122, pp 19-54 (1962).

12. Schaefer, H. J., "Protection Against the Solar Flare", Astronautics Vol 7, No. 8, pp 24-25 (1962).

13. Foelsche, T., "Radiation Hazards in Space" paper presented at Fall General Meeting of the AIEE, Detroit, Michigan, October 15-20, 1961.

be wise at this point, however, to feel that dose tolerances for all future missions will be as liberal as those proposed for Apollo. It seems certain that as weight becomes less of a problem the question will change from what can be tolerated to what would we like to tolerate. Also since the length of time over which detailed observations of solar proton events have been made is quite small and our statistics are few it cannot be said with any degree of certainty that we have observed the largest events which are possible. Also, it appears quite improper to correlate size or frequency of events with any other physical phenomena such as sun spot cycles when one considers that detailed observations have been made during but one cycle.

Models For Dose Calculations- Consider now the problem which has been referred to earlier- the selection of models for dose calculations. Much of the disagreement among dose calculations made by different persons results from differences in the models used. Three general types of models are depicted in Figs. 6(a) and 6(b) and 6(c). The pictured rays are for skin dose. The model in Fig. 6(a) involves the calculation of the dose in an infinitesimally small sample of tissue at the center of a spherical shield while in Fig. 6(b) a spherical tissue phantom is surrounded immediately by the shield. Figure 6(c) depicts a model similar to Fig. 6(b) where an attempt is made to assess the relative sizes of the man and the shielded volume. Figure 6(c), of course, represents a more accurate type of calculation than the others but requires knowledge of the vehicle dimensions which is not practical unless calculations are being made for a specific vehicle. Model (b) has the advantage of lending itself easily to depth-dose calculations while (a) can be used only for calculating a quantity which is representative of skin dose but should, in most cases be divided by roughly a factor of from one and one-half to two to allow for self-shielding.

It should be noted that the skin dose calculated using model (b) will always be less than that for (a) since the path length traversed by the radiation in penetrating the shield in (b) is greater than or equal to that for (a) at all angles. The same is true for (b) and (c) with the depth dose in (b) being less than that for (c) at every point except the center. It is obvious that the value for skin dose obtained for (c) will tend toward that for (a) as the shielded volume becomes large with repsect to the phantom. As an example of the different values which may be obtained by using (a) and (b), the skin dose for the Bailey "typical" flare behind 10 gm/cm^2 is$\sim$53/2=26 R for (a) and 10 R for (b). The correct value should lie between these values. The importance of making clear the techniques which are used in arriving at dose values is clearly seen.

On-Board Mass As Shielding- In arriving at a minimum weight vehicle-shield system one must make maximum use of any on-board mass (for other purposes) as shielding. There will always be a considerable amount of such mass on board a manned space vehicle and, indeed there are some persons who are expressing the rather naive viewpoint that the whole shielding program should be eliminated since the on-board equipment can more than take care of all the shielding problems for manned space flight by offering $\sim$10 gm/cm^2 of protection. It is obvious from the discussions in an earlier section that there probably exist more formidable problems than those resulting from solar protons unless we are willing to rule out, for manned operations, rather large regions of space near the earth as well as the use of some methods of propulsion without even trying to solve the problem. It has been shown that many more than 10 gm/cm^2 are involved in these cases.

The utilization of on-board mass as shielding is an area of consideration which, no doubt, will always appear more attractive than it turns out to be in practice. The most efficient use is hampered considerably by the fact that all vehicles can not be shields first and operational vehicles second. Also the types of equipment which are involved are far from being homogeneous in their mass distribution thus surely leaving relatively thin spots, or holes, in the protective shielding. The effects of such holes and the importance of detailed geometry in making penetration calculations are illustrated in Fig. 7.

The plots in Fig. 7 show the distribution of shielding thicknesses for a hypothetical spherical shield as a function of solid angle. The first example in the figure is that of a constant thickness shield having a thickness of 10 gm/cm^2. A dose calculation for the point at the center of the sphere using Bailey's "typical" flare yields a value of 53 Rads. The second distribution shows the effect of making 9% of the solid angle have a 2 gm/cm^2 thickness while 18% of the solid angle is increased to 14 gm/cm^2. While the average shield thickness for this case is still 10 gm/cm^2 the dose is now almost doubled or 103 Rads. For a vehicle where one is utilizing on-board mass as shielding the thin areas or holes will, without doubt, be scattered about more in the manner illustrated in the third distribution in Fig. 7. Here the total percentage distributions are the same as in the previous case with an average of 10 gm/cm^2. In this type of situation one must be careful how he makes his penetration calculation. The dose rate has been calculated by dividing the shield into different numbers of equal increments of solid angle, calculating the penetration through each, based on its average thickness, and summing over the increments. The results are given in the table in Fig. 7 for each of several numbers of increments chosen. From these results it is obvious that significant errors may be encountered unless one takes increments, at least in the

region of the irregularities, which are comparable to the dimensions of the irregularities. Also it should be noted that the effect of "holes" in a shield upon the dose received will be a strong function of position within the shielded region. Procedures for calculating dose rates within a vehicle should be capable of handling quite detailed geometry if they are reliable.

Secondary Radiation- From the curves shown earlier one must conclude that in future missions the use of quite thick shields, $\sim$60-100 gm/cm^2, may be needed to afford protection from Van Allen belt protons. On the other hand, based on the observations to date and present conceptions of tolerable doses shields well under 20 gm/cm^2 may suffice for the cases where solar protons are the controlling component. The question then arises as to the importance of secondary radiation production in the shield.

Figure 8 shows the relative importance (on a Rad basis) of the secondaries to the primaries as a function of shield thickness for the trapped protons (a) and the solar protons (b).[14] It appears from these curves that the secondaries will not be of major importance in cases where solar protons are the major component however, their importance in the case of the thick shields which may be needed for protection from Van Allen belt protons is obvious. Consequently, work devoted to the determination of data on secondary production must be continued in support of the long range problem.

General Approach to Shielding Problem

Figure 9 is a flow chart showing how the various parts of the long range space vehicle shielding program within the NASA fit together to yield a final vehicle shield design.

The blocks entitled Detailed Transport Calculations (and associated experiments), and Conceptual Studies (and associated experiments) fit properly into the Advanced Research and Technology area as does general work on the methods to be used in the block titled Dose Calculations. In these areas work is carried out on a continuing basis in support of the more specific work on particular vehicles signified by the blocks titled Space Vehicle Geometry, Shield Design, and Experimental Shield Verification as well as the more specific aspects of the Dose Calculations.

The detailed transport calculations should supply basic data for the dose calculations which, for the reason discussed in the previous section, should probably be restricted to rather simple transport considerations so as to accomodate rather complex geometries. The detailed transport techniques, on the other hand, could be developed to the point that they could be used to handle detailed geometry in special regions of a shield as is indicated. Conceptual Studies is

---

14. Allen, R. I. et al, Shielding Problems in Manned Space Vehicles Lockheed Nuclear Products Report No. 104 (1960)

a rather broad heading given to those studies which yield information on such subjects as the selection of shield materials, proper ordering of materials, weight optimization, general techniques for efficient utilization of on-board mass, methods for shield verification, and at this point studies of active shielding techniques. The experimental checks which are indicated include the generation of basic data as well as the verification of analytical techniques.

The results of the conceptual studies are, of course, fed into both the preliminary determination of the vehicle geometry and the block called Shield Design which is essentially the iteration process in arriving at a shield design. The final shield is then verified experimentally as the final step.

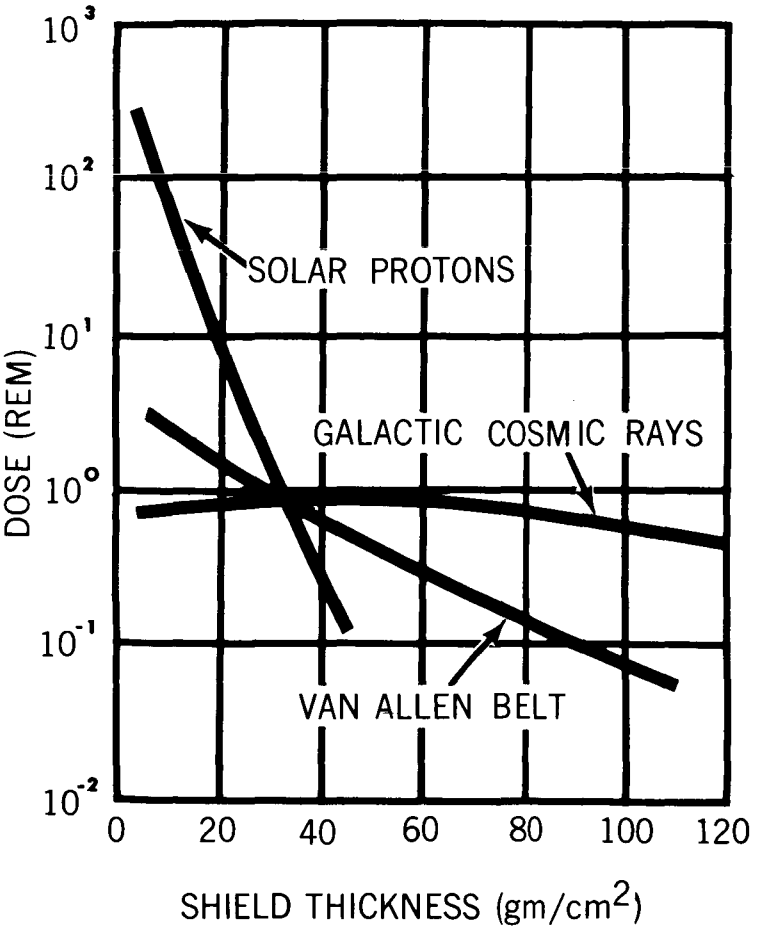

FIGURE 1

RADIATION ENVIRONMENT FOR TWO WEEK LUNAR MISSION

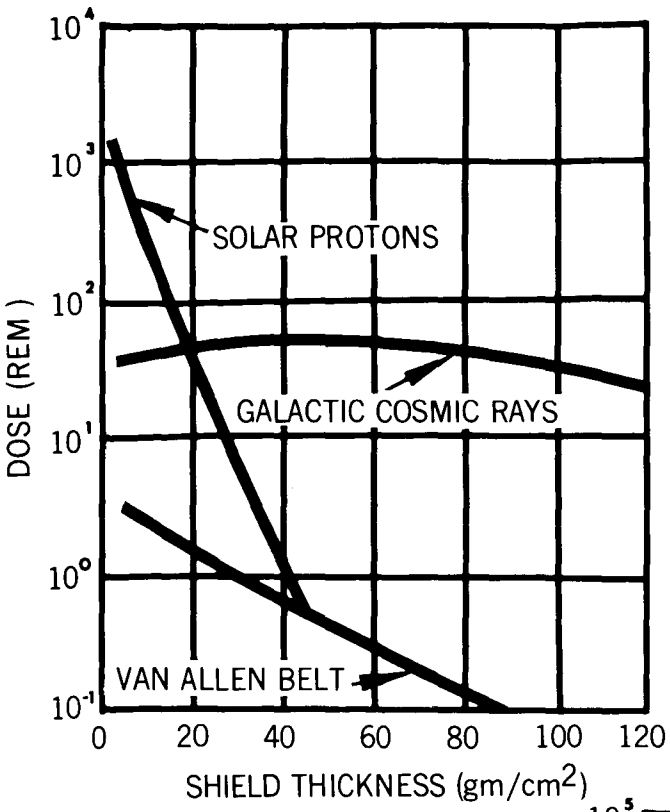

(A) HIGH THRUST

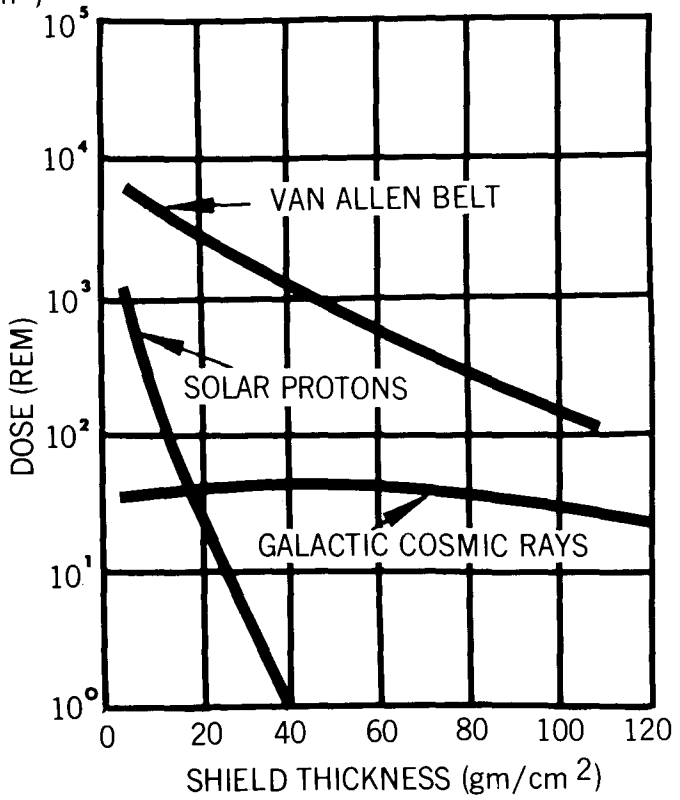

(B) LOW THRUST

FIGURE 2

RADIATION ENVIRONMENT FOR INTERPLANETARY MISSIONS

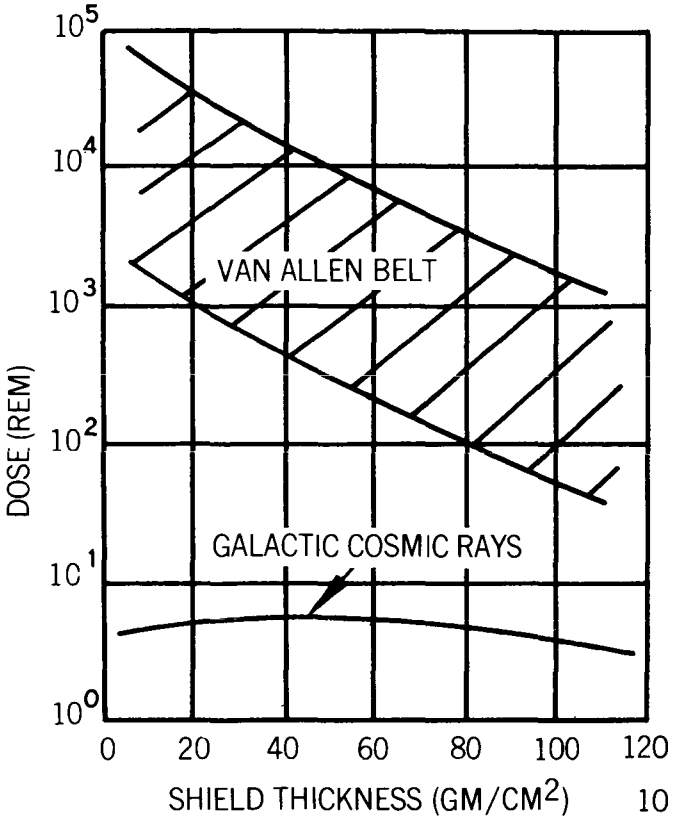

(A) EQUATORIAL ORBIT

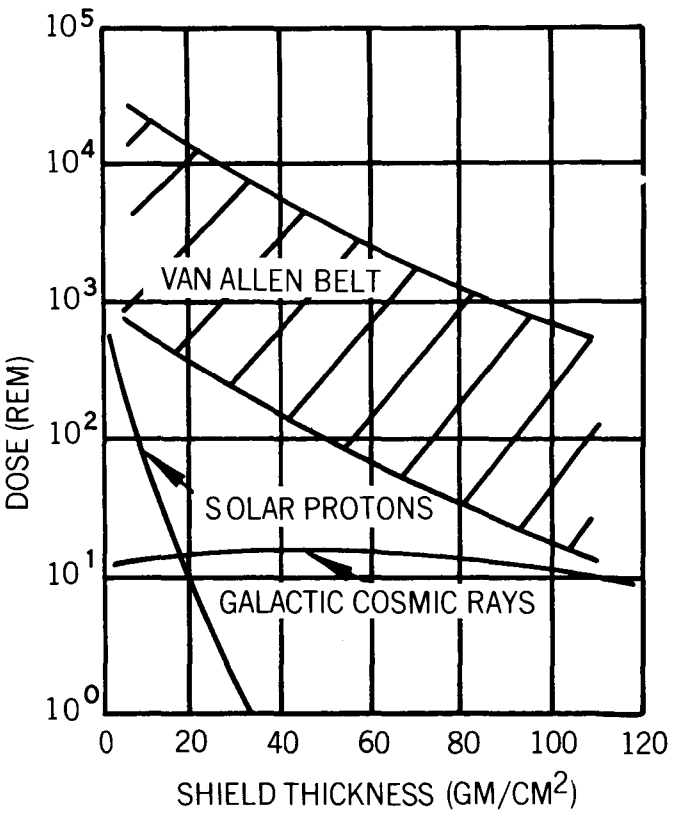

(B) POLAR ORBIT

FIGURE 3

RADIATION ENVIRONMENT FOR VEHICLES ORBITING IN VAN ALLEN BELT

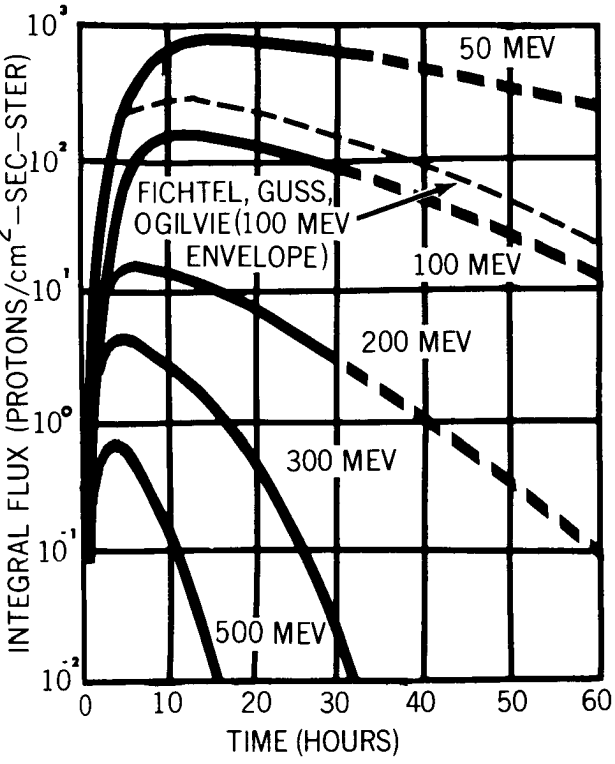

(A) TIME VARIATION OF INTEGRAL FLUX

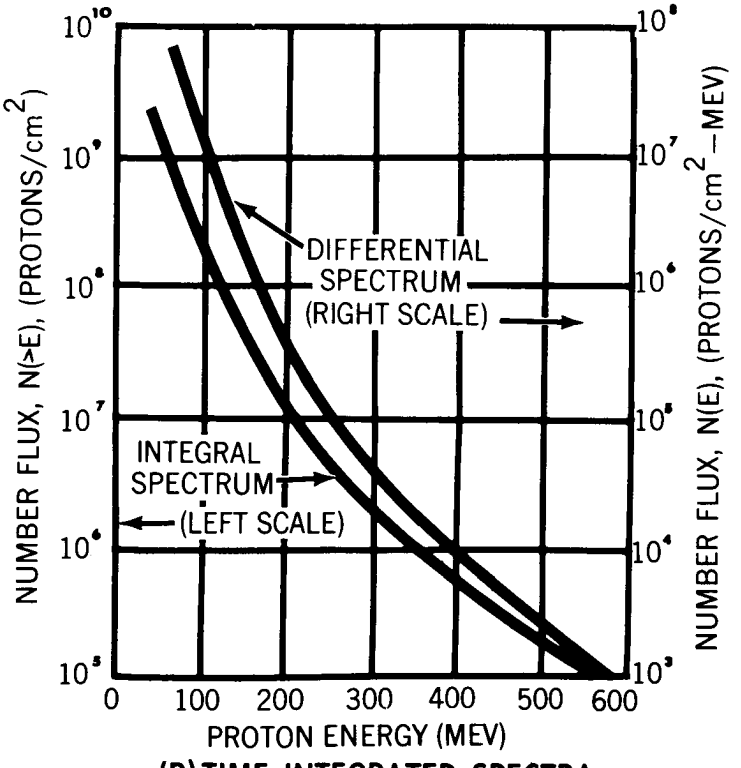

FIGURE 4 (B) TIME INTEGRATED SPECTRA

SPECTRAL CHARACTERISTICS OF BAILEY'S "TYPICAL" FLARE

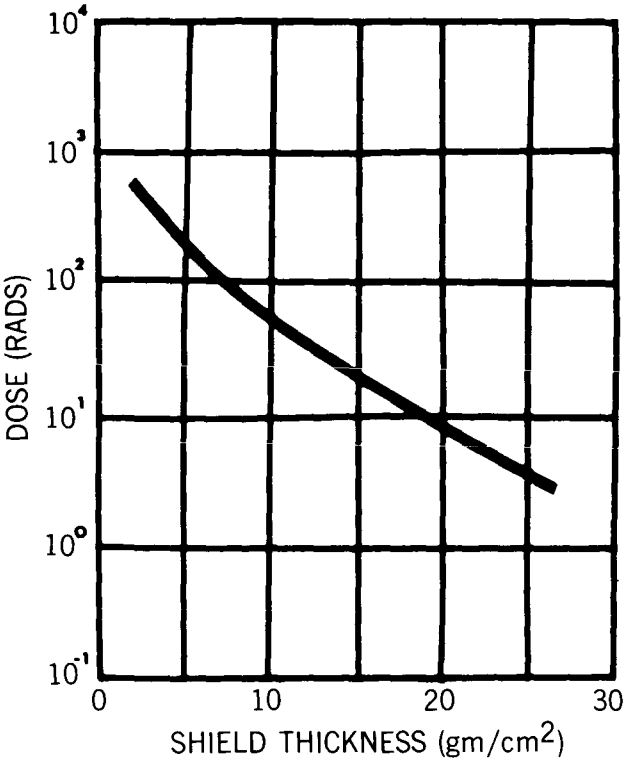

(A) EFFECT OF SHIELDING)

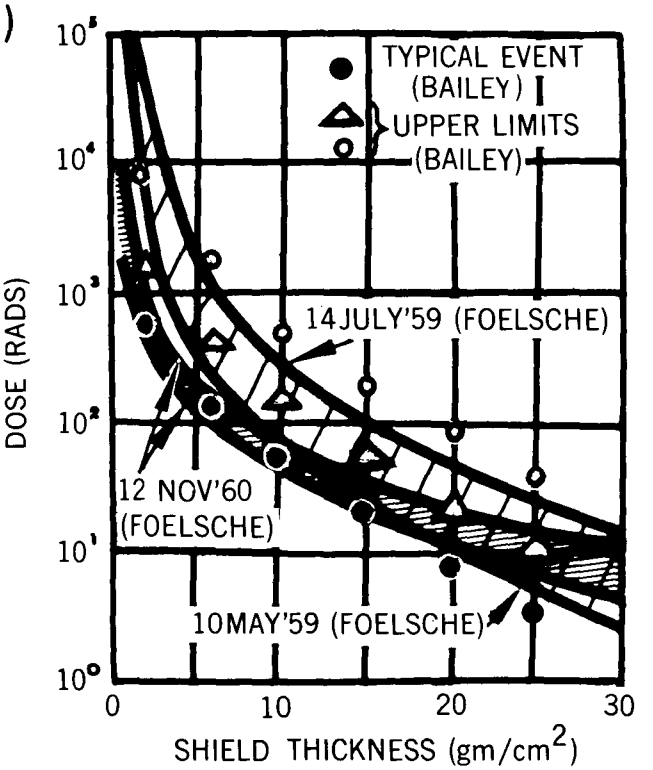

(B) COMPARISON WITH EARLIER ESTIMATES

FIGURE 5

DOSE FROM BAILEY'S "TYPICAL " FLARE

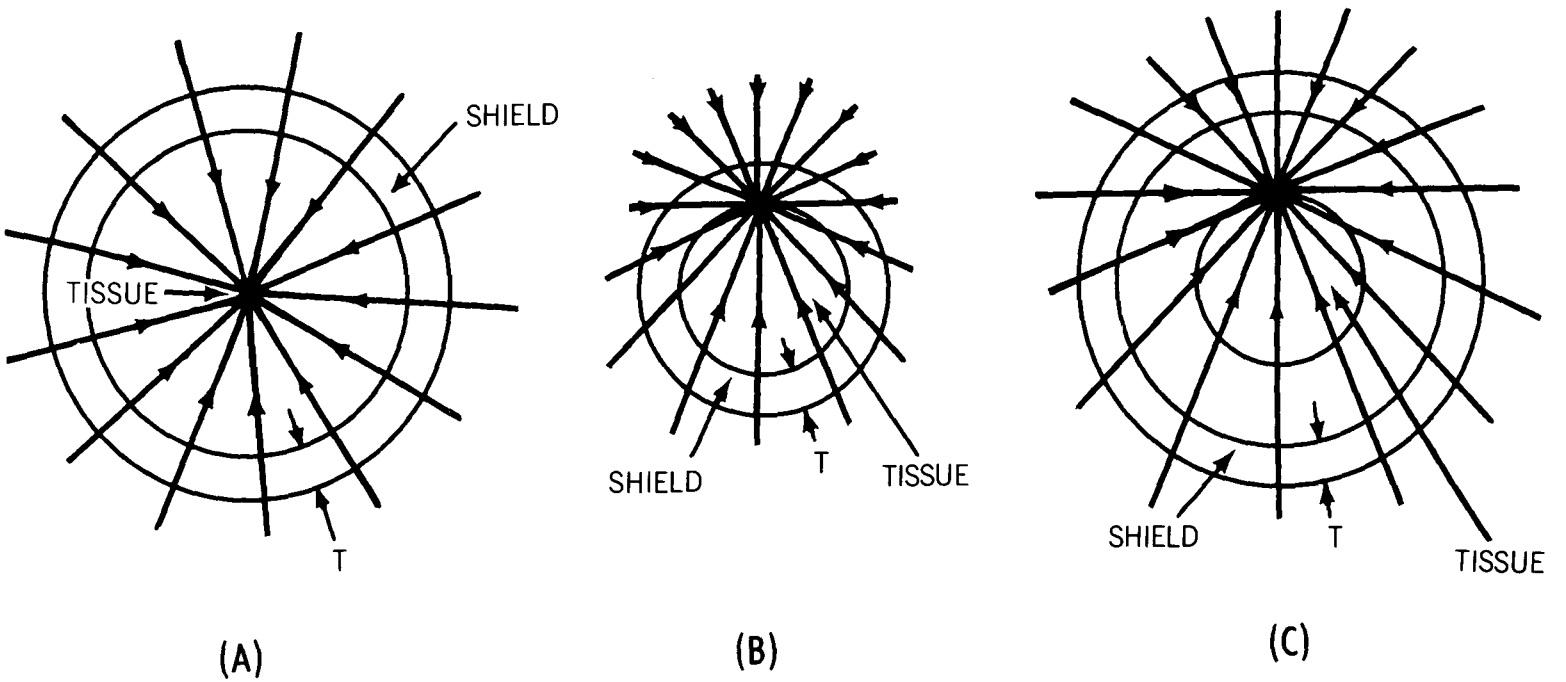

FIGURE 6

MODELS FOR CALCULATING DOSE

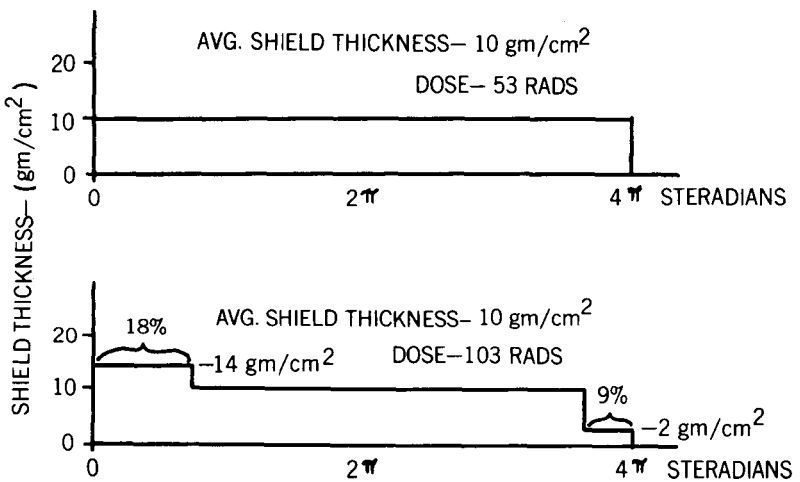

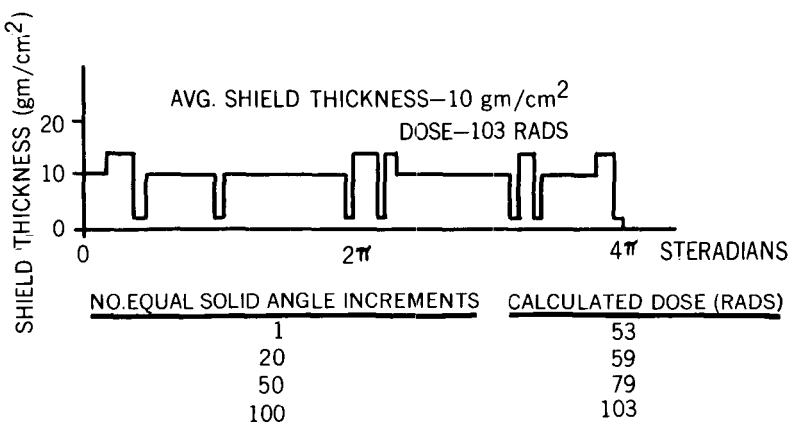

NO. EQUAL SOLID ANGLE INCREMENTS	CALCULATED DOSE (RADS)
1	53
20	59
50	79
100	103

FIGURE 7

UTILIZATION OF ON-BOARD MASS AS SHIELDING

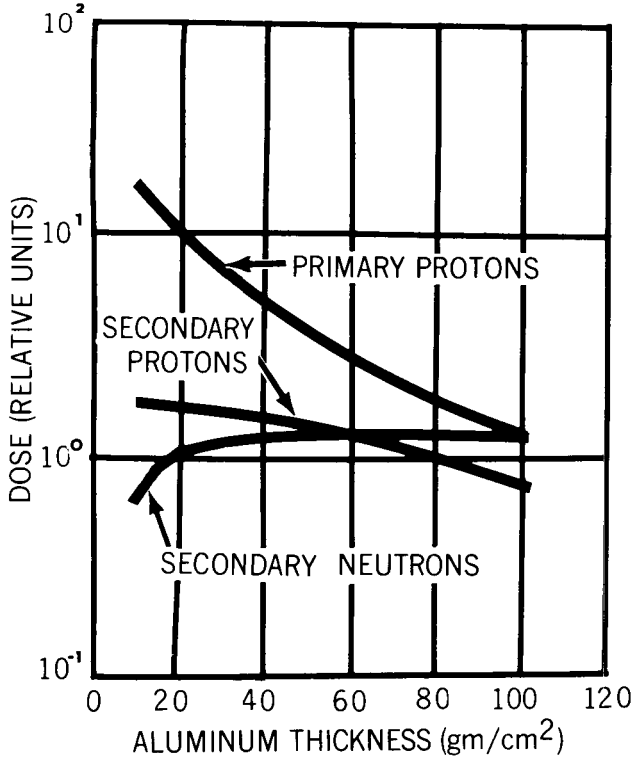

(A) TRAPPED PROTONS

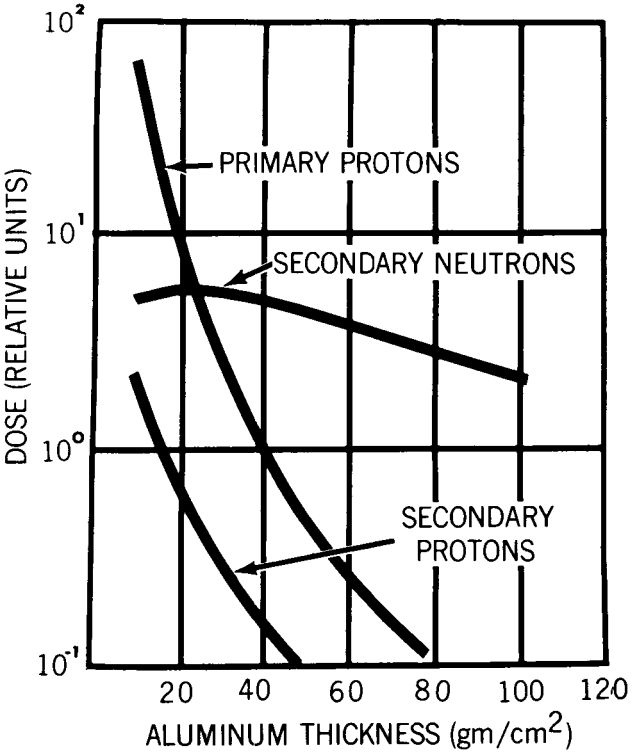

(B) SOLAR PROTONS

FIGURE 8

IMPORTANCE OF SECONDARY RADIATION

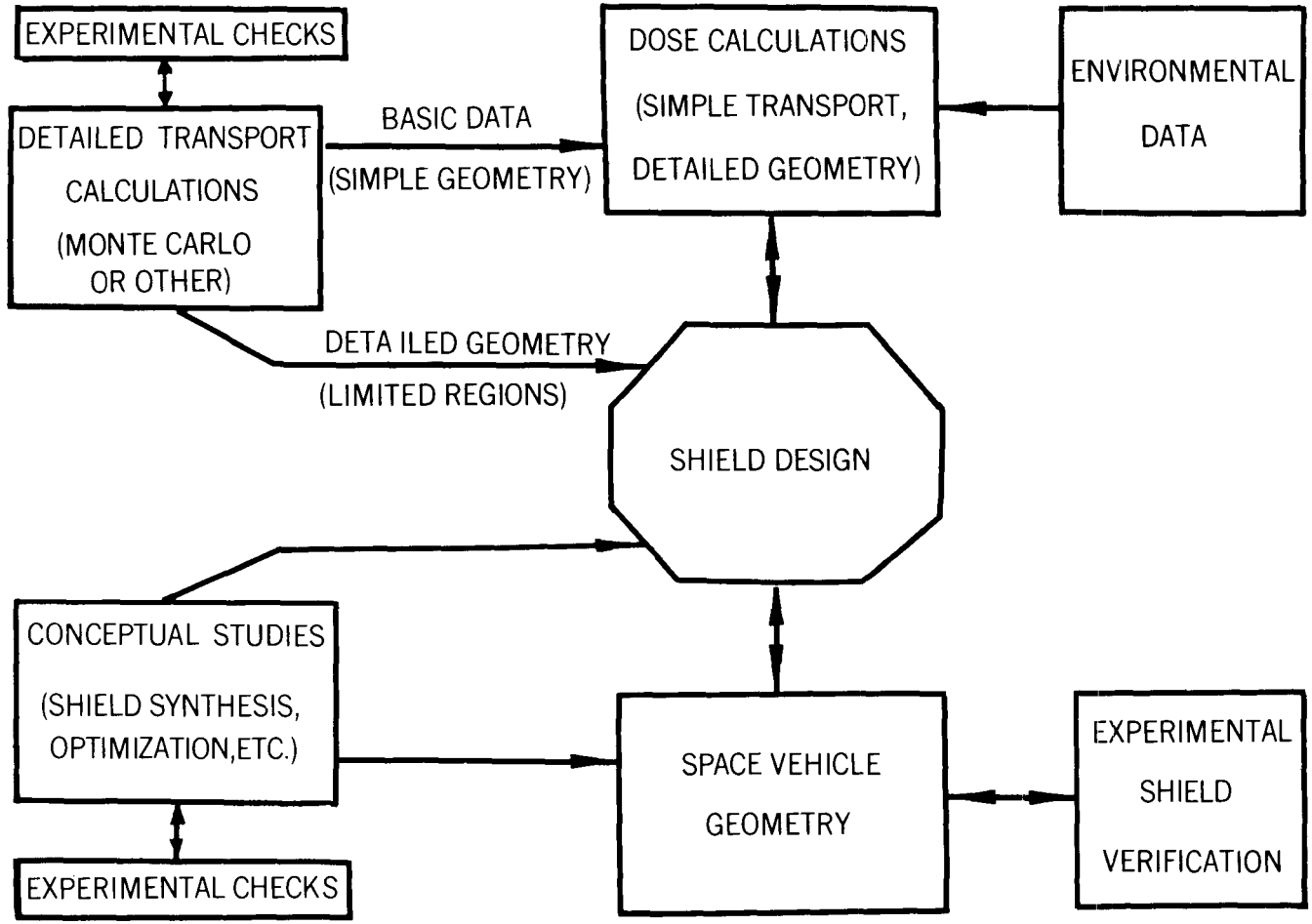

FLOW CHART FOR SPACE VEHICLE SHIELDING WORK

FIGURE 9

Paper E-2

COMPARISON OF MONTE CARLO AND IONIZATION CALCULATIONS FOR SPACECRAFT SHIELDING

K. A. More and O. L. Tiffany
Bendix Systems Division

ABSTRACT

Various methods have been used to calculate shield designs for manned space vehicles. The methods differ in the approximations used to describe the spacecraft geometry and the physical interactions of the space particles in the vehicle shield. Since calculation time is least for the methods with the most approximations, it is desirable to know what degree of approximation is permissible in designing shields. This paper compares the results of shield calculations using the Monte Carlo method and the more approximate ionization loss method.

The Monte Carlo method calculates the physical interactions following nuclear collisions and ionization loss. The ionization loss method considers only ionization loss of the incident protons. On a short-term mission the required shield is thin and the number of nuclear collisions by the incident protons is small. Therefore, both the increase in dose due to secondary particles from nuclear collisions and the decrease in dose due to nuclear absorption are small, and the dominant physical interaction is ionization loss. On the other hand, thick shields are required on long-term missions during which a large number of nuclear collisions will occur. The contribution to the astronaut's dose from the nuclear collision particles, especially the contribution from secondary neutrons, cannot be neglected. Consequently, there is a critical thickness in shield design at which shielding calculations must account for nuclear collisions.

To find this thickness, calculations were performed on a spherical shell aluminum spacecraft. The Monte Carlo code was basically the same one used in previous calculations, there

being added a subroutine for nuclear evaporation. The nuclear evaporation subroutine was patterned after the evaporation model used by Allen et al. The ionization loss calculation was taken directly from that part of the Monte Carlo program that computes ionization loss. Since the Monte Carlo calculation used the multigroup energy approximation, our ionization loss calculation also includes the multigroup approximation. While this method decreases the accuracy of an ionization loss calculation, its use here permits more direct comparison.

INTRODUCTION

During the last several years, different methods for calculating the radiation inside spacecraft have been tried. These methods have ranged from consideration of only the ionization loss of the protons to Monte Carlo treatments which take into account the three-dimensional processes in nuclear cascades. These calculations have been performed for geometries ranging from simple, one-material, spherical shell spacecraft to asymmetrical, multi-layered, spacecraft. But, because of the limitations of available computers it has been found necessary to limit calculations on complex geometry to simple calculation methods and to limit complex calculations to simple geometries. Thus, in order to perform calculations on the detailed designs of actual spacecraft, it has been necessary to develop approximate methods that give nearly the same results as the more exact methods. For this reason this paper aims to find how the simple calculation involving ionization loss compares with the complex Monte Carlo calculation for the simple, one-material, spherical shell, spacecraft geometry.

INPUT SPECTRA

The results presented in this paper are limited to missions of one year duration. The reason for this assumed duration was to smooth out the effects of solar flare fluctuations and to point out the differences in thick shields needed for long missions where the differences in calculation methods become consequential. The input proton spectra used in making the comparison between calculation methods were the expected yearly averages of cosmic protons during both periods of solar maximum and solar minimum. These averages were taken from data for spectra near the earth but outside of the man-made and natural radiation belts. The averages for solar flare

protons during solar maximum were obtained by normalizing the idealized spectrum derived by Bailey[1] to the average values[2] for the number of protons above 30 Mev and 100 Mev per year. These average values were an average of the three highest values reported by NASA for the years 1956, 1959, and 1960. The galactic cosmic ray spectra during solar maximum and solar minimum were taken from Bailey's paper. The input spectra used are shown in Figure 1.

METHOD OF CALCULATION

The Monte Carlo calculations were basically the same that we have used in the past[3]. The computer program was revised to include neutrons from evaporation and to include a different method for obtaining the dose inside the spacecraft. The approximate evaporation model developed by Allen et al[4] was incorporated as a subroutine in our program. We considered evaporation of both excited nuclei left after the intranuclear cascade and from compound nuclei formed by low-energy particle absorption. Since the limited data on intranuclear cascades prevented our considering cascades initiated by protons and neutrons below 150 Mev, we treated all collisions by particles below 150 Mev as producing compound nuclei.

The most significant modification to our previous calculations was in our method of obtaining the dose inside the spacecraft. In our previous calculations we found the radiation flux inside the spacecraft, assuming the inside was a vacuum. We then converted the radiation flux to dose by considering only the ionization loss this flux would have in plexiglass, the nearest material to tissue on which data were readily available for ionization loss.

Gibson[5] has computed the rate of energy removal of high-energy protons and neutrons in tissue as a function of particle energy. These energy removal rates include both ionization and nuclear collision mechanisms. We used his data in order to find the amount of energy removed by tissue inside the spacecraft from the neutrons and protons passing through the interior. Since no equivalent data were available for charged pions, only the ionization loss of the pions as they passed through the tissue was recorded. It should be noted that the energy removed from the particle bear is not necessarily deposited in the same location and no attempt was made at this time to determine the location at which the energy was absorbed. This can only be done when intranuclear cascade data are available for tissue. Our results can be interpreted as rads only if one assumes that

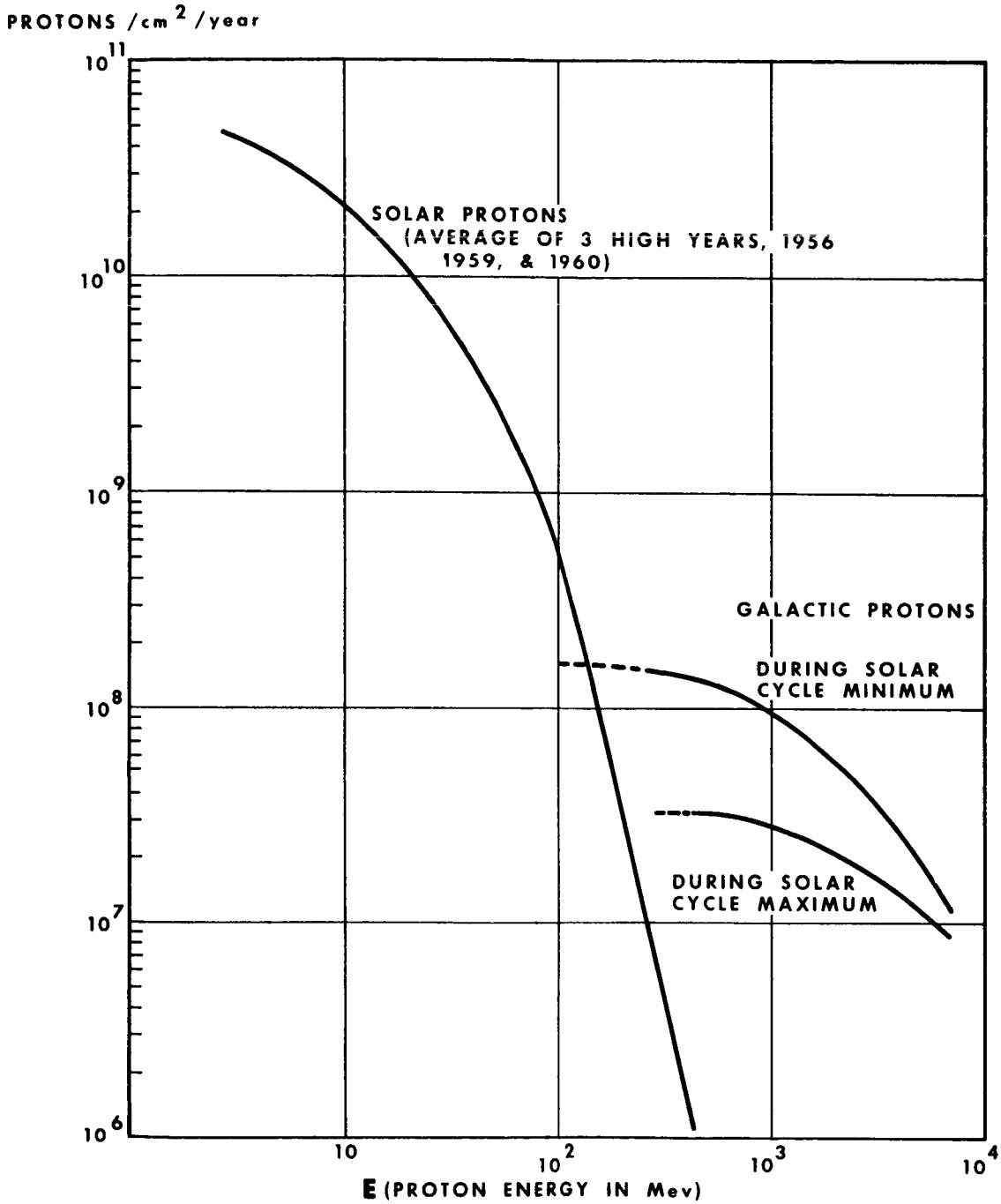

Figure 1 Omnidirectional Integrated Proton Flux. Number of Protons Having an Energy Greater Than E.

all the energy removed was absorbed in the tissue. In order to avoid any confusion on this subject, we have labeled our results energy removal dose and we define energy removal dose as the energy removed from a beam of particles by a gram of material.

The changes to our previous Monte Carlo computer program (to find the energy removal dose in tissue) were chosen to minimize the necessary modifications to the program while giving us enough information to compare ionization and Monte Carlo calculations and to account for the partial absorption of particles by the astronauts.

With the model used for this calculation it was assumed the inside of the spacecraft was homogeneously filled with tissue. The average energy lost by the particle in traversing the tissue was found by using Gibson's data for neutrons and protons, and ionization loss for pions. After summing all of the energy losses incurred by all the particles, the average energy loss per gram of tissue was found by dividing the total energy loss by the mass of tissue.

We began our calculations with a spherical shell spacecraft having inside dimensions comparable to the Apollo command module (inside diameter of 9 feet). The mass of tissue was taken to be 225 kg, which is roughly equivalent to the weight of three astronauts. This gives a density of .021 gm/cm^3 for the homogeneous tissue. Since this tissue density is thin, calculations were also carried out for a spherical shell spacecraft surrounding the same mass of tissue but having a density of one (inside radius of spacecraft equal to 37.33 cm). It will be seen that qualitatively the same conclusions are reached using either of these models for the tissue inside the spacecraft.

The ionization calculation used the ionization loss subroutine of the Monte Carlo program. This subroutine requires the incident proton spectrum to be divided into energy and angular groups. It is possible to treat ionization loss continuously by approximating the incident proton spectrum and proton range with power laws, and thus avoid energy groups. However, the use of the ionization subroutine was chosen here because it has the same approximations that were used in the Monte Carlo calculation. We believed this would give a sounder basis for comparing the two calculation methods.

Calculations were made for eighteen energy groups for the thin tissue and ten energy groups for the unit density tissue. The incident energies for these groups ranged from 10 Mev to 4000 Mev. The incident proton current, due to an assumed isotropic flux, was divided into 50 angular groups. The spacecraft walls were considered to be solid aluminum and the wall thickness was varied from 2 cm to 55.15 cm. The calculations were carried out on the Bendix G-20 computer.

DISCUSSION OF RESULTS

Three general conclusions can be drawn from our calculations: (1) For very thin spacecraft the predicted energy removal dose is nearly the same whether calculated by ionization loss or Monte Carlo. (2) The ionization loss calculation always predicted a higher energy removal dose than Monte Carlo. (3) For moderately thick spacecraft the energy removal dose for missions longer than a year was predicted to be higher during periods of solar minimum than solar maximum. These general conclusions were drawn from Figures 2 through 5. *

The first conclusion, that ionization loss and Monte Carlo should give nearly equal results for thin spacecraft was expected: because the probability of a nuclear collision in thin spacecraft is small so that the dominant shielding mechanism is ionization loss.

The second conclusion, that Monte Carlo results for the energy removal dose should be lower than for ionization loss was not predictable. There are two energy absorption processes: ionization loss and nuclear collisions. However, most of the nuclear collisions generate low-energy secondary particles and the dose from these low-energy secondaries may be higher than it would have been had the original particle passed through the tissue. Also, due to the energy difference between the parent particle and the secondary particles, the parent and secondary particles fall on different parts of the energy removal curve. Because of the nature of this curve, a high-energy proton may lose more energy per gm/cm^2 of path than low-energy secondaries. But, since there may be several secondary particles,

*Due to a question raised at the Gatlinburg conference on how Monte Carlo calculations compare with calculations based on ionization loss and exponential attenuation of the beam by nuclear collisions, the calculations for the latter case have been carried out and were added to Figures 2 through 5.

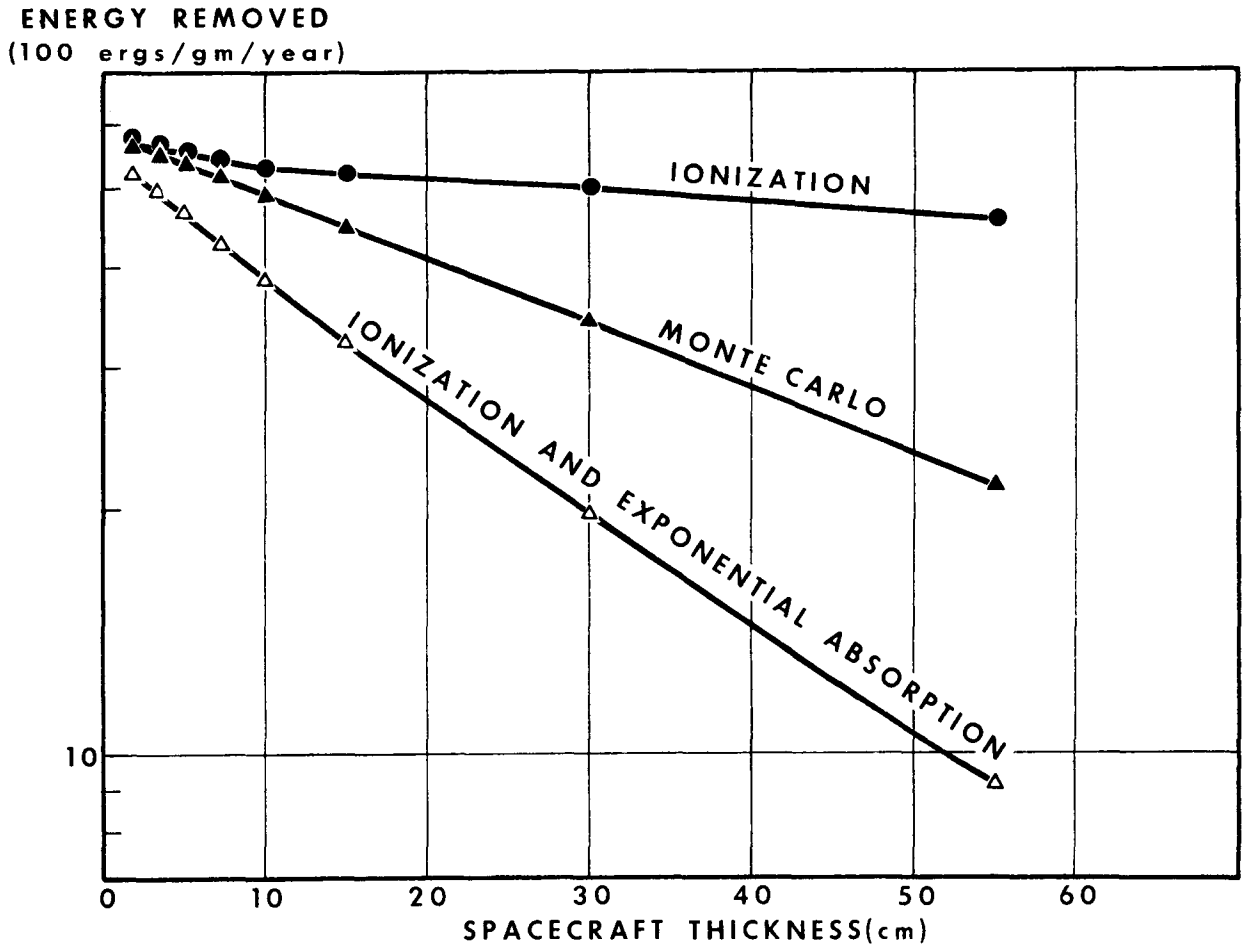

Figure 2 Comparison of Monte Carlo and Ionization Results for Aluminum Walled Spacecraft During Solar Minimum. Thin Tissue ($\rho = .021$)

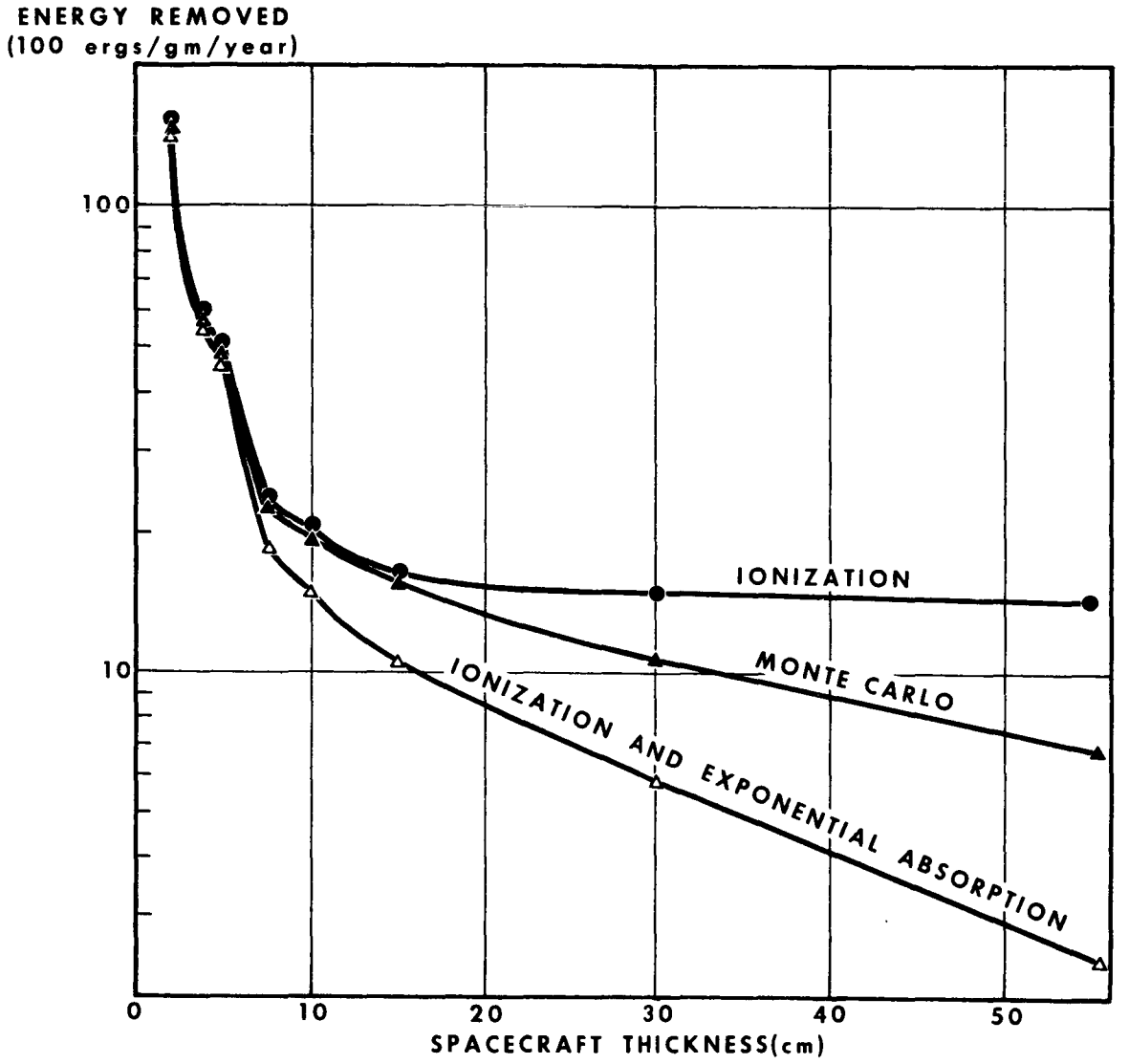

Figure 3 Comparison of Monte Carlo and Ionization Results for Aluminum Walled Spacecraft During Solar Maximum. Thin Tissue (ρ = .021).

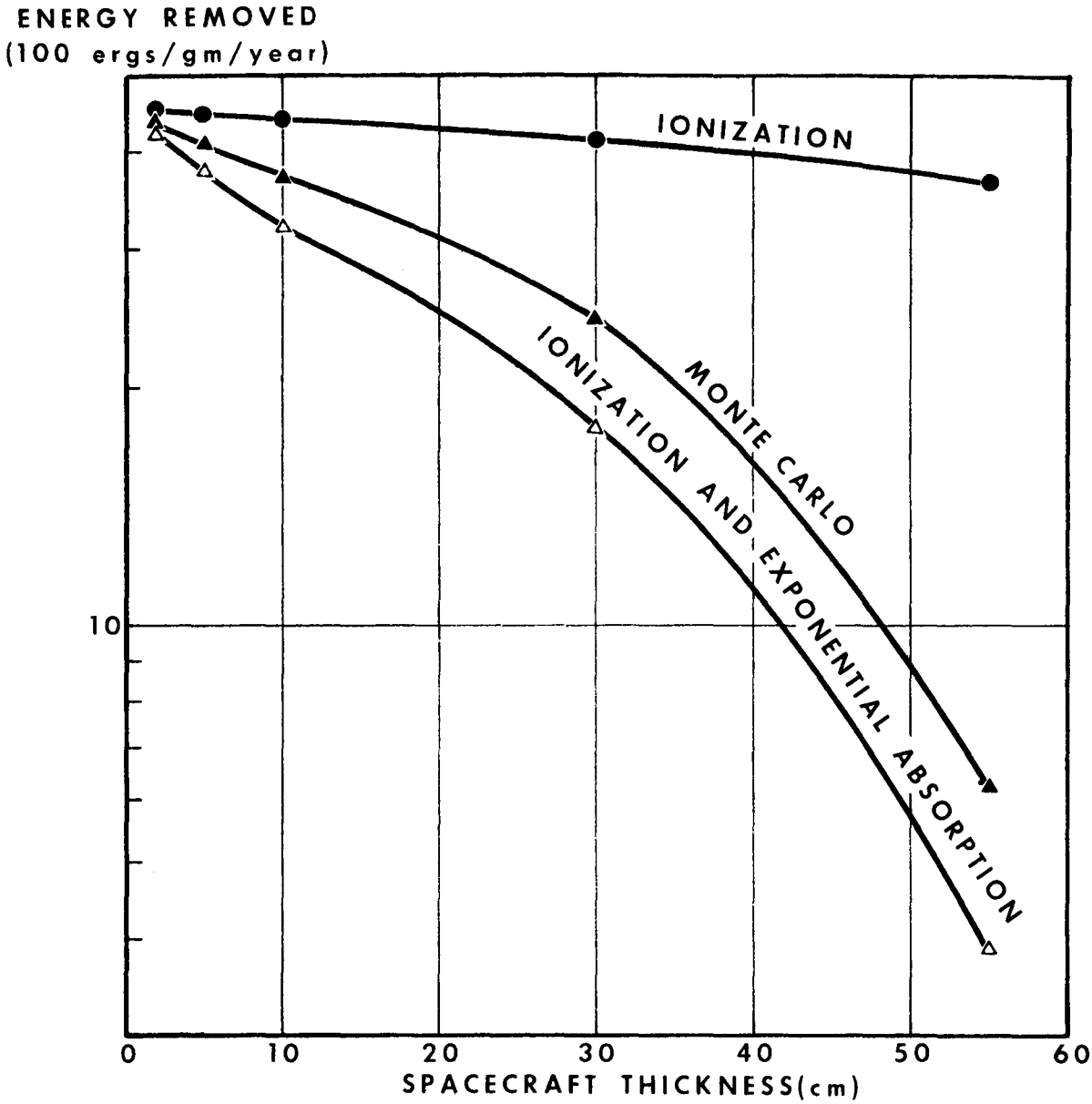

Figure 4 Comparison of Monte Carlo and Ionization Calculations for Aluminum Walled Spacecraft During Solar Minimum Normal Tissue (ρ = 1).

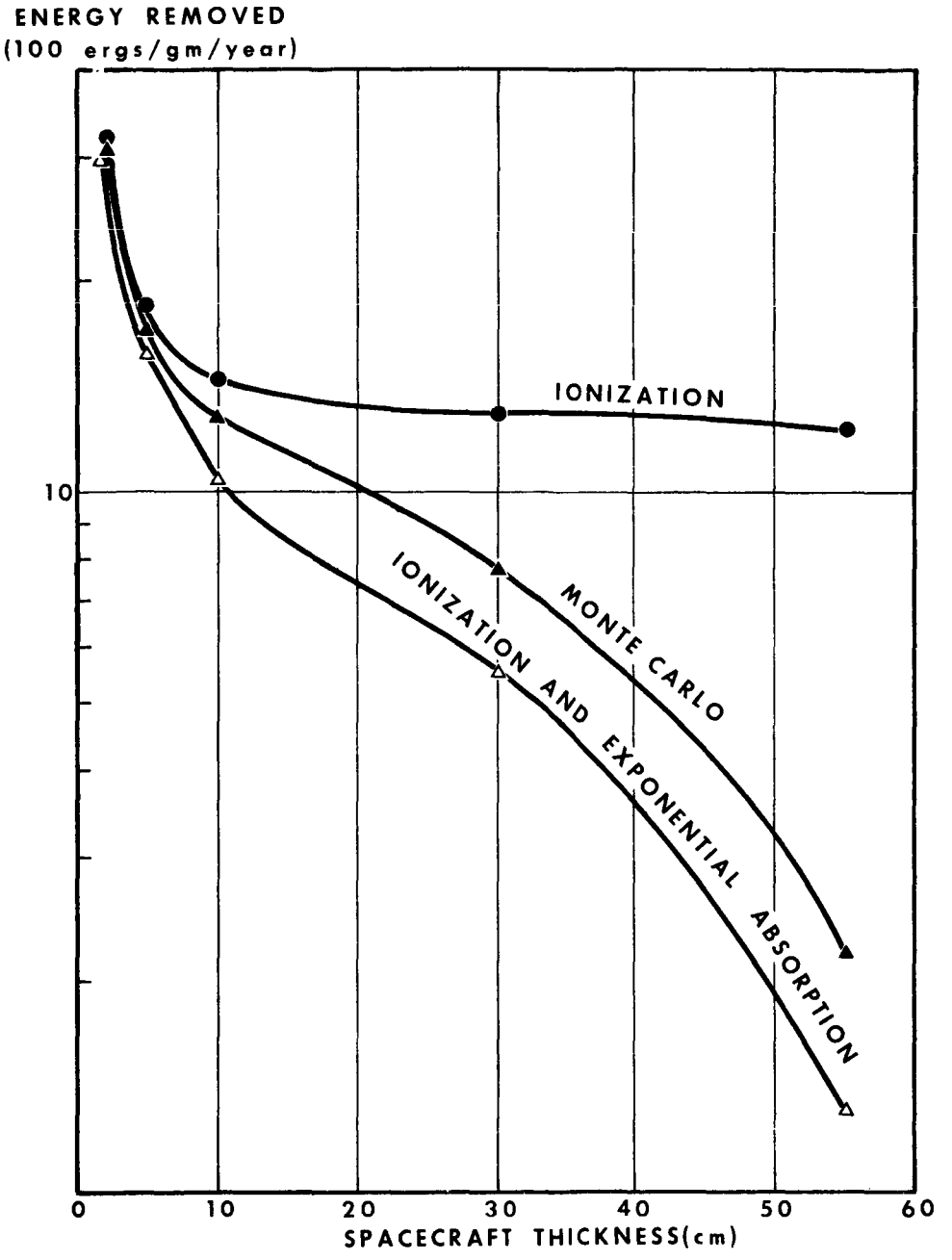

Figure 5 Comparison of Monte Carlo and Ionization Results for Aluminum Walled Spacecraft During Solar Maximum. Normal Tissue (ρ = 1).

the energy removal dose from all of the secondaries may be greater than it would have been had the parent particle passed through the tissue. Thus, with all of these mechanisms varying the energy removal dose, the only way to determine whether Monte Carlo results would be higher or lower than ionization results was to carry out the calculation.

The third conclusion, that the yearly energy removal dose for moderately thick spacecraft would be lower during solar maximum than solar minimum (see Figure 6), can be explained by the Forbush decreases during solar maximum and the large energy removal rates for high-energy particles. The Forbush decreases remove a considerable fraction of the galactic cosmic rays below 1 Gev, causing a considerable reduction in the energy removal dose. Moderately thick spacecraft, on the order of 5 cm thick, remove most of the solar flare particles below about 150 Mev. The solar flare protons above this energy that do penetrate the spacecraft fall into the minimum of the energy removal curve so that they contribute only a small dose. This can be seen in Figure 7 which shows the rapid attenuation of the energy removal dose from solar flare protons. Since the solar flare protons produce a minor dose and since there is a reduced number of cosmic rays during solar maximum, the dose should be higher during solar minimum, as our calculations show.

In the process of carrying out a Monte Carlo calculation, part of the results are the dose from both evaporation and secondary neutrons, and from pions. The pion dose that we found on the basis of only ionization loss of charged pions was two orders of magnitude less than the total energy removal dose, and therefore is of little interest. The neutron energy removal dose was an appreciable fraction of the total dose for all but the very thin spacecraft. During solar maximum, the evaporation neutron energy removal dose is higher than the secondary neutron dose for thin spacecraft (see Figure 8). The reason for this is the low production rate of secondary neutrons in thin spacecraft, and the high production rate of evaporation neutrons by solar flare protons in the 10 to 100 Mev energy range. In thicker spacecraft many of the evaporation neutrons are absorbed and more secondary neutrons are produced. This results in a nearly constant neutron energy removal dose with increasing spacecraft thickness.

The absence of low-energy protons during solar minimum changes this effect. During solar minimum the energy removed from evaporation neutrons was always less than from secondary neutrons (see Figure 9).

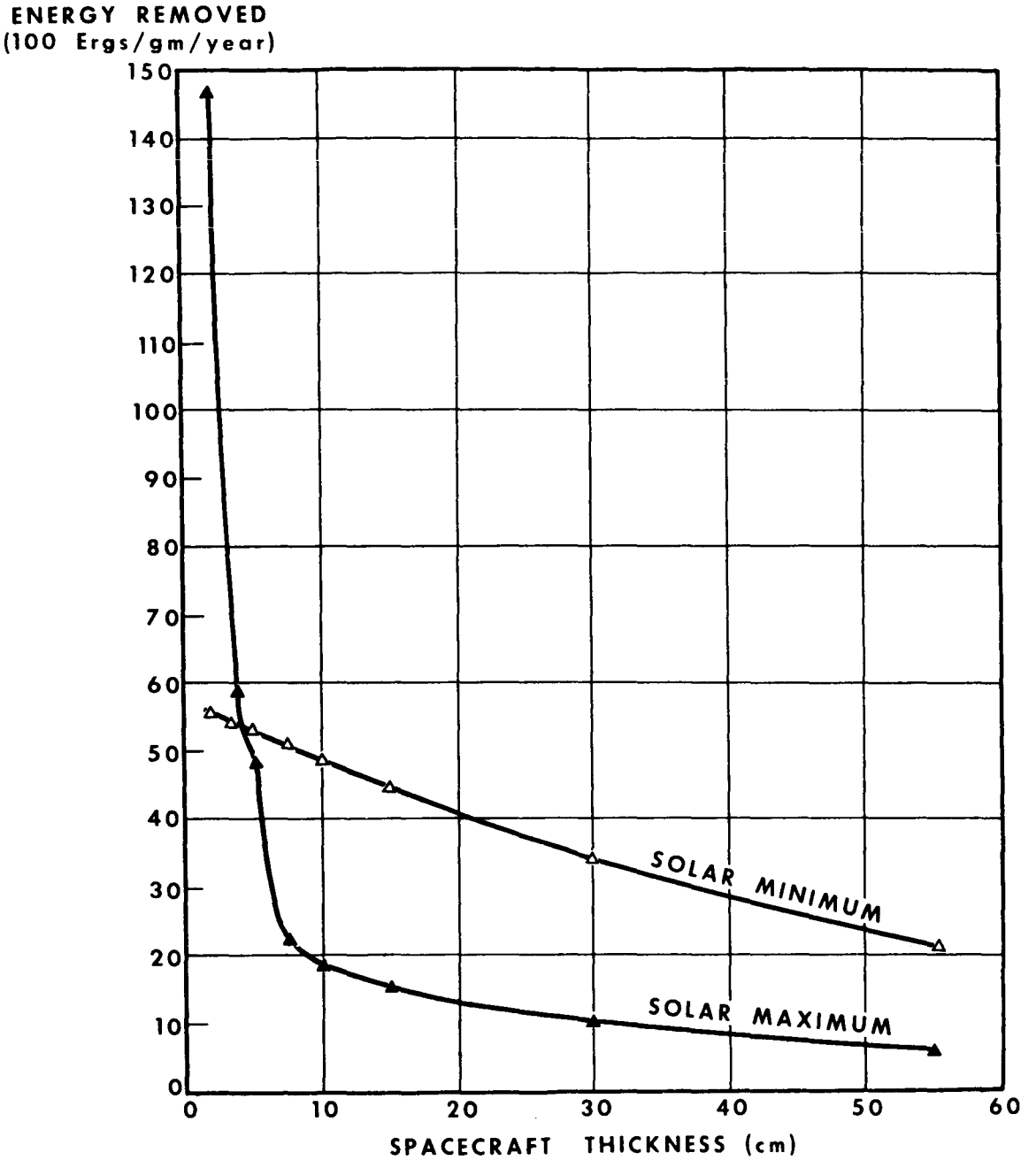

Figure 6 Comparison of Monte Carlo Results for Solar Cycle. Thin Tissue (ρ = . 021).

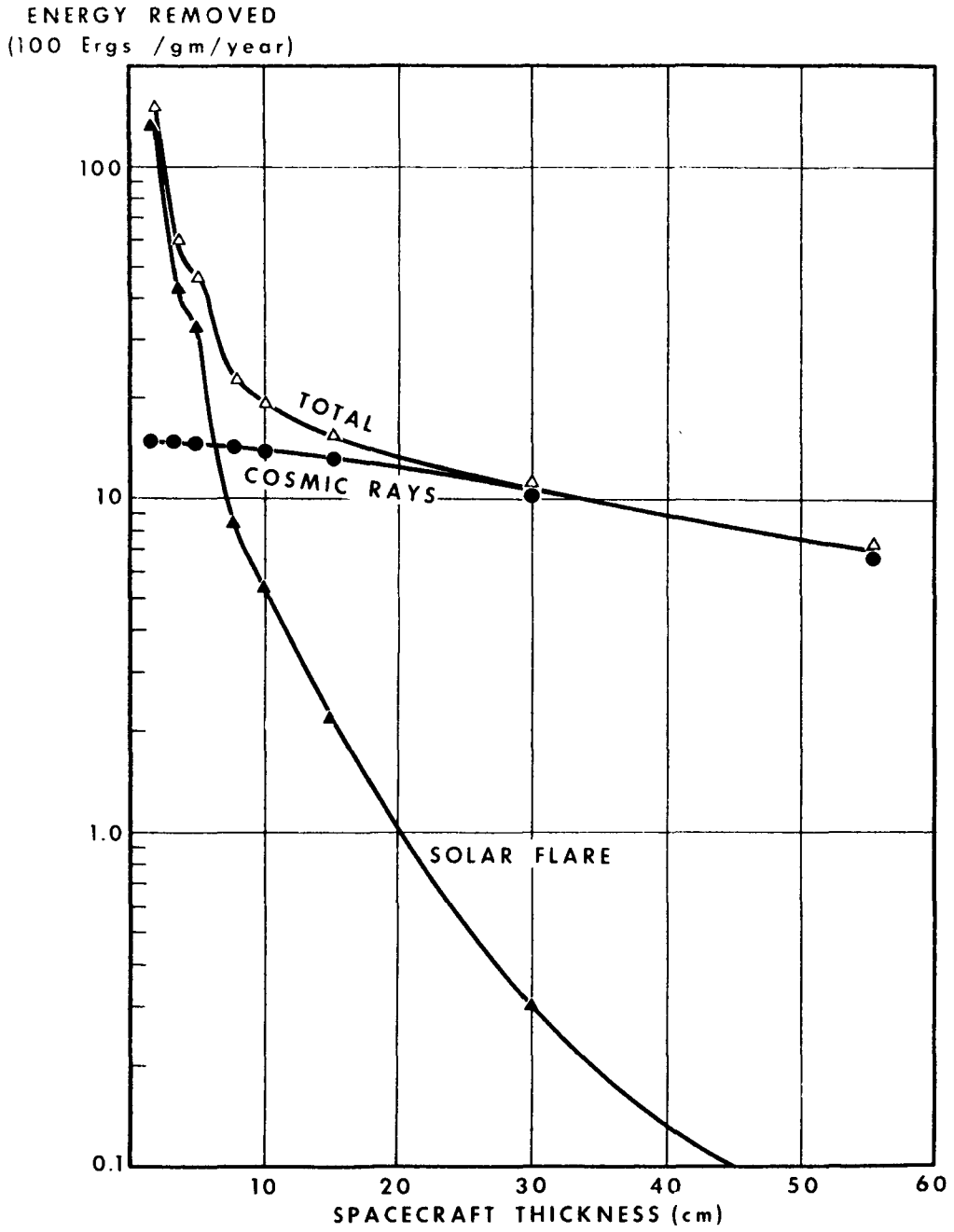

Figure 7 Monte Carlo Results for Solar Flare and Cosmic Ray Radiation in Spacecraft During Solar Maximum. Thin Tissue ($\rho = .021$).

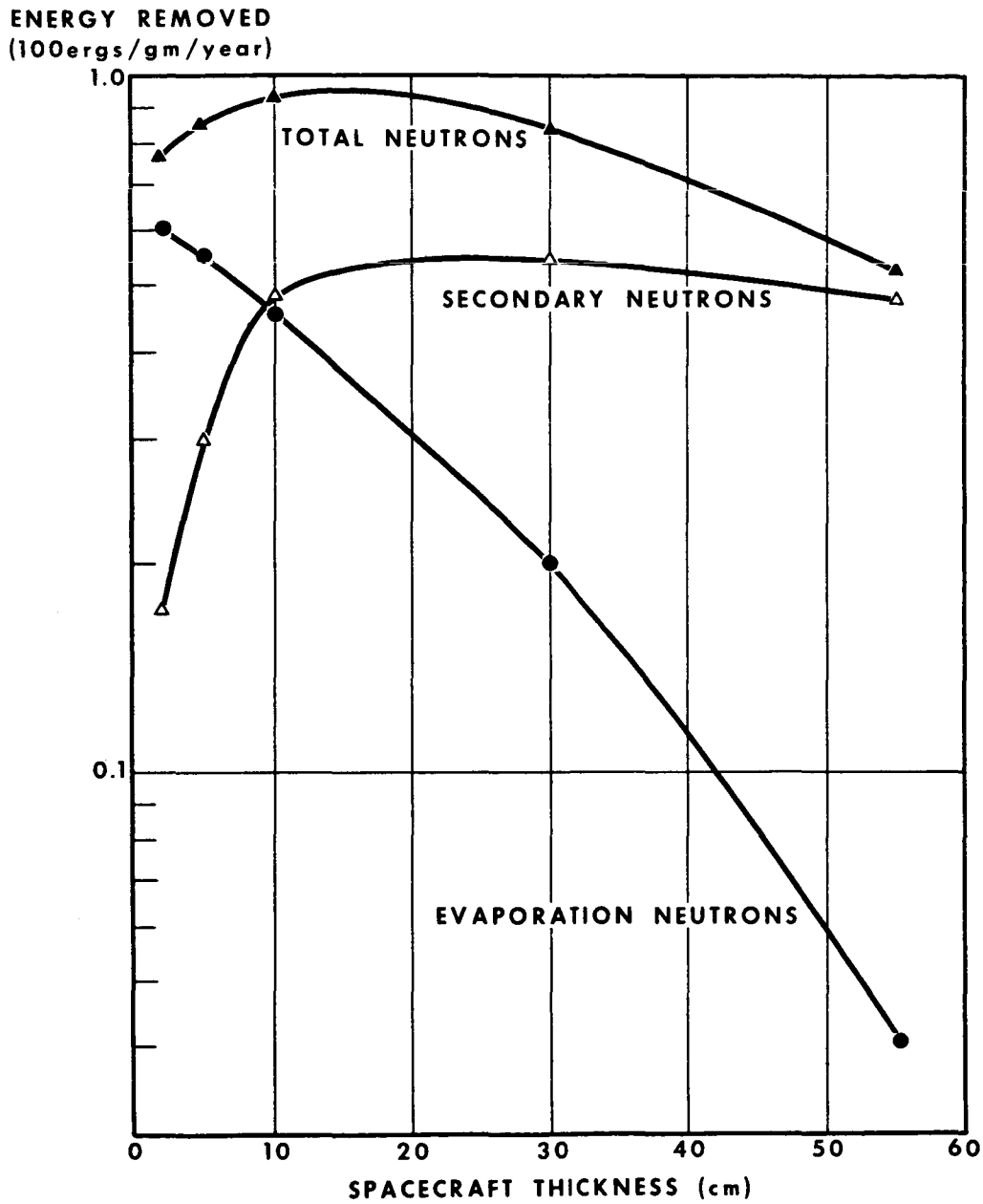

Figure 8 Energy Removed by Normal Tissue (ρ = 1.0) From Neutrons Produced in Aluminum Walled Spacecraft by Protons During Solar Maximum.

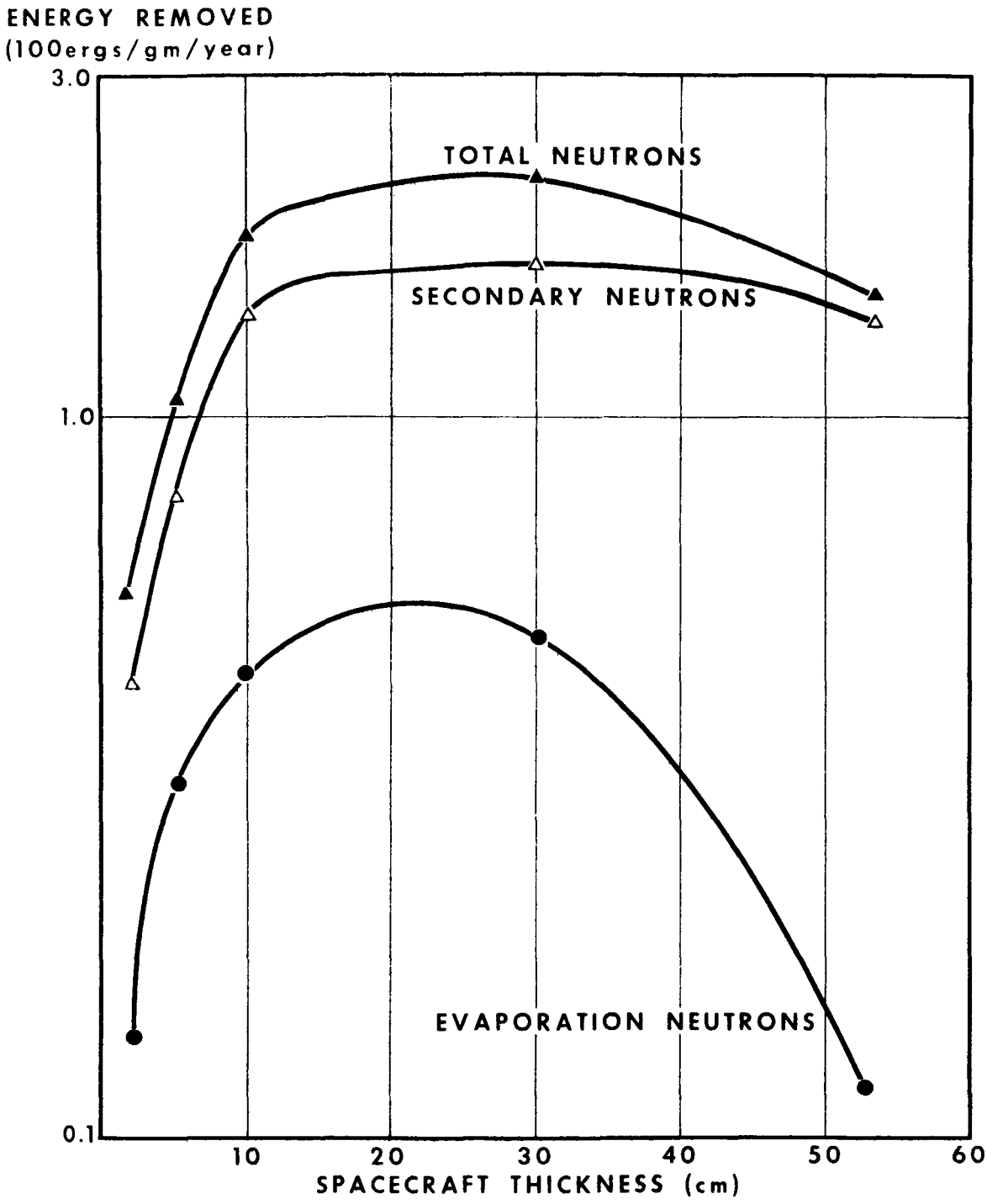

Figure 9 Energy Removed by Normal Tissue From Neutrons Produced in Aluminum Walled Spacecraft by Protons During Solar Minimum.

REFERENCES

1. Bailey, D.K., "Time Variations of the Energy Spectrum of Solar Cosmic Rays in Relation to the Radiation Hazard in Space," Journal of Geo. Rev., 67, No. 9, p. 391.

2. "Solar Proton Manual," edited by F. B. McDonald, X-611-62-122, NASA, Goddard Space Flight Center, Greenbelt, Md.

3. More, K.; Tiffany, O. L.; and Wainio, K., "Cosmic Ray Shower Production in Manned Space Vehicles," Chapter 8, Proceedings of the Conference on Medical and Biological Problems of Manned Space Flight, Nassau Conference, Nov. 1961, New York: Academic Press (In Publication 1962).

4. R. I. Allen et al, "Shielding Problems in Manned Space Flight," Annual Report - 1960, NASA Contract NAS 8-879, Lockheed Aircraft Corporation, Marietta, Georgia.

5. Gibson, G. A., "Energy Removed from Primary Proton and Neutron Beams by Tissue," ORNL-3260 Oak Ridge National Laboratory (1962).

ACKNOWLEDGEMENTS

We would like to acknowledge the continued support of I. H. McLaren and B. H. Colmery of the Bendix Systems Division. We would also like to thank Tom Cline, Arley Ferguson, and Harry Stigall of the Bendix Systems Division Data Processing Department for their invaluable assistance during the course of this investigation.

Paper E-3

NUCLEON-MESON CASCADE CALCULATIONS IN THE STRAIGHT-AHEAD APPROXIMATION

R. G. Alsmiller, Jr.
F. S. Alsmiller
J. E. Murphy*
Oak Ridge National Laboratory

Abstract

Nucleon-meson cascade calculations have been carried out for monoenergetic proton beams incident on aluminum shields. The results are used to obtain information for shielding against a solar flare proton spectrum.

A comparison between the one-dimensional cascade calculations and the more rigorous Monte Carlo calculations has been made. The two calculations are in very approximate agreement.

An IBM-7090 code which is being written to solve the nucleon-meson cascade equations is described.

In order to design shielding experiments for manned space vehicles, such as those being conducted at ORNL, it is necessary to know what energy regions are most important in the shielding problem. In order to give a preliminary answer to the question, nucleon-meson cascade calculations have been carried out in the straight-ahead approximation.

The method of calculation as well as the data used are given in detail in an ORNL report,[1] so only the results will be given here.

Let

$d(E_i,r)$ = the total dose rate per unit incident flux at a shield depth r from a monoenergetic proton beam of energy E_i

$d_s(E_i,r)$ = dose rate from secondary particles only per unit incident flux at a shield depth r from a monoenergetic proton beam of energy E_i.

---

*Central Data Processing Facility of the Oak Ridge Gaseous Diffusion Plant.

1. R. G. Alsmiller, Jr. and J. E. Murphy, Space Vehicle Shielding Studies: Calculation of the Attenuation of a Model Solar Flare and Monoenergetic Proton Beams by Aluminum Shields, ORNL-3317.

Using these functions, two "importance" functions, $I_1(E_i,r)$ and $I_2(E_i,r)$, are defined by

$$I_1(E_i,r) = d(E_i,r)\ F(E_i)$$

$$I_2(E_i,r) = d_s(E_i,r)\ F(E_i)$$

where

$F(E_i)$ = a solar flare proton spectrum.

If F is an isotropic angular flux incident on a spherical shell shield of thickness r, the importance functions must be multiplied by 4π steradians to obtain the total and secondary dose rates per unit incident energy range at the center of the spherical shell. If F is an isotropic angular flux incident on a slab shield, the importance functions must be Gross transformed[1] to obtain the dose rates per unit incident energy range at any given shield thickness. Since integrations over incident energies are required to obtain the dose rates from the flare, F, it is clear that the magnitude of I_1 is a measure of the importance of a given energy region in the incident spectrum for the determination of the total dose rate. Similarly, the magnitude of I_2 is a measure of the importance of a given energy region in the incident spectrum for the determination of the dose rate from secondary particles.

The importance functions for the case of a May 10th flare[2] on an aluminum shield are shown in Figs. 1 and 2. The dotted portions of the curves are drawn only for purposes of continuity and are, of course, not meant to be exact.

There are, of course, no discontinuities as shown in Fig. 1, rather, there is a very rapid variation in the regions where the discontinuities are shown. For a given curve (i.e., a given r) the discontinuity occurs at an energy such that the proton range at this energy is equal to r. To the right of the discontinuity the primary beam is contributing to the dose while to the left of the discontinuity only the secondary particles are contributing. It is clear that if one integrates under the curves in Fig. 1, most of the contribution to the integral will come from the region just to the right of the discontinuity, and thus, the primary dose is considerably more important than the secondary dose. It is clear that no single energy region can be singled out as being most important; rather the energy region of importance varies with the shield thickness. For a given shield thickness the energy region of most importance is that for which the proton range at this energy is just greater than the shield thickness.

---

2. W. L. Gill, Statement on the Approach to the Radiation Problem for Apollo, (submitted to National Academy of Sciences, Space Science Board, Working Group on Radiation Problems in Space Flight, Jan. 12-13, 1962).

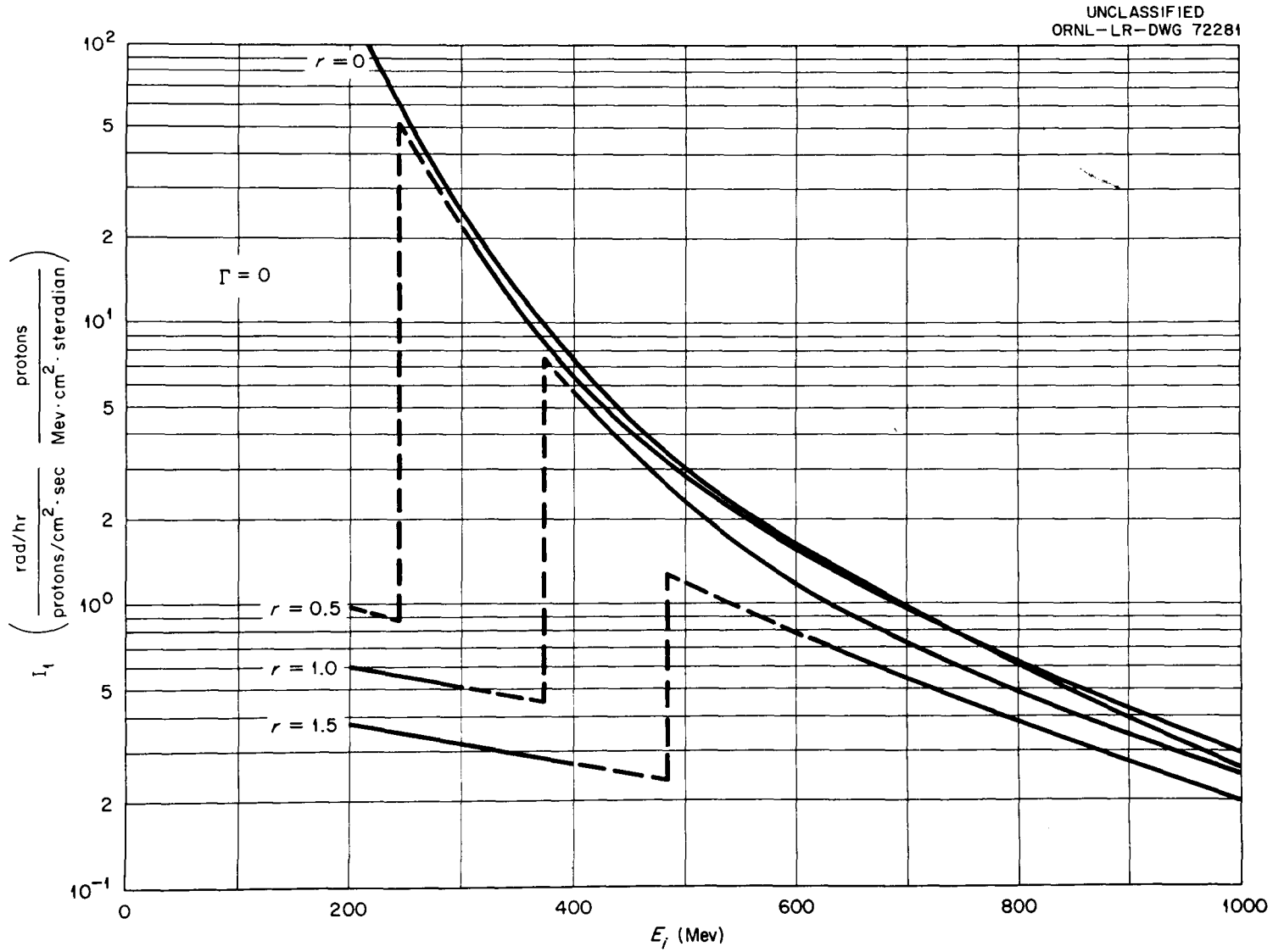

Fig. 1. First Importance Function vs Incident Energy
(r is measured in collision lengths = 93.80 g/cm^2)

The second importance function shown in Fig. 2 is of more interest since it is the secondary particles which will be the primary concern of the experimentalist. The curves in Fig. 2 are essentially flat over the energy region from 200 to 600 Mev. This is, of course, not precisely true,but the evaluation is not considered accurate enough to make the peaks significant.* Above 600 Mev the curves begin to fall off and thus these higher energies tend to be less important. No results are given for incident energies of less than 200 Mev because the computational method becomes very unreliable at the lower energies.

In general all energies from 200 to 600 Mev are of approximately the same importance in determining the dose from secondary particles. It must be understood that this statement is dependent on the particular flare used and could conceivably change if a very different flare spectrum were to be considered.

The straight-ahead approximation may not give accurate results at the low energies of interest in the shielding of manned space vehicles. The calculations discussed above were meant to give only preliminary answers until the more refined calculations of H. Bertini[3] and W. E. Kinney et al.[4] become available. These calculations are beginning to be available so it is now possible to obtain an estimate of the validity of the results discussed above.

In Fig. 3 the results for a 400 Mev proton beam incident on a slab as obtained in reference 1 are compared with the Monte Carlo calculations of W. E. Kinney et al.**,+ It must be emphasized that the data concerning high energy interactions used in the two calculations was not the same so the disagreement shown in the figure is not entirely due to the straight-ahead approximation. Also, the flux-to-dose conversion factors were taken to be the same in the two calculations, so the very approximate nature of these

---

3. H. W. Bertini, "Monte Carlo Calculations for Intranuclear Cascades," this report.

4. W. E. Kinney, "A Series of Monte Carlo Codes to Transport Nucleons Through Matter," this report.

*Note that the thinnest shield shown is 47 gm/cm^2. For thinner shields the peak in the curve becomes somewhat more pronounced and occurs at a lower energy.

**We wish to thank W. E. Kinney and his collaborators for allowing us to use their work prior to its publication.

+The pions and muons were included in all of the calculations in reference 1. They are not shown in Fig. 3 because for this low energy case they may be neglected.

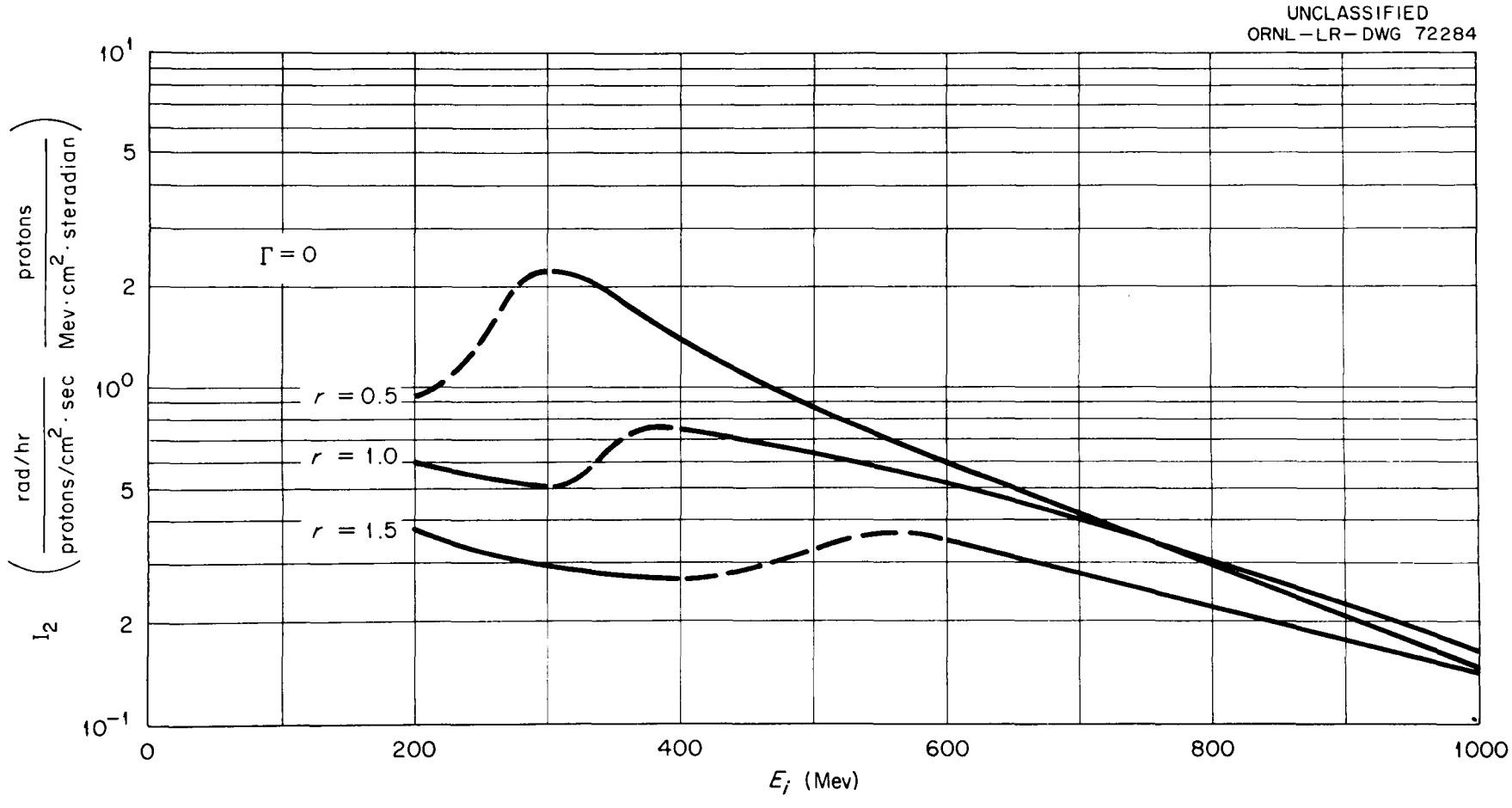

Fig. 2. Second Importance Function vs Incident Energy
(r is measured in collision lengths = 93.80 g/cm^2)

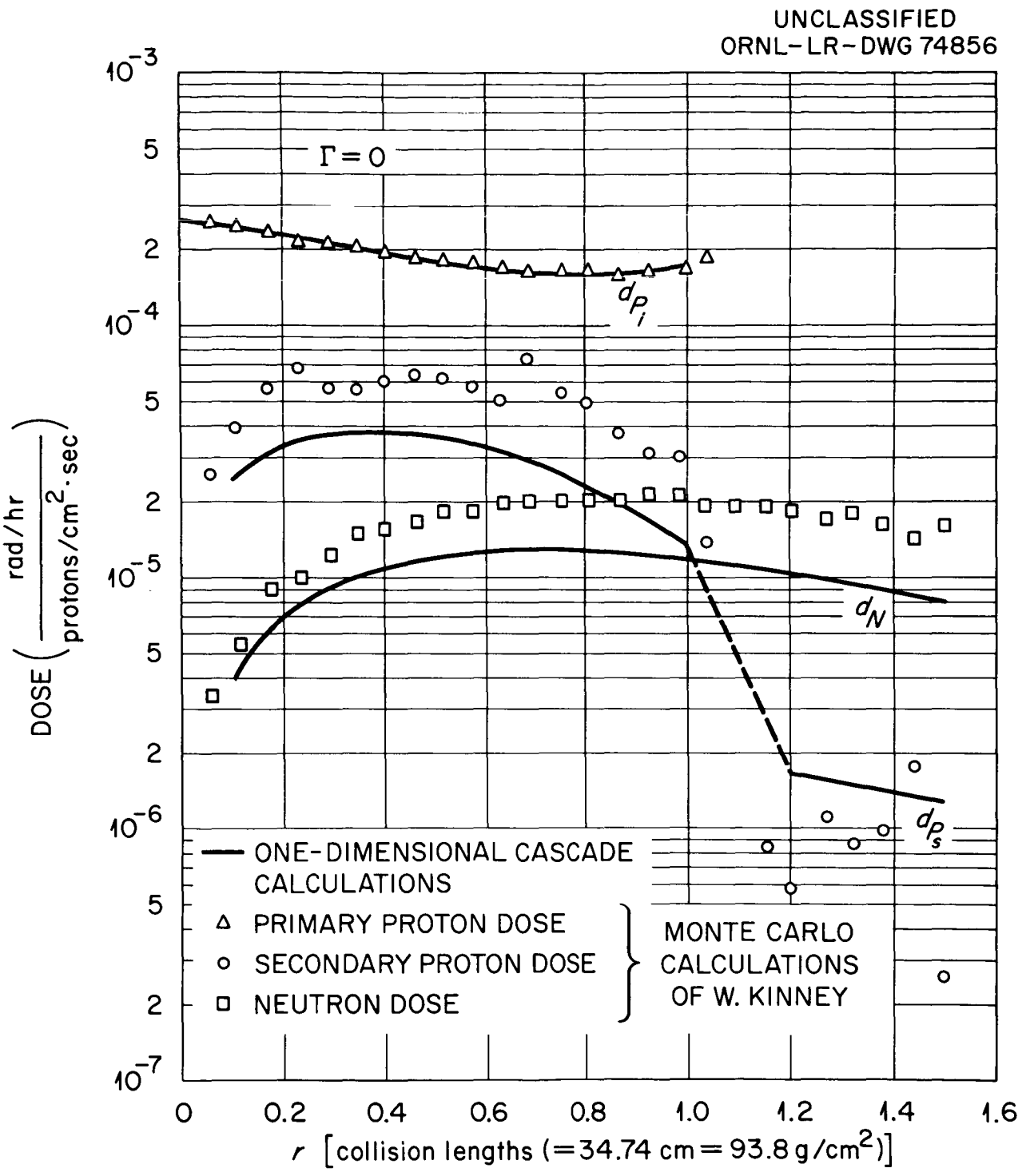

Dose vs Distance; 400-Mev Protons Incident.

Fig. 3.

conversion factors are incorporated in the Monte Carlo results.[1]

The two calculations are in good agreement insofar as the primary dose is concerned, but the Monte Carlo calculation gives a higher dose from both secondary protons and secondary neutrons. It is not possible to say how much of the discrepancy is due to the difference in data and how much is due to the straight-ahead approximation.

In general the results from the one-dimensionsl treatment leave much to be desired, but they are perhaps not so inaccurate as to invalidate the general conclusions drawn from Figs. 1 and 2.

Primarily because there is a lack of data concerning high-energy interactions, the IBM-7090 code written to solve the cascade equations included several approximations. Before long theoretical results for high-energy interactions will become available and make use of these approximations unnecessary; hence, a new code is being written which does not impose them.* At the same time several new features are being included so that the new code will be not only more accurate but also more efficient and more versatile.

The major improvements in the code are listed below:

1. Each of the secondary energy distributions, $F_{jk}(E',E)$, that is, the number of particles per unit energy of type j produced with energy E when a particle of type k and energy E' induces a nuclear reaction, may be an arbitrary function of E and E'. (The subscripts j and k take values N, P, and π corresponding to neutrons, protons, and pions.)

2. Monoenergetic sources, in addition to sources with a continuous energy distribution, may be considered.

3. The density of the medium in which the cascade takes place may be an arbitrary function of depth. (This allowance for density variation was introduced so that the propagation of cosmic rays in the atmosphere could be considered.)

4. The production of muons from the decay of pions is treated more rigorously.

5. A provision has been made for including neutron-proton elastic scattering in hydrogenous media. The slowing-down effect of this elastic scattering on the cascade neutrons is included, as is the introduction of the recoil protons into the cascade, but the method used is very approximate.

The basic approximation, the one-dimensional cascade treatment, is retained in the new code. The cascade components considered are neutrons,

---

*The coding is being done by R. G. Mashburn of the Central Data Processing Facility of the Oak Ridge Gaseous Diffusion Plant.

protons, charged pions, and charged muons; no distinction is made between positive and negative pions or positive and negative muons.

For numerical convenience all calculations will be done in terms of a lethargy variable u defined by

$$u = \ell n \frac{E_o}{E} ,$$

where E is the particle kinetic energy and E_o is an arbitrary energy which defines the zero of lethargy. However, the code will be written in such a way that all inputs (e.g., initial flux, secondary energy distribution, etc.) must be specified as a function of energy, and all outputs be given in energy.

The primary particle fluxes may be given analytically, and thus in the numerical calculation it will be convenient to separate the primary, $\phi_{ij}(E,r)$, and secondary, $\phi_{sj}(E,r)$ components.

The equations for the primary fluxes, to which we give the solutions, are the same as the equations for the secondary fluxes with the right-hand side set equal to zero. Although the equations will be coded in terms of lethargy, for clarity they are written here in terms of energy. The neutron, proton, and pion equations are:

$$\phi_{ij}(E,r) = \phi_j(E,0)(1 - C_j)\, e^{-Q_j(E)r} + Q_j(E_j,0)\, C_j \frac{S_j(E_j)}{S_j(E)}$$

$$\times \exp\left\{ - \int_E^{E_j} \left[\frac{Q_j(E') + \delta_{\pi j}\, Q_{\pi D}(E',r')}{S_j(E')} \right] dE' \right\} , \quad j = N,P,\pi, \qquad (1)$$

where

$$C_N = 0, \text{ or } 1;$$

$$C_P = 1;$$

$$C_\pi = 1;$$

$$\int_E^{E_j} \frac{dE'}{S_j(E')} = r; \text{ that is, } E_j = E_j(E,r),$$

$$\int_{E'}^{E_j} \frac{dE''}{S_j(E'')} = r'; \text{ that is, } r' = r'(E_j,E'),$$

$$\delta_{\pi j} = 1 \text{ if } j = \pi$$
$$= 0 \text{ if } j \neq \pi,$$

$$Q_{\pi D}(E,r) = \frac{C_\rho \lambda_o}{\rho \Lambda_\pi(E)} + \frac{(1 - C_\rho)\,\lambda_o}{\rho_c(r)\,\lambda_\pi(E)},$$

in which

$$\frac{1}{\Lambda_\pi(E)} = \frac{m_\pi}{\tau_\pi}\left[\frac{1}{E(E + 2m_\pi)}\right]^{1/2},$$

$$C_\rho = 0, \text{ or } 1$$

$$\frac{\partial}{\partial r}\phi_{sj}(E,r) + \left[Q_j(E) + \delta_{\pi j}\,Q_{\pi D}(E,r)\right]\phi_{sj}(E,r) - C_j\frac{\partial}{\partial E}\left[S_j(E)\,\phi_{sj}(E,r)\right]$$

$$= \sum_k \int_E^{E_{max}} F_{jk}(E',E)\,Q_k(E')\left[\phi_{ik}(E',r) + \phi_{sk}(E',r)\right]dE'$$

$$+ \delta_{Pj}\,H_R(E,r) + H_j(E,r), \qquad j,k = N,P,\pi, \tag{2}$$

where

$\phi_{iN}(E,r) = N_i(E,r)$

= primary neutron flux per unit energy from a neutron source at r = 0 with a continuous energy spectrum;

$\phi_{sN}(E,r) = N_s(E,r)$

= secondary neutron flux per unit energy;

$\phi_N(E,r) = N_i(E,r) + N_s(E,r)$

= total neutron flux per unit energy when there are no monoenergetic sources present; since $N_s(E,0) = 0$, then $\phi_N(E,0) = N_i(E,0)$ is one of the initial values which must be specified.

ϕ_{iP}, $\phi_{i\pi}$, etc. have similar definitions. Furthermore,

r = dimensionless distance variable defined by the relation $r = (\rho/\lambda_o)R$ if the density of the medium, ρ, is a constant, and by $r = [x(t) - x_o]/\lambda_o \cos\theta$, where $x(t) = \int_o^t \rho_c(t')\,dt'$, if the density of the medium, ρ_c, is a function of depth;

θ = angle of the flux with respect to the vertical; this angle is introduced so that the propagation of the cascade can be considered in a direction other than the vertical;

ρ = density of the medium, g/cm^3, if this density is constant;

R = distance in the direction θ, cm;

λ_o = an arbitrary constant with dimensions g/cm^2 which determines the units in which the dimensionless variable r is measured;

x_o = pressure, g/cm^2, at the point from which r is measured;

$\rho_c(t)$ = density of the medium, g/cm^3, as a function of position;

t = depth, cm;

C_j = constant which takes the value 0 or 1; the quantities C_P and C_π are always unity, but C_N may be 0 or 1; if $C_N = 1$, neutron slowing down (e.g., by elastic scattering from protons) is included; when $C_N = 0$, neutron slowing down is omitted;

$Q_j(E) = \frac{\lambda_o N_o}{A}\,\sigma_j(E)$;

$\sigma_j(E)$ = nonelastic cross section for particles of type j in the medium being considered;

N_o = Avogadro's number;

A = atomic weight of the nuclei in the medium;

$S_j(E) = \frac{\lambda N_o}{A} \epsilon_j(E)$;

$\epsilon_j(E)$ = atomic stopping cross section for particles of type j in the medium;

C_ρ = constant which takes value 0 or 1; when a medium of constant density is considered, $C_\rho = 1$; when a medium of variable density is considered, $C_\rho = 0$;

m_π = rest mass of the charged pion, Mev;

τ_π = mean life of the charged pion, sec, multiplied by the velocity of light, cm/sec;

$F_{jk}(E',E)dE$ = the number of secondary particles of type j in the energy interval E to E + dE produced by the nonelastic collision of a particle of type k of energy E'.

Still to be discussed are the source terms H_R and H_j. The equations without H_j are satisfactory if only sources with continuous energy distributions are to be considered; however, monoenergetic sources are most conveniently handled by introducing H_j. By utilizing the fact that the primary flux from a monoenergetic source may be calculated analytically, the number of secondary particles per unit energy range per unit volume, H_j, produced per second by the primary flux may be written

$$H_j = \sum_k F_{jk}(E_k^*,E)\, Q_k(E_k')\, \phi_{k\delta}(r)\, \Theta(E_k^* - E), \quad j,k = N,P,\pi \tag{3}$$

where

$$E_k' = E_{ok}(1 - C_k) + E_{Rk}\, C_k,$$

$$\phi_{k\delta} = \phi_{k\delta o}(1 - C_k)\, e^{-Q_k(E_{ok})r}$$

$$+ \phi_{k\delta o}\, C_k \exp\left\{ - \int_{E_{Rk}}^{E_{ok}} \left[\frac{Q_k(E') + \delta_{k\pi}\, Q_{\pi D}(E', r')}{S_k(E')} \right] dE' \right\}$$

$$\int_{E_{Rk}}^{E_{ok}} \frac{dE'}{S_k(E')} = r,$$

$$\int_{E'}^{E_{ok}} \frac{dE''}{S_k(E'')} = r',$$

$$\Theta(E_k - E) = 1 \text{ if } E_k - E \geq 0$$

$$= 0 \text{ if } E_k - E < 0,$$

$$\phi_{N\delta}(r) = N_\delta(r)$$

= flux strength of source neutrons which reach position r when a flux of $N_{\delta o}\delta(E - E_{oN})$ source neutrons start at the origin with energy E_{oN},

$N_{\delta o}$ = strength of neutron monoenergetic source,

E_{oN} = energy of monoenergetic neutron source,

E_{RN} = energy of monoenergetic source neutrons when they reach position r.

The other quantities, $\phi_{P\delta}$, $P_{\delta o}$, etc., have similar definitions.

The Θ functions are introduced into H_j to indicate that a particle of energy E' cannot produce secondary particles of energy greater than E'. The physically correct functions F_{jk} have the property

$$F_{jk}(E',E) = 0 , \qquad E \geq E' ,$$

so that the Θ functions are superfluous when these functions are used. In some cases, however, we use approximations to the F_{jk}'s which do not have this property,[5] and then it is necessary to introduce this property through the Θ functions.

The three terms in H_j correspond to the production of secondary particles of type j by the three kinds of monoenergetic sources allowed—neutrons, protons, and pions. The code will be written so that monoenergetic and continuous sources for all three types of particles may be considered simultaneously.

The term $H_R \delta_{jP}$ is introduced for the purpose of including recoil protons from neutron-proton elastic scattering in hydrogenous media. Assuming that when a neutron-proton collision takes place the neutron transfers, on the average, a given portion of its energy to the proton,

$$H_R = C_s \frac{S_N(KE)}{E} [N_i(E,r) + N_\delta(E,r)]$$

$$+ C_s \frac{K S_N[E_{RN}C_N + E_{oN}(1 - C_N)]}{E_{RN}C_N + E_{oN}(1 - C_N)} G[E_{RN}C_N + E_{oN}(1 - C_N),E]$$

$$\times N_\delta(r) \Theta[E_{RN}C_N + E_{oN}(1 - C_N) - E] , \qquad (4)$$

where

C_s = 0 or 1 and is introduced so that the recoil proton terms may be omitted; note that since C_s and C_N are specified separately it is possible to include the recoil protons and at the same time neglect the effects of elastic scattering on the neutrons;

5. R. G. Alsmiller, Jr. F. S. Alsmiller, J. E. Murphy, Nucleon-Meson Cascade Calculations: Transverse Shielding for a 45-Gev Electron Accelerator (Part I), ORNL-3289 (1962).

$1/K$ = fraction of the neutron's energy which on the average is given to the proton when a neutron-proton elastic scattering occurs;

$G(E',E)$ = energy distribution of the recoil proton when a neutron of energy E' is scattered by a proton; to be consistent with the first term in H_R we should have $G(E',E) = \frac{1}{K}\,\delta(E' - KE)$, but because of the difficulties associated with introducing a delta function into the equation we shall use an analytic function which approximates the delta function.

In writing Eq. 4 we assumed that $S_N(E)$ is given by

$$S_N(E) = n_P\,\sigma_E(E)\,\frac{E}{K} \quad ,$$

where n_P = number density of protons in the medium, and σ_E = elastic scattering cross section.

The muon equations are similar to those for the other cascade particles, but differ in one important way: since the small muon nuclear interactions are neglected, the muons do not produce neutrons, protons, or pions and thus do not take an active part in the cascade.

The muon equations are[6]

$$\mu_i(E,r) = \mu_i(E_\mu,0)\,\frac{S_\mu(E_\mu)}{S_\mu(E)}\,\exp\left[-\int_E^{E_\mu}\frac{Q_{\mu D}(E',r')}{S_\mu(E')}\,dE'\right] \qquad (5)$$

where

$$\int_E^{E_\mu}\frac{dE'}{S_\mu(E')} = r,$$

6. The form of the muon source term from pion decay is discussed in detail in Appendix 3 of Ref. 2. The secondary muon equation may be solved in quadrature, but in the present code the differential equation was found to be more convenient to use than the solution.

$$\int_{E'}^{E_\mu} \frac{dE''}{S_\mu(E'')} = r',$$

$$Q_{\mu D}(E,r) = \frac{C_\rho \lambda_o}{\rho \Lambda_\mu(E)} + \frac{(1 - C_\rho)\lambda_o}{\rho_c(R)\, \Lambda_\mu(E)},$$

$$\frac{1}{\Lambda_\mu(E)} = \frac{m_\mu}{\tau_\mu} \left[\frac{1}{E(E + 2m_\mu)} \right]^{1/2};$$

and

$$\frac{\partial}{\partial r} \mu_s(E,r) + Q_{\mu D}(E,r)\, \mu_s(E,r) + \frac{\partial}{\partial E} \left[S_\mu(E)\, \mu_s(E,r) \right]$$

$$= \int_{E_{\mu 1}}^{E_{\mu 2}} dE'\, F(E')\, Q_{\pi D}(E',r) \left[\pi_i(E',r) + \pi_s(E',r) \right]$$

$$+ \begin{cases} \pi_\delta(r)\, F(E_{R\pi})\, Q_{\pi D}(E_{R\pi},r), & E_{\mu i} \le E_{R\pi} \le E_{\mu 2}, \\ 0, & E_{\mu 2} < E_{R\pi} < E_{\mu 1}, \end{cases} \qquad (6)$$

where

$$F(E') = \frac{\left(\frac{m_\pi}{m_\mu} \right) E'}{2U_2 [E'(E' + 2m_\pi)]^{1/2}},$$

$$E_{\mu 1} = \frac{m_\pi}{m_\mu} \left\{ U_1(E + m_\mu) - U_2[E(E + 2m_\mu]^{\frac{1}{2}} \right\} - m_\pi,$$

$$E_{\mu 2} = \frac{m_\pi}{m_\mu} \left\{ U_1(E + m_\mu) + U_2[E(E + 2m_\mu)]^{\frac{1}{2}} \right\} - m_\pi.$$

Paper E-4

TRANSPORT CALCULATIONS FOR PROTON SHIELDING *

Gerald Litton, Rubin Goldstein, and Roger Wallace

Lawrence Radiation Laboratory
University of California
Berkeley, California

15149

Abstract

To calculate the dose rate and integrated dose behind a layer of material that shields against a proton flux it is necessary to know the effect of the shield on the incident flux. The work reported here investigates that effect.

The analysis takes into account both proton ionization energy loss and secondary-particle production, using the transport method of successive generations. The secondaries considered are protons, neutrons, and π mesons.

Introduction

The system chosen for analysis is a one-dimensional slab of width a, upon which is incident a uniform and isotropic proton flux with an arbitrary spectrum. An expression is developed for the uncollided proton flux, termed the primary flux, as a function of energy, angle, and position in the slab.

The first-generation secondary flux, i.e., the flux due to direct nuclear collisions of the primary flux, is then calculated. Similarly, a second-generation secondary flux, due to nuclear collisions of the first-generation flux is calculated. Succeeding generations of the secondary flux are calculated until the magnitude of the flux in a particular generation is sufficiently small to be neglected.

The secondary flux is subdivided into protons, neutrons, and π mesons, each of which is considered individually in the calculations.

---

* Work done under the auspices of the U. S. Atomic Energy Commission, and the Joint Atomic Energy Commission—NASA Space Radiation Program.

Primary Proton Flux

The primary or uncollided proton flux is given as

$$\phi_p^{(0)}(x, E, \mu) = \frac{1}{2\pi} \phi_0(E_0) \exp\left\{ - \int_E^{E_0} \frac{\Sigma_p(E')}{f(E')} \, dE' \right\}, \qquad (1)$$

where $\phi_0(E_0)$ = incident proton flux,

$\Sigma_p(E)$ = total macroscopic proton cross section of the slab medium,

$f(E)$ = ionization energy loss of the slab medium.

The relation between E and E_0 is given as

$$E_0 = E + \int_0^{x/\mu} f(E') \, dx' \, , \qquad (2)$$

which states that the initial proton energy E_0 is equal to the energy E at x plus the energy lost by ionization.

The exponential term in Eq. 1 represents the proton attenuation due to nuclear interactions.

Data on ionization energy loss are well known for a large number of elements. Similarly, low-energy proton cross sections are known. Unfortunately, only a small amount of high-energy cross-section data is available. Some estimates[1] and some experimental measurements[2] have been made. A useful approximation is the equivalence of neutron and proton cross sections at high energies, allowing the use of high-energy neutron cross-section data.[2]

Because of the complex form of f(E), the integration in Eqs. 1 and 2 must, in general, be performed numerically. The calculations are minimized by noting that the primary flux may be expressed as a function of two independent variables: E and x/μ.

Secondary Particle Fluxes

For the sake of brevity, meson fluxes are not discussed in the following sections. It is pertinent to note that the equations describing π^0 mesons are analogous to those describing neutrons. A similar correspondence exists for $\pi^{\pm}$ mesons and protons.

First-Generation Fluxes

The flux of particle i at some point $\vec{r}$, where i may represent protons or neutrons, is calculated by considering the production of i particles by proton interactions within a volume element at $\vec{r}'$, which contribute to the flux at $\vec{r}$, and then integrating over all $\vec{r}'$. The results for slab geometry are

$$\phi_i^{(1)}(x, E, \mu) = \frac{2\pi}{|\mu|} \int_{-1}^{1} d\mu' \int dE' \int_0^a dx' \, G(x';\mu) \Sigma_p(E') \, \phi_p^{(0)}(x', E', \mu') \cdot N_{ip}(E' \rightarrow E_0, |\mu''|) \cdot \exp[-h_i(E, x', x)] \tag{3}$$

with the following definitions:

The term μ'' is the cosine of the difference in angle between the direction fo the initial proton and the direction of the final particle i. It is related to μ and μ' by

$$\mu'' = \mu\mu' + \sqrt{[1 - (\mu)^2][1 - (\mu')^2]} \, . \tag{4}$$

The quantity E_0 is that energy which the particle i must have at x' so as to arrive at x with energy E. For neutrons, E_0 is identically E, but for protons, E_0 is greater than E by an amount equal to the ionization energy loss experienced by the proton in migrating from x' to x. The relationship between E and E_0 in this case is

$$E_0 = E + \int_0^{|(x'-x)/\mu|} f(E'') \, dx'' . \tag{5}$$

The function $G(x', \mu)$ serves to set the limits on the x' integration, and is defined by

$$G(x', \mu) = \begin{cases} 1 \ldots 0 < x' < x, & \text{for } \mu > 0, \\ 0 \ldots x < x' \leq a, & \text{for } \mu > 0, \\ 0 \ldots 0 \leq x' < x, & \text{for } \mu < 0, \\ 1 \ldots x < x' \leq a, & \text{for } \mu < 0. \end{cases} \tag{6}$$

The quantity $\exp[-h_i(E, x', x)]$ is the fraction of particles i that travel from x' to x without undergoing any nuclear interactions. The term $h_i(E, x', x)$ is given by

$$\begin{aligned} h_i(E, x', x) &= \Sigma_N(E) \frac{x'-x}{\mu} && \text{-- for neutrons,} \\ h_i(E, x', x) &= \int_E^{E_0} \frac{\Sigma p(E'')}{f(E'')} \, dE'' && \text{-- for protons,} \end{aligned} \tag{7}$$

where Σ_n = total macroscopic cross section for neutrons.

The superscripts attached to the fluxes denote generation number, with the primary proton flux being defined as the zero-order generation.

The function $N_{ij}(E' \rightarrow E_0, |\mu''|)$ represents the number of particles i with energy E_0 and direction μ produced per interaction of a proton of energy E' and direction μ'.

Higher-Generation Fluxes

The calculation of the higher-order fluxes is analogous to that for the first-generation fluxes, with one difference. Particles i may be produced not only by nuclear interactions of protons, but also from secondary neutrons and mesons. The expressions for the nth-generation fluxes are

$$\phi_i^{(N)}(x, E, \mu) = 2\pi \int_{-1}^{1} \frac{d\mu'}{|\mu|} \int dE' \int_0^a dx' \exp\left[-h_i(E, x', x)\right] G(x', \mu) \cdot \sum_j \phi_j^{(N-1)}(x', E', \mu') \Sigma_j(E') N_{ij}(E' \rightarrow E_0, |\mu''|) . \tag{8}$$

The summations in Eq. 8 extend over proton, neutron, and meson interactions.

Integral Evaluation

The integrals appearing in Eqs. 3 and 8 must be evaluated numerically for several reasons, the strongest of which is the complex form of the functions N_{ij}. Furthermore, the primary flux is in general specified as numerical data, as previously discussed.

At present, direct triple numerical integration of these equations appears to be the most likely method of attack.

Secondary-Particle Production

One of the major difficulties is the great lack of information about the function $N_{ij}(E' \rightarrow E_0, |\mu''|)$. The data that are available are due primarily to Metropolis[3] and Wallace and Moyer.[4]

The function N_{ij} represents the angular, energy, and number distributions of secondary particles j, and is, therefore, quite complicated. It is expected that more complete data on this function will be made available in the future.

Conclusions

The primary and secondary fluxes can, in principle, be determined to a high degree of accuracy by means of the foregoing analysis. In practice, however, there are two limitations on the obtainable accuracy, the more important by far being the lack of accurate data on high-energy cross sections and secondary-particle production.

The second limitation arises from truncation errors produced in the numerical integrations. The magnitude of these errors is determined by the sizes of the coordinate differences, which are unfortunately limited by computer capacities.

The desired end result is the fluxes of the various particles at the inner surface of the slab. A detailed knowledge of these fluxes is of major importance in determining the dose away from the inner slab surface.

REFERENCES

1. Burton J. Moyer (Lawrence Radiation Laboratory), Data Related to Nuclear Star Production by High-Energy Protons, unpublished data, 1961.

2. T. Coor, D. A. Hill, W. F. Hornyak, L. W. Smith, and G. Snow, Phys. Rev. 98, 1369 (1955).

3. N. Metropolis, R. Bivins, M. Storm, A. Turkevich, J. M. Miller, and G. Friedlander, Phys. Rev. 110, 185 (1958); and 110, 204 (1958).

4. R. W. Wallace and B. J. Moyer, Shielding and Activation Considerations for a Meson Factory, Lawrence Radiation Laboratory Report UCRL-10086, April 11, 1962 (unpublished).

Paper E-5

COMPARISON OF PRIMARY PROTON DOSE WITH THE DOSE FROM GAMMA RAYS PRODUCED BY INELASTIC SCATTERING OF SOLAR FLARE PROTONS

F. S. Alsmiller
R. G. Alsmiller, Jr.
D. K. Trubey
Oak Ridge National Laboratory

Abstract 15150

The primary proton dose resulting from solar flare (May 10, 1959) protons incident on an aluminum shield is compared with the dose from gamma rays produced by inelastic collisions of the primary protons. Both spherical shell and slab shields are considered.

Most of the radiation dose behind thin shields exposed to solar flare protons can be attributed to the primary protons. However, the possible importance of secondary gamma rays produced in proton nonelastic collisions has been pointed out recently by Madey et al.[1] They computed the gamma dose rate at the center of an aluminum spherical shell, as a function of shield thickness, and found it comparable to the primary proton dose at a thickness of about 12 cm. These results are based on the use of experimental values of the gamma spectrum and yield for 14-Mev protons[2] which were assumed to be the same for all proton energies above the Coulomb barrier up to 50 Mev.

---

1. R. Madey, A. G. Duneer, Jr., and T. J. Krieger, Gamma Dose from Solar Flare Protons Incident on an Aluminum Shield, Presented at the Annual Meeting of the American Nuclear Society, June 18-21, 1962 Boston, Mass.

2. T. Wakatsuki et al., J. Phys. Soc. Japan 15, 1141 (1960).

Since many questions remain, we have performed several further calculations for both spherical shell and infinite slab aluminum shields. The gamma spectrum is constructed from theoretical estimates of the gamma production cross sections[3] which are available for inelastic (n,n') neutron scattering in aluminum, for neutron energies from 0.9 to 18 Mev. We assume the gamma production cross sections for proton inelastic scattering can be approximated with sufficient accuracy by the relation

$$\sigma_{pp'\gamma}(E,E_\gamma) = \sigma_{nn'\gamma}(E - V_c,E_\gamma) \qquad (V_c \leq E \leq 22.3 \text{ Mev})$$

$$= \sigma_{nn'\gamma}(22.3 - V_c,E_\gamma) \quad (22.3 \text{ Mev} \leq E \leq E_{c_{max}}) , \qquad (1)$$

where V_c is the Coulomb potential barrier, E the incident proton energy, and E_γ the photon energy; $E_{c_{max}}$ is an upper limit on the proton energy, taken variously as 22.3 and 50 Mev.

In Fig. 1 we compare our curve of the gamma dose rate, d_γ, versus spherical shell thickness, with the result of Madey et al. for an isotropically incident differential proton flux,

$$P(E,0) = 3.1 \times 10^9 E^{-4.6} , \qquad (85 \text{ Mev} \leq E \leq 45 \times 10^3 \text{ Mev})$$

$$= 1.0 \times 10^6 E^{-2.8} , \qquad (5 \times 10^{-2} \text{ Mev} \leq E \leq 85 \text{ Mev}) , \qquad (2)$$

where P(E,0) has the units of protons cm^{-2}-sec^{-1}-$steradian^{-1}$-Mev^{-1}. The primary proton flux is calculated as a function of distance through the shield in the usual manner;[4] the proton stopping power in aluminum was computed from Sternheimer's[5] formula for E > 2 Mev, and from

---

3. E. S. Troubetzkoy, Fast Neutron Cross Sections of Iron, Silicon, Aluminum, and Oxygen, NDA-2111-3, Vol. C, 38,39.

4. R. G. Alsmiller, Jr., F. S. Alsmiller and J. E. Murphy, Nucleon-Meson Cascade Calculations in the Straight-Ahead Approximations, Paper E-3 this symposium.

5. R. M. Sternheimer, Phys. Rev. 115, 137 (1959).

tables[6] based on experimental values for $E < 2$ Mev. The proton total nonelastic collision cross section was taken mostly from the Monte Carlo calculation of Bertini above 30 Mev (see Paper D-3) and from Howerton's[7] compilation of neutron nonelastic cross sections for neutron energies below 15 Mev, using the same approximation as in Eq. 1; i.e.,

$$\sigma_{p,\text{nonel}}(E') = \sigma_{n,\text{nonel}}(E' - V_c). \qquad (3)$$

In the calculations for spherical shell shields, the photons are assumed to be produced by primary protons only, to have the same direction as the incident proton, and to be attenuated[8] exponentially through the shield. Photon flux-to-dose conversion factors for tissue were taken from ref 9.

The numerical differences in the estimates of the gamma dose rate shown in Fig. 1 are consistent with the differences in the assumed gamma spectrum. Fig. 1 also shows a comparison of the primary proton dose rate, $d_{P,dE/dx}$, calculated considering only the proton ionization energy losses in tissue,[10] with the results of Madey et al. No crossing between the gamma and proton curves occurs in our calculations; the gamma dose rate is less than 10% of the proton dose at a thickness of 25 g/cm^2 (9.3 cm).

The spherical shell calculations were repeated for the time-integrated May 10 solar flare spectrum,[11]

$$\begin{aligned} P(E,0) &= 0 && (0 \leq E < 5 \text{ Mev}) \\ &= 2.5 \times 10^{11} E^{-2.07} && (5 \text{ Mev} \leq E \leq 60 \text{ Mev}) \\ &= 5.486 \times 10^{14} E^{-3.95} && (60 \text{ Mev} \leq E \leq 10^3 \text{ Mev}) \end{aligned} \qquad (4)$$

---

6. American Institute of Physics Handbook, McGraw-Hill Book Co., Inc., 1957.
7. R. J. Howerton, Semi-Empirical Neutron Cross Sections, UCRL-5351 (1958).
8. G. W. Grodstein, X-ray Attenuation Coefficients from 10 Kev to 100 Mev, NBS Circular 583 (1957).
9. B. J. Henderson, Conversion of Neutron or Gamma-Ray Flux to Absorbed Dose Rate, XDC-59-8-179 (1959).
10. W. S. Snyder and J. Neufeld, Radiation Research 6, 67 (1957).
11. W. L. Gill, Statement on the Approach to the Radiation Problems for Apollo, submitted to the National Academy of Sciences, Space Science Board, Working Group on Radiation Problems in Space Flight, Jan. 12-13, 1962, NASA Manned Spacecraft Center, Life Systems Division.

(units are protons cm^{-2}-steradian^{-1}-Mev^{-1}), and are shown in Fig. 2. The curve labeled d_p is a total proton dose, in which not only the ionization losses but also the energy deposition by proton absorption in tissue is roughly accounted for by a method similar to that used by Gibson.[12]

The effect of varying the upper limit, $E_{c_{max}}$, on the energy of protons assumed capable of producing gamma rays, from 22.3 Mev to 50 Mev, is about a factor of two. At 25 g/cm^2 the gamma dose is less than 5% of the proton dose in Fig. 2.

These factors are changed very little in Fig. 3 in which we plot the dose results for the May 10 flare incident isotropically on an infinite slab shield. This is true even though three changes were made in the calculation. First, the photons were more realistically assumed to be emitted isotropically, rather than in the direction of the incident proton. Second, photon transport through the shield was calculated by means of the OGRE-P2 Monte Carlo code[13] which takes build-up of the photon flux into account. A major part of the gamma dose at the larger shielding distances is due to the "collided" photon flux, as opposed to the "uncollided" flux; only the latter was considered in the spherical shell cases.

Third, the primary proton flux is calculated as a function of position by taking into account the variation of path length with angle of incidence, and integrating over all angles; i.e., a Gross transformation is carried out. It is worth noting that the geometry effect is rather important, since the change from a spherical shell to a slab decreases the primary proton dose by almost a factor of 10.

On the basis of so few calculations, only very tentative conclusions can be drawn. In general, we find that with our cross sections the gamma dose is not so important as the calculations of Madey et al. would indicate. By comparing Figs. 1 and 2, it is clear that the ratio of the gamma dose to the primary proton dose at larger shield thicknesses is very dependent on the shape of the incident flare spectrum.

Finally, comparing the results of this paper with calculations of secondary neutron and proton dose,[4] it seems that in general the gamma rays are neither more nor less important than secondary nucleons.

---

12. W. A. Gibson, Energy Removal from Primary Proton and Neutron Beams by Tissue, ORNL-3260 (1962).

13. D. K. Trubey, S. K. Penny, and M. B. Emmett, OGRE-P2 - A Monte Carlo Program for Computing Gamma-Ray Leakage from Laminated Slabs Containing Distributed Sources, Neutron Physics Div. Ann. Progr. Rep. Sept. 1, 1962, ORNL-3360.

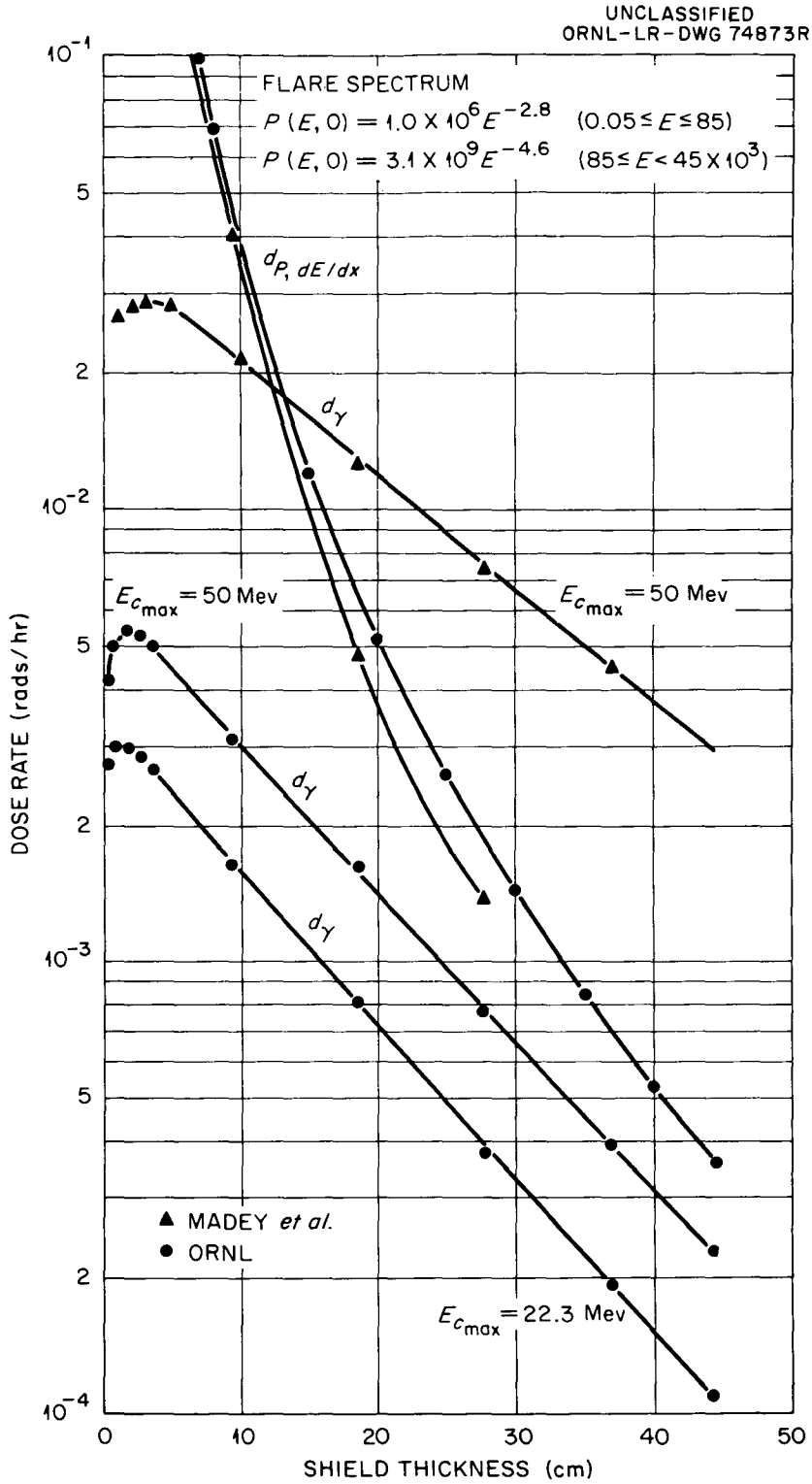

Fig. 1. Gamma and Primary Proton Dose Rates at the Center of a Spherical Aluminum Shell from Solar Flare Protons.

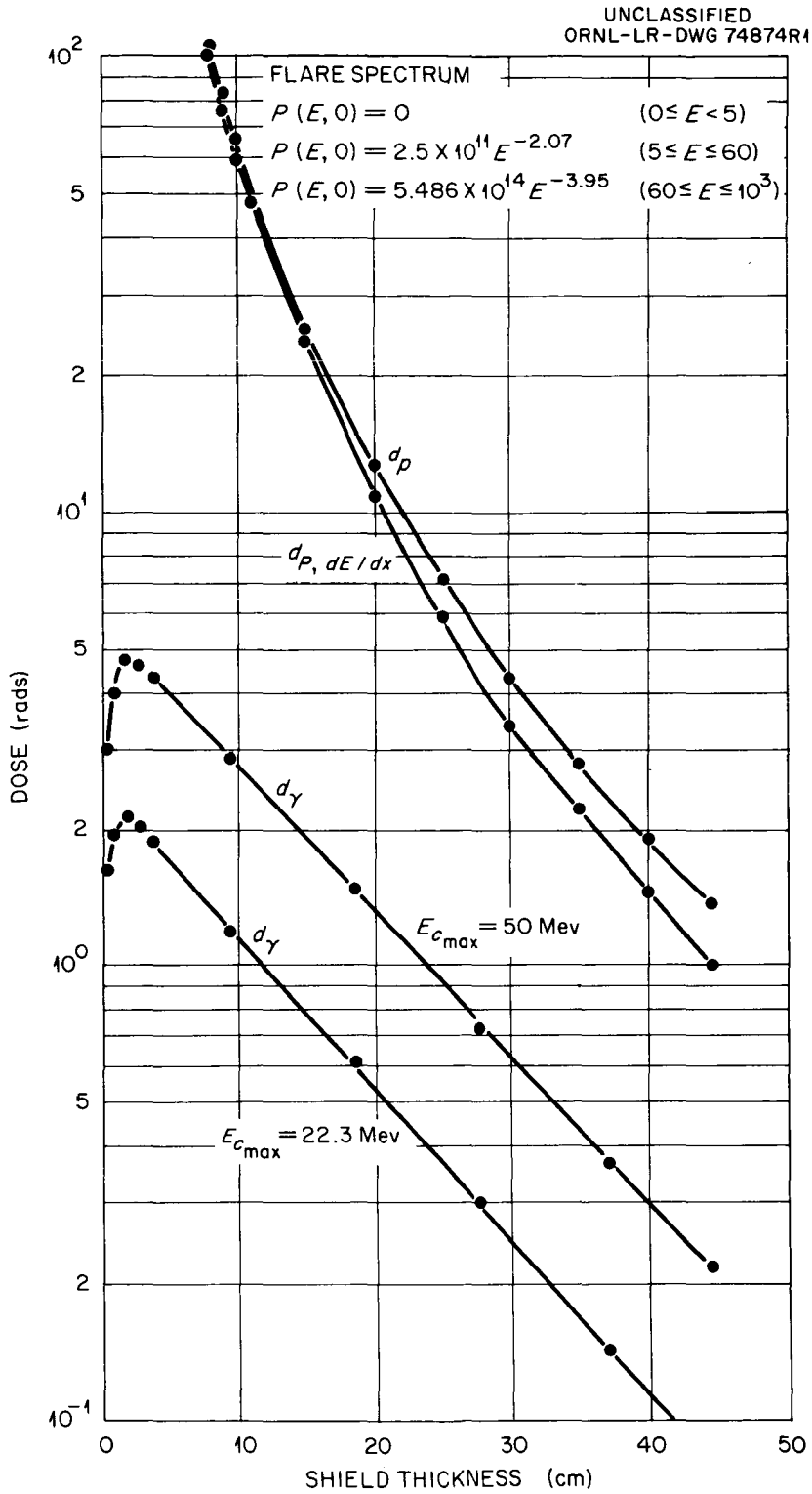

Fig. 2. Gamma and Primary Proton Doses at Center of Spherical Aluminum Shell from Solar Flare (May 10, 1959) Protons.

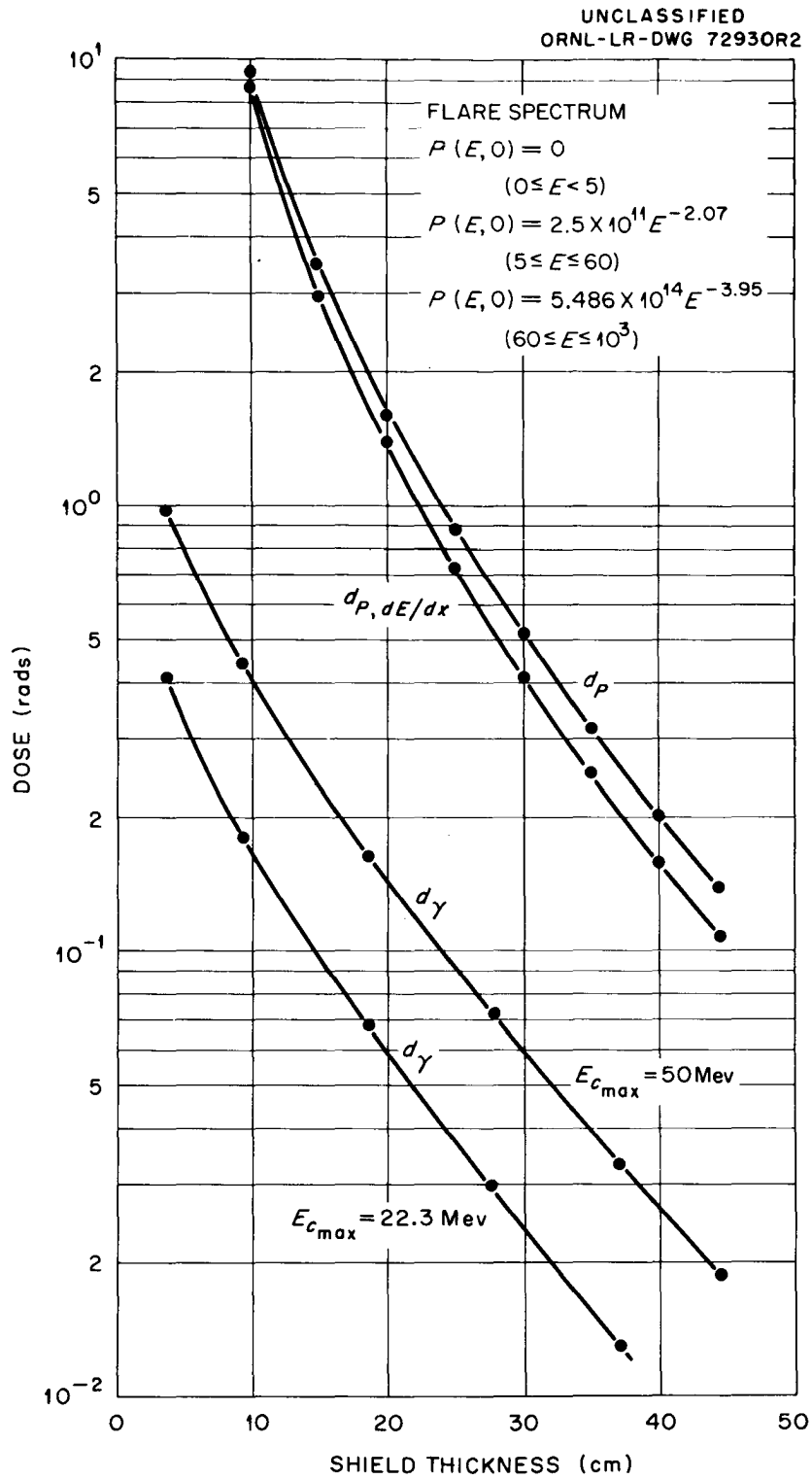

Fig. 3. Gamma and Primary Proton Doses from Solar Flare (May 10, 1959) Protons Incident on Aluminum Slab Shield.

Paper E-6

PROTON FLUXES ALONG TRAJECTORIES THROUGH THE INNER VAN ALLEN BELT

F. C. Perry
Aero-Space Division
The Boeing Company

1515 over Abstract

A method is formulated to calculate, by means of high-speed digital computing equipment, the total time-integrated proton flux for an arbitrary trajectory through the inner Van Allen belt. To this end, a map of the inner belt proton flux has been prepared in the (B,L) coordinate system, where B is computed from the 48-term spherical harmonic expansion of the earth's magnetic potential due to Finch and Leaton[1] and L is the McIlwain parameter.[2] This map is feasible, since the high-energy trapped proton component is generally quite stable with respect to geomagnetic activity.

The major souces of error inherent to the proton map in the (B,L) coordinate system are not to be found in the mathematical description of the geomagnetic field, but rather are to be found in positional inaccuracies of raw counting rate data, ambiguities connected with discrimination between protons and electrons, and time variations in the low energy proton component. This is especially true for large values of L ($L > 1.6$). Of interest are the marked differences between these proton flux contours and the proton flux contours calculated from the neutron albedo hypothesis.[3] Such differences indicate that other source mechanisms may well be important for populating the inner belt.

---

1. H. F. Finch and B. R. Leaton, The Earth's Main Magnetic Field - Epoch 1955.0, Monthly Notices R. Astron. Soc., Geophysical supplement, Vol. 7, 1957, pp 314-17.

2. C. E. McIlwain, J. Geophys. Res. 66, 3681-91 (1961).

3. A. M. Lenchek and S. F. Singer, J. Geophys. Res. 67, 1263 (1962).

15151

Values of the flux as a function of B and L are stored in a computer. Utilizing these values and given r, θ, and φ as a function of time for a trajectory of specified mission, the computer is programmed to (1) calculate B and L, (2) interpolate to obtain integral proton flux, and (3) integrate with respect to time along the trajectory to get the total integrated proton flux. The integrated proton flux can then be inserted, along with an appropriate differential spectrum, into a program[4] to calculate the total radiation dose received by the vehicle, components, and personnel (as modified by shielding). This is one of several computer programs which have been developed to assess the problem of radiation in space environment.

Introduction

In this paper the analysis leading to a calculational procedure to get integrated proton fluxes along trajectories is described in four sections. First, the general approach to the problem and its rationale are pointed out. Second, something is said about the coordinate system employed in developing a map of the inner belt protons. Third, a description is given of how the map was put together, the data utilized, and sources and magnitudes of possible errors; also, a comparison is made with a theoretical result based upon the cosmic-ray neutron albedo source mechanism. Fourth, the actual steps of programmed computation are delineated and examples are given of proton fluxes calculated along a few trajectories through the Inner Van Allen Belt.

General Approach to the Problem

As is well-known, the region of the inner belt is comprised of highly energetic protons of several million electron volts and thereby constitutes a possible radiation hazard to many space missions. The basic motivation in going to the trouble of developing a computer code to assess this radiation hazard is the feeling that the variety and complexity of space systems and subsystems warrant such an approach. For example, a question that may be asked by persons connected with space system hardware is "How long can transistor X be expected to

---

4. See paper by D. L. Dye in Session D.

function properly in space mission Y where the space mission is, say, characterized by a vehicle orbiting for 30 days at a certain inclination, etc.?" Due to the asymmetries inherent to the natural radiation belts, such a question (without the aid of automation) would entail a very laborious calculation to come up with even an order of magnitude estimate of the radiation. However, with a computer code the answer in terms of the total number of energetic protons per square centimeter can be estimated (in most cases to within much better than an order of magnitude) in a few minutes.

For the purpose of evaluating the radiation hazard to components and personnel, it would be desirable to know the differential energy spectrum of penetrating protons at every point of the inner belt (also, of course, as a function of time). Unfortunately, the spectrum itself has been measured at only a few positions in the region generally thought to be occupied by high energy protons. On the other hand, there has been a fair accumulation of counting rate data from satellites employing Geiger tubes. These detectors were sensitive to protons with energies above a specific threshold, and they detected radiation over a substantial volume of space. Therefore, our approach to the problem was to develop a spatial distribution of radiation based upon counting rate information (accounting separately for time variations), and then to make certain assumptions about the shape of the spectrum to be used in dose calculations.

The Coordinate System

To accomplish this task, a map of the inner belt proton flux has been prepared in the (B,L) coordinate system, where B is a representation of the earth's magnetic field[1] and L is the McIlwain parameter[2]. Several years ago it was realized that a dipole representation of the geomagnetic field was not adequate to systematize flux data[5]. As a result of this fact and attempts with other systems, the (B,L) coordinate system has been adopted as a standard in the systematization of measurements of the trapped corpuscular radiation.

The L parameter was invented by C. E. McIlwain and is the physical analog of the geomagnetic equatorial distance to a field line in the case of a dipole field. Figure 1 shows a typical example of surfaces of constant L and B. From the theory of adiabatic invariants as

---

5. S. Yoshida , G. H. Ludwig, and J. A. Van Allen, Distribution of Trapped Radiation in the Geomagnetic Field, J. Geophysical Research, 65, 807-813, 1960.

B.L. COORDINATE SYSTEM

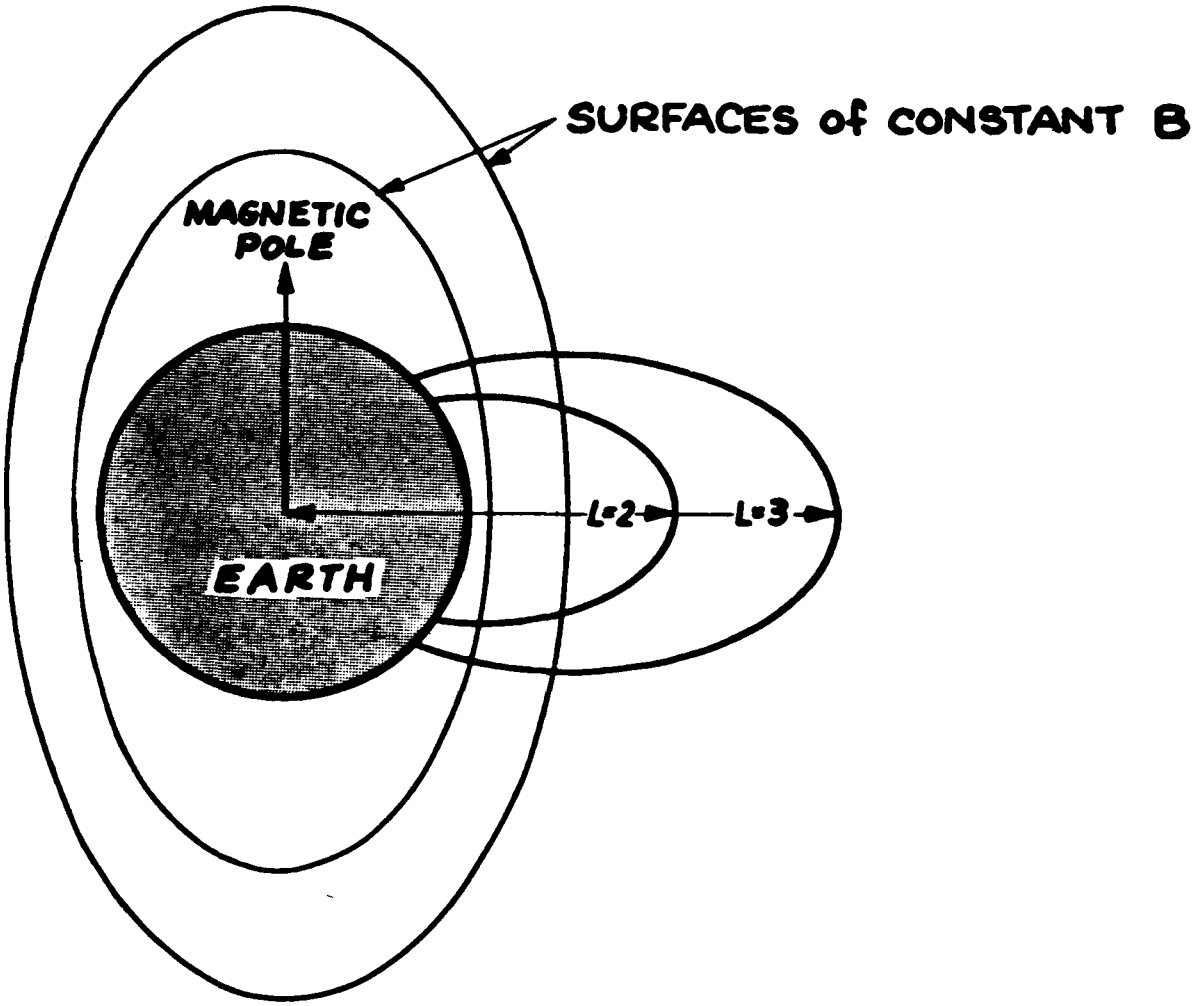

Figure 1

applied to particles trapped in the earth's magnetic field[6], we know, when the invariants are preserved, that the particle omnidirectional intensity is constant (to a good approximation) along loci of constant magnetic field and the longitudinal invariant. Since L is defined as a function only of B and I (longitudinal invariant), the same condition holds for particle intensity along loci of constant B and L. It also turns out, as one would expect from the definition of L, that the L parameter is approximately constant along magnetic field lines[2]. These facts imply, for our purposes, that geographic asymmetries will be smoothed out in a transformation from spherical spatial coordinates to the (B,L) coordinates, and our problem has been reduced from three to two dimensions (where computer interpolation is feasible).

Our procedure to compute B and L is as follows. The magnetic field is calculated from the 48-term spherical harmonic potential whose gaussian coefficients were computed by Finch and Leaton for epoch 1955.0 data[1]. The L parameter is calculated via the method of McIlwain from this magnetic field and the longitudinal invariant (also based upon the Finch and Leaton field). The longitudinal invariant itself is computed from a spherical harmonic expansion on shells of constant magnetic field. This expansion was devised by E. C. Ray and the coefficients were determined by fitting the series to values of I previously computed by Vestine.[7]

The method of computing B and L was not a critical factor in our analysis. The reasons for this are twofold: First, in the region where adequate flux data was available, comparisons were made between the values of B and L computed from a 512-term expansion kindly supplied by AFSWC[8] and the 48-term expansion[1]. The computed values always lay within the scatter deviation of points constituting isoflux contours. Second, in the region of scarce data, other errors by far exceeded those attributable to the (B,L) computational procedure (this will be explained in the next section).

In order to obtain the fullest advantage from a magnetic field representation, the coefficients should be updated every 10 years or

---

6. J. G. Northrup and E. Teller, Stability of the Adiabatic Motion of Charged Particles in the Earth's Magnetic Field, Phys. Rev. 117, 215-225, 1960.

7. E. C. Ray, NASA Goddard Space Flight Center, private communication, 1962.

8. D. C. Jensen and W. A. Whitaker, Spherical Harmonic Analysis of the Geomagnetic Field (abstract), J. Geophys. Research, 65, 2500, 1960.

less. A more recent magnetic field[9] should be used in an analysis such as the one presented here whenever better and more up-to-date flux data are available.

Data, Map, Errors, and Comparison with Theory

We discuss now the data that were used in the preparation of the inner belt proton map. Data in the form of true counting rates and spatial positions were taken from the satellites and space probes whose trajectories passed through the inner belt. The available information included the true counting rates of the unshielded 302 Geiger tube of Explorer IV already plotted in (B,L) coordinates by McIlwain,[2] and the Pioneer III[10] and IV[11] true counting rates. In all these vehicles the Anton 302 Geiger counter was the major information source, and the shielding was such as to make detection possible for directly penetrating protons with energies exceeding 30 Mev and directly penetrating electrons with energies exceeding about 2 Mev.

Counting rate data were also available from the detectors flown in the Explorer I[12] and Explorer VII[13] satellites. Both of these information sources were discarded for preparation of the present map for the reasons that: (1) the Explorer I counters saturated at the high counting rates and (2) the Geiger tube used on Explorer VII had an 18 Mev threshold for penetrating protons so that too many assumptions would have to be made in connection with the proton spectrum at low energies.

---

9. D. C. Jensen and J. C. Cain, An Interim Geomagnetic Field (abstract), J. Geophys. Research, 67, 3568-3569, 1962.

10. J. A. Van Allen and L. A. Frank, Radiation around the Earth to a Radial Distance of 107,400 km, Nature, Vol. 183, pp 430-434, February 14, 1959; IGY Satellite Report, Number 11, June 1960.

11. J. A. Van Allen and L. A. Frank, Radiation Measurements to 658,300 km with Pioneer IV, Nature, Vol. 184, pp 219-224, July 25, 1959; IGY Satellite Report, Number 11, June 1960.

12. SUI 61-3, Volumes I-V, Radiation Observations with Satellite 1958 Alpha (Explorer I).

13. G. Pizzella, C. E. McIlwain, and J. A. Van Allen, Time Variations of Intensity in the Earth's Inner Radiation Zone, October 1959 through December 1960, J. Geophys. Research, 67, 1235-1253, 1962.

The lower fringe of the inner belt was taken to be the McIlwain plot of Explorer IV true counting rates.[2] These counting rates were converted to omnidirectional proton flux ($E > 30$ Mev) by using the omnidirectional factor supplied by the Iowa group. Other experimental evidence which corroborates the Explorer IV fluxes derived in this manner are the Freden and White spectrum measurements[14], the Armstrong and Heckman spectrum measurements[15], and the Naugle and Kniffen experiment[16] (all of these utilizing emulsions and all measurements taken in the lower fringe of the inner belt).

In order to specify the peak and outer fringe of the high energy proton belt it was necessary to use the results of the space probes Pioneer III and IV. Both the trajectory of Pioneer IV and the outbound leg of the Pioneer III trajectory passed through a high latitude section of the inner belt, while the inbound leg of Pioneer III passed through the outer fringe of the inner belt very close to the geomagnetic equator. Counting rate data terminated at about 10,000 km geocentric distance on the inbound leg of Pioneer III; this point is believed to be close to the peak flux values in the inner belt. Omnidirectional fluxes were obtained from the equation given by Van Allen, namely $J = 1.6\,R$, where R is the true rate.

When flux positions for the outbound Pioneer III and IV trajectories were transformed to the (B,L) coordinates, marked inconsistencies were noted. The flux positions in (B,L) space for the inbound leg of Pioneer III were used to extrapolate the Explorer IV contours to the geomagnetic equator. The resulting contours seemed to average out the apparent inconsistencies between the Pioneer III and IV outbound legs in the outer fringe of the belt. The contour of maximum flux was taken to be 30,000 protons per square centimeter per second, based upon the work of Lenchek and Singer[3]. The result of these machinations is the plot of iso-proton flux contours shown in Fig. 2.

---

14. S. C. Freden and R. S. White, Trapped Proton and Cosmic-Ray Albedo Neutron Fluxes, J. Geophys. Research, 67, 25-29, 1962.

15. H. H. Heckman and A. H. Armstrong, Energy Spectrum of Geomagnetically Trapped Protons, J. Geophys. Research, 1255-1262, 1962.

16. J. E. Naugle and D. A. Kniffen, The Flux and Energy Spectra of the Protons in the Inner Van Allen Belt, J. Physical Society of Japan, Vol. 17, Supplement A-II, 118-122, 1962.

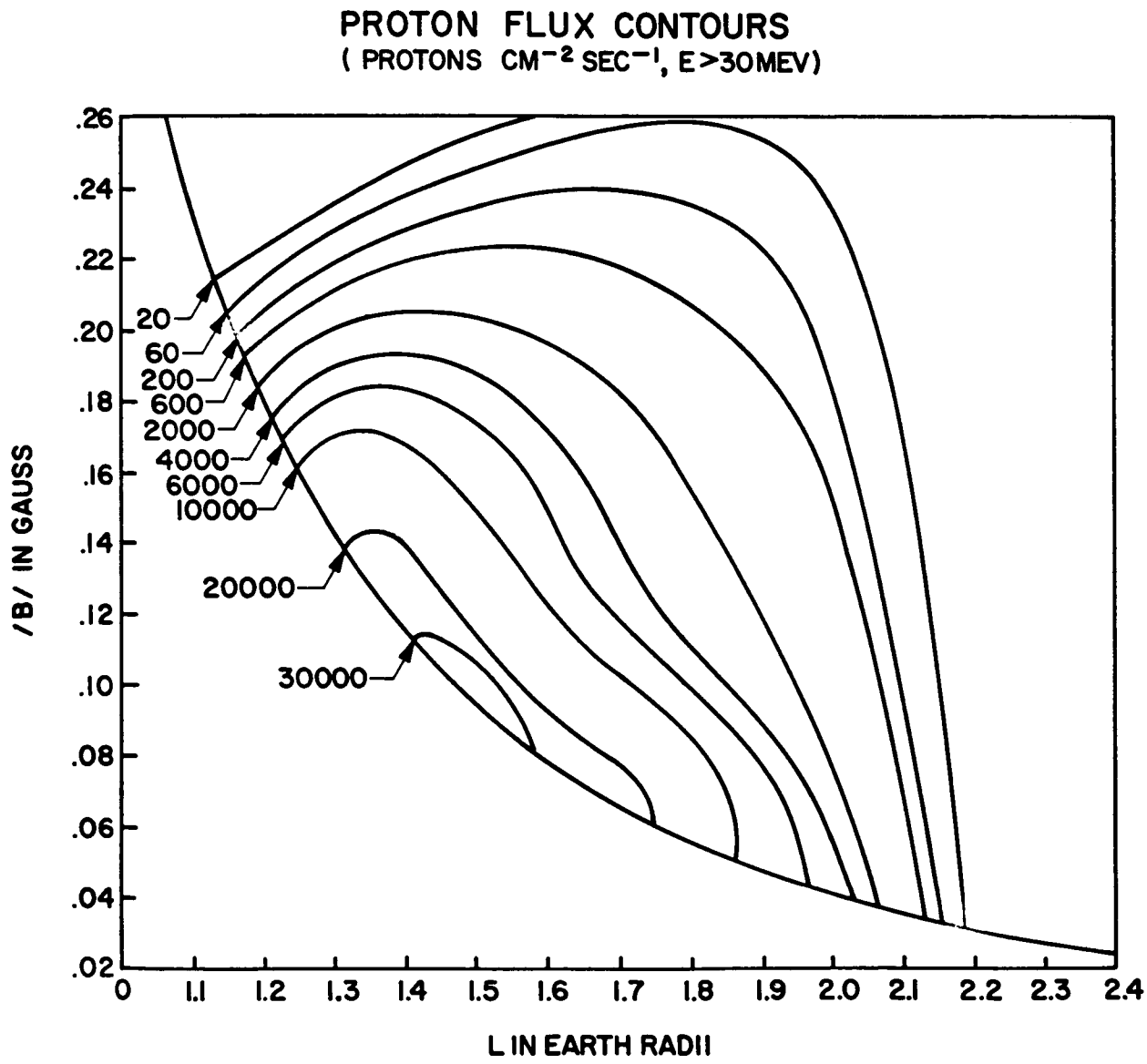
PROTON FLUX CONTOURS
(PROTONS CM⁻² SEC⁻¹, E>30MEV)
/B/ IN GAUSS
.26
.24
.22
.20
.18
.16
.14
.12
.10
.08
.06
.04
.02
20
60
200
600
2000
4000
6000
10000
20000
30000
0
1.1
1.2
1.3
1.4
1.5
1.6
1.7
1.8
1.9
2.0
2.1
2.2
2.3
2.4
L IN EARTH RADII

Figure 2

Now we discuss briefly the sources and magnitudes of possible errors inherent to this plot. There are several.

1. A major source of error is in the trajectory of Pioneer III (inbound leg). Van Allen estimates[10] the accuracy during the re-entry phase to be of the order of 1000 km. This amounts to a 10 percent error at the maximum of the belt. If all this error were to be found in the radial direction, it would amount to 1500 gamma in the magnetic field and .16 in the L parameter at the center of the belt. These, of course, are maximum errors. At the center of the belt this corresponds to believing the flux within about a factor of two. At larger values of L, i.e., toward the outer fringe of the belt, a 10 percent error in L may amount to flux errors of greater than an order of magnitude. Again this is undoubtedly a maximum estimate. More detailed knowledge is required to definitely establish the nature of the contours in the outer fringe region.

2. Errors in converting counting rates to omnidirectional flux. Van Allen estimates an uncertainty of $\pm$ 20 percent[10] in the omnidirectional factor of the 302 Geiger tube in Pioneer III; the Pioneer IV counter is supposed to be the same $\pm$ 10 percent[11]. For Explorer IV the error in conversion is not known but is presumed to be smaller.

3. Errors in determination of the nature of the radiation - discrimination between protons and electrons. The Iowa group estimates[13] tentatively on the basis of Explorer XII and other satellite information that the 302 Geiger tube aboard Explorer VII was counting the following particles:

   a. For $L < 1.8$, penetrating protons, $E > 18$ Mev.

   b. For $1.8 < L < 2.2$, comparable contributions of electrons and protons.

   c. For $L > 2.2$, penetrating electrons.

   Due to the somewhat different characteristics between the Geiger tubes aboard Explorer VII and the Pioneer probes, a pure proton contribution was ascribed to the Pioneer counting rates up to about $L = 2.0$. Above $L = 2.0$ the contours were arbitrarily joined to the equator in a manner symmetric to the lower fringe. Errors in the flux amounting to factors of two or three are possible here.

4. Errors from using the assumption of isotropic flux. There is practically no experimental information concerning the angular

distribution of inner belt protons, but certainly anisotropies exist.

5. Errors due to time variations in the belt. Investigations in this area using the Explorer VII data (Pizzella, et al.)[13] have indicated that there are time variations amounting to factors of two or three over a period of slightly more than a year when the data is averaged in a particular way. They found that some correlation may exist between magnetic storms (and accompanying solar proton events) and an enhancement of the inner belt protons. The picture is not clear to us yet, since the 302 Geiger tube in Explorer IV had a higher detection threshold than the tube in Explorer VII. This means that differences in counting rates may be due to either time variations or the different detection characteristics or a combination of both. If the changes are mainly attributable to low energy ($E < 40$ Mev) protons, perhaps from neutron albedo of solar protons arriving at the polar caps, then we are not in such bad shape (insofar as the radiation hazard is concerned). Such protons could be accounted for in the spectrum by looking at the 40 Mev threshold Geiger tube in Explorer IV.

A factor that should be remembered is that we are using 1958-59 data systematized by a magnetic field valid for 1955. It is felt that secular changes in the field up to the present time are of less importance than errors attributable to the data itself. A general conclusion regarding the errors in the proton map is that if in the heart of the belt the spectrum does not change radically from the one measured by Freden and White and others in the lower fringe (and this presumes that the cosmic-ray neutron albedo source mechanism is a likely source for the higher energy protons), then in this region the flux may be off by a factor of two or three. At larger values of L and at lower flux values (toward the slot), we may be off by an order of magnitude.

Of interest is a comparison between the proton map and a spatial distribution of inner belt protons calculated from the cosmic-ray neutron albedo source mechanism. Such a comparison is indicated in Fig. 3. The dashed distribution was originally computed by Lenchek and Singer[3] in spatial dipole coordinates, and it was then transformed to (B,L) coordinates. The neutron albedo-proton contours were computed for a 75 Mev threshold, so there should be some differences. In the regions near the geomagnetic equator the number of $E > 75$ Mev protons is less than the number of $E > 30$ Mev protons, as one might predict. At higher latitudes the number of $E > 75$ Mev protons exceeds that of the $E > 30$ Mev protons, which is contrary to expectation. If some low energy particles are due to the solar proton-neutron albedo mechanism, then one would expect that such a population would be most evident in the higher latitude regions of the inner belt. At any rate one can see that mechanisms other than the cosmic-ray neutron albedo may well be operative in the inner belt.

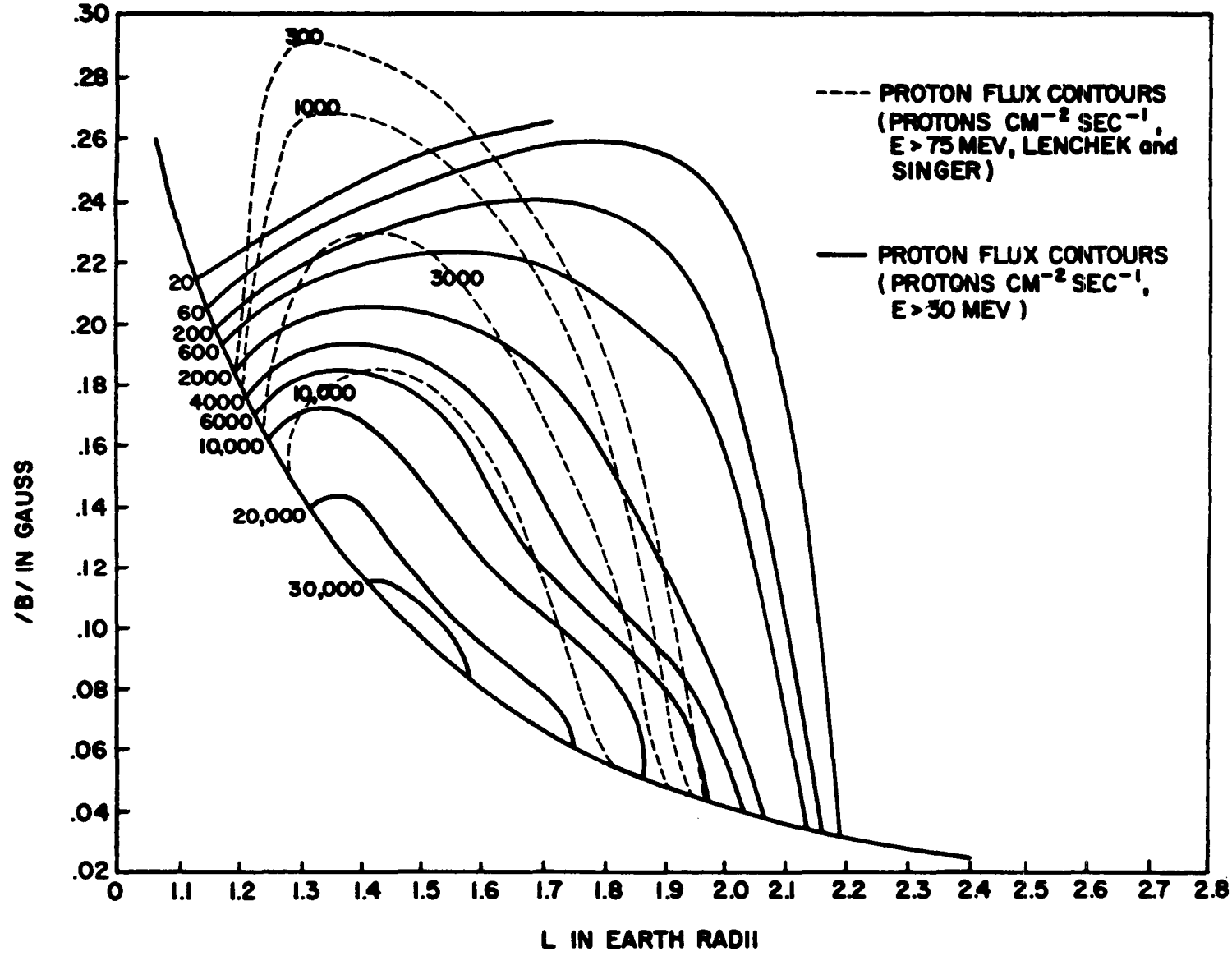
PROTON FLUX CONTOURS (PROTONS CM⁻² SEC⁻¹, E > 75 MEV, LENCHEK and SINGER)
PROTON FLUX CONTOURS (PROTONS CM⁻² SEC⁻¹, E > 30 MEV)
300
1000
3000
10,000
20
60
200
600
2000
4000
6000
10,000
20,000
30,000
/B/ IN GAUSS
.30
.28
.26
.24
.22
.20
.18
.16
.14
.12
.10
.08
.06
.04
.02
0
1.1
1.2
1.3
1.4
1.5
1.6
1.7
1.8
1.9
2.0
2.1
2.2
2.3
2.4
2.5
2.6
2.7
2.8
L IN EARTH RADII

Figure 3

Calculation of Integrated Proton Flux and Examples

Utilizing the previously described map of the inner belt, a method has been developed to calculate the integrated proton flux for an arbitrary trajectory. Values of the flux at magnetic field increments of 400 gamma and L parameter increments of .02 earth radii have been stored in a computer. These values (of flux) were obtained by logarithmic interpolation between the contours specified on the map. The computer program is designed to perform the following steps: (1) given a trajectory specified by the coordinates r, θ , φ , t (altitude, latitude, longitude, time), compute B and L at each point, (2) interpolate (linearly) in the stored flux values to get a flux at each point, and (3) integrate with respect to time along the trajectory to get the total proton flux for the duration of the mission.

The spectrum shape to be used along with the integrated flux in dose calculations is the latest one measured by Freden and White[14]. This spectrum is considered valid down to about 40 Mev. At lower energies and at higher latitudes there is some evidence for a steepening in the spectrum[16], possibly the result of protons from the solar proton-neutron albedo. The gammas as a function of B and L (assuming a power-law spectrum) have been computed[17] for energies between 30 and 40 Mev from counting rate data taken from the Explorer IV shielded Geiger tube, and these can be used in dose calculations if desired. However, it should be borne in mind that the lower energy component may well be subject to strong time variations.

In Fig. 4 are shown two examples of vehicle trajectories through the inner belt. The dashed curves represent a single polar circular orbit at an altitude of 1000 nautical miles; the total integrated flux per orbit was computed to be 2.5×10^7 protons per square centimeter. The dotted curves represent firstly the trajectory en route to an equatorial circular orbit, and secondly (the lopsided figure eight) a single equatorial circular orbit at an altitude of 2000 nautical miles; total integrated flux en route to orbit and per orbit are 5×10^7 and 2.7×10^8 protons per square centimeter, respectively.

Conclusions

1. Within the limits of available information a map of the high energy ($E > 30$ Mev) trapped protons has been prepared in the (B,L) coordinate system.

2. Errors in the proton map have been discussed. It is concluded that in the heart of the belt the flux is known to a factor of two

---

17. F. C. Perry and L. A. Oncley, to be published.

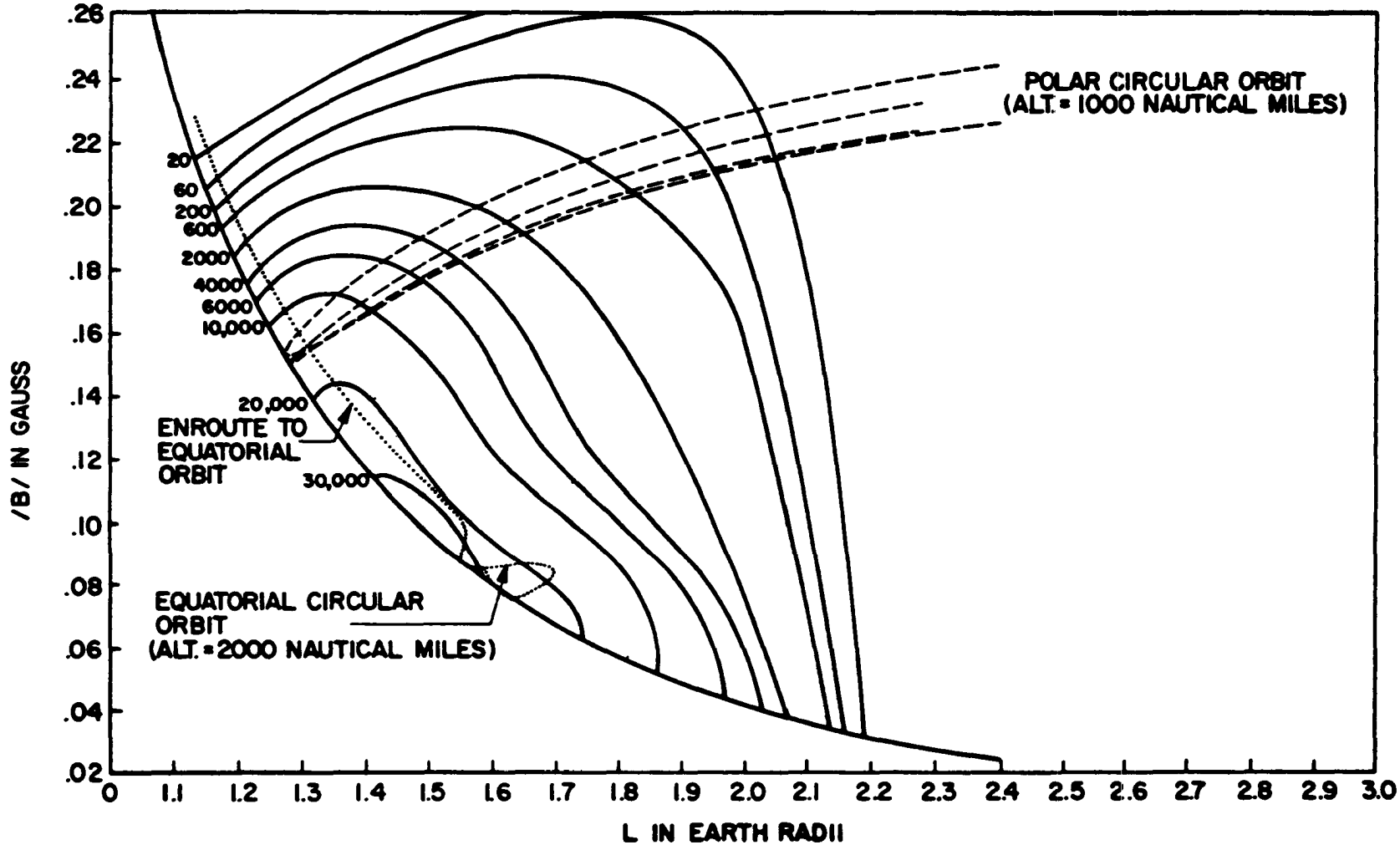
.26
.24
.22
.20
.18
.16
.14
.12
.10
.08
.06
.04
.02
/B/ IN GAUSS
0
1.1
1.2
1.3
1.4
1.5
1.6
1.7
1.8
1.9
2.0
2.1
2.2
2.3
2.4
2.5
2.6
2.7
2.8
2.9
3.0
L IN EARTH RADII
POLAR CIRCULAR ORBIT
(ALT.= 1000 NAUTICAL MILES)
20
60
200
600
2000
4000
6000
10,000
20,000
30,000
ENROUTE TO
EQUATORIAL
ORBIT
EQUATORIAL CIRCULAR
ORBIT
(ALT.=2000 NAUTICAL MILES)

Figure 4

or three; at larger L values we may be off by an order of magnitude.

3. Comparison of the proton map with a distribution based upon the cosmic-ray neutron albedo source mechanism, indicated that other sources may contribute to the trapped proton population.

4. The procedure to calculate the integrated proton flux along an arbitrary trajectory was outlined and a few examples given.

Paper E-7

A CALCULATIONAL PROCEDURE FOR ESTIMATING SPACE RADIATION EXPOSURE DURING LUNAR MISSIONS

R. A. Miller and W. Cranford
General Dynamics/Fort Worth

15152

Abstract

One problem concerned with manned space missions is the determination of shielding requirements for the protection of man from the hazards of space radiation. A space trajectory radiation exposure procedure (STREP) has been developed to estimate the magnitude of this radiation hazard by calculating the time-integrated spectra incident on a vehicle on a simulated trajectory during missions in cislunar space. STREP will calculate the dose received from radiation penetrating a thin shield. A brief description is given for the trajectory and radiation computational techniques. Some results are given for calculations of the integrated spectra and dose incident on a vehicle subjected to trapped radiation, cosmic radiation, and solar flare radiation during a lunar mission of about seven days.

Introduction

The problem described in this paper is concerned with one phase in determining the requirements for the protection of man from the hazards of space radiation. A computer program[1], STREP, has been developed at General Dynamics/Fort Worth under Air Force sponsorship to determine the magnitude of the radiation hazard to which manned space vehicles are exposed while on missions in cislunar or lunar space. The results of calculations of the time-integrated spectra incident on the vehicle from the various radiation components can be used as input for another procedure to compute the dose inside a shielded crew compartment. The computations made with STREP

1. W. Cranford, R. F. Falkenbury, and R. A. Miller, A Space Trajectory Radiation Exposure Procedure for Cislunar Missions. General Dynamics/Fort Worth Report FZK-9-178 (31 July 1962).

for two lunar missions - one in which the vehicle is beyond the earth's magnetic field during a solar flare, the other in which the vehicle is in a 24-hour orbit during the solar activity period - are described. Some results from calculations of the secondary components of the dose within a shielded crew compartment are shown as a function of polyethylene thickness.

Hazards to Space Missions

The discovery of ionizing radiations surrounding the earth has emphasized the existence of a hazard which must be assessed before manned space flight is feasible. From balloon observations, satellite measurements and earth-based monitoring systems, it is evident that the intensities of charged particles, both protons and electrons, are sufficiently great to create a radiation hazard.

The penetrating radiations to which a manned space vehicle will be exposed may be divided into four broad classifications: primary galactic cosmic radiation, trapped radiation, solar-flare radiation, and miscellaneous extraterrestrial radiation (Fig. 1). Of these categories, the greatest hazards to crews on lunar missions will be due to the solar-flare protons. The effects of solar flares within the vicinity of the earth are illustrated in Fig. 2.

Solar flares have an extreme time variability, which may depend to some extent on sunspot activity, since the flare frequency apparently varies roughly as the sunspot number with a period of approximately 11 years. During the peak sunspot cycle, Class 3+ flares may average one or more per month; however, during July 1959, three Class 3+ flares were observed within six days. The energy spectrum, measured 32 hours after onset, and other data for the 14 July 1959 flare are listed in Table 1. These data were used in the example described later in the paper.

Table 1. Solar Flare Data

Event	Spectrum (protons/cm^2-sec)	Energy Range (Mev)	Decay (hr)	Flare Duration (hr)
7-14-59	$1.5 \times 10^7 E^{-3.9}$	$30 < E < 1000$	t^{-2}	55.5

PRIMARY COSMIC RADIATION
- PROTONS
- HEAVY PARTICLES

TRAPPED RADIATION
- PROTONS
- ELECTRONS

SOLAR FLARE RADIATION
- PROTONS
- HEAVY PARTICLES
- GAMMAS
- ELECTRONS

MISCELLANEOUS RADIATION
- ALBEDO NEUTRONS
- AURORA BOREALIS GAMMAS

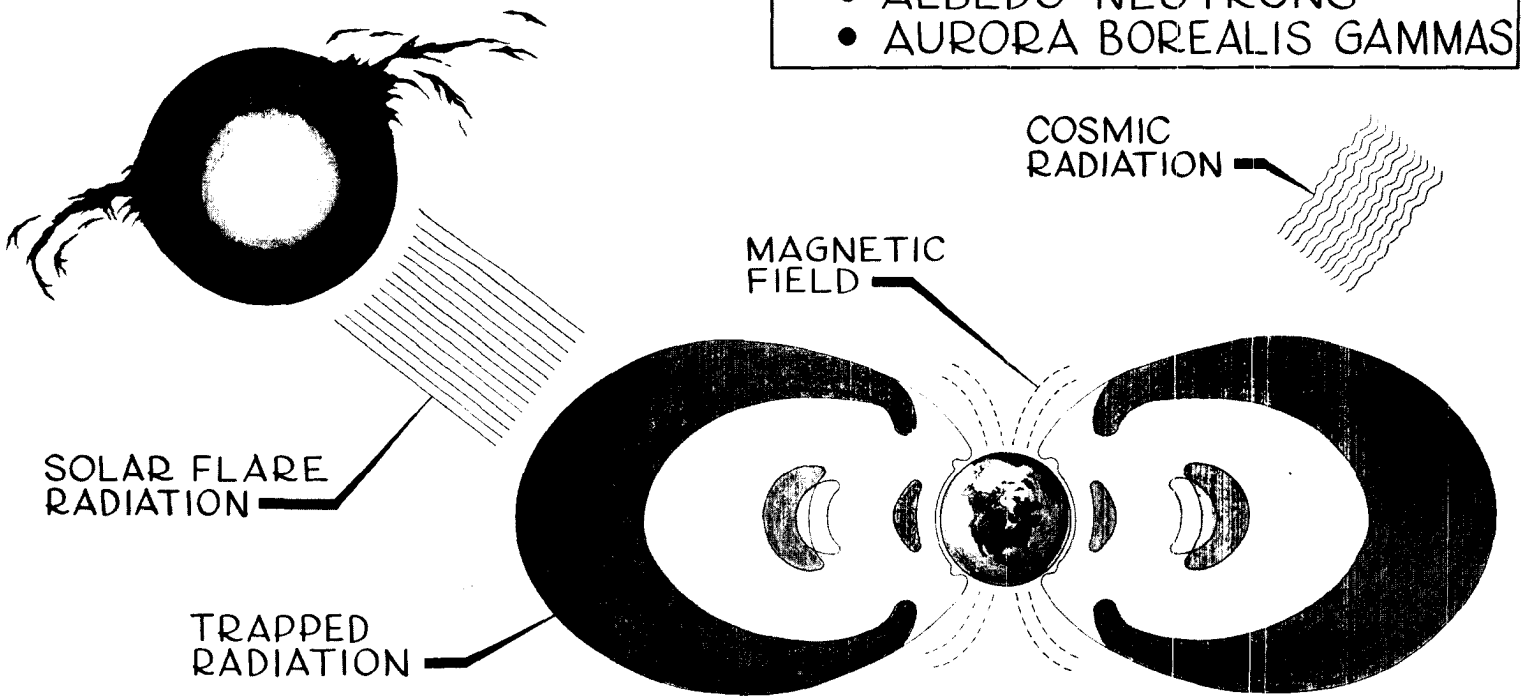

FIGURE 1. RADIATION HAZARDS TO SPACE MISSIONS

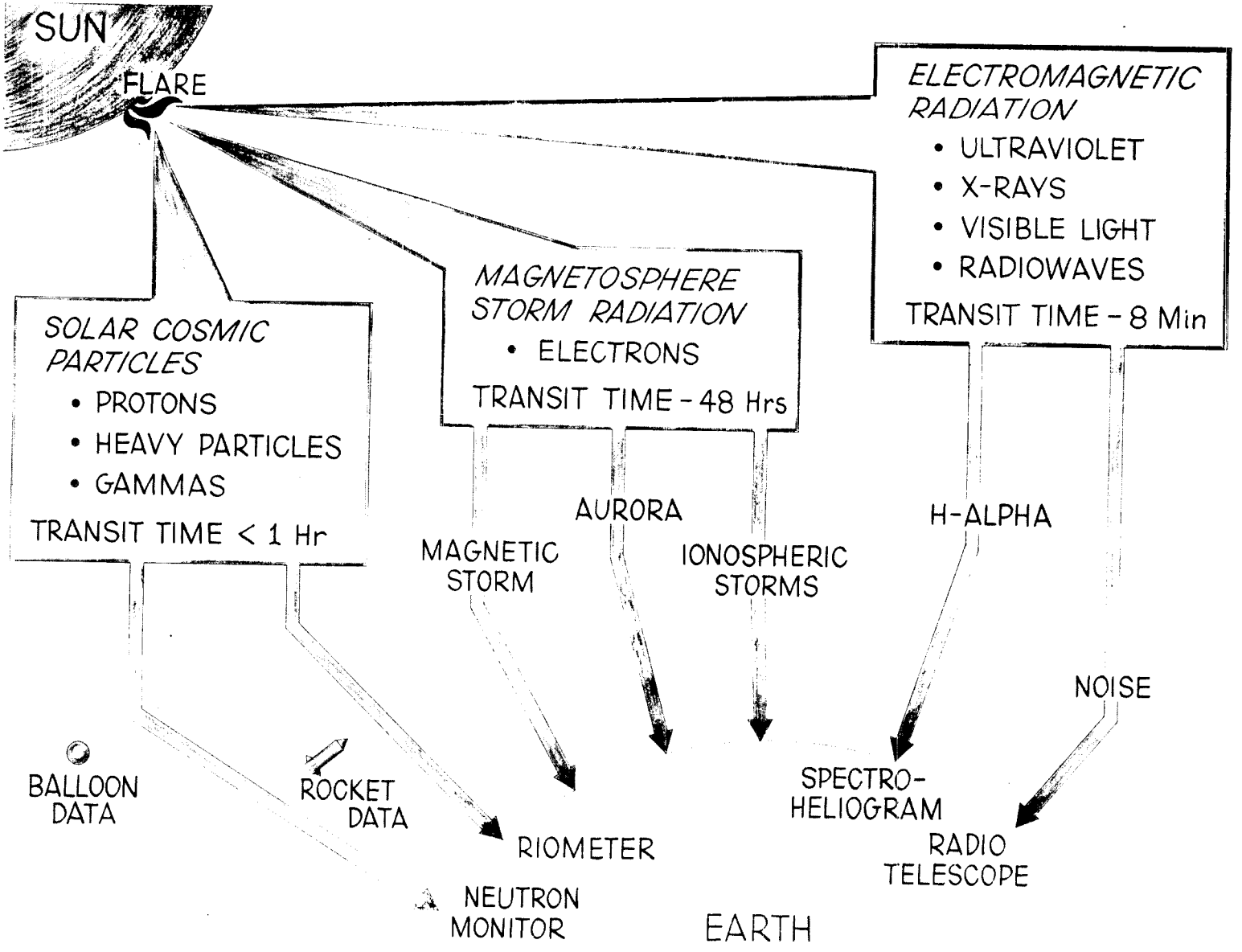

FIGURE 2. SOLAR FLARE EFFECTS

Calculation of Radiation Exposure

A procedure (STREP) which calculates the time-integrated spectra for mission trajectories will be described in the following sections. These spectra can be used in a second computer program (PAP) to calculate the primary and secondary proton and secondary neutron dose components within a shielded vehicle. STREP was designed to compute the time-integrated spectra for any combination of the several components of space radiations in lunar space. These components include the following: trapped protons and electrons; solar-flare protons, gammas, electrons, and heavy particles; cosmic-radiation protons and heavy particles; albedo neutrons; and aurora-borealis gamma radiation. The program will calculate the dose behind a thin shield at any time after the start of the mission.

Trajectory Calculations

General Considerations

The integration of the space-radiation spectra over a vehicle mission with experimental data for the radiation fields requires numerical integration with respect to time. Thus, this requirement infers the knowledge of the vehicle position as a function of time. The number and spacing in the set of positions in space, as well as the time required to obtain the desired accuracy under the assumption of accurate knowledge of the radiation field, influence the general approach to the trajectory computation problem. The spatial separation of the required points along the trajectory is governed by the gradients of the radiation field.

Since the problem has been confined to cislunar space and since no spatial dependence of the radiation components is known to exist in the vicinity of the moon, consideration is given only to the gradients induced by the earth. Such gradients are known to exist out to approximately ten earth radii, thereby defining a sphere of influence corresponding to the earth's magnetosphere. Outside this sphere of influence in cislunar space all types of radiation are assumed to be independent of position; however, time variation of the components, such as solar flares, will influence the integration. The greatest gradients are those associated with the trapped radiation regions. In practice, short time steps in integration are required inside the sphere of influence, whereas longer steps may be used for positions outside this region.

Trajectory Constraints

Since most of the space missions of immediate interest involve either close approach to an astronomical body other than the earth or several earth orbits, more than two points on the trajectory are necessary as input information for two-body calculations. The present version of STREP requires a number of positions, with associated times, determined by an external source which may include perturbation results. In order to reduce the number of positions required for input, the procedure solves the two-body problem by using an initial-position vector, estimated initial-velocity vector, and elapsed time to reach a second position. It computes the parameters of the free-fall orbit necessary to reach the second position at the proper time. The initial input velocity is used only to resolve the ambiguity of the direction of traversing the orbit. Once these parameters are established, STREP can compute any position along this trajectory leg which may be required by the radiation integration procedure. In this manner, a fast and efficient method for interpolation between known points on an accurately determined trajectory is provided, subject only to the restriction that the elapsed time is less than one orbital period in duration.

For free-fall trajectories inside the earth's magnetosphere, positions can be given at time intervals of less than one period. However, for thrust positions of the trajectory inside the sphere of influence, positions must be given every thirty seconds to maintain accurate integration. Outside the sphere of influence, for either thrust or free-fall legs, the positions must be given only when a change from thrust to free-fall, or vice versa, is evident. At each initial position of a free-fall orbit leg, an estimate of the velocity at this position must be given unless the previous leg was free-fall. The time from midnight of the day before the start of the mission must be specified with each position. Any number of thrust and free-fall legs may be used to describe the trajectory, with the required positional data given in any one of several different coordinate systems.

Time-Step Selections

For a trajectory in which burnout occurs below the inner radiation belt, calculations are begun from burnout as the first point. The first two points (P_1,P_2), shown in Fig. 3, and the elapsed time are used to compute orbit parameters for the first orbit leg of the trajectory. The radiation intensities are evaluated at the first point, P_1. A time step is calculated from the initial point by the equation

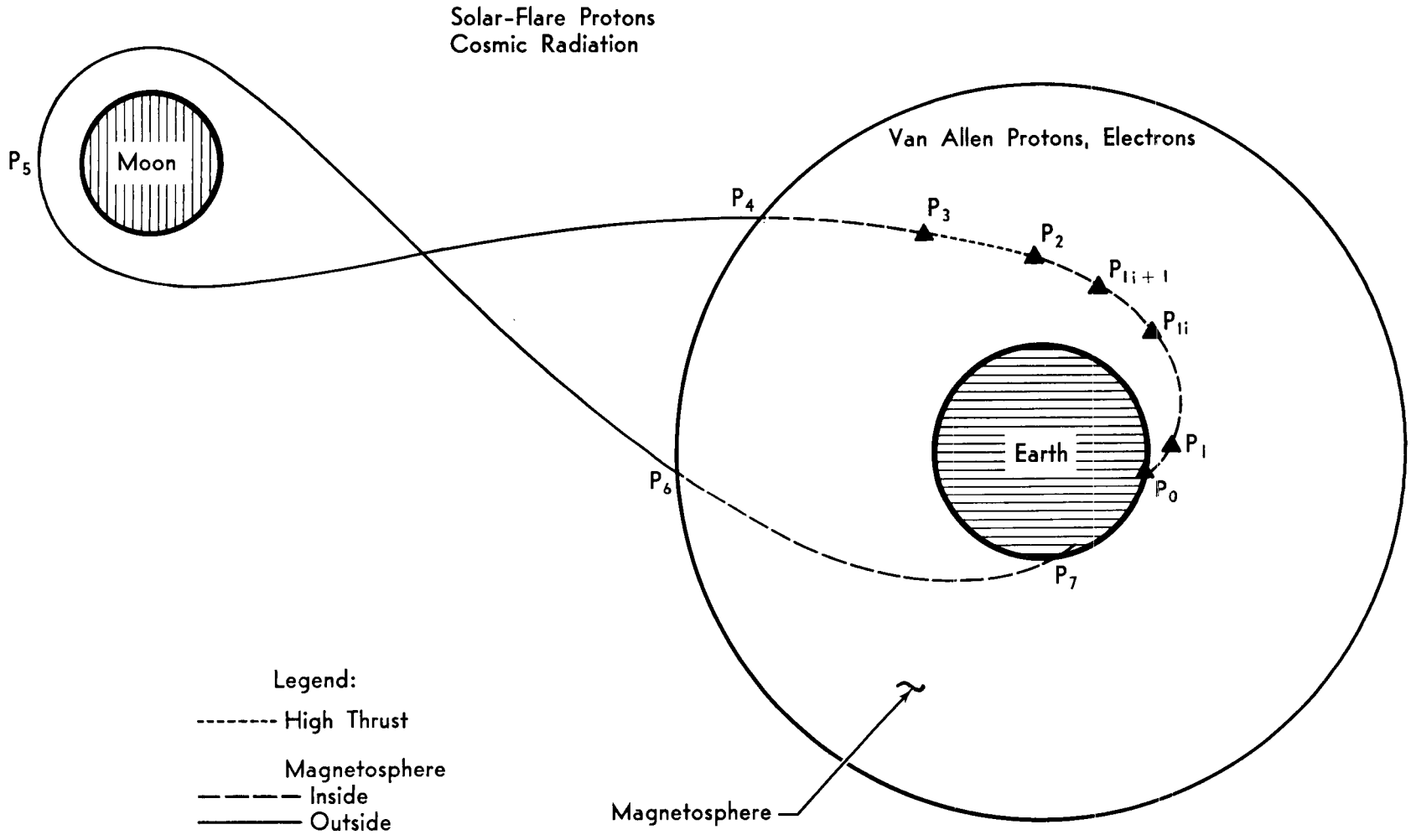

FIGURE 3. TRAJECTORY CHARACTERISTICS

$$\Delta t_1 = K\, r_e^{3/2}, \qquad (1)$$

where r_e is expressed in earth radii and K is an empirically determined constant. The radiation integration is performed with the integrand as a product of the intensity at the initial point and the time interval. The position at the end of the time interval is computed, the radiation intensities re-evaluated, and the radiation integration continued by adding the contribution from the new position. After a new time interval is found from the new position, the radiation integrals are increased by the contribution from the second step. This process is continued with the new position, P_{11} until the end (P_2) of the orbit leg is reached. The velocity at the end of this first leg is computed and is used as the initial estimate for parameters on the second leg (P_2,P_3). If the vehicle leaves the magnetosphere and the rest of the leg is entirely outside the sphere of influence, the remainder of the orbit leg is covered in one time step. This interpolation process is continued until the vehicle is outside the magnetosphere or else enters a high-thrust leg condition as indicated by a control number. In either of these cases, the two-body interpolations are not used until the vehicle is back within the magnetosphere or is on a low-thrust leg. Figure 4 shows the computational procedure in STREP.

Radiation Calculations

In addition to positions along the trajectory, data must be given to define the expected radiation environment for the mission. Although STREP does not predict the time of occurrence of solar flares or magnetic storms, any combination of these events with the associated times from the start of the mission may be used in describing the radiation environment. A maximum of ten changes - e.g., a total of ten different solar flares - could be programmed for each mission.

In general, the radiation environment is space-dependent. STREP considers cislunar space to be divided into two major domains by virtue of the earth's magnetic field. The first region is assumed to be a sphere with its center at the geomagnetic center. Inside this region all charged-particle radiation is modified by the effect of the earth's magnetic field on charged-particle intensities. An approximation is acquired through the reduction of the intensity at each energy by the solid-angle effect imposed by the cutoff energy and the distance from the earth's center. Outside this inner region, all types of radiation are assumed to be independent of space.

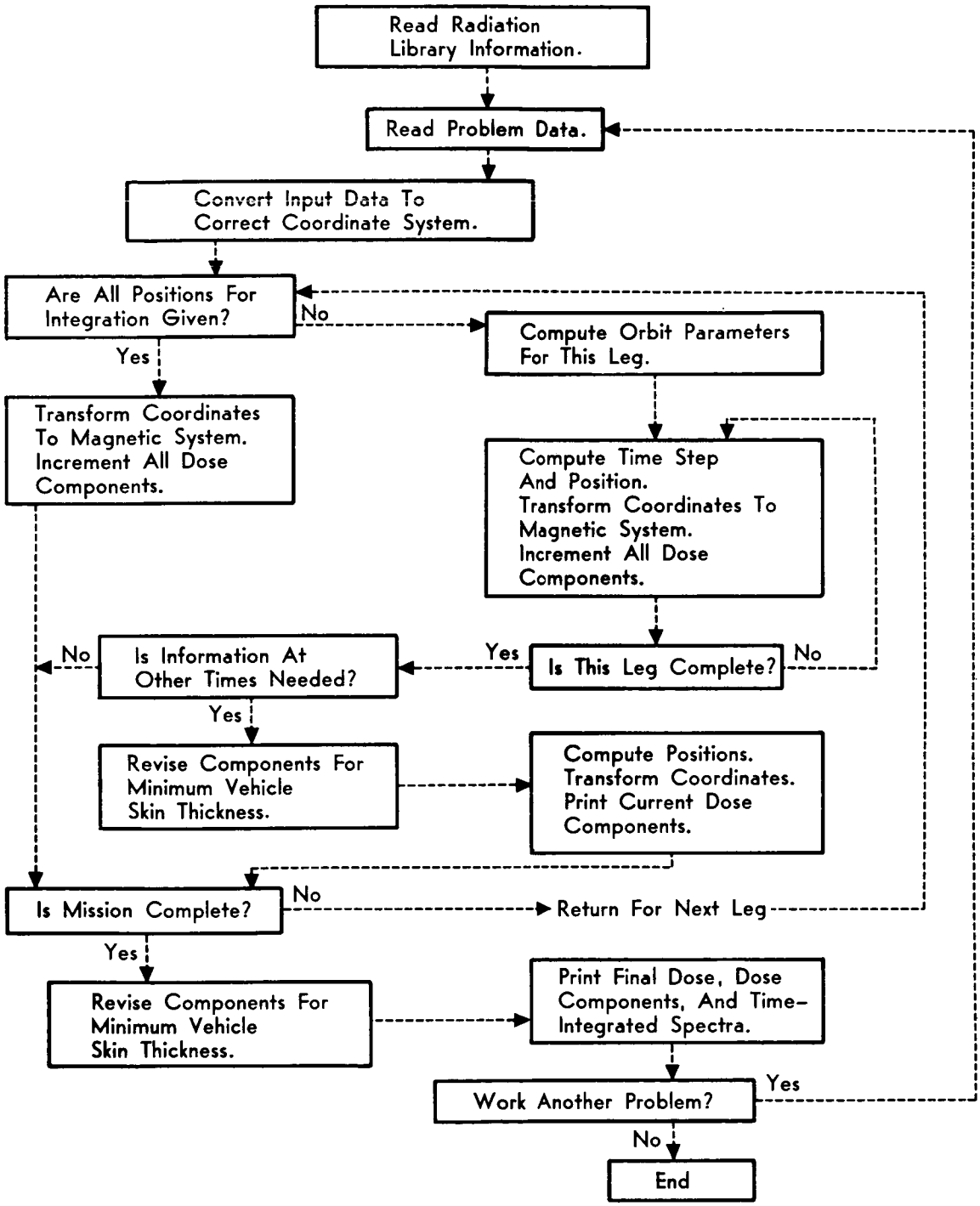

FIGURE 4. STREP FUNCTIONAL CHART

Trapped Radiation

The trapped radiation is assumed to be symmetric about an axis perpendicular to the equatorial plane and also symmetric with respect to the geomagnetic equator in a geomagnetic coordinate system. Under these assumptions, the data defining the space-dependent intensities are used in the form of a two-dimensional array in distance from the geomagnetic center and geomagnetic latitude. The intensity at a specified time is secured by linear interpolation with natural logarithms of the array, after transformation of the position to the geomagnetic coordinate system. Additional data required to define the spatial distribution of the trapped radiation are a maximum radius, minimum radius, and maximum latitude angle. After the intensity is calculated, the spectrum is computed from an expression of the form

$$\psi(E) = N_1 e^{-k_1 E} + N_2 E^{-k_2}, \qquad (2)$$

where the four parameters N_1, N_2, k_1, and k_2 are space-dependent. Provision is made to expand and contract the belts in case of a magnetic storm by insertion of new data at the proper time. After the activity has ceased, the original data may be re-inserted. The data for each component of the trapped radiation are secured from a separate library deck. In this manner, changes may be made in one component without modification of the other. A numerical integration is performed to secure the time-integrated spectra.

Solar-Flare Radiation

The spectra for solar-flare electrons, protons, and heavy particles are all computed by a formula similar to $\psi(E)$ with a decay factor t^{-k} and a normalization constant secured by an integration over the energy range. Inside the sphere of influence the integration with respect to time is numerical, since the intensities at each energy are modified by the effect of the geomagnetic field. A maximum of ten sets of constants for each flare is permissible, and as many as ten flares can be used during a mission to compute the radiation components. Outside the earth's magnetosphere, the spectra are integrated analytically in contrast to the numerical integration required by effects of the geomagnetic field on the charged-particle intensities.

Cosmic Radiation

The range of galactic particles is represented by protons for hydrogen and three types of heavy particles, namely:

Type A, (Helium); Type B ($2 \leq Z \leq 10$); and Type C ($Z > 10$). The spectra for protons and the heavy particles are computed by the formula

$$\phi(E) = H(E)\ C_1\ (C_2 + E)^{-k}, \tag{3}$$

where C_1, C_2, and k are determined from data for each type of spectral data, and H(E) is the modification produced on the spectra by the earth's magnetic field. Outside the sphere of influence, H(E) = 1.

Dose Calculations

The dose calculations are made for a vehicle skin with a thickness of 2 gm/cm^2. The charged-particle contributions are not attenuated through the skin of the vehicle. The portion of the spectrum which will not penetrate the skin is removed. The dose, for all charged particles except electrons, is calculated with the formula

$$D = A \int_{E_{cutoff}}^{E_{max}} \phi(E)/F(E)\ dE, \tag{4}$$

where A is constant to convert Mev to rads, $\phi(E)$ the time-integrated spectra, and F(E) an effective flux-to-dose conversion factor. The electron spectra are converted to gamma dose in the bremsstrahlung calculation by the formula

$$D_\gamma = \int_{E_{emin}}^{E_{max}} \phi(E_e) \int_0^{E_e} \frac{\psi(E_\gamma)\ e^{-u(E_\gamma)x}}{F(E_\gamma)}\ dE_\gamma E_e, \tag{5}$$

where $\psi(E_\gamma)$ is the gamma spectrum due to Wu[2], $\phi(E_e)$ the electron spectrum, E_e the electron energy, E_γ the gamma energy, $F(E_\gamma)$ a flux-to-dose conversion factor, and $e^{-u(E_\gamma)x}$ an attenuation factor for skin thickness x.

Radiation Calculations for a Lunar Mission

Trajectory and Environmental Data

The exposure of a shielded manned space vehicle to several radiation components while on two arbitrarily selected

---

2. B. T. Price, C. C. Horton, and K. T. Spinney, Radiation Shielding. New York: Pergamon Press (1957), 76

versions of a lunar mission was calculated with STREP to provide a functional evaluation of the procedure.

A trajectory of 149.2 hours duration[3] from the point of injection to the point of re-entry was used as a model. In the first trajectory, the vehicle was permitted to traverse the Van Allen regions, to proceed about the moon while exposed to a solar flare of the 14 July 1959 type, and then to return through the belts to the re-entry point. In this case, the flare was of 55.5 hours duration and was timed to begin onset at 12 hours after injection of the vehicle into its trajectory. The data for the solar-flare event is that listed in Table 1.

In the second case, the vehicle traversed the belts, proceeded beyond the magnetosphere, and received warning of probable flare activity six hours prior to onset. The vehicle returned to circle the earth in a 24-hour orbit (22,400-mile altitude) for 60 hours and then completed the lunar mission. A schematic drawing of these trajectories is shown in Fig. 5. The trajectory specifications[4] and radiation exposure conditions are listed in Table 2.

Table 2. Trajectory Specifications

Conditions	Trajectory 1	Trajectory 2
Radiation Exposure (hours after injection)		
Proton belt (exit)	.82	.82
Electron belt (exit)	3.4	3.4
Circular orbit (enter)		10.0
Solar Flare (onset)	12.0	12.0
Solar Flare (end)	67.5	67.5
Circular orbit (end)		70.0
Re-entry		
Time from injection (hr)	149.2	209.2
Altitude (miles)	75.77	75.77

3. J. P. Gapcynski and D. S. Woolston, Characteristics of Three Precision Circumlunar Trajectories for the Year 1968, NASA Report TN-D-1028 (March 1962).

4. Ibid.

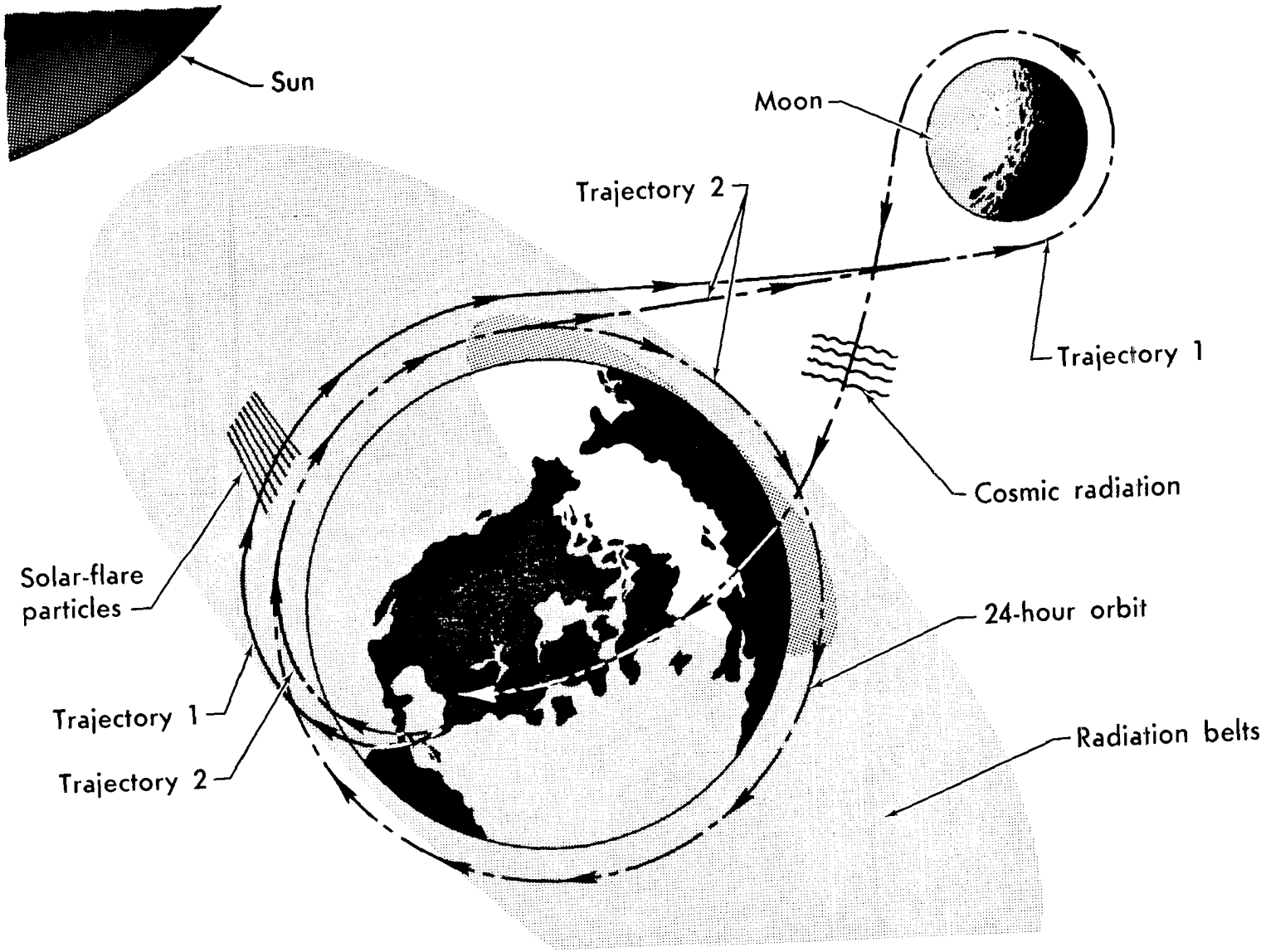

FIGURE 5. LUNAR TRAJECTORIES

A modification of Trajectory 1 consisting of a change of 30° in the longitude of the end point of the first leg after injection is designated by Trajectory 3. A portion of Trajectory 1 and Trajectory 3 through the Van Allen proton belt is shown in Fig. 6. This judiciously chosen alternate trajectory essentially avoided the radiation belts.

Some indications of the accuracy of STREP calculations of the required velocity can be seen from a comparison of the results in Table 3.

Table 3. Velocity Comparisons

Time (hr)	Velocity (ft/sec)	
	Reference 3	STREP
0	36,167	35,805
7.9	8,077	8,109
136.1	6,485	6,478
149.2	36,082	36,071

Spectra and Dose Calculations

The time-integrated spectra incident on the unshielded vehicle from solar-flare protons, Van Allen protons, and cosmic radiation for the trajectories are shown in Fig. 7. It will be noted that the solar-flare spectrum for Trajectory 2 is lower than that for Trajectory 1 in the energy range of from 30 to 300 Mev. This decrease for the lower-energy particles will reflect a decrease in the dose from secondary particles within a shield. Figure 8 shows the time-integrated spectra from Trajectory 1 for the three different types of heavy particles represented in STREP. A comparison of the time-integrated spectra for electrons during Trajectory 1 and Trajectory 2 is shown in Fig. 9. A slight increase of the electron spectrum, the heavy-particle spectrum, and cosmic-radiation spectrum was calculated for the 60 hours spent in the 24-hour orbit.

The results of the unshielded-dose calculations behind an aluminum skin of 2 gm/cm^2 thickness are summarized in Table 4 for the three trajectories. It may be noted that the dose from the Van Allen belt shows a decrease of from 14.3 rad for Trajectory 1 to 2.9 rad for Trajectory 3. It may be remarked that a geomagnetic equatorial orbit selected at about 2½ earth radii would have eliminated the contributions to the dose from the flare.

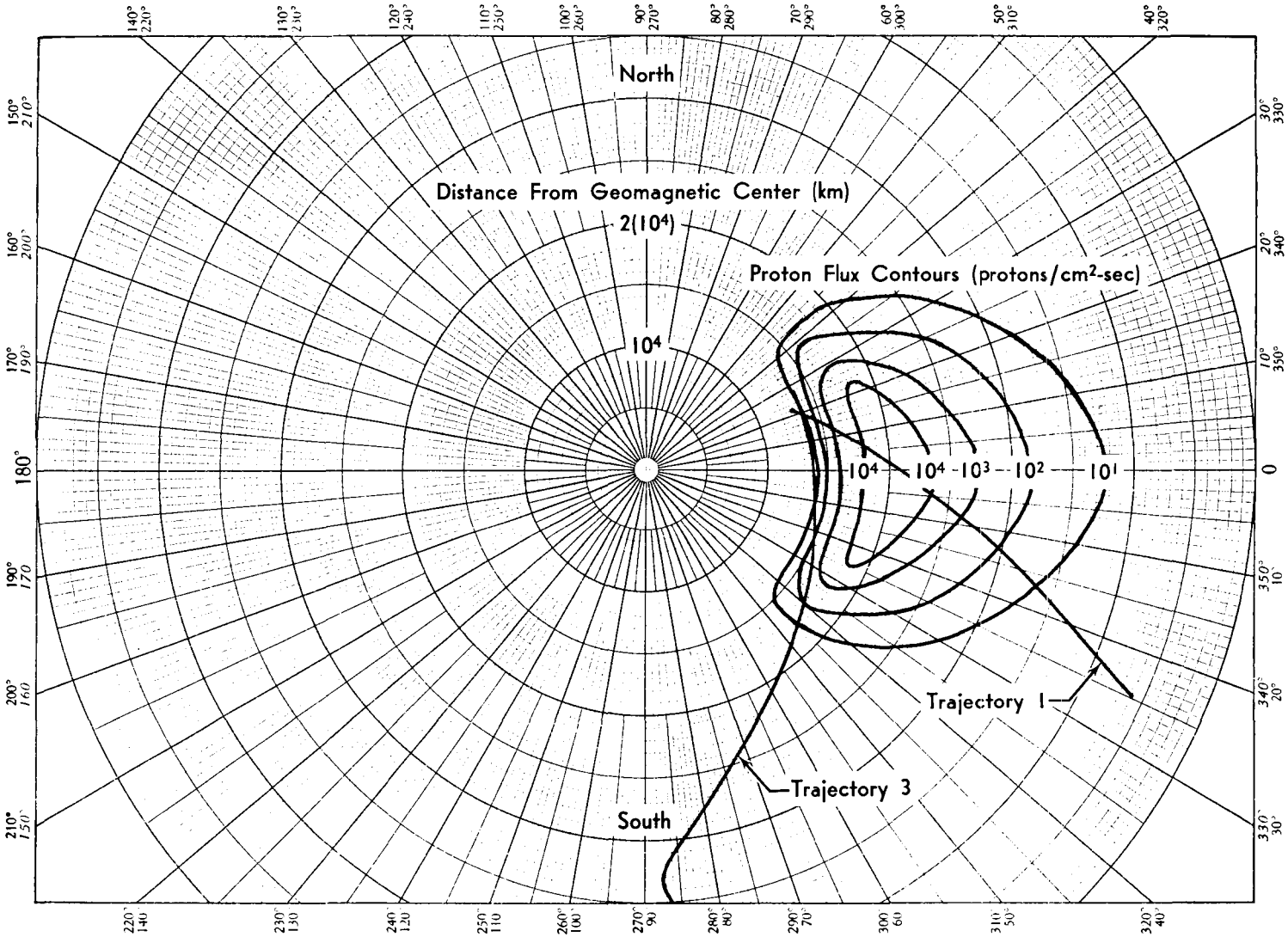

FIGURE 6. TRAJECTORIES THROUGH VAN ALLEN FROTON BELT

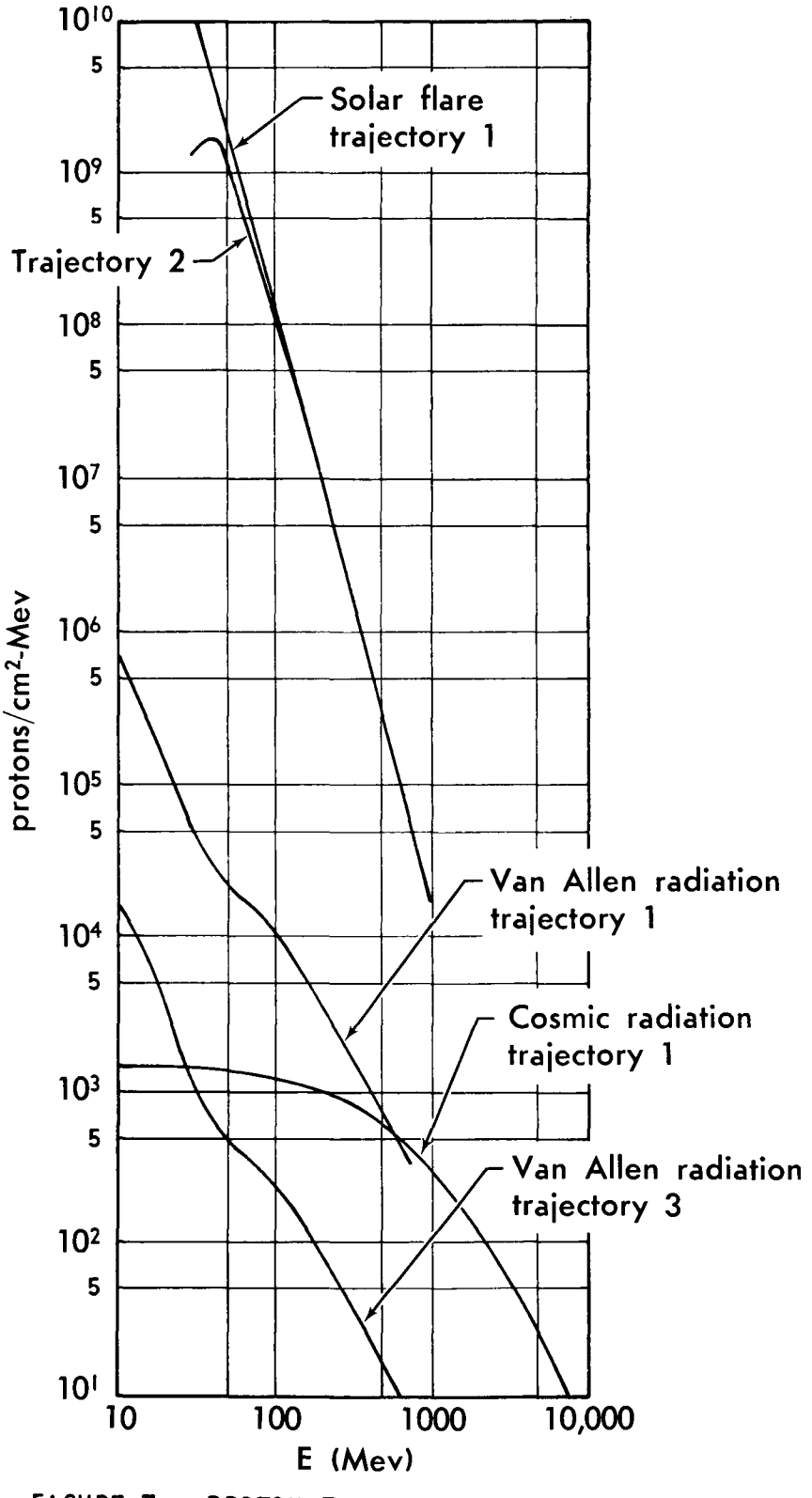

FIGURE 7. PROTON TIME-INTEGRATED SPECTRA

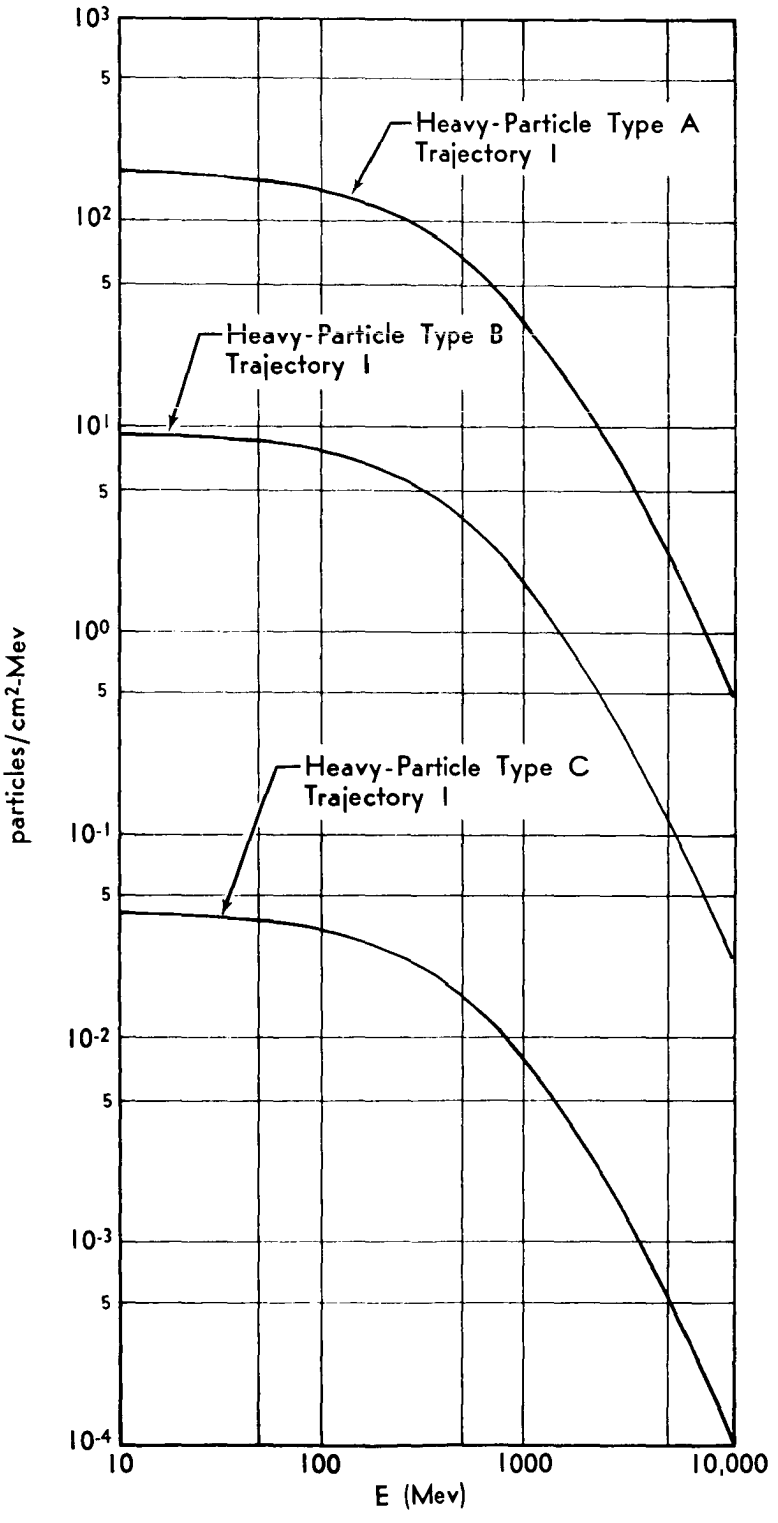

FIGURE 8. HEAVY-PARTICLE TIME-INTEGRATED SPECTRA

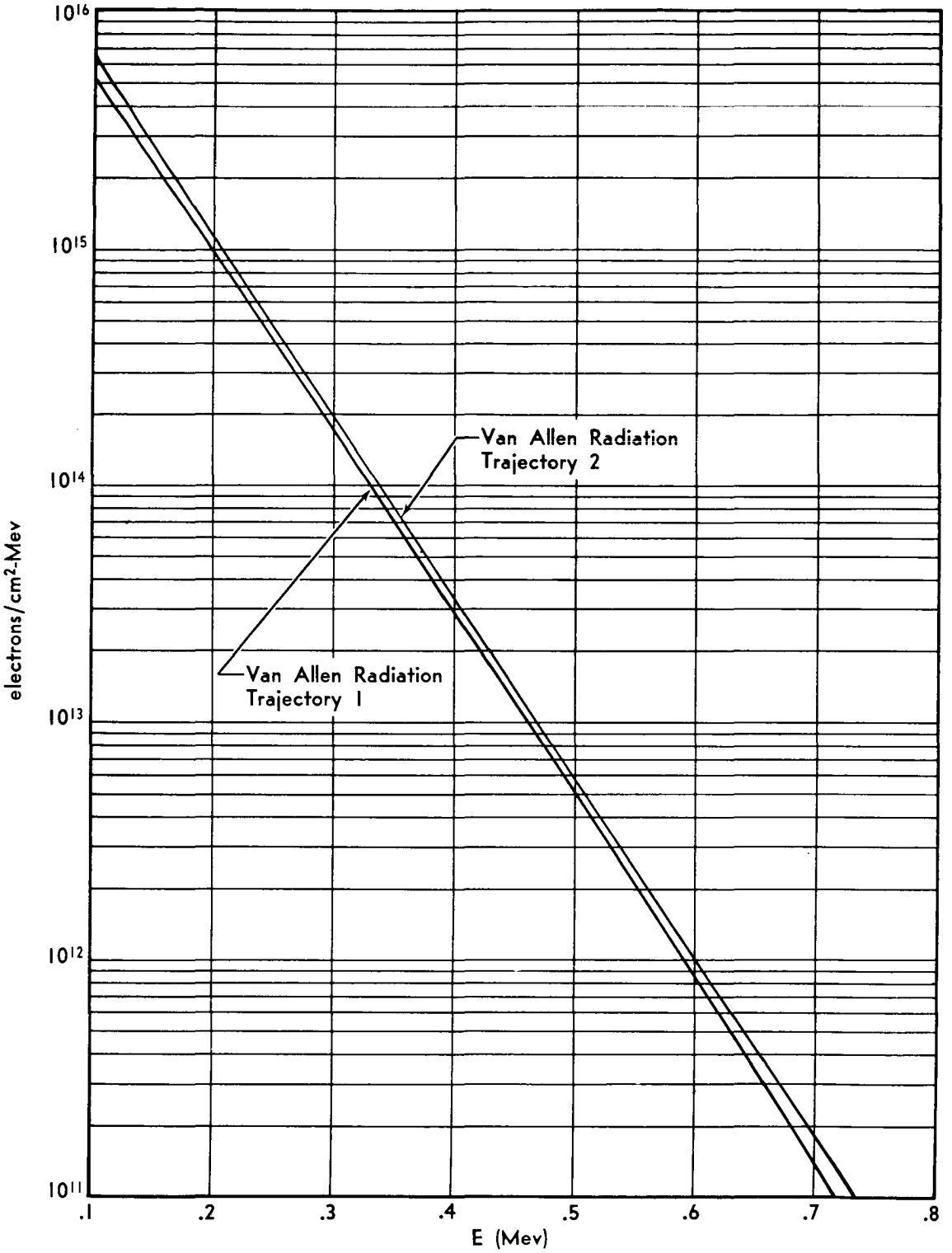

FIGURE 9. ELECTRON TIME-INTEGRATED SPECTRUM

Table 4. Unshielded-Dose Calculations

Component	Dose (rad)		
	Trajectory 1	Trajectory 2	Trajectory 3
Van Allen Protons	$3.1(10^{-1})$	$3.1(10^{-1})$	$6.8(10^{-3})$
Solar Flare Protons	$2.2(10^{4})$	$9.4(10^{3})$	$2.2(10^{4})$
Cosmic Protons	$6.2(10^{-2})$	$8.2(10^{-2})$	$6.2(10^{-2})$
Heavy Particle A	$2.7(10^{-2})$	$3.8(10^{-2})$	$2.7(10^{-2})$
Heavy Particle B	$7.9(10^{-3})$	$1.1(10^{-2})$	$7.9(10^{-3})$
Heavy Particle C	$2.5(10^{-5})$	$3.5(10^{-5})$	$2.5(10^{-5})$
Van Allen Electrons	$1.4(10^{1})$	$1.7(10^{1})$	$2.9(10^{0})$
Albedo Neutrons	$1.3(10^{-4})$	$2.7(10^{-4})$	$1.8(10^{-4})$

These dose values are for an essentially unshielded vehicle. The results of using the spectra output in another procedure[5] (PAP) are shown in Fig. 10 for lunar Trajectory 1. A fixed shield of 6 gm/cm^2 of aluminum backed with a variable thickness of polyethylene was assumed. The several components of the dose, primary and secondary, are shown as functions of the polyethylene thickness. It should be noted that the contribution to the dose from the secondary components begins to play an increasing role with increasing thickness of the shield. This contribution from the secondary component has been characteristic of other calculations for thick shields[5]. It is clear that for this flare a dose of 100 rads would be received under a composite shield of 6 gm/cm^2 of aluminum and 25 gm/cm^2 of polyethylene. The magnitude of this dose value indicates that for a flare with the characteristics of the 14 July 1959 event, considerable shielding will be required on lunar missions.

5. R. K. Wilson, R. A. Miller, and R. L. Kloster, A Study of Space Radiation Shielding Problems for Manned Vehicles. GD/FW Report FZK-144 (June 1962).

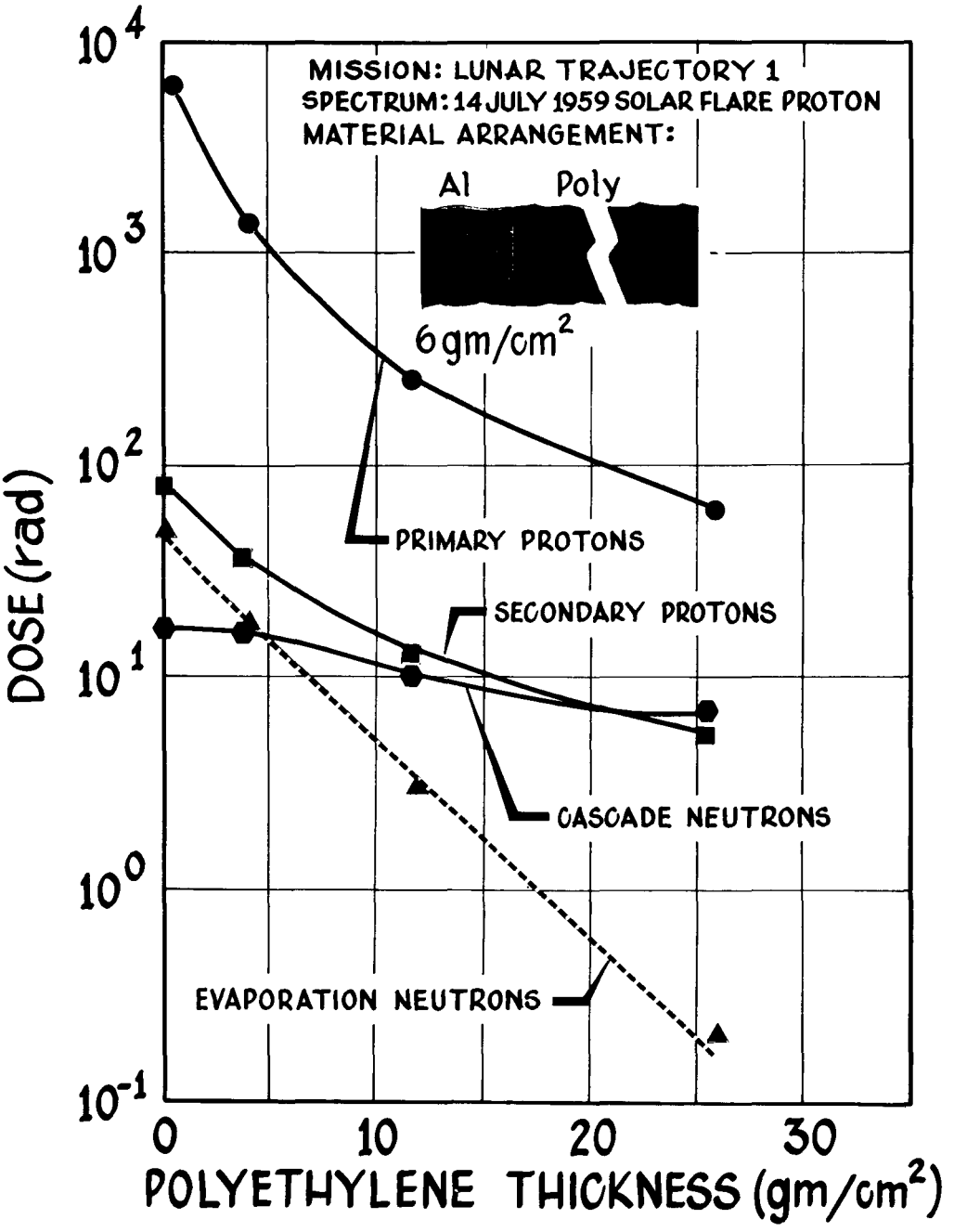

FIGURE 10. COMPOSITE-SHIELD DOSE

Summary

The procedure, STREP, may be utilized as a generation tool for a source of time-integrated spectra incident on a space vehicle during lunar missions. Since input requirements on the trajectory are positions and associated times, the procedure is independent of a particular calculational method for trajectories. The results from problems of interest indicate that the present version is adequate for lunar missions, provided a radiation field does not exist in the vicinity of the moon.

The calculations for a lunar mission during the active period of a particular solar flare indicate that an excessively high radiation dose may be received within a shielded vehicle. These calculations are predicated on the assumption that the radiation spectra as currently reported are reasonably correct. The results indicate the necessity of planning missions during quiet solar periods to avoid excessive shield weights to provide adequate protection.

Paper E-8

RADIATION DOSAGES FROM ELECTRONS AND BREMSSTRAHLUNG IN THE VAN ALLEN BELTS

S. L. Russak
The Martin Company
Baltimore 3, Maryland

Abstract

Radiation dose rates have been calculated for six electron spectra. The decrease in dose rate with shielding was determined--and in each case the electron dose becomes insignificant with 2 to 6 gm/cm^2 of aluminum. Electron bremsstrahlung dose rates versus absorber thickness were also calculated. Detailed dosage calculations for an Apollo-type spacecraft were made and mission dosages for four lunar trajectories are given, to show the effects of trajectory selection. These are compared with the dosages from protons and secondary neutrons in the Van Allen Belt. Doses as a function of orbital altitude, of inclination and of absorber thickness are also presented for the latest version of the inner belt.

Discussion

Over the past few years, a number of representations of the spectral distribution and intensity of geomagnetically trapped electrons have been evolved. We had had occasion to evaluate the radiation dosage that would result from exposure to these electrons and this paper reports on dosages from the six spectra shown in Fig. 1, namely: (1) the inner and (2) the outer zone integral spectra given by Van Allen[1] in 1959; (3) a composite inner and outer spectrum from the experimental data of Holley[2], together with Dessler's[3] interpretation of Walt's[4] data;

---

1. Van Allen, J. A., "The Geomagnetically Trapped Corpuscular Radiation," Journal of Geophys. Research, Vol. 64, No. 11, p 1683, 1959
2. Holley, F. E., "Radiation Measurements to 1500 Kilometers with Atlas Pods," Air Force Special Weapons Center, TR 60-9, 1960
3. Dessler, A. J., "Letters to the Editor," Journal of Geophys. Research, Vol. 65, No. 10, p 3487, 1960
4. Walt, M., Chase, L. F., Cladis, J. B., Imhof, W. L. and Knecht, D. J., "Energy Spectra and Altitude Dependence of Electrons Trapped in the Earth's Magnetic Field," Proceedings of First International Space Science Symposium, Nice, 1960

(4) the outer zone peak spectrum given by Van Allen in the Space Flight Report to the Nation; (5) an inner belt spectrum given recently by the SUI[5] group; and (6) the fission spectrum believed to be representative of the electrons at the peak of the artificial radiation belt[6].

For Spectra (3) and (5), the peak fluxes were extrapolated to the peak of the electron zone. The small detector dose rates from each of these distributions (evaluated between 0.001 and 5.0 Mev) are shown in Fig. 2, as a function of aluminum thickness. The rates vary from about 2×10^3 to 2×10^5 rad/hr under 0.03 gm/cm^2--with the electrons completely extinguished between 2 and 6 gm/cm^2. If we divide by the peak flux, J_o, we find that the highest dose per electron (remembering that J_o is the integral between 0.020 and 5 Mev) at absorber thickness above 0.1 gm/cm^2 comes--as expected--from the very flat fission spectrum.

Figure 3 shows the bremsstrahlung dose rates from these six spectra under aluminum thicknesses between 0.03 and 10 gm/cm^2. At 0.03 gm/cm^2 the dose rates extend from about 3 to 2500 rad/hr--considerably below the electron dose rates at that thickness. At 6 gm/cm^2 the X-ray dose rate extends from less than 0.1 rad/hr, for the new outer belt, to about 30 rad/hr for the fission electrons of the artificial belt. Quite a bit more can be obtained from further examination of these first three figures--for example, note the pronounced rising dose rate for the fission spectrum. It is less pronounced for the steeper Spectra (3) and (5) and no longer seen at 0.03 gm/cm^2 for the remaining, softer, electron spectra.

Let it suffice to say that the wide variation in form, or slope and intensity, of these spectra results in dose rates that are significantly different. In the case of thin absorbers, the electron dose rates are much more important than the X-rays. As we increase the absorber, the X-rays become more important--with the cross-over point varying among the different spectra.

---

5. Pizzella, G., Laughlin, C. D. and O'Brien, B. J., "Note on the Electron Energy Spectrum in the Inner Van Allen Belt," Journal of Geophys. Research, Vol. 67, No. 9, p 3281, 1962

6. Zerby, C. D. and Moran, H. S., "Tissue Dose Rate from Bremsstrahlung Radiation Behind an Idealized Apollo Vehicle Wall Exposed to Electrons in the Artificial Radiation Belt," presented at the Symposium on the Artificial Radiation Belt, Washington, D. C., September 1962

There is only a very limited amount of practical information that can be obtained with homogeneous spheres or slabs and peak fluxes. The next set of data is for a detailed Apollo configuration along several lunar trajectories. The method of analyzing the spacecraft shape and construction is illustrated in Fig. 4. This analysis was used over 200 area elements to define the command module. The electron fluxes at one longitude are shown in Fig. 5. A trimetric view of part of the inner zone is shown in Fig. 6.

The belts are symmetrical with respect to the position of the dip equator and magnetic intensity (B) as determined by using the AFSWC field solution of Jensen. The development of the radiation belt models is described in the last reference[7]. We are now setting up models in B, L coordinates for use with McIlwain's B, L program--and would welcome any recent spectral data in either B, L or World Map coordinates.

Bremsstrahlung doses on four Apollo trajectories from Cape Canaveral (bracketing the lunar month) are shown in Fig. 7. The first column, for the old inner and outer belts, shows total doses between 0.37 and 0.49 rad made up of between 0.08 and 0.15 rad from the inner and 0.29 to 0.41 rad from the outer region. The dose rate within the Apollo at the belt peak is shown along the top of the table. It is seen that traversal of the inner region along different trajectories gives from about 8% to 15% of one hour's exposure at the peak. For the outer belt, these values are between 38% and 53%.

The second column, for the composite outer and inner belt spectrum, gives total doses between 0.10 and 0.14 rad--depending on the trajectory selected. These calculations did not consider electrons above 1 Mev and it is estimated that these electrons would increase the doses by factors of 1.1, 3.3 and 1.3, for Spectra (1), (2) and (3)--respectively. This configuration carried 700 pounds of personal shielding--and electrons with incident averages as high as 5 Mev were extinguished before passing through all the materials. The bremsstrahlung dose time histories corresponding to the values of the first column are shown in Fig. 8. For comparison, the Van Allen Belt proton doses, as well as secondary neutron doses, are shown.

Note that the least favorable trajectory for protons results in doses comparable to the bremsstrahlung doses. The most favorable trajectory is an order of magnitude less--and neutron doses are still another order of magnitude lower.

---

7. Beck, A. J., Divita, E. and Russak, S. L., "Evaluation of Space Radiation Safety Procedures in the Design and Operation of Some Early Manned Lunar Vehicles," Proceedings of the Sixth Symposium on Ballistic Missile and Aerospace Technology, Academic Press, New York, 1962

Based upon these last data, some reasonable estimates may be made of the lunar mission dose, using the more recent inner and outer regions--Spectra (5) and (4). If we assume that the Apollo command module has some regions as thin as 2 gm/cm^2 of aluminum, the total inner belt dose on the least favorable trajectory would be less than 0.00001 rad from electrons and 0.295 rad from bremsstrahlung.

Corresponding outer belt doses would be 0.181 rad from electrons and 0.031 rad from X-rays--or a total of about 0.5 rad. For that portion of the command module having 6 gm/cm^2, only X-rays would be seen and the inner and outer belt dosages, respectively, would be 0.198 rad and 0.014 rad--or a total of less than 0.25 rad.

Also of interest, are the doses that would be received within an orbiting spacecraft. We have not yet analyzed a specific orbital spacecraft, but have made a series of calculations for aluminum spheres. This is of value in showing how the doses vary with the orbital parameters. Figure 9 shows dosages for 12 hours in the inner belt--Spectrum (5). The doses increase with altitude, such that the ratio of equatorial orbital doses at 300, 400, 600 and 1000 n mi to the dose from a stationary 12-hour exposure at the peak of the belt are--respectively--0.0063, 0.016, 0.091 and 0.36. Within each altitude, the effect of orbital inclination gives ratios to the equatorial orbit dose of 0.31 and 0.15, for 40° and 90°, respectively. The effect of increasing absorber has already been discussed.

If we look at the middle column in Fig. 9, assuming that orbiting laboratories might be no thicker than 1 gm/cm^2 over a considerable solid angle, then--at 300 n mi--a 50-rad dose would be received in about 110 days in an equatorial orbit and in about 2 years in a polar orbit. However, at 1000 n mi, these times are only about 2 and 4-1/2 days, respectively.

Therefore, depending on the position and duration of the mission, inner belt bremsstrahlung doses could be a factor in the design and operation of manned orbital laboratories.

Acknowledgements

The author would like to acknowledge the work of his colleagues at the Martin Company--Andrew Beck and Edward Divita--who developed the computer programs used to obtain the data reported upon. Credit is also due to Frank Roth and Leo Kossa, who coded these programs for the IBM 7090 machine.

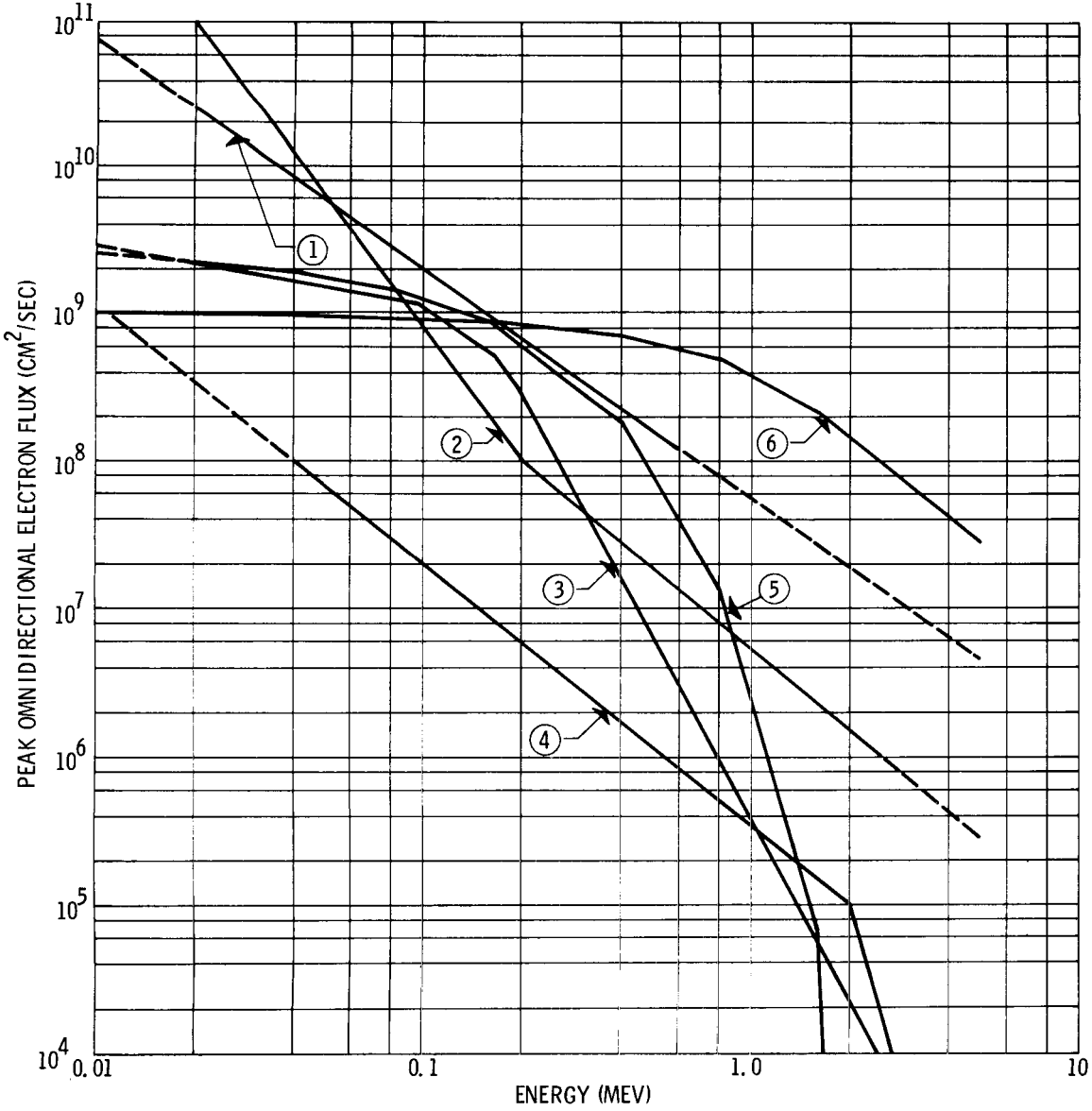

① 1959 INNER BELT, $J_0 = 2.5 \times 10^{10}$ (VAN ALLEN)

② 1959 OUTER BELT, $J_0 = 10^{11}$ (VAN ALLEN)

③ 1960 COMPOSITE, $J_0 = 2.2 \times 10^{9}$ (DESSLER; HOLLEY; WALT, ET AL.)

④ 1961 OUTER BELT, $J_0 = 3.2 \times 10^{8}$ (VAN ALLEN)

⑤ 1962 INNER BELT, $J_0 = 2.2 \times 10^{9}$ (PIZZELLA, LAUGHLIN & O'BRIEN)

⑥ FISSION SPECTRUM, $J_0 = 10^{9}$ (ZERBY AND MORAN)

Fig. 1. Integral Electron Kinetic Energy Spectra

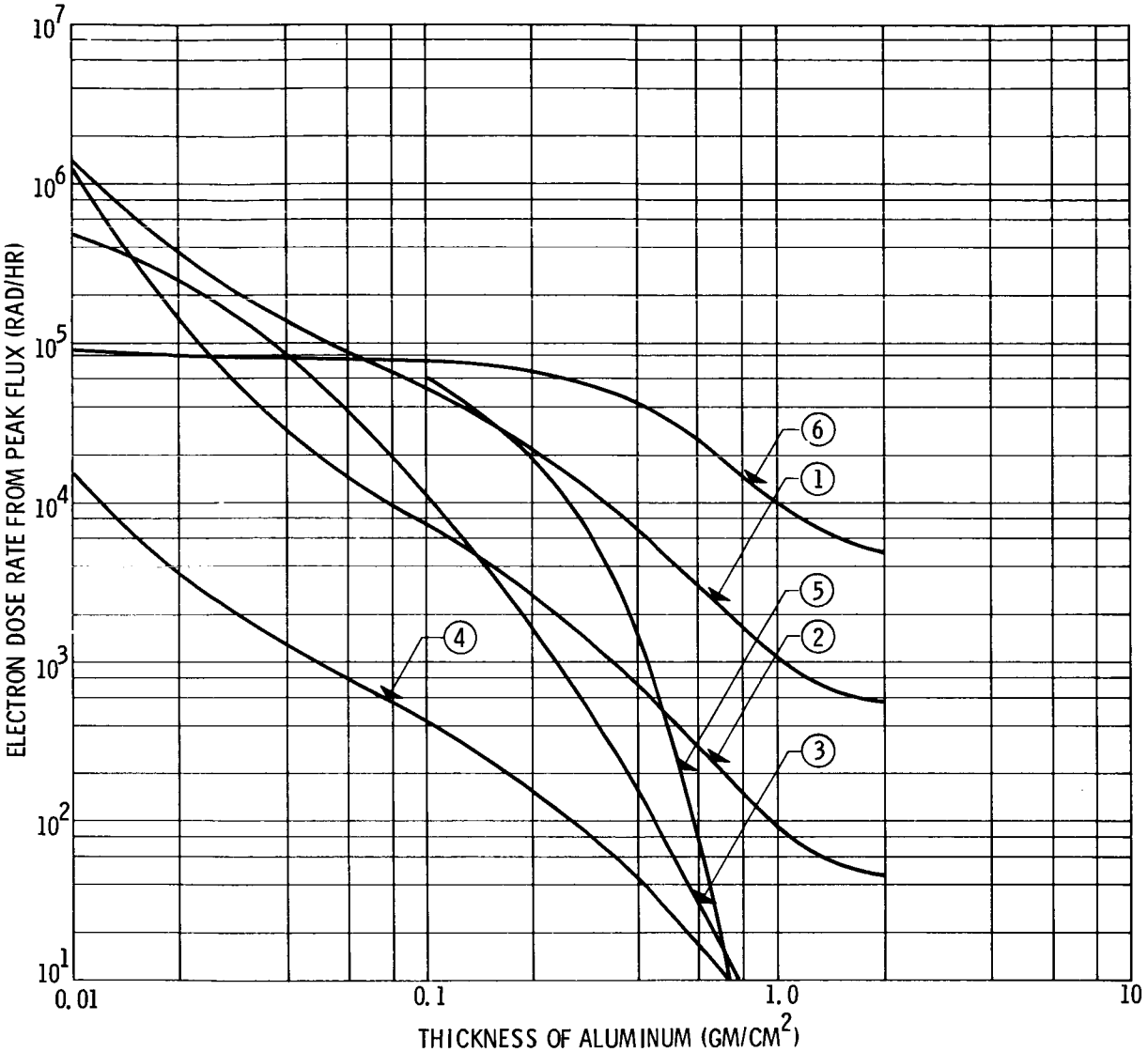

Fig. 2. Electron Dose Rates

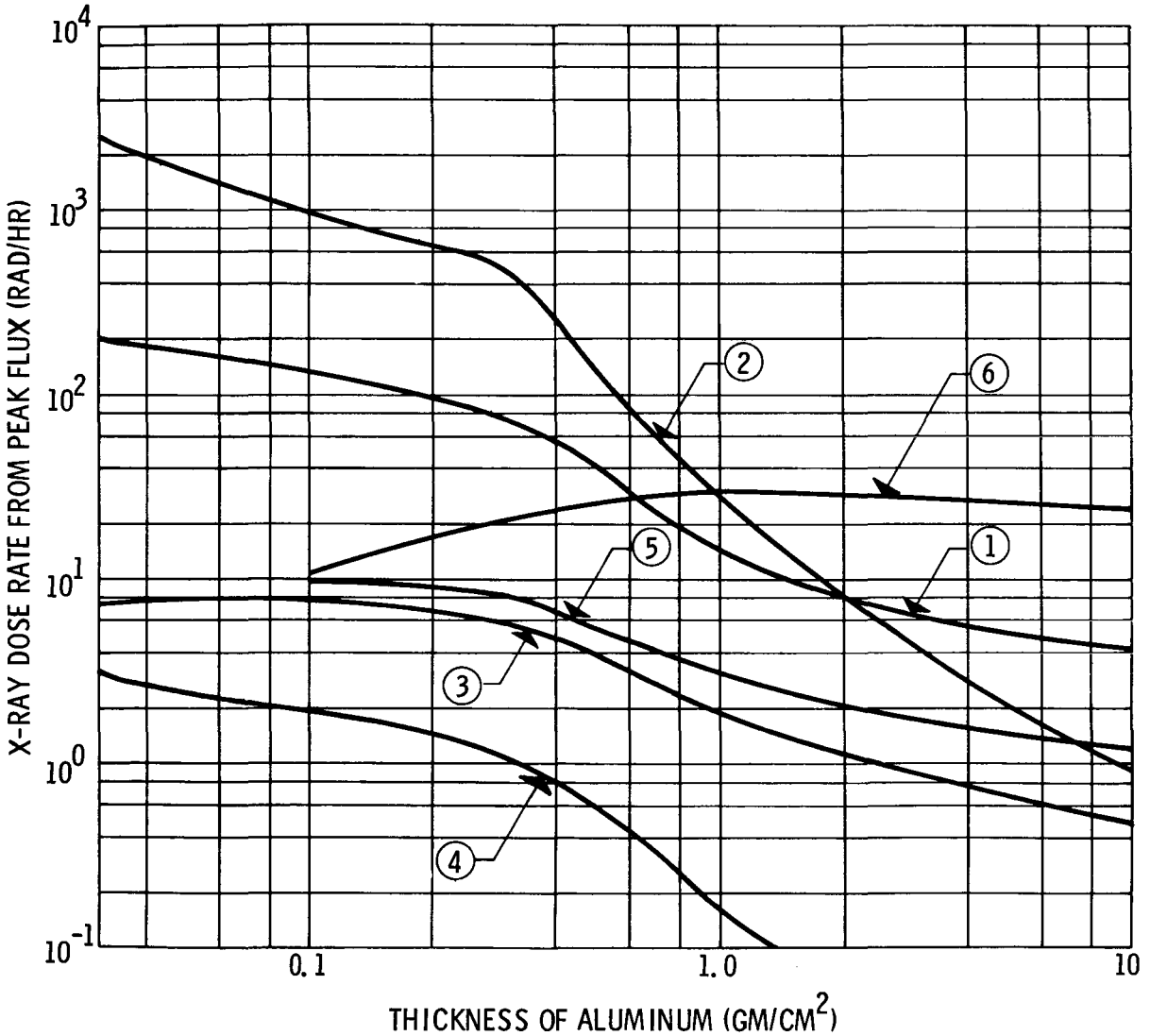

Fig. 3. X-Ray Dose Rates

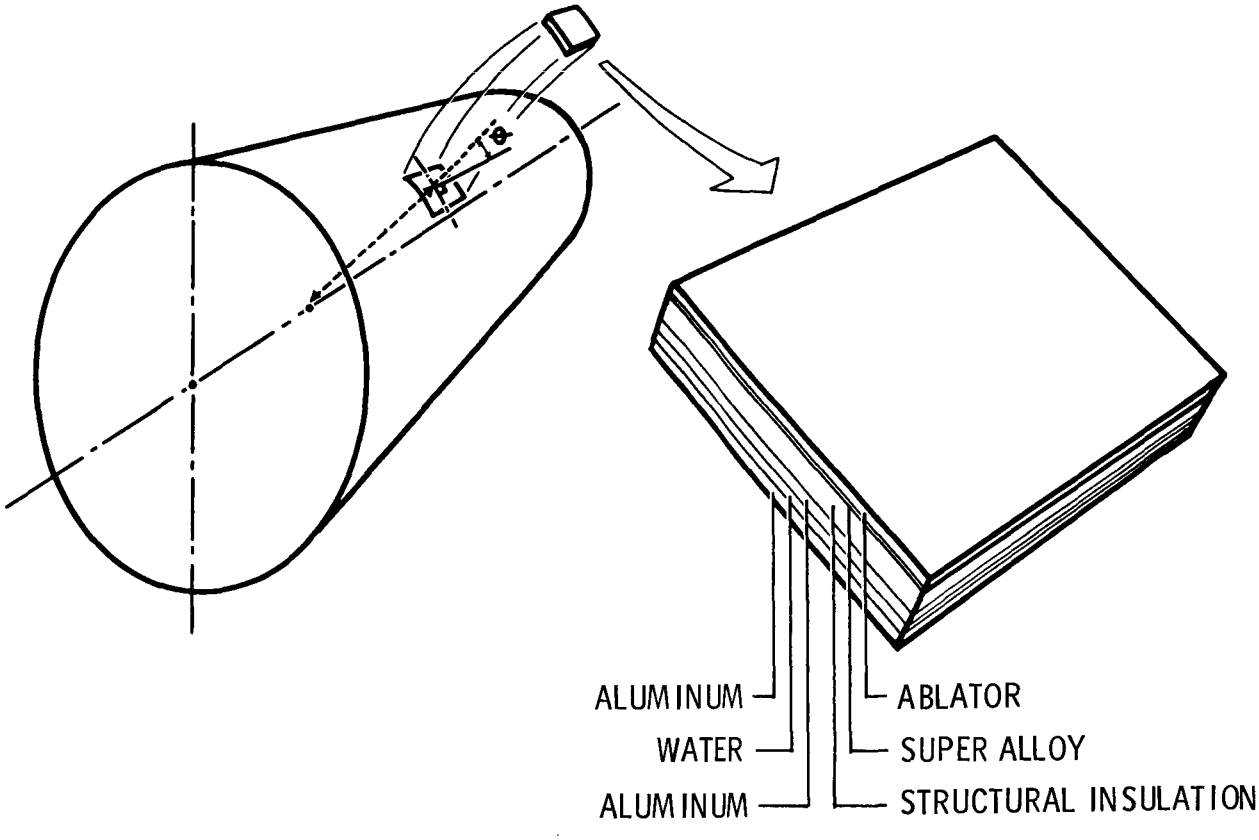

Fig. 4. Radiation Dose Calculation Schematic

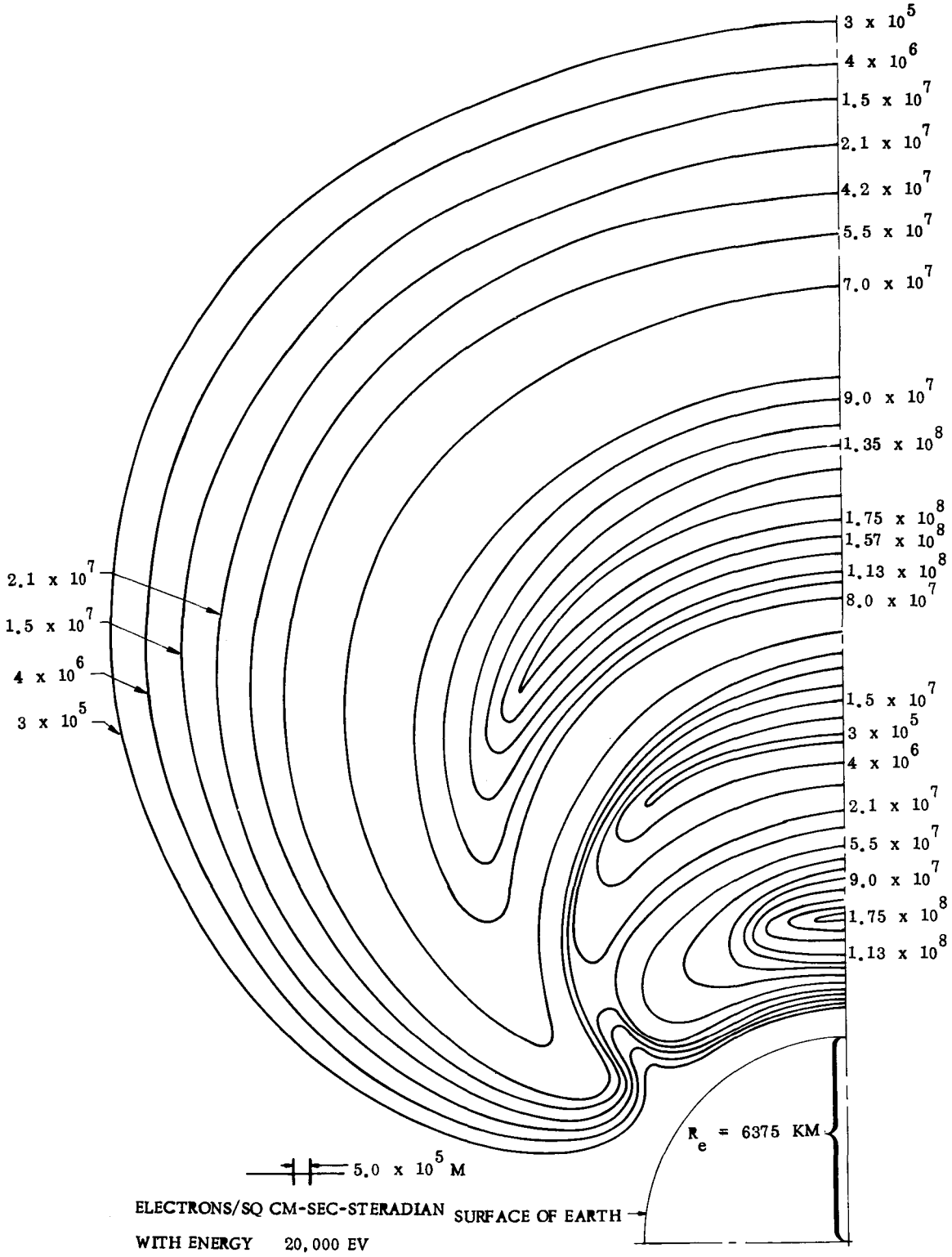

Fig. 5. Flux of Electrons at One Longitude in the Van Allen Belts

Fig. 6. Shape of Inner Van Allen Belt

LATITUDE AND LONGITUDE OF INJECTION POSITION	SPECTRUM NUMBER & PEAK DOSE RATE	
	① ② 1.0437 R/HR 0.7685 R/HR	③ ③ 0.24037 R/HR
-21.753^{0}	0.1531	0.0353
-102.524^{0}	0.3174	0.0923
	0.4705	0.1276
$+166.394^{0}$	0.0843	0.0194
$+31.953^{0}$	0.4053	0.1179
	0.4896	0.1373
-5.98^{0}	0.1529	0.0352
-127.23^{0}	0.3407	0.0992
	0.4936	0.1344
5.13^{0}	0.0815	0.0188
-141.599^{0}	0.2891	0.0841
	0.3706	0.1039

Fig. 7. Bremsstrahlung Radiation Doses Within Apollo Spacecraft on Four Lunar Trajectories

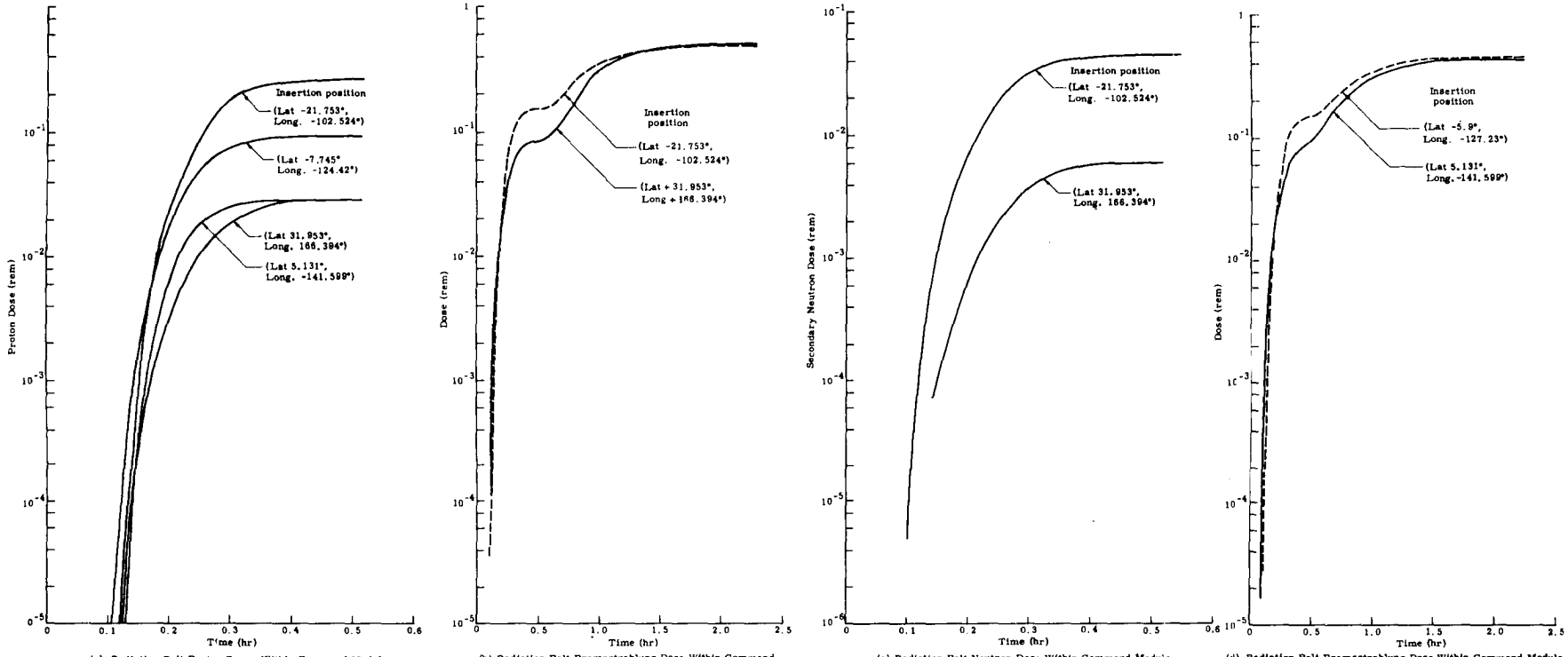

(a) Radiation Belt Proton Doses Within Command Module on Four Outgoing Lunar Trajectories

(b) Radiation Belt Bremsstrahlung Dose Within Command Module on Two Outgoing Lunar Trajectories

(c) Radiation Belt Neutron Dose Within Command Module on Two Outgoing Lunar Trajectories

(d) Radiation Belt Bremsstrahlung Dose Within Command Module on Two Outgoing Lunar Trajectories

Fig. 8. Radiation Dosages Along Various Trajectories for an Apollo Configuration in the Van Allen Belt

ALTITUDE (N MI)	ORBITAL INCLINATION (DEG)	ALUMINUM SPHERE THICKNESS (GM/CM^2)					
		0.1		1.0		2.0	
		ELECTRONS	X-RAYS	ELECTRONS	X-RAYS	ELECTRONS	X-RAYS
300	0	4.598×10^{3}	0.7569	1.137×10^{-3}	0.2301		0.1575
	40	1.444×10^{3}	0.2377	3.574×10^{-4}	0.0723	$<10^{-5}$	0.0494
	90	6.811×10^{2}	0.1121	1.686×10^{-4}	0.0341		0.0233
400	0	1.1690×10^{4}	1.9241	2.892×10^{-3}	0.5849		0.4003
	40	5.046×10^{3}	0.8306	1.248×10^{-3}	0.2525	$<10^{-5}$	0.1728
	90	3.693×10^{3}	0.6078	9.136×10^{-4}	0.1848		0.1264
600	0	6.634×10^{4}	10.9197	1.641×10^{-2}	3.3196		2.2716
	40	4.129×10^{4}	6.7964	1.021×10^{-2}	2.0661	$<10^{-4}$	1.4138
	90	2.359×10^{4}	3.8825	5.835×10^{-3}	1.1803		0.8077
1000	0	2.625×10^{5}	43.2147	6.495×10^{-2}	13.1373	1.803×10^{-4}	8.9898
	40	2.088×10^{5}	34.3755	5.166×10^{-2}	10.4502	1.434×10^{-4}	7.1510
	90	1.097×10^{5}	18.0597	2.714×10^{-2}	5.4901	7.534×10^{-5}	3.7569

Fig. 9. Twelve-Hour Orbital Dose (rad) Within Van Allen Belt

Paper E-9

SYNTHESIS OF MINIMUM WEIGHT PROTON SHIELDS*

A. D. Krumbein, P. S. Mittelman, E. S. Troubetzkoy,
F. Nakache, and J. Celnik
United Nuclear Corporation
Development Division – NDA
White Plains, New York

15154

Abstract

A shield optimization technique originally developed for reactor shields has been applied to proton shields. The cases of both spherical and nonspherical shields have been studied and the effects of certain special constraints and of secondary neutrons have been included in the analysis. The method indicates which materials should go into making up the minimum weight shield and what their order and the thickness of each material should be. The amount of weight saved is found to be a function of the radius of the shielded void and of the specified attenuation required.

Introduction

Recently a technique for the synthesis of minimum weight reactor shields has been developed at the United Nuclear Corporation in connection with advanced shielding work being carried out for the AEC. This technique had its origin in a series of suggestions made by Gale Young which were given mathematical verification by M. Slater. A fairly complete account of this theory can be found in Reference 1. This

---

*Work sponsored by National Aeronautics and Space Agency, Huntsville, under contract NAS8-2658.

1. E. S. Troubetzkoy, Minimum Weight Shield Synthesis, UNC-5017 (Part A) (1962).

shield synthesis technique has now been applied to the design of minimum weight proton shields. Starting with the radiation environment and given all the materials available which might be suitable as proton shields, and a specified allowable total dose in the shielded region, the synthesis technique indicates the proper materials and their disposition so as to obtain the minimum weight shield.

Minimum Weight Spherical Shields

For shielding against incident protons only, the problem is equivalent to designing a shield that will eliminate all protons below a given energy. This energy is so chosen that the dose from protons above that energy is below design levels. In the energy range from about 50 to 500 Mev one can write an approximate expression for the rate of energy loss per cm in a given material as:

$$\frac{dE}{dr} = A_i f(E), \tag{1}$$

where f(E) is the energy dependence of the proton stopping power of a reference material. In this work aluminum was chosen as the reference and A_i is then defined as the ratio of the proton energy loss with distance in the i^{th} material to the same loss in aluminum. A is called the proton relative stopping power. Figure 1 shows a plot of A vs energy for many materials of interest to space shielding. It is seen that the values of A are indeed fairly constant over the energy range indicated.

If a shield consisting of concentric spherical shells of radii r_0, r_1, ..., r_N, where r_0 is the void radius, and containing materials with relative stopping powers A_1, A_2, ..., A_N, has to stop protons with energies up to E_0, the following relationship has to be satisfied

$$\sum_{1}^{N} A_i (r_i - r_{i-1}) = \int_0^{E_0} \frac{dE}{f(E)} = K(E_0). \tag{2}$$

The last equality defines K, which is the equivalent aluminum thickness of the shield.

It can be shown that the choice of materials for the minimum weight shield can be obtained by the following prescription:

All materials available are plotted on a plane, the ordinate being A_i and the abscissa, the material density, ρ_i. Now one constructs for $\rho \geq 0$, the shortest curve $A = A(\rho)$ which lies above the material points. This curve will be a broken line whose vertices are the origin and certain pairs (A,ρ). The minimum weight shield will be made up only of materials whose coordinates are vertices of the broken line, the outermost shell being made up of the material vertex closest to the origin, the next outermost by the next material vertex, and so on. In general all materials will not be used but only some initial sequence governed by the restriction that the inner radius of the shield be equal to r_0. If $r_0 = 0$, all the materials on the broken line will be used. Figure 2 shows such a curve, which we call a "Young Diagram." The materials at the vertices are CH_2 (polyethylene), carbon, iron, and copper. As can be seen several other plastic materials might easily be used in place of polyethylene.

The method of Lagrange multipliers is used to locate the radii of the various layers of the minimum weight shield. From Eq. 2, the attenuation of the shield is:

$$K = \sum_{1}^{N} A_i \, (r_i - r_{i-1})$$

or

$$K + r_0 A_1 = \sum_{1}^{N} r_i \, (A_i - A_{i+1}) = K' \tag{3}$$

and the shield weight for the spherical case is given by:

$$W = \frac{4}{3} \pi \sum_{1}^{N} \rho_i \, (r_i^3 - r_{i-1}^3)$$

or

$$\frac{1}{4\pi} W = \sum_{1}^{N} \frac{r_i^3}{3} (\rho_i - \rho_{i+1}) - \frac{r_0^3}{3} \rho_1 \, . \tag{4}$$

What is now required is to minimize the shield weight subject to the condition of Eq. 3. We therefore construct the Lagrangian.

$$L = \frac{1}{4\pi} W - \mu K', \tag{5}$$

where μ is the Lagrangian multiplier.

The radii of the various layers of the minimum weight shield will then be obtained by minimizing L with respect to each r_i. Setting the derivatives of L with respect to each r_i equal to zero, we obtain:

$$r_i = \sqrt{\mu}\ \frac{(A_i - A_{i+1})^{1/2}}{(\rho_i - \rho_{i+1})^{1/2}} \ . \tag{6}$$

μ can then be obtained by substitution in Eq. 3 giving the following expression for the radius of each layer of a spherical shield:

$$r_i = \frac{K_0 + r_0 A_1}{\left[\sum_1^N \frac{(A_n - A_{n+1})^{3/2}}{(\rho_n - \rho_{n+1})^{1/2}}\right]} \ \frac{(A_i - A_{i+1})^{1/2}}{(\rho_i - \rho_{i+1})^{1/2}} \ . \quad i = 1, 2, \ldots, N \tag{7}$$

In order to investigate the application of the theory to a spherical shield, the parameter K/r_0 is used. The abscissa in Fig. 3 shows how different shielding materials enter the minimum weight shield as K/r_0 varies. For example, for the smallest practical value of void radius r_0 which can be considered, i.e., 25 cm or a small man-sized shield, a shield having a shielding equivalent of 20 g/cm^2 ($K/r_0 = 0.3$) would consist of iron, carbon and polyethylene in that order. If a shielding equivalent of 30 g/cm^2 ($K/r_0 = 0.44$) is desired, copper would also be a component of the minimum weight shield. On the other hand, if the shielded volume has a radius of 100 cm, below a shielding equivalent of about 22 g/cm^2 ($K/r_0 = 0.08$), the minimum weight shield consists only of polyethylene. Carbon must be added if higher shielding equivalents are desired but iron is not included in such a shield till a shielding equivalent of 55 g/cm^2 ($K/r_0 = 0.20$) is specified.

Conditionally Optimized Shields

The shield synthesis technique has been extended to include certain constraints which make the configurations more realistic. Two cases in particular have been considered:

1. The shield includes up to a certain volume, V, of a given material which primarily serves purposes other than shielding, e.g., electronic gear.
2. The shield must contain a shell of a given thickness of a given material, e.g., an aluminum "skin."

For the first case where the given material to be included is simulated by aluminum, Fig. 3 shows how the makeup of the shield changes both as a function of the amount of aluminum required and of K/r_0. The parameter used for the ordinate, the cube root of V over $4/3\,\pi r_0^3$, is essentially the ratio of the radius of the sphere of Al required, to the radius of the shielded void.

For the second case, for shielded regions of reasonable size with the necessary inclusion of an aluminum or titanium layer 1 cm thick, the minimum shield will consist of the metallic layer lying inside a layer of polyethylene. For both the special constraints we have discussed, the position of the required material in the shield is determined by its place on the "Young Diagram." However, depending on the value of K/r_0 and the amount of the required material to be included, one or another of the materials in the "Young sequence" may be omitted.

Treatment of Secondary Neutrons

Theory

It is believed that a significant contribution to the total dose inside a shielded vehicle traversing a proton flux region will be due to secondary neutrons arising from the interaction of the protons with the shielding material. We have, therefore, extended our shield optimization technique to include the effect of secondary neutrons. The model which was used is based on the following assumptions:

1. The secondary neutron flux inside the shielding material is a function of the incident proton flux at the outside of the shield and must be calculated explicitly for each proton environment. It is also obviously a function of the shielding material.

2. A power law dependence is assumed both for the impinging proton spectrum (Eq. 8) and for the proton attenuation in aluminum (Eq. 9), i.e.,

$$P_0(R,E') = C_1 \left[E'^{M} + \alpha\right]^{-1} \text{ , and} \tag{8}$$

$$\frac{dE}{dr} = C_2 E^{-N} , \tag{9}$$

where C_1, M, and α are constants determined by the particular proton environment and C_2 and N are determined by the properties of aluminum. For the solar flare of May 10, 1959, for example, we have taken $C_1 = 3.19 \times 10^{17}$ and M = 5. With $\alpha = 0$, this is an approximation to the Winckler spectrum[2] for that flare though in practice we have cut it off at about 7 Mev, the threshold of the (p,n) cross section for aluminum. When α is set equal to 5×10^6, the impinging proton spectrum is an approximation to the NASA spectrum[3] for that flare. Both of these calculated spectra are shown in Fig. 4.

From this, and using the previously given definition of K(r), viz.,

$$K(r) = \int_E^{E'} \frac{dE}{f(E)} = \int_r^R A(r)\, dr, \tag{10}$$

one can calculate the proton flux, P(r,E), throughout the shield as a function of position and energy. P(r,E) has the form:

$$P(r,E) = \frac{C_1 \left\{C_2[N+1]K(r) + E^{N+1}\right\}^{-\frac{N}{N+1}} E^N}{\left[C_2(N+1)K(r) + E^{N+1}\right]^{\frac{M}{N+1}} + \alpha} . \tag{11}$$

From this proton flux the secondary neutron source can be obtained from the expression:

---

2. J. R. Winckler and P. S. Bhavsar, J. of Geophys. Res., 65, 2637 (1960).

3. J. R. Winckler, Primary Cosmic Rays, Proceedings of Conference on Radiation Problems in Manned Space Flight, edited by G. J. Jacobs, NASA TN-D588, Appendix A (1960).

$$S\,[K(r)] = \int_0^{\infty} P(r,E)\ \sigma_{eff}(E)\,dE, \tag{12}$$

where $\sigma_{eff}(E)$ is the effective (p,n) cross section which takes into account multiple neutron production. The effective (p,n) cross sections as used were composed of two parts, those for the production of isotropic "evaporation" neutrons and those for the production of straight ahead "cascade" neutrons. The cross sections for evaporation were multiplied by 3/8 to take into account the isotropy of those neutrons. Figure 5 shows a typical curve of S[K(r)]. The point marked r = 0 is the asymptotic value of S for zero shielding thickness. S[K(r)] in any material is assumed proportional to the secondary neutron production in aluminum, viz.,

$$S[K(r)] = z(r)\ S_{Al}\,[K(r)]\,, \tag{13}$$

where z(r) is a function only of the material at r.

Finally, the total neutron production, $\Sigma\,[K(r)]$, is calculated from $S\,[K(r)]$ by

$$\Sigma[K(r)] = \int_0^{K(r)} S\,[K(r')]\,dK(r')\,. \tag{14}$$

It turns out that relatively large differences in the shapes of the curves of the effective (p,n) cross section as a function of energy result in relatively small differences (< 10%) in the shapes of the capital sigma curves. This has been borne out for Al, C, and Cu, the only elements for which we could find sufficient (p,n) data. Figure 6 shows a typical curve of the total neutron production for an approximation to the NASA spectrum for the flare of May 10, 1959, for which $\alpha = 5 \times 10^6$. For this case more than half of the neutrons are produced in the first few millimeters of aluminum.

The final assumption in the complete model is the exponential attenuation of the secondary neutrons using a parameter y(r) which is a function of material only. Because of lack of data on the energy spectrum of secondary neutrons from proton bombardment, the neutron

attenuation parameters used were calculated from the removal cross sections for fission neutrons.

Whereas in the pure proton case we had only two parameters A and ρ, when production and attenuation of secondary neutrons is included, we have four parameters, z and y being the additional ones. The materials defined by these four parameters are now to be plotted in a four-dimensional space, all the materials and their mixtures lying either inside or on a hypersurface P. This hypersurface is defined by a collection of tetrahedra, each tetrahedron in turn being defined by a set of four material points in the four-dimensional coordinate system A, y, z, ρ. This replaces the two-dimensional graph which was described previously, and which led to the "Young Diagram." Mixtures of materials are now possible since it was shown by Troubetzkoy[1] that up to an (n-1) material mixture is possible where n is the number of parameters used. Hence, for proton attenuation alone, only pure material layers are allowed, whereas for the present four parameter case, shielding layers consisting of up to three materials are possible.

The method of Lagrange multipliers is again used to determine the shield configurations and requires that the total weight be minimized with respect to the four parameters subject to the constraints that:

1. the total dose (both from primary protons and secondary neutrons) to the inside of the shield be equal or less than a certain specified dose $\overline{D}$, and
2. a point (A,y,z,ρ) lies inside or on the hypersurface P.

The results show that:

1. in joining two regions in the optimum shield, it is permissible to add or delete only one material;
2. the innermost and outermost regions must be composed of pure materials.

Figures 7 and 8 give the possible shield configurations for 2, 3, 4, 5, and 6 region shields. The actual materials used in the optimum shields, however, are functions of r_0 and $\overline{D}$. The following comments can be made on these configurations:

1. All materials in adjacent regions must lie on the same tetrahedron of the hypersurface.

2. Three material regions can occur only in relatively complex shields containing five or more regions. Even in a five-region shield such a mixture is contained in only one of six possible configurations. In a six-region shield, three material mixtures are contained in only two of ten possible configurations.

Numerical Results

Because of a lack of sufficient data on (p,n) cross sections, we have only been able to calculate, according to this model, shields containing Al, C, and CH_2. The results of some sample calculations are given in Table 1. The weight savings for the minimum weight configuration for this flare proton spectrum, as can be seen, are small. Aluminum, and presumably iron and copper if they had been included in the calculations, do not enter into the optimum shields for these permitted dose values and void radii. For decreased values of $\overline{D}$, i.e., for heavier shielding requirements, the optimum configuration will be expected to represent an increasingly substantial saving over a one-material shield. Another point to be noted is that for this proton spectrum the dose inside the lightest weight shields is contributed mainly by protons. The materials used, C and CH_2, though they have low values of A_i, produce only small numbers of secondary neutrons. Therefore, for a fairly soft proton spectrum, such as we have used here, their proton attenuation is sufficient to make them the most desirable materials for the optimum shield within the permitted dose requirements we have set. For harder spectra, such as the Van Allen belt or the giant flare of Feb. 23, 1956, better proton attenuators will be required in the optimum shield and other materials besides C and CH_2 will come in.

Extension to Other Geometries

Slater[4] has shown that the shield optimization technique has validity in geometries other than spherical as long as the volume function is a convex function of some typical dimension. As before, one considers the condition that at every point on the shield the cutoff energy for protons is constant. This was originally interpreted as allowing the design of a shield for protons normally incident as this was believed to lead

4. M. Slater, Private Communication.

Table 1. Optimum Spherical Shields for the May 10, 1959 Flare – Effect of Secondary Neutrons is Included

Void Radius, cm	Materials	Total Dose Requirement, rem	Proton Dose, rem	Neutron Dose, rem	Total Weight, kg
0	Al	70	39	31	0.37
0	C	70	64	6	0.16
0	CH_2	70	67	3	0.51
0	C + CH_2	70	65	5	0.15
20	Al	70	39	31	50.9
20	C	70	64	6	32.8
20	CH_2	70	67	3	30.0
20	C + CH_2	70	66.5	3.5	29.9
20	Al	24.3	5.1	19.2	215
20	C	24.3	19.0	5.3	74.5
20	CH_2	24.3	22.3	2.0	70.6
20	C + CH_2	24.3	21.3	3.0	68.3

An RBE of 1.3 is assumed as the average over the energy range of the protons.

to a conservative result since protons entering normally would be attenuated less than protons coming from any other direction. This turned out not to be strictly true for certain shield regions but the errors involved have been calculated and turn out to be extremely small (fractions of a percent).

The problem of the minimum weight shield was solved for the general case of a convex volume void assuming normally incident particles, again using the method of Lagrange multipliers. The particular cases of the right cylinder, cone, and truncated cone were investigated. For the particular case of the right cylinder of inner radius r_0 and height h_0, the radius of the i^{th} circular shell in the shield is given by:

$$r_i = \left[\frac{K + r_0 A_1}{\sum_{1}^{N} \frac{(A_n - A_{n+1})^2}{(\rho_n - \rho_{n+1})}} \right] \left(\frac{A_i - A_{i+1}}{\rho_i - \rho_{i+1}} \right) . \qquad (15)$$

The same expression gives the radii of the various conical shield regions for a cone of the same height and base radius as the right cylinder, if for r_0 in Eq. 15 we substitute S_0, the normal distance from the axis of the cone to the void surface. In the conical shield each shield layer is bounded by a conical surface and the number of materials required varies with S_0, decreasing for a complete cone, from the total number available from the Young Diagram, at the top of the cone, to a smaller number as one proceeds toward the base. For truncated cones, the number of materials used even at the top of the cone can be less than the total number available and depends on the relative values of the upper and lower radii of the cone.

Table 2 compares several convex optimum shields of different shapes and sizes with all aluminum and all polyethylene shields. It is seen that, as in the case of spherical shields, the percentage weight saved by using an optimum configuration increases with decreasing void radius and with increasing prescribed attenuation.

Some attempts have been made to ease the constraint that the shield be required to remove all incident protons of energy below a certain specified energy, particularly for volumes near the bottom of the cone. In the calculations carried out thus far, additional weight savings have been achieved and by applying the method to other less important portions of the shielded volume still lighter shields may be obtained.

Table 2. Optimum Convex Shields of Several Types

Type of Void	Height, cm	Radius, cm	Attenuation, cm of Al	Shield Weights: Optimum, kg	Shield Weights: All Al, kg	Shield Weights: All CH_2, kg	% Savings
Conical	200	50	3.7	338	439	362	7
Conical	200	50	11.1	1195	1573	1470	23
Conical	200	25	11.1	621	813	857	31
Cylindrical	200	25	11.1	1102	1366	1312	19
Cylindrical	100	10	11.1	266	360	430	35
Cylindrical	200	50	11.1	2112	2644	2218	5
Truncated conical	200	Lower 100 Upper 50	11.1	3478	4555	3792	9
Conical	100	100	11.1	2090	3258	2788	33

Conclusion

Though for usable voids (25 cm in radius or greater), the optimization method for the spherical case reveals that a simple one- or two-layer carbonaceous shield is best, the method can provide much useful information for space shield design for the more practical nonspherical shapes and special constraints. In addition, as more shielding is required, say for longer space voyages, the method should also prove useful.

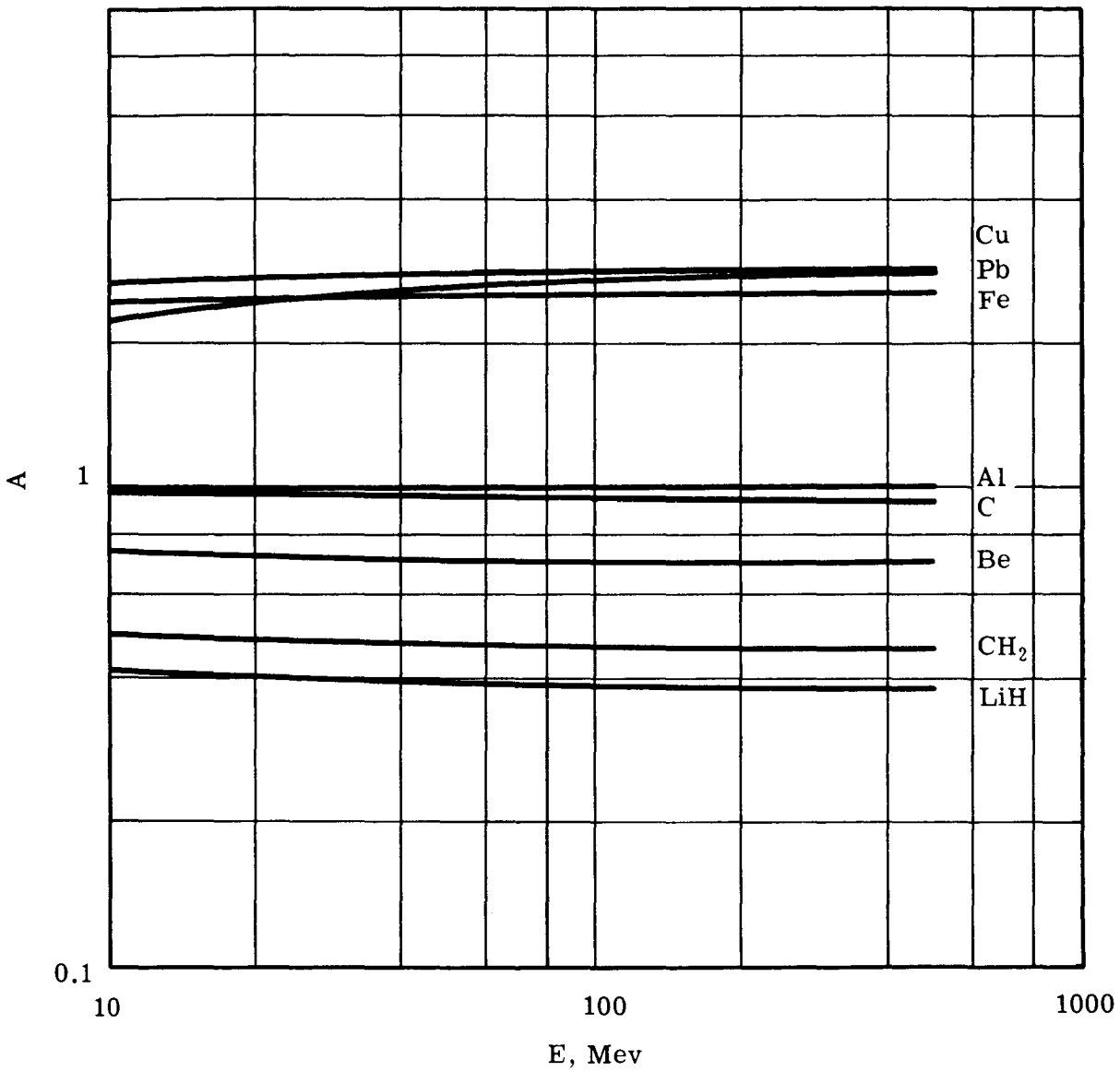

Fig. 1 — The Proton Relative Stopping Power as a Function of Proton Energy for a Number of Elements and Compounds (Al is taken as the standard)

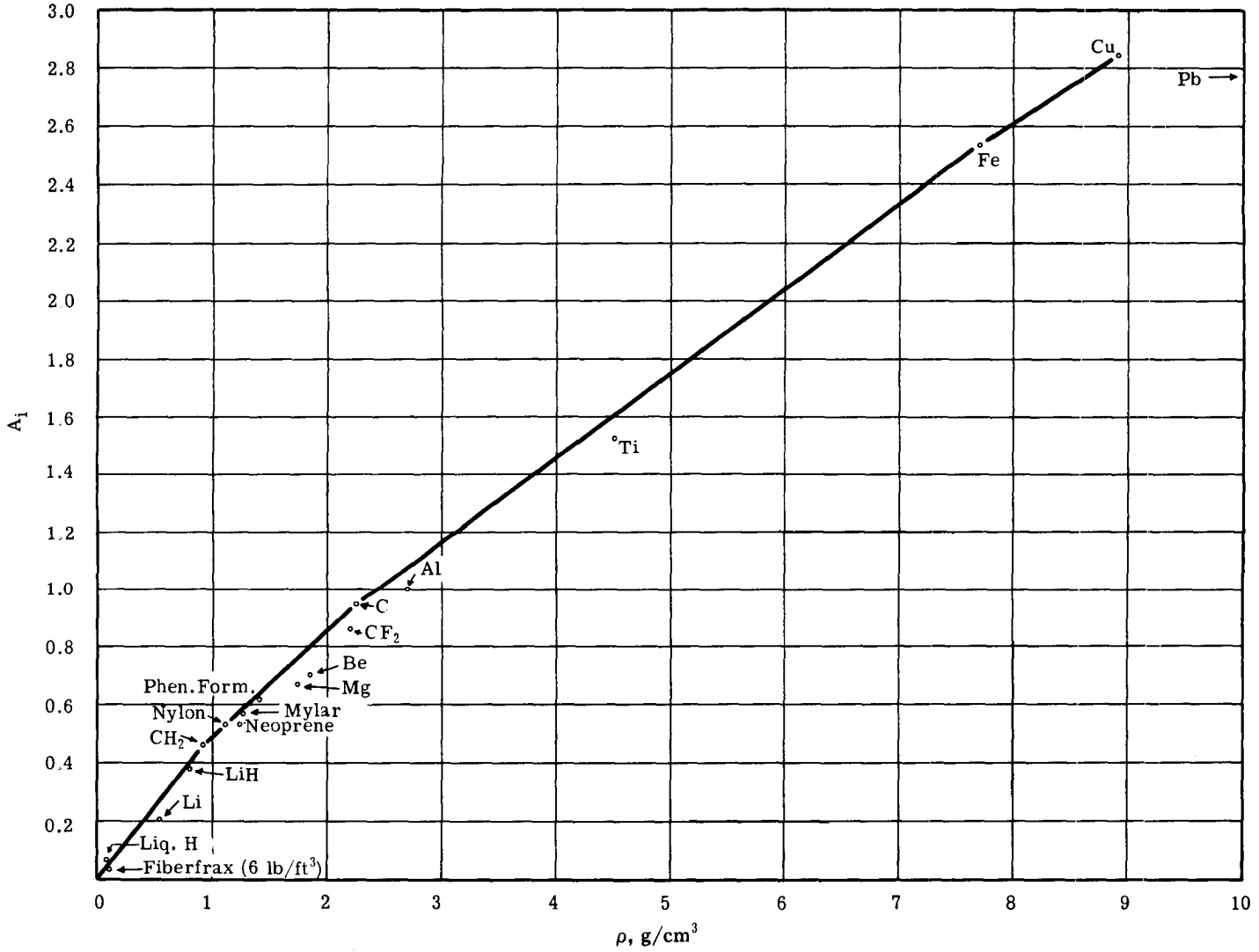

Fig. 2 — Proton Relative Stopping Power (calculated for 300 Mev protons), as a Function of Material Density for a Number of Elements and Compounds

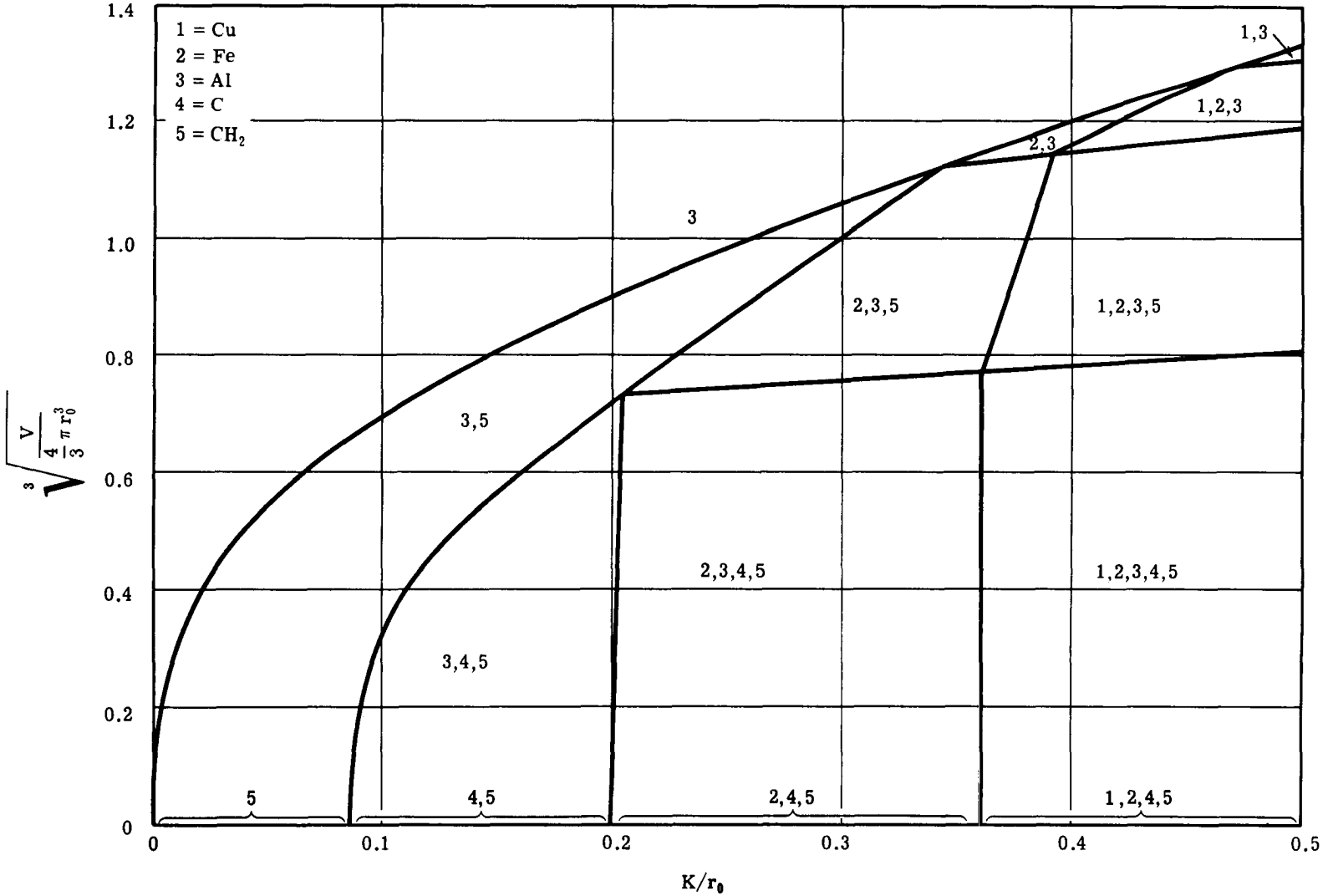

Fig. 3 — Materials to be Included in an Optimized Spherical Shield as a Function of K/r_0 and Required Amounts of Aluminum

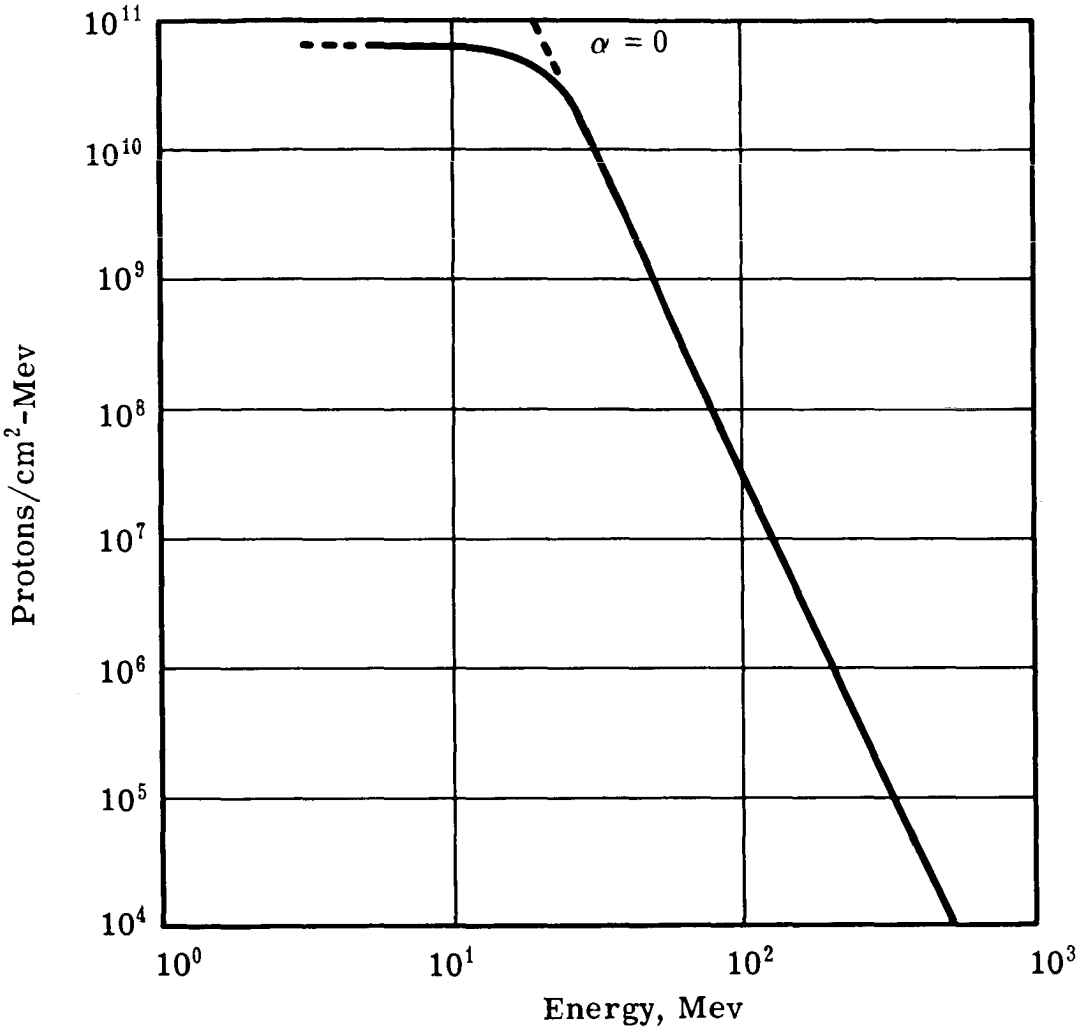

Fig. 4 — Calculated Approximation to the Proton Spectrum of the Flare of May 10, 1959; $\alpha = 0$ – Winckler Spectrum; $\alpha = 5 \times 10^6$ – NASA Spectrum.

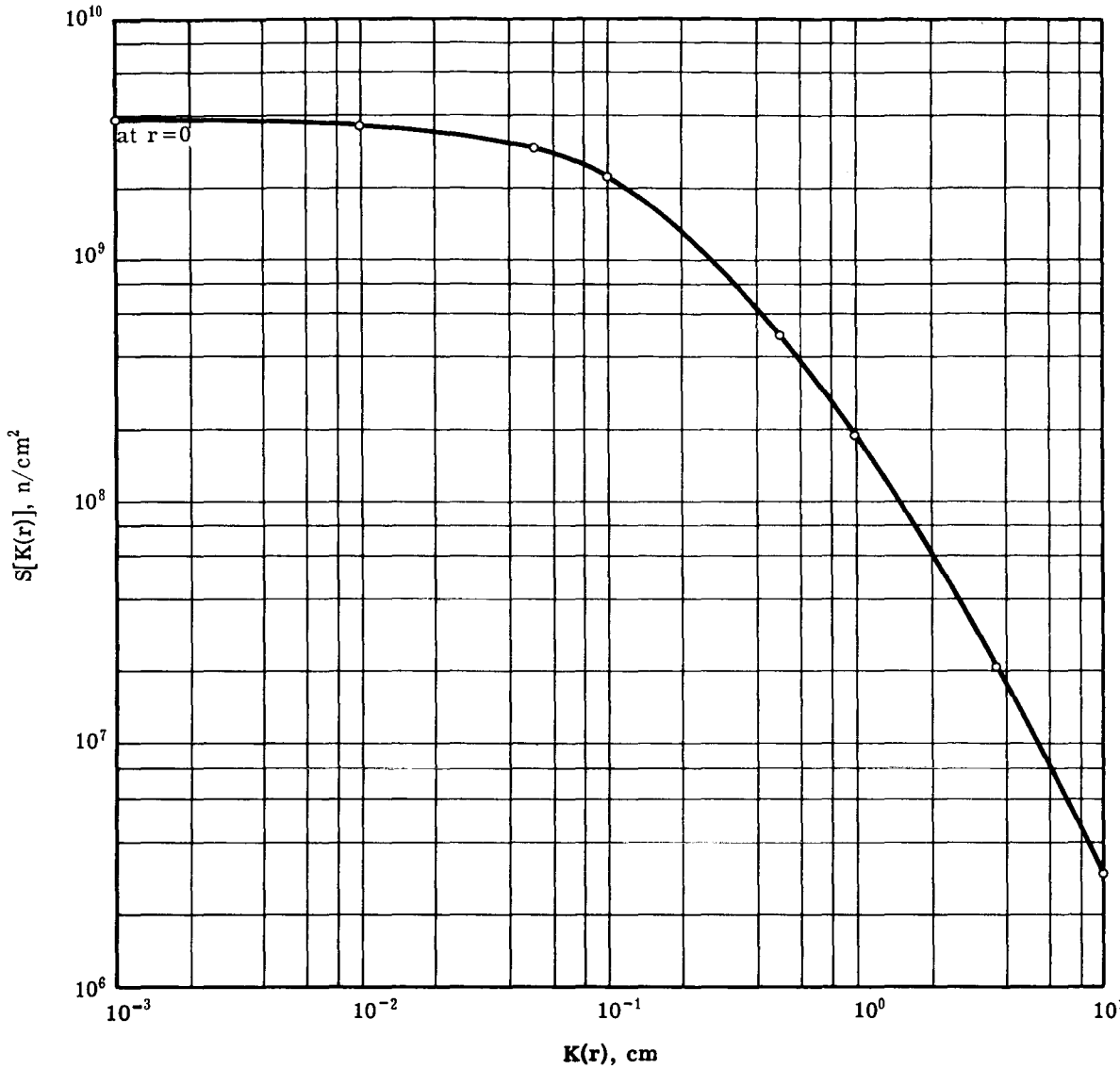

Fig. 5 — Secondary Neutron Source Inside the Shielding Material as a Function of the Equivalent Depth into Aluminum for the May 10, 1959 Flare – NASA Spectrum

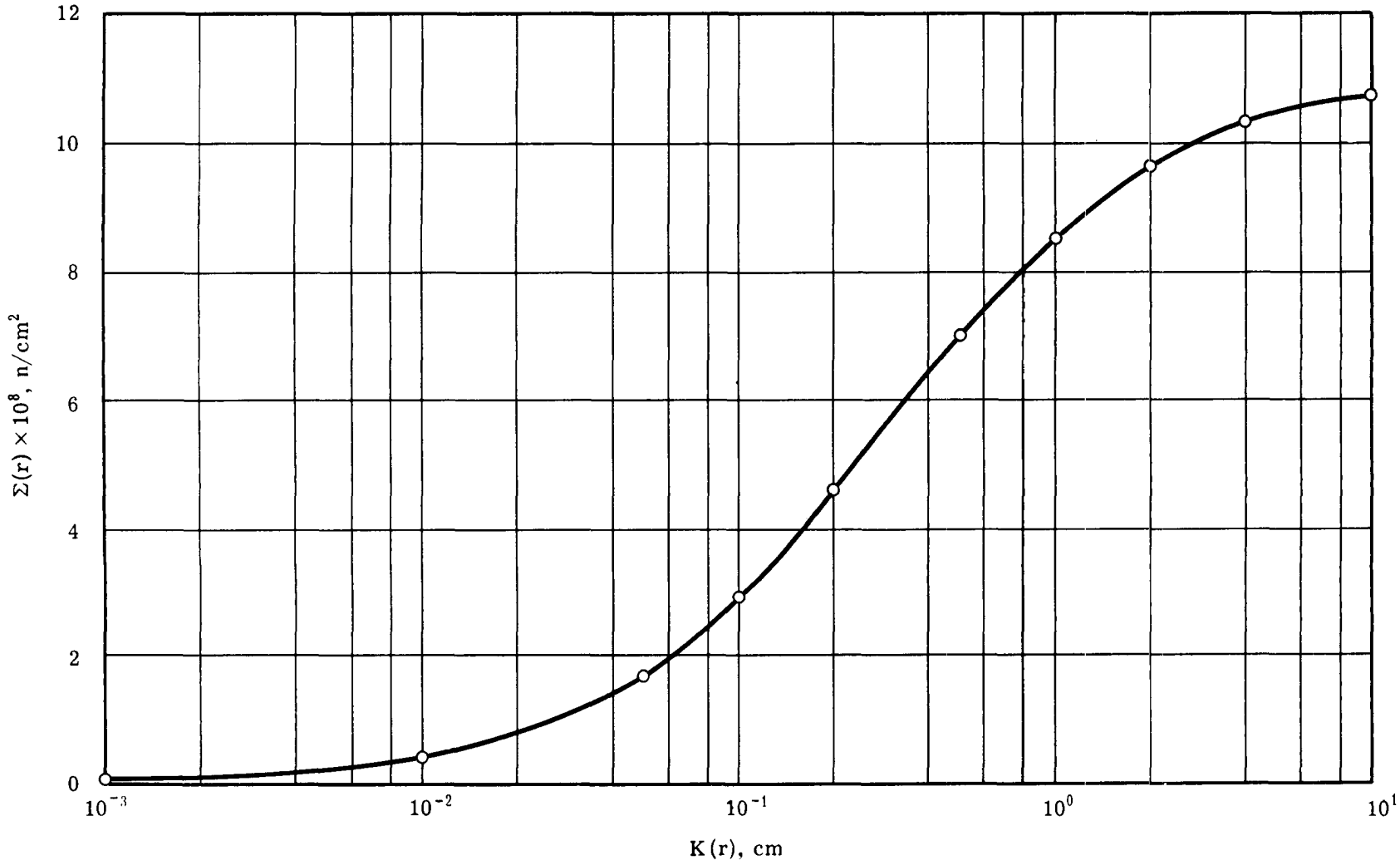

Fig. 6 — Total Secondary Neutron Production as a Function of Equivalent Thickness of Aluminum for May 10, 1959 Flare – NASA Spectrum

Two-region shield

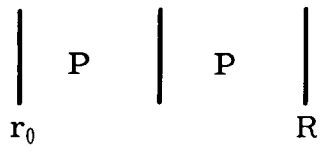

P = pure material
2M = two-material mixture
3M = three-material mixture

Three-region shield

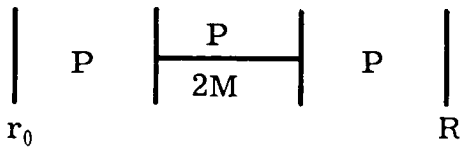

Four-region shield

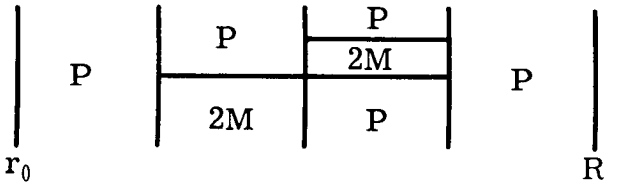

Five-region shield

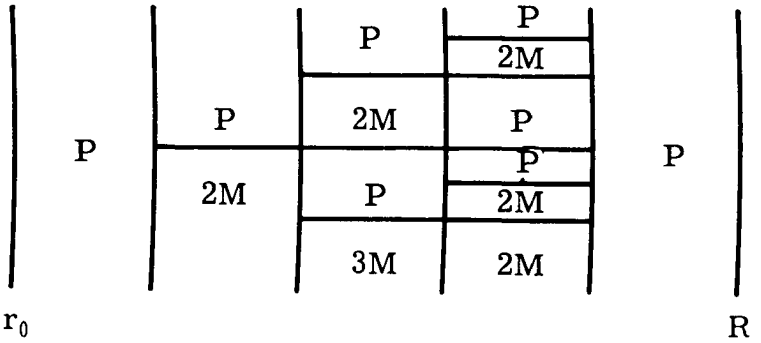

Fig. 7 — Possible configurations for shields containing from 2 to 5 regions

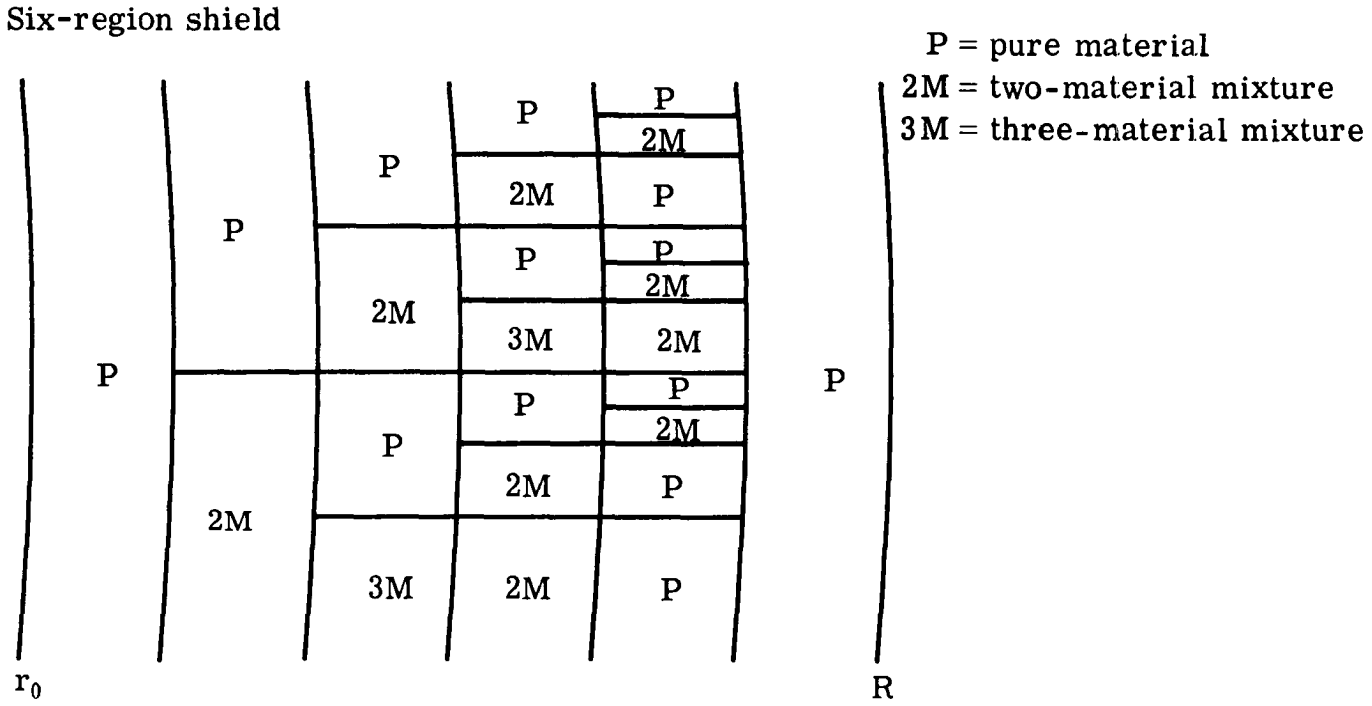

Fig. 8 — Possible configurations for shields containing 6 regions

Paper F-1

THE PROSPECTS FOR ACTIVE SHIELDING*

R. H. Levy**

Avco-Everett Research Laboratory
Everett, Massachusetts

I. Introduction

Shielding the astronaut against the various forms of penetrating radiation likely to be encountered on a space trip is one of many difficult problems facing the space ship designer. Perhaps it is fair to say that at this stage it is the most uncertain of all the environmental factors which must be considered in the design.

Estimates of the shielding required for the first travelers to the moon are low, but as permissible doses decline, the shielding requirement will increase. Again, we may anticipate a desire to fly extended missions in those regions near the earth (or other planets) where substantial fluxes of trapped radiation are to be found, thus imposing a severe shielding requirement on the designer. Interplanetary travel involving substantial transit times will make the occurrence of large solar flares during the trip virtually certain, and here again a sizable shielding problem is involved. Finally, for any mission, as the number of individuals undertaking it increases, permissible radiation doses will decrease, so that shielding will inevitably grow in importance as the era of space flight progresses.

It is the purpose of this note to make some general remarks on various methods of shielding which might be used other than the standard one of interposing a substantial amount of matter between the astronaut and the radiation. The importance of such methods is directly related to the

* This work was supported by the Office of Naval Research, Department of the Navy, under Contract No. Nonr-2524(00).

** Principal Research Scientist.

weight involved in bulk shielding. We shall in this note consider only the radiation hazard due to high energy protons since it appears at present that such protons constitute the most important natural source of danger to the astronaut.

II. Electrostatic Shielding

In order to stop a proton with an electrostatic field, the necessary potential rise in the field (in volts) must be numerically equal to the energy of the proton (in electron volts). Thus, one must at once consider potentials in the order of 10^7 to 10^9 volts.

Two methods of obtaining such potentials may be discussed. In the first, one maintains a positive charge on the space ship such that its potential relative to infinity has the required value V. This has the immediate result that electrons will bombard the ship, each having an energy equal to V electron volts. Thus, one has exchanged one form of radiation for another. Since the stopping of electrons with such energies will involve substantial production of highly penetrating bremsstrahlung, the advantage of such a method is not obvious. Furthermore, in order to maintain the potential, one would have to accelerate electrons away from the ship with this same energy V. This operation is quite difficult by itself, but, in addition, will consume a substantial amount of power.

An alternative method of generating the required potential drop would be to maintain it between, say, two concentric spherical shells. The achievement of the necessary potentials in this way is at present beyond the reach of ground based machines; and the space environment would not appear to make the problem any easier, especially since the conductors would both be essentially unshielded against galactic cosmic rays.

III. Magnetic Shielding

Magnetic shielding using superconducting field coils appears to offer an attractive shielding method provided only that the engineering problems involved in the construction of the large coils involved prove to

be tractable. It has been shown[1] that in such a shield the heaviest item by far would be the structure required to contain the magnetic stresses. In this note we shall use a theorem[2] on the minimum (ideal) weight of this structure to estimate the minimum (ideal) weight of a magnetic shield. In this way we will obtain some impression of the gains which are potentially available in a magnetic shield.

The structural weight theorem states that if it is required to confine a magnetic field containing energy E_M by using a structural material having density ρ and allowable stress σ , the mass of material required (M_s) is always greater than $E_M (\rho/\sigma)$,

$$M_s \geq \frac{\rho}{\sigma} \quad E_M \tag{1}$$

The equality holds only if each element of the structure is in tension and at its allowable stress. The quantity ρ/σ is a property only of the structural material. For our purposes it is conveniently quoted in kilograms of structure per joule of stored magnetic energy, but may be more familiar when quoted as a specific strength in inches, being the length of a wire of the material that could support itself under gravity. Two examples are quoted in Table I, the one for aluminum being somewhat conservative, and the one for titanium being somewhat optimistic.

Table I

Strength of Materials

	Aluminum	Titanium (-423°F)
Stress	50,000 psi	230,000 psi
Strength to Weight	7.8×10^{-6} kg/joule	2.9×10^{-6} kg/joule
	$.52 \times 10^{6}$ inches	1.4×10^{6} inches

An extremely simplified view of the shielding problem is shown in Fig. 1. We consider the surface of a shielded region. Outside this surface we have a uniform magnetic field B parallel to the surface; the thickness of the magnetic field is Δ. Now it is clear at once that if proton trajectories are to be strongly affected by the magnetic field, the thickness of the

magnetic field must be of the order of the proton Larmor radius. A more detailed study shows that the "worst" proton is the one that approaches in the direction illustrated in Fig. 1. To shield against this proton it is clear that Δ must be one Larmor diameter. Thus, $\Delta = 2p/eB$ where p/e is the momentum to charge ratio of the incident proton. Now, the energy in the field per unit surface area is just $(B^2/2\mu_o) \cdot \Delta$, and with this surface distribution of energy we can (by the structural theorem) associate a structural mass per unit surface area. This mass per unit area can be regarded as a "range" in the same sense that once calculates the "range" of a proton in a solid material. Denoting it by R_B we find

$$R_B = \frac{\rho}{\sigma} \quad \frac{B^2}{2\mu_o} \cdot \Delta = \frac{\rho}{\sigma} \quad \frac{(2p/e)^2}{2\mu_o} \cdot \frac{1}{\Delta} \qquad (2)$$

With this formula we can now compare, say, aluminum as a bulk material for stopping protons and aluminum as a structural material for supporting field coils for stopping protons. This comparison is shown in Fig. 2 for a value of ρ/σ between the two values quoted in Table I.

The first thing to note from this figure is that magnetic shielding improves as we go to larger sizes and lower fields. Of course, at some point it is no longer reasonable to neglect the contributions of the superconductor, insulation, etc. to the total mass; but the general trend of the numbers is certainly correct.

Since the results shown in Fig. 2 appear to be encouraging, it is appropriate here to list the idealizations which led to them, and which will be violated, more or less, in a real system.

1. Every element of the structure is in tension, and the cross section of each element is such that the tension is the maximum allowable.
2. The magnetic field is uniform and parallel to the surface of the shielded region.
3. The weight of the system is entirely in the structure required to support the magnetic stresses.

We will not in this note proceed to more detailed consideration of the errors involved in these assumptions; we will, however, define the

limit on how much progress can be made in the direction of reducing the weight of a magnetic shield simply by increasing its size and decreasing the field strength.

It is clear that one cannot expect to gain much beyond the point where Δ becomes of the order of the size of the shielded region. We will make this point quantitatively by resorting to a further idealization. We imagine a spherical shielded region or radius R, as illustrated in Fig. 3, surrounded by a magnetic field of thickness Δ. Now this configuration is topologically impossible since div B = 0 and a magnetically shielded region must always be multiply connected. Thus, in considering the results we will obtain from the idealization of Fig. 3, we will have to bear in mind that there is a topological factor to be considered in estimating real weights; or, alternatively, some part of the surface must be shielded by solids. With this limitation in mind we proceed by noting that Δ must still be one Larmor diameter. The volume occupied by the magnetic field is

$$\frac{4\pi}{3} (R + \Delta)^3 - \frac{4\pi}{3} R^3 \tag{3}$$

so that the minimum structural mass is, from Eq. (1),

$$M_s = \frac{\rho}{\sigma} \frac{1}{2\mu_o} \left(\frac{2p}{e}\right)^2 \frac{4\pi}{3} \left[\frac{3R^2}{\Delta} + 3R + \Delta\right] \tag{4}$$

The last term in this expression clearly has a minimum when $\Delta = \sqrt{3}\, R$ verifying our assertion that Δ should be of the order of magnitude of the size of the shielded region. With this value of Δ, the minimum weight is

$$M_s = \frac{\rho}{\sigma} \frac{1}{2\mu_o} \left(\frac{2p}{e}\right)^2 \frac{4\pi}{3} (3 + 2\sqrt{3})\, R \tag{5}$$

and this quantity is shown in Fig. 4 for various values of the proton energy. Also shown in Fig. 4 are the corresponding weights for solid spherical shields having thicknesses appropriate to the proton energy. It is seen that here again for all reasonable sizes of the shielded volume and energies of the incident proton stream there is an advantage to be realized by shielding magnetically. However, this is, as has been pointed out, an idealized

calculation. It is not possible at present to estimate with much precision just what penalty is involved in going from the idealized situation of Fig. 4 to some real situation. However, in Fig. 5 a shield is illustrated for which the weight was calculated in Ref. 1. For 100 m^3 shielded volume and for 1 Bev protons the weight was found to be about 3×10^5 kg, and this point is marked on Fig. 4 as a "Real Magnetic Calculation." The difference between this weight and the ideal weight of 10^4 kg can be interpreted as a measure both of the prospects for magnetic shielding and of the ingenuity which has to date been exercised in the design of such shields. Further study of magnetic shields is clearly warranted and some effort should be made to pin down the real weight and operating problems involved with actual hardware. In this connection it is worth pointing out that each kg of structure in Fig. 4 corresponds to something on the order of a megajoule of stored magnetic energy. The superconducting coil with the largest energy storage known to the author to be presently functioning[3] has an energy storage of 45,000 joules, at leat three orders of magnitude smaller than anything that might be useful for radiation shielding.

IV. Explosive Shielding

One final method of shielding seems worthy of mention, although its operation is many orders more undertain than those discussed. Furthermore, the reason for discussing it is chiefly to point out that it apparently cannot be done.

The method in question is illustrated in schematic form in Fig. 6. The principle is as follows: An explosion with a yield in the megaton range takes place in an ionized medium containing a weak magnetic field. A large fraction of the energy released in the explosion is tied up in the kinetic energy of the debris of the bomb, its case, etc. All this material can be expected to be ionized, and in its expansion it will interact with the ambient magnetic field in such a way as to make a large bubble empty of both field and plasma. In this way the field lines in the interplanetary plasma will be bent around the outside of the bubble, and individual high energy protons might be expected to follow these field lines around the outside of the hole.

The difficulty with this method is not in protecting the space ship from the effects of the explosion, for the size of the bubble must be many times the radius of the earth and the bomb could easily be exploded a safe distance from the ship. In fact, it seems likely that such a bubble could be made and might persist for some minutes. However, the magnetic field produced in this way cannot exclude the high energy protons even in the extreme case where the size of the bubble is large compared to the Larmor radius of the incident protons. For it is easy to find proton paths which go through the bubble. The existence of such paths, when taken together with the form of Liouville's theorem suitable for the motion of charged particles in a magnetic field,[4] guarantees that the flux in the interior is just the same as that in the exterior. Thus, no advantage appears possible from this method.

In conclusion it may be worth pointing out that this is a fortunate circumstance. For if it were not so, one might expect the magnetosphere to act somewhat like the bubble described above, in that the interplanetary field lines to some extent go around it. Then, if there were a shielding effect, we would have to conclude that measurements of the flux of solar protons made within the magnetosphere were suspect and that the intensity of these protons in free space might be much higher than suspected. There is, at present, no evidence of such an effect, although there is not much evidence from beyond the magnetosphere.

Acknowledgment

The author wishes to thank Dr. H. Petschek for the many helpful discussions in the course of this work.

REFERENCES

1. Levy, R. H., "Radiation Shielding of Space Vehicles by Means of Superconducting Coils," Avco-Everett Research Laboratory Research Report 106, April, 1961; ARS Journal, Vol. 31, p. 1568, November, 1961.
2. Levy, R. H., "Author's Reply to Willinski's Comment on 'Radiation Shielding of Space Vehicles by Means of Superconducting Coils,'" ARS Journal, Vol. 32, p. 787, May, 1961.
3. Electronics, p. 56, November 16, 1962.
4. Lemaitre, G., "Contributions A La Theorie Des Effets De Latitude Et D'Asymetrie Des Rayons Cosmiques," Ann. Soc. Sci. de Bruxelles, A54, p. 162, 1934.

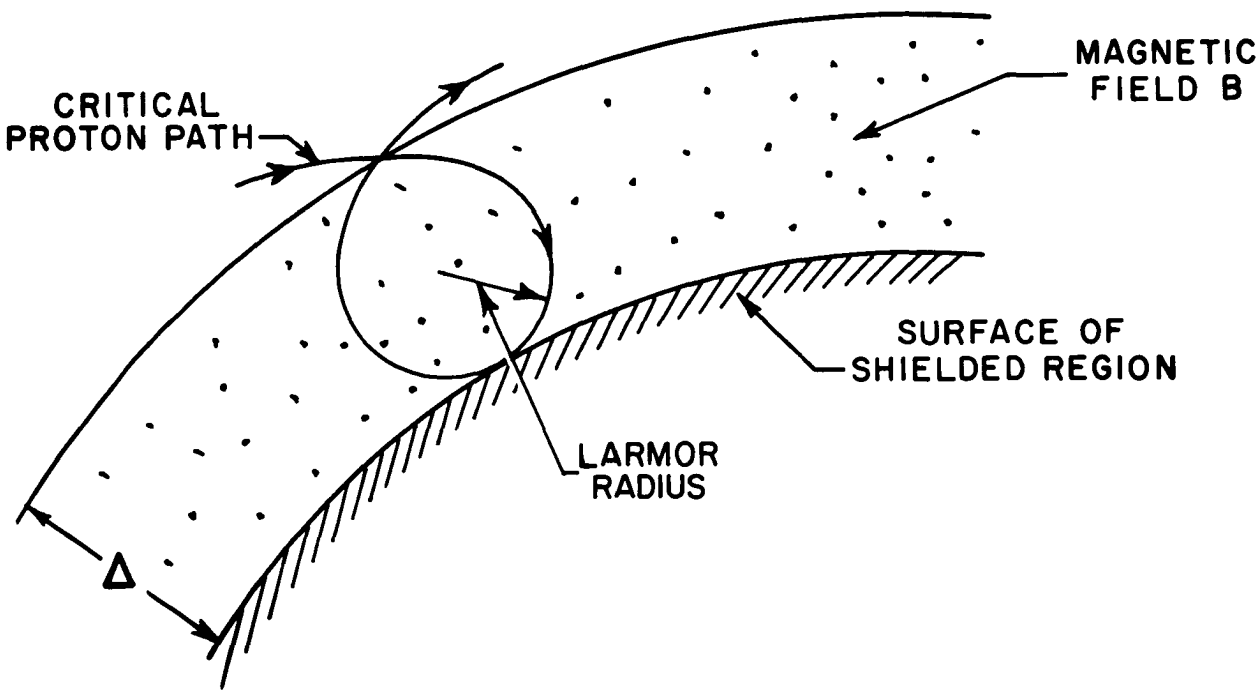

Fig. 1 This figure illustrates in a schematic manner the way in which a surface may be shielded against charged particle radiation with a magnetic field which is parallel to the surface.

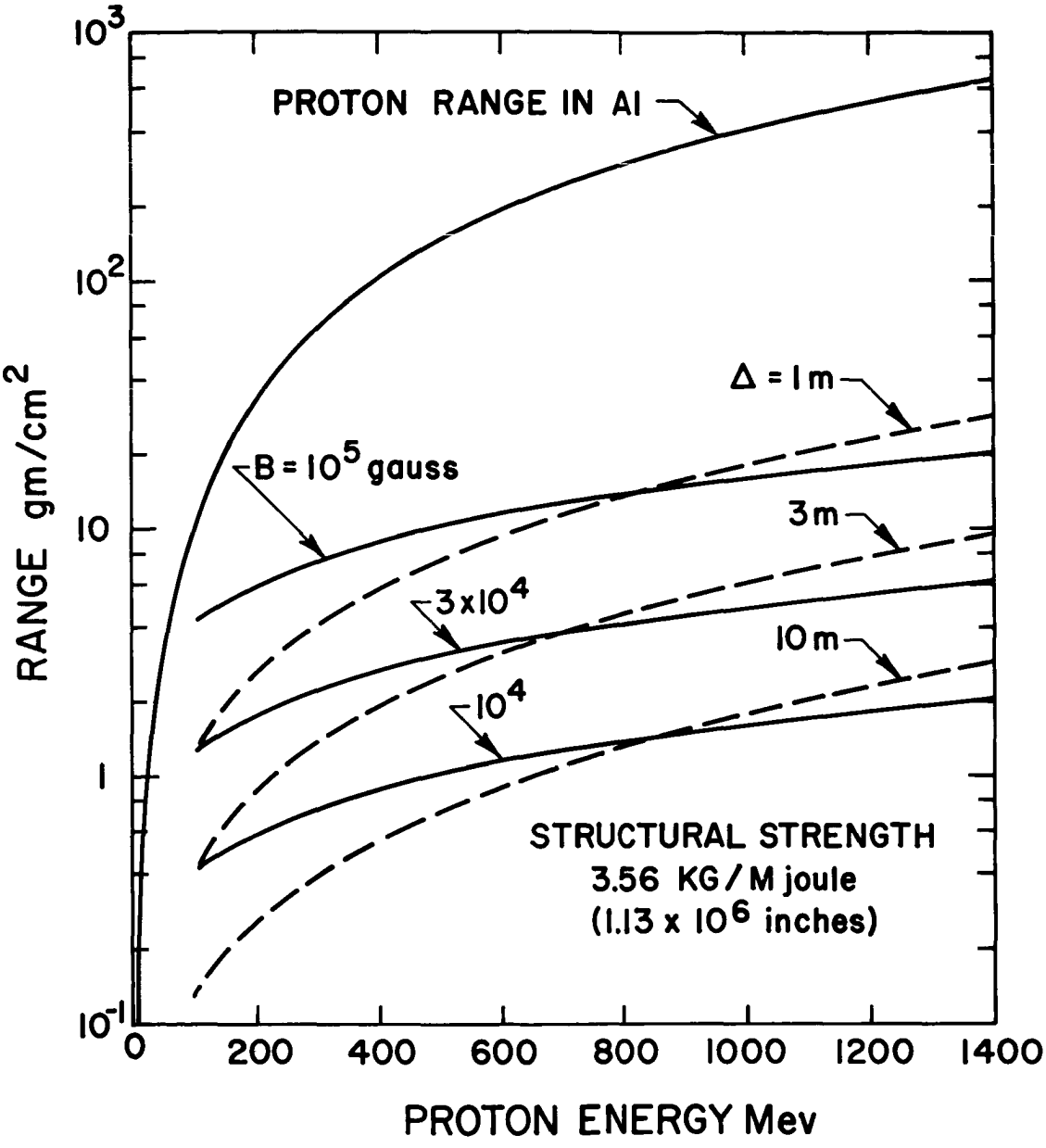

Fig. 2 This graph gives the mass per unit area (under idealizing assumptions) of a magnetic shield and compares it with the mass per unit area of a bulk shield for various field strengths and sizes.

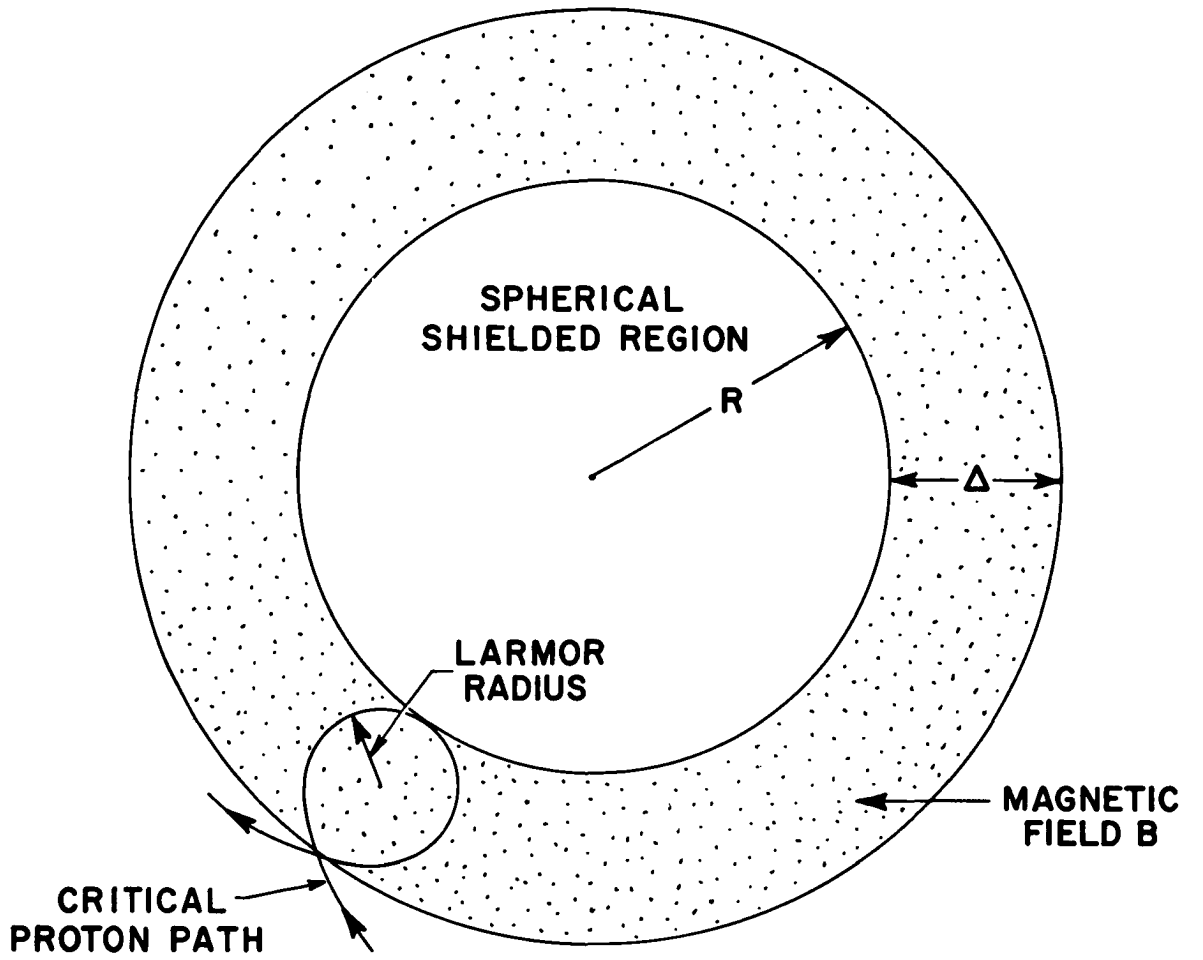

Fig. 3 This figure illustrates in a schematic manner the way in which a spherical cavity might be shielded with a magnetic field. Note that the field configuration shown is impossible; it does, however, represent a reasonable idealization of a practical configuration.

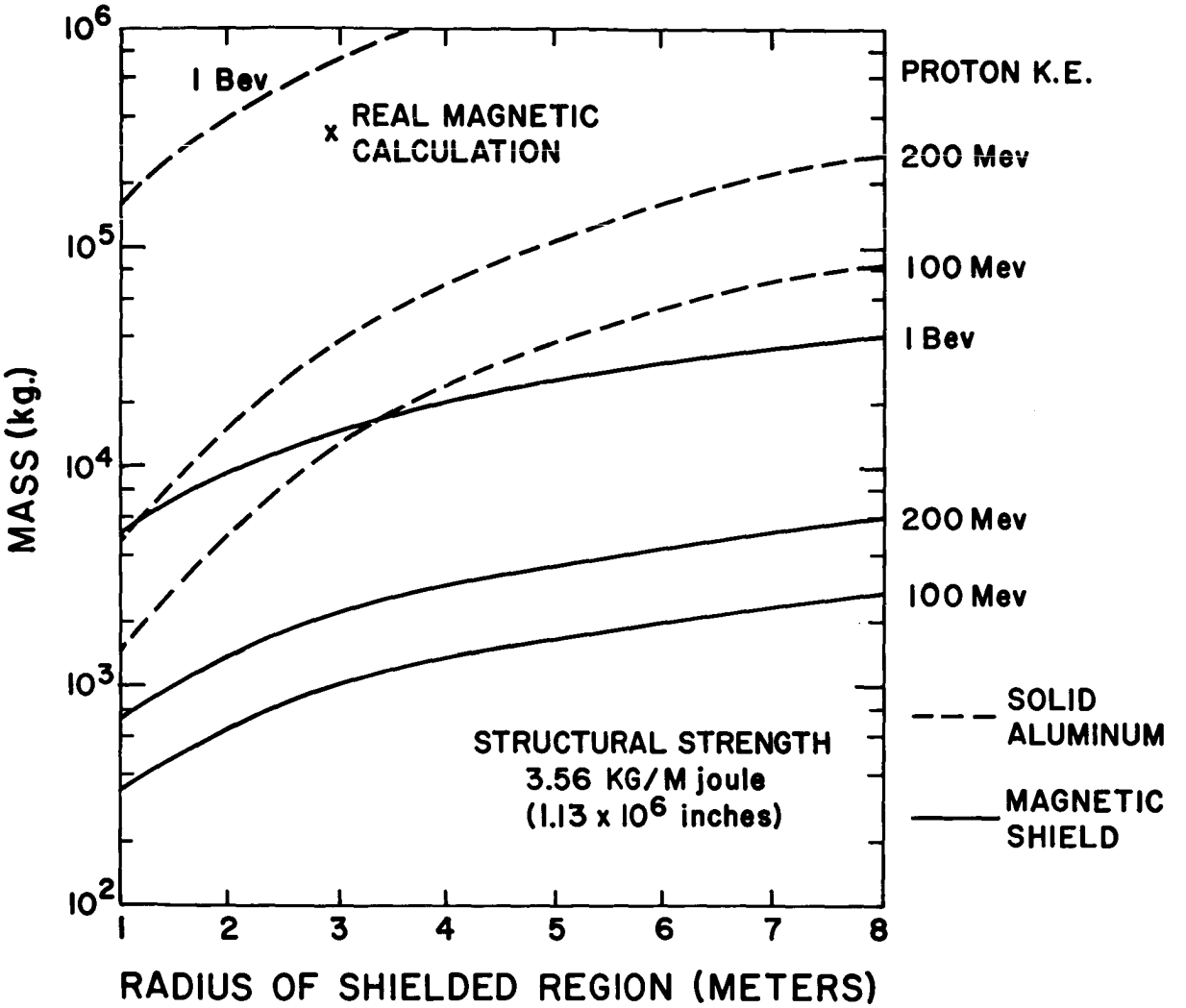

Fig. 4 This graph gives the mass (under idealizing assumptions) of the magnetic shield illustrated in Fig. 3. It also gives the mass of the bulk shield required to perform the same task, not counting secondaries, and, in addition, a more realistic calculation of a magnetic shield from Ref. 1.

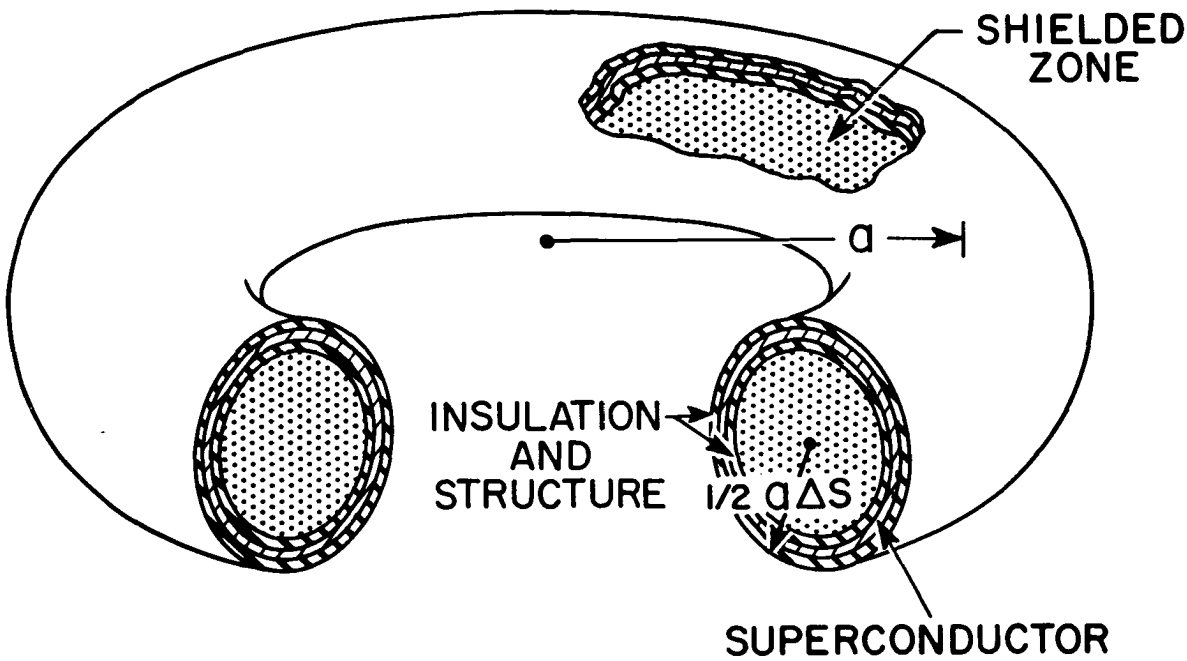

Fig. 5 This magnetic shield was discussed in Ref. 1. The shielded volume is tubular in shape, and the magnetic field is confined to the exterior of the shielded volume.

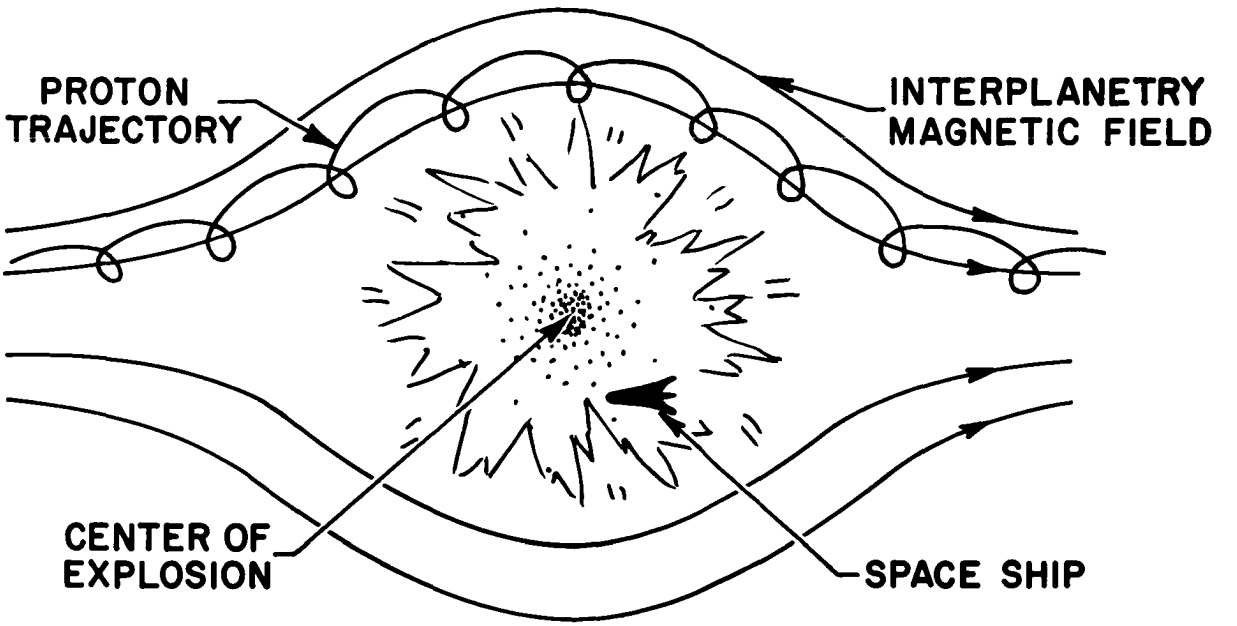

Fig. 6 This figure illustrates the explosive method of shielding discussed in the text. The size of the hole made in the magnetic field should be greater than the Larmor radius of the incident protons.

Paper F-2

SHIELDING OF SPACE VEHICLES BY MAGNETIC FIELDS

N. Edmonson, C. D. Verwers and F. L. Gibbons
General Dynamics/Fort Worth

Abstract

Protons emitted by solar flares represent a significant radiation hazard to crew members of an interplanetary space vehicle. Shielding the vehicle from charged particles by the use of magnetic fields is an obvious possibility. Reduction of secondary radiation otherwise produced in bulk shielding is an added incentive to study magnetic shielding. The feasibility of this type of shielding was reported by R. H. Levy, who utilized the properties of new superconducting materials. A program has been initiated at General Dynamics/Fort Worth to study various aspects of magnetic shielding of space vehicles. In one phase of the program, a procedure has been formulated and coded for the IBM-7090 computer for rapidly computing the field of an optimized superconducting solenoid.

In another phase, samples of NbZr wire have been irradiated with neutral particles from two sources. Preliminary results are now available. Irradiation with 10^{11} neutrons per cm^2 from the D-T reaction showed no change in the critical current versus magnetic field curve. Irradiation with 10^{16} neutrons (>2.9 Mev) per cm^2 showed a slight downward shift in the critical current. It is difficult to say whether this shift was due to the irradiation or due to the environment during the irradiation.

Introduction

A program for studying the magnetic shielding of space vehicles against charged space radiations was initiated approximately a year ago at the NARF facility of General Dynamics/Fort Worth. Two assumptions are basic in this program:

1. Magnetic shielding against charged space radiations is feasible for space vehicles;

2. Superconductors even more effective than existing superconductors will be developed.

The first assumption was based on a study by R. H. Levy[1]. The second assumption was made after a survey of the literature[2,3] and after conferences with many active research workers in the field of superconductivity.

This program was broken down into the subdivisions:

1. Design of optimized superconducting magnets;

2. Shielding effects of magnetic fields against charged particles;

3. Optimized solenoid configurations for shielding prescribed volumes;

4. Structural support design, refrigeration, and power sources for a superconducting electromagnet system;

5. Protection of the superconducting magnet system against quenches;

6. Experimental investigation of the effects of different kinds of radiations, particularly neutrons and protons on the properties of superconducting materials.

Work is being actively carried out on phases 1, 2, and 6. In this paper, a discussion is given of the analytical and experimental activities at GD/FW.

---

1. R. H. Levy, Radiation Shielding of Space Vehicles by Means of Superconducting Coils. Avco-Everett Research Laboratory (April 1961, Contract AF04(647)-278.

2. J. E. Kunzler, "Superconductivity in High Fields." Rev. of Mod. Phys., 33, 4 (October 1961).

3. J. J. Haak, G. D. Cody, P. R. Aron, and H. E. Hitchcock, (RCA Labs, Princeton, N. J.), "Some Physical Properties of Deposited Nb_3Sn." High Magnetic Fields, MIT Press (Cambridge) and John Wiley and Sons, Inc., (New York), 1962.

Problems and Computational Techniques for Superconducting Magnets

For a given temperature in the temperature range for which a given material is superconducting, there is for any transverse magnetic-field strength within a definite range of magnetic-field strengths a current I_c, the critical current, so that for currents less than I_c the superconductor behaves as a superconductor and for currents greater than I_c the superconductor behaves as a conventional or normal conductor. The superconductor goes normal or quenches at $I = I_c$. This experimental fact is added to the classical methods for computing the magnetic fields arising from current-carrying circuits to develop methods for computing the fields due to superconducting electromagnets. For example, at a given location within the windings of a superconducting solenoid, the transverse magnetic field would be the vector sum of the transverse external magnetic field and the field generated by the solenoid. The current carries by the superconducting winding at this point would be fixed from above by this total transverse magnetic-field strength. Methods for computing the magnetic-field intensities generated by superconducting solenoids have been developed by a number of workers[4,5]. These methods are discussed in Reference 6.

To apply these methods, it is necessary to have procedures for rapidly computing the field due to a superconducting solenoid both within and without the solenoid structure.

A IBM-7090 computer FORTRAN code, MAGFI, based on classical formulae for solenoids having a rectangular cross section, has been prepared. This code, furnishes a very fast means for mapping the field of a solenoid.

---

4. R. W. Boom, and R. S. Livingston, "Superconducting Solenoids." 1961 Western Electronics Show and Convention, San Francisco, August 22-25, 1961.

5. W. F. Gauster and C. E. Parker, "Some Concepts for the Design of Superconducting Solenoids." High Magnetic Fields. pp. 3-13. MIT Press (Cambridge) and John Wiley and Sons, Inc. (New York), 1962.

6. N. Edmonson, Magnetic Field Shielding Against Charged Space Radiations. GD/FW Report FZK-9-181 (to be published).

If the magnetic field of a solenoid is mapped by MAGFI, the solenoid requirements for superconducting material and structural support for the superconductors can be reduced in the following way. In general, the maximum field of a rectangular solenoid occurs at the longitudinal midpoint of the inner surface of the solenoid. The field decreases in all directions from this point. Thus, if the solenoid were wound in ring-shaped segments, the number of turns in each segment could be reduced and the current raised in accordance with the critical current-magnetic field relation of the superconducting material, so as to keep the ampere-turn constant. This technique would lead to a reduction in material and size for the solenoid for the same magnetic field strength. An optimization procedure is currently being developed for the IBM-7090.

Shielding Effects of a Magnetic Field

The shielding effect of a magnetic field is investigated by use of Störmer's concept of "forbidden regions" and by computations of the orbits of individual charged particles in a magnetic field.

The basic concepts of Störmer's theory are given in References 7 and 8. Both of these references are concerned with geomagnetic effects on charged particles. The geomagnetic field is approximated by a dipole. For the much smaller space vehicle, the dipole approximation is not sufficiently accurate. A more realistic approach is to compute the vector potential of a loop current. The equivalent solenoid may then be computed. Perhaps a more realistic procedure is to compute a solenoid optimized as described earlier and then to compute the vector potential of each one of the ring-shaped segments of the solenoid. Then the total vector potential of the solenoid is the result of a summation of the elementary vector potentials. The computations of the vector potential of a ring-shaped current is a classical procedure to be found in any advanced treatise on electromagnetism[9]. Its application to the determination of regions open to charged particles and closed (or forbidden) to charged particles is discussed in References 1 and 6.

---

7. M. S. Vallarta, "Theory of Geomagnetic Effects," Handbuch der Physik, Band XLVI/1, 88, Springer, Gottingen, 1961.

8. C. Störmer, Polar Aurora, Clarendon Press, Oxford, 1955.

9. W. R. Smythe, "Static and Dynamic Electricity," 2nd Ed., New York; McGraw-Hill Book Co., (1950).

In applying the Störmer procedure to shielding problems, a shut-off energy is selected, so that the total dose for all charged particles having energies above this shut-off energy is tolerable. For more exact information about the effects of charged particles in the neighborhood of this pre-selected shut-off energy orbit, computations may be necessary. Such computations are classical[7-10].

The Experimental Program

A major goal of the present experimental program at GD/FW is to investigate the effects of neutral particle irradiation on a superconducting material. At present, the principal interest in superconductors at GD/FW is for use in producing a large volume magnetic field for shielding a space vehicle. Clearly, magnetic shielding is not effective against neutral particles; however, in the event that the space vehicle is nuclear-powered, it is essential to determine whether neutral radiation will affect the superconducting properties of the material. The techniques developed during the phase of neutral irradiation can be used during the later phase of charged-particle irradiation.

The maximum current density of a superconducting material or alloy is not only a function of the environmental conditions during its use, but also its purity, crystal structure, and the manufacturing process used to produce the material. Work-hardening during the manufacturing process makes some materials better superconductors. For example, the maximum current density of extruded NbZr wire increases by 50% between 20- and 10-mil wire. Since it is known that irradiating a material can change the structural strength and crystal structure, one may expect a change in maximum current density after irradiation. Changes are particularly expected at low temperatures, where lattice defects may remain frozen in the material.

---

7. Ibid.
8. Ibid.
9. Ibid.
10. L. Paige, Electrodynamics, New York, Van Nostrand.

Measurement of the critical current (I_c) as a function of an applied external magnetic field is the method selected to observe changes due to irradiation. The critical current is described as the current necessary to cause a small resistive voltage to appear across the sample. All measurements are made in liquid helium at ambient pressure (approx. 4.2°K) and in a magnetic field of 10 to 15 Kgauss.

NbZr wire being used in the experiment is 0.014 inch in diameter, hard drawn (>99% reduction), and of a Nb 25 at. % Zr alloy.

The Dewar used is a conventional liquid-nitrogen-jacketed, glass, helium Dewar with a liquid helium capacity of approximately one and one-half liters. Current leads are brought into the dewar through liquid nitrogen to decrease liquid-helium boiloff. This setup allowed about 45 minutes working time. (See Fig. 1.)

The circuit used to measure the critical current is shown in Fig. 2. A Keithly Model 149 millimicrovoltmeter is used to measure the voltage across the sample. Its output is attached to the y axis of a Sylvania Type B-281 x-y recorder with the x axis attached to a precision resistor through a D-C amplifier to record the current. The current is supplied by two large storage batteries and controlled through a transistorized series amplifier.

The sample holder (see Fig. 3) is cut so that it will fit into the 5/8-in.-diam Dewar tip and hold the sample in the center of the Dewar. The sample is mounted parallel and coincident to the center plane midway between the poles of the magnet. All samples are copper-plated, except for three lengths between the four contact points. The contact between the superconductor and current lead is made by winding 12 inches of wire around the current lead and then soft-soldering with 60/40 lead-tin or indium. The contact resistance with these junctions was on the order of 5×10^{-6} ohms.

Two pieces of NbZr wire were irradiated at ambient temperature in the Ground Test Reactor and compared with control samples. The total neutron flux was 10^{17} neutrons (>2.9 Mev) per cm^2. X-ray diffraction and optical magnifications to x 1000 showed no observable change in the crystal structure. The micro-hardness test, using a Knoop micro-hardness tester and converting the readings to the Rockwell "c" hardness scale, showed a change of from 30.5 to 28.6 on the hardness scale after irradiation. Another sample that was completely annealed by heating changed from 30.8 to 25.1. Due to the dependence of the current density on work-hardening these

measurements indicate a plausible explanation for any possible change in the critical current due to irradiation.

Three different samples have been irradiated in the Ground Test Reactor at ambient temperature, with a total flux of $>10^{16}$ neutrons (>2.9 Mev) per cm^2. Preliminary results of several measurements of the critical current before and after irradiation are shown on the bottom curve of Fig. 4.

Effects of neutron irradiation are being studied by irradiating samples with 14.2-Mev neutrons from the D-T reaction using a Cockcroft-Walton type accelerator. The critical current as a function of the magnetic field is measured before, during, and after irradiation with the sample temperature kept at $4.2^{o}K$ during the experiment. Preliminary results of this irradiation are shown by the top curve of Fig. 4.

Summary of Experimental Results

The upper curve of the accelerator irradiation shows no significant change, but the lower curve with reactor irradiation is suggestive of a downward shift in the critical current curve. One other sample was irradiated at the accelerator and two other samples were irradiated with the reactor. Those data show similar trends. However, the reproducibility from one run to the next and between samples leaves something to be desired. The spread in the points is comparable to the apparent effects observed with the reactor irradiation. Note that the accelerator exposure was only 10^{11} neutrons compared to more than 10^{16} from the reactor.

The data then seem to suggest that there may be an effect at the higher exposures, but our experimental techniques must be improved to reach a firm conclusion. This will be the next step in this current phase in the experimental program at GD/FW. Beyond that, the next phase in the overall program will include the construction and testing of optimized magnets.

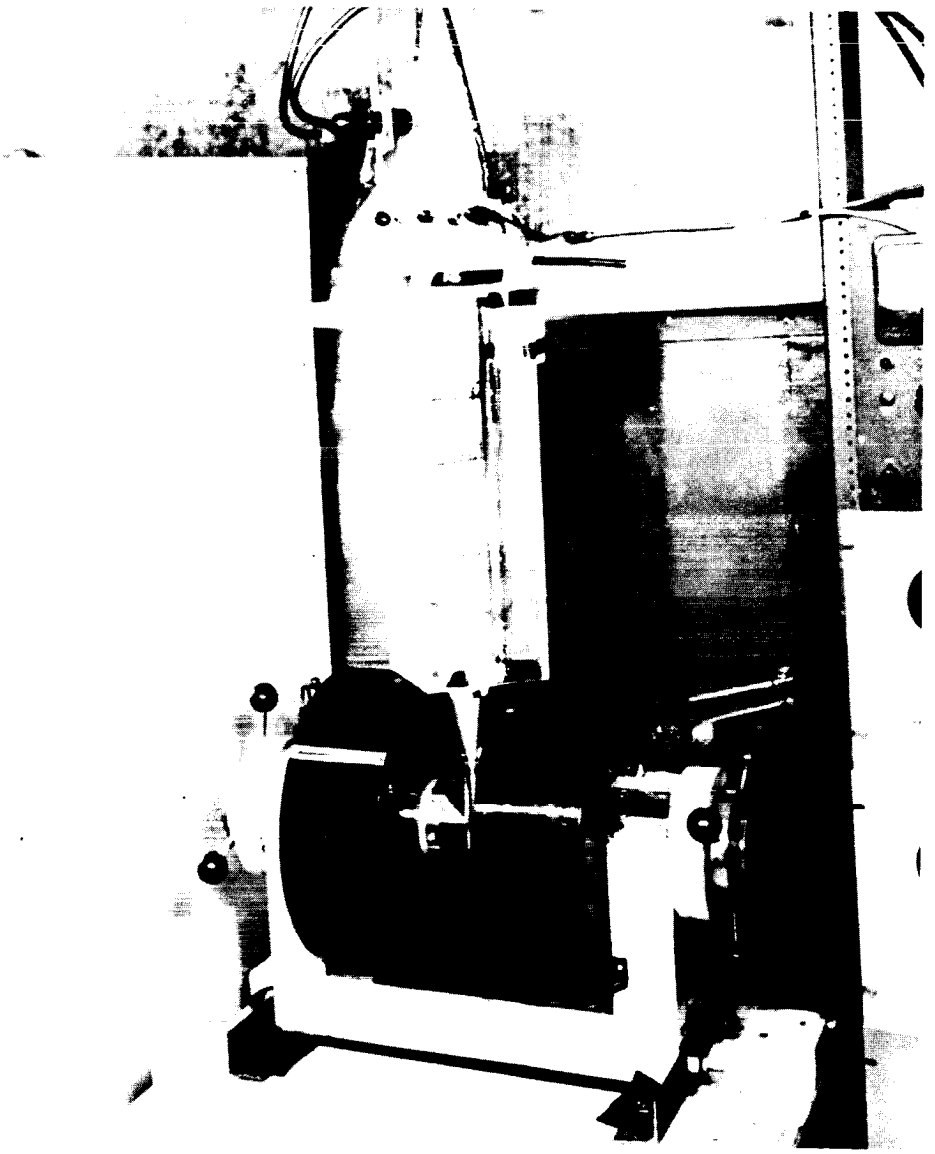

FIGURE 1. DEWAR AND MAGNET

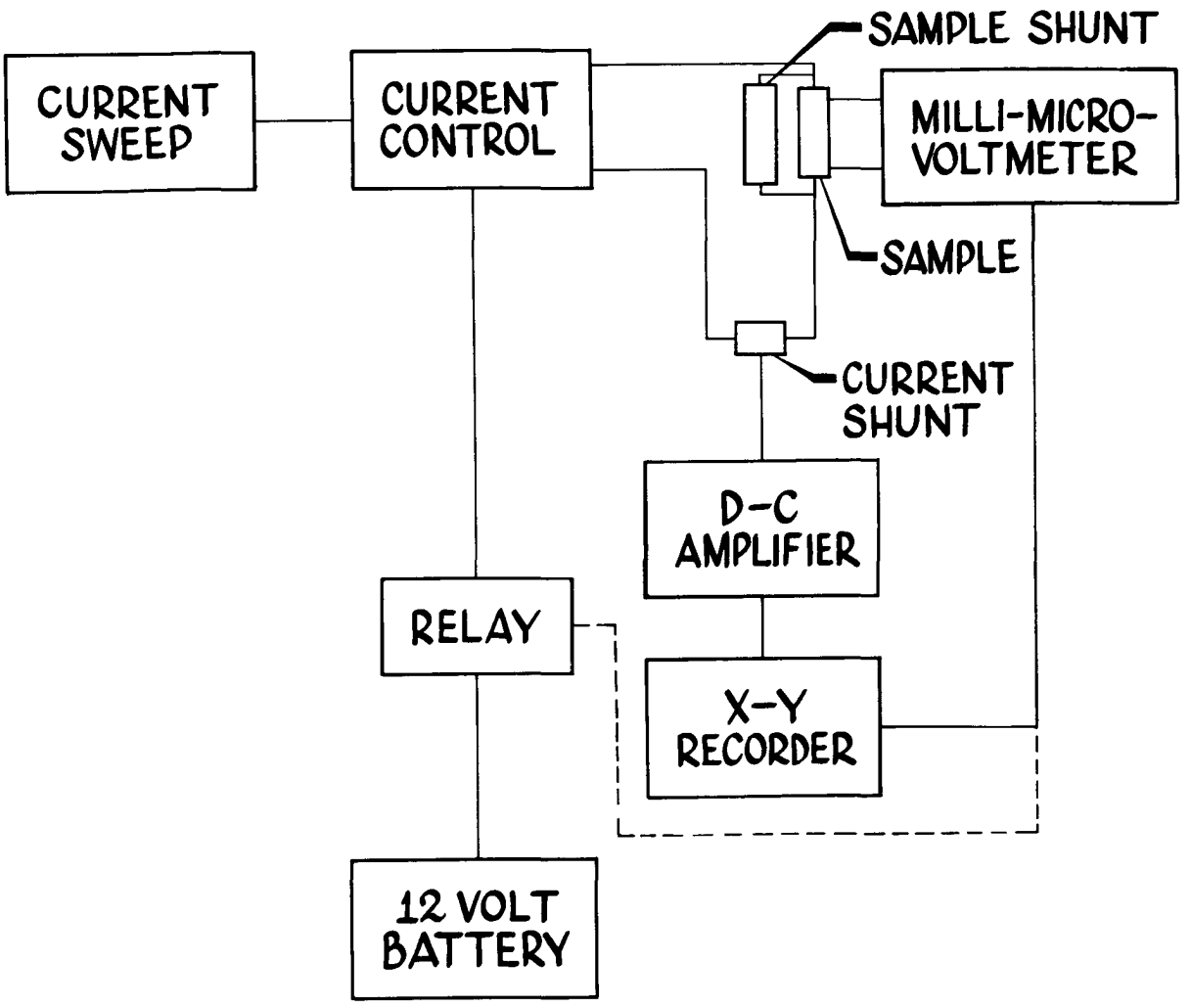

FIGURE 2. BLOCK DIAGRAM OF ELECTRICAL CIRCUIT

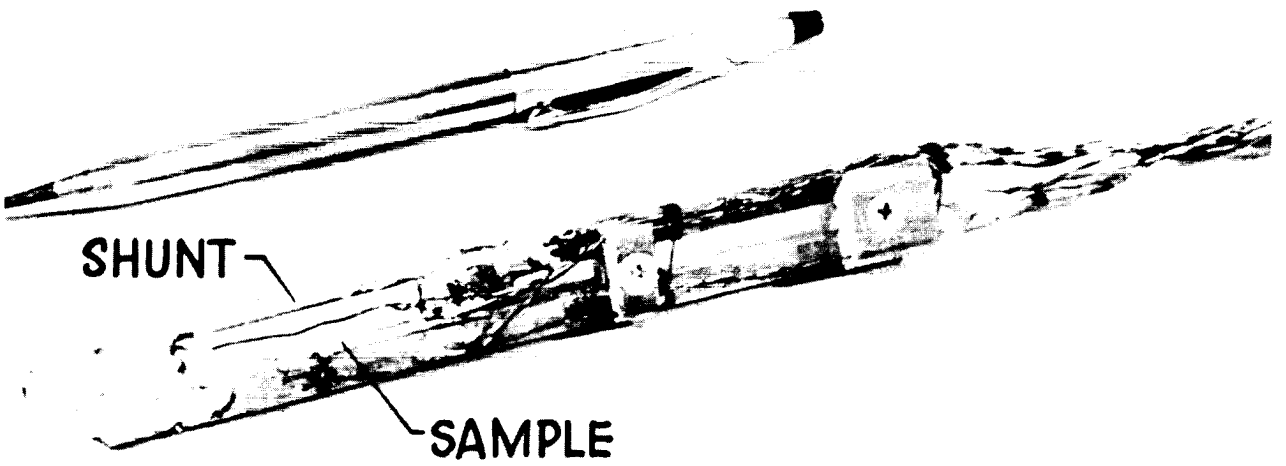

FIGURE 3. SAMPLE HOLDER WITH NbZr SAMPLE

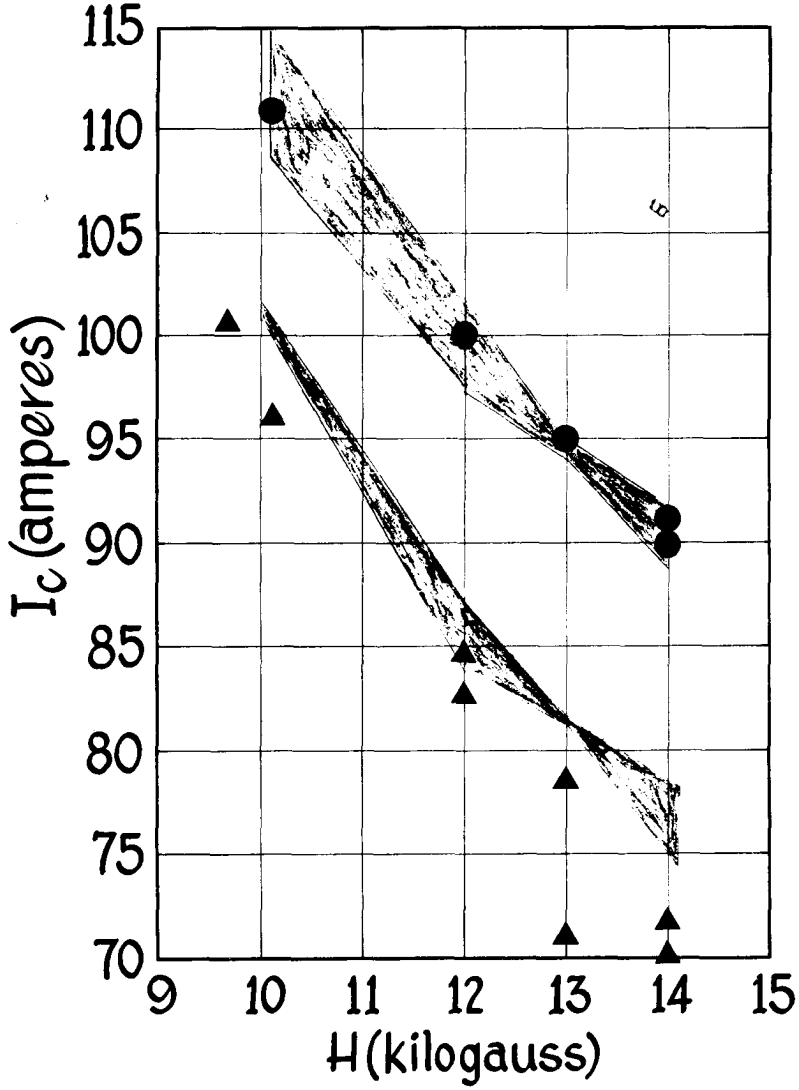

NbZr SAMPLE "C"
14 Mev NEUTRON IRRADIATION

▩ PRE-IRRADIATION
(DATA SPREAD IN 4 RUNS)
JUNCTION RESISTANCE-5.3$\mu\Omega$

● POST IRRADIATION-1.2×10^{11} n/cm^2
JUNCTION RESISTANCE-8.3$\mu\Omega$

NbZr SAMPLE "B"
REACTOR IRRADIATION

▩ PRE-IRRADIATION (2 RUNS)
JUNCTION RESISTANCE-5.6$\mu\Omega$

▲ POST-IRRADIATION $>10^{16}$ n/cm^2
JUNCTION RESISTANCE-15$\mu\Omega$

FIGURE 4. PRELIMINARY RESULTS

Paper F-3

THE COMBINATION OF ACTIVE AND PASSIVE SHIELDING

J. M. Norwood
General Dynamics/Fort Worth

15156

Abstract

It is conceivable that improved shielding of space vehicles against high-energy charged-particle radiation can be obtained by combining active and passive shielding. Methods of shielding calculations and some preliminary observations pertaining to active-passive shielding are given. An analysis based upon the field of a magnetic dipole indicates that weight savings in bulk shielding can be accomplished.

Introduction

A space vehicle can, of course, be protected against high-energy, charged-particle radiation by either a passive bulk shield or an active magnetic shield. The weight, however, of a passive shield may be excessive[1], and magnetic shielding apparently provides inadequate protection against charged particles incident from certain directions and no protection from neutrons and gamma rays. It is conceivable that improved shielding with reduced weight can be obtained by combining the two shielding methods. Possibly, thick bulk shielding will be required only in regions of the magnetic field which provide weak active shielding, with relatively thin bulk shielding being sufficient elsewhere. These possibilities warrant examination, thus a limited investigation has been undertaken for that purpose. Some preliminary observations and shielding calculation methods are presented.

The Mathematical Formulation of the Problem

The combination active-passive shielding problem can be separated into two parts: (1) the passive shielding problem with the complication of a magnetic field, and (2) the active

1. R. K. Wilson, R. A. Miller, and R. L. Kloster, A Study of Space Radiation Shielding Problems for Manned Vehicles. GD/FW Report FZK-144 (June 1962).

shielding problem which must be solved to find the magnetically shielded regions and to determine the charged-particle intensity on the surface of the bulk shield in the unshielded regions. The intensity of incident charged particles is assumed to be known, and the dose calculation problem is ignored. Preliminary information pertaining to the feasibility of active-passive shielding can be obtained without dose calculations by computing the total number of particles which penetrate the shield.

Passive Shielding

Motion Through Bulk Material. Those particles of primary radiation which penetrate the magnetic field into the bulk shield move through the bulk material under the influence of the magnetic field and a slowing down force. If it is assumed that the slowing-down force is directed backwards along the trajectory, that it is independent of the magnetic field and of the path, and that there is no straggling, the path can be computed from the following equations:

$$\frac{d\vec{R}}{ds} = \vec{\Omega} = \frac{\vec{v}}{v}, \tag{1}$$

$$\frac{d\vec{\Omega}}{ds} = \frac{q\sqrt{1-\beta^2}}{m_p c^2 \beta}\,\vec{\Omega} \times \vec{B}, \tag{2}$$

the Bethe-Bloch equation[2]

$$-\frac{dE}{ds} = \frac{4\pi e^2 q^2 NZ}{m_e v^2}\left[\ell n \frac{2m_e c^2}{I(Z)} + \ell n \frac{\beta^2}{1-\beta^2} - \beta^2\right], \tag{3}$$

and the relativistic kinetic energy equation

$$U + m_p c^2 = \frac{m_p c^2}{\sqrt{1-\beta^2}} = E. \tag{4}$$

$\vec{R}$ is the particle position vector, s the arc length of the path, $\vec{\Omega}$ a unit vector along the path, $\vec{v}$ particle velocity, c the speed of light, m_p and q particle mass and charge, respectively, and $\vec{B}$ the magnetic field vector. E is particle energy, m_e and e electron mass and charge, respectively, Z

---

2. S. K. Allison and S. D. Warshaw, Rev. Mod. Phys. 25, (1953), 779.

the atomic number of the shielding material, N the number of atoms of shielding material per cubic centimeter, I(Z) the mean excitation potential (approximately equal to 12.5 Z electron volts), and $\beta = v/c$. If the bulk shield is composed of more than one element, dE/ds is assumed to equal the sum of a set of equations of the form of Eq. 3, one equation for each element.

The Differential Form of The Transport Equation. The transport theory formulation of the passive shielding problem in terms of the integro-differential equation is

$$\vec{v} \cdot \nabla_R N(\vec{R},\vec{P}) + \left[q\vec{v} \times \vec{B} + \frac{\vec{v}}{v}\frac{dE}{ds}\right] \cdot \nabla_P N(\vec{R},\vec{P})$$

$$+ v(\sigma_t - \sigma_{sl}) N(\vec{R},\vec{P}) = \int \sigma_s(\vec{P}' \rightarrow \vec{P}) v' N(\vec{R},\vec{P}') d^3\vec{P}'. \qquad (5)$$

$N(\vec{R},\vec{P})$ is the particle density in phase space at the point in phase space $(\vec{R},\vec{P})$, where $\vec{R}$ and $\vec{P}$ are position and momentum vectors, respectively; ∇_R and ∇_P are the usual ∇ operators, but the former denotes differentiation with respect to the space coordinates and the later with respect to the momentum coordinates. The parameter σ_t is the total cross section, and $\sigma_s(\vec{P} \rightarrow \vec{P})$ is the usual function denoting the probability that a charged particle of momentum $\vec{P}'$ will undergo a nuclear collision at the point $\vec{R}$ and give rise to a charged particle of momentum $\vec{P}$. Equation 5 is written in terms of only one type of particle, but it can, of course, be generalized to include all types.

The parameter σ_{sl} is an abbreviation for the expression

$$\sigma_{sl} = -\frac{1}{v\,P^2}\frac{d}{dP}\left\langle P^2 \frac{dE}{ds}\right\rangle \qquad (6)$$

and arises from the fact that volume in phase space is not conserved within the bulk material because of inelastic collisions with electrons. An expression for σ_{sl} derived from the Bethe-Bloch equation is

$$\sigma_{sl} = \frac{8\pi\, e^2 q^2 NZ}{m_p m_e c^4}\frac{\sqrt{1-\beta^2}}{\beta^2}\left[\ell n \frac{\beta^2}{1-\beta^2} + \frac{1}{\beta^2} + \ell n \frac{2m_e c^2}{I(Z)} - 1\right]. \qquad (7)$$

Values of σ_{sl} and σ_t for carbon are compared in Table 1.

Table 1. Comparison of Parameters for Carbon

U (Mev)	σ_{s1} (cm^{-1})	σ_t (cm^{-1})
100	0.034	0.019
200	0.015	0.017
500	0.006	0.018

The Integral Form of The Transport Equation. The transport equation for active-passive shielding can also be formulated as an integral equation, and as such its functional form is unaltered by the presence or absence of the magnetic field. With N in terms of $\vec{R}$, $\vec{E}$, and $\vec{\Omega}$, the integral equation is

$$vN(\vec{R},E,\vec{\Omega})S(s) = v_oN(\vec{R}_o,E_o,\vec{\Omega}_o)S(o)e^{-\ell(o,s)}$$

$$+\int_o^s\left[\iint\sigma_s\left\{E'',\vec{\Omega}''\rightarrow E(s'),\vec{\Omega}(s')\right\}\ v''N\left\{\vec{R}(s'),E'',\vec{\Omega}''\right\}dE''\ d\Omega''\right]$$

$$x\ S(s')e^{-\ell(s',s)}\ ds'\ , \qquad (8)$$

where

$$S(s) = \frac{dE(s)}{ds} \qquad (9)$$

and

$$\ell(s',s) = \int_{s'}^{s}\sigma_t\left\{E(s'')\right\}ds'' \ . \qquad (10)$$

Integration of Eq. 8 is carried out along the path of a particle in the increment of volume in phase space of $d^3\vec{R}dEd\Omega$ as the volume increment moves along the arc from point $\vec{R}_o$ to $\vec{R}$ (Fig. 1).

The arc can be obtained by integrating Eqs. 1 through 4. The first term on the right of Eq. 8 represents the primaries which enter the shield at $\vec{R}_o$ with energy E_o and direction $\vec{\Omega}_o$ and which reach $\vec{R}$ with energy E and direction $\vec{\Omega}$. The second term represents secondaries which reach $\vec{R}$ with energy E and direction $\vec{\Omega}$ from all points $\vec{R}(s'')$ along the arc $0 \leq s'' < s$. Terms of the form $e^{-\ell}$ represent attenuation due to nuclear processes.

Shielding calculations are performed for a given shield configuration by summing the total number of particles which

reach the interior of the bulk shield from all possible paths through the shield. That is, the total number I of particles, which cross the inner surface is calculated by integrating $\vec{v} \cdot \vec{\Omega}\ v\ N(\vec{R},E,\vec{\Omega})$ over the inner surface of the shield, over all directions $\vec{\Omega}$ into the shield, and over all energies E; $\vec{v}$ is a unit normal to the inner surface and $v\ N(\vec{R},E,\vec{\Omega})$ is given by Eq. 8.

$$I = \int dS \int d\Omega \int_0^\infty dE\ \vec{v} \cdot \vec{\Omega}\ v\ N(\vec{R},E,\vec{\Omega}). \tag{11}$$

If desired, dose calculations can be performed by including a flux-to-dose conversion factor behind the energy integral. However, dose calculations are ignored in this paper.

It can be shown by a modification of Liouville's theorem[3] that if the incident charged-particle flux is isotropic and homogeneous at infinity (an assumption which is adequate for present purposes), it is isotropic and homogeneous everywhere in a magnetic field except in magnetically shielded regions, where it is zero. Thus, if secondaries can be neglected in Eq. 8, then Eq. 11 can be written as

$$I = \int dS \int d\Omega \int_{E^*(\vec{R},\vec{\Omega})}^\infty dE_o\ \frac{1}{4\pi}\ \Phi(\vec{R},E_o,\vec{\Omega})\ \vec{v} \cdot \vec{\Omega}\ e^{-\ell\{E_o,E(\vec{R},E_o,\vec{\Omega})\}} \tag{12}$$

where

$$\begin{aligned} \Phi(\vec{R},E_o,\vec{\Omega}) &= \Phi(E_o) \text{ in non-shielded regions} \\ &= 0 \text{ in shielded regions.} \end{aligned} \tag{13}$$

Magnetic shielding will be discussed in the next section. $E^*(\vec{R},\vec{\Omega})$ is the minimum energy required of particles at the outer bulk shield surface to reach the inner surface at $\vec{R}$ with direction of motion $\vec{\Omega}$. The parameter ℓ is written in terms of E_o and E instead of s' = 0 and s' = s.

Evidently, active-passive bulk shielding calculations are executed in the same manner as passive shielding calculations with zero magnetic field. Active-passive bulk shielding calculations are much more complicated, however, because of nonlinear particle paths through the bulk material. Speci-

---

3. W. F. G. Swann, Phys. Rev. 44, 224 (1933).

fically, loss of symmetry due to nonlinear particle paths results in the necessity of performing more integrations, or conversely, linear paths lead to symmetry which renders certain integrations trivial.

Active-Passive Shielding

A realistic solution to the combined active-passive shielding problem is dependent upon the geometry chosen for the shielding configuration. Since such a configuration has not been selected at this time, only investigations of a preliminary nature can be undertaken. Indeed, one object of such investigations is to determine optimum active-passive configurations.

The tentative analysis to follow is based upon the Störmer analysis of a dipole field[4,5]. According to the Störmer analysis, a volume of space at the magnetic equator of the dipole field is completely shielded from charged particle radiation of a given energy. Outside this volume, there is a region of space which is shielded against all particles except those which possess directions of motion inside a given cone of directions (the Störmer cone). Since the sizes of the partially and completely shielded regions are functions of energy and since these regions decrease in size as incident-particle energy decreases, the position of the magnetically-shielded regions relative to the position of the bulk shield is a function of energy.

For a fixed passive shield, the boundary of the completely magnetically shielded region will lie outside the bulk shield for low-energy particles and inside for very-high-energy particles. Thus, the active shield will stop the low-energy particles, while the passive shield must stop the high-energy particles. But if the bulk shield is to stop the high-energy particles, it will be quite thick, in which case its presence will negate the usefulness of the magnetic shield.

This analysis applies to the volume about the magnetic equator. At the magnetic poles, the component of $\vec{\Omega}$ parallel to the axis of the field, $\vec{\Omega}_{//}$, is not affected by the field, since by Eq. 2, $d\vec{\Omega}_{//}/ds = 0$. Consequently, $\vec{\Omega}_{//}$ is constant, and by Eq. 1 the component of $\vec{R}$ in the $\vec{\Omega}_{//}$ direction is

---

4. L. Janossy, Cosmic Rays. Oxford, (1950), Chap. VII.

5. R. F. Tooper and W. O. Davies, Electromagnetic Shielding of Space Vehicles. Armour Research Foundation, IAS Paper No. 62-156 (June 1962).

$\vec{R}_{\parallel} = s\vec{\Omega}_{\parallel}$. Thus, the necessary thickness of the bulk shield at the poles is independent of the presence or absence of the magnetic field.

It appears that thick bulk shielding is needed everywhere, thus rendering the active shield useless. But the preceding analysis ignores several things. First, the dipole field is not very realistic, although one is led to believe that it represents many of the shielding properties of any magnetic field; second, it ignores the fact that the magnetic field bends the path of a charged particle as it traverses the bulk shield; and third, it neglects the partially shielded region.

In the partially shielded region at the magnetic equator, the solid angle subtended by the cone of allowed directions (which opens to the east) decreases in size as energy decreases. After consideration is given to take advantage of this fact and the turning effect of the magnetic field, an active-passive shield with reduced bulk shield weight can be constructed so that no particle of energy less than a maximum energy can penetrate it. The shield is designed so that lower-energy particles have directions of incidence which lie closer to the bulk shield surface and their paths inside the bulk shield tend to bend away from the inner surface (Fig. 2).

Computational Results. Calculations were made for a spherically shaped bulk shield and a magnetic field independent of position within the bulk shield. A dipole field was assumed to exist outside the bulk shield. The outer diameter of the bulk shield was taken as 2 meters and the magnitude of the magnetic field intensity within the material was 37,500 gauss. At points on the magnetic equator, it was found that a shield thickness of 5.3 gm/cm^2 of polyethylene would completely stop protons of energy of 100 Mev or less; at the poles, where the effect of the magnetic field is minimum, the necessary thickness is 7.1 gm/cm^2. No calculations were made at magnetic latitudes other than at the equator and at the poles, but if it is assumed that the inner surface of the bulk shield is an ellipsoid of revolution (the shielding being thinner at the equator) as opposed to a spherical inner surface, the weight saving in shielding material is some 1200 lb or 16% of the whole.

Conclusions

Although it appears that active-passive shielding may be a useful concept, a more comprehensive study is indicated. Calculations for more realistic geometries would be desirable. For example, an active shielding analysis for a large diameter circular loop or solenoid would be more reasonable as a basis for active-passive shielding calculations. Another possible geometry is Levy's torus with concentric windings centered on the axis of symmetry[6].

6. R. H. Levy, Radiation Shielding of Space Vehicles by Means of Superconducting Coils. Avco-Everett Research Laboratory, Research Report 106 (April 1961).

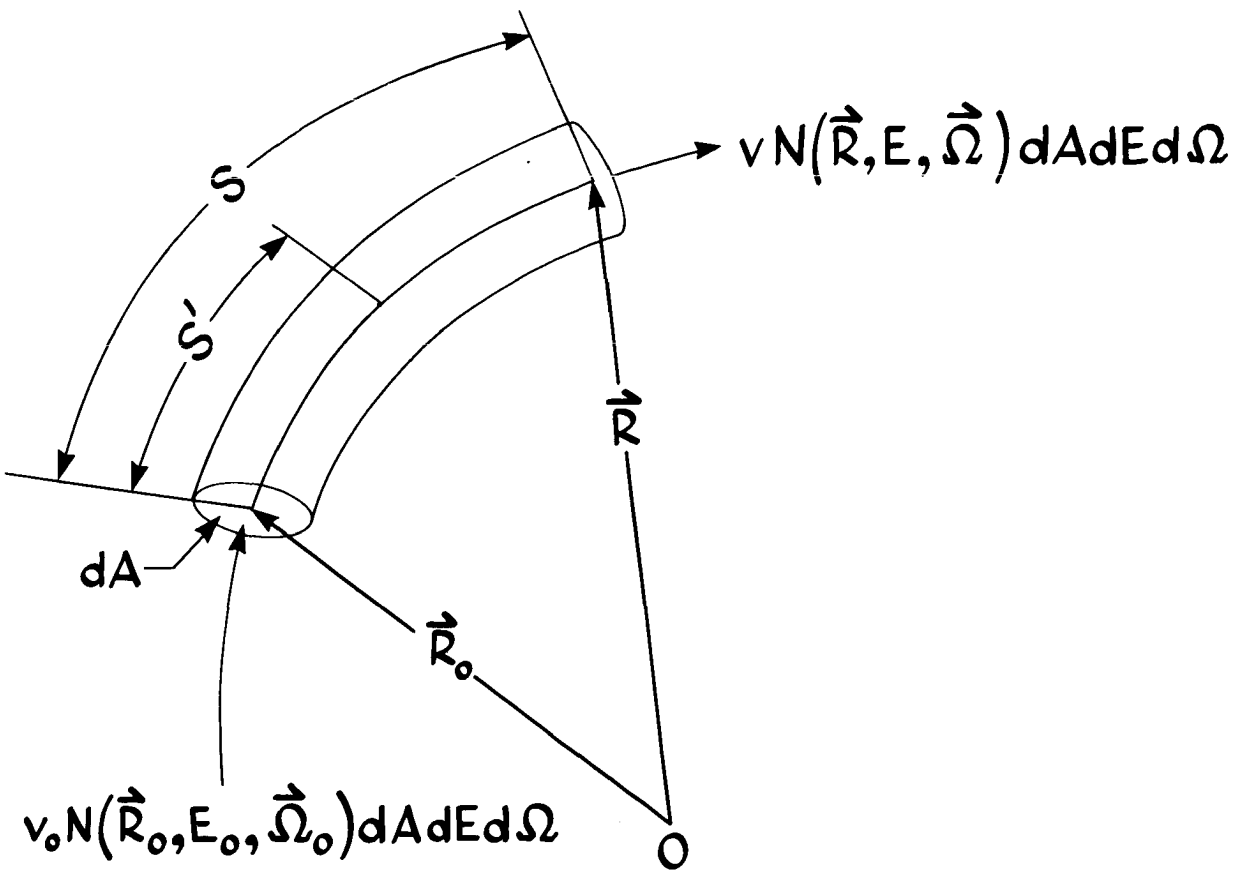

FIGURE 1. CHARGED PARTICLE FLUX ALONG AN ARC

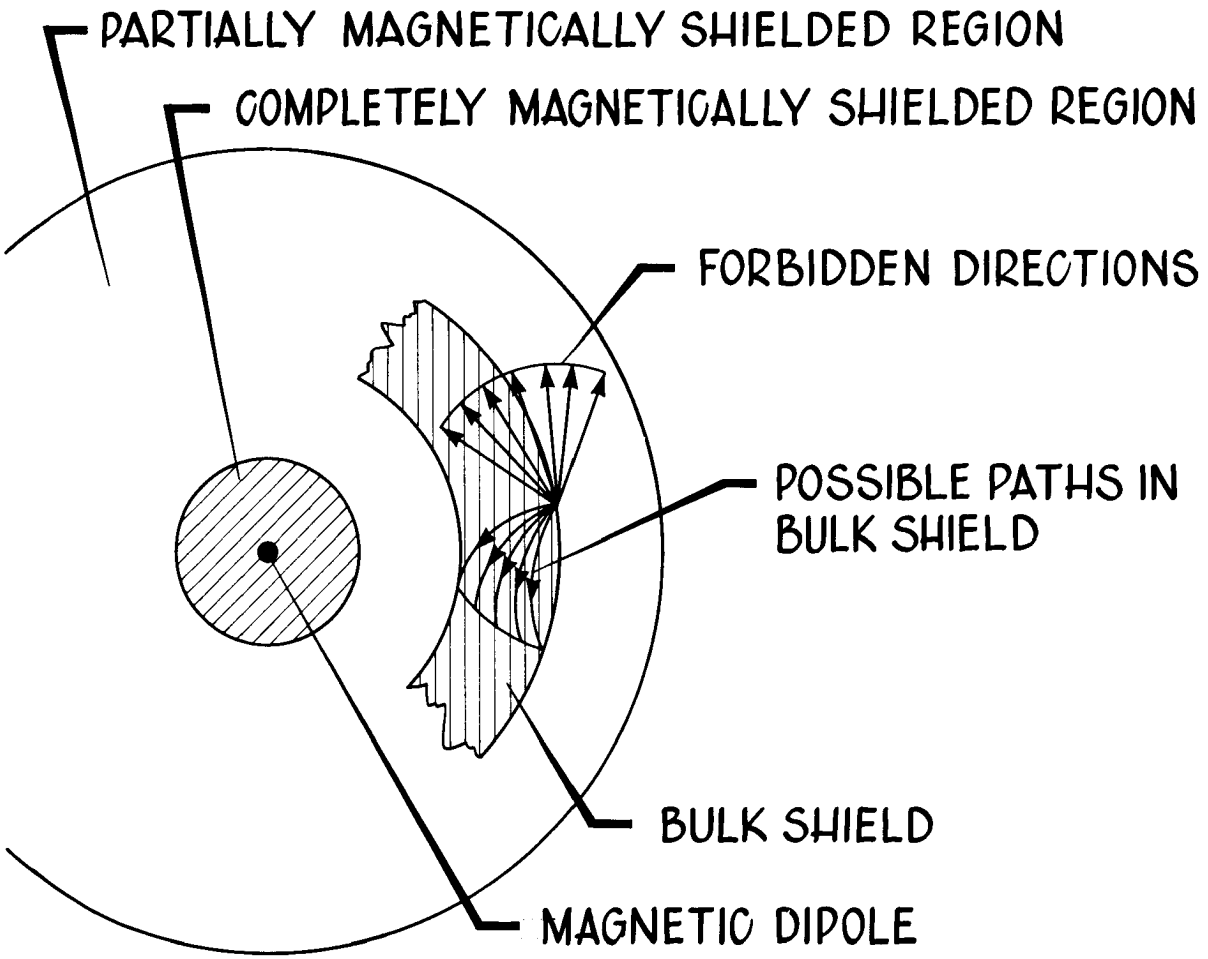

FIGURE 2. SHIELDING IN THE EQUATORIAL PLANE

Paper F-4

TECHNIQUES USED IN SHIELDING CALCULATIONS FOR HIGH-ENERGY ACCELERATORS: APPLICATIONS TO SPACE SHIELDING*

Roger Wallace and Charles Sondhaus

Lawrence Radiation Laboratory
University of California
Berkeley, California

15157

Abstract

The prediction for the secondary neutron spectrum produced inside of a thick shield is described. The multiplicity of cascade and evaporation secondaries as well as subsequent moderation of the secondary spectrum is described quantitatively. Experimental thick-target neutron yields, as well as Monte Carlo cascade data, are the basis for these estimates.

Introduction

The principle differences between shielding a man in space and shielding the crew of a large accelerator are that the tolerance levels for the space ship are higher, and the integrated incident dose is lower. This reduces the thickness of shield in the space ship relative to that in the accelerator. The detailed investigation of this difference is not the subject of this paper. We only attempt to show how approximate estimates for the shielding of accelerators can be made. These methods and the data used in them are applicable to the space-ship problem.

The spectrum of protons incident on a space ship is both continuous and somewhat softer than the monoenergetic protons that would emerge from a high-energy accelerator in the several-hundred-MeV region. This difference tends to reduce greatly the number of secondary neutrons produced and emphasizes the role of primary protons that may actually penetrate the space-ship wall. Such wall penetration by protons is not characteristic of accelerator-shield situations. The companion paper by Sondhaus and Wallace[1] describes the penetration of a thick shield by protons, whereas this paper is largely limited to neutron considerations. For high-energy accelerators it has been found that the gamma-ray dose outside of a very thick shield is only a modest fraction of the neutron dose. This conclusion may not be true in the case of space shielding where the shield may be somewhat thinner and the gamma-ray dose a more important fraction of the neutron dose.

*Work done under the auspices of the U. S. Atomic Energy Commission, and the Joint Atomic Energy Commission--NASA Space Radiation Program.

The technique generally used to estimate shielding is that developed by B. J. Moyer.[2a, 3, 4] While each proton produces a variety of particles as it undergoes collision in the shield, only the neutrons are of biological significance. For protons striking an extended thick target, the total neutron production as a function of energy for carbon, aluminum, copper, and lead is shown in Fig. 1. This total neutron production consists of two parts: "cascade" and "evaporation" neutrons. There are also cascade protons. The cascade particles that are knocked out during the immediate passage of the incident proton by direct interactions between the proton and the individual nucleons in a target nucleus have been extensively treated by Metropolis.[5] The cascade particles, because of momentum conservation, are strongly concentrated in the forward direction relative to the incident-proton direction. Due to their long mean free paths only those cascade particles having energies above 150 MeV need be considered in shielding. Cascade particles would be rather unimportant as secondaries from protons below 100 MeV.

The remainder of the secondary particles are produced by evaporation from the nucleus after the initial proton passage as a result of the excitation energy that is left behind in the nucleus. The evaporation process gives off neutrons isotropically. There has been some augmentation of these curves to allow for a plural cascade within the target nucleus.

The cascade yields of neutrons and protons resulting from either neutron or proton bombardment are shown in Fig. 2. The synthesis of the resulting secondary neutron spectrum results from three parts:

(1) the cascade neutrons above 20 MeV,

(2) the evaporation-neutron spectrum that is peaked in the few MeV region, and

(3) the resulting thermal spectrum which arises from the degradation of the energy of the other two neutron sources.

This three-part synthesis is a natural division of this otherwise far too complex problem for a simple estimate. Of course, the problem is not too complex for a computer approach. The cascade neutrons above 150 MeV are the only part of the spectrum which must initially be considered in the evaluation of the thickness of the shield. This results from the neutrons of lower energy having attenuation lengths substantially shorter than those above 150 MeV. It is only this penetrating high-energy component that controls the shield thickness, as can be seen in Fig. 3. There is a plateau in the half-value thicknesses of concrete shielding above 150 MeV. The conclusions that one reaches about concrete are also applicable to most other materials (with the exception of hydrogen) on a gram for gram basis. A thick shield made of liquid hydrogen would need special consideration.

There is, of course, a buildup and an establishment of equilibrium in the secondary neutron spectrum in the first few outer layers of the shield. After equilibrium is established in one or two half-value layers, no further change in the shape of the neutron spectrum occurs with depth in the shield, only an attenuation of the entire spectrum as the highest-energy primaries are attenuated.

Cascade Particles

The spectra of cascade particles computed by Metropolis are shown in Fig. 4 for 460 and 1840 MeV incident protons on aluminum. These spectra seem not to differ very much from each other except of course at the highest energies. These spectra are characteristic of somewhat lower energies as well. These spectra, multiplied by the appropriate normalization factors (given in Fig. 7), are shown in the energy region above 50 MeV on Fig. 5 for incident proton energies of 450, 600, and 850 MeV. It is seen that below about 100 MeV the cascade spectra are essentially the same. These spectra have not yet been degraded by passage through hydrogenous material, therefore no thermal peak is present.

The angular distribution of the cascade particles of Metropolis et al. [5] has been augmented by Moyer using data on the angular distribution of the prongs of nuclear-emulsion stars from the Bevatron and from cosmic rays. Such an angular distribution is shown in Fig. 6. The distribution shown is normalized for 6.2-GeV protons on copper; however, the angular distribution is not sensitive to energy. It is hoped that the extremely valuable work of Metropolis et al., which has served as a basis for so many shielding calculations, will soon be augmented by additional Monte Carlo computations from the Oak Ridge Group.

The number of cascade neutrons per incident proton as a function of proton energy for a variety of target materials is given in Fig. 7. It is seen that for the high energies there is a monatonic increase in the number of cascade neutrons with A, whereas for the energy region below 200 MeV the low-A materials actually have a higher neutron production than the high-A materials.

The number of cascade protons per incident proton as a function of proton energy and target A is shown in Fig. 8. These curves bear a resemblance to those for neutron production in Fig. 7 and the same conclusion can be drawn with respect to production in the light elements. It should be noted that in the energy region near 500 MeV the Fig. 8 cascade-proton curves are in the reverse order with the highest proton production coming from the low A's and the lowest proton production coming from the high A's in contrast to the Fig. 7 cascade-neutron case. Above 1000 MeV the low-A curve does cross over the others but the others still remain in the inverted order. This particular fact is of only minor importance to our present problem since cascade protons have a very limited range and it is really the cascade neutrons that one must consider.

After the shielding thickness becomes quite thick, a similar set of curves could be provided giving neutrons per incident neutron and protons per incident neutron as a function of A and energy. These additional curves would only be useful for some specialized accelerator-shielding situations. In the space-vehicle case we do not have a sufficient number of incident neutrons to concern us and the incident proton case is overwhelmingly dominant.

Evaporation Particles

The most important source of neutrons is the evaporation process. Several authors[6-9] have treated the evaporation of nucleons from nuclei that have been excited by very high-energy neutrons or protons. These evaporation neutrons will provide the low-energy end of our spectrum. Nuclear evaporation is somewhat analogous to the evaporation of the liquid on an atomic scale. The resulting particle spectra are obtained by estimating an excitation energy E_1 for the nucleus as a whole. This estimation, due to Moyer,[5] is shown in detail for A from 20 to 220 in Fig. 9. This set of curves gives the "excitation" energy E_1 left behind in a nucleus by a proton or neutron of energy E. This energy is then considered as a thermal kinetic-energy source for eventual evaporation.

The nuclear temperature produced by the deposition of energy E_1 in a nucleus A by an incident neutron or proton is shown in Fig. 10. Note that nuclear temperatures for the light elements have plateaus in the region of several hundred MeV, making the change in temperature in this region with incident proton energy quite small.

The excitation energy is related to the square of an effective nuclear "temperature" by an empirical parameter[6] (A/10); thus we have

$$E_1 = (A/10)\tau^2, \tag{1}$$

where E_1 is the nuclear excitation in MeV, and A is the atomic weight of the nucleus. This empirical equation is shown in Fig. 11 for four different values of A. It is seen that the light elements have higher nuclear temperatures than heavy elements for a particular excitation energy. Figures 9, 10, and 11 represent a three-dimensional surface in a space whose coordinates are the total nuclear excitation energy, nuclear temperature and bombarding-proton energy.

The evaporation spectrum itself is given by Eq. (2). The E in front of the exponential instead of the usual $E^{1/2}$ which appears in the

$$N(E)dE = (E/\tau^2)e^{-(E/\tau)}dE \tag{2}$$

Maxwellian energy distribution is necessary to account for the fact that N(E) is a flux density rather than a numerical density.

To estimate the complete spectrum penetrating the shield, it is now necessary to fit this modified Maxwellian low-energy evaporation end of the spectrum to the Metropolis cascade high-energy tail. This transition fit is made after the area under each individual spectrum has been normalized to the estimated total production of each spectrum's particular component (as given in Table I for the case of aluminum or shown for other A's and E's in Figs. 1, 7, and 12). Note that in Table I it is appropriate for the sum of "cascade" and "evaporation" neutrons to not equal the "total" neutrons. The "total" production is per incident particle on a thick target. The "cascade" and "evaporation" production are per inelastic collision at the quoted energy. The sum of these two productions can be either less than or greater than the "total," depending on the ratio of inelastic-collision proton removal to electromagnetic dE/dx proton energy loss. The total neutron production per inelastic collision and the ratio of the evaporation to the cascade process both as a function of energy and A are given in detail in Figs. 13 and 14. The electromagnetic energy loss changes with proton energy, while the inelastic cross sections are quite constant with energy above 100 MeV as seen in Fig. 15. It is seen that for the lightweight elements the number of evaporation neutrons is quite constant at about one neutron per proton over a wide energy range.

More details of this process are available, such as the suppression of the low-energy particles by the Coulomb barrier, as treated by Dostrovsky[6] and Le Couteur.[7] Particles other than neutrons, such as H, H^2, and H^3, as well as multiple-charged particles, such as He^3 and He^4 can also be estimated as given in Figs. 16 through 20. The doubly charged particles have their evaporation spectrum peaks at about twice the energy of the proton spectrum peak for a nucleus of the same excitation. The angular distribution of the particles emitted in connection with nuclear evaporation is of course isotropic. The evaporation particles produced in an internal target have no chance of their own of penetrating the main shield directly, except for the inner one or two mean free paths of the shield. Therefore, evaporation particles are mainly of interest with regard to the radioactivity that they may induce in the accelerator hardware. This problem is probably not of particular importance for space-craft shielding. The evaporation particles are far more important for inducing radioactivity than are the cascade neutrons, since evaporation particles are considerably more numerous and their energy is more favorable for capture. More extensive data is available on evaporation particles.

Attenuation of the Total Spectrum

Generally the fit between the two parts of the spectra as shown in Fig. 5 is done by eye. Greater accuracy is not appropriate to the degree of approximation which we are making. Direct measurements of shield thickness required for a given attenuation factor, using beams of restricted width, have been made for concrete, water, and a few other materials, but probably not for the materials of interest in

space-craft shielding. Light-weight elements, such as contained in concrete, have shielding values very little different for different A's; this value is mainly proportional to the number of grams of shield per cm^2. A thick shield provides neutron attenuation by absorbing, degrading, or deviating the neutrons by nuclear collisions. At the high energies characteristic of cascade particles, elastically scattered particles are so strongly peaked in forwardly directed diffraction patterns that essentially no geometric deviation or energy loss occurs. Thus, as the incident neutron energy is increased from values characteristic of the evaporation region to values associated with the cascade region, the value of the effective removal cross section for neutrons by a shield decreases from the value of the total cross section to the value of the inelastic cross section. This effect is shown in Tables 2, 3, and 4, from Patterson, [2b] as applied to the elements present in concrete. It is seen that $n\sigma_a(cm^{-1})$ is a figure of merit for the efficiency of each element in the concrete. Table 4 emphasizes the importance of the heavier elements as the neutron energy is raised. Several points calculated from these data for concrete, by Patterson, are plotted in Fig. 21 together with several experimental values for energies from 1 MeV to 4.5 GeV. The agreement between the experimental and calculated values is quite good. The same data appeared in CGS units in Fig. 3. These data only apply to thick shields and poor geometry situations. The companion paper presented by C. Sondhaus[1] will outline some deviations from this which are characteristic of somewhat thinner shields where the proton beam may be considered to survive in a geometrical fashion.

The measurements of σ_{total} and $\sigma_{reaction}$ for various nuclei as a function of neutron energy up to 5 GeV are given by Coor et al.[10] and Atkinson et al.[11] and are shown in Lindenbaum[12] (see Fig. 21). This experimental work shows that the attenuation of neutrons in the high-energy region is essentially constant.

Radiation Emerging from the Shield

Now that the spectrum and angular distribution of the neutrons produced in the target and accelerator hardware by the primary protons have been estimated, a secondary calculation can be made of the penetration of the outer shield by these neutrons. This can be done by using similar data for cascade and evaporation particles produced by neutrons, instead of protons as shown in Figs. 2, 9, 10, 12, and 16 through 20, secured from the same sources as that given earlier for incident protons. The evaporation data are the same as those for incident protons, whereas the cascade values are not. As would be expected, the neutrons are more numerous in neutron-induced cascades than in proton-induced cascades, and vice versa for proton-induced cascades. Cascade-produced mesons gradually increase in importance from 500-MeV incident energy on up. They do not become a controlling factor in the energy range considered in space shielding.

The flux of particles present inside the space-ship shield or outside the accelerator shield now consists of (a) directly transmitted primary neutrons of energy > 150 MeV (from the spectra shown in Fig. 5), and (b) evaporation fragments produced by the high-energy neutrons that suffer inelastic collisions in the last layers of the shield. The number of cascade neutrons making evaporation neutrons and protons by inelastic collisions within a last layer of the shield wall of thickness x is

$$N = N_o(e^{x/\lambda} - 1), \tag{3}$$

where x is measured in from the shielded side of the shield, and λ is the mean free path for inelastic collisions of the cascade neutrons. Assume that half of the evaporation neutrons emerge. This is an obvious overestimate of the number of evaporation neutrons but it will to some extent be compensated for by the further multiplication of a fraction of the cascade neutrons in secondary collisions which again increases the number of evaporation neutrons emerging from the shield. Few of the protons produced in the cascade events in the early part of the shield will emerge from the shield, because of range limitations. There will, however, be protons arising from the evaporation processes emerging from the shield.

Considering a final layer of the shield $x = \lambda$, one mean free path thick, and using the spectra shown in Fig. 5 and values of λ shown in Fig. 15 from Lindenbaum,[12] we estimate that in a particular case each cascade neutron produced in the outer shield will be accompanied by 0.6 fast neutrons and 0.3 protons when it emerges from the shield.

There may also be a small flux of thermal neutrons and gamma rays. The gammas come from thermal neutron capture by the H of the shield (if present) and also from nuclear de-excitations associated with evaporation processes. Typically, the numerical value of the thermal neutron flux is only a few times that of the fast neutrons, so the relative dosage from the thermal neutrons is negligible, if we take RBE values into account, in comparison with the fast neutrons. Ionization-chamber measurements of the gamma-ray dosage are typically one-quarter or less than that arising from fast neutrons.

If one wishes to make an estimate of the spectrum of epithermal neutrons that will be produced by moderation of the cascade and evaporation neutrons and will extend below the evaporation peak, the slowing down spectrum can be approximated by assuming that each emission increment $Q(E_1)\Delta E_1$ gives rise to a flux increment with spectrum $1/E - 1/E_1$. Thus, by integration, the slowing down flux has the spectrum

$$\phi(E) = K_1 \int_E^{E_{max}} Q(E_1)\left(\frac{1}{E} - \frac{1}{E_1}\right) dE_1 . \tag{4}$$

This slowing down flux spectrum is joined by continuity of slope of the thermal spectrum,

$$\phi_{th} = K_2 E^{1/2} e^{-(E/kT)}, \tag{5}$$

which are normalized by requiring the integral from zero energy to 1/2 eV to give the value[13]

$$\phi_{th} = 1.25 \frac{Q}{S}, \tag{6}$$

where Q is the total source strength of fast neutrons and S is the surface area over which they are thermalized (in cm^2).

Conclusions

The data that is presently available and pertinent to the shielding of high-energy proton accelerators has been presented. An approximate method for estimating the neutrons produced in the shield and released into the cabin has been outlined. The production curves for heavier secondaries have been given. Data for meson production, although available, are not included. Should the shield consist of liquid hydrogen, some revision of the data would be necessary since the lowest atomic weight included is A = 20 and the production of neutrons in a liquid hydrogen shield arises through different processes. Neither cascade nor evaporation are possible for H. Various modes of meson production accompanied by neutron production are the only sources of neutrons from H. While data for this type of neutron production is available it has not been accumulated and converted to a useful form for shielding purposes. It is probably true however that neutron production from the hydrogen shield would be considerably reduced relative to that from a shield of higher atomic weight. In general, on a weight basis, a hydrogen shield should be considerably more effective than an equal mass per cm^2 of any other type of material; this difference might be a factor of 2. This is probably not enough to dictate the use of liquid hydrogen relative to other shielding materials, unless it happens to be unusually convenient for propulsion and energy storage reasons, since its low density and temperature make its storage very difficult.

References

1. C. Sondhaus and R. Wallace, Solar Proton Exposure Simulation with the 184-Inch Cyclotron, Lawrence Radiation Laboratory Report UCRL-10447, November 1962 (unpublished).

2a. B. J. Moyer, Method of Calculation of the Shielding Enclosure for the Berkeley Bevatron, in First International Symposium on Protection Near Large Accelerators, Saclay, France, January 1962 (to be published).

2b. H. Wade Patterson, The Effect of Shielding on Radiation Produced by the 730-MeV Synchrocyclotron and the 6.3 GeV Proton Synchrotron at the Lawrence Radiation Laboratory (UCRL-10061, January 1962, in First International Symposium on Protection Near Large Accelerators, Saclay, January 1962 (to be published).

3. B. J. Moyer, Data Related to Nuclear Star Production by High-Energy Protons, Lawrence Radiation Laboratory, June 20, 1961 (private communication).

4. B. J. Moyer, Shielding and Radiation Calculations for USNRDL Cyclotron, Lawrence Radiation Laboratory, October 11, 1960 (private communication).

5. N. Metropolis, R. Bivins, M. Storm, A. Turkevich, J. M. Miller, and G. Friedlander, Phys. Rev. 110, (1958) pp. 185 and 204.

6. I. Dostrovsky, P. Robinowitz, and R. Bivins, Phys. Rev. 111, 1659 (1958).

7. K. J. Le Couteur, Proc. Phys. Soc. (London) A63, 259 (1950).

8. Y. Fujimoto and Y. Yamaguchi, Progr. Theoret. Phys. (Kyoto) 4, 468 (1950); ibid., 5, 787.

9. R. W. Deutsch, Phys. Rev. 97, 1110-23 (1955).

10. T. Coor, D. A. Hill, W. F. Hornyak, L. W. Smith, and G. Snow, Phys. Rev. 98, 1369 (1955).

11. J. H. Atkinson, W. N. Hess, V. Perez-Mendez, and R. Wallace, Phys. Rev. 98, 1369 (1955).

12. S. J. Lindenbaum, Shielding of High-Energy Accelerators, in Ann. Rev. Nucl. Sci. 11, 213 (1961).

13. H. W. Patterson and R. Wallace, A Method of Calibrating Slow-Neutron Detectors, Lawrence Radiation Laboratory Report UCRL-8359, July 1958 (unpublished).

Table 1. Secondary cascade and evaporation-particle production, nuclear excitation energy and temperature for aluminum targets in proton beams of three different energies.

Proton energy (MeV)	Total neutron thick target yield (n/p)on Al	No. cascade[a] neutrons per incident proton on Al per inelastic collision	No. cascade[a] protons per incident proton on Al per inelastic collision	Total[a] no. cascade nucleons per incident proton on Al per inelastic collision	Residual[a] nuclear excitation E_1 (MeV)	Residual[a] nuclear temperature τ (MeV)	No. evaporation neutrons per incident neutron or proton per inelastic collision
450	1.3	1.30	1.85	3.15	63	4.3	1.30
600	2.1	1.40	2.05	3.45	72	4.5	1.50
850	3.3	1.55	2.25	3.80	88	4.9	1.60

a. See ref. 3.

Table 2. N atoms/cm^3 for Berkeley concrete ($\times 10^{22}$).

O	4.73
H	1.73
Si	1.57
Ca	0.26
Al	0.17
Fe	0.053
Na	0.028
K	0.028
Mg	0.013

Table 3. Assumed relation between σ_a, the neutron-attenuation cross section, and σ_{tot}, the total neutron cross section

(MeV)	
1	$\sigma_a = 1.00\ \sigma_{tot}$
5	$\sigma_a = 0.65\ \sigma_{tot}$
14	$\sigma_a = 0.055\sigma_{tot}$
≥ 150	$\sigma_a = 0.50\ \sigma_{tot}$

Table 4. $N\sigma_a(cm^{-1})$ for various elements ($\times 10^{-2}$).

	1 MeV	14 MeV	270 MeV
O	16	4.4	0.89
H	7.8	0.64	0.026
Si	4.7	1.7	0.41
Ca	0.78	0.33	0.10
Al	0.51	0.16	0.05
Fe	0.16	0.045	0.028

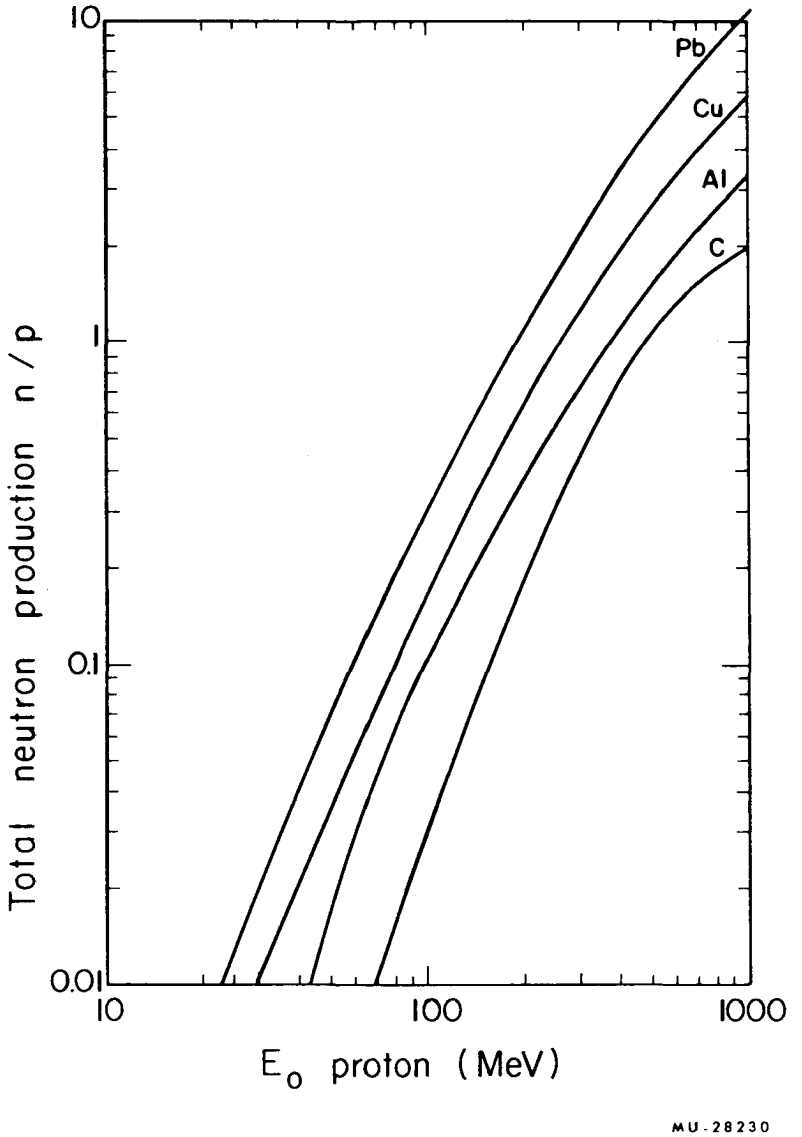

Fig. 1. Measured total neutron yields per proton stopping in a thick target for C, Al, Cu, and Pb, from Moyer.

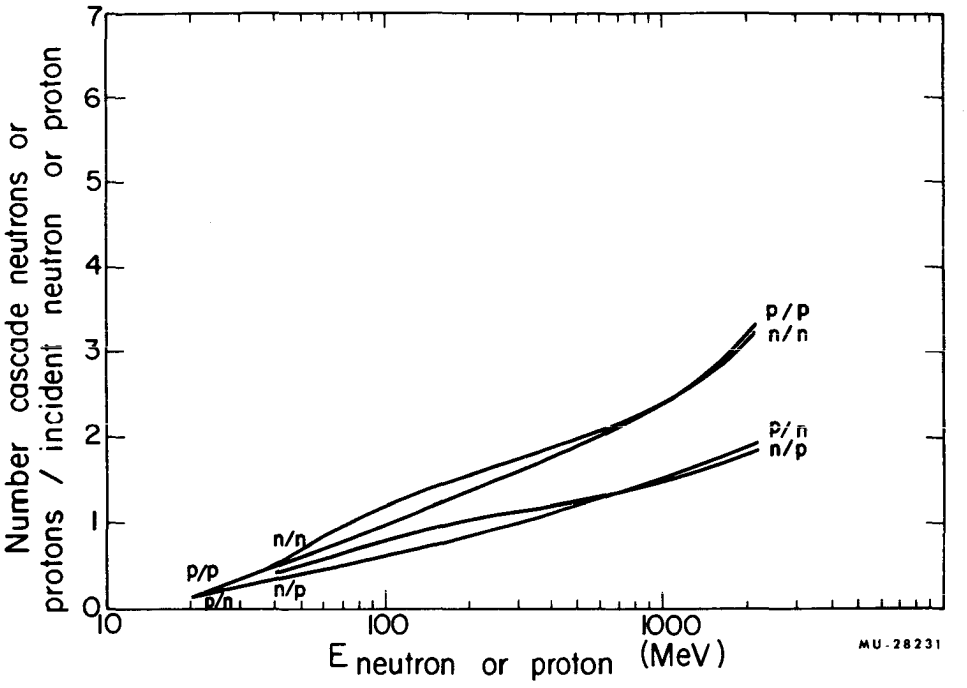

Fig. 2. Estimated cascade neutrons and protons produced by incident neutrons or protons of energy E_n on nuclei near A = 20 per incident particle per inelastic collision, from Metropolis et al.[5]

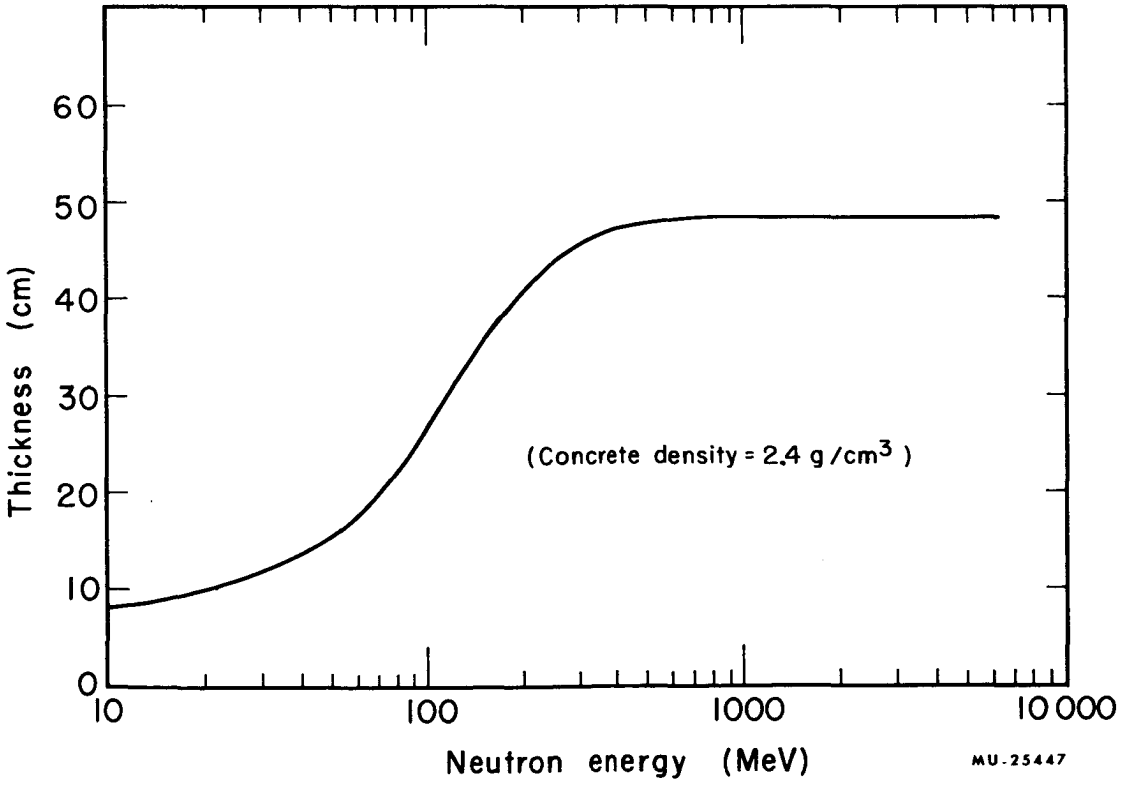

Fig. 3. Half-value reduction thickness for high-energy neutrons in ordinary concrete.

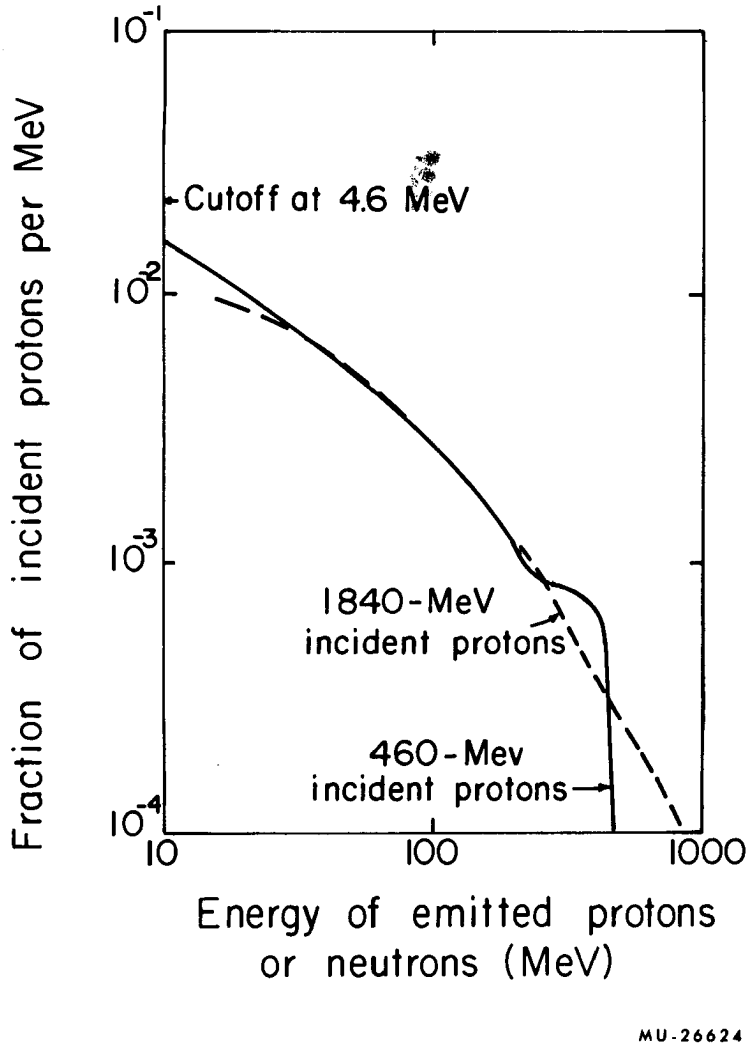

Fig. 4. Energy spectra of cascade nucleons emitted from aluminum, from Metropolis et al. [5]

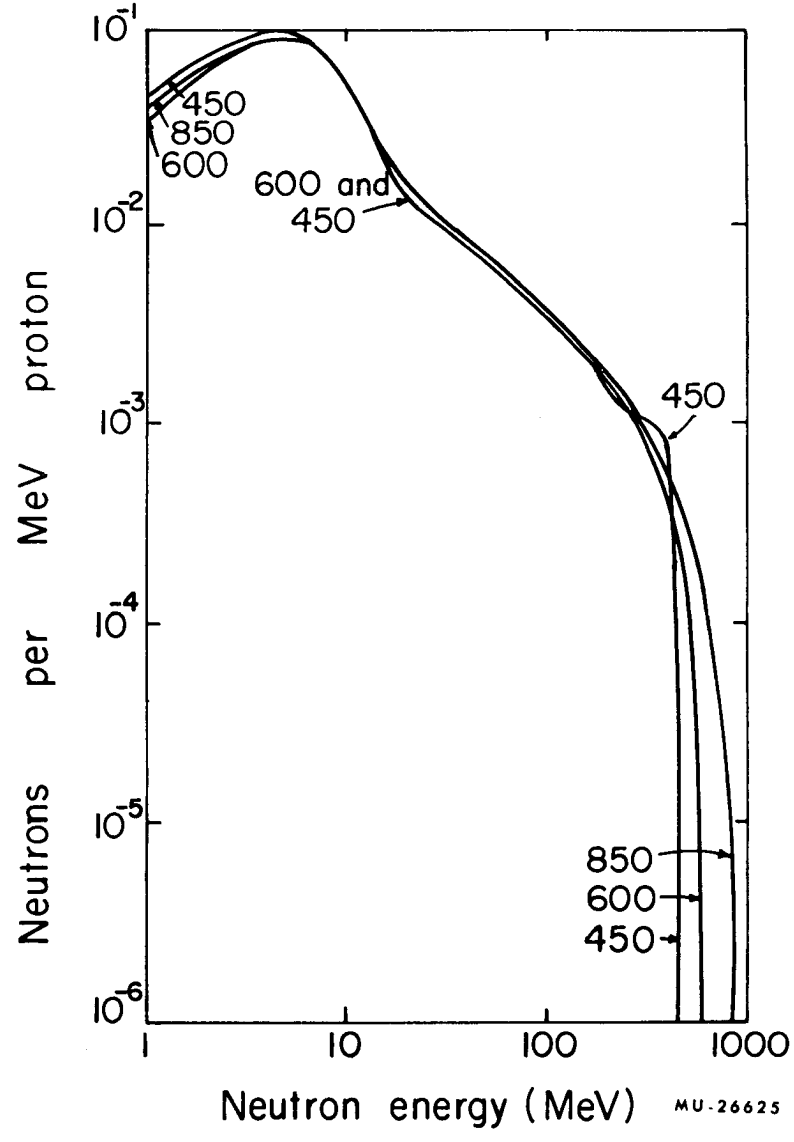

Fig. 5. Cascade and evaporation-neutron emission spectra from 450-, 600-, and 850-MeV protons on aluminum, per incident proton.

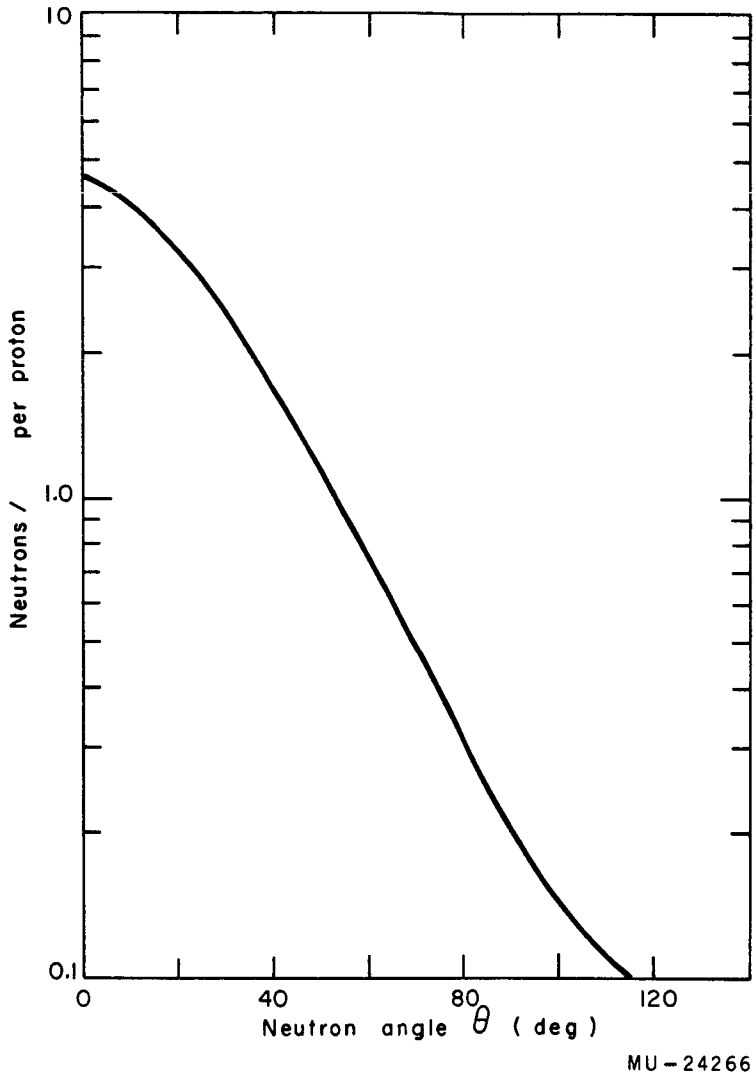

Fig. 6. Angular distribution of neutrons, over 150 MeV in energy, from a single collision in Cu by 6.3-GeV protons (normalized to 8 neutrons/proton), from Metropolis et al. [5]

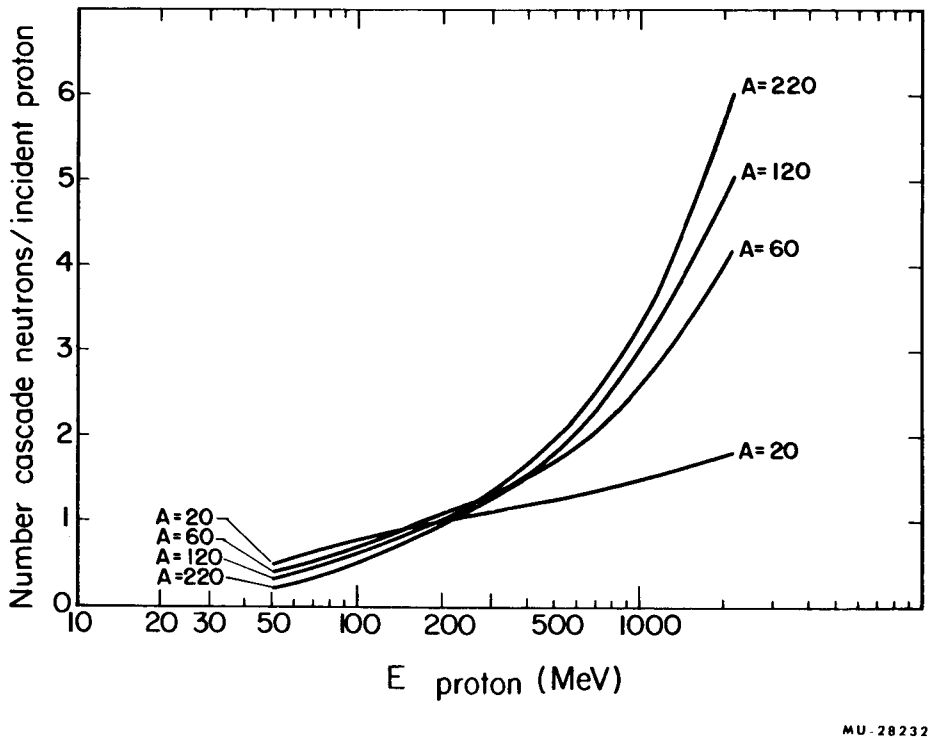

Fig. 7. Number of cascade neutrons per incident proton as a function of proton energy and target A, from Metropolis et al. [5]

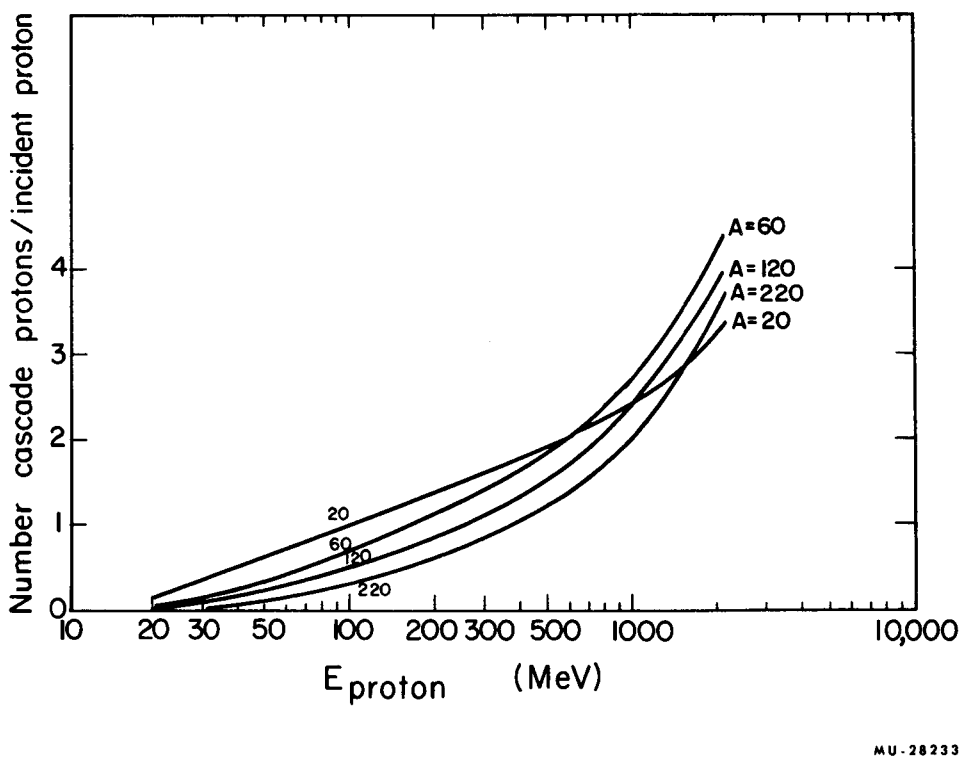

Fig. 8. Number of cascade protons per incident proton per inelastic collision as a function of proton energy and target A, from Metropolis et al. [5]

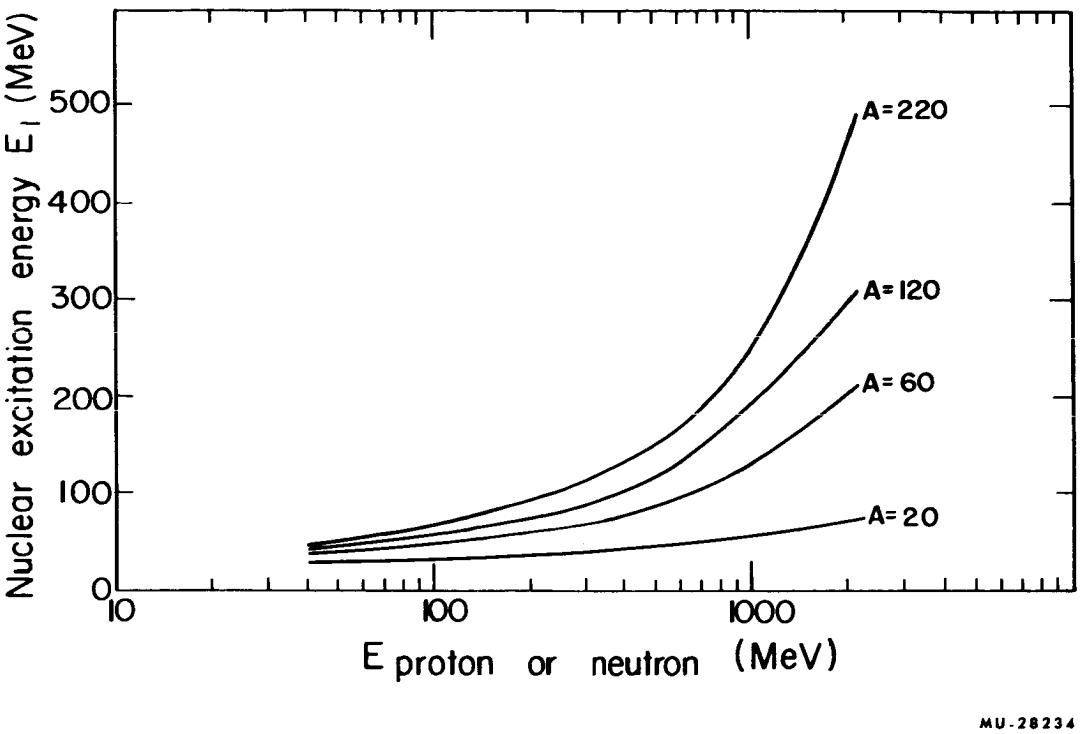

Fig. 9. Average nuclear excitation energy E_1 deposited in nucleus A by an incident neutron or proton of energy E in one inelastic collision.

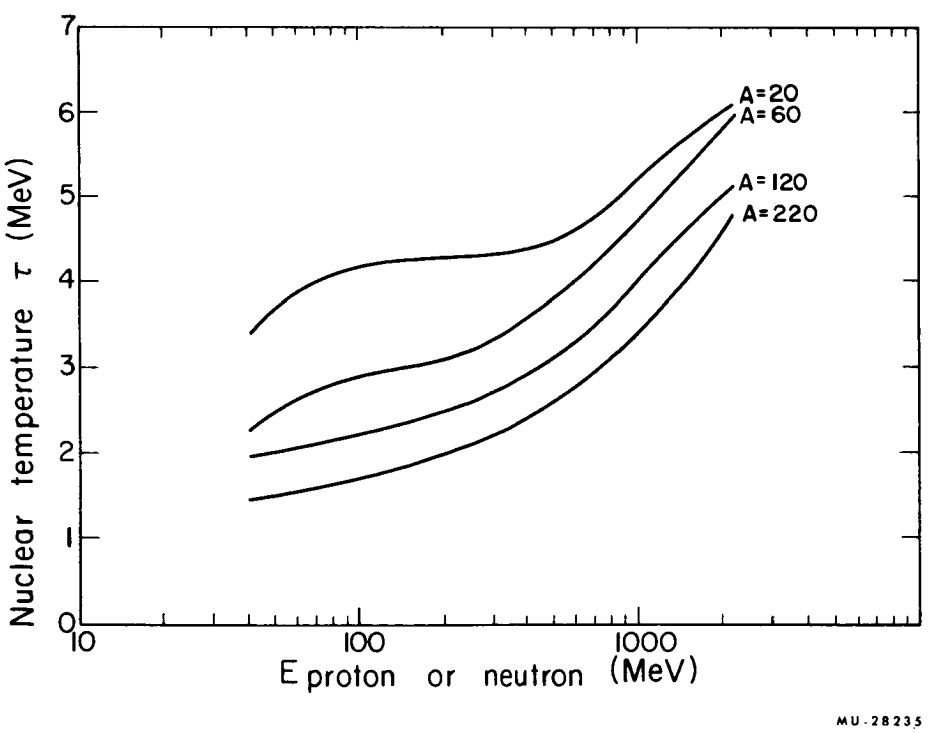

Fig. 10. Estimated residual nuclear temperature produced in nucleus A after excitation by a neutron or proton of energy E in one inelastic collision, from Metropolis et al. [5]

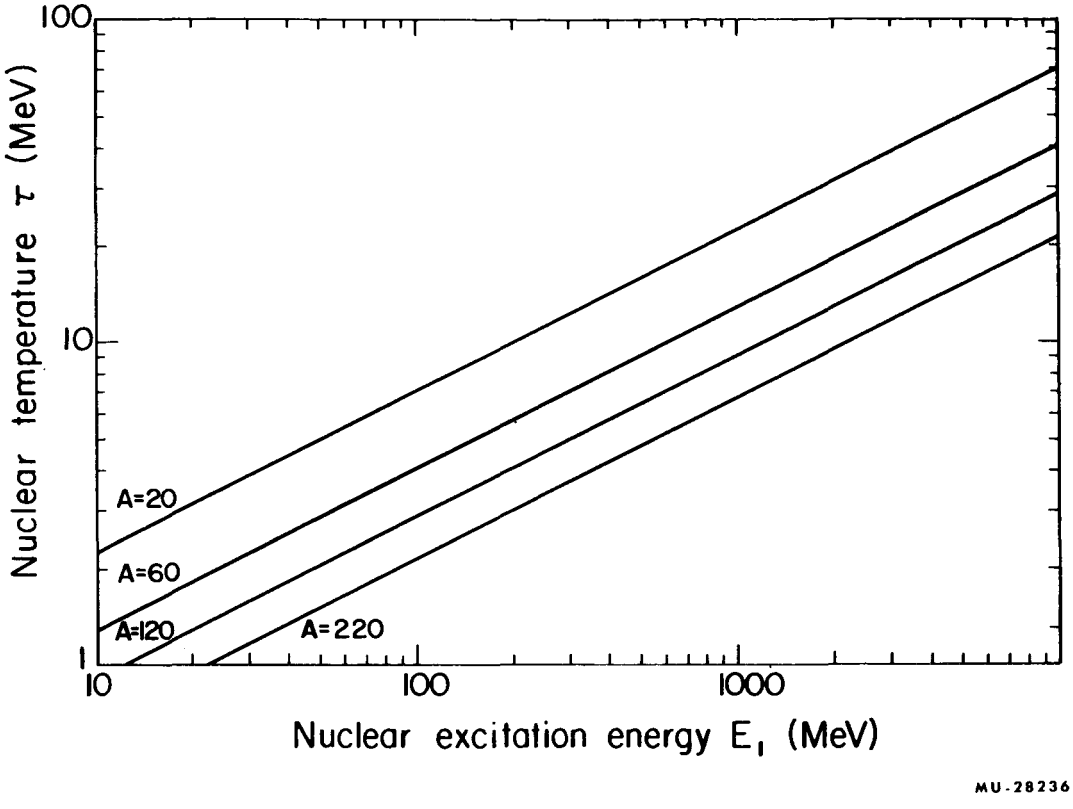

Fig. 11. Nuclear temperature τ vs nuclear excitation energy E_1 for various A's.

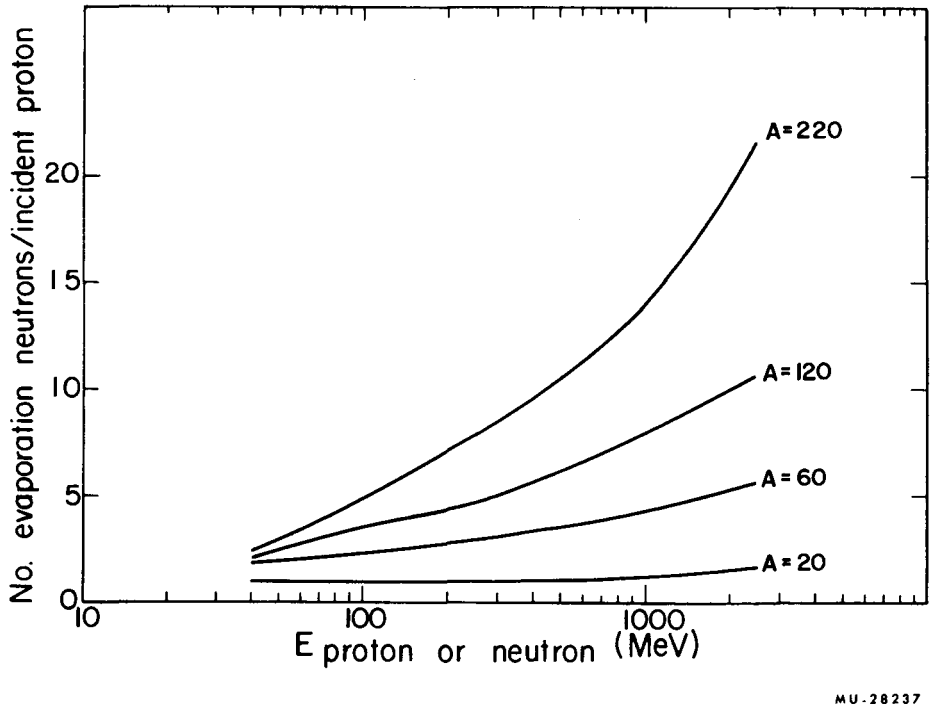

Fig. 12. Estimated number of evaporation neutrons produced per incident neutron or proton of energy E per inelastic collision, from Metropolis et al.

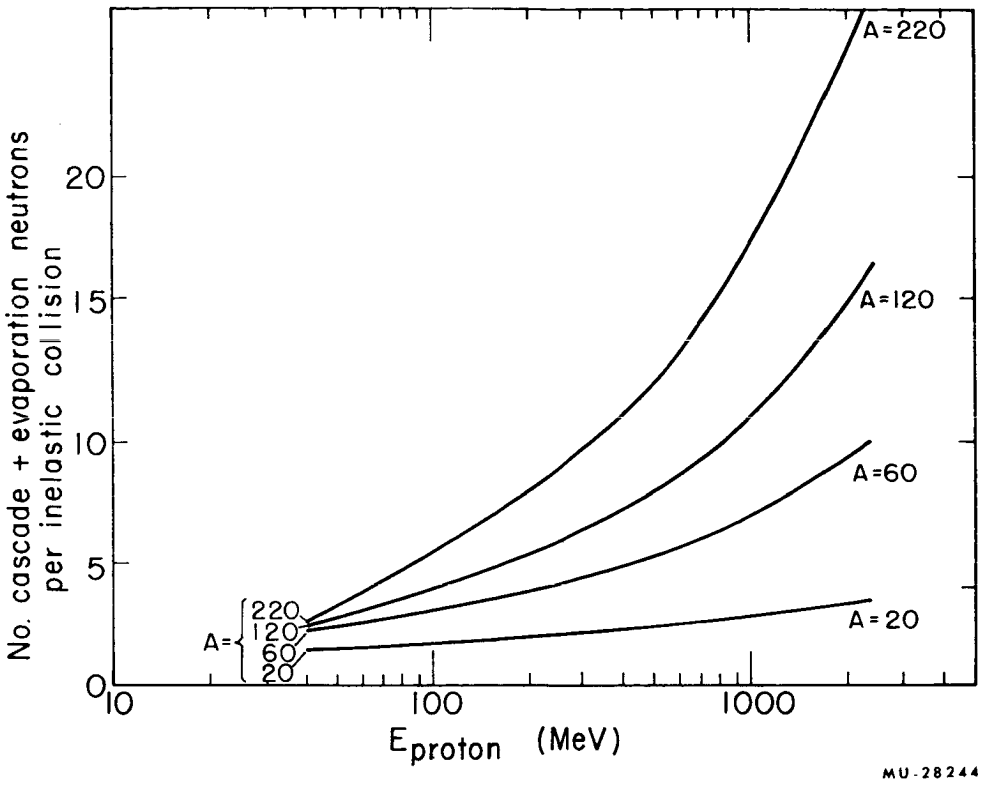

Fig. 13. Average number of evaporation protons per incident proton or neutron on various A's per inelastic collision vs energy of the incident particle, from Metropolis et al.

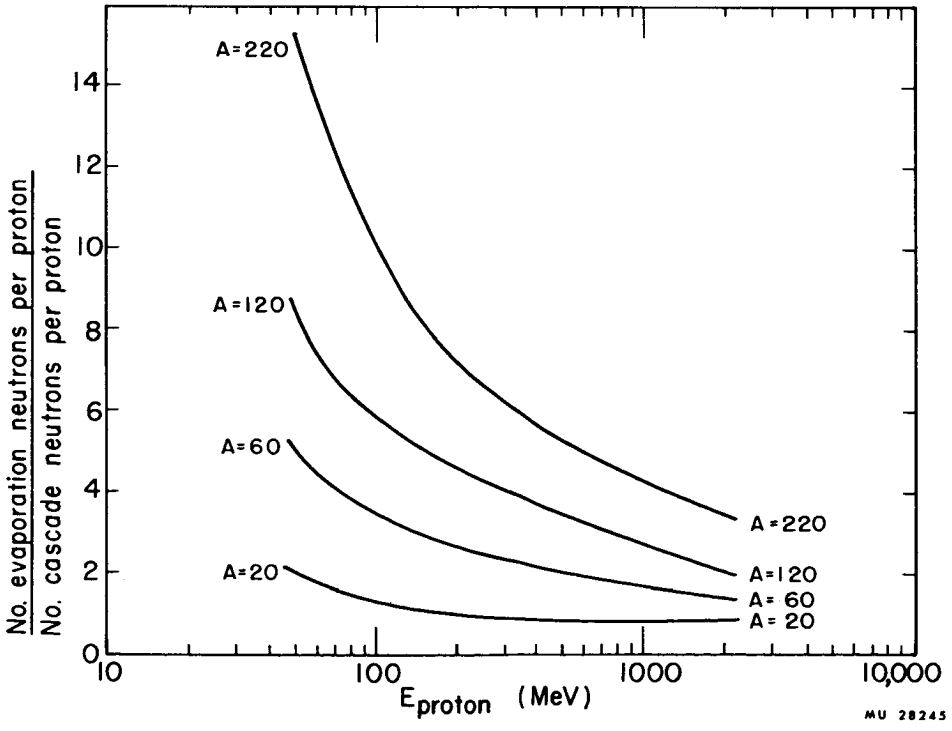

Fig. 14. Average number of evaporation H^2 per incident proton or neutron on various A's per inelastic collision vs energy of the incident particle, from Metropolis et al.

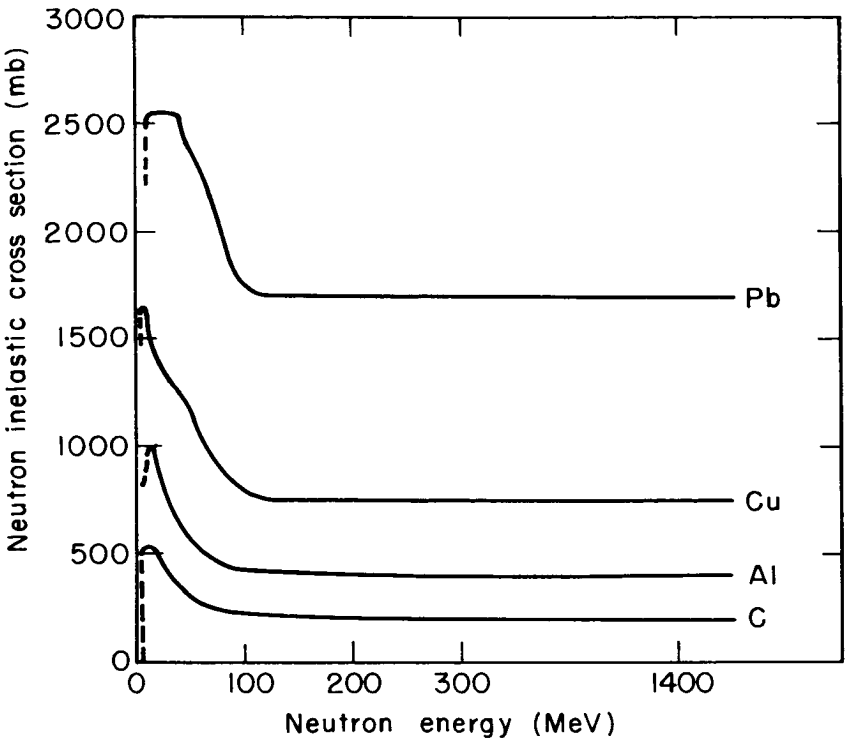

Fig. 15. Average number of evaporation H^3 per incident proton or neutron on various $\overline{A's}$ per inelastic collision vs energy of the incident particle, from Metropolis et al.

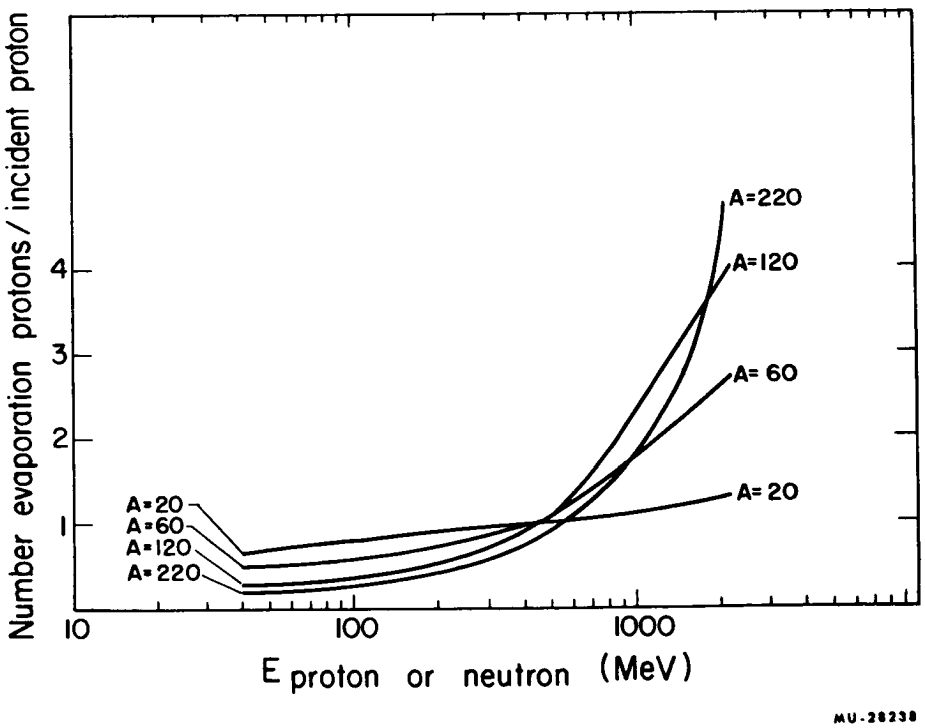

Fig. 16. Average number of evaporation He^3 per incident proton or neutron on various $\overline{A's}$ per inelastic collision vs energy of the incident particle, from Metropolis et al.

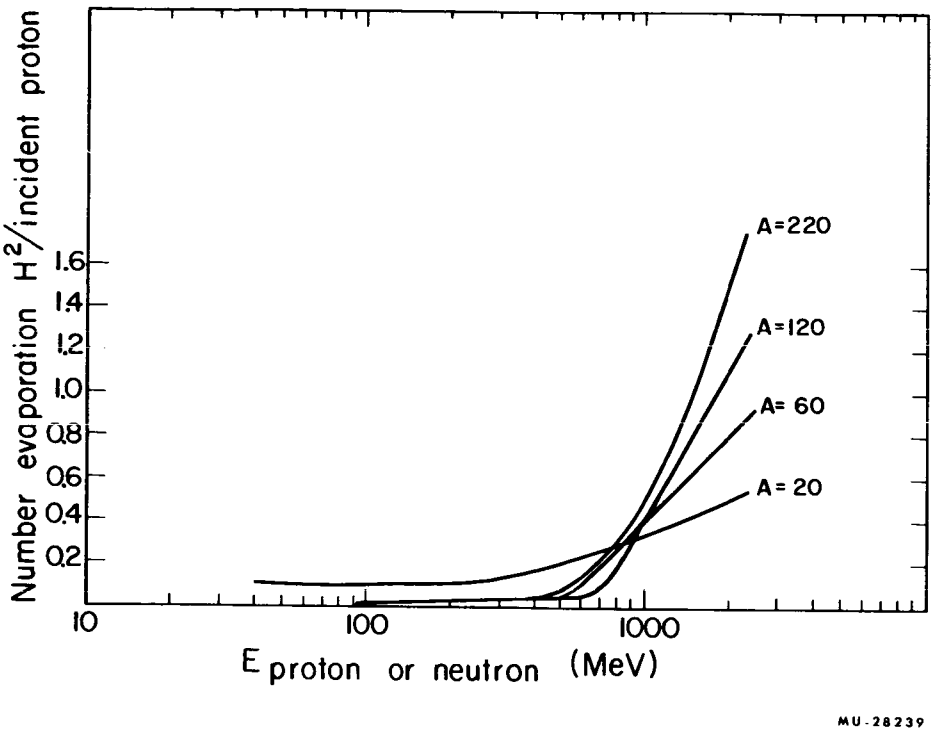

Fig. 17. Average number of evaporation He^4 per incident proton or neutron on various A's per inelastic collision vs energy of the incident particle, from Metropolis et al.

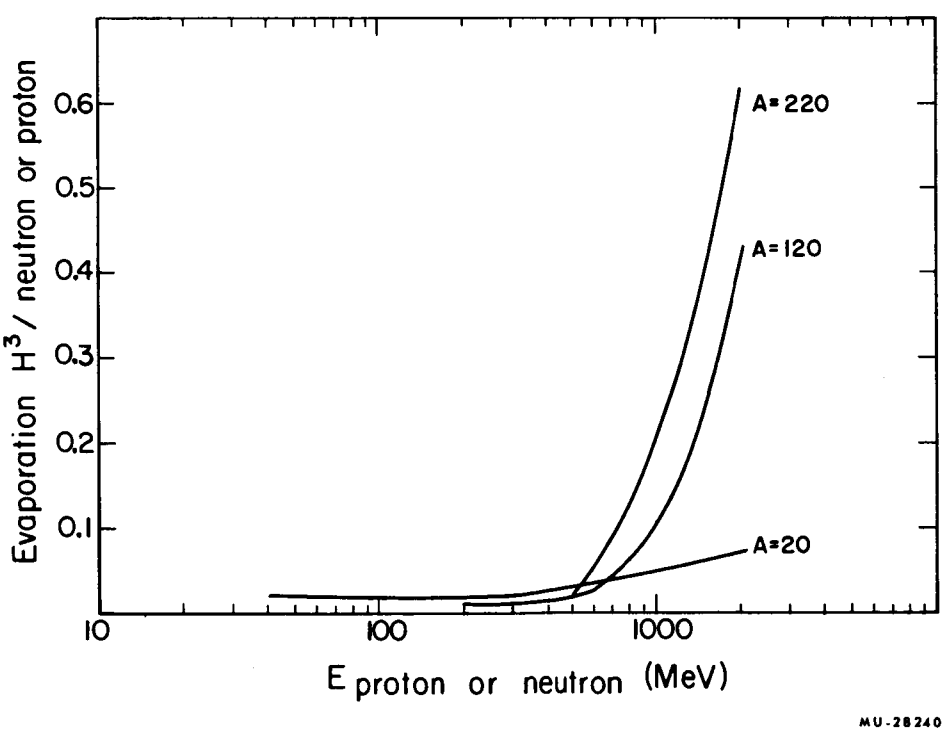

Fig. 18. Neutron inelastic cross-sections for C, Al, Cu, and Pb vs incident neutron energy, from Lindenbaum. [12]

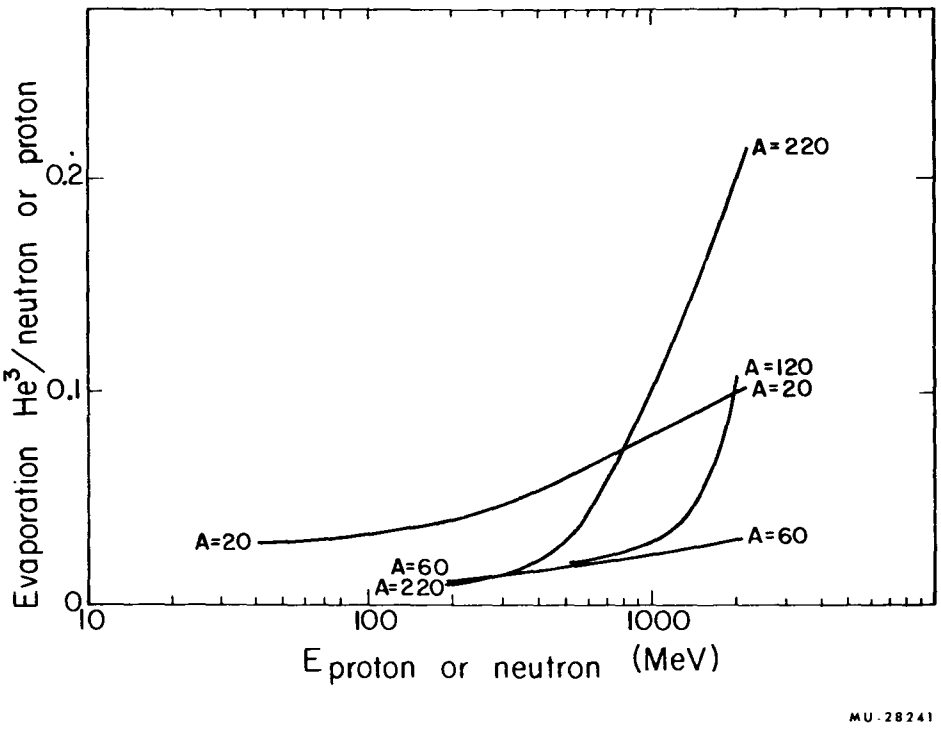

Fig. 19. Attenuation of neutrons in ordinary concrete. At 90 and 270 MeV, measurements were made at the 184-Inch 340-MeV cyclotron. At 4.5 GeV the measurement was made at the Bevatron.

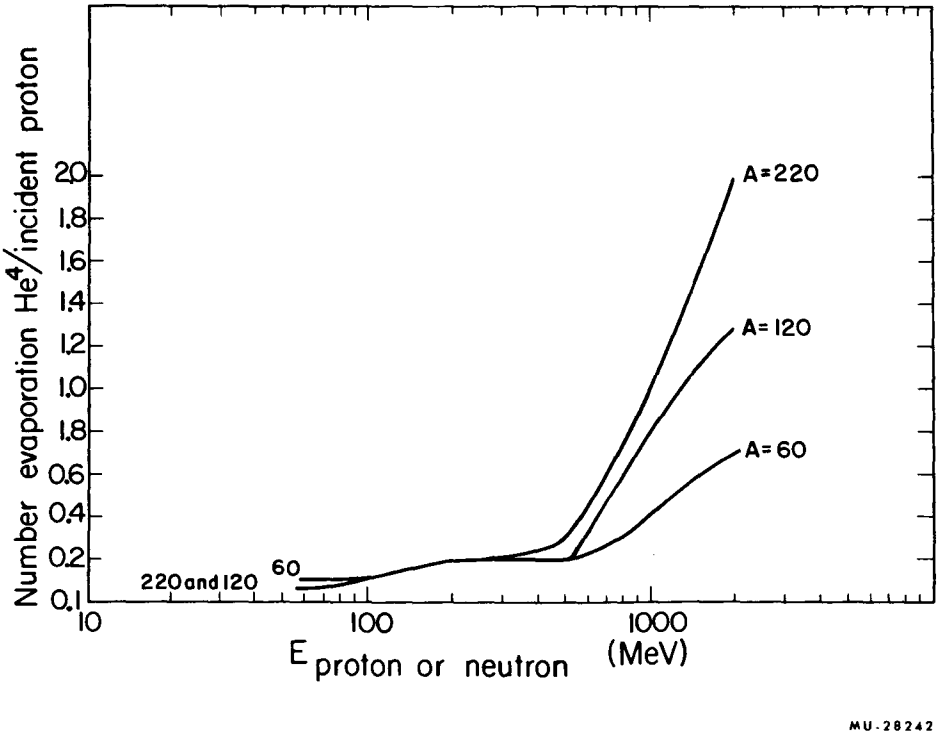

Fig. 20. Total neutron production per inelastic collision = cascade + evaporation as a function of the incident proton energy.

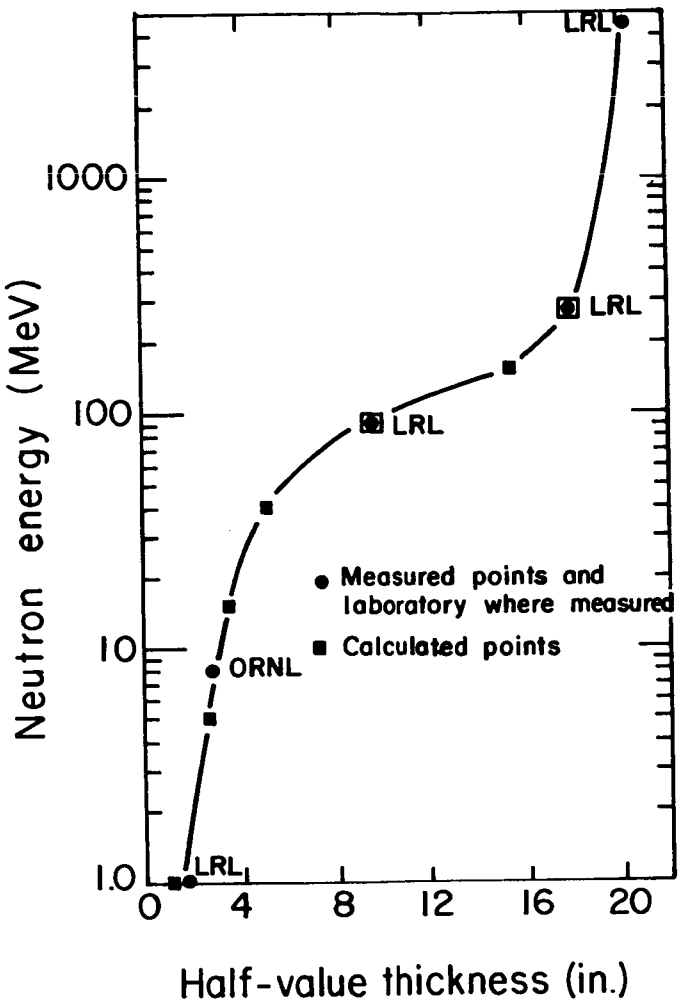

Fig. 21. Ratio of evaporation neutrons to cascade neutrons per inelastic collision as a function of the incident proton energy.

Paper F-5

SOME EXPERIMENTS ON THE PASSAGE OF HIGH-ENERGY PROTONS IN DENSE MATTER

S. P. Shen

Department of Physics, New York University
University Heights, New York, New York

Abstract

1515?

A series of experiments designed to study the nuclear cascade resulting from the passage of 1 to 3 GeV protons in matter has been in progress at the Brookhaven Cosmotron. Preliminary results on the fluxes of fast neutrons (upper limits) and of strongly-interacting particles above 50 MeV are summarized here (Fig. 1 and Table 1). The four cases studied are: 1-GeV protons on Fe, on chondritic material, and on $C_5H_8O_2$, and 3-GeV protons on Fe.

I. Introduction

The passage in matter of low-energy radiation up to about 0.1 GeV (1 GeV = 10^9 eV) has been studied almost throughout the history of nuclear physics.[1] The passage in matter of particles of extremely high energy (above 100 GeV) has been studied in recent years in connection with Auger showers in the atmosphere and "jet" showers in nuclear emulsions.[2] In the intermediate region, viz., from about 0.1 to 100 GeV (hereafter referred to as the "high-energy" region), interest has been less pronounced although considerable data do exist for the case of average cosmic rays passing through the atmosphere.[3] Recently, interest in this energy range has been given renewed impetus by three superficially distinct but basically identical problems: (1) depth variation of nuclide production by cosmic rays in the atmoshpere, in meteorites, and in other astonomical objects, (2) depth dosimetry of high-

energy particles in tissue and in other absorbers, and (3) shielding of energetic particles in space and of the radiation emerging from particle accelerators.

The passage of high-energy protons differs from that of protons of lower energy mainly in that the former survive far enough in the absorber for inelastic nuclear interactions to take place. These interactions give rise to secondaries, and often to a succession of secondaries constituting what is known as a nuclear cascade. Thus, the study of the passage of high-energy protons consists largely in the study of the accompanying nuclear cascade. The nuclear cascade has been reviewed and discussed from the shielding standpoint elsewhere.[4]

Here, we will summarize briefly for this symposium several recent experiments on the passage in dense matter of monoenergetic protons of 1 and 3 GeV. The use of a narrow beam of artificially accelerated protons in these experiments made possible the study of their passage under well-defined conditions not available in cosmic-ray experiments. The reader should also refer to the nuclide-production experiments of Fireman and Zaehringer,[5] Goel, Rayudu, and Shedlovsky,[6] Shedlovsky,[7] and Honda,[8] to the shielding experiments of Tinlot,[9] and Citron, Hoffmann and Passow,[10] and those reviewed by Lindenbaum,[11] as well as to the dosimetric experiments of Shal'nov[12] and Sondhaus.[13] Some of the questions dealt with here are discussed in greater detail from the shielding standpoint in a forthcoming review article.[14]

II. Nuclear-Cascade Studies at the Cosmotron

A series of joint irradiations at the external beam of the Brookhaven Cosmotron involving several institutions was initiated in the fall of 1961. Since then, four irradiations have taken place. This section briefly summarizes some preliminary results on the nuclear-cascade experiments undertaken during these irradiations. Full details and discussions of these experiments will appear elsewhere.

In all these experiments, the basic arrangement has been the same. A narrow (< 3 cm^2 area) and nearly parallel beam of 1 or 3 GeV protons impinges perpendicularly on the center of the face (usually 1 ft by 1 ft) of a thick absorber

made of either iron, chondritic material,* or $C_5H_8O_2$ ("Plexiglas").

At various depths of interest inside the absorber are "sandwiched" very thin Al foils (usually 1 ft by 1 ft by 0.0025 g/cm^2 thick), with their flat faces normal to the beam direction. After the irradiation, which varies from 10 to 90 min in duration, the Al foils are removed, and the F^{18} and Na^{24} activities induced in each foil counted, without chemistry, by means of calibrated counters. F^{18} and Na^{24} can be produced in Al by the following reactions:

$$Al^{27}(N, X)\ F^{18},$$

$$Al^{27}(N, X)\ Na^{24},$$

and $$Al^{27}(n, \text{alpha})\ Na^{24},$$

where N stands for strongly-interacting particles (nucleons and charged pions) exceeding about 50 MeV, n stands for neutrons below 50 MeV, and X for the particles emerging from the reactions. From the measured F^{18} activity, one can deduce roughly the flux of N, which in turn allows the flux of n to be found, again roughly, from the measured Na^{24} activity. Henceforth, the symbols N will stand for the flux of strongly-interacting particles exceeding about 50 MeV, and n for the flux of fast neutrons between about 7 and 20 MeV. This method of measuring separately N and n when both types are present is described together with its variations and present limitations in detail elsewhere. Although at present the results obtained in this way are only approximate, it is felt that they are nevertheless of some interest in view of the current lack of data on the nuclear cascade.

Figure 1 ("intensity-depth curves") shows the smoothed variation of N and n with depth in the absorber for the four

---

* Material whose composition closely simulates that of chondrites, a common type of stone meteorite. Chief constituents are roughly, by weight: 35% O; 25% Fe; 20% Si; 15% Mg. The Moon is probably chondritic. We are indebted to Dr. J. P. Shedlovsky and his colleagues for providing the chondritic absorber and for permitting us to conduct our experiment in it in conjunction with theirs.

cases studied. The fours cases and the total thickness (T_o) of each absorber are listed, respectively, in the first and second columns of Table 1. Since, for each case we also made measurements (not shown here) of the lateral spread of the cascade at several depths, it has been possible to correct for the loss of particles through the sides of the absorber at great depths. This correction has already been made for the curves in Fig. 1, so that these in effect represent the integral N or n (the integration being taken over an infinite plane normal to the beam) found at various depths in an absorber of the specified total thickness but of infinite lateral extension.

Note that the ordinate in Fig. 1 is logarithmic, and is expressed in units of particles per incident primary proton. The F^{18} and Na^{24} counting rates are such that the statistical counting error is almost always negligible. For the N-curves, we estimate that the absolute values given by the ordinate have an overall error not exceeding 25%. On the other hand, the relative heights of points within each N-curve are subject to a much smaller error. The absolute values given for the n-curves should be regarded as upper limits; this is not because such neutrons were not detected (they were), but because we have chosen to use, in these preliminary results, a weighted average cross-section for Al^{27} (n, alpha) Na^{24} that we know to be too low for our cases and therefore very "safe". Thus, the four n-curves are too high by about the same factor. Note, however, that even these upper limits are interestingly low for chondrite and $C_5H_8O_2$. The relative heights within each n-curve should be quite accurate for depths greater than the maximum in the curve; for smaller depths, the relative heights may be altered slightly when the upper limits are later converted to actual values. Each curve in Fig. 1 represents the average behavior of the individual cascades induced by at least 8×10^{12} incident protons, and in one case by as many as 8×10^{13} protons. The total number of incident primaries for the 3-GeV bombardment of Fe is still somewhat uncertain at this writing; for this case, therefore, the ordinate gives upper limits for both N and n.

III. Parameters of the Intensity-Depth Curves

We now consider the intensity-depth curve in general, intorduce some parameters for specifying its more salient features, and finally use these parameters to specify the curves in Fig. 1.

Suppose an idealized detector detects the flux (or ionization, or energy deposition, etc.) of some arbitrarily chosen component (e.g., 7-MeV gamma rays; protons above 14 MeV) at every depth inside a dense absorber bombarded by high-energy protons. Consider the function

$$f_{det}(x, T_o),$$

where f, for the moment, stands for the flux, the subscript "det" stands for the detected component (so that f_{det} is the flux of the detected component), the variable x is the depth in the absorber, and T_o the fixed total thickness of the absorber. Now, in analogy with the curves shown in Fig. 1, one would expect the function $f_{det}(x, T_o)$ to assume the general shape shown by the curve so labelled in Fig. 2.

There is however, no need to restrict ourselves to the flux. Henceforth, let the symbol f stand for either flux, or energy deposition, or RBE dose, etc. (each of these quantities of course is ultimately some function of the flux of the component in question). One would expect that $f_{det}(x, T_o)$, even in this larger sense, would still take on the general shape of the curve so labelled in Fig. 2.* The dashed straight line labelled $f_{prim}(x)$ represents f due to the primaries alone. The detected component of course may or may not include the primaries.

It is convenient to regard the intensity-depth curve $f_{det}(x, T_o)$ as composed of four regions (see Fig. 2): pre-maximum, approach (to equilibrium), equilibrium, and exit.

---

* The exact shape of $f_{det}(x, T_o)$ of course depends on the functional form of f. In addition, Sondhaus[13] has observed, superposed on the nuclear cascade, the effect of the small fraction ($< 10\%$ for 730-MeV primaries) of electromagnetically-stopped primaries.[4] On the other hand, no effect due to electromagnetically-stopped primaries is obvious in the nuclide-production curves of Goel, Rayudu, and Shedlovsky[6] at 440 MeV, where such stopped primaries should account for some 20% of the incident beam. This is understandable, since one would expect the stopped primaries to show themselves in a much more pronounced manner when the total ionization is measured, as in Sondhaus' case, than when some quantity directly related to the flux is measured, as in the case of Goel et al.

The pre-maximum region may not exist if the detected component includes the primaries themselves. The equilibrium region may not be strictly reached in some cases save at very great depths where the radiation is no longer detectable.

Imagine now our finite absorber to be indefinitely extended in both the front and rear directions (i.e., the absorber is now infinitely long), then the intensity-depth curve would no longer have the shape of $f_{det}(x, T_o)$, but would instead assume the shape of a straight line identical or parallel (depending on the primary flux) to the line labelled $f_{det}(x,\infty)$. The deviation of the actual intensity-depth curve $f_{det}(x, T_o)$ from this straight line except in the equilibrium region can be thought of as due to the "missing" front and rear parts of the absorber. Thus, the "missing" front part fails to supply the forward-moving particles that would fill the area between $f_{det}(x,\infty)$ and $f_{det}(x, T_o)$ near the front; similarly, the "missing" rear part of the absorber fails to supply the backward-moving (albedo*) particles that would fill the corresponding area in the exit region. This deviation, in shape, of $f_{det}(x, T_o)$ from $f_{det}(x,\infty)$ is called the transition effect, a term used here in a more extended sense than usual. One may say that the pre-maximum and approach regions together constitute the entrance transition, and the exit region constitutes the exit transition.

If, instead of the fixed thickness T_o, we were to use an absorber of variable thickness T and detect the chosen component behind the absorber, then the "intensity-thickness" curve $f_{det}(T)$ should be expected to assume the general shape of the curve so labelled in Fig. 2. Obviously, the intensity-thickness curve can be derived from the intensity -depth curve $f_{det}(x, T_o)$ by subtracting from the latter the appropriate albedo flux at every depth x (except in the exit region, where part of the albedo is already absent). No attempt is made here to derive the intensity-thickness curves in this way from the empirical intensity-depth curves shown in Fig. 1, although this should be achievable provided one has a rough

---

* The backward-moving or albedo particles come from the backward moving secondaries emerging from the inelastic nuclear interactions. The flux of albedo particles for a given detected component is of course different for different depths x.

idea of the albedo flux as a function of depth, e.g., from the calculations in progress[15] at Oak Ridge.**

Quantities of interest in Fig. 2 are:

(a) Attenuation mean free path λ_{att}: it is customary to fit regions more or less below the transition maximum with a single exponential with exponent x/λ_{att}. Sometimes the approach region takes on a straight-line appearance only because the experimental points are few and far apart;

(b) Location of the transition maximum or "optimum depth" (term borrowed from electron-photon cascade theory): x_{max};

(c) Surface albedo per primary, defined as $f_{det}(0, T_o) - f_{prim}(0)$ if the detected component includes the primaries, or $f_{det}(0, T_o)$ if the detected component does not include the primaries;

(d) "Maximum-to-surface" ratio: $f_{det}(x_{max}, T_o)/f_{det}(0, T_o)$;

(e) "Maximum-to-primary" ratio: $f_{det}(x_{max}, T_o)/f_{prim}(0)$;

(f) Build-up factor:[17] $f_{det}(x, T_o)/f_{prim}(x)$;

** Even from the shielding standpoint, it is not certain that intensity-thickness curves are indispensable. For even when one knows in detail the radiation emerging from behind a shield, one will still be confronted with the problem of depth dosimetry of this complicated radiation. It seems that the ultimate day-to-day handling of the space-radiation shielding problem must rely on estimates based on calculations in which the shield, tissue, and even the air in between could be treated as a continuous absorber. At present, nuclear-cascade calculations have few empirical data with which to compare results. If the purpose of cascade calculations is (from the space radiation shielding standpoint) to check the validity of cascade calculations, then comparison of intensity-depth curves alone would probably suffice. From the standpoint of the physics of the nuclear cascade also, $f_{det}(T)$ is as a rule neither more nor less interesting than $f_{det}(x, T_o)$, provided T_o is not too small. On the other hand, intensity-thickness curves can be measured in far greater detail and with far more elaborate detectors[16] than intensity-depth curves.

(g) $f_{det}(x, T_o)/f_{det}(0, T_o)$;

(h) $f_{det}(x, T_o)/f_{prim}(0)$;

(i) "Critical" depth x_c, defined such that $f_{det}(x_c, T_o)/f_{prim}(0) = 1$ and $x_c \neq 0$.

Quantities (h) and (i) are of particular interest to shielding and dosimetry of high-energy particles. Thus, if f stands for the total RBE dose, then, for monoenergetic primaries, any shield thinner than x_c would be meaningless and in fact harmful.

Table 1 lists the values of some of the above parameters for the intensity-depth curves of Fig. 1. N and n have the same meansings as before. Note that, in Table 1, f stands for the flux, and not for some function of the flux. An attenuation mean free path has been arbitrarily fitted even to cases where much of the decrease is obviously not exponential. The $C_5H_8O_2$ curves in Fig. 1 are examples of the exit region merging into the pre-maximum region, resulting in an apparent maximum which is not the transition maximum of Fig. 2. In such cases, the "maximum" in Table 1 refers to this apparent maximum. Upper limits are indicated by an asterisk.

IV. Remarks

We will not here enter into any detailed discussion of the results shown in Fig. 1 and Table 1 beyond noting the following points of interest to high-energy shielding and dosimetry:

(a) The variation, with primary energy and with absorber mass number, of the quantities listed in Table 1 is generally in qualitative agreement with even the crudest of cascade theories, such as the energy-independent one based on the work of Martin.[18, 4] Quantitative comparison with detailed calculations based on transport theory is not yet feasible at present.

(b) The value of x_c and the apparent λ_{att} ($\gtrsim 110$ g/cm^2) (see Fig. 1) of the N-curve for chondritic material suggest that chondrites are poorer cosmic-ray shields than sometimes assumed. Bearing in mind that there are many cosmic rays above 1 GeV and that meteorites

are bombarded isotropically (both facts tend to make shielding far less effective than shown in Fig. 1), the result in Fig. 1 further reduces the possibility that shielding might explain the abnormally low Ne^{21} and Al^{26} contents of the two chondrites recently discussed by Anders.[19] It also makes less puzzling the nearly constant Al^{26} content of most chondrite specimens examined,[20, 21] and sets a lower limit on the pre-atmospheric mass of those chondrites whose various specimens do show dissimilar Al^{26} contents.[20]

(c) The components measured in these experiments, viz., N and n, are suitable bases for dose estimates. The quantity $N(x, T_o)$ is, in effect, the backbone of the nuclear cascade. From it, one can readily obtain the rate of inelastic nuclear interactions in the absorber material itself or in some other material (e.g., emulsion, tissue). From the interaction rate, one could then estimate as a function of depth the dose due to the interactions, including local absorption of the recoil nuclei and light fragments (e.g., He, Li, Be, B). Furthermore, adopting a fast-neutron spectral shape,[22] one can extrapolate the values of n (7 to 20 MeV) to include the flux in the dosimetrically-interesting range of, say, 1 to 30 MeV. One can then calculate, as a function of depth, the dose and RBE dose due to the fast neutrons by using the usual flux-to-dose factors.

(d) Despite the hydrogen deficiency of $C_5H_8O_2$ as compared to tissue ($C_5H_{40}O_{18}N$), the N and n measured here should be roughly valid for a true tissue absorber. This is because hydrogen deficiency should not seriously affect the development of the higher-energy components of the cascade, including fast neutrons; rather it would affect mainly the slow-neutron flux and the fast-neutron energy deposition, neither of which is directly measured here. Of course, when one now tries to calculate the fast-neutron dose in tissue from the measured n, the correct tissue composition should be used (i.e., use the usual flux-to-dose factors for tissue).

(e) The $C_5H_8O_2$ curve in Fig. 1 gives 0.12 as the maximum number of 7 to 20 MeV neutrons (per primary) emerging from the 30 g/cm^2 (10-inch) thick slab bombarded by 1-GeV protons. The maximum number of slow neutrons below 2 eV emerging from this slab was also measured, but data reduction is still incomplete at this writing. This

type of information is of some interest to the interpretation of measurements of fast cosmic-ray neutrons in the atmosphere and in space using BF_3 counters surrounded by a hydrocarbon moderator.[23]

---

1. See, e.g., H. A. Bethe and J. Ashkin, "Passage of Radiations Through Matter," Experimental Nuclear Physics, edited by E. Segre, Vol. 1, p. 166, John Wiley & Sons, New York, 1953.

2. See, e.g., papers in J. Phys. Soc. Japan 17, Suppl. A-III (1962) (Proc. Int'l. Cosmic-Ray Conf.).

3. See, e.g., R. K. Soberman, Phys. Rev. 102, 1399 (1956); W. N. Hess, H. W. Patterson, R. Wallace, and E. L. Chupp, Phys. Rev. 116, 445 (1959).

4. S. P. Shen, Aerospace Med. 32, 901 (1961); Astronautica Acta 8, 228 (1962).

5. E. L. Fireman and J. Zaehringer, Phys. Rev. 107, 1695 (1957).

6. P. S. Goel, G. V. S. Rayudu, and J. P. Shedlovsky, Progress Report (Nuclear Chemistry) Dept. of Chemistry, Carnegie Institute of Technology, Pittsburgh, Pa., 1959-60 (p. 38), 1960-61 (p. 74), 1961-62 (pp. 60, 67).

7. J. P. Shedlovsky (to be published).

8. M. Honda, J. Geophys. Research (to be published).

9. J. H. Tinlot, Brookhaven National Laboratory Internal Report 750 (T-276) (Mu-p No. 18) (1961).

10. A. Citron, L. Hoffmann, and C. Passow, Nucl. Instr. and Meth. 14, 97 (1961).

11. S. J. Lindenbaum, Annual Review of Nuclear Science 11, 213 (1961).

12. M. I. Shal'nov, Soviet J. Atomic Energy 4, 735 (1958).

13. C. A. Sondhaus, these Proceedings.

14. S. P. Shen, Astronautica Acta (to be published).

15. Papers by the Oak Ridge groups in these Proceedings.

16. F. C. Maienschein t al., these Proceedings.

17. B. J. Moyer, "Build-up Factors," Proceedings of the Conference on the Shielding of High-Energy Accelerators, TID-7545, p. 96 (1957).

18. G. R. Martin, Geochimica et Cosmochimica Acta 3, 288 (1953).

19. E. Anders, Science 138, 431 (1962), and references 1, 2 and 3 therein.

20. M. W. Rowe, "Quantitative Measurement of Gamma-Ray Emitting Radio nuclides in Meteorites," preprint, 1962.

21. S. P. Shen and G. R. Laurer, unpublished results of a gamma-spectrometric survey (in progress) of meteorite specimens in New York museums.

22. R. Wallace and C. A. Sondhaus, these Proceedings.

23. S. A. Korff and R. B. Mendell, private communication.

Acknowledgements

We wish to thank Professor S. A. Korff for his continued interest and hospitality. We are indebted to Drs. R. Davis, Jr., J. P. Shedlovsky, and R. W. Stoenner for their generous and invaluable help during these experiments, and to Dr. W. H. Moore and the Cosmotron staff for their cooperation. The joint irradiations were ably coordinated by Professor Shedlovsky, representing Carnegie Institute of Technology. The interest of Dr. F. W. Wendt is also much appreciated. This work was supported in part by the NASA, the AFOSR, and the Research Corporation.

Table I. Parameters of the Intensity-Depth Curves of Fig. 1.

	T_o (g/cm^2)	x_{max} (g/cm^2)		λ_{att} (g/cm^2)		"Max.-to-surface" ratio		"Max.-to primary" ratio		x_c (g/cm^2)		Surface albedo (particles per primary)	
		N	n	N	n	N	n	N	n	N	n	N	n
1-GeV on Fe	740	40	70	120	120	1.3	2.5*	1.3	-	120	-	0	0.3
1-GeV on chondrite	120	35	45	-	-	1.3	2.7*	1.3	-	85	-	.045	.089
1-GeV on $C_5H_8O_2$	30.4	22	22	-	-	1.25	4.10*	1.25	-	-	-	.027	.032
3-GeV on Fe	703	60	90	200	200	3	3*	6.8*	-	400*	-	0.8*	1*

*Upper limit.

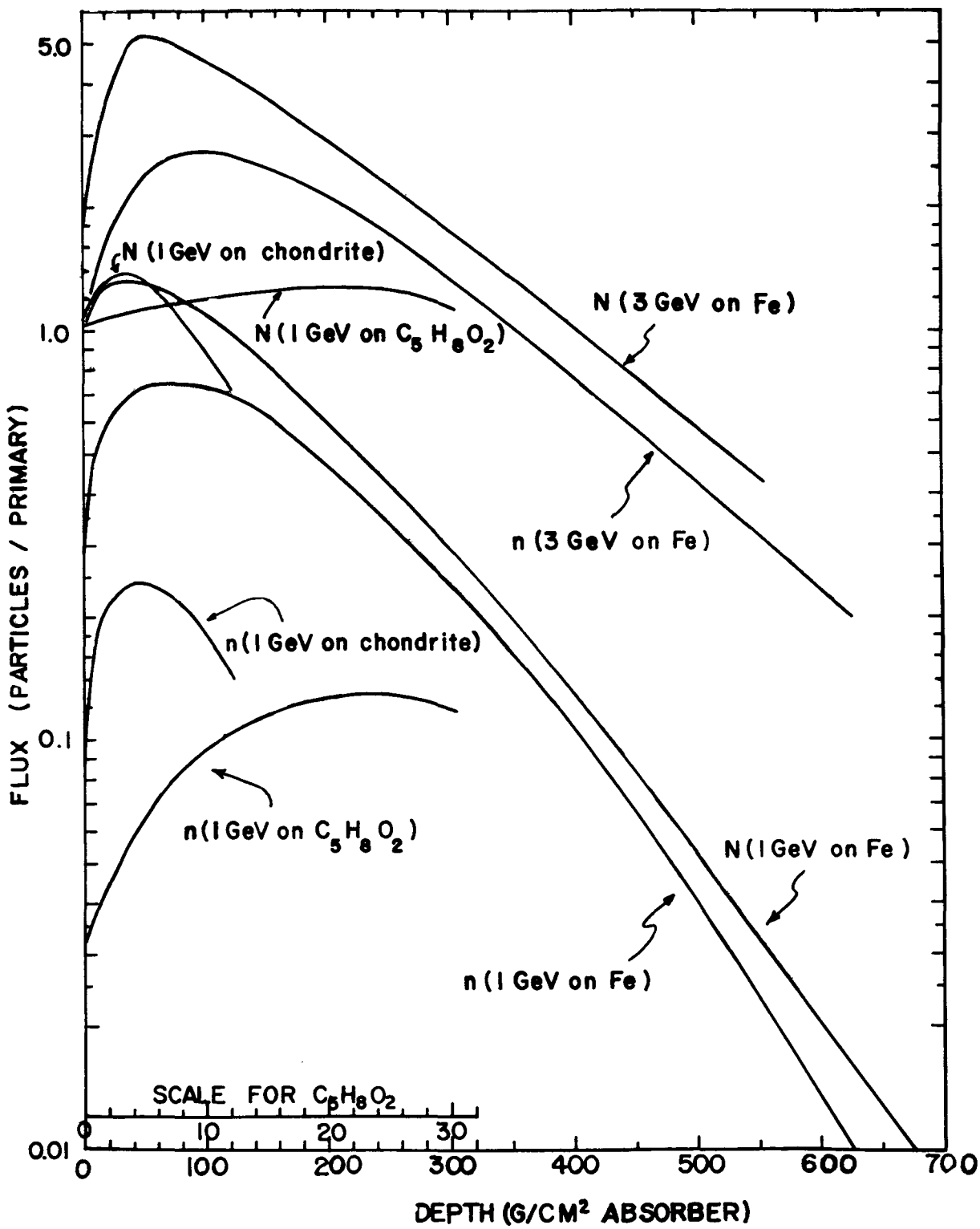

Fig. I Intensity - depth curves for N and n (n-curves are upper limits; see text). Note the expanded abscissa scale for $C_5H_8O_2$.

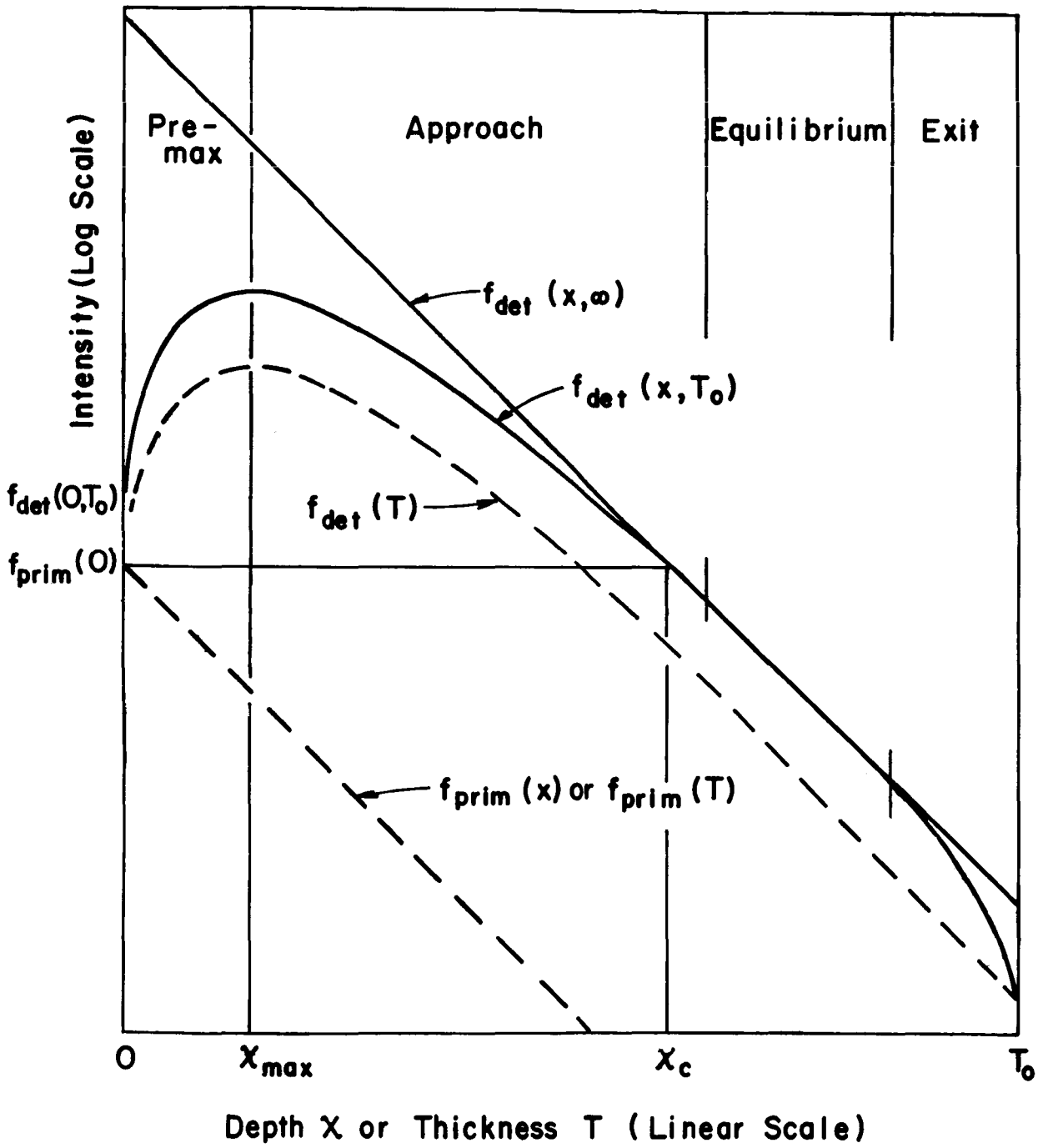

Fig. 2 Some idealized intensity - depth and intensity - thickness curves.

Paper F-6

THE BIOLOGICAL HAZARDS OF π AND μ MESONS

B.L. Murphy, P. Kitching and H.B. Knowles
Yale University

Abstract

The biological hazard of both kinds of π and μ mesons has been very roughly evaluated for the purpose of estimating shielding about a meson factory. Certain processes relative to the probable interactions of stopped mesons are discussed in detail because of their relevance to shielding against high energy proton fluxes. In particular, stopping π^- mesons appear to be of the order of ten times more dangerous than neutrons of the same energy, and the importance of this ratio is noted for the case of thin space shields. Techniques for an improved calculation of the hazard are considered.

Introduction

As the last paper of this conference, it seems appropriate to remark that a number of our ideas have been revised in the last three days. In addition, our results are no more than a very rough estimate of the personnel hazard induced by mesons necessitated by a particular problem. It is hoped that these results will be revised in the near future when a proper computer Monte Carlo calculation is made.

Our interest in this problem has been connected with the design of a 750 Mev proton linear accelerator with a very high beam intensity, specifically, 1 milliampere

average current of high energy protons with suitable targets and magnetic optical devices, we expect to produce meson beams of the intensities shown in Table I. Justification for these values is given in a recent design study status report.[1]

Table 1. Expected Meson Beams $\Delta p/p = 1\%$

Meson	Intensity (number/sec)
π^+	10^9
π^-	10^8
μ^+	$\sim 10^8$
μ^-	$\sim 10^7$

It will be noted that these beams are analyzed and thus have a relatively narrow energy spread. This is not the case with the pions produced by a white spectrum of protons such as might be found in the inner Van Allen belt. It should be remarked that most nuclear physicists have assumed that rather large intensities of high energy protons were to be found in many space environments; many of the papers presented here have presented evidence to the contrary, and it is therefore not certain how pertinent the behavior of mesons is to the space radiation hazard problem, however important it may be to the designers of a meson factory. However, the findings are presented in the hope that they will be re-examined and incorporated into calculations relating to problems of radiation hazard during passage through regions of intense high energy proton fluxes.

Electromagnetic Interaction of Mesons with Tissue

If the human body is taken to be 30 cm thick, mesons of all kinds with kinetic energies above approximately 100 Mev penetrate the body and behave much as do protons in energy loss by ionization. One significant difference should be indicated: π mesons have a mass about one-seventh, and μ mesons a mass about one-ninth that of a proton. As Dr. H. J. Schaefer pointed out in his very informative talk, the tissue dose from protons is not localized because so many high energy delta rays are produced and the energy loss is diffused by these. Because the mesons will in general, produce delta

rays of maximum energies nine and seven times those produced by protons, their ionization loss will result in an even more diffuse tissue dose. No account was taken of this effect in the calculations to be presented here; an early modification of this study will be the calculation of an L.E.T. spectrum of the sort that Dr. Schaefer presented.

Mesons stopping within the body also exhibit a different stopping power behavior from that of heavy charged particles. If compared to protons, directly, a pion has one seventh and a muon one-ninth the residual range as a proton of the same velocity. Thus, π^+ and μ^+ mesons should reproduce the L.E.T. vs range curve of the proton in miniature, including the recombination effects, known to set in at about 40 kilovolts proton kinetic energy. In the terminology of Dr. Schaefer, the "thin-down" region is reduced to 1/7 or 1/9. The negative particles do not recombine and therefore rise to a higher value of L.E.T. These effects are shown schematically in Figure 1, in which the proton Bragg curve is approximately compared to that of the four kinds of mesons and also to that for the alpha particle. The latter undergoes double recombination and therefore has a peak of ionization only about 2.5 times that of the proton, rather than the 4 times expected on the simple theory. Figure 1 thus indicates some of the peculiarities of mesons. If the abscissa is noted, one might infer that the mesons would be less dangerous than protons for cells of order of 5 to 10 microns diameter, and about equally dangerous for cells of the order of one micron, which is the size of the meson thin-down region. On the left hand vertical scale are plotted some rbe values recommended by the NCRP (as functions of L.E.T. only); it is seen that the rbe is even harder to evaluate in this case than is usual, because the stopping mesons differ from protons first, in that their delta rays are more energetic, second, in that the effect more critically depends on all size, and third, in that the negative mesons behave quite differently in the last fraction of a micron than do the positive mesons. We chose an rbe of 5 for stopping mesons on a very conservative basis.

Terminal Interactions of Mesons With Tissue

After depositing their kinetic energy in tissue and coming to rest, mesons also differ from other charged particles in that they proceed to deposit some significant fraction of their rest energy. The negative mesons again differ from the

positive mesons by undergoing capture by the Coulomb field of a nucleus. If we note that tissue is well represented by $C_7H_{70}O_{32}N_2$ [2] capture on hydrogen would appear to be common, but if this should occur the neutral mesic hydrogen atom undergoes a sufficient number of thermal collisions to cause mesons always to be captured in the stronger Coulomb potential of one of the heavier nuclei. Details of this process are not well known; it is possible that the proton receives some of the capture energy. Once the negative meson is in the 2s level of, for example, an oxygen atom, its optical transitions rate[3] is much smaller than its Auger transition, as shown in Table 2.[3] The latter is just large enough to permit the π^- to get to the 1S orbit before it decays.

Table 2 Lifetimes and Transition Probabilities For π^- and μ^- Mesons In Oxygen

	π^-	μ^-
Mean Life	2.5×10^{-8} sec.	2×10^{-6} sec
Transition Probabilities		
Optical		
$2s \longrightarrow 2p^*$	1×10^{4}/sec	2×10^{4}/sec
$2p \longrightarrow 1s$	5×10^{15}/sec	1×10^{15}/sec
Auger		
$2s \longrightarrow 1s$	1×10^{8}/sec	2×10^{9}/sec

* The 2s meson level lies slightly above the 2p level because of the penetrating s orbit together with the small meson-nucleus radius.

However, this particular meson interacts strongly with the nucleus and is always absorbed by it in about 10^{-18} sec. The μ^- in the 1s orbit interacts so weakly that it undergoes nuclear absorbtion in water only about 17 per cent of the time.[4] The positive mesons undergo normal decay processes, as shown in Table 3. The complicated capture products of π^- mesons were taken from the emulsion data of Van der haeghe and Demeur, using only the oxygen stars.

Table 3 Behavior of Stopped Mesons in Tissue

MESON	TERMINUS	PRODUCTS	COMMENT
μ^+	Decay	34 Mev e^+ (Avg.)	e^+ annihilation
μ^-	**Decay - 83%	34 Mev e^- (Avg.)	
	Capture - 17 %	2 to 3n,	Excited nucleus $\bar{E}_n$ = 20 Mev
π^+	Decay	4.14 Mev μ^+	μ^+ decays
π^-	**Capture	(a) C^{12*} + p+3n (68%)	$\bar{E}_\alpha$ = 7 Mev
(O^{16} only noted)		(b) 3 α + p+3n (17%)	$\bar{E}_p$ = 8 Mev
		(c) 2 α + 3p + 5n, etc.	$\bar{E}_n$ = 20 Mev

** Auger electrons also emitted

Calculation of Energy Deposition and Dose

The various processes indicated in Table 3 are evaluated on a very elementary basis. For energy deposition W' (Mev/cm) we write

$$D(\text{rads/particle/cm}^2) = \frac{1.6\ 10^{-6}\ \text{ergs/mev}}{100\ \text{ergs/g-rad} \times 19/\text{cm}^3}\ W'\ (\text{Mev/cm})$$

and approximate W' by

$$W' = \frac{W\ (\text{total Mev deposited})}{30\ \text{cm}}$$

The latter equation is extremely crude and is particularly inaccurate when the energy of the mesons lost to range is considered for the worst case (π^-) the error is of less significance, as will be shown. We can thus calculate the energy deposition in rads per hour per unit flux as a function of incident meson kinetic energy as shown in Figure 2.

(a) energy loss by ionization
(b) electrons from $\mu^\pm$ decay
(c) neutrons from μ^- capture

(d) muons from π^+ decay
(e) neutrons from π^- capture
(f) protons from π^- capture
(g) alpha particles plus heavy fragments from π capture.

These are now to be evaluated by use of an rbe and added for each process. We have elected the NCRP values of rbe because we are dealing with chronic exposures, although the validity of these values for this problem is, as noted, not at all clear. In particular for the energy loss process (a), rbe = 5 is used for meson energies below 100 Mev and, rbe = 2 for penetrating mesons (refer to Fig. 1). For process (b) rbe = 1 is used, and for processes (c), (d), (e) and (f) a nominal rbe value of 10 is used. Progress (g) is assigned an rbe of 20, the usual value for particles above mass four. From these values, the rem for each particle at each energy can be evaluated and these are plotted in Fig. 3. Also shown, for comparison, is the equivalent value for neutrons.[1]

Discussion

The extremely flat characteristic of the low energy π^- dose curve is the most significant feature of Fig. 3, and it indicates that the proton, neutron, and heavy particle fragments are of particular hazard following the capture of a π^- meson. The hazard may be worse than shown, in that all of these star fragments are very localized (in a more microscopic sense than that used by Schaefer) and a monoenergetic negative pion beam could produce a very serious internal radiation burn. With respect to space applications Metropolis, et. al show that protons near an energy of 700 Mev produce about 10 neutrons per inelastic collision, compared to about 0.5 of a negative pion.[6] Because the data of Fig. 3 suggests that the negative pions are each about 10 times more dangerous to a human than are neutrons, the negative pion flux behind a thin shield may be of the order of 30 to 50 per cent as dangerous as are the neutrons. Neither will be as serious as are the penetrating protons, but the π^- secondaries from inelastic processes should not be neglected, because of the extremely localized nature of the biological damage.

1. Internal Report Y-6 A Progress Report On The Design Of A Very High Intensity Linear Accelerator For Protons At An Energy Of 750 Mev. Yale University October 30, 1962.

2. W. A. Gibson, Energy Removed from Primary Proton and Neutron Beams by Tissue, ORNL 61-6-48 p. 5 (1961).

3. Table adapted from R. E. Marshak Meson Physics Chap. 5, p. 178, McGraw Hill, New York (1952).

4. H. K. Ticho, Phys. Rev. 74, 1337, (1948).

5. G. Van der haeghe and M. Demeur, Nuovo Cim 4 (Series 10), 931 (1956 Suppl.).

6. N. Metropolis, R. Bivins, M. Storm, J. M. Miller, G. Friedlander and Anthony Turkevitch, Phys. Rev. 110, 204, (1958).

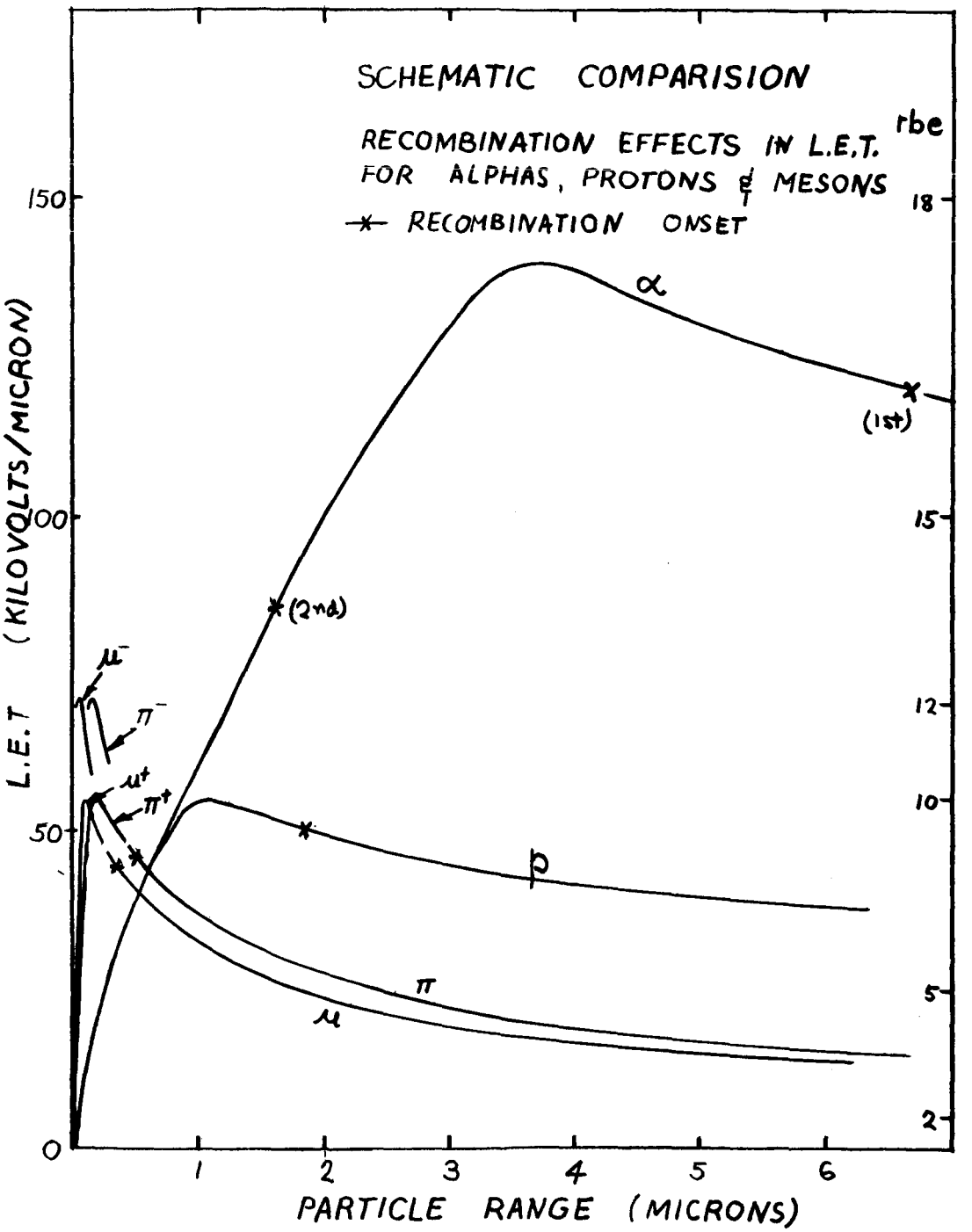
SCHEMATIC COMPARISION
RECOMBINATION EFFECTS IN L.E.T.
FOR ALPHAS, PROTONS & MESONS
RECOMBINATION ONSET
rbe
L.E.T (KILOVOLTS/MICRON)
150
100
50
0
18
15
12
10
5
2
α
(1st)
(2nd)
μ⁻
π⁻
μ⁺
π⁺
p
π
μ
1
2
3
4
5
6
PARTICLE RANGE (MICRONS)

FIG. 1

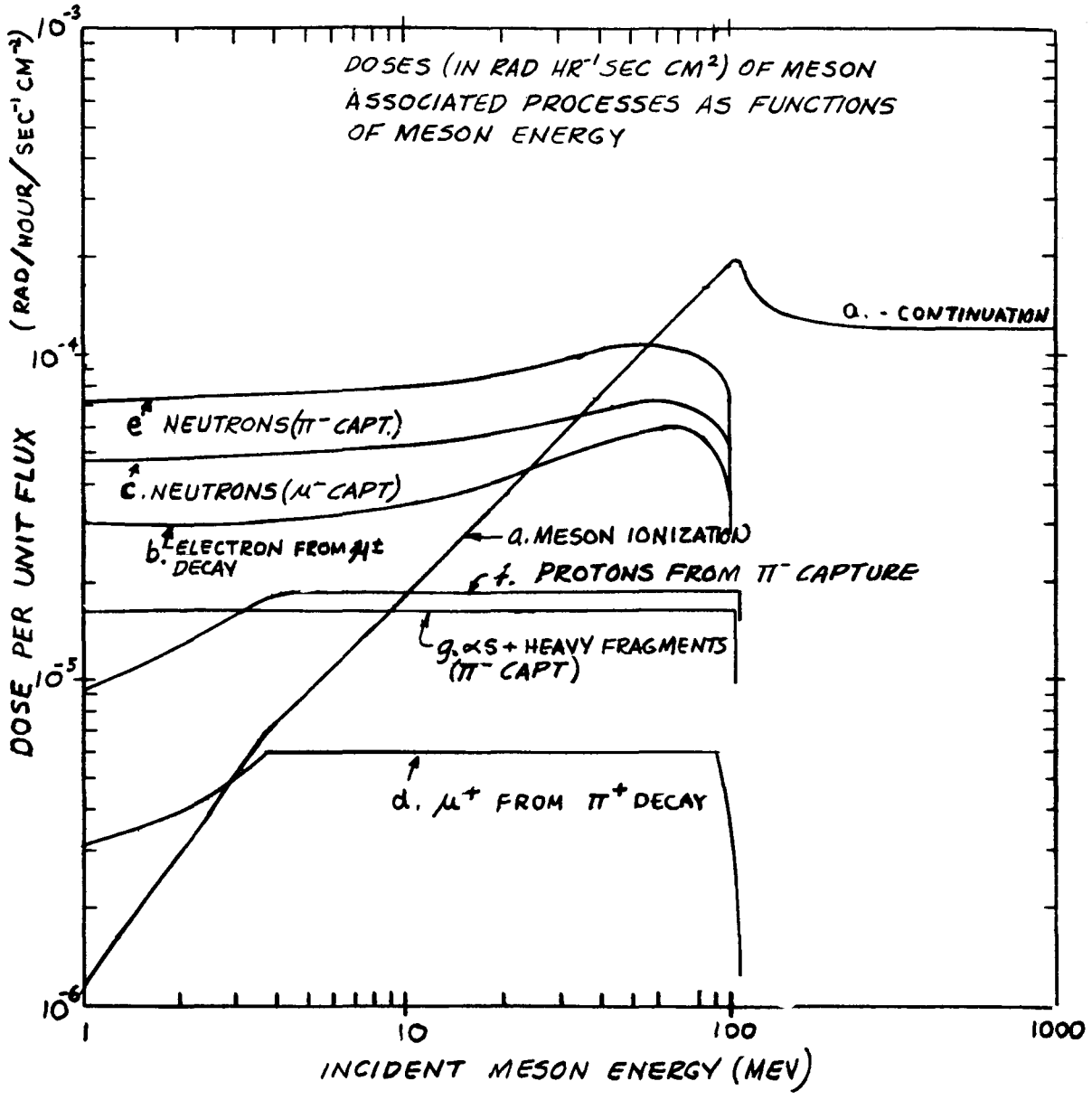
DOSES (IN RAD HR⁻¹ SEC CM²) OF MESON ASSOCIATED PROCESSES AS FUNCTIONS OF MESON ENERGY
DOSE PER UNIT FLUX (RAD/HOUR/SEC⁻¹ CM⁻²)
10⁻³
10⁻⁴
10⁻⁵
10⁻⁶
a. - CONTINUATION
e. NEUTRONS (π⁻ CAPT.)
c. NEUTRONS (μ⁻ CAPT)
b. ELECTRON FROM μ± DECAY
a. MESON IONIZATION
f. PROTONS FROM π⁻ CAPTURE
g. ∝S + HEAVY FRAGMENTS (π⁻ CAPT)
d. μ⁺ FROM π⁺ DECAY
1
10
100
1000
INCIDENT MESON ENERGY (MEV)

FIG. 2

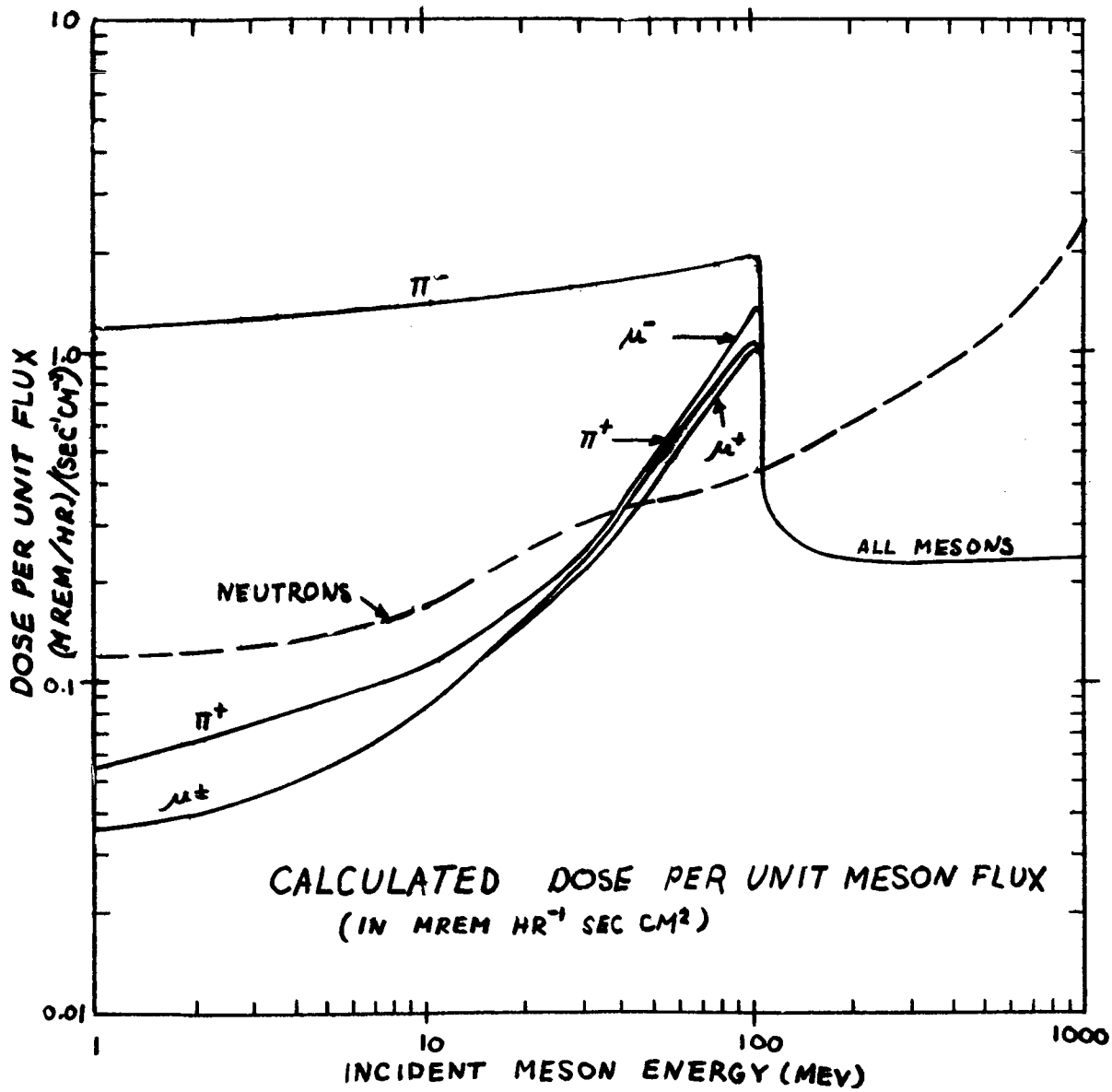
10
1.0
0.1
0.01
DOSE PER UNIT FLUX
(MREM/HR)/(SEC⁻¹CM⁻²)
π⁻
μ⁻
π⁺
μ⁺
ALL MESONS
NEUTRONS
π⁺
μ±
CALCULATED DOSE PER UNIT MESON FLUX
(IN MREM HR⁻¹ SEC CM²)
1
10
100
1000
INCIDENT MESON ENERGY (MEV)

FIG. 3.